➢ НАУЧНОМ ВЕЋУ

ИНСТИТУТА ЗА ФИЗИКУ У БЕОГРАДУ


*Београд, 7. 7. 2017.*

---

**ПРЕДМЕТ: Молба за покретање поступка за стицање звања научни сарадник**

---

Поштовани,

Молим Научно веће Института за физику у Београду да покрене поступак за мој избор у звање научног сарадника, пошто испуњавам услове које је прописало Министарство просвете, науке и технолошког развоја за стицање овог звања.


Прилажем следећу документацију:

1. Мишљење руководиоца пројекта с предлогом чланова комисије за избор у звање;
2. Стручну биографију;
3. Преглед научне активности;
4. Елементе за квалитативну анализу;
5. Елементе за квантитативну анализу;
6. Списак објављених радова разврстан по категоријама;
7. Извод из матичне књиге рођених с белешком о промени презимена;
8. Решење о нострификацији, докторску диплому и превод дипломе на енглески и српски језик;
9. Доказе за наводе под тачкама 2 и 4;
10. Податке о цитираности према Web of Science;
11. Копије објављених радова и докторску дисертацију.


Срдачно,

*Дуња Поповић*

Др Дуња Поповић (презиме: Stoltz од 2007. до 2015. године)

*професор струковних студија*

Висока техничко-технолошка школа струковних студија

Косанчићева 36, 37000 Крушевац

## Научном већу Института за физику у Београду

Београд, 7. јул 2017. године

**Предмет:**     **Мишљење о избору др Дуње Поповић у звање научни сарадник са предлогом комисије**

Др Дуња Поповић (ex. Столц) је запослена као професор струковних студија у Високој техничко-технолошкој школи струковних студија у Крушевцу. Докторирала је 2005. године на Универзитету Сарске области у Немачкој, а након тога је била постдокторски истраживач на Универзитету у Карлстаду и Краљевском техничком институту (КТН) у Шведској, као и у Камерлинг Онес лабораторији Универзитета у Лајдену у Холандији. С обзиром да испуњава све предвиђене услове у складу са Правилником о поступку, начину вредновања и квантитативном исказивању научноистраживачких резултата истраживача МПНТР, предлажем покретање поступка за избор др Дуње Поповић у звање научни сарадник.

За састав комисије за избор др Дуње Попвић у звање научни сарадник предлажем:

(1) др Ненад Лазаревић, виши научни сарадник, Институт за физику у Београду
(2) академик Зоран Поповић, научни саветник, Институт за физику у Београду
(3) др Антун Балаж, научни саветник, Институт за физику у Београду
(4) др Саша Дмитровић, доцент Физичког факултета Универзитета у Београду

Руководилац пројекта ОН171017

др Антун Ђалаж
научни саветник

# Стручна биографија

Дуња Поповић је рођена 27. 3. 1977. године у Београду.

Дипломирала је 1999. године на Физичком факултету Универзитета у Београду, студијска група теоријска физика, са просечном оценом 9.61 и дипломским радом *Анализа генеричког модела стохастичке резонанце* (ментор: проф. др Сава Милошевић). Током студија је била стипендиста Републичке фондације Србије и САНУ. На Приматијади 1996. године у Лепенском Виру рад *Хаотично кретање побуђеног клатна* који је представила, проглашен је за најбољи истраживачки рад.

Дипломски рад из експерименталне физике урадила је на Универзитету у Фрибургу (Universität Freiburg, Université de Fribourg) у Швајцарској 2000. године на тему *Oxidation of Quasicrystal Surfaces* (ментор: Dr Dušanka Naumović, Dr Philipp Aebi, Prof. dr Louis Schlapbach) са оценом 5.5 (највиша оцена 6). Учествовала је у сарадњи са швајцарским синхротроном SLS.

Докторирала је 2005. године на Универзитету Сарске области (Universität des Saarlandes) у Немачкој с дисертацијом *Quasiparticle band dispersion in the vicinity of the Fermi surface in quasi-two dimensional systems* (ментор: Prof. Dr. rer. nat. Dr. h. c. mult. Stefan Hüfner) и оценом врло добар (magna cum laude) и стекла звање *doctor rerum naturalium* (доктор природних наука). Током израде доктората била је ангажована као асистент у настави за лабораторијске вежбе и члан Међународне групе за тренинг истраживача GRK 532 – Физичке методе испитивања структуре нових материјала (приложено уверење). Дисертација је објављена 2009. године у издању VDM Verlag Dr. Müller, Saarbrücken под насловом *Quasiparticle band dispersion in quasi-two dimensional systems – in the vicinity of the Fermi surface*. Докторат је признат Решењем Министарства просвете, науке и технолошког развоја број: 612-01-01541/2015-06 од 27. 01. 2016. године као диплома докторских академских студија трећег степена високог образовања у оквиру области интердисциплинарних, мултидисциплинарних и трансдисциплинарних студија, ради запошљавања.

Као истраживач Дуња Поповић је била ангажована годину дана на Универзитету у Карлстаду (Karltads Universitet) у Шведској код Prof. dr Lars Johansson са стипендијом универзитета, годину дана на Краљевском техничком институту (Kungliga Tekniska högskolan – KTH, Royal Institute of Technology) у Стокхолму у Шведској код Prof. dr Mats Göthelid, Prof. dr Ulf Karlsson са стипендијом Göran Gustafsson и две године у Камерлинг Онес Лабораторији у Лајдену (Universiteit Leiden) у Холандији код Prof. dr Joost W. Frenken. У Шведској је поред ангажовања на универзитету била и корисник Max-Lab синхротрона, а током рада у Холандији корисник синхротрона ESRF. У Холандији је руководила реализацијом Reactor-STM пројекта у оквиру Real-Nano конзорцијума између водећих холандских универзитета и индустрије са циљем развоја инструмента за испитивање катализатора под индустријским условима. У оквиру овог ангажовања завршила је Пројект-менаџмент курс и сарађивала са компанијом Albemarle.

Од 2009. до 2013. је запослена као forskare-assistent (assistent professor, односно доцент у Србији) на Краљевском техничком институту у Стокхолму, Шведска, у групи Prof. dr Ulf Karlsson. Ангажована је као предавач, истраживач и корисник Max-Lab синхротрона, по сопственом пројекту који је одобрио Шведски научни савет (Vetenskapsrådet). Као доцент је похађала курсеве за истраживачко менторство организован за предаваче у Стокхолму. Године 2010. добила је награду шведске фондације Göran Gustafsson за младе истраживаче.

Од 2016. године ради на Високој техничко-технолошкој школи струковних студија у Крушевцу као професор струковних студија за ужу област физика. Аутор је два уџбеника у издању Школе, *Климатске промене* и *Микроелектроника и наноелектроника*.

Објавила је укупно 23 рецензирана рада, који су цитирани 312 пута, односно 296 пута без сопствених цитата. Хиршов индекс јој је 7. Била је учесник више међународних конференција и радионица, а завршила је и двомесечну радионицу HERCULES (Higher European Course for Users of Large Experimental Systems), реализован у Греноблу и Паризу, у Француској, где је награђена за најбољи постер. Одржала је један позвани семинар на ETH у Цириху 2002. године. Има радно искуство на синхротронима SLS (Swiss Light Source) у Швајцарској, ESRF (European Synchrotron Radiation Facility) и Soleil у Француској и Max-Lab у Шведској. Сарађивала је са истраживачким групама које се баве теоријом, компјутерским моделовањем, експериментом и припремом узорака.

# Преглед научних активности

Научно-истраживачки рад др Дуње Поповић представља комбиноване примене две савремене експерименталне технике – угаоно разложене фотолектронске спектроскопије (angle-resolved photoelectron spectroscopy, ARPES) и скенирајуће тунелујуће микроскопије (scanning tunnelling microscopy, STM) у испитивању начина на које структурне промене доводе до модификација електронске структуре површина, са импликацијама на нивоу од фундаменталног разумевања физичких процеса до њихове индустријске примене.

## Дихалогениди прелазних метала

Високотемпературна суперпроводност је пре петнаест година било веома актуелно поље истраживања и разматрање појаве псеудопроцепа на Ферми површи као прекурзора суперпроводног стања код једињења бизмута инспирисало је студије на једноставнијим слојевитим системима, попут дихалогенида прелазних метала. Студирајући својства 1Т-фамилије: $TaSe_2$, $TaS_2$, $TiSe_2$, установљено је да се равне површине могу добити уклањањем површинског слоја у ултрависоком вакууму и да се оне формирају увек између две металне равни. [D3] Псеудопроцеп који се код ових материјала формира у близини Ферми површи доводи се у везу са таласима густине наелектрисања, који су последица атомских реконструкција површи. [A1] Формирање три групе еквивалентних атома под дејством таласа густине наелектрисања на површини која је претходно имала хексагоналну симетрију, доводи до цепања зона на три субзоне, које се региструју фотоелектронском спектроскопијом и виде у DFT прорачунима (wien2k кôд) зонске дисперзије. [A1] Притом субзоне имају периодичност одређену атомском реконструкцијом, али спектрални интензитет остаје изражен дуж нереконструисане зонске структуре. [A1] Да је електронска структура у директној спрези са атомском потврђује скенирајућа тунелујућа микроскопија, где се подешавањем напона тунеловања може тунеловати у појединачне субзоне и скенирањем с тим напоном видети само они атоми који учествују у формирању дате субзоне. [B8, D5]

[A1] Bovet, M., Popović, D., Clerc, F., Koitzsch, C., Probst, U., Bucher, E., Berger, H., Naumović, D., and Aebi, P. (2004). Psudogapped Fermi surfaces of 1T-TaS$_2$ and 1T-TaSe$_2$: A charge density wave effect, *Phys. Rev. B 69*, 125117.

[B8] Stoltz, D., Bielmann, M., Bovet, M., Schlapbach, L., Berger, H. (2007). Tunneling evidence for spatial location of the charge-density-wave induced band splitting in 1T-TaS$e_2$, *Phys. Rev. B, 76*, 073410.

[D3] Stoltz, D., Stoltz, S. E. (2007). X-ray photoelectron diffraction investigation of the cleavage plane in 1T-transition metal dichalcogenides, *Physica B, 398*, 172.

[D5] Stoltz, D., Bielmann, M., Schlapbach, L., Bovet, M., Berger, H., Göthelid, M., Stoltz, S. E., Starnberg, H. I. (2008). Atomic origin of the scanning tunneling microscopy images of charge-density-waves on 1T-TaSe$_2$, *Physica B, 403*, 2207.

## Површинска стања

Код површина или танких филмова племенитих метала као што су сребро и злато у *L*-процепу пројектоване зонске структуре јављају се површинска стања као последица електронске локализације. Површинска стања се карактеришу комплексним таласним бројем, па експоненцијално опада њихов интензитет ка унутрашњости материјала, а одсечен је и ван њега, дајући просторну локализацију. То даје могућност модификовања оваквих стања променама атомске структуре површине. Док раст Ag на Au(111) површини при ниским температурама даје неуређен филм, на собној температури настаје раст слој-по-слој и детектују се дискретни помераји енергије минимума дисперзије зоне са повећањем броја моноатомских слојева, да би се при 10 моноатомских слојева појавило површинско стање и валентна зона сребра, упоредо са стањима квантне јаме филма сребра у пројектованом *sp*-процепу злата, у складу са прорачуном који је дала DFT (wien2k код). [B3] Линијом Ar I измерено је смањење спин-орбит цепања површинског стања злата са повећањем дебљине филма сребра. [B3, A2]

[A2] Cercellier, H., Fagot-Revurat, Y., Kierren, B., Reinert, F., <u>Popović, D.</u>, and Malterre, D. (2004). Spin-orbit splitting of the Shockley state in the Ag/Au(111) interface, *Phys. Rev. B 70*, 193412.

[B3] <u>Popović, D.</u>, Reinert, F., Huefner, S., Grigoryan, V. G., Springborg, M., Cercellier, H., Fagot-Revurat, Y., Kierren, B. and Malterre, D. (2005). High-resolution photoemission on Ag/Au(111): Spin-orbit splitting and electronic localization of the surface state, *Phys. Rev. B, 72*, 045419.

Квантне јаме, површинска стања, интерфејс стања и површинске резонанце су даље посматране на систему који је релевантан за примене – злату на полупроводничкој површини 4H-SiC(0001), код кога се може добити широк спектар различитих реконструкција у зависности од услова припреме површине, а самим тим и веома различита електронска стања. [B5, B6, D4]

[B5] <u>Stoltz, D.</u>, Stoltz, S. E., Johansson, L. S. O. (2007). Surface resonance on the (6√3x6√3)- R30º-reconstructed 5 ML Au on (√3x√3)-R30 º-4H-SiC(0001), *Surf. Sci., 601*, 2508.

[B6] <u>Stoltz, D.</u>, Stoltz, S. E. and Johansson, L. S. O. (2007). A high-resolution core-level photoemission study of the Au/4H-SiC(0001)-(√3x√3) interface, *J. Phys.: Condens. Matter 19*, 266006.

[D4] <u>Stoltz, D.</u>, Stoltz, S. E., Johansson, L. S. O. (2008). Two-dimensional states in the electronic structure of Au/(√3x√3)-R30º-4H-SiC(0001), *J. of Elec. Spec. and Rel. Phen. 163*, 1.

## Структурна анализа фотоелектронском дифракцијом

Електронска својства материјала могу се модификовати допирањем. Фотоелектронском дифракцијом X-зрацима (XPD) на линијама карактеристичним за одређени хемијски елемент може се идентификовати његово атомско окружење, а на основу упоређивања се дифрактограмима свих других елемената у недопираном материјалу закључити чије место ови атоми заузимају, што је демонстрирано на примеру допирања Bi2212 елементима Pb и Dy. [D1] У комбинацији са прорачунима који узимају у обзир једноструко (SSC) или вишеструко расејање (MSCD) фотоелектронска дифракција (PED) може дати информацију о површинској равни у случају припреме површине у ултрависоком вакууму код слојевитих дихалогенида прелазних метала [D3] и бити од помоћи при одређивању атомске структуре

површинске реконструкције силицијум карбида, где је од посебне користи хемијска осетљивост фотоелектронске технике [D2].

[D1] Popović, D., Bovet, M., Berger, H., and Aebi P. (2005). Fingerprinting substitution sites in Pb,Dy-$Bi_2Sr_2Ca_1Cu_2O_{8+\delta}$ using X-ray Photoelectron Diffraction, *Eur. Phys. J. Appl. Phys. 30*, 171-174.

[D2] Stoltz, D., Stoltz, S. E., Widstrand, S. M., Johansson, L. S. O. (2007). Investigation of surface structure related features in the multiple-scattering simulations of photoelectron diffraction of 3C-SiC(001)-c(4x2), *Physica B, 395*, 130.

[D3] Stoltz, D., Stoltz, S. E. (2007). X-ray photoelectron diffraction investigation of the cleavage plane in 1T-transition metal dichalcogenides, *Physica B, 398*, 172.

## Складиштење водоника

Потенцијал Mg за складиштење водоника је испитиван због веома повољног односа масе магнезијум хидрида и апорпционог капацитета Mg. Танки филмови Mg на површини Мo(110) апсорбују водоник дуж интерфејса, али филмови Mg-Ni задржавају формирани хидрид на површини [B4], а апсорпција и термална десорпција водоника се могу понављати без нарушавања структуре материјала [B7].

[B4] Stoltz, S. E., Popović, D. (2007). A high-resolution core-level study of Ni-catalyzed absorption and desorption of hydrogen in Mg films, *Surf. Sci., 601*, 1507.

[B7] Stoltz, S. E. and Stoltz, D. (2007). Spectroscopic evidence for reversible hydrogen storage in unordered $Mg_5Ni_1$ thin films, *J. of Phys.: Cond. Matter, 19*, 446010.

## Катализа под индустријским условима

*ReactorSTM* је скенирајући тунелујући микроскоп оперативан у условима високих температура (до 600 K) и високих притисака (до 6 bar) у чијем дизајнирању и конструисању сам учествовала у групи Prof. dr Joost W. Frenken. [C2] Намењен је проучавању хемијских процеса на површинама троструких катализатора изложених протоку гасова. Сматра се *operando* инструментом јер функционише са варијабилним протоком гасова кроз простор веома мале запремине између површине катализатора и врха игле скенера и може мерити с атомском резолуцијом и великим бројем фрејмова у секунди у реалном времену. Упркос томе што се локално посматрају услови високог притиска и температуре, све је смештено у систем са ултрависоким вакуумом који је вибрационо изолован, што представља велики технички изазов. У хетерогеној катализи су степеници места повишене каталитичке активности, чија густина одређује стабилност оксида на површини и руководи осцилацијама константе реакције оксидације угљен-моноксида на површини паладијума при атмосферском притиску. [A4]

[A4] Hendriksen, B. L. M., Ackermann, M. D., van Rijn, R., Stoltz, D., Popa, I., Balmes, O., Resta, A., Wermeille, D., Felici, R., Ferrer, S., Frenken, J. W. M. (2010). The role of steps in surface catalysis and reaction oscillations, *Nature Chemistry, 2*, 730-734.

[C2] Herbschleb, C. T., van der Tuijn, P. C., Roobol, S. B., Navarro, V., Bakker, J. W., Liu, Q., Stoltz, D. Canas-Ventura, M. E., Verdoes, G., van Spronsen, M. A., Bergman, M., Crama, L., Taminiau, I., Ofitserov, A., van Baarle, G. J. C., and Frenken, J. W. M. (2014). The ReactorSTM: Atomically resolved scanning tunneling microscopy under high-pressure, high-temperature catalytic reaction conditions, *Rev. Sci. Instr. 85*, 083703.

**Оксидација и корозија површина**

Како у катализи, тако и у техници и екологији, испитивање оксидације и корозије материјала игра велику улогу.

За квазикристале је откривено да имају повољнија својства за пресвлачење тигања од тефлона, што је подстакло изучавање њиховог понашања при оксидацији. Површина Al-Pd-Mn показује од свих елемената најинтензивнију оксидацију Mn, као и интензивнију оксидацију Al у квазикристалу него у Al(111), са достизањем сатурације испод 50 L кисеоника. [B1]

[B1] Popović, D., Naumovic, D., Bovet, M., Koitzsch, C., Schlapbach, L., Aebi, P. (2001). Oxidation of Al-Pd-Mn quasicrystal surfaces, *Surf. Sci. 492/3*, 294.

Корозија оксида прелазних метала је изучавана систематски на оксидима гвожђа, цинка и бакра. У случају оксида гвожђа, апсорбовани сумпор-диоксид и вода интерагују са гвожђем из супстрата и формирају гвожђе-сулфат који прати реконструкцију чисте површине [B9], тако да је чак STM-ом могуће видети његову атомску структуру [A3]. На начин апсорпције воде и сумпор-диоксида не утиче само моноатомски слој на површини, о чему сведоче разлике које се јављају код површине Zn(0001) и Zn-терминисане површине ZnO(0001). [C1] Апсорпција воде може потпуно променити структуру Zn-терминисане ZnO(0001) површине формирањем троугаоних структура при нижим дозама воде или потпуном урушавању правилне структуре при дозама преко 20 L. [A5] Дефекти на површини, попут шупљина бакра код $Cu_2O$(111), окружени су јонима кисеоника са незасићеним везама, који су центри за апсорпцију производа хемијских реакција воде и сумпор-диоксида на површини. [A6] Променом температуре може се постићи да на површини $Cu_2O$(111) буде апсорбована само молекуларна или молекуларна и дисосована вода, односно да се сумпор-диоксид на њој задржи у форми $SO_3$ или $SO_4$. [A6]

[A3] Stoltz, D., Önsten, A., Karlsson, U. O. and Göthelid, M. (2007). High resolution spectroscopic and microscopic signatures of ordered growth of ferrous sulfate in $SO_2$ assisted corrosion of $Fe_3O_4$(100), *Appl. Phys. Lett., 91*, 093107.

[A5] Önsten, A., Stoltz, D., Palmgren, P., Yu, S., Göthelid, M. and Karlsson, U. O. (2010). Water Adsorption on ZnO(0001): Transition from Triangular Surface Structures to a Disordered Hydroxyl Terminated phase, *J. Phys. Chem. C, 114*, 11157.

[A6] Önsten, A., Weissenrieder, J., Stoltz, D., Yu, S., Göthelid, M. and Karlsson, U. O. (2013). Role of Defects in Surface Chemistry on $Cu_2O$(111), *J. Phys. Chem. C. 117*, 19357.

[B9] Stoltz, D., Önsten, A., Karlsson, U. O., and Göthelid, M. (2008). Scanning tunneling microscopy of Fe- and O-sublattices on $Fe_3O_4$(100), *Ultramicroscopy, 108*, 540.

[C1] Önsten, A., Stoltz, D., Palmgren, P., Yu S., Claesson, T., Göthelid, M. and Karlsson, U. O. (2013). $SO_2$ interaction with Zn(0001) and ZnO(0001) and the influence of water, *Surf.Sci. 608*, 31.

# Елементи за квалитативну анализу рада

## 1. Квалитет научних резултата

Научни ниво и значај резултата
Кандидаткиња има 6 радова категорије М21а (међународни часопис изузетне вредности), 10 радова категорије М21 (врхунски међународни часопис), 2 рада категорије М22 (истакнути међународни часопис) и 5 радова категорије М23 (међународни часопис) .

Утицајност
Најцитиранији рад кандидаткиње има 89 цитата.

Цитираност
Према Web of Science радови кандидаткиње су укупно цитирани 312 пута (296 пута без сопствених цитата). Хиршов индекс кандидаткиње је 7.

Параметри квалитета часописа
- Једна публикација у часопису *Nature Chemistry* (2010), ИФ=17.927
- Две публикације у часопису *Journal of Physical Chemistry C*, ИФ=4.524, 4.805
- Једна публикација у часопису *Applied Physics Letters*, ИФ=4.127
- Једна публикација у часопису *Journal of Chemical Physics*, ИФ=3.333
- Четири публикације у часопису *Physical Review B*, ИФ=3.185-3.327
- Једна публикација у часопису *Ultramicroscopy*, ИФ=2.629
- Две публикације у часопису *Journal of Physics: Condensed Matter*, ИФ=2.145
- Четири публикације у часопису *Surface Science*, ИФ=1.880-2.385
- Једна публикација у часопису *Review of Scientific Instruments*, ИФ=1.614
- Једна публикација у часопису *Journal of Electron Spectroscopy and Related Phenomena*, ИФ=1.290
- Једна публикација у часопису *Surface Review and Letters*, ИФ=0.886
- Три публикације у часопису *Physica B*, ИФ=0.872
- Једна публикација у часопису *European Physics Journal: Applied Physics*, ИФ=0.745

Укупни ИФ свих публикација кандидаткиње је 69.949.

Степен самосталности и степен учешћа аутора у реализацији резултата
Од укупно 23 рада, кандидаткиња је први аутор 12 публикација, што је подразумевало самостално постављање и извођење експеримената, обраду и интерпретацију резултата и писање публикације. Кандидаткиња је други аутор 5 публикација и у трећи аутор у једној публикацији, што је подразумевало учешће или консултовање око извођења експеримената, заједничку анализу и интерпретацију

резултата са првим аутором. Улога у осталим публикацијама је негде консултативна при анализи резултата, а негде водећа и самостална улога у реализацији једног дела пројекта.

Награде
Кандидаткиња је добитник награде шведске фондације Göran Gustafsson за младе истраживаче 2010. године.

Број аутора
Укупно 9 публикација кандидаткиње реализовано је у оквиру једне експерименталне групе, 12 публикација представља колаборацију две групе са различитих установа, 1 публикација садржи резултате рада 3 групе (2 експерименталне и 1 теоријска) и у изради 1 публикације су учествовали аутори са 5 различитих установа. (Ово су реални бројеви установа, који су мањи од бројева који се појављују на публикацијама, а који узимају у обзир да је неко променио установу од тренутка мерења до тренутка објављивања резултата.)

Примењивост научних резултата
Експериментални систем *ReactorSTM* представљен у публикацији у *Review of Scientific Instruments* сада је комерцијални производ који продаје холандска фирма Leiden Probe Microscopy.

## 2. Ангажованост у формирању научних кадрова

Кандидаткиња је током докторских студија радила као асистент за лабораторијске вежбе у Немачкој и Швајцарској (2000-2005), а током четири године била је предавач курса Наука о површинама (Surface science) на КТН у Шведској (2009-2013).

## 3. Нормирање броја коауторских радова

Сви радови су експериментални, осим рада [D2] који је нумеричка симулација, али има мање од 5 аутора, па није потребно да му се број бодова нормира. Нормирање је извршено код 2 рада категорије М21а, 2 рада категорије М21, 1 рада категорије М22 и 1 рада категорије М23, чиме је укупан збир М бодова смањен са 171 на 154.69, тј. за 16.31, што не мења значајно резултате.

## 4. Руковођење пројектима, потпројектима и пројектним задацима

Кандидаткиња је руководила реализацијом *ReactorSTM* пројекта на Универзитету у Лајдену у Холандији у оквиру Nimic (Nano-imaging in realistic conditions) - Real-Nano конзорцијума између академије и индустрије. (Доказ: евалуациони лист после прве године ангажовања.) То је подразумевало координацију рада механичке радионице, електричне радионице, докторанда и дипломанда; управљање буџетом од милион

евра; израду временског плана реализације и праћење реализације пројекта; размену са партнерима у индустрији и сарадњу са снабдевачима.

Кандидаткиња је написала предлог пројекта који је усвојио Шведски научни савет и на основу кога је ангажована као доцент на четири године на КТН у Шведској. О самосталном писању пројекта и развоју у самостаног истраживача сведочи доказ из претходне тачке у коме се то помиње, као и приложени уговори о раду у Шведској у којима се наводи да је финансирање пројекта изнео Шведски научни савет.

## 5. Утицај научних резултата

Публикације кандидаткиње цитирани су 312 пута (296 пута без сопствених цитата), а чак 6 публикација објављено је у међународним часописима изузетних вредности. Најцитиранија публикација је цитирана 89 пута. Хиршов индекс кандидаткиње је 7.

## 6. Конкретни научни допринос кандидата у реализацији резултата у научним центрима у земљи и иностранству

Кандидаткиња је све резултате остварила у иностранству. Радила је на пет различитих Универзитета у Швајцарској, Немачкој, Холандији и Шведској. Рад на докторској дисертацији подразумевао је самосталност у експерименталном раду, обради и интерпретацији резултата и укључио је сарадњу са теоретичарима са истог Универзитета, који су радили нумеричке прорачуне за вршена експериментална мерења. Један део резултата урађен је у колаборацији са групом из Нансија у Француској, о чему сведоче заједничке публикације. Кандидаткиња је током прве постдок позиције реализовала нову поставку у синхротронској лабораторији Max-Lab у Шведској, а о том и даљим ангажовањима на овом синхротрону сведоче годишњи извештаји ове установе. Сарађивала је на студији о складиштењу водоника која је у потпуности изведена у овој лабораторији са још једном постдоком (S. Stoltz). Од тада је иницијатор и реализатор истраживања силицијум карбида и танких филмова злата на њему. У оквиру постдокторског ангажовања на КТН кандидаткиња је узела учешће у дугорочном истраживању корозије прелазних метала под утицајем воде и сумпор-диоксида у коме је учествовала и једна докторанткиња (A. Önsten), а које ће се продужити и на период у току кога је кандидаткиња радила као доцент на истој установи. У оквиру постдокторског ангажовања у Холандији допринела је развоју сложеног инструмента представљеног у публикацији у часопису *Review of Scientific Instruments* који је постао комерцијални производ који до данас продаје компанија Leiden Probe Microscopy. Кандидаткиња је на свим радним местима учествовала у промотивним активностима и данима отворених врата. За пројекат са којим је добила позицију доцента, кандидаткиња је добила Göran Gustafsson награду за младе истраживаче у Шведској.

# Елементи за квантитативну анализу рада

Кандидаткиња је објавила укупно 23 рада који су разврстани по категоријама као што је приказано у табели испод.

| КАТЕГОРИЈА | БРОЈ РАДОВА | М БОДОВА ПО РАДУ | УКУПНО М БОДОВА | НОРМИРАНИ БРОЈ М БОДОВА |
|---|---|---|---|---|
| M21a | 6 | 10 | 60 | 52.69 |
| M21 | 10 | 8 | 80 | 74.71 |
| M22 | 2 | 5 | 10 | 6.79 |
| M23 | 5 | 3 | 15 | 14.5 |
| M70 | 1 | 6 | 6 | 6 |

Поређење са минималним квантитативним резултатима потребним за избор у звање научни сарадник приказано је у табели испод.

| КАТЕГОРИЈА | МИНИМАЛНИ БРОЈ М БОДОВА | НОРМИРАНИ БРОЈ М БОДОВА КАНДИДАТА |
|---|---|---|
| УКУПНО | 16 | 154.69 |
| M10+M20+M31+M32+M33+M41+M42 | 10 | 154.69 |
| M11+M12+M21+M22+M23 | 6 | 154.69 |

# Списак објављених радова по категоријама

## Радови у међународним часописима изузетних вредности (М21а)

[A1]

Bovet, M., <u>Popović, D.</u>, Clerc, F., Koitzsch, C., Probst, U., Bucher, E., Berger, H., Naumović, D., and Aebi, P. (2004). Psudogapped Fermi surfaces of 1T-TaS$_2$ and 1T-TaSe$_2$: A charge density wave effect, *Phys. Rev. B 69*, 125117. (цитиран 28 пута)

[A2]

Cercellier, H., Fagot-Revurat, Y., Kierren, B., Reinert, F., <u>Popović, D.</u>, and Malterre, D. (2004). Spin-orbit splitting of the Shockley state in the Ag/Au(111) interface, *Phys. Rev. B 70*, 193412. (цитиран 42 пута)

[A3]

<u>Stoltz, D.</u>, Önsten, A., Karlsson, U. O. and Göthelid, M. (2007). High resolution spectroscopic and microscopic signatures of ordered growth of ferrous sulfate in SO$_2$ assisted corrosion of Fe$_3$O$_4$(100), *Appl. Phys. Lett., 91*, 093107. (цитиран 4 пута)

[A4]

Hendriksen, B. L. M., Ackermann, M. D., van Rijn, R., <u>Stoltz, D.</u>, Popa, I, Balmes, O., Resta, A., Wermeille, D., Felici, R., Ferrer, S., Frenken, J. W. M. (2010). The role of steps in surface catalysis and reaction oscillations, *Nature Chemistry, 2*, 730-734. (цитиран 89 пута)

[A5]

Önsten, A., <u>Stoltz, D.</u>, Palmgren, P., Yu, S., Göthelid, M. and Karlsson, U. O. (2010). Water Adsorption on ZnO(0001): Transition from Triangular Surface Structures to a Disordered Hydroxyl Terminated phase, *J. Phys. Chem. C, 114*, 11157. (цитиран 34 пута)

[A6]

Önsten, A., Weissenrieder, J., <u>Stoltz, D.</u>, Yu, S., Göthelid, M. and Karlsson, U. O. (2013). Role of Defects in Surface Chemistry on Cu$_2$O(111), *J. Phys. Chem. C. 117*, 19357. (цитиран 7 пута)

## Радови у врхунским међународним часописима (М21)

[B1]

<u>Popović, D.</u>, Naumovic, D., Bovet, M., Koitzsch, C., Schlapbach, L., Aebi, P. (2001). Oxidation of Al-Pd-Mn quasicrystal surfaces, *Surf. Sci. 492/3*, 294. (цитиран 17 пута)

[B2]

Hayoz, J., Koitzsch, C., Popović, D., Bovet, M., Naumović, D. and Aebi, P. (2002). Angle-scanned photoemission on $YbH_x$: Relevance for switchable mirrors, *Surf. Rev. Lett. 9 (1)*, 235. (цитиран 2 пута)

[B3]

Popović, D., Reinert, F., Huefner, S., Grigoryan, V. G., Springborg, M., Cercellier, H., Fagot-Revurat, Y., Kierren, B. and Malterre, D. (2005). High-resolution photoemission on Ag/Au(111): Spin-orbit splitting and electronic localization of the surface state, *Phys. Rev. B, 72*, 045419. (цитиран 28 пута)

[B4]

Stoltz, S. E., Popović, D. (2007). A high-resolution core-level study of Ni-catalyzed absorption and desorption of hydrogen in Mg films, *Surf. Sci., 601*, 1507. (цитиран 7 пута)

[B5]

Stoltz, D., Stoltz, S. E., Johansson, L. S. O. (2007). Surface resonance on the $(6\sqrt{3}x6\sqrt{3})$- R30º-reconstructed 5 ML Au on $(\sqrt{3}x\sqrt{3})$-R30 º-4H-SiC(0001), *Surf. Sci., 601*, 2508. (цитиран 1 пут)

[B6]

Stoltz, D., Stoltz, S. E. and Johansson, L. S. O. (2007). A high-resolution core-level photoemission study of the Au/4H-SiC(0001)-$(\sqrt{3}x\sqrt{3})$ interface, *J. Phys.: Condens. Matter 19*, 266006. (цитиран 3 пута)

[B7]

Stoltz, S. E. and Stoltz, D. (2007). Spectroscopic evidence for reversible hydrogen storage in unordered $Mg_5Ni_1$ thin films, *J. of Phys.: Cond. Matter, 19*, 446010. (цитиран 0 пута)

[B8]

Stoltz, D., Bielmann, M., Bovet, M., Schlapbach, L., Berger, H. (2007). Tunneling evidence for spatial location of the charge-density-wave induced band splitting in 1T-TaS$e_2$, *Phys. Rev. B, 76*, 073410. (цитиран 2 пута)

[B9]

Stoltz, D., Önsten, A., Karlsson, U. O., and Göthelid, M. (2008). Scanning tunneling microscopy of Fe- and O-sublattices on $Fe_3O_4$(100), *Ultramicroscopy, 108*, 540. (цитиран 6 пута)

[B10]

Göthelid, M., Tymczenko, M., Chow, W., Ahmadi, S., Yu, S., Bruhn, B., Stoltz, D., Von Schenck, H., Weissenrieder, J., and Sun, C. (2012). Surface concentration dependent structures of iodine on Pd(110), *J. Chem. Phys. 137*, 204703. (цитиран 5 пута)

**Радови у истакнутим међународним часописима (М22)**

[C1]

Önsten, A., <u>Stoltz, D.</u>, Palmgren, P., Yu S., Claesson, T., Göthelid, M. and Karlsson, U. O. (2013). $SO_2$ interaction with Zn(0001) and ZnO(0001) and the influence of water, *Surf.Sci. 608*, 31. (цитиран 3 пута)

[C2]

Herbschleb, C. T., van der Tuijn, P. C., Roobol, S. B., Navarro, V., Bakker, J. W., Liu, Q., <u>Stoltz, D.</u>, Canas-Ventura, M. E., Verdoes, G., van Spronsen, M. A., Bergman, M., Crama, L., Taminiau, I., Ofitserov, A., van Baarle, G. J. C., and Frenken, J. W. M. (2014). The ReactorSTM: Atomically resolved scanning tunneling microscopy under high-pressure, high-temperature catalytic reaction conditions, *Rev. Sci. Instr. 85*, 083703. (цитиран 16 пута)

**Радови у међународним часописима (М23)**

[D1]

<u>Popović, D.</u>, Bovet, M., Berger, H., and Aebi P. (2005). Fingerprinting substitution sites in Pb,Dy-$Bi_2Sr_2Ca_1Cu_2O_{8+\delta}$ using X-ray Photoelectron Diffraction, *Eur. Phys. J. Appl. Phys. 30*, 171-174. (цитиран 1 пут)

[D2]

<u>Stoltz, D.</u>, Stoltz, S. E., Widstrand, S. M., Johansson, L. S. O. (2007). Investigation of surface structure related features in the multiple-scattering simulations of photoelectron diffraction of 3C-SiC(001)-c(4x2), *Physica B, 395*, 130. (цитиран 2 пута)

[D3]

<u>Stoltz, D.</u>, Stoltz, S. E. (2007). X-ray photoelectron diffraction investigation of the cleavage plane in 1T-transition metal dichalcogenides, *Physica B, 398*, 172. (цитиран 1 пут)

[D4]

<u>Stoltz, D.</u>, Stoltz, S. E., Johansson, L. S. O. (2008). Two-dimensional states in the electronic structure of Au/($\sqrt{3}$x$\sqrt{3}$)-R30º-4H-SiC(0001), *J. of Elec. Spec. and Rel. Phen. 163*, 1. (цитиран 0 пута)

[D5]

<u>Stoltz, D.</u>, Bielmann, M., Schlapbach, L., Bovet, M., Berger, H., Göthelid, M., Stoltz, S. E., Starnberg, H. I. (2008). Atomic origin of the scanning tunneling microscopy images of charge-density-waves on 1T-$TaSe_2$, *Physica B, 403*, 2207. (цитиран 0 пута)

**Објављена докторска дисертација (М70)**

[Е1]

Докторат је одбрањен на колоквијуму 11. 3. 2005. године у Сарбрикену, Немачка. Докторска диплома је издата 18. 3. 2005. године. Дисертација је публикована:

Stoltz, D. (2009). *Quasiparticle band dispersion in quasi-two dimensional systems – in the vicinity of the Fermi surface*, VDM Verlag Dr. Müller, Saarbrücken, ISBN: 978-3639200584.

Образац 6

# МКР

## РЕПУБЛИКА СРБИЈА

ГРАД __БЕОГРАД__

ОПШТИНА _____

# ИЗВОД ИЗ МАТИЧНЕ КЊИГЕ РОЂЕНИХ

У матичну књигу рођених која се води за матично подручје __САВСКИ ВЕНАЦ__, под текућим бројем __529__ за годину __1977__ извршен је упис рођења:

| Име | ДУЊА | | женски |
|---|---|---|---|
| Презиме | ПОПОВИЋ | | (пол) |
| Дан, месец, година и час рођења | 27. (ДВАДЕСЕТСЕДМИ) МАРТ 1977. ГОДИНЕ У 14.25 ЧАС. | | |
| Место и општина-град рођења, а ако је лице рођено у иностранству и држава | БЕОГРАД, ХЕРОЈА МИЛАНА ТЕПИЋА 1 | | |
| Јединствени матични број грађана | 2 7 0 3 9 7 7 8 6 0 1 9 | | |
| Држављанство | РЕПУБЛИКЕ СРБИЈЕ | | |

| Подаци о родитељима | оца | мајке |
|---|---|---|
| Име | ПРЕДРАГ | РАДИЦА |
| Презиме (и презиме пре закључења брака) | ПОПОВИЋ | ПОПОВИЋ РОЂ. ПАВЛОВИЋ |
| Јединствени матични број грађана | | |
| Дан, месец и година рођења | 05.01.1953. | 25.03.1954. |
| Место и општина-град рођења, а ако је лице рођено у иностранству и држава | КЊАЖЕВАЦ | ЈАСИКА |
| Држављанство | СФРЈ | СФРЈ |
| Пребивалиште и адреса | БЕОГРАД, НИШКА 3 | БЕОГРАД, НИШКА 3 |

Накнадни уписи и забелешке:

РЕШЕЊЕМ ОПШТИНА КРУШЕВАЦ, КРУШЕВАЦ, БР. 204-215 ОД 29.06.1992., ДРЖАВЉАНСТВО УПИСАНО У МКР ЗАКЉУЧИЛА БРАК 10.02.2007., СТОКХОЛМ,ШВЕДСКА, СУПРУЖНИК: СВЕН ЕРИК СТОЛТЗ, А ЧИЊЕНИЦА БРАКА УПИСАНА У ДОМАЋУ МКВ: КРУШЕВАЦ, ОПШТИНА КРУШЕВАЦ, ТКБР 265/2011.ПО ЗАКЉУЧЕНОМ БРАКУ ПРОМЕНИЛА ПРЕЗИМЕ НА СТОЛТЗ.БРАК ЗАКЉУЧЕН СА СУПРУЖНИКОМ: СВЕН ЕРИК СТОЛТЗ РАЗВЕДЕН ПРЕСУДОМ ПРВОСТЕПЕНИ СУД, ЛУНДУ, ШВЕДСКА, БР.Т5068-07 ОД 19.12.2007 ГОД., ПРИЗНАТО РЕШЕЊЕМ ВИШИ СУД, КРУШЕВАЦ, ПЗ БР.4/2013, 07.02.2014 РЕШЕЊЕМ, ГУ, КРУШЕВАЦ

Број: _____

У __БЕОГРАДУ__

дана __20.03.2015.__

(М.П.)

Потпис матичара

БРАНКА ШЕРБУЛА КОКОТ

1 1 4 7 2 7 9

Република Србија
**МИНИСТАРСТВО ПРОСВЕТЕ,**
**НАУКЕ И ТЕХНОЛОШКОГ РАЗВОЈА**
Број: 612-01-01541/2015-06
Датум: 27.01.2016. године
Немањина 22-26
Б е о г р а д
ЈК

На основу члана 105б. став 4. Закона о високом образовању („Службени гласник РС", бр. 76/05, аутентично тумачење – 100/07, 97/08, 44/10, 93/12, 89/13, 99/14, 45/15 – аутентично тумачење и 68/15), члана 192. став 1. Закона о општем управном поступку („Службени гласник СРЈ", бр. 33/97 и 31/01, „Службени гласник РС", број 30/10) и члана 23. став 2 Закона о државној управи („Службени гласник РС", бр. 79/05, 101/07 и 95/10), решавајући по захтеву Дуње Поповић из Крушевца за признавање високошколске исправе издате у СР Немачкој, ради запошљавања,

министар просвете, науке и технолошког развоја доноси

**Р Е Ш Е Њ Е**

Диплома, коју је 18.03.2005. године на име Дуња Поповић, издао Универзитет Сарске области (Universitat des Saarlandes), СР Немачка, о успешно савладаном програму докторских студија из главне области студија: Факултет природних наука и технологије II, Физика и мехатроника, (Naturwissenschaftlish-Technische Fakultat II/Physik und Mechatronik), звање/квалификација: Doktor der Naturwissenschaften (doctor rerum naturalium, Dr Rer.nat); **признаје** се као диплома докторских академских студија трећег степена високог образовања, у оквиру области интердисциплинарних, мултидисциплинарних и трансдисциплинарних студија, ради запошљавања.

**О б р а з л о ж е њ е**

Овом министарству обратила се Дуња Поповић из Крушевца (у даљем тексту подносилац захтева), захтевом за признавање дипломе Универзитет сарске области, СР Немачка, ради запошљавања.

Уз захтев, подносилац захтева доставио је:
1) оверену копију дипломе издате 18.03.2005. године, коју је издао Универзитет сарске области (Universitat des Saarlandes), СР Немачка, Doktor der Naturwissenschaften (doctor rerum naturalium, Dr. Rer.nat);
2) оверени превод дипломе на српски језик;
3) оверени превод додатка дипломи на српском језику;
4) транскрипт оцена на српском језику;
5) радну биографију;
6) пријавни формулар;
7) доказ о уплати таксе.

Чланом 105 б. став 4. прописано је да Министар доноси решење о професионалном признавању у року од 90 дана од дана пријема уредног захтева.

Одредбама члана 192. Закона о општем управном поступку прописано је да на основу одлучних чињеница утврђених у поступку орган надлежан за решавање доноси решење у управној ствари која је предмет поступка.

Одредбама члана 23. став 2. Закона о државној управи прописано је да Министар представља Министарство, доноси прописе и решења у управним и другим појединачним стварима и одлучује о другим питањима из делокруга Министарства.

Чланом 104. став 1. Закона о високом образовању, прописано је да признавање стране високошколске исправе јесте поступак којим се имаоцу те исправе утврђује право на наставак образовања, односно на запошљавање. Поступак признавања стране високошколске исправе спроводи се у складу са одредбама овог закона, ако међународним уговором није предвиђено другачије.

Сходно одредбама члана 105. став 1. и 6. Закона о високом образовању и васпитању, ENIC/NARIC центар при Министарству просвете, науке и технолошког развоја, прибавио је релевантне информације о студијском програму на ком је стечена диплома из става 2. тачка 1) образложења овог решења.

У складу са чланом 105. став 4. Закона о високом образовању, комисија коју је именовао министар извршила је прво вредновање студијског програма на коме је стечена диплома из става 2. тачка 1) образложења овог решења, и дала предлог за признавање дипломе ради запошљавања.

Подносилац захтева је доставио доказ о уплати таксе у складу са чланом 2. став 1. Правилника о висини таксе за професионално признавање страних високошколских исправа („Службени гласник РС", број 83/2015).

Имајући у виду наведено, решено је као у диспозитиву овог решења.

**Упутство о правном средству:** Ово решење је коначно у управном поступку и против истог може се покренути управни спор. Тужба се подноси Управном суду у року од 30 дана од дана пријема овог решења.

Решење доставити:
- Дуњи Поповић, ул. Косовска бр. 51, 37000 Крушевац;
- Архиви.

МИНИСТАР

др Срђан Вербић

# URKUNDE

DIE FAKULTÄT PROMOVIERT

**Frau Dunja Popović**

geboren am 27. März 1977 in Belgrad (Jugoslawien)

ZUM

**DOKTOR DER NATURWISSENSCHAFTEN**

(doctor rerum naturalium, Dr. rer. nat.)

NACHDEM SIE IN EINEM ORDENTLICHEN PROMOTIONSVERFAHREN
DURCH DIE DISSERTATION

**Quasiparticle band dispersion in the vicinity of the Fermi surface in quasi-two dimensional systems**

BEGUTACHTET VON

**Herrn Univ.-Prof. Dr. rer. nat. Dr. h. c. mult. S. Hüfner**
**Herrn Univ.-Prof. Dr. rer. nat. U. Hartmann**

SOWIE DURCH DAS ABSCHLIESSENDE KOLLOQUIUM AM 11. MÄRZ 2005 IHRE
WISSENSCHAFTLICHE QUALIFIKATION NACHGEWIESEN HAT
MIT DER GESAMTNOTE
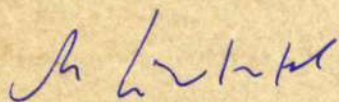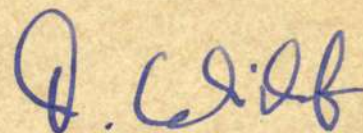
**sehr gut**
**(magna cum laude)**

SAARBRÜCKEN, DEN 18.03.2005

DIE UNIVERSITÄTSPRÄSIDENTIN

DER DEKAN

# TRANSLATION

Scientific-Technical Faculty II
Physics and Mechatronics

# CERTIFICATE

**The Faculty**

confers on

**Mrs. Dunja POPOVIC**
born on March 27, 1977 in Belgrade (Yugoslavia)

**the degree of a Doctor of Natural Sciences**
(doctor rerum naturalium; Dr. rer. nat.)

after having proved her scientific qualification within an orderly
doctoral procedure by the thesis

**QUASIPARTICLE BAND DISPERSION IN THE VICINITY OF THE
FERMI SURFACE IN QUASI-TWO DIMENSIONAL SYSTEMS**

assessed by

**Univ.-Prof. Dr. rer. nat. Dr. h.c. mult. S. Hüfner**
**Univ.-Prof. Dr. rer. nat. U. Hartmann**

and by the final colloquy on March 11, 2005.

She obtained the final grade

**VERY GOOD
(MAGNA CUM LAUDE)**

**Saarbrücken, March 18, 2005**

(signature: Prof. Dr. M. Wintermantel)          (signature: Thomas Wichert)

**THE PRESIDENT**                                          **THE DEAN**

Elisabeth M. Müller-Perich

ELISABETH M. MÜLLER-PERICH
Für die Gerichte des Saarlandes
und die saarländischen Notare
allgemein vereidigte
Dolmetscherin / Übersetzerin

This is to certify that the copy
corresponds to the original in
German language

Elisabeth M. Müller-Perich

**Deutsch-Französische
Hochschule**

**Université
franco-allemande**

# Certificate

**International Research Training**

**Group, GRK 532**

*Physical Methods for the Structural
Investigation of New Materials*

## Dunja Popovic

was a member of the GRK 532
during her PhD at the Saarland
University, under the supervision of
Prof. Dr. Stefan Hüfner.

**DFG**

Saarbrücken/Sarrebruck
12/03/2005

CENTRE NATIONAL
DE LA RECHERCHE
SCIENTIFIQUE

Université du
LUXEMBOURG

The participation in seminars and workshops organised by the GRK 532 as well as other
activities of the grant holder are listed in the appendix.

UNIVERSITÉ LOUIS PASTEUR STRASBOURG

UNIVERSITÉ DE METZ

inpl
nancy

UNIVERSITÄT
DES
SAARLANDES

**Deutsch-Französische
Hochschule**

**Université
franco-allemande**

# Zertifikat | Certificat

**Europäisches Graduiertenkolleg,** | **Réseau Européen de Formation**

**GRK 532** | **des doctorants, GRK 532**

*Physikalische Methoden in der
Strukturellen Erforschung Neuer
Materialen* | *Nouveaux Matériaux et
Développement de Nouvelles
Méthodes Physiques pour leur
Etude Structurale*

## *Dunja Popovic*

war während ihrer Doktorarbeit
bei Prof. Dr. Stefan Hüfner
an der Universität des Saarlandes
Mitglied des GRK 532 | A été membre du GRK 532 durant
son doctorat à l'Université de la Sarre,
sous la direction du Pr. Dr. Stefan
Hüfner

**DFG**

Saarbrücken/Sarrebruck
12/03/2005

**CNRS** CENTRE NATIONAL
DE LA RECHERCHE
SCIENTIFIQUE

Université du
LUExEMBOURG

Prof. Dr. M. Veith
(Sprecher des GRK 532)

Prof. Dr. A. Hamm
(Deutsch-Französische Hochschule/
Université Franco-Allemande)

Prof. J.-F. Muller
(Université de Metz)

*b.w.* | *t.s.v.p.*

**ulp** UNIVERSITÉ LOUIS PASTEUR STRASBOURG

**UNIVERSITÉ DE METZ**

**inpl** nancy

**UNIVERSITÄT
DES
SAARLANDES**

# Appendix to Certificate
## List of Participated Events:

a) Lectures

| Title | Lecturer | Date |
|---|---|---|
| Synthesis of CVD-Single-Source Precursors for the preparation of thin films and modification of their surfaces | Veith | 17/09/2002 |
| XPS for the analysis of surfaces | Hüfner | 17/09/2002 |
| Mass-Spectrometry and its Application in Material and Life Science | Muller | 14/01/2003 |
| Protein investigation on the level of molecules and cells | Bernhardt | 12/05/2003 |
| Mass Spectrometry and Proteomics | Leize | 12/12/2003 |
| N-N and N-O Bond Containing Pseudopeptides: Synthesis, Structural Studies and Applications | Jamart | 14/06/2004 |

b) Workshops

| Title | Location | Date |
|---|---|---|
| Preparation and physical characterisation of Inorganic Molecules and Materials | Veith, Hüfner; Saarbrücken | 11/12/2002 |
| Laser - Matter Interaction - Applications in Mass Spectrometry | Muller; Metz | 11/03/2003 |
| Computer-Aided Massbalancing | Heinzle; Saarbrücken | 11/07/2003 |
| Introduction to Cells and Overview on Flow of Information in Living Systems | Bernhardt; Saarbrücken | 12/09/2003 |
| Mass Spectrometers (ESI-MS MALDI TOF-TOF, Q-TOF) | Albrecht, van Dorselaer; Strasbourg | 22/03/2004 |
| Solid Phase Synthesis of Organic Compounds (SPOC), Solid Phase Synthesis of Peptides (SPPS) and 1D and 2D NMR | Jamart; Nancy | 09/07/2004 |

c) Seminars

| Location | Date |
|---|---|
| Homburg | 07/11/2002 |
| La Petite Pierre | 22/05/2003 |
| Achern/Strasbourg | 04/12/2003 |

d) Presentations

| Title (oral/posters) | Event | Date |
|---|---|---|
| Introduction to ESCA and High Resolution UPS (oral) | Workshop A | 11-12/12/2002 |

Saarbrücken, 01.09.2004

_____
Speaker of the Graduiertenkolleg

_____
Supervisor

1b

# Annotation to the Structure and Benefit of the International Research Training Group (GRK)

Educational Events take place in "series" comprising each one lecture, workshop and seminar, where the lecture and workshop are given/organised by one research group of the Graduiertenkolleg.

There are 3 series of events per year plus the individual research stays in partner laboratories.

All the events are given in English, the international scientific communication language.

Members in the Gradiertenkolleg (GRK) are: student members (qualifying students, doctorants, post-doctorants; as grant-holders or financed externally), assistants/maîtres de conférence/chargés de recherche (supervising doctorants), group leaders (head of laboratory or university professor). External speakers (young or renown guests) take part in the seminars.

Lectures:

Group leaders introduce their field of research in a comprehensive way to strengthen interdisciplinary education.
Duration: typically 1-2 hour
Participants: student members, group leaders

Workshops:

In the workshops, the students of one research group practically present their working techniques to the other groups and teach them on basic handlings.
Duration: typically one day
Participants: student members

Seminars:

In the seminars, the doctorants and post-doctorants present their latest results to the members; external speakers from industries and institutional research give insight in up-to-date developments.
Duration: typically 2 days
Participants: all members, invited external speakers

Laboratory Stays and Visits:

In individual stays in partner laboratories abroad, the students learn and apply new techniques, dive into a foreign culture and thereby qualify for a "co-tutelle du thèse" - a bilateral doctoral degree.
Duration: up to 6 months (stays), several weeks (visits)
Participants: student members

Presentations (oral/poster):

During the seminars and evaluation events of the GRK, doctorants and post-doctorants give presentations on their latest results in front of renowned researchers in the respective field. The presentations serve to reflect the actual state of the respective research and train the presentation skills of the students.
Duration: 10-20 minutes + discussion
Participants: student members (presenting), all members (discussion)

By this (pilot) project in the German-French-Luxemburg graduate education, the candidates get an exceptional possibility to enlarge their interdisciplinary knowledge, train their international presentation skills, increase their mobility and language competence, get cross-border research experience and contacts, and organise conferences, workshops and seminars for their needs.

CENTRE NATIONAL DE LA RECHERCHE SCIENTIFIQUE

UNIVERSITÉ PARIS-SUD XI

CĒÂ

INP Grenoble

UNIVERSITÉ JOSEPH FOURIER
SCIENCES, TECHNOLOGIE, MÉDECINE

## ATTESTATION D'ETUDES

## H E R C U L E S

- - - - - - - -

**FORMATION DOCTORALE EUROPEENNE POUR LES UTILISATEURS DES GRANDS INSTRUMENTS**
*HIGHER EUROPEAN RESEARCH COURSE FOR USERS OF LARGE EXPERIMENTAL SYSTEMS*

**Année Universitaire**     **2001 - 2002**
*Academic Year*

**POPOVIC Dunja**   né(e) le *(born)*  27/03/77  à *(in)*  Belgrade

inscrit(e) en Thèse de Doctorat à :                    **Université   de   Fribourg**
*registered in the Doctoral Programme of :*
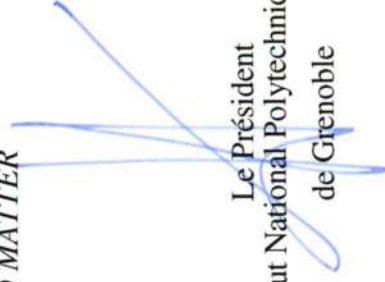
a suivi du 17 février au 28 mars 2002 l'enseignement de :         **HERCULES 2002**
*has attended from 17 February to 28 March 2002 the Course :*

NEUTRONS ET RAYONNEMENT SYNCHROTRON POUR LA PHYSIQUE ET LA CHIMIE DE LA MATIERE CONDENSEE
*NEUTRON AND SYNCHROTRON RADIATION FOR PHYSICS AND CHEMISTRY OF CONDENSED MATTER*

A Grenoble, le 28 mars 2002

Le Président
de l'Université Paris-Sud XI

Le Président
de l'Institut National Polytechnique
de Grenoble

Le Président
de l'Université Joseph Fourier
Grenoble 1
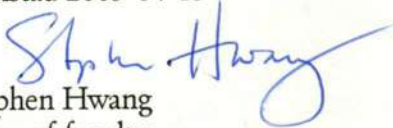
# Karlstad University Post-doctoral fellowship

Karlstad University awards a post-doctoral fellowship to promote the career of a young promising scientist and to increase the university's international research exchange.

The Karlstad University Post-doctoral fellowship of 2005 is hereby awarded to Dunja Popovic. The fellowship entitles the receiver a sum of 200 000 swedish crowns for the purpose of a stay at Karlstad University for one year from 2005-04-13 to 2006-04-12.

Karlstad 2005-04-13

Stephen Hwang
Dean of faculty

By signing below I accept the fellowship and ensure that it will only be used for the intended purpose. I understand that if it is used for other purposes, I must return the entire fellowship.

Karlstad ...18.04.2005.

Dunja Popovic

# Göran Gustafssons Stiftelse

FÖR FRÄMJANDE AV VETENSKAPLIG FORSKNING
VID UPPSALA UNIVERSITET OCH KUNGL. TEKNISKA HÖGSKOLAN

# DUNJA STOLTZ

## 2007 års Göran Gustafsson-postdoktor

STOCKHOLM 27 APRIL 2007

Kristian Gustafsson

*Gustafssonstiftelsen stöder unga forskare*

Universiteit Leiden

Faculty of Science

# Form
# Performance & Development Interview

## I.   General Information

| | |
|---|---|
| Name employee | Dunja Stoltz |
| Job title | Postdoc |
| Institute / Division | LION |
| Section / Department | /Interface Physics Group |
| Superior / Supervisor | Joost Frenken |
| Assessment Authority | Prof.Dr. J.M. van Ruitenbeek |
| P&D period | 20 juni 2007 tot 9 april 2008 |
| Date previous interview | 20 juni 2007 |
| Date of P&D interview | 9 april 2008 |
| Annual report enclosed | Nee |

This form consists of two sections:
A – Assessment
B – Agreements, this part of the P&D interview is also suitable for use as an interview report.

Explanation letter codes Section A - Assessment
A       Exceeds requirements
B       Meets requirements
C       Does not (yet) fully meet requirements
D       Does not meet requirements

# Section A – Assessment

## 1. Assessment of achieved results in P&D period
To be filled out by superior

### 1.1 Performance agreements

| Performance area position [1] | Achieved results | Score |
| --- | --- | --- |
| • Good job performance | | |
| • Opzetten HP-STM project | Helemaal gebeurd | A |
| • Ontwerp PH-STM opstellingen | Vrijwel voltooid | A |
| • | | |
| • | | |
| Further clarification scores | | |

| Other performance areas [2] | Achieved results | Score |
| --- | --- | --- |
| • | | |
| • | | |
| • | | |
| Further clarification scores | | |

### 1.2 Competencies, development & other topics

| Agreement | Achieved results | Score |
| --- | --- | --- |
| • Projectmanagement | Cursus wordt inmiddels gevolgd en stevig in de praktijk gebracht | B |
| • Ontwikkeling naar een volledig zelfstandige junior onderzoeker | Krijgt sterk gestalte in het HP-SPM project; 2e ontwikkeling is het schrijven van research proposal | A |
| • | | |

---

[1] Applicable performance areas as listed in the initial Performance & Development Interview and from the VSNU HAY profile.
[2] Other applicable performance areas.

| | Further clarification scores | |
|---|---|---|

Click for digital competence list (Dutch version only)

**2.     Employee statement (not obligatory)**

| |
|---|
| |

# Signatures for Agreements & processing³

| | Signature | Date |
|---|---|---|
| Employee | Seen / Approved ⁴ | 9 april 2008 |
| Superior | | 9 april 2008 |
| Assessment authority | | 29 april 200 8 |

**Yearly increment**

| Only to be signed by Scientific Director / Assessment authority | Yes/No |
|---|---|
| As a result of this assessment the yearly increment will be assigned. | |
| Further clarification/Signature | |

**HRM Department**

| | Signature | Date |
|---|---|---|
| HRM advisor | | 200 |
| HRM administrator | | 200 |
| Yearly increment processed in SAP | | 200 |

---

³ Also see D&P regulation
⁴ Delete what is not applicable

# Section B - Agreements

This section deals with SMART agreements concerning expected achievements based on the performance areas from the VSNU HAY Profile, designated tasks, competencies and the personal development of the employee. For instance: career agreements, courses / trainings etc.

## 1.1 Performance areas

| Performance area position[5] | Goals | Deadline |
|---|---|---|
| • Good job performance | | |
| • HP-STM opstelling: | voltooid en volledig operationeel | eind 2008 |
| • Eerste meetserie met nieuwe opstelling | voltooid en geanalyseerd | voorjaar 2009 |
| • Publicatie instrument | draft klaar | eind 2008 |
| • Publicatie eerste metingen | draft klaar | medio 2009 |

| Other performance areas [6] | Goals | Deadline |
|---|---|---|
| • | | |
| • | | |
| • | | |

## 1.2 Competencies

| Agreement | Goals | Deadline |
|---|---|---|
| • projectmanagement | cursus afmaken | medio 2008 |
| • oppervlakte-katalyse | aan de hand van eerste resultaten verder inwerken tot volledige expert op dit gebied | medio 2009 |
| • | | |
| • | | |

---

[5] Applicable performance areas from the VSNU HAY profile.
[6] Other applicable performance areas

## 1.3 Development

| Agreement | Goals | Deadline |
|---|---|---|
| • verzelfstandiging | gehonoreerd onderzoeksvoorstel (Zweden) | eind 2008 |
| • | | |
| • | | |
| • | | |

## 2. Other topics covered in the Interview/remarks (interview report)

Dunja gaat verder nadenken over de carriere na de postdoctijd. Voor een deel doet ze dat al in de vorm van het research proposal dat ze momenteel schrijft. Afgesproken is om op dit punt expliciet terug te komen aan het eind van 2008.

Dunja gaat zich opgeven voor tenminste 1 conferentie (b.v. ECOSS in Liverpool) in 2008, waar zij haar werk zal presenteren.

Dunja blijft betrokken bij de SXRD experimenten van Richard van Rijn bij ESRF in Grenoble.

# Signatures for Agreements & processing[7]

| | Signature | | Date |
|---|---|---|---|
| Employee | Seen / Approved [8] | | 9 april 2008 |
| Superior | | | 9 april 2008 |
| Assessment authority | | | 29 april 2008 |

---

[7] Employees signs as seen / approved, superior as agreed, assessment authority as seen
[8] Delete what is not applicable

| | Signature | Date |
|---|---|---|
| HRM Advisor | | 200 |
| HRM administration | | 200 |

# Göran Gustafssons Stiftelse

FÖR FRÄMJANDE AV VETENSKAPLIG FORSKNING
VID UPPSALA UNIVERSITET OCH KUNGL. TEKNISKA HÖGSKOLAN

## DUNJA STOLTZ

har 2010 tilldelats Gustafssonpriset till unga forskare

STOCKHOLM 23 APRIL 2010

*Kristian Gustafsson*

*Gustafssonstiftelsen stöder unga forskare*

# Web of Science

## Marked List 23 records

Save | Open/Manage | ✕ Clear

**23** total records on the Marked List
Output author, title, source, abstract, and times cited for all records in the Marked List.

**23** records from *Web of Science Core Collection*
Output complete data from this product for these records.

**Output Records** [ ➕ Show Output Options ] | **5K**

Sort by: Publication Date -- oldest to newest ▾        Page 1 of 1

**Create Citation Report**

≡ **Analyze Results**

1. **Oxidation of Al-Pd-Mn quasicrystal surfaces**

   By: Popovic, D; Naumovic, D; Bovet, M; et al.
   SURFACE SCIENCE   Volume: 492   Issue: 3   Pages: 294-304   Published: OCT 20 2001

   Full Text from Publisher | View Abstract

   Times Cited: 17
   *(from Web of Science Core Collection)*

   Usage Count

2. **Angle-scanned photoemission on YbHx: relevance for switchable mirrors**

   By: Hayoz, J; Koitzsch, C; Popovic, D; et al.
   Conference: 13th International Conference on Vacuum Ultraviolet Radiation Physics (VUV-13) Location: TRIESTE, ITALY Date: JUL 23-27, 2001
   SURFACE REVIEW AND LETTERS   Volume: 9   Issue: 1   Pages: 235-241   Published: FEB 2002

   Full Text from Publisher | View Abstract

   Times Cited: 2
   *(from Web of Science Core Collection)*

   Usage Count

3. **Pseudogapped Fermi surfaces of 1T-TaS2 and 1T-TaSe2: A charge density wave effect**

   By: Bovet, M; Popovic, D; Clerc, F; et al.
   PHYSICAL REVIEW B   Volume: 69   Issue: 12   Article Number: 125117   Published: MAR 2004

   View Abstract

   Times Cited: 28
   *(from Web of Science Core Collection)*

   Usage Count

4. **Spin-orbit splitting of the Shockley state in the Ag/Au(111) interface**

   By: Cercellier, H; Fagot-Revurat, Y; Kierren, B; et al.
   PHYSICAL REVIEW B   Volume: 70   Issue: 19   Article Number: 193412   Published: NOV 2004

   View Abstract

   Times Cited: 42
   *(from Web of Science Core Collection)*

   Usage Count

5. **Fingerprinting substitution sites in Pb, Dy-Bi2Sr2Ca1Cu2O8+delta using X-ray Photoelectron Diffraction**

   By: Popovic, D; Bovet, M; Berger, H; et al.
   EUROPEAN PHYSICAL JOURNAL-APPLIED PHYSICS   Volume: 30   Issue: 3   Pages: 171-174   Published: JUN 2005

   View Abstract

   Times Cited: 1
   *(from Web of Science Core Collection)*

   Usage Count

6. **High-resolution photoemission on Ag/Au(111): Spin-orbit splitting and electronic localization of the surface state**

   By: Popovic, D; Reinert, F; Hufner, S; et al.
   PHYSICAL REVIEW B   Volume: 72   Issue: 4   Article Number: 045419   Published: JUL 2005

   View Abstract

   Times Cited: 42
   *(from Web of Science Core Collection)*

   Usage Count

7. **A high-resolution core-level study of Ni-catalyzed absorption and desorption of hydrogen in Mg-films**

By: Stoltz, S. E.; Popovic, D.
SURFACE SCIENCE   Volume: 601   Issue: 6   Pages: 1507-1512   Published: MAR 15 2007

Full Text from Publisher    View Abstract

Times Cited: **7**
*(from Web of Science Core Collection)*

Usage Count

8. **Investigation of surface structure related features in the multiple-scattering simulations of photoelectron diffraction of 3C-SiC(001)-c(4 x 2)**

By: Stoltz, D.; Stoltz, S. E.; Widstrand, S. M.; et al.
PHYSICA B-CONDENSED MATTER   Volume: 395   Issue: 1-2   Pages: 130-137   Published: MAY 31 2007

Full Text from Publisher    View Abstract

Times Cited: **2**
*(from Web of Science Core Collection)*

Usage Count

9. **Surface resonance on the (6 root 3 x 6 root 3)-R30 degrees-reconstructed 5 ML Au on (root 3 x root 3)-R30 degrees-4H-SiC(0001)**

By: Stoltz, D.; Stoltz, S. E.; Johansson, L. S. O.
SURFACE SCIENCE   Volume: 601   Issue: 12   Pages: 2508-2511   Published: JUN 15 2007

Full Text from Publisher    View Abstract

Times Cited: **1**
*(from Web of Science Core Collection)*

Usage Count

10. **A high-resolution core-level photoemission study of the Au/4H-SiC(0001)-(root 3 x root 3) interface**

By: Stoltz, D.; Stoltz, S. E.; Johansson, L. S. O.
JOURNAL OF PHYSICS-CONDENSED MATTER   Volume: 19   Issue: 26   Article Number: 266006   Published: JUL 4 2007

View Abstract

Times Cited: **3**
*(from Web of Science Core Collection)*

Usage Count

11. **X-ray photoelectron diffraction investigation of the cleavage plane in IT-transition metal dichalcogenides**

By: Stoltz, D.; Stoltz, S. E.
PHYSICA B-CONDENSED MATTER   Volume: 398   Issue: 1   Pages: 172-177   Published: AUG 1 2007

Full Text from Publisher    View Abstract

Times Cited: **1**
*(from Web of Science Core Collection)*

Usage Count

12. **Tunneling evidence for spatial location of the charge-density-wave induced band splitting in 1T-TaSe2**

By: Stoltz, D.; Bielmann, M.; Bovet, M.; et al.
PHYSICAL REVIEW B   Volume: 76   Issue: 7   Article Number: 073410   Published: AUG 2007

View Abstract

Times Cited: **2**
*(from Web of Science Core Collection)*

Usage Count

13. **High resolution spectroscopic and microscopic signatures of ordered growth of ferrous sulfate in SO2 assisted corrosion of Fe3O4(100)**

By: Stoltz, D.; Onsten, A.; Karlsson, U. O.; et al.
APPLIED PHYSICS LETTERS   Volume: 91   Issue: 9   Article Number: 093107   Published: AUG 27 2007

View Abstract

Times Cited: **4**
*(from Web of Science Core Collection)*

Usage Count

14. **Spectroscopic evidence for reversible hydrogen storage in unordered Mg5Ni1 thin films**

By: Stoltz, S. E.; Stoltz, D.
JOURNAL OF PHYSICS-CONDENSED MATTER   Volume: 19   Issue: 44   Article Number: 446010   Published: NOV 7 2007

View Abstract

Times Cited: **0**
*(from Web of Science Core Collection)*

Usage Count

15. **Two-dimensional states in the electronic structure of Au/(root 3 x root 3)-R30 degrees-4H-SiC(0001)**

By: Stoltz, D.; Stoltz, S. E.; Johansson, L. S. O.
JOURNAL OF ELECTRON SPECTROSCOPY AND RELATED PHENOMENA   Volume: 163   Issue: 1-3   Pages: 1-6   Published: APR 2008

Full Text from Publisher    View Abstract

Times Cited: **0**
*(from Web of Science Core Collection)*

Usage Count

16. **Scanning tunneling microscopy of Fe- and O-sublattices on Fe(3)O(4)(100)**

By: Stoltz, D.; Oensten, A.; Karlsson, U. O.; et al.

Times Cited: **6**
*(from Web of Science Core*

ULTRAMICROSCOPY   Volume: 108   Issue: 6   Pages: 540-544   Published: MAY 2008

[ Full Text from Publisher ]     [ View Abstract ]

Usage Count

17.   **Atomic origin of the scanning tunneling microscopy images of charge-density-waves on 1T-TaSe2**

By: Stoltz, D.; Bielmann, M.; Schlapbach, L.; et al.
PHYSICA B-CONDENSED MATTER   Volume: 403   Issue: 13-16   Pages: 2207-2210   Published: JUL 1 2008

[ Full Text from Publisher ]     [ View Abstract ]

Times Cited: 0
*(from Web of Science Core Collection)*

Usage Count

18.   **Water Adsorption on ZnO(0001): Transition from Triangular Surface Structures to a Disordered Hydroxyl Terminated phase**

By: Onsten, Anneli; Stoltz, Dunja; Palmgren, Pal; et al.
JOURNAL OF PHYSICAL CHEMISTRY C   Volume: 114   Issue: 25   Pages: 11157-11161   Published: JUL 1 2010

[ View Abstract ]

Times Cited: 34
*(from Web of Science Core Collection)*

Usage Count

19.   **The role of steps in surface catalysis and reaction oscillations**

By: Hendriksen, Bas L. M.; Ackermann, Marcelo D.; van Rijn, Richard; et al.
NATURE CHEMISTRY   Volume: 2   Issue: 9   Pages: 730-734   Published: SEP 2010

[ View Abstract ]

Times Cited: 89
*(from Web of Science Core Collection)*

Usage Count

20.   **Surface concentration dependent structures of iodine on Pd(110)**

By: Gothelid, Mats; Tymczenko, Michael; Chow, Winnie; et al.
JOURNAL OF CHEMICAL PHYSICS   Volume: 137   Issue: 20   Article Number: 204703   Published: NOV 28 2012

[ View Abstract ]

Times Cited: 5
*(from Web of Science Core Collection)*

Usage Count

21.   **SO2 interaction with Zn(0001) and ZnO(0001) and the influence of water**

By: Onsten, Anneli; Stoltz, Dunja; Palmgren, Pal; et al.
SURFACE SCIENCE   Volume: 608   Pages: 31-43   Published: FEB 2013

[ Full Text from Publisher ]     [ View Abstract ]

Times Cited: 3
*(from Web of Science Core Collection)*

Usage Count

22.   **Role of Defects in Surface Chemistry on Cu2O(111)**

By: Onsten, Anneli; Weissenrieder, Jonas; Stoltz, Dunja; et al.
JOURNAL OF PHYSICAL CHEMISTRY C   Volume: 117   Issue: 38   Pages: 19357-19364   Published: SEP 26 2013

[ View Abstract ]

Times Cited: 7
*(from Web of Science Core Collection)*

Usage Count

23.   **The ReactorSTM: Atomically resolved scanning tunneling microscopy under high-pressure, high-temperature catalytic reaction conditions**

By: Herbschleb, C. T.; van der Tuijn, P. C.; Roobol, S. B.; et al.
REVIEW OF SCIENTIFIC INSTRUMENTS   Volume: 85   Issue: 8   Article Number: 083703   Published: AUG 2014

[ View Abstract ]

Times Cited: 16
*(from Web of Science Core Collection)*

Usage Count

▲ Back to top

Sort by: [ Publication Date -- oldest to newest ▼ ]     Show: [ 25 per page ▼ ]     Page [ 1 ]   of  1

*23 records matched your query of the 37,941,506 in the data limits you selected.*

| Web of Science | InCites | Journal Citation Reports | Essential Science Indicators | EndNote | | Sign In ▼ | Help | English ▼ |

# Web of Science

| Search | Search Results | | My Tools ▼ | Search History | Marked List   23 |

## Citation report for 23 results from Web of Science Core Collection   between   1996 ▼   and   2017 ▼   Go

You searched for: **From Marked List: ...More**

This report reflects citations to source items indexed within Web of Science Core Collection. Perform a Cited Reference Search to include citations to items not indexed within Web of Science Core Collection.

Export Data:   Save to Text File ▼

**Total Publications** ⤢
**23**

1995     2014

**h-index** ⓘ
**7**

**Sum of Times Cited** ⓘ
**312**

**Citing articles** ⓘ
**291**
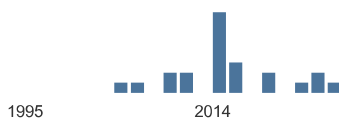
**Average citations per item** ⓘ
**13.57**

**Without self citations** ⓘ
**296**

**Without self citations** ⓘ
**281**

### Sum of Times Cited per Year
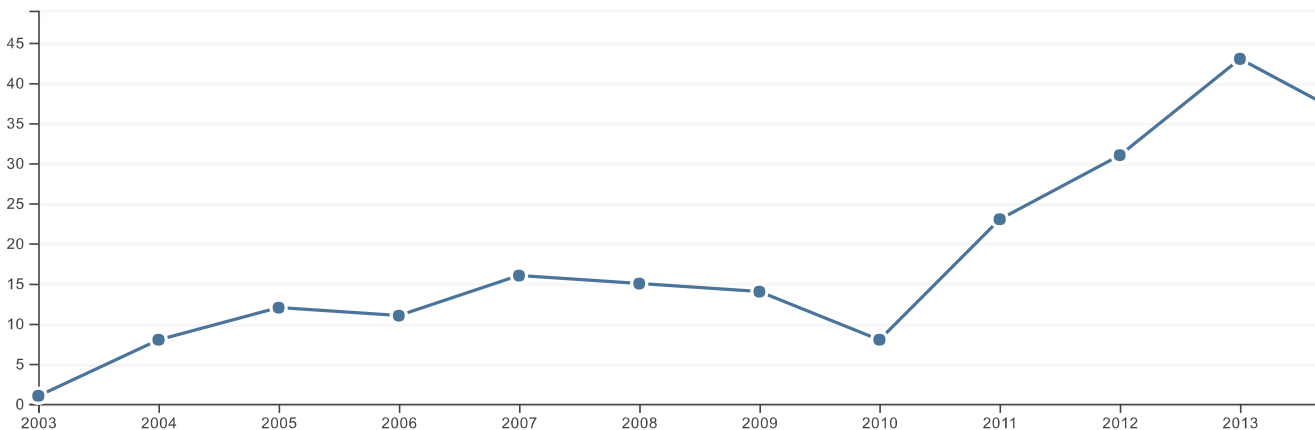


Sort by:   Times Cited -- highest to lowest ▼     Page [1] of 3

| | | 2013 ◄ | 2014 | 2015 | 2016 | 2017 ► | Total | Average Citations per Year |
|---|---|---|---|---|---|---|---|---|
| Use the checkboxes to remove individual items from this Citation Report | | | | | | | | |
| ↓   or restrict to items published between   1996 ▼   and   2017 ▼   Go | | 43 | 35 | 33 | 48 | 14 | 312 | 20.80 |
| ☐ 1. **The role of steps in surface catalysis and reaction oscillations** ☑ | | 16 | 15 | 13 | 15 | 7 | 89 | 11.12 |
| By: Hendriksen, Bas L. M.; Ackermann, Marcelo D.; van Rijn, Richard; et al. | | | | | | | | |

NATURE CHEMISTRY   Volume: 2   Issue: 9   Pages: 730-734   Published: SEP 2010

2. **High-resolution photoemission on Ag/Au(111): Spin-orbit splitting and electronic localization of the surface state**

By: Popovic, D; Reinert, F; Hufner, S; et al.
PHYSICAL REVIEW B   Volume: 72   Issue: 4   Article Number: 045419
Published: JUL 2005

| 3 | 1 | 5 | 4 | 2 | 42 | 3.23 |

3. **Spin-orbit splitting of the Shockley state in the Ag/Au(111) interface**

By: Cercellier, H; Fagot-Revurat, Y; Kierren, B; et al.
PHYSICAL REVIEW B   Volume: 70   Issue: 19   Article Number: 193412
Published: NOV 2004

| 3 | 1 | 0 | 0 | 0 | 42 | 3.00 |

4. **Water Adsorption on ZnO(0001): Transition from Triangular Surface Structures to a Disordered Hydroxyl Terminated phase**

By: Onsten, Anneli; Stoltz, Dunja; Palmgren, Pal; et al.
JOURNAL OF PHYSICAL CHEMISTRY C   Volume: 114   Issue: 25   Pages: 11157-11161   Published: JUL 1 2010

| 9 | 7 | 4 | 5 | 0 | 34 | 4.25 |

5. **Pseudogapped Fermi surfaces of 1T-TaS2 and 1T-TaSe2: A charge density wave effect**

By: Bovet, M; Popovic, D; Clerc, F; et al.
PHYSICAL REVIEW B   Volume: 69   Issue: 12   Article Number: 125117
Published: MAR 2004

| 1 | 3 | 4 | 3 | 0 | 28 | 2.00 |

6. **Oxidation of Al-Pd-Mn quasicrystal surfaces**

By: Popovic, D; Naumovic, D; Bovet, M; et al.
SURFACE SCIENCE   Volume: 492   Issue: 3   Pages: 294-304   Published: OCT 20 2001

| 1 | 2 | 0 | 0 | 1 | 17 | 1.00 |

7. **The ReactorSTM: Atomically resolved scanning tunneling microscopy under high-pressure, high-temperature catalytic reaction conditions**

By: Herbschleb, C. T.; van der Tuijn, P. C.; Roobol, S. B.; et al.
REVIEW OF SCIENTIFIC INSTRUMENTS   Volume: 85   Issue: 8   Article Number: 083703   Published: AUG 2014

| 0 | 0 | 4 | 9 | 3 | 16 | 4.00 |

8. **Role of Defects in Surface Chemistry on Cu2O(111)**

By: Onsten, Anneli; Weissenrieder, Jonas; Stoltz, Dunja; et al.
JOURNAL OF PHYSICAL CHEMISTRY C   Volume: 117   Issue: 38   Pages: 19357-19364   Published: SEP 26 2013

| 0 | 1 | 1 | 5 | 0 | 7 | 1.40 |

9. **A high-resolution core-level study of Ni-catalyzed absorption and desorption of hydrogen in Mg-films**

By: Stoltz, S. E.; Popovic, D.
SURFACE SCIENCE   Volume: 601   Issue: 6   Pages: 1507-1512   Published: MAR 15 2007

| 1 | 1 | 1 | 1 | 0 | 7 | 0.64 |

10. **Scanning tunneling microscopy of Fe- and O-sublattices on Fe(3)O(4)(100)**

By: Stoltz, D.; Oensten, A.; Karlsson, U. O.; et al.
ULTRAMICROSCOPY   Volume: 108   Issue: 6   Pages: 540-544   Published: MAY 2008

| 4 | 0 | 0 | 1 | 0 | 6 | 0.60 |

Select Page     Save to Text File

Sort by: Times Cited -- highest to lowest       Page 1 of 3

*23 records matched your query of the 37,941,506 in the data limits you selected.*

# Web of Science

| Search | Search Results | | My Tools ▾ | Search History | Marked List   23 |

## Citation report for 23 results from Web of Science Core Collection   between    1996 ▾   and   2017 ▾    Go

You searched for: **From Marked List: ...More**

This report reflects citations to source items indexed within Web of Science Core Collection. Perform a Cited Reference Search to include citations to items not indexed within Web of Science Core Collection.

Export Data:   Save to Text File   ▾

| **Total Publications** ⤢ | **_h_-index** ⓘ | **Sum of Times Cited** ⓘ | **Citing articles** ⓘ |
|---|---|---|---|
| **23** | **7** | **312** | **291** |

| **Average citations per item** ⓘ | **Without self citations** ⓘ | **Without self citations** ⓘ |
|---|---|---|
| 1995   2014 | | |
| **13.57** | **296** | **281** |

### Sum of Times Cited per Year



Sort by:   Times Cited -- highest to lowest ▾      Page [2] of 3

| | 2013 ◀ | 2014 | 2015 | 2016 | 2017 ▶ | Total | Average Citations per Year |
|---|---|---|---|---|---|---|---|
| Use the checkboxes to remove individual items from this Citation Report | | | | | | | |
| ↓   or restrict to items published between   1996 ▾   and   2017 ▾   Go | 43 | 35 | 33 | 48 | 14 | 312 | 20.80 |
| ☐ 11. **Surface concentration dependent structures of iodine on Pd(110)** ☑ | 0 | 2 | 1 | 2 | 0 | 5 | 0.83 |
| By: Gothelid, Mats; Tymczenko, Michael; Chow, Winnie; et al. | | | | | | | |

JOURNAL OF CHEMICAL PHYSICS   Volume: 137   Issue: 20    Article Number: 204703   Published: NOV 28 2012

**12. High resolution spectroscopic and microscopic signatures of ordered growth of ferrous sulfate in SO2 assisted corrosion of Fe3O4(100)**

By: Stoltz, D.; Onsten, A.; Karlsson, U. O.; et al.
APPLIED PHYSICS LETTERS   Volume: 91   Issue: 9    Article Number: 093107   Published: AUG 27 2007

| 2 | 0 | 0 | 2 | 0 | 4 | 0.36 |
|---|---|---|---|---|---|------|

**13. SO2 interaction with Zn(0001) and ZnO(0001) and the influence of water**

By: Onsten, Anneli; Stoltz, Dunja; Palmgren, Pal; et al.
SURFACE SCIENCE   Volume: 608   Pages: 31-43   Published: FEB 2013

| 1 | 1 | 0 | 0 | 1 | 3 | 0.60 |
|---|---|---|---|---|---|------|

**14. A high-resolution core-level photoemission study of the Au/4H-SiC(0001)-(root 3 x root 3) interface**

By: Stoltz, D.; Stoltz, S. E.; Johansson, L. S. O.
JOURNAL OF PHYSICS-CONDENSED MATTER   Volume: 19   Issue: 26   Article Number: 266006   Published: JUL 4 2007

| 0 | 0 | 0 | 1 | 0 | 3 | 0.27 |
|---|---|---|---|---|---|------|

**15. Tunneling evidence for spatial location of the charge-density-wave induced band splitting in 1T-TaSe2**

By: Stoltz, D.; Bielmann, M.; Bovet, M.; et al.
PHYSICAL REVIEW B   Volume: 76   Issue: 7    Article Number: 073410   Published: AUG 2007

| 0 | 1 | 0 | 0 | 0 | 2 | 0.18 |
|---|---|---|---|---|---|------|

**16. Investigation of surface structure related features in the multiple-scattering simulations of photoelectron diffraction of 3C-SiC(001)-c(4 x 2)**

By: Stoltz, D.; Stoltz, S. E.; Widstrand, S. M.; et al.
PHYSICA B-CONDENSED MATTER   Volume: 395   Issue: 1-2   Pages: 130-137   Published: MAY 31 2007

| 2 | 0 | 0 | 0 | 0 | 2 | 0.18 |
|---|---|---|---|---|---|------|

**17. Angle-scanned photoemission on YbHx: relevance for switchable mirrors**

By: Hayoz, J; Koitzsch, C; Popovic, D; et al.
Conference: 13th International Conference on Vacuum Ultraviolet Radiation Physics (VUV-13) Location: TRIESTE, ITALY Date: JUL 23-27, 2001
SURFACE REVIEW AND LETTERS   Volume: 9   Issue: 1   Pages: 235-241   Published: FEB 2002

| 0 | 0 | 0 | 0 | 0 | 2 | 0.12 |
|---|---|---|---|---|---|------|

**18. X-ray photoelectron diffraction investigation of the cleavage plane in IT-transition metal dichalcogenides**

By: Stoltz, D.; Stoltz, S. E.
PHYSICA B-CONDENSED MATTER   Volume: 398   Issue: 1   Pages: 172-177   Published: AUG 1 2007

| 0 | 0 | 0 | 0 | 0 | 1 | 0.09 |
|---|---|---|---|---|---|------|

**19. Surface resonance on the (6 root 3 x 6 root 3)-R30 degrees-reconstructed 5 ML Au on (root 3 x root 3)-R30 degrees-4H-SiC(0001)**

By: Stoltz, D.; Stoltz, S. E.; Johansson, L. S. O.
SURFACE SCIENCE   Volume: 601   Issue: 12   Pages: 2508-2511   Published: JUN 15 2007

| 0 | 0 | 0 | 0 | 0 | 1 | 0.09 |
|---|---|---|---|---|---|------|

**20. Fingerprinting substitution sites in Pb, Dy-Bi2Sr2Ca1Cu2O8+delta using X-ray Photoelectron Diffraction**

By: Popovic, D; Bovet, M; Berger, H; et al.
EUROPEAN PHYSICAL JOURNAL-APPLIED PHYSICS   Volume: 30   Issue: 3   Pages: 171-174   Published: JUN 2005

| 0 | 0 | 0 | 0 | 0 | 1 | 0.08 |
|---|---|---|---|---|---|------|

Select Page   |   Save to Text File

Sort by: Times Cited -- highest to lowest

Page 2 of 3

*23 records matched your query of the 37,941,506 in the data limits you selected.*

*23 records matched your query of the 37,941,506 in the data limits you selected.*

| Web of Science | InCites | Journal Citation Reports | Essential Science Indicators | EndNote | | Sign In ▼ | Help | English ▼ |

# Web of Science

| Search | Search Results | | | My Tools ▼ | Search History | Marked List 23 |

## Citation report for 23 results from Web of Science Core Collection  between  1996 ▼  and  2017 ▼   Go

You searched for: **From Marked List: ...More**

This report reflects citations to source items indexed within Web of Science Core Collection. Perform a Cited Reference Search to include citations to items not indexed within Web of Science Core Collection.

Export Data:  Save to Text File  ▼

**Total Publications**  ⤢

**23**

1995    2014
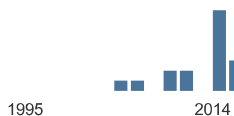
**h-index** ⓘ

**7**

**Average citations per item** ⓘ

**13.57**

**Sum of Times Cited** ⓘ

**312**

**Without self citations** ⓘ

**296**

**Citing articles** ⓘ

**291**

**Without self citations** ⓘ

**281**

**Sum of Times Cited per Year**
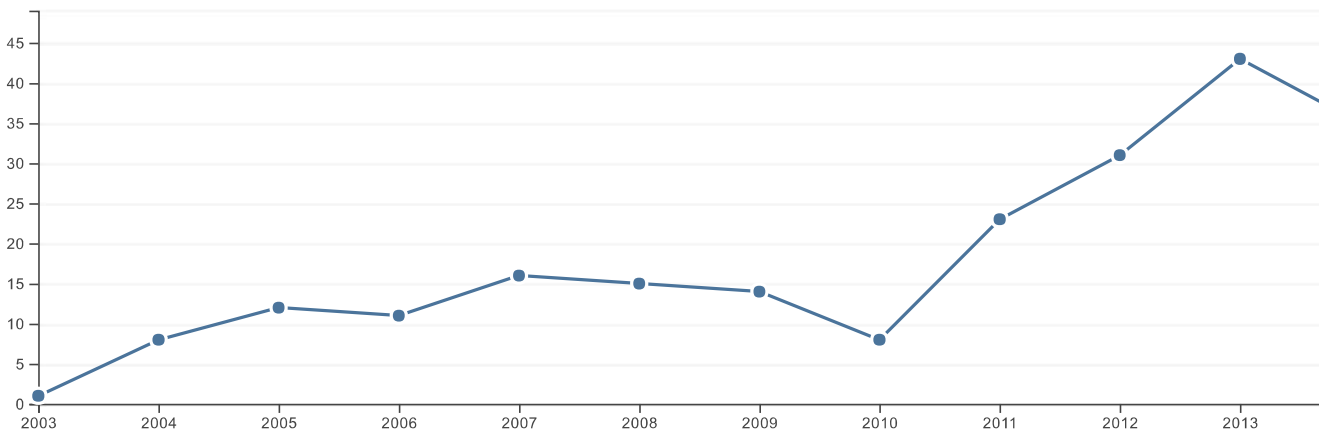


Sort by: Times Cited -- highest to lowest ▼

Page 3 of 3

|  | 2013 ◄ | 2014 | 2015 | 2016 | 2017 ► | Total | Average Citations per Year |
|---|---|---|---|---|---|---|---|
| Use the checkboxes to remove individual items from this Citation Report | | | | | | | |
| or restrict to items published between 1996 ▼ and 2017 ▼  Go | 43 | 35 | 33 | 48 | 14 | 312 | 20.80 |
| 21. **Atomic origin of the scanning tunneling microscopy images of charge-density-waves on 1T-TaSe2** <br> By: Stoltz, D.; Bielmann, M.; Schlapbach, L.; et al. | 0 | 0 | 0 | 0 | 0 | 0 | 0.00 |

PHYSICA B-CONDENSED MATTER    Volume: 403   Issue: 13-16   Pages:
2207-2210   Published: JUL 1 2008

22.  **Two-dimensional states in the electronic structure of Au/(root
     3 x root 3)-R30 degrees-4H-SiC(0001)**

     By: Stoltz, D.; Stoltz, S. E.; Johansson, L. S. O.                          0      0      0      0      0      0      0.00
     JOURNAL OF ELECTRON SPECTROSCOPY AND RELATED PHENOMENA
      Volume: 163   Issue: 1-3   Pages: 1-6   Published: APR 2008

23.  **Spectroscopic evidence for reversible hydrogen storage in
     unordered Mg5Ni1 thin films**

     By: Stoltz, S. E.; Stoltz, D.                                              0      0      0      0      0      0      0.00
     JOURNAL OF PHYSICS-CONDENSED MATTER   Volume: 19   Issue: 44
       Article Number: 446010   Published: NOV 7 2007

☐ Select Page          🖶  ✉          Save to Text File      ▾

---

Sort by:  Times Cited -- highest to lowest   ▾                                  Page  3    of  3

*23 records matched your query of the 37,941,506 in the data limits you selected.*

---

# Web of Science

Search | Search Results | My Tools ▾ | Search History | Marked List 23

## Citing Articles: 17
*(from Web of Science Core Collection)*

**For:** Oxidation of Al-Pd-Mn quasicrystal surfaces **...Less**

**Times Cited Counts**

18 in All Databases

17 in Web of Science Core Collection

0 in BIOSIS Citation Index

1 in Chinese Science Citation Database

0 data sets in Data Citation Index

0 publication in Data Citation Index

0 in Russian Science Citation Index

0 in SciELO Citation Index

**View Additional Times Cited Counts**

**Refine Results**

Search within results for...

### Publication Years ▼
- [ ] 2004 (5)
- [ ] 2014 (2)
- [ ] 2009 (2)
- [ ] 2008 (2)
- [ ] 2007 (1)

**more options / values...**

**Refine**

### Web of Science Categories ▼
- [ ] CHEMISTRY PHYSICAL (9)
- [ ] PHYSICS CONDENSED MATTER (8)
- [ ] MATERIALS SCIENCE MULTIDISCIPLINARY (5)
- [ ] METALLURGY METALLURGICAL ENGINEERING (3)
- [ ] ENGINEERING CHEMICAL (1)

**more options / values...**

**Refine**

### Document Types ▼
- [ ] ARTICLE (12)
- [ ] REVIEW (5)
- [ ] BOOK CHAPTER (1)

**more options / values...**

**Refine**

---

Sort by: Publication Date -- newest to oldest ▾

Page 1 of 1

- [ ] Select Page | 🖥 ✉ 5K
- Save to Other File Formats ▾ | **Add to Marked List**

**Create Citation Report**

**≡ Analyze Results**

1. **Al62Cu25Fe12 and Quasicrystalline Phases and Their Influence on Oxidation**

   By: Lucena Agostinho Jamshidi, Lourdes Cristina; Rodbari, Reza Jamshidi; Nascimento, Luciano; et al.
   ORBITAL-THE ELECTRONIC JOURNAL OF CHEMISTRY Volume: 9 Issue: 1 Pages: 27-35 Published: JAN-MAR 2017

   **Full Text from Publisher** | **View Abstract**

   Times Cited: 0
   *(from Web of Science Core Collection)*

   Usage Count

2. **Formation of less-known structurally complex zeta(b) and orthorhombic quasicrystalline approximant epsilon(n) on solidification of selected Al-Pd-Cr alloys**

   By: Adamech, M.; Cernickova, I.; Duriska, L.; et al.
   MATERIALS CHARACTERIZATION Volume: 97 Pages: 189-198 Published: NOV 2014

   **Full Text from Publisher** | **View Abstract**

   Times Cited: 0
   *(from Web of Science Core Collection)*

   Usage Count

3. **Fine structure of phases of epsilon-family in Al73.8Pd11.9Co14.3 alloy**

   By: Cernickova, Ivona; Svec, Peter; Watanabe, Shinichi; et al.
   JOURNAL OF ALLOYS AND COMPOUNDS Volume: 609 Pages: 73-79 Published: OCT 5 2014

   **Full Text from Publisher** | **View Abstract**

   Times Cited: 3
   *(from Web of Science Core Collection)*

   Usage Count

4. **STM and XPS investigation of the oxidation of the Al-4(Cr,Fe) quasicrystal approximant**

   By: Parle, J. K.; Beni, A.; Dhanak, V. R.; et al.
   APPLIED SURFACE SCIENCE Volume: 283 Pages: 276-282 Published: OCT 15 2013

   **Full Text from Publisher** | **View Abstract**

   Times Cited: 7
   *(from Web of Science Core Collection)*

   Usage Count

5. **Surface oxidation of the icosahedral Ag-In-Yb quasicrystal**

   By: Nugent, P. J.; Simutis, G.; Dhanak, V. R.; et al.
   PHYSICAL REVIEW B Volume: 82 Issue: 1 Article Number: 014201 Published: JUL 9 2010

   **View Abstract**

   Times Cited: 6
   *(from Web of Science Core Collection)*

   Usage Count

6. **Oxygen-induced surface faceting of the threefold-symmetry surface of icosahedral AlPdMn quasicrystal**

   By: Burkardt, S.; Erbudak, M.
   SURFACE SCIENCE Volume: 603 Issue: 14 Pages: 2248-2253 Published: JUL 15 2009

   **Full Text from Publisher** | **View Abstract**

   Times Cited: 1
   *(from Web of Science Core Collection)*

   Usage Count

**Organizations-Enhanced** ▼

☐ SWISS FEDERAL INSTITUTE OF TECHNOLOGY ZURICH (4)

☐ BOGAZICI UNIVERSITY (4)

☐ UNITED STATES DEPARTMENT OF ENERGY DOE (3)

☐ IOWA STATE UNIVERSITY (3)

☐ AMES NATIONAL LABORATORY (3)

more options / values...

**Refine**

**Funding Agencies** ◀

**Open Access** ◀

**Authors** ◀

**View all options**

*For advanced refine options, use*

**Analyze Results**

---

☐ 7. **High-temperature surface oxidation of the decagonal AlCoNi quasicrystal**

By: Burkardt, S.; Erbudak, M.; Mader, R.
SURFACE SCIENCE　Volume: 603　Issue: 6　Pages: 867-872　Published: MAR 15 2009

**Full Text from Publisher**　**View Abstract**

Times Cited: **8**
*(from Web of Science Core Collection)*

Usage Count

☐ 8. **Bulk and surface structure of the clean and adsorbate-covered decagonal Al-Co-Ni quasicrystal**

By: Burkardt, S.; Deloudi, S.; Erbudak, M.; et al.
JOURNAL OF PHYSICS-CONDENSED MATTER
　Volume: 20　Issue: 31　Article Number: 314006　Published: AUG 6 2008

**View Abstract**

Times Cited: **11**
*(from Web of Science Core Collection)*

Usage Count

☐ 9. **Quasicrystal surfaces**

By: Thiel, Patricia A.
ANNUAL REVIEW OF PHYSICAL CHEMISTRY　Book Series: Annual Review of Physical Chemistry　Volume: 59　Pages: 129-152　Published: 2008

**View Abstract**

Times Cited: **28**
*(from Web of Science Core Collection)*

Usage Count

☐ 10. **Formation of a well ordered ultrathin aluminum oxide film on icosahedral AlPdMn quasicrystal**

By: Longchamp, J.-N.; Burkardt, S.; Erbudak, M.; et al.
PHYSICAL REVIEW B　Volume: 76　Issue: 9　Article Number: 094203　Published: SEP 2007

**View Abstract**

Times Cited: **11**
*(from Web of Science Core Collection)*

Usage Count

☐ 11. **Oxidation kinetics of the quasicrystalline i-AlCuFe phase compared with that of crystalline omega-AlCuFe and pure aluminum**

By: Rouxel, D; Gil-Gavatz, M; Pigeat, P; et al.
JOURNAL OF NON-CRYSTALLINE SOLIDS　Volume: 351　Issue: 10-11　Pages: 802-809　Published: APR 15 2005

**Full Text from Publisher**　**View Abstract**

Times Cited: **14**
*(from Web of Science Core Collection)*

Usage Count

☐ 12. **Friction and adhesion properties of clean and oxidized Al-Ni-Co decagonal quasicrystals: a UHV atomic force microscopy/scanning tunneling microscopy study**

By: Park, JY; Ogletree, DF; Salmeron, M; et al.
TRIBOLOGY LETTERS　Volume: 17　Issue: 3　Pages: 629-636　Published: OCT 2004

**View Abstract**

Times Cited: **53**
*(from Web of Science Core Collection)*

Usage Count

☐ 13. **Structure and oxidation at quasicrystal surfaces**

By: Thiel, PA
PROGRESS IN SURFACE SCIENCE　Volume: 75　Issue: 3-8　Pages: 191-204　Published: AUG 2004

**Full Text from Publisher**　**View Abstract**

Times Cited: **11**
*(from Web of Science Core Collection)*

Usage Count

☐ 14. **Structure and electronic structure of quasicrystal and approximant surfaces: a photoemission study**

By: Naumovic, D
PROGRESS IN SURFACE SCIENCE　Volume: 75　Issue: 3-8　Pages: 205-225　Published: AUG 2004

**Full Text from Publisher**　**View Abstract**

Times Cited: **4**
*(from Web of Science Core Collection)*

Usage Count

☐ 15. **Corrosion behaviour of Al-Cu-Fe alloys containing a quasicrystalline phase**

By: Huttunen-Saarivirta, E; Tiainen, T

Times Cited: **12**
*(from Web of Science Core Collection)*

MATERIALS CHEMISTRY AND PHYSICS   Volume: 85
Issue: 2-3   Pages: 383-395   Published: JUN 15 2004

**Full Text from Publisher**        **View Abstract**

16.  **Microstructure, fabrication and properties of quasicrystalline Al-Cu-Fe alloys: a review**

By: Huttunen-Saarivirta, E
JOURNAL OF ALLOYS AND COMPOUNDS   Volume: 363
Issue: 1-2   Pages: 150-174   Published: JAN 28 2004

**Full Text from Publisher**        **View Abstract**

Times Cited: **92**
*(from Web of Science Core Collection)*

17.  **X-ray photoelectron diffraction. Possibilities of surface structural analysis**

By: Shalaeva, EV; Kuznetsov, MV
JOURNAL OF STRUCTURAL CHEMISTRY   Volume: 44
Issue: 3   Pages: 465-498   Published: MAY-JUN 2003

**View Abstract**

Times Cited: **3**
*(from Web of Science Core Collection)*

Select Page        **5K**

Save to Other File Formats    ▾    **Add to Marked List**

Sort by:   Publication Date -- newest to oldest   ▾

Show:   25 per page   ▾

Page [ 1 ]   of   1

*17 records matched your query of the 37,941,506 in the data limits you selected.*

| Web of Science | InCites | Journal Citation Reports | Essential Science Indicators | EndNote | | Sign In ▾ | Help | English ▾ |

# Web of Science

| Search | Search Results | | My Tools ▾ | Search History | Marked List   23 |

## Citing Articles: 2
*(from Web of Science Core Collection)*

**For:** Angle-scanned photoemission on YbHx: relevance for switchable mirrors **...Less**

### Times Cited Counts

2 in All Databases

2 in Web of Science Core Collection

0 in BIOSIS Citation Index

0 in Chinese Science Citation Database

0 data sets in Data Citation Index

0 publication in Data Citation Index

0 in Russian Science Citation Index

0 in SciELO Citation Index

**View Additional Times Cited Counts**

---

**Refine Results**

---

Search within results for...

---

### Publication Years ▼

☐ 2007 (1)

☐ 2005 (1)

**more options / values...**

**Refine**

### Web of Science Categories ▼

☐ PHYSICS CONDENSED MATTER (1)

☐ PHYSICS APPLIED (1)

**more options / values...**

**Refine**

### Document Types ▼

☐ ARTICLE (2)

**Refine**

### Organizations-Enhanced ▼

☐ UNIVERSITY OF NEUCHATEL (1)

☐ SAARLAND UNIVERSITY (1)

☐ ROYAL INSTITUTE OF TECHNOLOGY (1)

☐ LUND UNIVERSITY (1)

☐ ECOLE POLYTECHNIQUE FEDERALE DE LAUSANNE (1)

**more options / values...**

---

Sort by:   Publication Date -- newest to oldest ▾     Page [1] of 1

☐ Select Page    🗔 ✉ **5K**

Save to Other File Formats   ▾   **Add to Marked List**

**Create Citation Report**

≡ **Analyze Results**

1. **X-ray photoelectron diffraction investigation of the cleavage plane in IT-transition metal dichalcogenides**

   By: Stoltz, D.; Stoltz, S. E.
   PHYSICA B-CONDENSED MATTER   Volume: 398   Issue: 1   Pages: 172-177   Published: AUG 1 2007

   **Full Text from Publisher**    **View Abstract**

   Times Cited: **1**
   *(from Web of Science Core Collection)*

   Usage Count

2. **Fingerprinting substitution sites in Pb, Dy-Bi2Sr2Ca1Cu2O8+delta using X-ray Photoelectron Diffraction**

   By: Popovic, D; Bovet, M; Berger, H; et al.
   EUROPEAN PHYSICAL JOURNAL-APPLIED PHYSICS   Volume: 30   Issue: 3   Pages: 171-174   Published: JUN 2005

   **View Abstract**

   Times Cited: **1**
   *(from Web of Science Core Collection)*

   Usage Count

☐ Select Page    🗔 ✉ **5K**

Save to Other File Formats   ▾   **Add to Marked List**

Sort by:   Publication Date -- newest to oldest ▾     Page [1] of 1

Show:   25 per page ▾

*2 records matched your query of the 37,941,506 in the data limits you selected.*

**Refine**

Funding Agencies ◀

Open Access ◀

Authors ◀

**View all options**

*For advanced refine options, use*

**Analyze Results**

| Web of Science | InCites | Journal Citation Reports | Essential Science Indicators | EndNote | | Sign In ▾ | Help | English ▾ |

# Web of Science

| Search | Search Results | | | My Tools ▾ | Search History | Marked List | 23 |

## Citing Articles: 28
*(from Web of Science Core Collection)*

**For:** Pseudogapped Fermi surfaces of 1T-TaS2 and 1T-TaSe2: A charge density wave effect ...Less

### Times Cited Counts

28 in All Databases

28 in Web of Science Core Collection

0 in BIOSIS Citation Index

0 in Chinese Science Citation Database

0 data sets in Data Citation Index

0 publication in Data Citation Index

0 in Russian Science Citation Index

0 in SciELO Citation Index

**View Additional Times Cited Counts**

---

## Refine Results

*Search within results for...*

**Filter results by:**

☐ Highly Cited in Field (2)

**Refine**

### Publication Years ▾

☐ 2015 (4)
☐ 2012 (4)
☐ 2005 (4)
☐ 2016 (3)
☐ 2014 (3)

more options / values...

**Refine**

### Web of Science Categories ▾

☐ PHYSICS CONDENSED MATTER (18)
☐ PHYSICS APPLIED (5)
☐ PHYSICS MULTIDISCIPLINARY (4)
☐ MATERIALS SCIENCE MULTIDISCIPLINARY (4)
☐ NANOSCIENCE NANOTECHNOLOGY (3)

more options / values...

**Refine**

### Document Types ▾

☐ ARTICLE (22)
☐ REVIEW (5)

---

Sort by: Publication Date -- newest to oldest ▾

Page 1 of 1

☐ Select Page    🗗 ✉ **5K**

Save to Other File Formats ▾    **Add to Marked List**

**Create Citation Report**

**≣ Analyze Results**

☐ 1. **Raman spectroscopy of transition metal dichalcogenides**

By: Saito, R.; Tatsumi, Y.; Huang, S.; et al.
JOURNAL OF PHYSICS-CONDENSED MATTER
Volume: 28 Issue: 35 Article Number: 353002 Published: SEP 7 2016

**View Abstract**

Times Cited: **7**
*(from Web of Science Core Collection)*

Usage Count

☐ 2. **Nature of charge density waves and superconductivity in 1T-TaSe2-xTex**

By: Liu, Y.; Shao, D. F.; Li, L. J.; et al.
PHYSICAL REVIEW B Volume: 94 Issue: 4 Article Number: 045131 Published: JUL 20 2016

**View Abstract**

Times Cited: **5**
*(from Web of Science Core Collection)*

Usage Count

☐ 3. **Epitaxial 2D MoSe2 (HfSe2) Semiconductor/2D TaSe2 Metal van der Waals Heterostructures**

By: Tsoutsou, Dimitra; Aretouli, Kleopatra E.; Tsipas, Polychronis; et al.
ACS APPLIED MATERIALS & INTERFACES Volume: 8 Issue: 3 Pages: 1836-1841 Published: JAN 27 2016

**View Abstract**

Times Cited: **6**
*(from Web of Science Core Collection)*

Usage Count

☐ 4. **Electronic and magnetic properties of 1T-TiSe2 nanoribbons**

By: Ozaydin, H. D.; Sahin, H.; Kang, J.; et al.
2D MATERIALS Volume: 2 Issue: 4 Article Number: 044002 Published: DEC 2015

**View Abstract**

Times Cited: **2**
*(from Web of Science Core Collection)*

Usage Count

☐ 5. **Pseudogap from ARPES experiment: Three gaps in cuprates and topological superconductivity**

By: Kordyuk, A. A.
LOW TEMPERATURE PHYSICS Volume: 41 Issue: 5 Pages: 319-341 Published: MAY 2015

**Full Text from Publisher**    **View Abstract**

Times Cited: **17**
*(from Web of Science Core Collection)*

Usage Count

☐ 6. **Zone-Folded Phonons and the Commensurate-Incommensurate Charge-Density-Wave Transition in 1T-TaSe2 Thin Films**

By: Samnakay, R.; Wickramaratne, D.; Pope, T. R.; et al.
NANO LETTERS Volume: 15 Issue: 5 Pages: 2965-2973 Published: MAY 2015

**View Abstract**

Times Cited: **15**
*(from Web of Science Core Collection)*

Usage Count

PROCEEDINGS PAPER (1)

more options / values...

**Refine**

## Organizations-Enhanced ▼

UNIVERSITY OF NEUCHATEL (6)

ECOLE POLYTECHNIQUE
FEDERALE DE LAUSANNE (6)

CHINESE ACADEMY OF
SCIENCES (6)

TOHOKU UNIVERSITY (4)

UNIVERSITY OF KIEL (3)

more options / values...

**Refine**

Funding Agencies ◀

Open Access ◀

Authors ◀

**View all options**

*For advanced refine options, use*

**Analyze Results**

---

7. **Science and technology roadmap for graphene, related two-dimensional crystals, and hybrid systems**

By: Ferrari, Andrea C.; Bonaccorso, Francesco; Fal'ko, Vladimir; et al.
NANOSCALE   Volume: 7   Issue: 11   Pages: 4598-4810
Published: 2015

View Abstract

Times Cited: **478**
*(from Web of Science Core Collection)*

**Highly Cited Paper**

Usage Count

8. **Spin polarization driven by a charge-density wave in monolayer 1T-TaS2**

By: Zhang, Qingyun; Gan, Li-Yong; Cheng, Yingchun; et al.
PHYSICAL REVIEW B   Volume: 90   Issue: 8   Article
Number: 081103   Published: AUG 6 2014

View Abstract

Times Cited: **6**
*(from Web of Science Core Collection)*

Usage Count

9. **Coexistence of superconductivity and charge-density-wave domain in 1T-FexTa1-xSSe**

By: Liu, Y.; Lu, W. J.; Li, L. J.; et al.
APPLIED PHYSICS LETTERS   Volume: 104   Issue: 25
Article Number: 252601   Published: JUN 23 2014

View Abstract

Times Cited: **2**
*(from Web of Science Core Collection)*

Usage Count

10. **How fast can a Peierls-Mott insulator be melted?**

By: Sohrt, C.; Stange, A.; Bauer, M.; et al.
FARADAY DISCUSSIONS   Volume: 171   Pages: 243-257
Published: 2014

View Abstract

Times Cited: **14**
*(from Web of Science Core Collection)*

Usage Count

11. **Superconductivity and bandwidth-controlled Mott metal-insulator transition in 1T-TaS2-xSex**

By: Ang, R.; Miyata, Y.; Ieki, E.; et al.
PHYSICAL REVIEW B   Volume: 88   Issue: 11   Article
Number: 115145   Published: SEP 30 2013

View Abstract

Times Cited: **21**
*(from Web of Science Core Collection)*

Usage Count

12. **Real-Space Coexistence of the Melted Mott State and Superconductivity in Fe-Substituted 1T-TaS2**

By: Ang, R.; Tanaka, Y.; Ieki, E.; et al.
PHYSICAL REVIEW LETTERS   Volume: 109   Issue: 17
Article Number: 176403   Published: OCT 23 2012

View Abstract

Times Cited: **20**
*(from Web of Science Core Collection)*

Usage Count

13. **Fe-doping-induced superconductivity in the charge-density-wave system 1T-TaS2**

By: Li, L. J.; Lu, W. J.; Zhu, X. D.; et al.
EPL   Volume: 97   Issue: 6   Article Number: 67005
Published: MAR 2012

View Abstract

Times Cited: **20**
*(from Web of Science Core Collection)*

Usage Count

14. **Pseudogap in the chain states of YBa2Cu3O6.6**

By: Zabolotnyy, V. B.; Kordyuk, A. A.; Evtushinsky, D.; et al.
PHYSICAL REVIEW B   Volume: 85   Issue: 6   Article
Number: 064507   Published: FEB 8 2012

View Abstract

Times Cited: **12**
*(from Web of Science Core Collection)*

Usage Count

15. **Effect of Fe-doping on charge density wave in 1T-TaS2: Instability and induced superconductivity**

By: Li, Lijun; Lu, Wenjian; Zhu, Xiangde; et al.
Book Group Author(s): IOP
Conference: 26th International Conference on Low Temperature
Physics (LT) Location: Beijing, PEOPLES R CHINA Date: AUG
10-17, 2011

Times Cited: **0**
*(from Web of Science Core Collection)*

Usage Count

26TH INTERNATIONAL CONFERENCE ON LOW
TEMPERATURE PHYSICS (LT26), PTS 1-5   Book Series:
Journal of Physics Conference Series   Volume: 400   Article
Number: UNSP 022061   Published: 2012

**Full Text from Publisher**        **View Abstract**

16. **On the origin of charge-density waves in select
    layered transition-metal dichalcogenides**

    By: Rossnagel, K.
    JOURNAL OF PHYSICS-CONDENSED MATTER
    Volume: 23   Issue: 21   Article Number: 213001   Published:
    JUN 1 2011

    **View Abstract**

Times Cited: **128**
*(from Web of Science Core
Collection)*

**Highly Cited Paper**

**Usage Count**

17. **Electron-phonon coupling in compressed 1T-TaS2:
    Stability and superconductivity from first principles**

    By: Liu, Amy Y.
    PHYSICAL REVIEW B   Volume: 79   Issue: 22   Article
    Number: 220515   Published: JUN 2009

    **View Abstract**

Times Cited: **16**
*(from Web of Science Core
Collection)*

**Usage Count**

18. **Atomic origin of the scanning tunneling microscopy
    images of charge-density-waves on 1T-TaSe2**

    By: Stoltz, D.; Bielmann, M.; Schlapbach, L.; et al.
    PHYSICA B-CONDENSED MATTER   Volume: 403   Issue:
    13-16   Pages: 2207-2210   Published: JUL 1 2008

    **Full Text from Publisher**        **View Abstract**

Times Cited: **0**
*(from Web of Science Core
Collection)*

**Usage Count**

19. **Fermi surface of layered compounds and bulk
    charge density wave systems**

    By: Clerc, F.; Battaglia, C.; Cercellier, H.; et al.
    JOURNAL OF PHYSICS-CONDENSED MATTER
    Volume: 19   Issue: 35   Article Number: 355002   Published:
    SEP 5 2007

    **View Abstract**

Times Cited: **20**
*(from Web of Science Core
Collection)*

**Usage Count**

20. **The Fermi surface of Sn/Ge(111) and Pb/Ge(111)**

    By: Tejeda, A.; Cortes, R.; Lobo, J.; et al.
    JOURNAL OF PHYSICS-CONDENSED MATTER
    Volume: 19   Issue: 35   Article Number: 355008   Published:
    SEP 5 2007

    **View Abstract**

Times Cited: **8**
*(from Web of Science Core
Collection)*

**Usage Count**

21. **Tunneling evidence for spatial location of the charge-
    density-wave induced band splitting in 1T-TaSe2**

    By: Stoltz, D.; Bielmann, M.; Bovet, M.; et al.
    PHYSICAL REVIEW B   Volume: 76   Issue: 7   Article
    Number: 073410   Published: AUG 2007

    **View Abstract**

Times Cited: **2**
*(from Web of Science Core
Collection)*

**Usage Count**

22. **Lattice-distortion-enhanced electron-phonon
    coupling and Fermi surface nesting in 1T-TaS2**

    By: Clerc, F.; Battaglia, C.; Bovet, M.; et al.
    PHYSICAL REVIEW B   Volume: 74   Issue: 15   Article
    Number: 155114   Published: OCT 2006

    **View Abstract**

Times Cited: **26**
*(from Web of Science Core
Collection)*

**Usage Count**

23. **Fermi-surface-induced lattice distortion in NbTe2**

    By: Battaglia, C; Cercellier, H; Clerc, F; et al.
    PHYSICAL REVIEW B   Volume: 72   Issue: 19   Article
    Number: 195114   Published: NOV 2005

    **View Abstract**

Times Cited: **16**
*(from Web of Science Core
Collection)*

**Usage Count**

24. **Continuous tuning of electronic correlations by alkali adsorption on layered 1T-TaS2**

By: Rossnagel, K; Rotenberg, E; Koh, H; et al.
PHYSICAL REVIEW LETTERS    Volume: 95    Issue: 12
    Article Number: 126403    Published: SEP 16 2005

View Abstract

Times Cited: **10**
*(from Web of Science Core Collection)*

**Usage Count**

25. **Low-energy quasiparticle states at superconductor/charge-density-wave interfaces**

By: Bobkova, IV; Barash, YS
PHYSICAL REVIEW B    Volume: 71    Issue: 14    Article
Number: 144510    Published: APR 2005

View Abstract

Times Cited: **5**
*(from Web of Science Core Collection)*

**Usage Count**

26. **First-principle study of materials involved in incommensurate transitions**

By: Caracas, R; Gonze, X
ZEITSCHRIFT FUR KRISTALLOGRAPHIE    Volume: 220
    Issue: 5-6    Pages: 511-520    Published: 2005

View Abstract

Times Cited: **4**
*(from Web of Science Core Collection)*

**Usage Count**

27. **High-resolution angle-resolved photoemission study of incommensurate charge-density-wave compound CeTe3**

By: Komoda, H; Sato, T; Souma, S; et al.
PHYSICAL REVIEW B    Volume: 70    Issue: 19    Article
Number: 195101    Published: NOV 2004

View Abstract

Times Cited: **26**
*(from Web of Science Core Collection)*

**Usage Count**

28. **Spin-orbit splitting in the valence bands of 1T-TaS2 and 1T-TaSe2**

By: Clerc, F; Bovet, M; Berger, H; et al.
JOURNAL OF PHYSICS-CONDENSED MATTER
    Volume: 16    Issue: 18    Pages: 3271-3278    Published: MAY 12 2004

View Abstract

Times Cited: **13**
*(from Web of Science Core Collection)*

**Usage Count**

Select Page        5K

Save to Other File Formats    ▼        Add to Marked List

Sort by:    Publication Date -- newest to oldest    ▼

Show:    50 per page    ▼

Page  1    of  1

*28 records matched your query of the 37,941,506 in the data limits you selected.*

# Web of Science

Search | Search Results | My Tools ▼ | Search History | Marked List 23

## Citing Articles: 42
*(from Web of Science Core Collection)*

**For:** Spin-orbit splitting of the Shockley state in the Ag/Au(111) interface ...Less

**Times Cited Counts**

42 in All Databases

42 in Web of Science Core Collection

0 in BIOSIS Citation Index

0 in Chinese Science Citation Database

0 data sets in Data Citation Index

0 publication in Data Citation Index

0 in Russian Science Citation Index

0 in SciELO Citation Index

**View Additional Times Cited Counts**

## Refine Results

Search within results for...

### Publication Years ▼

☐ 2009 (6)
☐ 2006 (6)
☐ 2005 (6)
☐ 2011 (5)
☐ 2012 (4)

more options / values...

**Refine**

### Web of Science Categories ▼

☐ PHYSICS CONDENSED MATTER (25)
☐ PHYSICS MULTIDISCIPLINARY (8)
☐ CHEMISTRY PHYSICAL (5)
☐ PHYSICS APPLIED (3)
☐ MATERIALS SCIENCE MULTIDISCIPLINARY (3)

more options / values...

**Refine**

### Document Types ▼

☐ ARTICLE (37)
☐ REVIEW (5)
☐ PROCEEDINGS PAPER (3)

more options / values...

**Refine**

---

Sort by: Publication Date -- newest to oldest ▼

Page 1 of 1

☐ Select Page | 🖨 ✉ 5K

Save to Other File Formats ▼ | **Add to Marked List**

**Create Citation Report**

📋 **Analyze Results**

☐ 1. **Spin-polarized quantum confinement in nanostructures: Scanning tunneling microscopy**

By: Oka, Hirofumi; Brovko, Oleg O.; Corbetta, Marco; et al.
REVIEWS OF MODERN PHYSICS Volume: 86 Issue: 4 Pages: 1127-1168 Published: OCT 3 2014

**View Abstract**

Times Cited: **16**
*(from Web of Science Core Collection)*

Usage Count

☐ 2. **Effect of spin-orbit coupling on atomic-like and delocalized quantum well states in Au overlayers on W(110) and Mo(110)**

By: Shikin, A. M.; Rybkina, A. A.; Rusinova, M. V.; et al.
NEW JOURNAL OF PHYSICS Volume: 15 Article Number: 125014 Published: DEC 10 2013

**Full Text from Publisher** | **View Abstract**

Times Cited: **4**
*(from Web of Science Core Collection)*

Usage Count

☐ 3. **Surface segregation of silver atoms on Au-Ag alloys according to data of laser-heating induced temperature potential shifts, XPS and conventional electrochemical methods**

By: Manzhos, Roman A.; Krivenko, Aleksandr G.; Doronin, Sergey V.; et al.
JOURNAL OF ELECTROANALYTICAL CHEMISTRY Volume: 704 Pages: 175-182 Published: SEP 1 2013

**Full Text from Publisher** | **View Abstract**

Times Cited: **8**
*(from Web of Science Core Collection)*

Usage Count

☐ 4. **Rashba split surface states in BiTeBr**

By: Eremeev, S. V.; Rusinov, I. P.; Nechaev, I. A.; et al.
NEW JOURNAL OF PHYSICS Volume: 15 Article Number: 075015 Published: JUL 17 2013

**Full Text from Publisher** | **View Abstract**

Times Cited: **26**
*(from Web of Science Core Collection)*

Usage Count

☐ 5. **Decay of Shockley surface state by randomly adsorbed Bi atoms at Ag(111) surfaces**

By: Fukumoto, Hiroyuki; Aoki, Yuki; Hirayama, Hiroyuki
PHYSICAL REVIEW B Volume: 86 Issue: 16 Article Number: 165311 Published: OCT 11 2012

**View Abstract**

Times Cited: **4**
*(from Web of Science Core Collection)*

Usage Count

☐ 6. **Modification of the surface-state occupancy on noble metal films with stacking fault arrays**

By: Mishra, Puneet; Uchihashi, Takashi; Nakayama, Tomonobu
APPLIED PHYSICS LETTERS Volume: 100 Issue: 14 Article Number: 141609 Published: APR 2 2012

**View Abstract**

Times Cited: **1**
*(from Web of Science Core Collection)*

Usage Count

7. **Electronic structure study of ultrathin Ag(111) films modified by a Si(111) substrate and root 3 x root 3-Ag2Bi surface**

By: Ogawa, M.; Sheverdyaeva, P. M.; Moras, P.; et al.
JOURNAL OF PHYSICS-CONDENSED MATTER Volume: 24 Issue: 11 Article Number: 115501 Published: MAR 21 2012

**View Abstract**

Times Cited: **1**
*(from Web of Science Core Collection)*

**Usage Count**

8. **Electronic substrate-mediated interactions**

By: Han, Patrick; Weiss, Paul S.
SURFACE SCIENCE REPORTS Volume: 67 Issue: 2 Pages: 19-81 Published: FEB 1 2012

**Full Text from Publisher** **View Abstract**

Times Cited: **43**
*(from Web of Science Core Collection)*

**Usage Count**

9. **One-dimensional surface states on a striped Ag thin film with stacking fault arrays**

By: Uchihashi, Takashi; Mishra, Puneet; Kobayashi, Katsuyoshi; et al.
PHYSICAL REVIEW B Volume: 84 Issue: 19 Article Number: 195466 Published: NOV 28 2011

**View Abstract**

Times Cited: **4**
*(from Web of Science Core Collection)*

**Usage Count**

10. **Current-induced spin-orbit torques**

By: Gambardella, Pietro; Mihai Miron, Ioan
PHILOSOPHICAL TRANSACTIONS OF THE ROYAL SOCIETY A-MATHEMATICAL PHYSICAL AND ENGINEERING SCIENCES Volume: 369 Issue: 1948 Pages: 3175-3197 Published: AUG 13 2011

**View Abstract**

Times Cited: **74**
*(from Web of Science Core Collection)*

**Usage Count**

11. **Growth and crystalline structure of Ag layers on Au(111)**

By: Jurczyszyn, M.; Morawski, I.; Nowicki, M.
THIN SOLID FILMS Volume: 519 Issue: 18 Pages: 6196-6201 Published: JUL 1 2011

**Full Text from Publisher** **View Abstract**

Times Cited: **4**
*(from Web of Science Core Collection)*

**Usage Count**

12. **Slab Thickness Dependence of Rashba Splitting on Au(111) Surface: First-Principles and Model Analyses**

By: Kosugi, Taichi; Miyake, Takashi; Ishibashi, Shoji
JOURNAL OF THE PHYSICAL SOCIETY OF JAPAN Volume: 80 Issue: 7 Article Number: 074713 Published: JUL 2011

**Full Text from Publisher** **View Abstract**

Times Cited: **15**
*(from Web of Science Core Collection)*

**Usage Count**

13. **Surface versus bulk contributions to the Rashba splitting in surface systems**

By: Nuber, A.; Braun, J.; Forster, F.; et al.
PHYSICAL REVIEW B Volume: 83 Issue: 16 Article Number: 165401 Published: APR 1 2011

**View Abstract**

Times Cited: **23**
*(from Web of Science Core Collection)*

**Usage Count**

14. **Scanning tunneling microscopy of Bi- induced Ag(111) surface structures**

By: Kato, Chiaki; Aoki, Yuki; Hirayama, Hiroyuki
PHYSICAL REVIEW B Volume: 82 Issue: 16 Article Number: 165407 Published: OCT 5 2010

**View Abstract**

Times Cited: **7**
*(from Web of Science Core Collection)*

**Usage Count**

15. **Surface and bulk electronic structures of LaFeAsO studied by angle-resolved photoemission spectroscopy**

Times Cited: **27**
*(from Web of Science Core Collection)*

By: Yang, L. X.; Xie, B. P.; Zhang, Y.; et al.
PHYSICAL REVIEW B   Volume: 82   Issue: 10     Article
Number: 104519   Published: SEP 23 2010

**View Abstract**

Usage Count

16.  **Electronic structures and related properties of Ag-Au
     bulks and surfaces**

     By: Gong, H. R.
     MATERIALS CHEMISTRY AND PHYSICS   Volume: 123
     Issue: 1   Pages: 326-330   Published: SEP 1 2010

     **Full Text from Publisher**          **View Abstract**

Times Cited: **8**
*(from Web of Science Core
Collection)*

Usage Count

17.  **The work function and electronic structure of
     coherent Ag-Au interfaces**

     By: Gong, H. R.
     SOLID STATE COMMUNICATIONS   Volume: 149   Issue:
     47-48   Pages: 2143-2145   Published: DEC 2009

     **Full Text from Publisher**          **View Abstract**

Times Cited: **6**
*(from Web of Science Core
Collection)*

Usage Count

18.  **Transition between Tamm-like and Shockley-like
     surface states in optically induced photonic
     superlattices**

     By: Malkova, Natalia; Hromada, Ivan; Wang, Xiaosheng; et al.
     PHYSICAL REVIEW A   Volume: 80   Issue: 4     Article
     Number: 043806   Published: OCT 2009

     **View Abstract**

Times Cited: **10**
*(from Web of Science Core
Collection)*

Usage Count

19.  **Origin and manipulation of the Rashba splitting in
     surface alloys**

     By: Bentmann, H.; Forster, F.; Bihlmayer, G.; et al.
     EPL   Volume: 87   Issue: 3     Article Number: 37003
     Published: AUG 2009

     **View Abstract**

Times Cited: **45**
*(from Web of Science Core
Collection)*

Usage Count

20.  **Thickness dependence of Shockley-type surface
     states of Ag(111) ultrathin films on Si(111)7X7
     substrates**

     By: Sawa, Keiichi; Aoki, Yuki; Hirayama, Hiroyuki
     PHYSICAL REVIEW B   Volume: 80   Issue: 3     Article
     Number: 035428   Published: JUL 2009

     **View Abstract**

Times Cited: **16**
*(from Web of Science Core
Collection)*

Usage Count

21.  **Modification of Shockley surface state by long-chain
     n-alkane: Photoemission study on
     tetratetracontane/Au(111) interface**

     By: Kanai, K.; Ouchi, Y.; Seki, K.
     THIN SOLID FILMS   Volume: 517   Issue: 11   Pages: 3276-
     3280   Published: APR 2 2009

     **Full Text from Publisher**          **View Abstract**

Times Cited: **9**
*(from Web of Science Core
Collection)*

Usage Count

22.  **Recent ARPES experiments on quasi-1D bulk
     materials and artificial structures**

     By: Grioni, M.; Pons, S.; Frantzeskakis, E.
     JOURNAL OF PHYSICS-CONDENSED MATTER
     Volume: 21   Issue: 2     Article Number: 023201   Published:
     JAN 14 2009

     **View Abstract**

Times Cited: **25**
*(from Web of Science Core
Collection)*

Usage Count

23.  **Influence of reconstruction on the surface state of
     Au(110)**

     By: Nuber, Andreas; Higashiguchi, Mitsuharu; Forster, Frank; et
     al.
     PHYSICAL REVIEW B   Volume: 78   Issue: 19     Article
     Number: 195412   Published: NOV 2008

Times Cited: **27**
*(from Web of Science Core
Collection)*

Usage Count

24. **Tunneling conductance of a two-dimensional electron gas with Rashba spin-orbit coupling**

By: Srisongmuang, B.; Pairor, P.; Berciu, M.
PHYSICAL REVIEW B   Volume: 78   Issue: 15   Article Number: 155317   Published: OCT 2008

View Abstract

**Times Cited: 21**
*(from Web of Science Core Collection)*

**Usage Count**

25. **Two-dimensional states in the electronic structure of Au/(root 3 x root 3)-R30 degrees-4H-SiC(0001)**

By: Stoltz, D.; Stoltz, S. E.; Johansson, L. S. O.
JOURNAL OF ELECTRON SPECTROSCOPY AND RELATED PHENOMENA   Volume: 163   Issue: 1-3   Pages: 1-6   Published: APR 2008

Full Text from Publisher    View Abstract

**Times Cited: 0**
*(from Web of Science Core Collection)*

**Usage Count**

26. **The Shockley-type surface state on Ar covered Au(111): High resolution photoemission results and the description by slab-layer DFT calculations**

By: Forster, F.; Bendounan, A.; Reinert, F.; et al.
SURFACE SCIENCE   Volume: 601   Issue: 23   Pages: 5595-5604   Published: DEC 1 2007

Full Text from Publisher    View Abstract

**Times Cited: 20**
*(from Web of Science Core Collection)*

**Usage Count**

27. **ARPES and STS investigation of Shockley states in thin metallic films and periodic nanostructures**

By: Malterre, D.; Kierren, B.; Fagot-Revurat, Y.; et al.
NEW JOURNAL OF PHYSICS   Volume: 9   Article Number: 391   Published: OCT 31 2007

Full Text from Publisher    View Abstract

**Times Cited: 34**
*(from Web of Science Core Collection)*

**Usage Count**

28. **Real-space pseudopotential method for spin-orbit coupling within density functional theory**

By: Naveh, Doron; Kronik, Leeor; Tiago, Murilo L.; et al.
PHYSICAL REVIEW B   Volume: 76   Issue: 15   Article Number: 153407   Published: OCT 2007

View Abstract

**Times Cited: 10**
*(from Web of Science Core Collection)*

**Usage Count**

29. **Local detection of spin-orbit splitting by scanning tunneling spectroscopy**

By: Ast, Christian R.; Wittich, Gero; Wahl, Peter; et al.
PHYSICAL REVIEW B   Volume: 75   Issue: 20   Article Number: 201401   Published: MAY 2007

View Abstract

**Times Cited: 63**
*(from Web of Science Core Collection)*

**Usage Count**

30. **Electronic excitations in metals and at metal surfaces**

By: Chulkov, E. V.; Borisov, A. G.; Gauyacq, J. P.; et al.
CHEMICAL REVIEWS   Volume: 106   Issue: 10   Pages: 4160-4206   Published: OCT 11 2006

**Times Cited: 152**
*(from Web of Science Core Collection)*

**Usage Count**

31. **Systematic studies on surface modifications by ARUPS on Shockley-type surface states**

By: Forster, F.; Bendounan, A.; Ziroff, J.; et al.
Conference: 23rd European Conference on Surface Science (ECOSS-23) Location: Freie Univ, Berlin, GERMANY Date: SEP 04-09, 2005
SURFACE SCIENCE   Volume: 600   Issue: 18   Special Issue: SI   Pages: 3870-3874   Published: SEP 15 2006

Full Text from Publisher    View Abstract

**Times Cited: 26**
*(from Web of Science Core Collection)*

**Usage Count**

32. **Ag nanostructures on Au(788): A self-assembled**

**Times Cited: 11**

**superlattice of metallic quantum resonators**

By: Didiot, Clement; Pons, Stephane; Kierren, Bertrand; et al.
Conference: 23rd European Conference on Surface Science
(ECOSS-23) Location: Freie Univ, Berlin, GERMANY Date:
SEP 04-09, 2005
SURFACE SCIENCE    Volume: 600    Issue: 18   Special
Issue: SI   Pages: 3917-3920   Published: SEP 15 2006

Full Text from Publisher          View Abstract

---

33. **Electronic structure of an ordered Pb/Ag(111) surface alloy: Theory and experiment**

By: Pacile, D.; Ast, C. R.; Papagno, M.; et al.
PHYSICAL REVIEW B   Volume: 73   Issue: 24     Article
Number: 245429   Published: JUN 2006

View Abstract

---

34. **Higher-order contributions to Rashba and Dresselhaus effects**

By: Cartoixa, X.; Wang, L. -W.; Ting, D. Z. -Y.; et al.
PHYSICAL REVIEW B   Volume: 73   Issue: 20     Article
Number: 205341   Published: MAY 2006

View Abstract

---

35. **Interplay between structural, chemical, and spectroscopic properties of Ag/Au(111) epitaxial ultrathin films: A way to tune the Rashba coupling**

By: Cercellier, H.; Didiot, C.; Fagot-Revurat, Y.; et al.
PHYSICAL REVIEW B   Volume: 73   Issue: 19     Article
Number: 195413   Published: MAY 2006

View Abstract

---

36. **Imaging a buried interface by scanning tunneling spectroscopy of surface states in a metallic system**

By: Didiot, C; Vedeneev, A; Fagot-Revurat, Y; et al.
PHYSICAL REVIEW B   Volume: 72   Issue: 23     Article
Number: 233408   Published: DEC 2005

View Abstract

---

37. **Surface state scattering at a buried interface**

By: Schiller, F; Keyling, R; Chulkov, EV; et al.
PHYSICAL REVIEW LETTERS   Volume: 95   Issue: 12
Article Number: 126402   Published: SEP 16 2005

View Abstract

---

38. **Influence of the reconstruction in Ag/Cu(111) on the surface electronic structure: Quantitative analysis of the induced band gap**

By: Bendounan, A; Forster, F; Ziroff, J; et al.
PHYSICAL REVIEW B   Volume: 72   Issue: 7     Article
Number: 075407   Published: AUG 2005

View Abstract

---

39. **Photoelectron spectroscopy - An overview**

By: Hufner, S; Schmidt, S; Reinert, F
Conference: Workshop on Hard X-Ray Photoelectron
Spectroscopy Location: Grenoble, FRANCE Date: SEP 11-12,
2003
Sponsor(s): ESRF; FOCUS GmbH; Gammadata Scienta; MB
Sci AB; SPECS GmbH
NUCLEAR INSTRUMENTS & METHODS IN PHYSICS
RESEARCH SECTION A-ACCELERATORS
SPECTROMETERS DETECTORS AND ASSOCIATED
EQUIPMENT   Volume: 547   Issue: 1   Pages: 8-23
Published: JUL 21 2005

Full Text from Publisher          View Abstract

40. **High-resolution photoemission on Ag/Au(111): Spin-orbit splitting and electronic localization of the surface state**

By: Popovic, D; Reinert, F; Hufner, S; et al.
PHYSICAL REVIEW B    Volume: 72    Issue: 4    Article Number: 045419   Published: JUL 2005

**View Abstract**

**Times Cited: 42**
*(from Web of Science Core Collection)*

**Usage Count**

41. **Photoemission spectroscopy – from early days to recent applications**

By: Reinert, F; Hufner, S
NEW JOURNAL OF PHYSICS    Volume: 7    Article Number: 97   Published: APR 29 2005

**Full Text from Publisher**    **View Abstract**

**Times Cited: 63**
*(from Web of Science Core Collection)*

**Usage Count**

42. **Rare gases on noble-metal surfaces: An angle-resolved photoemission study with high energy resolution**

By: Forster, F; Hufner, S; Reinert, F
JOURNAL OF PHYSICAL CHEMISTRY B    Volume: 108    Issue: 38   Pages: 14692-14698   Published: SEP 23 2004

**View Abstract**

**Times Cited: 49**
*(from Web of Science Core Collection)*

**Usage Count**

Select Page        🗔  ✉  **5K**

Save to Other File Formats        ▾        **Add to Marked List**

Sort by:  Publication Date -- newest to oldest  ▾

Show:  50 per page  ▾

Page 1  of  1

*42 records matched your query of the 37,941,506 in the data limits you selected.*

Web of Science | InCites | Journal Citation Reports | Essential Science Indicators | EndNote | Sign In ▾ | Help | English ▾

# Web of Science

Search | Search Results | My Tools ▾ | Search History | Marked List 23

## Citing Articles: 1
*(from Web of Science Core Collection)*

**For:** Fingerprinting substitution sites in Pb, Dy-Bi2Sr2Ca1Cu2O8+delta using X-ray Photoelectron Diffraction **...Less**

**Times Cited Counts**

1 in All Databases

1 in Web of Science Core Collection

0 in BIOSIS Citation Index

0 in Chinese Science Citation Database

0 data sets in Data Citation Index

0 publication in Data Citation Index

0 in Russian Science Citation Index

0 in SciELO Citation Index

**View Additional Times Cited Counts**

## Refine Results

*Search within results for...*

### Publication Years ▼
☐ 2007 (1)

**Refine**

### Web of Science Categories ▼
☐ PHYSICS CONDENSED MATTER (1)

**Refine**

### Document Types ▼
☐ ARTICLE (1)

**Refine**

### Organizations-Enhanced ▼
☐ ROYAL INSTITUTE OF TECHNOLOGY (1)
☐ LUND UNIVERSITY (1)

**more options / values...**

**Refine**

### Funding Agencies ◀

### Open Access ◀

Sort by: Publication Date -- newest to oldest ▾　　　　Page [1] of 1

☐ Select Page　　🖶 ✉ **5K**

Save to Other File Formats ▾　　**Add to Marked List**

**Create Citation Report**

≡ **Analyze Results**

☐ **1.** **X-ray photoelectron diffraction investigation of the cleavage plane in IT-transition metal dichalcogenides**

By: Stoltz, D.; Stoltz, S. E.

PHYSICA B-CONDENSED MATTER　Volume: 398　Issue: 1　Pages: 172-177　Published: AUG 1 2007

**Full Text from Publisher** | **View Abstract**

**Times Cited: 1**
*(from Web of Science Core Collection)*

**Usage Count**

☐ Select Page　　🖶 ✉ **5K**

Save to Other File Formats ▾　　**Add to Marked List**

Sort by: Publication Date -- newest to oldest ▾　　　　Page [1] of 1

Show: 50 per page ▾

*1 records matched your query of the 37,941,506 in the data limits you selected.*

## Authors ◀

**View all options**

*For advanced refine options, use*

**Analyze Results**

Web of Science | InCites | Journal Citation Reports | Essential Science Indicators | EndNote | Sign In ▾ | Help | English ▾

# Web of Science

Search | Search Results | My Tools ▾ | Search History | Marked List 23

## Citing Articles: 42
*(from Web of Science Core Collection)*

**For:** High-resolution photoemission on Ag/Au(111): Spin-orbit splitting and electronic localization of the surface state **...Less**

### Times Cited Counts

42 in All Databases

42 in Web of Science Core Collection

0 in BIOSIS Citation Index

1 in Chinese Science Citation Database

0 data sets in Data Citation Index

0 publication in Data Citation Index

0 in Russian Science Citation Index

0 in SciELO Citation Index

**View Additional Times Cited Counts**

## Refine Results

*Search within results for...*

**Filter results by:**

☐ Highly Cited in Field (1)

**Refine**

### Publication Years ▼

☐ 2008 (6)
☐ 2015 (5)
☐ 2011 (5)
☐ 2007 (5)
☐ 2016 (4)

more options / values...

**Refine**

### Web of Science Categories ▼

☐ PHYSICS CONDENSED MATTER (19)
☐ PHYSICS MULTIDISCIPLINARY (11)
☐ PHYSICS APPLIED (5)
☐ CHEMISTRY PHYSICAL (5)
☐ MATERIALS SCIENCE MULTIDISCIPLINARY (3)

more options / values...

**Refine**

### Document Types ▼

☐ ARTICLE (39)

---

Sort by: Publication Date -- newest to oldest ▾

Page 1 of 1

☐ Select Page    🖼 ✉ 5K

Save to Other File Formats ▾ | **Add to Marked List**

**Create Citation Report**

≡ **Analyze Results**

☐ 1. **Tunable Rashba spin splitting in quantum-spin Hall-insulator AsF bilayers**

By: Zhao, Jun; Guo, Wanlin; Ma, Jing
NANO RESEARCH   Volume: 10   Issue: 2   Pages: 491-502
Published: FEB 2017

**View Abstract**

Times Cited: 0
*(from Web of Science Core Collection)*

Usage Count

☐ 2. **Films based on group IV-V-VI elements for the design of a large-gap quantum spin Hall insulator with tunable Rashba splitting**

By: Jia, Yi-zhen; Ji, Wei-xiao; Zhang, Chang-wen; et al.
RSC ADVANCES   Volume: 7   Issue: 19   Pages: 11636-11643   Published: 2017

**View Abstract**

Times Cited: 0
*(from Web of Science Core Collection)*

Usage Count

☐ 3. **Newtype large Rashba splitting in quantum well states induced by spin chirality in metal/topological insulator heterostructures**

By: Chang, Ching-Hao; Chang, Tay-Rong; Jeng, Horng-Tay
NPG ASIA MATERIALS   Volume: 8   Article Number: e332
Published: NOV 2016

**Full Text from Publisher** | **View Abstract**

Times Cited: 0
*(from Web of Science Core Collection)*

Usage Count

☐ 4. **Nonvortical Rashba Spin Structure on a Surface with C-1h Symmetry**

By: Annese, Emilia; Kuzumaki, Takuya; Mueller, Beate; et al.
PHYSICAL REVIEW LETTERS   Volume: 117   Issue: 1
Article Number: 016803   Published: JUN 30 2016

**View Abstract**

Times Cited: 1
*(from Web of Science Core Collection)*

Usage Count

☐ 5. **Theoretical aspects of the Edelstein effect for anisotropic two-dimensional electron gas and topological insulators**

By: Johansson, Annika; Henk, Juergen; Mertig, Ingrid
PHYSICAL REVIEW B   Volume: 93   Issue: 19   Article Number: 195440   Published: MAY 26 2016

**View Abstract**

Times Cited: 1
*(from Web of Science Core Collection)*

Usage Count

☐ 6. **Formation of Ideal Rashba States on Layered Semiconductor Surfaces Steered by Strain Engineering**

By: Ming, Wenmei; Wang, Z. F.; Zhou, Miao; et al.
NANO LETTERS   Volume: 16   Issue: 1   Pages: 404-409
Published: JAN 2016

**View Abstract**

Times Cited: 10
*(from Web of Science Core Collection)*

Usage Count

REVIEW (3)
PROCEEDINGS PAPER (1)

more options / values...

**Refine**

**Organizations-Enhanced** ▼

UNIVERSITY OF WURZBURG (7)
UNIVERSITY OF TOKYO (4)
UNIVERSITY OF BASQUE COUNTRY (4)
KARLSRUHE INSTITUTE OF TECHNOLOGY (4)
HIROSHIMA UNIVERSITY (4)

more options / values...

**Refine**

**Funding Agencies** ◄

**Open Access** ◄

**Authors** ◄

**View all options**

*For advanced refine options, use*

**Analyze Results**

---

7.  **Spin-orbit coupling at surfaces and 2D materials**

    By: Krasovskii, E. E.
    JOURNAL OF PHYSICS-CONDENSED MATTER
    Volume: 27  Issue: 49   Article Number: 493001  Published:
    DEC 16 2015

    **View Abstract**

    **Times Cited: 7**
    *(from Web of Science Core Collection)*

    **Usage Count**

8.  **Surface confined quantum well state in MoS2(0001) thin film**

    By: Sun, Jia-Tao; Song, S. R.; Meng, S.; et al.
    APPLIED PHYSICS LETTERS  Volume: 107  Issue: 16
    Article Number: 161602  Published: OCT 19 2015

    **View Abstract**

    **Times Cited: 1**
    *(from Web of Science Core Collection)*

    **Usage Count**

9.  **Recent progress in Rashba spin orbit coupling on metal surface**

    By: Gong Shi-Jing; Duan Chun-Gang
    ACTA PHYSICA SINICA  Volume: 64  Issue: 18  Special
    Issue: SI   Article Number: 187103  Published: SEP 20 2015

    **View Abstract**

    **Times Cited: 2**
    *(from Web of Science Core Collection)*

    **Usage Count**

10. **Theory of unconventional spin states in surfaces with non-Rashba spin-orbit interaction**

    By: Nakajin, Kokin; Murakami, Shuichi
    PHYSICAL REVIEW B  Volume: 91  Issue: 24   Article
    Number: 245428  Published: JUN 22 2015

    **View Abstract**

    **Times Cited: 2**
    *(from Web of Science Core Collection)*

    **Usage Count**

11. **Symmetry induced peculiar Rashba effect on thallium adsorbed Si(111) surfaces**

    By: Sakamoto, Kazuyuki; Oda, Tatsuki; Kimura, Akio; et al.
    JOURNAL OF ELECTRON SPECTROSCOPY AND
    RELATED PHENOMENA  Volume: 201  Special Issue: SI
    Pages: 88-91  Published: MAY 2015

    **Full Text from Publisher**   **View Abstract**

    **Times Cited: 0**
    *(from Web of Science Core Collection)*

    **Usage Count**

12. **Rashba splitting and relativistic energy shifts in In/Si(111) nanowires**

    By: Gerstmann, U.; Vollmers, N. J.; Luecke, A.; et al.
    PHYSICAL REVIEW B  Volume: 89  Issue: 16   Article
    Number: 165431  Published: APR 30 2014

    **View Abstract**

    **Times Cited: 7**
    *(from Web of Science Core Collection)*

    **Usage Count**

13. **Enhancing and reducing the Rashba-splitting at surfaces by adsorbates: Na and Xe on Bi/Cu(111)**

    By: Bentmann, Hendrik; Reinert, Friedrich
    NEW JOURNAL OF PHYSICS  Volume: 15   Article
    Number: 115011  Published: NOV 19 2013

    **Full Text from Publisher**   **View Abstract**

    **Times Cited: 11**
    *(from Web of Science Core Collection)*

    **Usage Count**

14. **Origin of giant Rashba spin splitting in Bi/Ag surface alloys**

    By: Bian, G.; Wang, X.; Miller, T.; et al.
    PHYSICAL REVIEW B  Volume: 88  Issue: 8   Article
    Number: 085427  Published: AUG 21 2013

    **View Abstract**

    **Times Cited: 15**
    *(from Web of Science Core Collection)*

    **Usage Count**

15. **Rashba split surface states in BiTeBr**

    By: Eremeev, S. V.; Rusinov, I. P.; Nechaev, I. A.; et al.
    NEW JOURNAL OF PHYSICS  Volume: 15   Article
    Number: 075015  Published: JUL 17 2013

    **Full Text from Publisher**   **View Abstract**

    **Times Cited: 26**
    *(from Web of Science Core Collection)*

    **Usage Count**

16. **Large spin-orbit splitting of surface states in ultrathin Au (111) films**

By: Li, Zhongyao; Gong, Shijing; Yang, Zhongqin
PHYSICS LETTERS A   Volume: 377   Issue: 1-2   Pages: 129-132   Published: DEC 3 2012

[ Full Text from Publisher ]   [ View Abstract ]

**Times Cited: 3**
*(from Web of Science Core Collection)*

**Usage Count**

17. **Direct Observation of Interband Spin-Orbit Coupling in a Two-Dimensional Electron System**

By: Bentmann, Hendrik; Abdelouahed, Samir; Mulazzi, Mattia; et al.
PHYSICAL REVIEW LETTERS   Volume: 108   Issue: 19   Article Number: 196801   Published: MAY 7 2012

[ View Abstract ]

**Times Cited: 29**
*(from Web of Science Core Collection)*

**Usage Count**

18. **Electronic structure study of ultrathin Ag(111) films modified by a Si(111) substrate and root 3 x root 3-Ag2Bi surface**

By: Ogawa, M.; Sheverdyaeva, P. M.; Moras, P.; et al.
JOURNAL OF PHYSICS-CONDENSED MATTER   Volume: 24   Issue: 11   Article Number: 115501   Published: MAR 21 2012

[ View Abstract ]

**Times Cited: 1**
*(from Web of Science Core Collection)*

**Usage Count**

19. **Li+-ion neutralization on metal surfaces and thin films**

By: Chen, Lin; Shen, Jie; Jia, Juanjuan; et al.
PHYSICAL REVIEW A   Volume: 84   Issue: 5   Article Number: 052901   Published: NOV 15 2011

[ View Abstract ]

**Times Cited: 13**
*(from Web of Science Core Collection)*

**Usage Count**

20. **Current-induced spin-orbit torques**

By: Gambardella, Pietro; Mihai Miron, Ioan
PHILOSOPHICAL TRANSACTIONS OF THE ROYAL SOCIETY A-MATHEMATICAL PHYSICAL AND ENGINEERING SCIENCES   Volume: 369   Issue: 1948   Pages: 3175-3197   Published: AUG 13 2011

[ View Abstract ]

**Times Cited: 74**
*(from Web of Science Core Collection)*

**Usage Count**

21. **Electronic localization of quantum-well states in Ag/Au(111) metallic heterostructures**

By: Forster, F.; Gergert, E.; Nuber, A.; et al.
PHYSICAL REVIEW B   Volume: 84   Issue: 7   Article Number: 075412   Published: AUG 3 2011

[ View Abstract ]

**Times Cited: 8**
*(from Web of Science Core Collection)*

**Usage Count**

22. **Slab Thickness Dependence of Rashba Splitting on Au(111) Surface: First-Principles and Model Analyses**

By: Kosugi, Taichi; Miyake, Takashi; Ishibashi, Shoji
JOURNAL OF THE PHYSICAL SOCIETY OF JAPAN   Volume: 80   Issue: 7   Article Number: 074713   Published: JUL 2011

[ Full Text from Publisher ]   [ View Abstract ]

**Times Cited: 15**
*(from Web of Science Core Collection)*

**Usage Count**

23. **Surface versus bulk contributions to the Rashba splitting in surface systems**

By: Nuber, A.; Braun, J.; Forster, F.; et al.
PHYSICAL REVIEW B   Volume: 83   Issue: 16   Article Number: 165401   Published: APR 1 2011

[ View Abstract ]

**Times Cited: 23**
*(from Web of Science Core Collection)*

**Usage Count**

24. **Peculiar Rashba Splitting Originating from the Two-**

**Times Cited: 72**
*(from Web of Science Core*

**Dimensional Symmetry of the Surface**

By: Sakamoto, Kazuyuki; Kakuta, Haruya; Sugawara, Katsuaki; et al.
PHYSICAL REVIEW LETTERS   Volume: 103   Issue: 15
   Article Number: 156801   Published: OCT 9 2009

   **View Abstract**

25.  **Understanding intensities of angle-resolved photoemission with circularly polarized radiation from a Cu(111) surface state**

By: Mulazzi, M.; Rossi, G.; Braun, J.; et al.
PHYSICAL REVIEW B   Volume: 79   Issue: 16   Article Number: 165421   Published: APR 2009

   **View Abstract**

Times Cited: 17
*(from Web of Science Core Collection)*

Usage Count

26.  **Abrupt Rotation of the Rashba Spin to the Direction Perpendicular to the Surface**

By: Sakamoto, Kazuyuki; Oda, Tatsuki; Kimura, Akio; et al.
PHYSICAL REVIEW LETTERS   Volume: 102   Issue: 9
   Article Number: 096805   Published: MAR 6 2009

   **View Abstract**

Times Cited: 77
*(from Web of Science Core Collection)*

Usage Count

27.  **Modification of the Cu(110) Shockley surface state by an adsorbed pentacene monolayer**

By: Scheybal, A.; Mueller, K.; Bertschinger, R.; et al.
PHYSICAL REVIEW B   Volume: 79   Issue: 11   Article Number: 115406   Published: MAR 2009

   **View Abstract**

Times Cited: 39
*(from Web of Science Core Collection)*

Usage Count

28.  **Interplay between electronic states and structure during Au faceting**

By: Schiller, F.; Corso, M.; Cordon, J.; et al.
NEW JOURNAL OF PHYSICS   Volume: 10   Article Number: 113017   Published: NOV 14 2008

   **Full Text from Publisher**      **View Abstract**

Times Cited: 3
*(from Web of Science Core Collection)*

Usage Count

29.  **Plasmons in the presence of Tamm-Shockley states with Rashba splitting at noble metal surfaces**

By: Farid, A. M.; Mishchenko, E. G.
PHYSICAL REVIEW B   Volume: 78   Issue: 20   Article Number: 205434   Published: NOV 2008

   **View Abstract**

Times Cited: 1
*(from Web of Science Core Collection)*

Usage Count

30.  **An energy-dependent photoemission study on line-shape analysis in determining the absolute coverage of metallic thin films**

By: Cheng, Cheng-Maw; Tsuei, Ku-Ding; Luh, Dah-An
JOURNAL OF PHYSICS D-APPLIED PHYSICS   Volume: 41   Issue: 19   Article Number: 195302   Published: OCT 7 2008

   **View Abstract**

Times Cited: 3
*(from Web of Science Core Collection)*

Usage Count

31.  **Tunneling conductance of a two-dimensional electron gas with Rashba spin-orbit coupling**

By: Srisongmuang, B.; Pairor, P.; Berciu, M.
PHYSICAL REVIEW B   Volume: 78   Issue: 15   Article Number: 155317   Published: OCT 2008

   **View Abstract**

Times Cited: 21
*(from Web of Science Core Collection)*

Usage Count

32.  **Precise determination of absolute coverage of thin films by layer-resolved surface states**

By: Cheng, Cheng-Maw; Tsuei, Ku-Ding; Tsai, Chi-Ting; et al.

Times Cited: 7
*(from Web of Science Core Collection)*

Usage Count

APPLIED PHYSICS LETTERS   Volume: 92   Issue: 16
Article Number: 163102   Published: APR 21 2008

**View Abstract**

33. **Two-dimensional states in the electronic structure of Au/(root 3 x root 3)-R30 degrees-4H-SiC(0001)**

By: Stoltz, D.; Stoltz, S. E.; Johansson, L. S. O.
JOURNAL OF ELECTRON SPECTROSCOPY AND RELATED PHENOMENA   Volume: 163   Issue: 1-3   Pages: 1-6   Published: APR 2008

**Full Text from Publisher**    **View Abstract**

Times Cited: 0
*(from Web of Science Core Collection)*

Usage Count

34. **The Shockley-type surface state on Ar covered Au(111): High resolution photoemission results and the description by slab-layer DFT calculations**

By: Forster, F.; Bendounan, A.; Reinert, F.; et al.
SURFACE SCIENCE   Volume: 601   Issue: 23   Pages: 5595-5604   Published: DEC 1 2007

**Full Text from Publisher**    **View Abstract**

Times Cited: 20
*(from Web of Science Core Collection)*

Usage Count

35. **The two dimensional Kondo model with Rashba spin-orbit coupling**

By: Malecki, Justin
JOURNAL OF STATISTICAL PHYSICS   Volume: 129   Issue: 4   Pages: 741-757   Published: NOV 2007

**View Abstract**

Times Cited: 20
*(from Web of Science Core Collection)*

Usage Count

36. **Surface resonance on the (6 root 3 x 6 root 3)-R30 degrees-reconstructed 5 ML Au on (root 3 x root 3)-R30 degrees-4H-SiC(0001)**

By: Stoltz, D.; Stoltz, S. E.; Johansson, L. S. O.
SURFACE SCIENCE   Volume: 601   Issue: 12   Pages: 2508-2511   Published: JUN 15 2007

**Full Text from Publisher**    **View Abstract**

Times Cited: 1
*(from Web of Science Core Collection)*

Usage Count

37. **Giant spin splitting through surface alloying**

By: Ast, Christian R.; Henk, Juergen; Ernst, Arthur; et al.
PHYSICAL REVIEW LETTERS   Volume: 98   Issue: 18
Article Number: 186807   Published: MAY 4 2007

**View Abstract**

Times Cited: 382
*(from Web of Science Core Collection)*

**Highly Cited Paper**

Usage Count

38. **Local detection of spin-orbit splitting by scanning tunneling spectroscopy**

By: Ast, Christian R.; Wittich, Gero; Wahl, Peter; et al.
PHYSICAL REVIEW B   Volume: 75   Issue: 20   Article Number: 201401   Published: MAY 2007

**View Abstract**

Times Cited: 63
*(from Web of Science Core Collection)*

Usage Count

39. **Electronic excitations in metals and at metal surfaces**

By: Chulkov, E. V.; Borisov, A. G.; Gauyacq, J. P.; et al.
CHEMICAL REVIEWS   Volume: 106   Issue: 10   Pages: 4160-4206   Published: OCT 11 2006

Times Cited: 152
*(from Web of Science Core Collection)*

Usage Count

40. **Systematic studies on surface modifications by ARUPS on Shockley-type surface states**

By: Forster, F.; Bendounan, A.; Ziroff, J.; et al.
Conference: 23rd European Conference on Surface Science (ECOSS-23) Location: Freie Univ, Berlin, GERMANY Date: SEP 04-09, 2005
SURFACE SCIENCE   Volume: 600   Issue: 18   Special Issue: SI   Pages: 3870-3874   Published: SEP 15 2006

**Full Text from Publisher**    **View Abstract**

Times Cited: 26
*(from Web of Science Core Collection)*

Usage Count

41.  **Higher-order contributions to Rashba and Dresselhaus effects**

By: Cartoixa, X.; Wang, L. -W.; Ting, D. Z. -Y.; et al.
PHYSICAL REVIEW B   Volume: 73   Issue: 20   Article
Number: 205341   Published: MAY 2006

**View Abstract**

**Times Cited: 29**
*(from Web of Science Core Collection)*

**Usage Count**

42.  **Interplay between structural, chemical, and spectroscopic properties of Ag/Au(111) epitaxial ultrathin films: A way to tune the Rashba coupling**

By: Cercellier, H.; Didiot, C.; Fagot-Revurat, Y.; et al.
PHYSICAL REVIEW B   Volume: 73   Issue: 19   Article
Number: 195413   Published: MAY 2006

**View Abstract**

**Times Cited: 77**
*(from Web of Science Core Collection)*

**Usage Count**

Select Page          📄 ✉ *5K*

Save to Other File Formats        ▼      **Add to Marked List**

Sort by:   Publication Date -- newest to oldest        ▼

Show:   50 per page        ▼

Page [1]   of  1

*42 records matched your query of the 37,941,506 in the data limits you selected.*

Web of Science | InCites | Journal Citation Reports | Essential Science Indicators | EndNote | Sign In ▾ | Help | English ▾

# Web of Science

Search | Search Results | My Tools ▾ | Search History | Marked List 23

## Citing Articles: 7
*(from Web of Science Core Collection)*

**For:** A high-resolution core-level study of Ni-catalyzed absorption and desorption of hydrogen in Mg-films ...**More**

### Times Cited Counts
8 in All Databases
7 in Web of Science Core Collection
0 in BIOSIS Citation Index
1 in Chinese Science Citation Database
0 data sets in Data Citation Index
0 publication in Data Citation Index
0 in Russian Science Citation Index
0 in SciELO Citation Index
**View Additional Times Cited Counts**

## Refine Results

*Search within results for...*

### Filter results by:
☐ Highly Cited in Field (1)

**Refine**

### Publication Years ▾
☐ 2016 (1)
☐ 2015 (1)
☐ 2014 (1)
☐ 2013 (1)
☐ 2010 (1)
**more options / values...**

**Refine**

### Web of Science Categories ▾
☐ MATERIALS SCIENCE MULTIDISCIPLINARY (3)
☐ CHEMISTRY PHYSICAL (3)
☐ PHYSICS CONDENSED MATTER (2)
☐ ENERGY FUELS (2)
☐ ELECTROCHEMISTRY (2)
**more options / values...**

**Refine**

### Document Types ▾
☐ ARTICLE (6)
☐ PROCEEDINGS PAPER (2)

---

Sort by: Publication Date -- newest to oldest ▾

Page 1 of 1

☐ Select Page  🖶 ✉ **5K**

Save to Other File Formats ▾ | **Add to Marked List**

**Create Citation Report**

▤ **Analyze Results**

☐ 1. **A first-principles study on interaction of Mg/Ni interface and its hydrogen absorption characteristics**

By: Chen, Yuying; Dai, Jianhong; Xie, Ruiwen; et al.
SURFACE SCIENCE   Volume: 649   Pages: 133-137   Published: JUL 2016

**Full Text from Publisher** | **View Abstract**

Times Cited: 0
*(from Web of Science Core Collection)*

**Usage Count**

☐ 2. **Investigation of interfaces in Mg/Nb multilayer thin films**

By: Junkaew, A.; Ham, B.; Zhang, X.; et al.
COMPUTATIONAL MATERIALS SCIENCE   Volume: 108   Pages: 212-225   Part: A   Published: OCT 2015

**Full Text from Publisher** | **View Abstract**

Times Cited: 4
*(from Web of Science Core Collection)*

**Usage Count**

☐ 3. **Superior electrochemical hydrogen storage properties of binary Mg-Y thin films**

By: Wang, Yanyan; Xin, Gongbiao; Li, Wei; et al.
INTERNATIONAL JOURNAL OF HYDROGEN ENERGY   Volume: 39   Issue: 9   Pages: 4373-4379   Published: MAR 18 2014

**Full Text from Publisher** | **View Abstract**

Times Cited: 3
*(from Web of Science Core Collection)*

**Usage Count**

☐ 4. **Method of Preparation Magnesium-based Alloy Film and Its Hydrogen Storage Performance**

By: Kan Hongmin; Zhang Ning; Wang Xiaoyang
Edited by: Zeng, JM; Zhu, HX; Kong, JY
Conference: 2nd International Conference on Chemical, Material and Metallurgical Engineering (ICCMME 2012) Location: Kunming, PEOPLES R CHINA Date: DEC 15-16, 2012
Sponsor(s): Wuhan Univ Sci & Technol; Auckland Univ Technol; Guangxi Univ
ADVANCES IN CHEMICAL, MATERIAL AND METALLURGICAL ENGINEERING, PTS 1-5   Book Series: Advanced Materials Research   Volume: 634-638   Pages: 2588-2591   Published: 2013

**View Abstract**

Times Cited: 0
*(from Web of Science Core Collection)*

**Usage Count**

☐ 5. **Hydrogen storage in Mg: A most promising material**

By: Jain, I. P.; Lal, Chhagan; Jain, Ankur
Conference: 1st International Conference on Hydrogen Production (ICH2P09) Location: Univ Ontario, Inst Technol, Oshawa, CANADA Date: MAY 03-06, 2009
INTERNATIONAL JOURNAL OF HYDROGEN ENERGY   Volume: 35   Issue: 10   Special Issue: SI   Pages: 5133-5144   Published: MAY 2010

**Full Text from Publisher** | **View Abstract**

Times Cited: 380
*(from Web of Science Core Collection)*

**Highly Cited Paper**

**Usage Count**

☐ 6. **Hydrogen storage and cycling properties of a**

Times Cited: 22

vanadium decorated Mg nanoblade array on a Ti coated Si substrate

*(from Web of Science Core Collection)*

By: He, Yuping; Zhao, Yiping

**Usage Count**

NANOTECHNOLOGY   Volume: 20   Issue: 20   Article Number: 204008   Published: MAY 20 2009

**View Abstract**

7. **Spectroscopic evidence for reversible hydrogen storage in unordered Mg5Ni1 thin films**

**Times Cited: 0**
*(from Web of Science Core Collection)*

By: Stoltz, S. E.; Stoltz, D.

**Usage Count**

JOURNAL OF PHYSICS-CONDENSED MATTER   Volume: 19   Issue: 44   Article Number: 446010   Published: NOV 7 2007

**View Abstract**

Select Page    🖨 ✉ **5K**

Save to Other File Formats ▾    **Add to Marked List**

---

## Left sidebar

more options / values...

**Refine**

**Organizations-Enhanced** ▼

- ☐ SHENYANG UNIVERSITY (1)
- ☐ PEKING UNIVERSITY (1)
- ☐ NATL SCI TECHNOL DEV AGCY NSTDA (1)
- ☐ LUND UNIVERSITY (1)
- ☐ LEIDEN UNIVERSITY (1)

more options / values...

**Refine**

**Funding Agencies** ◀

**Open Access** ◀

**Authors** ◀

**View all options**

*For advanced refine options, use*

**Analyze Results**

---

Sort by:   Publication Date -- newest to oldest ▾     Page [1] of 1

Show:   50 per page ▾

*7 records matched your query of the 37,941,506 in the data limits you selected.*

Web of Science | InCites | Journal Citation Reports | Essential Science Indicators | EndNote | Sign In ▼ | Help | English ▼

# Web of Science

Search | Search Results | My Tools ▼ | Search History | Marked List  23

## Citing Articles: 2
*(from Web of Science Core Collection)*

**For:** Investigation of surface structure related features in the multiple-scattering simulations of photoelectron diffraction of 3C-SiC(001)-c(4 x 2) **...Less**

**Times Cited Counts**

2 in All Databases

2 in Web of Science Core Collection

0 in BIOSIS Citation Index

0 in Chinese Science Citation Database

0 data sets in Data Citation Index

0 publication in Data Citation Index

0 in Russian Science Citation Index

0 in SciELO Citation Index

**View Additional Times Cited Counts**

### Refine Results

*Search within results for...*

**Publication Years**    ▼

☐ 2013 (2)

**Refine**

**Web of Science Categories**    ▼

☐ PHYSICS MULTIDISCIPLINARY (1)

☐ PHYSICS MATHEMATICAL (1)

☐ PHYSICS CONDENSED MATTER (1)

☐ PHYSICS APPLIED (1)

**more options / values...**

**Refine**

**Document Types**    ▼

☐ ARTICLE (2)

**Refine**

**Organizations-Enhanced**    ▼

☐ GUIZHOU UNIVERSITY (2)

☐ UNIV ANSHUN (1)

☐ ANSHUN UNIV (1)

**more options / values...**

**Refine**

Sort by: Publication Date -- newest to oldest ▼

Page [1] of 1

☐ Select Page    🗗  ✉  **5K**

Save to Other File Formats    ▼    **Add to Marked List**

**Create Citation Report**

☰ **Analyze Results**

☐ 1. **MICROSTRUCTURAL EVOLUTION OF SiC DURING MELTING PROCESS**

By: Yan, Wanjun; Xie, Quan; Gao, Tinghong; et al.
MODERN PHYSICS LETTERS B   Volume: 27   Issue: 31
Article Number: 1350231   Published: DEC 20 2013

**Full Text from Publisher**    **View Abstract**

**Times Cited: 1**
*(from Web of Science Core Collection)*

**Usage Count**

☐ 2. **Melting kinetics of bulk SiC using molecular dynamics simulation**

By: Yan WanJun; Gao TingHong; Guo XiaoTian; et al.
SCIENCE CHINA-PHYSICS MECHANICS & ASTRONOMY   Volume: 56   Issue: 9   Pages: 1699-1704
Published: SEP 2013

**View Abstract**

**Times Cited: 0**
*(from Web of Science Core Collection)*

**Usage Count**

☐ Select Page    🗗  ✉  **5K**

Save to Other File Formats    ▼    **Add to Marked List**

Sort by: Publication Date -- newest to oldest ▼

Page [1] of 1

Show: 50 per page ▼

*2 records matched your query of the 37,941,506 in the data limits you selected.*

**Funding Agencies** ◀

**Open Access** ◀

**Authors** ◀

**View all options**

*For advanced refine options, use*

**Analyze Results**

Web of Science | InCites | Journal Citation Reports | Essential Science Indicators | EndNote | Sign In ▾ | Help | English ▾

# Web of Science

Search | Search Results | My Tools ▾ | Search History | Marked List 23

## Citing Articles: 1
*(from Web of Science Core Collection)*

**For:** Surface resonance on the (6 root 3 x 6 root 3)-R30 degrees-reconstructed 5 ML Au on (root 3 x root 3)-R30 degrees-4H-SiC(0001)
**...Less**

**Times Cited Counts**

1 in All Databases

1 in Web of Science Core Collection
0 in BIOSIS Citation Index
0 in Chinese Science Citation Database
0 data sets in Data Citation Index
0 publication in Data Citation Index
0 in Russian Science Citation Index
0 in SciELO Citation Index

**View Additional Times Cited Counts**

## Refine Results

Search within results for...

### Publication Years ▾
☐ 2008 (1)

**Refine**

### Web of Science Categories ▾
☐ SPECTROSCOPY (1)

**Refine**

### Document Types ▾
☐ ARTICLE (1)

**Refine**

### Organizations-Enhanced ▾
☐ LUND UNIVERSITY (1)
☐ LEIDEN UNIVERSITY (1)
☐ KARLSTAD UNIVERSITY (1)

**more options / values...**

**Refine**

### Funding Agencies ◀

### Open Access ◀

---

Sort by: Publication Date -- newest to oldest ▾    Page [1] of 1

☐ Select Page    🗗 ✉ 5K
Save to Other File Formats ▾    **Add to Marked List**

**Create Citation Report**

**≡ Analyze Results**

☐ 1. **Two-dimensional states in the electronic structure of Au/(root 3 x root 3)-R30 degrees-4H-SiC(0001)**

By: Stoltz, D.; Stoltz, S. E.; Johansson, L. S. O.
JOURNAL OF ELECTRON SPECTROSCOPY AND RELATED PHENOMENA    Volume: 163    Issue: 1-3    Pages: 1-6    Published: APR 2008

**Full Text from Publisher**    **View Abstract**

**Times Cited: 0**
*(from Web of Science Core Collection)*

**Usage Count**

☐ Select Page    🗗 ✉ 5K
Save to Other File Formats ▾    **Add to Marked List**

---

Sort by: Publication Date -- newest to oldest ▾    Page [1] of 1

Show: 50 per page ▾

*1 records matched your query of the 37,941,506 in the data limits you selected.*

**Authors** ◀

**View all options**

*For advanced refine options, use*

**Analyze Results**

| Web of Science | InCites | Journal Citation Reports | Essential Science Indicators | EndNote | | Sign In ▼ | Help | English ▼ |

# Web of Science

| Search | Search Results | | My Tools ▼ | Search History | Marked List 23 |

## Citing Articles: 3
*(from Web of Science Core Collection)*

**For:** A high-resolution core-level photoemission study of the Au/4H-SiC(0001)-(root 3 x root 3) interface
**...Less**

### Times Cited Counts

3 in All Databases

3 in Web of Science Core Collection

0 in BIOSIS Citation Index

0 in Chinese Science Citation Database

0 data sets in Data Citation Index

0 publication in Data Citation Index

0 in Russian Science Citation Index

0 in SciELO Citation Index

**View Additional Times Cited Counts**

---

## Refine Results

*Search within results for...*

### Publication Years ▼

☐ 2016 (1)
☐ 2010 (1)
☐ 2008 (1)

more options / values...

**Refine**

### Web of Science Categories ▼

☐ PHYSICS CONDENSED MATTER (2)
☐ SPECTROSCOPY (1)

more options / values...

**Refine**

### Document Types ▼

☐ ARTICLE (3)

**Refine**

### Organizations-Enhanced ▼

☐ MAX PLANCK SOCIETY (1)
☐ LUND UNIVERSITY (1)
☐ LEIDEN UNIVERSITY (1)
☐ KARLSTAD UNIVERSITY (1)
☐ ECOLE POLYTECHNIQUE FEDERALE DE LAUSANNE (1)

---

Sort by: Publication Date -- newest to oldest ▼     Page [1] of 1

☐ Select Page    ▣ ✉ 5K

Save to Other File Formats ▼    **Add to Marked List**

**Create Citation Report**

☰ **Analyze Results**

☐ 1. **Noble-metal intercalation process leading to a protected adatom in a graphene hollow site**

By: Nair, M. Narayanan; Cranney, M.; Jiang, T.; et al.
PHYSICAL REVIEW B   Volume: 94   Issue: 7   Article Number: 075427   Published: AUG 22 2016

**View Abstract**

Times Cited: 0
*(from Web of Science Core Collection)*

**Usage Count**

☐ 2. **Electronic decoupling of an epitaxial graphene monolayer by gold intercalation**

By: Gierz, Isabella; Suzuki, Takayuki; Weitz, R. Thomas; et al.
PHYSICAL REVIEW B   Volume: 81   Issue: 23   Article Number: 235408   Published: JUN 4 2010

**View Abstract**

Times Cited: **114**
*(from Web of Science Core Collection)*

**Usage Count**

☑ 3. **Two-dimensional states in the electronic structure of Au/(root 3 x root 3)-R30 degrees-4H-SiC(0001)**

By: Stoltz, D.; Stoltz, S. E.; Johansson, L. S. O.
JOURNAL OF ELECTRON SPECTROSCOPY AND RELATED PHENOMENA   Volume: 163   Issue: 1-3   Pages: 1-6   Published: APR 2008

**Full Text from Publisher**    **View Abstract**

Times Cited: 0
*(from Web of Science Core Collection)*

**Usage Count**

☐ Select Page    ▣ ✉ 5K

Save to Other File Formats ▼    **Add to Marked List**

---

Sort by: Publication Date -- newest to oldest ▼    Page [1] of 1

Show: 50 per page ▼

*3 records matched your query of the 37,941,506 in the data limits you selected.*

more options / values...

**Refine**

**Funding Agencies** ◀

**Open Access** ◀

**Authors** ◀

**View all options**

*For advanced refine options, use*

**Analyze Results**

Web of Science | InCites | Journal Citation Reports | Essential Science Indicators | EndNote | | Sign In ▾ | Help | English ▾

# Web of Science

| Search | Search Results | | My Tools ▾ | Search History | Marked List 23 |

## Citing Articles: 1
*(from Web of Science Core Collection)*

**For:** X-ray photoelectron diffraction investigation of the cleavage plane in IT-transition metal dichalcogenides
**...Less**

### Times Cited Counts

1 in All Databases

1 in Web of Science Core Collection

0 in BIOSIS Citation Index

0 in Chinese Science Citation Database

0 data sets in Data Citation Index

0 publication in Data Citation Index

0 in Russian Science Citation Index

0 in SciELO Citation Index

**View Additional Times Cited Counts**

---

## Refine Results

*Search within results for...*

### Publication Years ▾

☐ 2012 (1)

**Refine**

### Web of Science Categories ▾

☐ PHYSICS CONDENSED MATTER (1)

☐ CHEMISTRY PHYSICAL (1)

more options / values...

**Refine**

### Document Types ▾

☐ ARTICLE (1)

**Refine**

### Organizations-Enhanced ▾

☐ URAL FEDERAL UNIVERSITY (1)

☐ RUSSIAN ACADEMY OF SCIENCES (1)

more options / values...

**Refine**

### Funding Agencies ◀

---

Sort by: Publication Date -- newest to oldest ▾

Page 1 of 1

☐ Select Page  🗗 ✉ 5K

Save to Other File Formats ▾  **Add to Marked List**

**Create Citation Report**

≣ **Analyze Results**

☐ 1. **Characterization of 1T-TiSe2 surface by means of STM and XPD experiments and model calculations**

By: Kuznetsov, M. V.; Ogorodnikov, I. I.; Vorokh, A. S.; et al.
SURFACE SCIENCE   Volume: 606   Issue: 23-24   Pages: 1760-1770   Published: DEC 2012

**Full Text from Publisher**   **View Abstract**

**Times Cited: 9**
*(from Web of Science Core Collection)*

**Usage Count**

☐ Select Page  🗗 ✉ 5K

Save to Other File Formats ▾  **Add to Marked List**

---

Sort by: Publication Date -- newest to oldest ▾

Page 1 of 1

Show: 50 per page ▾

*1 records matched your query of the 37,941,506 in the data limits you selected.*

**Open Access** ◀

**Authors** ◀

**View all options**

*For advanced refine options, use*

**Analyze Results**

**Web of Science**    InCites    Journal Citation Reports    Essential Science Indicators    EndNote                    Sign In ▾    Help    English ▾

# Web of Science

| Search | Search Results | | My Tools ▾ | Search History | Marked List 23 |

## Citing Articles: 2
*(from Web of Science Core Collection)*

**For:** Tunneling evidence for spatial location of the charge-density-wave induced band splitting in 1T-TaSe2
**...Less**

**Times Cited Counts**

2 in All Databases

2 in Web of Science Core Collection

0 in BIOSIS Citation Index

0 in Chinese Science Citation Database

0 data sets in Data Citation Index

0 publication in Data Citation Index

0 in Russian Science Citation Index

0 in SciELO Citation Index

**View Additional Times Cited Counts**

## Refine Results

*Search within results for...*

### Publication Years ▾

☐ 2014 (1)
☐ 2008 (1)

**more options / values...**

**Refine**

### Web of Science Categories ▾

☐ PHYSICS CONDENSED MATTER (2)

**Refine**

### Document Types ▾

☐ ARTICLE (2)

**Refine**

### Organizations-Enhanced ▾

☐ SWISS FEDERAL LABORATORIES FOR MATERIALS SCIENCE TECHNOLOGY EMPA (1)
☐ ROYAL INSTITUTE OF TECHNOLOGY (1)
☐ LUND UNIVERSITY (1)
☐ LEIDEN UNIVERSITY (1)
☐ ECOLE POLYTECHNIQUE FEDERALE DE LAUSANNE (1)

**more options / values...**

Sort by: Publication Date -- newest to oldest ▾          Page [1] of 1

☐ Select Page          5K
  Save to Other File Formats  ▾    **Add to Marked List**

**Create Citation Report**

≡ **Analyze Results**

☐ 1.  **Three-dimensional metallic and two-dimensional insulating behavior in octahedral tantalum dichalcogenides**

By: Darancet, Pierre; Millis, Andrew J.; Marianetti, Chris A.
PHYSICAL REVIEW B   Volume: 90   Issue: 4   Article Number: 045134   Published: JUL 25 2014

**View Abstract**

**Times Cited: 17**
*(from Web of Science Core Collection)*

**Usage Count**

☑ 2.  **Atomic origin of the scanning tunneling microscopy images of charge-density-waves on 1T-TaSe2**

By: Stoltz, D.; Bielmann, M.; Schlapbach, L.; et al.
PHYSICA B-CONDENSED MATTER   Volume: 403   Issue: 13-16   Pages: 2207-2210   Published: JUL 1 2008

**Full Text from Publisher**    **View Abstract**

**Times Cited: 0**
*(from Web of Science Core Collection)*

**Usage Count**

☐ Select Page          5K
  Save to Other File Formats  ▾    **Add to Marked List**

Sort by: Publication Date -- newest to oldest ▾          Page [1] of 1

Show: 50 per page ▾

*2 records matched your query of the 37,941,506 in the data limits you selected.*

| | **Refine** |
|---|---|
| **Funding Agencies** | ◀ |
| **Open Access** | ◀ |
| **Authors** | ◀ |

**View all options**

*For advanced refine options, use*

**Analyze Results**

# Web of Science

Search | Search Results | My Tools ▾ | Search History | Marked List 23

## Citing Articles: 4
*(from Web of Science Core Collection)*

**For:** High resolution spectroscopic and microscopic signatures of ordered growth of ferrous sulfate in SO2 assisted corrosion of Fe3O4(100)
**...Less**

### Times Cited Counts

4 in All Databases

4 in Web of Science Core Collection

0 in BIOSIS Citation Index

0 in Chinese Science Citation Database

0 data sets in Data Citation Index

0 publication in Data Citation Index

0 in Russian Science Citation Index

0 in SciELO Citation Index

**View Additional Times Cited Counts**

### Refine Results

Search within results for...

**Publication Years** ▾

☐ 2016 (2)
☐ 2013 (2)

more options / values...

**Refine**

**Web of Science Categories** ▾

☐ CHEMISTRY PHYSICAL (4)
☐ PHYSICS CONDENSED MATTER (2)
☐ PHYSICS ATOMIC MOLECULAR CHEMICAL (1)
☐ NANOSCIENCE NANOTECHNOLOGY (1)
☐ MATERIALS SCIENCE MULTIDISCIPLINARY (1)

more options / values...

**Refine**

**Document Types** ▾

☐ ARTICLE (3)
☐ REVIEW (1)

more options / values...

**Refine**

**Organizations-Enhanced** ▾

---

Sort by: Publication Date -- newest to oldest ▾     Page 1 of 1

☐ Select Page     🗗 ✉ 5K

Save to Other File Formats ▾     **Add to Marked List**

**Create Citation Report**

📊 **Analyze Results**

☐ 1. **Molecular degradation of D35 and K77 sensitizers when exposed to temperatures exceeding 100 degrees C investigated by photoelectron spectroscopy**

By: Oscarsson, Johan; Fredin, Kristofer; Ahmadi, Sareh; et al.
PHYSICAL CHEMISTRY CHEMICAL PHYSICS   Volume: 18   Issue: 12   Pages: 8598-8607   Published: MAR 28 2016

**View Abstract**

**Times Cited: 1**
*(from Web of Science Core Collection)*

**Usage Count**

☐ 2. **Iron oxide surfaces**

By: Parkinson, Gareth S.
SURFACE SCIENCE REPORTS   Volume: 71   Issue: 1   Pages: 272-365   Published: MAR 2016

**Full Text from Publisher**     **View Abstract**

**Times Cited: 18**
*(from Web of Science Core Collection)*

**Usage Count**

☐ 3. **Role of Defects in Surface Chemistry on Cu2O(111)**

✅ By: Onsten, Anneli; Weissenrieder, Jonas; Stoltz, Dunja; et al.
JOURNAL OF PHYSICAL CHEMISTRY C   Volume: 117   Issue: 38   Pages: 19357-19364   Published: SEP 26 2013

**View Abstract**

**Times Cited: 7**
*(from Web of Science Core Collection)*

**Usage Count**

☐ 4. **SO2 interaction with Zn(0001) and ZnO(0001) and the influence of water**

✅ By: Onsten, Anneli; Stoltz, Dunja; Palmgren, Pal; et al.
SURFACE SCIENCE   Volume: 608   Pages: 31-43   Published: FEB 2013

**Full Text from Publisher**     **View Abstract**

**Times Cited: 3**
*(from Web of Science Core Collection)*

**Usage Count**

☐ Select Page     🗗 ✉ 5K

Save to Other File Formats ▾     **Add to Marked List**

---

Sort by: Publication Date -- newest to oldest ▾     Page 1 of 1

Show: 50 per page ▾

*4 records matched your query of the 37,941,506 in the data limits you selected.*

☐ ROYAL INSTITUTE OF
　　TECHNOLOGY (2)

☐ VIENNA UNIVERSITY OF
　　TECHNOLOGY (1)

☐ UPPSALA UNIVERSITY (1)

**more options / values...**

| | **Refine** |
|---|---|

| **Funding Agencies** | ◀ |
|---|---|

| **Open Access** | ◀ |
|---|---|

| **Authors** | ◀ |
|---|---|

**View all options**

*For advanced refine options, use*

**Analyze Results**

# Web of Science

| Search | Search Results | | My Tools ▾ | Search History | Marked List   23 |

## Citing Articles: 6
*(from Web of Science Core Collection)*

**For:** Scanning tunneling microscopy of Fe- and O-sublattices on Fe(3)O(4) (100) ...Less

### Times Cited Counts

**6 in All Databases**

6 in Web of Science Core Collection

1 in BIOSIS Citation Index

0 in Chinese Science Citation Database

0 data sets in Data Citation Index

0 publication in Data Citation Index

0 in Russian Science Citation Index

0 in SciELO Citation Index

**View Additional Times Cited Counts**

### Refine Results

Search within results for...

**Publication Years**   ▼

☐ 2013 (4)

☐ 2016 (1)

☐ 2010 (1)

more options / values...

**Refine**

**Web of Science Categories**   ▼

☐ PHYSICS CONDENSED MATTER (3)

☐ CHEMISTRY PHYSICAL (2)

☐ NANOSCIENCE NANOTECHNOLOGY (1)

☐ MICROSCOPY (1)

☐ MATERIALS SCIENCE MULTIDISCIPLINARY (1)

more options / values...

**Refine**

**Document Types**   ▼

☐ ARTICLE (5)

☐ REVIEW (1)

☐ PROCEEDINGS PAPER (1)

more options / values...

**Refine**

**Organizations-Enhanced**   ▼

---

Sort by: Publication Date -- newest to oldest ▾     Page [1] of 1

☐ Select Page     🗔  ✉  5K

Save to Other File Formats ▾     **Add to Marked List**

**Create Citation Report**

☰ **Analyze Results**

☐ 1. **Iron oxide surfaces**

By: Parkinson, Gareth S.
SURFACE SCIENCE REPORTS   Volume: 71   Issue: 1   Pages: 272-365   Published: MAR 2016

**Full Text from Publisher**   **View Abstract**

Times Cited: **18**
*(from Web of Science Core Collection)*

Usage Count

☐ 2. **Order-disorder phase transition on the (100) surface of magnetite**

By: Bartelt, Norman C.; Nie, Shu; Starodub, Elena; et al.
PHYSICAL REVIEW B   Volume: 88   Issue: 23   Article Number: 235436   Published: DEC 30 2013

**View Abstract**

Times Cited: **8**
*(from Web of Science Core Collection)*

Usage Count

☐ 3. **Real-space imaging of the Verwey transition at the (100) surface of magnetite**

By: de la Figuera, Juan; Novotny, Zbynek; Setvin, Martin; et al.
PHYSICAL REVIEW B   Volume: 88   Issue: 16   Article Number: 161410   Published: OCT 29 2013

**View Abstract**

Times Cited: **9**
*(from Web of Science Core Collection)*

Usage Count

☐ 4. **Micromagnetism in (001) magnetite by spin-polarized low-energy electron microscopy**

By: de la Figuera, Juan; Vergara, Lucia; N'Diaye, Alpha T.; et al.
Conference: 8th International Workshop on Low Energy Electron Microscopy and Photoemission Electron Microscopy (LEEM/PEEM) Location: Hong Kong, PEOPLES R CHINA Date: NOV 11-15, 2012
Sponsor(s): SPECS; ELMITEC; Omicron; Focus; Toyama; HKUST, Sch Sci; HKUST, Inst Adv Study
ULTRAMICROSCOPY   Volume: 130   Special Issue: SI   Pages: 77-81   Published: JUL 2013

**Full Text from Publisher**   **View Abstract**

Times Cited: **11**
*(from Web of Science Core Collection)*

Usage Count

☐ 5. **X-ray Photoemission and Density Functional Theory Study of the Interaction of Water Vapor with the Fe3O4(001) Surface at Near-Ambient Conditions**

By: Kendelewicz, T.; Kaya, S.; Newberg, J. T.; et al.
JOURNAL OF PHYSICAL CHEMISTRY C   Volume: 117   Issue: 6   Pages: 2719-2733   Published: FEB 14 2013

**View Abstract**

Times Cited: **34**
*(from Web of Science Core Collection)*

Usage Count

☐ 6. **Structure, charge distribution, and electron hopping dynamics in magnetite (Fe3O4) (100) surfaces from first principles**

By: Skomurski, Frances N.; Kerisit, Sebastien; Rosso, Kevin M.

Times Cited: **30**
*(from Web of Science Core Collection)*

Usage Count

UNITED STATES DEPARTMENT
OF ENERGY DOE (5)

UNIVERSITY OF CALIFORNIA
SYSTEM (3)

UNIVERSITY OF CALIFORNIA
BERKELEY (3)

LAWRENCE BERKELEY
NATIONAL LABORATORY (3)

CSIC INSTITUTO DE QUIMICA
FISICA ROCASOLANO IQFR (3)

**more options / values...**

**Refine**

**Funding Agencies** ◀

**Open Access** ◀

**Authors** ◀

**View all options**

*For advanced refine options, use*

**Analyze Results**

GEOCHIMICA ET COSMOCHIMICA ACTA   Volume: 74
Issue: 15   Pages: 4234-4248   Published: AUG 1 2010

**Full Text from Publisher**     **View Abstract**

☐   Select Page     🖸 ✉ *5K*

Save to Other File Formats    ▾    **Add to Marked List**

Sort by:   Publication Date -- newest to oldest   ▾      Page ☐   of   1

Show:   50 per page   ▾

*6 records matched your query of the 37,941,506 in the data limits you selected.*

| Web of Science | InCites | Journal Citation Reports | Essential Science Indicators | EndNote | Sign In ▼ | Help | English ▼ |

# Web of Science

| Search | Search Results | | My Tools ▼ | Search History | Marked List 23 |

## Citing Articles: 33
*(from Web of Science Core Collection)*

**For:** Water Adsorption on ZnO(0001): Transition from Triangular Surface Structures to a Disordered Hydroxyl Terminated phase **...Less**

### Times Cited Counts

**34 in All Databases**

34 in Web of Science Core Collection

0 in BIOSIS Citation Index

0 in Chinese Science Citation Database

0 data sets in Data Citation Index

0 publication in Data Citation Index

0 in Russian Science Citation Index

0 in SciELO Citation Index

**View Additional Times Cited Counts**

---

## Refine Results

*Search within results for...*

### Publication Years ▼

- ☐ 2013 (8)
- ☐ 2014 (7)
- ☐ 2012 (6)
- ☐ 2016 (5)
- ☐ 2015 (4)

**more options / values...**

**Refine**

### Web of Science Categories ▼

- ☐ MATERIALS SCIENCE MULTIDISCIPLINARY (18)
- ☐ CHEMISTRY PHYSICAL (18)
- ☐ NANOSCIENCE NANOTECHNOLOGY (11)
- ☐ PHYSICS CONDENSED MATTER (5)
- ☐ PHYSICS APPLIED (3)

**more options / values...**

**Refine**

### Document Types ▼

- ☐ ARTICLE (31)
- ☐ PROCEEDINGS PAPER (2)
- ☐ REVIEW (1)

**more options / values...**

**Refine**

---

Sort by: Publication Date -- newest to oldest ▼

Page 1 of 1

☐ Select Page 🖶 ✉ 5K

Save to Other File Formats ▼    **Add to Marked List**

**Create Citation Report**

**Analyze Results**

☐ 1. **Defects/vacancies engineering and ferromagnetic behavior in pure ZnO and ZnO doped with Co nanoparticles**

By: Aljawf, Rezq Naji; Rahman, F.; Kumar, Shalendra
MATERIALS RESEARCH BULLETIN Volume: 83 Pages: 108-115 Published: NOV 2016

**Full Text from Publisher** **View Abstract**

Times Cited: **3**
*(from Web of Science Core Collection)*

Usage Count

☐ 2. **Identifying the sources of ferromagnetism in sol-gel synthesized Zn1-xCoxO (0 <= x <= 0.10) nanoparticles**

By: Beltran, J. J.; Barrero, C. A.; Punnoose, A.
JOURNAL OF SOLID STATE CHEMISTRY Volume: 240 Pages: 30-42 Published: AUG 2016

**Full Text from Publisher** **View Abstract**

Times Cited: **1**
*(from Web of Science Core Collection)*

Usage Count

☐ 3. **D2O Interaction with Planar ZnO(0001) Bilayer Supported on Au(111): Structures, Energetics and Influence of Hydroxyls**

By: Deng, Xingyi; Sorescu, Dan C.; Lee, Junseok
JOURNAL OF PHYSICAL CHEMISTRY C Volume: 120 Issue: 15 Pages: 8157-8166 Published: APR 21 2016

**View Abstract**

Times Cited: **2**
*(from Web of Science Core Collection)*

Usage Count

☐ 4. **The origin of facet selectivity and alignment in anatase TiO2 nanoparticles in electrolyte solutions: implications for oriented attachment in metal oxides**

By: Sushko, M. L.; Rosso, K. M.
NANOSCALE Volume: 8 Issue: 47 Pages: 19714-19725 Published: 2016

**View Abstract**

Times Cited: **1**
*(from Web of Science Core Collection)*

Usage Count

☐ 5. **Effect of Water on Ethanol Conversion over ZnO**

By: Rahman, Muhammad Mahfuzur .; Davidson, Stephen D.; Sun, Junming; et al.
TOPICS IN CATALYSIS Volume: 59 Issue: 1 Pages: 37-45 Published: JAN 2016

**View Abstract**

Times Cited: **3**
*(from Web of Science Core Collection)*

Usage Count

☐ 6. **Stabilization of Ultrathin Zinc Oxide Films on Metals: Reconstruction versus Hydroxylation**

By: Liu, Bo-Hong; Boscoboinik, J. Anibal; Cui, Yi; et al.
JOURNAL OF PHYSICAL CHEMISTRY C Volume: 119 Issue: 14 Pages: 7842-7847 Published: APR 9 2015

**View Abstract**

Times Cited: **7**
*(from Web of Science Core Collection)*

Usage Count

## Organizations-Enhanced ▼

- [ ] UNITED STATES DEPARTMENT OF ENERGY DOE (4)
- [ ] UPPSALA UNIVERSITY (3)
- [ ] PACIFIC NORTHWEST NATIONAL LABORATORY (3)
- [ ] GEORGIA INSTITUTE OF TECHNOLOGY (2)
- [ ] FU JEN CATHOLIC UNIVERSITY (2)

**more options / values...**

**Refine**

## Funding Agencies ◄

## Open Access ◄

## Authors ◄

**View all options**

*For advanced refine options, use*

**Analyze Results**

---

7. **Zinc Oxide Nanostructures for NO2 Gas-Sensor Applications: A Review**

By: Kumar, Rajesh; Al-Dossary, O.; Kumar, Girish; et al.
NANO-MICRO LETTERS   Volume: 7   Issue: 2   Pages: 97-120   Published: APR 2015

Full Text from Publisher    View Abstract

**Times Cited: 40**
*(from Web of Science Core Collection)*

**Usage Count**

8. **Ultrasensitive and Ultraselective impedimetric Detection of Cr(VI) Using Crown Ethers as High-Affinity Targeting Receptors**

By: Wei, Juan; Guo, Zheng; Chen, Xing; et al.
ANALYTICAL CHEMISTRY   Volume: 87   Issue: 3   Pages: 1991-1998   Published: FEB 3 2015

View Abstract

**Times Cited: 11**
*(from Web of Science Core Collection)*

**Usage Count**

9. **Phase and structure development of spontaneously ambient-grown ZnO center dot xH(2)O and TiO2 center dot xH(2)O nanostructures towards oxide single crystals**

By: Yang, Nai-Hao; Chang, Shou-Yi; Liu, Chien-Yen; et al.
RSC ADVANCES   Volume: 5   Issue: 44   Pages: 35061-35069   Published: 2015

View Abstract

**Times Cited: 0**
*(from Web of Science Core Collection)*

**Usage Count**

10. **A series of copper-free ternary oxide catalysts ZnAlCex used for hydrogen production via dimethyl ether steam reforming**

By: Zhang, Lijie; Meng, Ming; Wang, Xiaojing; et al.
JOURNAL OF POWER SOURCES   Volume: 268   Pages: 331-340   Published: DEC 5 2014

Full Text from Publisher    View Abstract

**Times Cited: 5**
*(from Web of Science Core Collection)*

**Usage Count**

11. **Large-scale SCC-DFTB calculations of reconstructed polar ZnO surfaces**

By: Huber, Stefan E.; Hellstrom, Matti; Probst, Michael; et al.
SURFACE SCIENCE   Volume: 628   Pages: 50-61   Published: OCT 2014

Full Text from Publisher    View Abstract

**Times Cited: 2**
*(from Web of Science Core Collection)*

**Usage Count**

12. **Studies on the adsorption of chromium(VI) onto 3-Mercaptopropionic acid coated superparamagnetic iron oxide nanoparticles**

By: Burks, T.; Avila, M.; Akhtar, F.; et al.
JOURNAL OF COLLOID AND INTERFACE SCIENCE   Volume: 425   Pages: 36-43   Published: JUL 1 2014

Full Text from Publisher    View Abstract

**Times Cited: 29**
*(from Web of Science Core Collection)*

**Usage Count**

13. **Zinc Oxide Nanoparticles Catalyze Rapid Hydrolysis of Poly( lactic acid) at Low Temperatures**

By: Qu, Meng; Tu, Huilin; Amarante, Miranda; et al.
JOURNAL OF APPLIED POLYMER SCIENCE   Volume: 131   Issue: 11   Article Number: 40287   Published: JUN 5 2014

View Abstract

**Times Cited: 8**
*(from Web of Science Core Collection)*

**Usage Count**

14. **Electrochemically deposited ZnO films: an XPS study on the evolution of their surface hydroxide and defect composition upon thermal annealing**

By: Marrani, Andrea Giacomo; Caprioli, Fabrizio; Boccia, Alice; et al.
JOURNAL OF SOLID STATE ELECTROCHEMISTRY   Volume: 18   Issue: 2   Pages: 505-513   Published: FEB 2014

View Abstract

**Times Cited: 12**
*(from Web of Science Core Collection)*

**Usage Count**

15. **Formation of Copper Nanoparticles on ZnO Powder by a Surface-Limited Reaction**

By: Kung, Hsuan; Teplyakov, Andrew V.
JOURNAL OF PHYSICAL CHEMISTRY C   Volume: 118
Issue: 4   Pages: 1990-1998   Published: JAN 30 2014

View Abstract

**Times Cited: 6**
*(from Web of Science Core Collection)*

**Usage Count**

16. **Transparent Conducting Oxides of Relevance to Organic Electronics: Electronic Structures of Their Interfaces with Organic Layers**

By: Li, Hong; Winget, Paul; Bredast, Jean-Luc
CHEMISTRY OF MATERIALS   Volume: 26   Issue: 1
Special Issue: SI   Pages: 631-646   Published: JAN 14 2014

View Abstract

**Times Cited: 20**
*(from Web of Science Core Collection)*

**Usage Count**

17. **Face-Selective Etching of ZnO during Attachment of Dyes**

By: Palacios-Lidon, E.; Pickup, D. F.; Johnson, P. S.; et al.
JOURNAL OF PHYSICAL CHEMISTRY C   Volume: 117
Issue: 36   Pages: 18414-18422   Published: SEP 12 2013

View Abstract

**Times Cited: 6**
*(from Web of Science Core Collection)*

**Usage Count**

18. **An SCC-DFTB Repulsive Potential for Various ZnO Polymorphs and the ZnO-Water System**

By: Hellstrom, Matti; Jorner, Kjell; Bryngelsson, Maria; et al.
JOURNAL OF PHYSICAL CHEMISTRY C   Volume: 117
Issue: 33   Pages: 17004-17015   Published: AUG 22 2013

View Abstract

**Times Cited: 9**
*(from Web of Science Core Collection)*

**Usage Count**

19. **Structures and Mechanisms of Water Adsorption on ZnO(0001) and GaN(0001) Surface**

By: Ye, Honggang; Chen, Guangde; Niu, Haibo; et al.
JOURNAL OF PHYSICAL CHEMISTRY C   Volume: 117
Issue: 31   Pages: 15976-15983   Published: AUG 8 2013

View Abstract

**Times Cited: 6**
*(from Web of Science Core Collection)*

**Usage Count**

20. **Density Functional Study of the First Wetting Layer on the GaN (0001) Surface**

By: Chen, Yun-Wen; Kuo, Jer-Lai
JOURNAL OF PHYSICAL CHEMISTRY C   Volume: 117
Issue: 17   Pages: 8774-8783   Published: MAY 2 2013

View Abstract

**Times Cited: 11**
*(from Web of Science Core Collection)*

**Usage Count**

21. **High CO2 Selectivity of ZnO Powder Catalysts for Methanol Steam Reforming**

By: Halevi, Barr; Lin, Sen; Roy, Aaron; et al.
JOURNAL OF PHYSICAL CHEMISTRY C   Volume: 117
Issue: 13   Pages: 6493-6503   Published: APR 4 2013

View Abstract

**Times Cited: 11**
*(from Web of Science Core Collection)*

**Usage Count**

22. **Surface defect mediated magnetic interactions and ferromagnetism in Cr/Co Co-doped ZnO nanoparticles**

By: Aljawfi, Rezq Naji; Rahman, F.; Batoo, Khalid Mujasam
JOURNAL OF MAGNETISM AND MAGNETIC MATERIALS   Volume: 332   Pages: 130-136   Published: APR 2013

Full Text from Publisher    View Abstract

**Times Cited: 17**
*(from Web of Science Core Collection)*

**Usage Count**

23. **SO2 interaction with Zn(0001) and ZnO(0001) and the influence of water**

By: Onsten, Anneli; Stoltz, Dunja; Palmgren, Pal; et al.

**Times Cited: 3**
*(from Web of Science Core Collection)*

**Usage Count**

SURFACE SCIENCE   Volume: 608   Pages: 31-43
Published: FEB 2013

**Full Text from Publisher**    **View Abstract**

24. **Various post-annealing treatments on aluminum doped zinc oxide films fabricated by ion beam co-sputtering**

By: Hsu, Jin-Cherng; Chen, Yu-Yun; Chiang, Yueh-Sheng; et al.
Edited by: Teherani, FH; Look, DC; Rogers, DJ
Conference: Conference on Oxide-Based Materials and Devices IV Location: San Francisco, CA Date: FEB 03-06, 2013
Sponsor(s): SPIE
OXIDE-BASED MATERIALS AND DEVICES IV   Book Series: Proceedings of SPIE   Volume: 8626   Article Number: 86261J
Published: 2013

**View Abstract**

Times Cited: 0
*(from Web of Science Core Collection)*

Usage Count

25. **ONIOM study of dissociated hydrogen and water on ZnO surface**

By: Martins, Joao B. L.; Taft, Carlton A.; Longo, Elson; et al.
Conference: 16th Brazilian Symposium of Theoretical Chemistry (SBQT) Location: Ouro Preto, BRAZIL Date: NOV 20-23, 2011
INTERNATIONAL JOURNAL OF QUANTUM CHEMISTRY   Volume: 112   Issue: 19   Special Issue: SI
Pages: 3223-3227   Published: OCT 5 2012

**View Abstract**

Times Cited: 5
*(from Web of Science Core Collection)*

Usage Count

26. **Polarity-dependent photoemission of in situ cleaved zinc oxide single crystals**

By: Heinhold, Robert; Allen, Martin Ward
JOURNAL OF MATERIALS RESEARCH   Volume: 27
Issue: 17   Pages: 2214-2219   Published: SEP 2012

**View Abstract**

Times Cited: 3
*(from Web of Science Core Collection)*

Usage Count

27. **Zinc Oxide as a Model Transparent Conducting Oxide: A Theoretical and Experimental Study of the Impact of Hydroxylation, Vacancies, Interstitials, and Extrinsic Doping on the Electronic Properties of the Polar ZnO (0002) Surface**

By: Li, Hong; Schirra, Laura K.; Shim, Jaewon; et al.
CHEMISTRY OF MATERIALS   Volume: 24   Issue: 15
Pages: 3044-3055   Published: AUG 14 2012

**View Abstract**

Times Cited: 62
*(from Web of Science Core Collection)*

Usage Count

28. **Hydrogen-induced disruption of the ZnO(0001) polar surface**

By: Nishidate, Kazume; Hasegawa, Masayuki
PHYSICAL REVIEW B   Volume: 86   Issue: 3   Article Number: 035412   Published: JUL 9 2012

**View Abstract**

Times Cited: 2
*(from Web of Science Core Collection)*

Usage Count

29. **Bimetallic Nickel-Cobalt Nanosized Layers Supported on Polar ZnO Surfaces: Metal-Support Interaction and Alloy Effects Studied by Synchrotron Radiation X-ray Photoelectron Spectroscopy**

By: Law, Y. T.; Skala, T.; Pis, I.; et al.
JOURNAL OF PHYSICAL CHEMISTRY C   Volume: 116
Issue: 18   Pages: 10048-10056   Published: MAY 10 2012

**View Abstract**

Times Cited: 10
*(from Web of Science Core Collection)*

Usage Count

30. **Spectroscopic ellipsometry studies on various zinc oxide films deposited by ion beam sputtering at room temperature**

By: Hsu, Jin-Cherng; Lin, Yung-Hsin; Wang, Paul W.; et al.

Times Cited: 3
*(from Web of Science Core Collection)*

Usage Count

APPLIED OPTICS   Volume: 51   Issue: 9   Pages: 1209-1215   Published: MAR 20 2012

**View Abstract**

☐ 31. **Simulation of reconstructions of the polar ZnO(0001) surfaces**

By: Meskine, H.; Mulheran, P. A.
PHYSICAL REVIEW B   Volume: 84   Issue: 16   Article Number: 165430   Published: OCT 20 2011

**View Abstract**

Times Cited: **15**
*(from Web of Science Core Collection)*

Usage Count

☐ 32. **Room Temperature Water Splitting at the Surface of Magnetite**

By: Parkinson, Gareth S.; Novotny, Zbynek; Jacobson, Peter; et al.
JOURNAL OF THE AMERICAN CHEMICAL SOCIETY   Volume: 133   Issue: 32   Pages: 12650-12655   Published: AUG 17 2011

**View Abstract**

Times Cited: **50**
*(from Web of Science Core Collection)*

Usage Count

☐ 33. **Polarity effects in the x-ray photoemission of ZnO and other wurtzite semiconductors**

By: Allen, M. W.; Zemlyanov, D. Y.; Waterhouse, G. I. N.; et al.
APPLIED PHYSICS LETTERS   Volume: 98   Issue: 10   Article Number: 101906   Published: MAR 7 2011

**View Abstract**

Times Cited: **38**
*(from Web of Science Core Collection)*

Usage Count

☐ Select Page      🖫 ✉ *5K*

Save to Other File Formats   ▾     **Add to Marked List**

Sort by:   Publication Date -- newest to oldest   ▾

Show:   50 per page   ▾

Page [1]  of  1

*33 records matched your query of the 37,941,506 in the data limits you selected.*

| Web of Science | InCites | Journal Citation Reports | Essential Science Indicators | EndNote | | Sign In ▾ | Help | English ▾ |

# Web of Science

| Search | Search Results | | My Tools ▾ | Search History | Marked List 23 |

## Citing Articles: 87
*(from Web of Science Core Collection)*

**For:** The role of steps in surface catalysis and reaction oscillations
**...Less**

**Times Cited Counts**

89 in All Databases

89 in Web of Science Core Collection

7 in BIOSIS Citation Index

1 in Chinese Science Citation Database

0 data sets in Data Citation Index

0 publication in Data Citation Index

0 in Russian Science Citation Index

0 in SciELO Citation Index

**View Additional Times Cited Counts**

### Refine Results

*Search within results for...*

**Filter results by:**

- ☐ Highly Cited in Field (4)

**Refine**

**Publication Years** ▾

- ☐ 2016 (15)
- ☐ 2013 (15)
- ☐ 2014 (14)
- ☐ 2015 (13)
- ☐ 2012 (13)

**more options / values...**

**Refine**

**Web of Science Categories** ▾

- ☐ CHEMISTRY PHYSICAL (55)
- ☐ NANOSCIENCE NANOTECHNOLOGY (21)
- ☐ MATERIALS SCIENCE MULTIDISCIPLINARY (21)
- ☐ CHEMISTRY MULTIDISCIPLINARY (20)
- ☐ PHYSICS CONDENSED MATTER (17)

**more options / values...**

**Refine**

**Document Types** ▾

- ☐ ARTICLE (78)

---

Sort by: Publication Date -- newest to oldest ▾          Page 1 of 2

☐ Select Page     🗔  ✉  5K

Save to Other File Formats ▾     **Add to Marked List**

**Create Citation Report**

≡ **Analyze Results**

☐ 1. **Ceria-supported small Pt and Pt3Sn nanoparticles for NOx-assisted soot oxidation**

By: Andana, Tahrizi; Piumetti, Marco; Bensaid, Samir; et al.
APPLIED CATALYSIS B-ENVIRONMENTAL   Volume: 209   Pages: 295-310   Published: JUL 15 2017

**Full Text from Publisher**     **View Abstract**

Times Cited: 0
*(from Web of Science Core Collection)*

**Usage Count**

☐ 2. **In Situ Optical Reflectance Difference Observations of CO Oxidation over Pd(100)**

By: Onderwaater, Willem G.; Taranovskyy, Andriy; van Baarle, Gertjan C.; et al.
JOURNAL OF PHYSICAL CHEMISTRY C   Volume: 121   Issue: 21   Pages: 11407-11415   Published: JUN 1 2017

**View Abstract**

Times Cited: 0
*(from Web of Science Core Collection)*

**Usage Count**

☐ 3. **Tuning the work function of stepped metal surfaces by adsorption of organic molecules**

By: Jiang, Yingda; Li, Jingtai; Su, Guirong; et al.
JOURNAL OF PHYSICS-CONDENSED MATTER   Volume: 29   Issue: 20   Article Number: 204001   Published: MAY 24 2017

**View Abstract**

Times Cited: 0
*(from Web of Science Core Collection)*

**Usage Count**

☐ 4. **An In situ TEM study of the surface oxidation of palladium nanocrystals assisted by electron irradiation**

By: Zhang, Dejiong; Jin, Chuanhong; Tian, He; et al.
NANOSCALE   Volume: 9   Issue: 19   Pages: 6327-6333   Published: MAY 21 2017

**View Abstract**

Times Cited: 0
*(from Web of Science Core Collection)*

**Usage Count**

☐ 5. **Surface-Electronic-State-Modulated, Single-Crystalline (001) TiO2 Nanosheets for Sensitive Electrochemical Sensing of Heavy-Metal Ions**

By: Zhou, Wen-Yi; Liu, Jin-Yun; Song, Jie-Yao; et al.
ANALYTICAL CHEMISTRY   Volume: 89   Issue: 6   Pages: 3386-3394   Published: MAR 21 2017

**View Abstract**

Times Cited: 0
*(from Web of Science Core Collection)*

**Usage Count**

☐ 6. **From dull to shiny: A novel setup for reflectance difference analysis under catalytic conditions**

By: Onderwaater, Willem G.; Taranovskyy, Andriy; Bremmer, G. Marien; et al.
REVIEW OF SCIENTIFIC INSTRUMENTS   Volume: 88   Issue: 2   Article Number: 023704   Published: FEB 2017

**View Abstract**

Times Cited: 1
*(from Web of Science Core Collection)*

**Usage Count**

REVIEW (7)
PROCEEDINGS PAPER (3)
MEETING ABSTRACT (1)
EDITORIAL MATERIAL (1)

more options / values...

**Refine**

## Organizations-Enhanced ▼

UNITED STATES DEPARTMENT OF ENERGY DOE (10)
LUND UNIVERSITY (10)
EUROPEAN SYNCHROTRON RADIATION FACILITY ESRF (9)
MAX PLANCK SOCIETY (7)
LAWRENCE BERKELEY NATIONAL LABORATORY (7)

more options / values...

**Refine**

## Funding Agencies ◀

## Open Access ◀

## Authors ◀

**View all options**

*For advanced refine options, use*

**Analyze Results**

---

7. **Strain Dependent Light-off Temperature in Catalysis Revealed by Planar Laser-Induced Fluorescence**

By: Blomberg, Sara; Zetterberg, Johan; Zhou, Jianfeng; et al.
ACS CATALYSIS  Volume: 7  Issue: 1  Pages: 110-114  Published: JAN 2017

**View Abstract**

Times Cited: **2**
*(from Web of Science Core Collection)*

**Usage Count**

8. **Whither Goest Thou, Catalysis**

By: Augustine, Robert L.
CATALYSIS LETTERS  Volume: 146  Issue: 12  Pages: 2393-2416  Published: DEC 2016

**View Abstract**

Times Cited: **0**
*(from Web of Science Core Collection)*

**Usage Count**

9. **2D and 3D imaging of the gas phase close to an operating model catalyst by planar laser induced fluorescence**

By: Blomberg, Sara; Zhou, Jianfeng; Gustafson, Johan; et al.
JOURNAL OF PHYSICS-CONDENSED MATTER  Volume: 28  Issue: 45  Article Number: 453002  Published: NOV 16 2016

**View Abstract**

Times Cited: **3**
*(from Web of Science Core Collection)*

**Usage Count**

10. **Combined scanning probe microscopy and x-ray scattering instrument for in situ catalysis investigations**

By: Onderwaater, Willem G.; van der Tuijn, Peter C.; Mom, Rik V.; et al.
Conference: 21st Topical Conference on High-Temperature Plasma Diagnostics Location: Madison, WI Date: JUN 05-09, 2016
REVIEW OF SCIENTIFIC INSTRUMENTS  Volume: 87  Issue: 11  Article Number: 113705  Published: NOV 2016

**View Abstract**

Times Cited: **0**
*(from Web of Science Core Collection)*

**Usage Count**

11. **Comparing the catalytic activity of the water gas shift reaction on Cu(321) and Cu(111) surfaces: Step sites do not always enhance the overall reactivity**

By: Prats, Hector; Gamallo, Pablo; Illas, Francesc; et al.
JOURNAL OF CATALYSIS  Volume: 342  Pages: 75-83  Published: OCT 2016

**Full Text from Publisher**    **View Abstract**

Times Cited: **1**
*(from Web of Science Core Collection)*

**Usage Count**

12. **Formation of Second-Generation Nanoclusters on Metal Nanoparticles Driven by Reactant Gases**

By: Tao, Franklin Feng; Nguyen, Luan; Zhang, Shiran; et al.
NANO LETTERS  Volume: 16  Issue: 8  Pages: 5001-5009  Published: AUG 2016

**View Abstract**

Times Cited: **5**
*(from Web of Science Core Collection)*

**Usage Count**

13. **In-Situ TEM on Epitaxial and Non-Epitaxial Oxidation of Pd and Reduction of PdO at P=0.2-0.7 bar and T=20-650 degrees C**

By: Yokosawa, Tadahiro; Tichelaar, Frans D.; Zandbergen, Henny W.
EUROPEAN JOURNAL OF INORGANIC CHEMISTRY  Issue: 19  Pages: 3094-3102  Published: JUL 2016

**View Abstract**

Times Cited: **0**
*(from Web of Science Core Collection)*

**Usage Count**

14. **Reversed Hysteresis during CO Oxidation over Pd75Ag25(100)**

By: Fernandes, Vasco R.; Van den Bossche, Maxime; Knudsen, Jan; et al.

Times Cited: **0**
*(from Web of Science Core Collection)*

**Usage Count**

ACS CATALYSIS   Volume: 6   Issue: 7   Pages: 4154-4161
Published: JUL 2016

**View Abstract**

---

15.  **Active Site Dependent Reaction Mechanism over Ru/CeO2 Catalyst toward CO2 Methanation**

By: Wang, Fei; He, Shan; Chen, Hao; et al.
JOURNAL OF THE AMERICAN CHEMICAL SOCIETY
Volume: 138   Issue: 19   Pages: 6298-6305   Published: MAY 18 2016

**View Abstract**

Times Cited: **8**
*(from Web of Science Core Collection)*

**Usage Count**

---

16.  **CO oxidation on large high-index faceted Pd nanostructures**

By: Sreedhala, S.; Sudheeshkumar, V.; Vinod, C. P.
JOURNAL OF CATALYSIS   Volume: 337   Pages: 138-144
Published: MAY 2016

**Full Text from Publisher**   **View Abstract**

Times Cited: **1**
*(from Web of Science Core Collection)*

**Usage Count**

---

17.  **A versatile instrument for ambient pressure x-ray photoelectron spectroscopy: The Lund cell approach**

By: Knudsen, Jan; Andersen, Jesper N.; Schnadt, Joachim
SURFACE SCIENCE   Volume: 646   Special Issue: SI
Pages: 160-169   Published: APR 2016

**Full Text from Publisher**   **View Abstract**

Times Cited: **6**
*(from Web of Science Core Collection)*

**Usage Count**

---

18.  **Ab Initio Thermodynamics and First-Principles Microkinetics for Surface Catalysis**

By: Reuter, Karsten
CATALYSIS LETTERS   Volume: 146   Issue: 3   Pages: 541-563   Published: MAR 2016

**View Abstract**

Times Cited: **12**
*(from Web of Science Core Collection)*

**Usage Count**

---

19.  **Insight into the adsorption and dissociation of water over different CuO(111) surfaces: The effect of surface structures**

By: Zhang, Jin; Zhang, Riguang; Wang, Baojun; et al.
APPLIED SURFACE SCIENCE   Volume: 364   Pages: 758-768   Published: FEB 28 2016

**Full Text from Publisher**   **View Abstract**

Times Cited: **1**
*(from Web of Science Core Collection)*

**Usage Count**

---

20.  **A hot tip: imaging phenomena using in situ multi-stimulus probes at high temperatures**

By: Nonnenmann, Stephen S.
NANOSCALE   Volume: 8   Issue: 6   Pages: 3164-3180
Published: FEB 14 2016

**View Abstract**

Times Cited: **2**
*(from Web of Science Core Collection)*

**Usage Count**

---

21.  **Evolution of self-sustained kinetic oscillations in the catalytic oxidation of propane over a nickel foil**

By: Kaichev, V. V.; Teschner, D.; Saraev, A. A.; et al.
JOURNAL OF CATALYSIS   Volume: 334   Pages: 23-33
Published: FEB 2016

**Full Text from Publisher**   **View Abstract**

Times Cited: **6**
*(from Web of Science Core Collection)*

**Usage Count**

---

22.  **Low temperature platinum atomic layer deposition on nylon-6 for highly conductive and catalytic fiber mats**

By: Mundy, J. Zachary; Shafiefarhood, Arya; Li, Fanxing; et al.
JOURNAL OF VACUUM SCIENCE & TECHNOLOGY A
Volume: 34   Issue: 1   Article Number: 01A152   Published: JAN 2016

**View Abstract**

Times Cited: **1**
*(from Web of Science Core Collection)*

**Usage Count**

23. **X-ray photoemission analysis of clean and carbon monoxide-chemisorbed platinum(111) stepped surfaces using a curved crystal**

By: Walter, Andrew L.; Schiller, Frederik; Corso, Martina; et al.
NATURE COMMUNICATIONS　Volume: 6　Article Number: 8903　Published: NOV 2015

Full Text from Publisher | View Abstract

**Times Cited: 7**
*(from Web of Science Core Collection)*

**Usage Count**

24. **Formation of surface oxides and Ag2O thin films with atomic oxygen on Ag(111)**

By: Derouin, Jonathan; Farber, Rachael G.; Heslop, Stacy L.; et al.
SURFACE SCIENCE　Volume: 641　Pages: L1-L4　Published: NOV 2015

Full Text from Publisher | View Abstract

**Times Cited: 8**
*(from Web of Science Core Collection)*

**Usage Count**

25. **Direct Visualization of Catalytically Active Sites at the FeO-Pt(111) Interface**

By: Kudernatsch, Wilhelmine; Peng, Guowen; Zeuthen, Helene; et al.
ACS NANO　Volume: 9　Issue: 8　Pages: 7804-7814　Published: AUG 2015

View Abstract

**Times Cited: 13**
*(from Web of Science Core Collection)*

**Usage Count**

26. **Operando spatially and time-resolved X-ray absorption spectroscopy and infrared thermography during oscillatory CO oxidation**

By: Gaenzler, Andreas M.; Casapu, Maria; Boubnov, Alexey; et al.
JOURNAL OF CATALYSIS　Volume: 328　Special Issue: SI　Pages: 216-224　Published: AUG 2015

Full Text from Publisher | View Abstract

**Times Cited: 21**
*(from Web of Science Core Collection)*

**Usage Count**

27. **Nanohole-Structured and Palladium-Embedded 3D Porous Graphene for Ultrahigh Hydrogen Storage and CO Oxidation Multifunctionalities**

By: Kumar, Rajesh; Oh, Jung-Hwan; Kim, Hyun-Jun; et al.
ACS NANO　Volume: 9　Issue: 7　Pages: 7343-7351　Published: JUL 2015

View Abstract

**Times Cited: 29**
*(from Web of Science Core Collection)*

**Usage Count**

28. **Nanocatalysis: size- and shape-dependent chemisorption and catalytic reactivity**

By: Cuenya, Beatriz Roldan; Behafarid, Farzad
SURFACE SCIENCE REPORTS　Volume: 70　Issue: 2　Pages: 135-187　Published: JUN 2015

Full Text from Publisher | View Abstract

**Times Cited: 30**
*(from Web of Science Core Collection)*

**Usage Count**

29. **Reconstruction of steps on the Cu(111) surface induced by sulfur**

By: Walen, Holly; Liu, Da-Jiang; Oh, Junepyo; et al.
JOURNAL OF CHEMICAL PHYSICS　Volume: 142　Issue: 19　Article Number: 194711　Published: MAY 21 2015

View Abstract

**Times Cited: 4**
*(from Web of Science Core Collection)*

**Usage Count**

30. **Synchrotron X-Ray Scattering as a Tool for Characterising Catalysts on Multiple Length Scales**

By: Hudspeth, Jessica M.; Kvashnina, Kristina O.; Kimber, Simon A. J.; et al.
Conference: NextLab Location: IFP Energies nouvelles, Rueil-Malmaison, FRANCE Date: APR 02-04, 2014
OIL & GAS SCIENCE AND TECHNOLOGY-REVUE D IFP ENERGIES NOUVELLES　Volume: 70　Issue: 3　Pages: 429-436　Published: MAY-JUN 2015

**Times Cited: 0**
*(from Web of Science Core Collection)*

**Usage Count**

**Full Text from Publisher**    **View Abstract**

31.  **Catalytic Reaction Processes Revealed by Scanning Probe Microscopy**

By: Jiang, Peng; Bao, Xinhe; Salmeron, Miquel
ACCOUNTS OF CHEMICAL RESEARCH   Volume: 48
Issue: 5   Pages: 1524-1531   Published: MAY 2015

**View Abstract**

Times Cited: **6**
(from Web of Science Core Collection)

**Usage Count**

32.  **Influence of Subsurface Oxygen in the Catalytic CO Oxidation on Pd(111)**

By: Wrobel, Rafal J.; Becker, Stefan; Weiss, Helmut
JOURNAL OF PHYSICAL CHEMISTRY C   Volume: 119
Issue: 10   Pages: 5386-5394   Published: MAR 12 2015

**View Abstract**

Times Cited: **4**
(from Web of Science Core Collection)

**Usage Count**

33.  **Multi-lattice Kinetic Monte Carlo Simulations from First Principles: Reduction of the Pd(100) Surface Oxide by CO**

By: Hoffmann, Max J.; Scheffler, Matthias; Reuter, Karsten
ACS CATALYSIS   Volume: 5   Issue: 2   Pages: 1199-1209
Published: FEB 2015

**View Abstract**

Times Cited: **9**
(from Web of Science Core Collection)

**Usage Count**

34.  **Visible to near-infrared plasmon-enhanced catalytic activity of Pd hexagonal nanoplates for the Suzuki coupling reaction**

By: Trinh, T. Thuy; Sato, Ryota; Sakamoto, Masanori; et al.
NANOSCALE   Volume: 7   Issue: 29   Pages: 12435-12444
Published: 2015

**View Abstract**

Times Cited: **7**
(from Web of Science Core Collection)

**Usage Count**

35.  **The study of the active surface for CO oxidation over supported Pd catalysts**

By: Weng, Xuefei; Yuan, Xiang; Li, Huan; et al.
SCIENCE CHINA-CHEMISTRY   Volume: 58   Issue: 1
Special Issue: SI   Pages: 174-179   Published: JAN 2015

**View Abstract**

Times Cited: **2**
(from Web of Science Core Collection)

**Usage Count**

36.  **Trends in the Adsorption and Dissociation of Water Clusters on Flat and Stepped Metallic Surfaces**

By: Pekoez, Rengin; Woerner, Svenja; Ghiringhelli, Luca M.; et al.
JOURNAL OF PHYSICAL CHEMISTRY C   Volume: 118
Issue: 51   Pages: 29990-29998   Published: DEC 25 2014

**View Abstract**

Times Cited: **10**
(from Web of Science Core Collection)

**Usage Count**

37.  **CO Oxidation on the Pd(111) Surface**

By: Duan, Zhiyao; Henkelman, Graeme
ACS CATALYSIS   Volume: 4   Issue: 10   Pages: 3435-3443
Published: OCT 2014

**View Abstract**

Times Cited: **12**
(from Web of Science Core Collection)

**Usage Count**

38.  **A high pressure X-ray photoelectron spectroscopy study of oxidation and reduction of Rh(100) and Rh nanoparticles**

By: Blomberg, S.; Westerstrom, R.; Martin, N. M.; et al.
SURFACE SCIENCE   Volume: 628   Pages: 153-158
Published: OCT 2014

**Full Text from Publisher**    **View Abstract**

Times Cited: **7**
(from Web of Science Core Collection)

**Usage Count**

39.  **Surface-Step-Induced Oscillatory Oxide Growth**

Times Cited: **11**

By: Li, Liang; Luo, Langli; Ciston, Jim; et al.
PHYSICAL REVIEW LETTERS    Volume: 113   Issue: 13
Article Number: 136104   Published: SEP 25 2014

**View Abstract**

40.  **Influence of Step Geometry on the Reconstruction of
     Stepped Platinum Surfaces under Coadsorption of
     Ethylene and CO**

By: Zhu, Zhongwei; Barroo, Cedric; Lichtenstein, Leonid; et al.
JOURNAL OF PHYSICAL CHEMISTRY LETTERS
Volume: 5   Issue: 15   Pages: 2626-2631   Published: AUG 7
2014

**View Abstract**

Times Cited: 4

41.  **Palladium Nanoparticles Supported on Nitrogen-
     Doped Carbon Nanofibers: Synthesis,
     Microstructure, Catalytic Properties, and Self-
     Sustained Oscillation Phenomena in Carbon
     Monoxide Oxidation**

By: Stonkus, Olga A.; Kibis, Lidiya S.; Podyacheva, Olga Yu.;
et al.
CHEMCATCHEM   Volume: 6   Issue: 7   Pages: 2115-2128
Published: JUL 2014

**View Abstract**

Times Cited: 16

42.  **What drives spontaneous oscillations during CO
     oxidation using O-2 over supported Rh/Al2O3
     catalysts?**

By: Figueroa, Santiago J. A.; Newton, Mark A.
JOURNAL OF CATALYSIS   Volume: 312   Pages: 69-77
Published: APR 2014

**Full Text from Publisher**          **View Abstract**

Times Cited: 9

43.  **Atomic scale insights into the initial oxidation of
     Ru(0001) using atomic**

By: Herd, Benjamin; Over, Herbert
SURFACE SCIENCE   Volume: 622   Pages: 24-34
Published: APR 2014

**Full Text from Publisher**          **View Abstract**

Times Cited: 10

44.  **Iron Catalyzed Asymmetric Hydrogenation of
     Ketones**

By: Li, Yanyun; Yu, Shenluan; Wu, Xiaofeng; et al.
JOURNAL OF THE AMERICAN CHEMICAL SOCIETY
Volume: 136   Issue: 10   Pages: 4031-4039   Published: MAR
12 2014

**View Abstract**

Times Cited: 81

45.  **Vicinal Rutile TiO2 Surfaces and Their Interactions
     with O-2**

By: Rieboldt, Felix; Bechstein, Ralf; Besenbacher, Flemming;
et al.
JOURNAL OF PHYSICAL CHEMISTRY C   Volume: 118
Issue: 7   Pages: 3620-3628   Published: FEB 20 2014

**View Abstract**

Times Cited: 8

46.  **Characterizing nano-scale electrocatalysis during
     partial oxidation of methane**

By: Lee, Daehee; Kim, Dongha; Kim, Joosun; et al.
SCIENTIFIC REPORTS   Volume: 4   Article Number: 3937
Published: FEB 3 2014

**Full Text from Publisher**          **View Abstract**

Times Cited: 3

47.  **CO Oxidation on Pd(100) Versus PdO(101)-(root 5 x**

Times Cited: 12

**root 5)R27 degrees First-Principles Kinetic Phase Diagrams and Bistability Conditions**

By: Hoffmann, Max J.; Reuter, Karsten
TOPICS IN CATALYSIS　Volume: 57　Issue: 1-4　Pages: 159-170　Published: FEB 2014

**View Abstract**

*(Collection)*

**Usage Count**

---

48. **Recent advances in heterogeneous selective oxidation catalysis for sustainable chemistry**

By: Guo, Zhen; Liu, Bin; Zhang, Qinghong; et al.
CHEMICAL SOCIETY REVIEWS　Volume: 43　Issue: 10　Pages: 3480-3524　Published: 2014

**View Abstract**

**Times Cited: 134**
*(from Web of Science Core Collection)*

**Highly Cited Paper**

**Usage Count**

---

49. **Generation of surface steps on Pt(977) induced by the catalytic oxidation of CO**

By: Balmes, O.; Prevot, G.; Torrelles, X.; et al.
JOURNAL OF CATALYSIS　Volume: 309　Pages: 33-37　Published: JAN 2014

**Full Text from Publisher**　　**View Abstract**

**Times Cited: 5**
*(from Web of Science Core Collection)*

**Usage Count**

---

50. **Kinetics and Active Surfaces for CO Oxidation on Pt-Group Metals Under Oxygen Rich Conditions**

By: Chen, Mingshu; Zheng, Yanping; Wan, Huilin
TOPICS IN CATALYSIS　Volume: 56　Issue: 15-17　Pages: 1299-1313　Published: NOV 2013

**View Abstract**

**Times Cited: 7**
*(from Web of Science Core Collection)*

**Usage Count**

---

Select Page　　　　5K

Save to Other File Formats　　▼　　**Add to Marked List**

---

Sort by: Publication Date -- newest to oldest　　▼

Show: 50 per page　　▼

Page [ 1 ] of 2

*87 records matched your query of the 37,941,506 in the data limits you selected.*

---

# Web of Science

| Search | Search Results | | My Tools ▾ | Search History | Marked List   23 |

## Citing Articles: 87
*(from Web of Science Core Collection)*

**For:** The role of steps in surface catalysis and reaction oscillations **...More**

**Times Cited Counts**

89 in All Databases

89 in Web of Science Core Collection

7 in BIOSIS Citation Index

1 in Chinese Science Citation Database

0 data sets in Data Citation Index

0 publication in Data Citation Index

0 in Russian Science Citation Index

0 in SciELO Citation Index

**View Additional Times Cited Counts**

---

**Refine Results**

*Search within results for...*

**Filter results by:**

☐ Highly Cited in Field (4)

**Refine**

**Publication Years** ▼

☐ 2016 (15)
☐ 2013 (15)
☐ 2014 (14)
☐ 2015 (13)
☐ 2012 (13)

**more options / values...**

**Refine**

**Web of Science Categories** ▼

☐ CHEMISTRY PHYSICAL (55)
☐ NANOSCIENCE NANOTECHNOLOGY (21)
☐ MATERIALS SCIENCE MULTIDISCIPLINARY (21)
☐ CHEMISTRY MULTIDISCIPLINARY (20)
☐ PHYSICS CONDENSED MATTER (17)

**more options / values...**

**Refine**

**Document Types** ▼

☐ ARTICLE (78)
☐ REVIEW (7)

---

Sort by:   Publication Date -- newest to oldest ▾      Page 2 of 2

☐ Select Page    🗗 ✉ 5K

Save to Other File Formats ▾    **Add to Marked List**

**Create Citation Report**

**☰ Analyze Results**

☐ 51. **In-situ X-ray diffraction studies of the catalytic CO oxidation on Pd surfaces and clusters at real working conditions**

By: Balmes, Olivier; van Rijn, Richard; Frenken, Joost W. M.; et al.
Conference: 246th National Meeting of the American-Chemical-Society (ACS) Location: Indianapolis, IN Date: SEP 08-12, 2013
Sponsor(s): Amer Chem Soc
ABSTRACTS OF PAPERS OF THE AMERICAN CHEMICAL SOCIETY   Volume: 246   Meeting Abstract: 122-CATL
Published: SEP 8 2013

**Times Cited: 0**
*(from Web of Science Core Collection)*

Usage Count

☐ 52. **Structure and Chemical State of the Pt(557) Surface during Hydrogen Oxidation Reaction Studied by in Situ Scanning Tunneling Microscopy and X-ray Photoelectron Spectroscopy**

By: Zhu, Zhongwei; Melaet, Gerome; Axnanda, Stephanus; et al.
JOURNAL OF THE AMERICAN CHEMICAL SOCIETY   Volume: 135   Issue: 34   Pages: 12560-12563   Published: AUG 28 2013

**View Abstract**

**Times Cited: 12**
*(from Web of Science Core Collection)*

Usage Count

☐ 53. **Influence of Anion Adsorption on the Parallel Reaction Pathways in the Oscillatory Electro-oxidation of Methanol**

By: Nagao, Raphael; Cantane, Daniel A.; Lima, Fabio H. B.; et al.
JOURNAL OF PHYSICAL CHEMISTRY C   Volume: 117   Issue: 29   Pages: 15098-15105   Published: JUL 25 2013

**View Abstract**

**Times Cited: 15**
*(from Web of Science Core Collection)*

Usage Count

☐ 54. **Correlating Catalytic Methanol Oxidation with the Structure and Oxidation State of Size-Selected Pt Nanoparticles**

By: Merte, Lindsay R.; Ahmadi, Mahdi; Behafarid, Farzad; et al.
ACS CATALYSIS   Volume: 3   Issue: 7   Pages: 1460-1468   Published: JUL 2013

**View Abstract**

**Times Cited: 21**
*(from Web of Science Core Collection)*

Usage Count

☐ 55. **Structure of Clean and Adsorbate-Covered Single-Crystal Rutile TiO2 Surfaces**

By: Pang, Chi Lun; Lindsay, Robert; Thornton, Geoff
CHEMICAL REVIEWS   Volume: 113   Issue: 6   Pages: 3887-3948   Published: JUN 2013

**Times Cited: 125**
*(from Web of Science Core Collection)*

**Highly Cited Paper**

Usage Count

☐ 56.

**Times Cited: 27**

PROCEEDINGS PAPER (3)

MEETING ABSTRACT (1)

EDITORIAL MATERIAL (1)

**more options / values...**

| Refine |

## Organizations-Enhanced ▼

UNITED STATES DEPARTMENT OF ENERGY DOE (10)

LUND UNIVERSITY (10)

EUROPEAN SYNCHROTRON RADIATION FACILITY ESRF (9)

MAX PLANCK SOCIETY (7)

LAWRENCE BERKELEY NATIONAL LABORATORY (7)

**more options / values...**

| Refine |

**Funding Agencies** ◄

**Open Access** ◄

**Authors** ◄

**View all options**

*For advanced refine options, use*

| Analyze Results |

**Improved Low-Temperature CO Oxidation Performance of Pd Supported on La-Stabilized Alumina**

By: Gaudet, Jason R.; de la Riva, Andrew; Peterson, Eric J.; et al.
ACS CATALYSIS  Volume: 3  Issue: 5  Pages: 846-855
Published: MAY 2013

| View Abstract |

57. **Inhibition of water dissociation on a pitted Pt(111) surface: First principles study**

By: Qian, Yumin; Hamada, Ikutaro; Otani, Minoru; et al.
CATALYSIS TODAY  Volume: 202  Pages: 163-167
Published: MAR 15 2013

| Full Text from Publisher |  | View Abstract |

58. **In situ XPS study of self-sustained oscillations in catalytic oxidation of propane over nickel**

By: Kaichev, V. V.; Gladky, A. Yu.; Prosvirin, I. P.; et al.
SURFACE SCIENCE  Volume: 609  Pages: 113-118
Published: MAR 2013

| Full Text from Publisher |  | View Abstract |

59. **Improving Spin-Transport by Disorder**

By: Chadov, Stanislav; Kiss, Janos; Felser, Claudia
ADVANCED FUNCTIONAL MATERIALS  Volume: 23
Issue: 7  Pages: 832-838  Published: FEB 18 2013

| View Abstract |

60. **Visualization of Surfaces of Pt and Ni Model Catalysts in Reactive Environments Using Ambient Pressure High Temperature Scanning Tunneling Microscopy and Understanding the Restructurings of Surfaces of Model Metal Catalysts under Reaction Conditions at Near Ambient Pressure**

By: Luan Nguyen; Cheng, Fang; Zhang, Shiran; et al.
JOURNAL OF PHYSICAL CHEMISTRY C  Volume: 117
Issue: 2  Pages: 971-977  Published: JAN 17 2013

| View Abstract |

61. **Water adsorption and dissociation on Ni surface: Effects of steps, dopants, coverage and self-aggregation**

By: Huang, Yucheng; Ling, Chongyi; Jin, Meng; et al.
PHYSICAL CHEMISTRY CHEMICAL PHYSICS  Volume:
15  Issue: 41  Pages: 17804-17817  Published: 2013

| View Abstract |

62. **THE RADIOCARBON INTRACAVITY OPTOGALVANIC SPECTROSCOPY SETUP AT UPPSALA**

By: Eilers, Gerriet; Persson, Anders; Gustavsson, Cecilia; et al.
Conference: 21st International Radiocarbon Conference
Location: Paris, FRANCE Date: 2012
RADIOCARBON  Volume: 55  Issue: 2-3  Pages: 237-250
Published: 2013

| View Abstract |

63. **The CO oxidation mechanism and reactivity on PdZn alloys**

By: Johnson, Ryan S.; DeLaRiva, Andrew; Ashbacher, Valerie; et al.
PHYSICAL CHEMISTRY CHEMICAL PHYSICS  Volume:
15  Issue: 20  Pages: 7768-7776  Published: 2013

| View Abstract |

64. **Self-sustained carbon monoxide oxidation oscillations on size-selected platinum nanoparticles at atmospheric pressure**

By: Jensen, Robert; Andersen, Thomas; Nierhoff, Anders; et al.
PHYSICAL CHEMISTRY CHEMICAL PHYSICS   Volume: 15   Issue: 8   Pages: 2698-2702   Published: 2013

[ View Abstract ]

**Times Cited: 9**
*(from Web of Science Core Collection)*

**Usage Count**

65. **Active Surface Oxygen for Catalytic CO Oxidation on Pd(100) Proceeding under Near Ambient Pressure Conditions**

By: Toyoshima, Ryo; Yoshida, Masaaki; Monya, Yuji; et al.
JOURNAL OF PHYSICAL CHEMISTRY LETTERS   Volume: 3   Issue: 21   Pages: 3182-3187   Published: NOV 1 2012

[ View Abstract ]

**Times Cited: 30**
*(from Web of Science Core Collection)*

**Usage Count**

66. **First-principles investigations of O-2 dissociation on low-coordinated Pd ensembles over stepped Au surfaces**

By: Yuan, D. W.; Liu, Z. R.; Xu, Si.
PHYSICS LETTERS A   Volume: 376   Issue: 45   Pages: 3432-3438   Published: OCT 1 2012

[ Full Text from Publisher ]   [ View Abstract ]

**Times Cited: 5**
*(from Web of Science Core Collection)*

**Usage Count**

67. **A mechanistic study of H2S adsorption and dissociation on Cu2O(111) surfaces: Thermochemistry, reaction barrier**

By: Zhang, Riguang; Liu, Hongyan; Li, Jingrui; et al.
APPLIED SURFACE SCIENCE   Volume: 258   Issue: 24   Pages: 9932-9943   Published: OCT 1 2012

[ Full Text from Publisher ]   [ View Abstract ]

**Times Cited: 28**
*(from Web of Science Core Collection)*

**Usage Count**

68. **Highly Oxidized Palladium Nanoparticles Comprising Pd4+ Species: Spectroscopic and Structural Aspects, Thermal Stability, and Reactivity**

By: Kibis, Lidiya S.; Stadnichenko, Andrey I.; Koscheev, Sergei V.; et al.
JOURNAL OF PHYSICAL CHEMISTRY C   Volume: 116   Issue: 36   Pages: 19342-19348   Published: SEP 13 2012

[ View Abstract ]

**Times Cited: 37**
*(from Web of Science Core Collection)*

**Usage Count**

69. **In Situ Ambient Pressure XPS Study of CO Oxidation Reaction on Pd(111) Surfaces**

By: Toyoshima, Ryo; Yoshida, Masaaki; Monya, Yuji; et al.
JOURNAL OF PHYSICAL CHEMISTRY C   Volume: 116   Issue: 35   Pages: 18691-18697   Published: SEP 6 2012

[ View Abstract ]

**Times Cited: 44**
*(from Web of Science Core Collection)*

**Usage Count**

70. **Structure of the Rh2O3(0001) surface**

By: Blomberg, S.; Lundgren, E.; Westerstrom, R.; et al.
SURFACE SCIENCE   Volume: 606   Issue: 17-18   Pages: 1416-1421   Published: SEP 2012

[ Full Text from Publisher ]   [ View Abstract ]

**Times Cited: 8**
*(from Web of Science Core Collection)*

**Usage Count**

71. **Structural Modification of Platinum Model Systems under High Pressure CO Annealing**

By: McCarthy, D. N.; Strebel, C. E.; Johansson, T. P.; et al.
JOURNAL OF PHYSICAL CHEMISTRY C   Volume: 116   Issue: 29   Pages: 15353-15360   Published: JUL 26 2012

[ View Abstract ]

**Times Cited: 8**
*(from Web of Science Core Collection)*

**Usage Count**

72. **Packing Defects into Ordered Structures: Strands on**

**Times Cited: 14**

**TiO2**

By: Bechstein, R.; Kristoffersen, H. H.; Vilhelmsen, L. B.; et al.
PHYSICAL REVIEW LETTERS    Volume: 108   Issue: 23
  Article Number: 236103   Published: JUN 7 2012

[View Abstract]

*(from Web of Science Core Collection)*

**Usage Count**

---

73.  **Surface Chemistry of Ruthenium Dioxide in Heterogeneous Catalysis and Electrocatalysis: From Fundamental to Applied Research**

By: Over, Herbert
CHEMICAL REVIEWS    Volume: 112   Issue: 6   Pages: 3356-3426   Published: JUN 2012

Times Cited: **217**
*(from Web of Science Core Collection)*

**Highly Cited Paper**

**Usage Count**

---

74.  **Unraveling the mechanism of the NO reduction by CO on gold based catalysts**

By: Fajin, Jose L. C.; Cordeiro, M. Natalia D. S.; Gomes, Jose R. B.
JOURNAL OF CATALYSIS    Volume: 289   Pages: 11-20
  Published: MAY 2012

[Full Text from Publisher]    [View Abstract]

Times Cited: **14**
*(from Web of Science Core Collection)*

**Usage Count**

---

75.  **Operando Studies of Catalyst Surfaces during Catalysis and under Reaction Conditions: Ambient Pressure X-Ray Photoelectron Spectroscopy with a Flow-Cell Reactor**

By: Tao, Franklin (Feng)
CHEMCATCHEM    Volume: 4   Issue: 5   Pages: 583-590
  Published: MAY 2012

[View Abstract]

Times Cited: **15**
*(from Web of Science Core Collection)*

**Usage Count**

---

76.  **Formation of Nanometer-Sized Surface Platinum Oxide Clusters on a Stepped Pt(557) Single Crystal Surface Induced by Oxygen: A High-Pressure STM and Ambient-Pressure XPS Study**

By: Zhu, Zhongwei; Tao, Franklin (Feng); Zheng, Fan; et al.
NANO LETTERS    Volume: 12   Issue: 3   Pages: 1491-1497
  Published: MAR 2012

[View Abstract]

Times Cited: **48**
*(from Web of Science Core Collection)*

**Usage Count**

---

77.  **Oscillatory Behavior during the Catalytic Partial Oxidation of Methane: Following Dynamic Structural Changes of Palladium Using the QEXAFS Technique**

By: Stoetzel, Jan; Frahm, Ronald; Kimmerle, Bertram; et al.
JOURNAL OF PHYSICAL CHEMISTRY C   Volume: 116
  Issue: 1   Pages: 599-609   Published: JAN 12 2012

[View Abstract]

Times Cited: **19**
*(from Web of Science Core Collection)*

**Usage Count**

---

78.  **In Situ Oxidation Study of Pt(110) and Its Interaction with CO**

By: Butcher, Derek R.; Grass, Michael E.; Zeng, Zhenhua; et al.
JOURNAL OF THE AMERICAN CHEMICAL SOCIETY
  Volume: 133   Issue: 50   Pages: 20319-20325   Published: DEC 21 2011

[View Abstract]

Times Cited: **57**
*(from Web of Science Core Collection)*

**Usage Count**

---

79.  **Steps on rutile TiO2(110): Active sites for water and methanol dissociation**

By: Martinez, Umberto; Vilhelmsen, Lasse B.; Kristoffersen, Henrik H.; et al.
PHYSICAL REVIEW B   Volume: 84   Issue: 20   Article Number: 205434   Published: NOV 16 2011

[View Abstract]

Times Cited: **41**
*(from Web of Science Core Collection)*

**Usage Count**

☐ 80.  **First-Principles Study of Water Dissociation on PdZn near Surface Alloys**

By: Huang, Yucheng; Chen, Zhao-Xu
JOURNAL OF PHYSICAL CHEMISTRY C   Volume: 115
  Issue: 38   Pages: 18752-18760   Published: SEP 29 2011

**View Abstract**

**Times Cited: 17**
*(from Web of Science Core Collection)*

**Usage Count**

☐ 81.  **Structural and chemical states of palladium in Pd/Al2O3 catalysts under self-sustained oscillations in reaction of CO oxidation**

By: Slavinskaya, E. M.; Stonkus, O. A.; Gulyaev, R. V.; et al.
APPLIED CATALYSIS A-GENERAL   Volume: 401   Issue:
1-2   Pages: 83-97   Published: JUL 15 2011

**Full Text from Publisher**       **View Abstract**

**Times Cited: 27**
*(from Web of Science Core Collection)*

**Usage Count**

☐ 82.  **Catalytic oxidation of CO on Ir(100)**

By: Erikat, I. A.; Hamad, B. A.; Khalifeh, J. M.
PHYSICA STATUS SOLIDI B-BASIC SOLID STATE
PHYSICS   Volume: 248   Issue: 6   Pages: 1425-1430
  Published: JUN 2011

**View Abstract**

**Times Cited: 9**
*(from Web of Science Core Collection)*

**Usage Count**

☐ 83.  **Oxidation of stepped Pt(111) studied by x-ray photoelectron spectroscopy and density functional theory**

By: Bandlow, Jochen; Kaghazchi, Payam; Jacob, Timo; et al.
PHYSICAL REVIEW B   Volume: 83   Issue: 17     Article
Number: 174107   Published: MAY 11 2011

**View Abstract**

**Times Cited: 19**
*(from Web of Science Core Collection)*

**Usage Count**

☐ 84.  **Structure, Chemical Composition, And Reactivity Correlations during the In Situ Oxidation of 2-Propanol**

By: Paredis, Kristof; Ono, Luis K.; Mostafa, Simon; et al.
JOURNAL OF THE AMERICAN CHEMICAL SOCIETY
  Volume: 133   Issue: 17   Pages: 6728-6735   Published: MAY
4 2011

**View Abstract**

**Times Cited: 31**
*(from Web of Science Core Collection)*

**Usage Count**

☐ 85.  **Nanoparticulate Pd Supported Catalysts: Size-Dependent Formation of Pd(I)/Pd(0) and Their Role in CO Elimination**

By: Iglesias-Juez, Ana; Kubacka, Anna; Fernandez-Garcia,
Marcos; et al.
JOURNAL OF THE AMERICAN CHEMICAL SOCIETY
  Volume: 133   Issue: 12   Pages: 4484-4489   Published: MAR
30 2011

**View Abstract**

**Times Cited: 28**
*(from Web of Science Core Collection)*

**Usage Count**

☐ 86.  **Surface structure and reactivity of Pd(100) during CO oxidation near ambient pressures**

By: van Rijn, R.; Balmes, O.; Resta, A.; et al.
PHYSICAL CHEMISTRY CHEMICAL PHYSICS   Volume:
13   Issue: 29   Pages: 13167-13171   Published: 2011

**View Abstract**

**Times Cited: 53**
*(from Web of Science Core Collection)*

**Usage Count**

☐ 87.  **Descriptors controlling the catalytic activity of metallic surfaces toward water splitting**

By: Fajin, Jose L. C.; Cordeiro, M. Natalia D. S.; Illas,
Francesc; et al.
JOURNAL OF CATALYSIS   Volume: 276   Issue: 1   Pages:
92-100   Published: NOV 19 2010

**Full Text from Publisher**       **View Abstract**

**Times Cited: 40**
*(from Web of Science Core Collection)*

**Usage Count**

Select Page

5K

Save to Other File Formats    ▼    **Add to Marked List**

Sort by:   Publication Date -- newest to oldest    ▼        Page   2   of   2

Show:   50 per page    ▼

*87 records matched your query of the 37,941,506 in the data limits you selected.*

Web of Science | InCites | Journal Citation Reports | Essential Science Indicators | EndNote | Sign In ▾ | Help | English ▾

# Web of Science

Search | Search Results | My Tools ▾ | Search History | Marked List 23

## Citing Articles: 5
*(from Web of Science Core Collection)*

**For:** Surface concentration dependent structures of iodine on Pd(110)
**...Less**

### Times Cited Counts
5 in All Databases
5 in Web of Science Core Collection
0 in BIOSIS Citation Index
0 in Chinese Science Citation Database
0 data sets in Data Citation Index
0 publication in Data Citation Index
0 in Russian Science Citation Index
0 in SciELO Citation Index
**View Additional Times Cited Counts**

### Refine Results

Search within results for...

**Publication Years** ▾
☐ 2016 (2)
☐ 2014 (2)
☐ 2015 (1)
more options / values...
**Refine**

**Web of Science Categories** ▾
☐ CHEMISTRY PHYSICAL (5)
☐ NANOSCIENCE NANOTECHNOLOGY (2)
☐ MATERIALS SCIENCE MULTIDISCIPLINARY (2)
☐ PHYSICS CONDENSED MATTER (1)
☐ PHYSICS ATOMIC MOLECULAR CHEMICAL (1)
more options / values...
**Refine**

**Document Types** ▾
☐ ARTICLE (5)
**Refine**

**Organizations-Enhanced** ▾
☐ VIENNA UNIVERSITY OF TECHNOLOGY (2)
☐ UPPSALA UNIVERSITY (2)

---

Sort by: Publication Date -- newest to oldest ▾          Page 1 of 1

☐ Select Page      🖶 ✉ 5K

Save to Other File Formats ▾      **Add to Marked List**

**Create Citation Report**

≡ **Analyze Results**

☐ 1. **TiOx thin films grown on Pd(100) and Pd(111) by chemical vapor deposition**

By: Farstad, M. H.; Ragazzon, D.; Groenbeck, H.; et al.
SURFACE SCIENCE   Volume: 649   Pages: 80-89
Published: JUL 2016

**Full Text from Publisher** | **View Abstract**

Times Cited: 1
*(from Web of Science Core Collection)*

Usage Count

☐ 2. **Structure of Low and High Coverage Phases of Bromine on Pd(110)**

By: Huber, Veronika; Bikaljevic, Djuro; Redinger, Josef; et al.
JOURNAL OF PHYSICAL CHEMISTRY C   Volume: 120   Issue: 25   Pages: 13523-13530   Published: JUN 30 2016

**View Abstract**

Times Cited: 0
*(from Web of Science Core Collection)*

Usage Count

☐ 3. **Surface composition of PdCuAu ternary alloys: a combined LEIS and XPS study**

By: Tarditi, Ana M.; Imhoff, Carolina; Miller, James B.; et al.
SURFACE AND INTERFACE ANALYSIS   Volume: 47   Issue: 7   Pages: 745-754   Published: JUL 2015

**View Abstract**

Times Cited: 5
*(from Web of Science Core Collection)*

Usage Count

☐ 4. **Degenerate Phases of Iodine on Pt(110) at Half-Monolayer Coverage**

By: Oberkalmsteiner, Nadja; Cordin, Michael; Duerrbeck, Stefan; et al.
JOURNAL OF PHYSICAL CHEMISTRY C   Volume: 118   Issue: 51   Pages: 29919-29927   Published: DEC 25 2014

**View Abstract**

Times Cited: 2
*(from Web of Science Core Collection)*

Usage Count

☐ 5. **Site-dependent charge transfer at the Pt(111)-ZnPc interface and the effect of iodine**

By: Ahmadi, Sareh; Agnarsson, Bjorn; Bidermane, Ieva; et al.
JOURNAL OF CHEMICAL PHYSICS   Volume: 140   Issue: 17   Article Number: 174702   Published: MAY 7 2014

**View Abstract**

Times Cited: 5
*(from Web of Science Core Collection)*

Usage Count

☐ Select Page      🖶 ✉ 5K

Save to Other File Formats ▾      **Add to Marked List**

Sort by: Publication Date -- newest to oldest ▾          Page 1 of 1

Show: 50 per page ▾

*5 records matched your query of the 37,941,506 in the data limits you selected.*

UNIVERSITY OF INNSBRUCK (2)

CHALMERS UNIVERSITY OF
TECHNOLOGY (2)

LUND UNIVERSITY (1)

**more options / values...**

| | **Refine** |
|---|---|

**Funding Agencies** ◀

**Open Access** ◀

**Authors** ◀

**View all options**

*For advanced refine options, use*

**Analyze Results**

| Web of Science | InCites | Journal Citation Reports | Essential Science Indicators | EndNote | | Sign In ▾ | Help | English ▾ |

# Web of Science

| Search | Search Results | | My Tools ▾ | Search History | Marked List   23 |

## Citing Articles: 3
*(from Web of Science Core Collection)*

**For:** SO2 interaction with Zn(0001) an
d ZnO(0001) and the influence of wate
r ...**More**

**Times Cited Counts**

3 in All Databases

3 in Web of Science Core Collection

0 in BIOSIS Citation Index

0 in Chinese Science Citation Database

0 data sets in Data Citation Index

0 publication in Data Citation Index

0 in Russian Science Citation Index

0 in SciELO Citation Index

**View Additional Times Cited Counts**

---

### Refine Results

*Search within results for...*

---

**Publication Years** ▼

☐ 2017 (1)
☐ 2014 (1)
☐ 2013 (1)

**more options / values...**

**Refine**

---

**Web of Science Categories** ▼

☐ MATERIALS SCIENCE
MULTIDISCIPLINARY (2)
☐ PHYSICS CONDENSED MATTER
(1)
☐ PHYSICS APPLIED (1)
☐ NANOSCIENCE
NANOTECHNOLOGY (1)
☐ ENGINEERING ELECTRICAL
ELECTRONIC (1)

**more options / values...**

**Refine**

---

**Document Types** ▼

☐ ARTICLE (3)

**Refine**

---

**Organizations-Enhanced** ▼

☐ UNIVERSITY OF CANTERBURY (2)
☐ ABERYSTWYTH UNIVERSITY (2)

---

Sort by:   Publication Date -- newest to oldest ▾      Page | 1 | of 1

☐ Select Page    ▣ ✉ **5K**

Save to Other File Formats ▾   **Add to Marked List**

**Create Citation Report**

**☰ Analyze Results**

☐ 1. **Lasing from ZnO Nanocrystals in ZnO-ZnS
Microbelts**

By: Nghia, N. V.; Dung, N. D.; Huy, P. T.; et al.
JOURNAL OF ELECTRONIC MATERIALS    Volume: 46
  Issue: 6   Pages: 3295-3300   Published: JUN 2017

**View Abstract**

Times Cited: **0**
*(from Web of Science Core
Collection)*

**Usage Count**

☐ 2. **Stability of the Surface Electron Accumulation
Layers on the Nonpolar (10(1)over-bar0) and
(11(2)over-bar0) Faces of ZnO**

By: Heinhold, Robert; Cooil, Simon P.; Evans, D. Andrew; et al.
JOURNAL OF PHYSICAL CHEMISTRY C    Volume: 118
  Issue: 42   Pages: 24575-24582   Published: OCT 23 2014

**View Abstract**

Times Cited: **10**
*(from Web of Science Core
Collection)*

**Usage Count**

☐ 3. **Influence of polarity and hydroxyl termination on the
band bending at ZnO surfaces**

By: Heinhold, R.; Williams, G. T.; Cooil, S. P.; et al.
PHYSICAL REVIEW B    Volume: 88   Issue: 23    Article
Number: 235315   Published: DEC 30 2013

**View Abstract**

Times Cited: **24**
*(from Web of Science Core
Collection)*

**Usage Count**

☐ Select Page    ▣ ✉ **5K**

Save to Other File Formats ▾   **Add to Marked List**

Sort by:   Publication Date -- newest to oldest ▾      Page | 1 | of 1

Show:   50 per page ▾

*3 records matched your query of the 37,941,506 in the data limits you selected.*

HANOI UNIVERSITY OF SCIENCE
TECHNOLOGY (1)

GLOBAL INNOVAT CTR (1)

**more options / values...**

|  | **Refine** |
|---|---|

**Funding Agencies** ◄

**Open Access** ◄

**Authors** ◄

**View all options**

*For advanced refine options, use*

**Analyze Results**

| Web of Science | InCites | Journal Citation Reports | Essential Science Indicators | EndNote | | Sign In ▼ | Help | English ▼ |

# Web of Science

| Search | Search Results | | My Tools ▼ | Search History | Marked List  23 |

## Citing Articles: 7
*(from Web of Science Core Collection)*

**For:** Role of Defects in Surface Chemistry on Cu2O(111) **...Less**

**Times Cited Counts**

7 in All Databases

7 in Web of Science Core Collection

0 in BIOSIS Citation Index

1 in Chinese Science Citation Database

0 data sets in Data Citation Index

0 publication in Data Citation Index

0 in Russian Science Citation Index

0 in SciELO Citation Index

**View Additional Times Cited Counts**

---

| **Refine Results** |

*Search within results for...*

### Publication Years ▼
- ☐ 2016 (5)
- ☐ 2015 (1)
- ☐ 2014 (1)

**more options / values...**

**Refine**

### Web of Science Categories ▼
- ☐ CHEMISTRY PHYSICAL (6)
- ☐ MATERIALS SCIENCE MULTIDISCIPLINARY (5)
- ☐ NANOSCIENCE NANOTECHNOLOGY (4)
- ☐ PHYSICS APPLIED (2)
- ☐ MATERIALS SCIENCE COATINGS FILMS (1)

**more options / values...**

**Refine**

### Document Types ▼
- ☐ ARTICLE (6)
- ☐ REVIEW (1)

**more options / values...**

**Refine**

### Organizations-Enhanced ▼
- ☐ ROYAL INSTITUTE OF TECHNOLOGY (3)

---

Sort by:  Publication Date -- newest to oldest ▼

Page 1 of 1

☐ Select Page    5K

Save to Other File Formats ▼    **Add to Marked List**

**Create Citation Report**

**Analyze Results**

☐ 1. **CuCo Hybrid Oxides as Bifunctional Electrocatalyst for Efficient Water Splitting**

By: Kuang, Min; Han, Peng; Wang, Qihao; et al.
ADVANCED FUNCTIONAL MATERIALS   Volume: 26   Issue: 46   Pages: 8555-8561   Published: DEC 13 2016

**View Abstract**

Times Cited: **4**
*(from Web of Science Core Collection)*

Usage Count

☐ 2. **Copper(I)-Based p-Type Oxides for Photoelectrochemical and Photovoltaic Solar Energy Conversion**

By: Sullivan, Ian; Zoellner, Brandon; Maggard, Paul A.
CHEMISTRY OF MATERIALS   Volume: 28   Issue: 17   Pages: 5999-6016   Published: SEP 13 2016

**View Abstract**

Times Cited: **4**
*(from Web of Science Core Collection)*

Usage Count

☐ 3. **One-dimensional Cu-based catalysts with layered Cu-Cu2O-CuO walls for the Rochow reaction**

By: Li, Jing; Zhang, Zailei; Ji, Yongjun; et al.
NANO RESEARCH   Volume: 9   Issue: 5   Pages: 1377-1392   Published: MAY 2016

**View Abstract**

Times Cited: **0**
*(from Web of Science Core Collection)*

Usage Count

☐ 4. **The Surface Structure of Cu2O(100)**

By: Soldemo, Markus; Stenlid, Joakim Halldin; Besharat, Zahra; et al.
JOURNAL OF PHYSICAL CHEMISTRY C   Volume: 120   Issue: 8   Pages: 4373-4381   Published: MAR 3 2016

**View Abstract**

Times Cited: **1**
*(from Web of Science Core Collection)*

Usage Count

☐ 5. **Reactivity at the Cu2O(100):Cu-H2O interface: a combined DFT and PES study**

By: Stenlid, J. H.; Soldemo, M.; Johansson, A. J.; et al.
PHYSICAL CHEMISTRY CHEMICAL PHYSICS   Volume: 18   Issue: 44   Pages: 30570-30584   Published: 2016

**View Abstract**

Times Cited: **0**
*(from Web of Science Core Collection)*

Usage Count

☐ 6. **Cooperative Effects in Water Binding to Cuprous Oxide Surfaces**

By: Riplinger, Christoph; Carter, Emily A.
JOURNAL OF PHYSICAL CHEMISTRY C   Volume: 119   Issue: 17   Pages: 9311-9323   Published: APR 30 2015

**View Abstract**

Times Cited: **2**
*(from Web of Science Core Collection)*

Usage Count

☐ 7. **Self-Assembled Monolayers as Inhibitors for the Atmospheric Corrosion of Copper Induced by Formic**

Times Cited: **10**
*(from Web of Science Core*

PRINCETON UNIVERSITY (1)

NORTH CAROLINA STATE UNIVERSITY (1)

NANYANG TECHNOLOGICAL UNIVERSITY NATIONAL INSTITUTE OF EDUCATION NIE SINGAPORE (1)

NANYANG TECHNOLOGICAL UNIVERSITY (1)

**more options / values...**

**Refine**

**Funding Agencies** ◀

**Open Access** ◀

**Authors** ◀

**View all options**

*For advanced refine options, use*

**Analyze Results**

Acid: A Comparison between Hexanethiol and Hexaneselenol

By: Hosseinpour, Saman; Gothelid, Mats; Leygraf, Christofer; et al.
JOURNAL OF THE ELECTROCHEMICAL SOCIETY
Volume: 161   Issue: 1   Pages: C50-C56   Published: 2014

**View Abstract**

Select Page      🗗  ✉  **5K**

Save to Other File Formats       ▼      **Add to Marked List**

Sort by:   Publication Date -- newest to oldest   ▼              Page ⌷1⌷ of  1

Show:   50 per page   ▼

*7 records matched your query of the 37,941,506 in the data limits you selected.*

Collection)

**Usage Count**

| Web of Science | InCites | Journal Citation Reports | Essential Science Indicators | EndNote | | Sign In ▾ | Help | English ▾ |

# Web of Science

| Search | Search Results | | | My Tools ▾ | Search History | Marked List   23 |

## Citing Articles: 16
*(from Web of Science Core Collection)*

**For:** The ReactorSTM: Atomically resolved scanning tunneling microscopy under high-pressure, high-temperature catalytic reaction conditions **...Less**

### Times Cited Counts

**16 in All Databases**

16 in Web of Science Core Collection

2 in BIOSIS Citation Index

0 in Chinese Science Citation Database

0 data sets in Data Citation Index

0 publication in Data Citation Index

0 in Russian Science Citation Index

0 in SciELO Citation Index

**View Additional Times Cited Counts**

### Refine Results

*Search within results for...*

**Filter results by:**

☐ Highly Cited in Field (1)

**Refine**

### Publication Years ▼

☐ 2016 (9)
☐ 2015 (4)
☐ 2017 (3)

**more options / values...**

**Refine**

### Web of Science Categories ▼

☐ CHEMISTRY PHYSICAL (9)
☐ PHYSICS APPLIED (3)
☐ NANOSCIENCE NANOTECHNOLOGY (3)
☐ MATERIALS SCIENCE MULTIDISCIPLINARY (3)
☐ INSTRUMENTS INSTRUMENTATION (3)

**more options / values...**

**Refine**

### Document Types ▼

☐ ARTICLE (14)
☐ REVIEW (2)

---

Sort by:   Publication Date -- newest to oldest ▾        Page [1] of 1

☐ Select Page    🗗 ✉ **5K**

Save to Other File Formats ▾    **Add to Marked List**

**Create Citation Report**

☰ **Analyze Results**

☐ 1. **Operando chemistry of catalyst surfaces during catalysis**

By: Dou, Jian; Sun, Zaicheng; Opalade, Adedamola A.; et al.
**CHEMICAL SOCIETY REVIEWS**   Volume: 46   Issue: 7 Pages: 2001-2027   Published: APR 7 2017

**View Abstract**

Times Cited: 0
*(from Web of Science Core Collection)*

Usage Count

☐ 2. **In situ TEM observation of the Boudouard reaction: multi-layered graphene formation from CO on cobalt nanoparticles at atmospheric pressure**

By: Bremmer, G. Marien; Zacharaki, Eirini; Sjastad, Anja O.; et al.
**FARADAY DISCUSSIONS**   Volume: 197   Pages: 337-351 Published: APR 1 2017

**View Abstract**

Times Cited: 0
*(from Web of Science Core Collection)*

Usage Count

☐ 3. **Atomic-Scale Structural Evolution of Rh(110) during Catalysis**

By: Luan Nguyen; Liu, Lacheng; Assefa, Solomon; et al.
**ACS CATALYSIS**   Volume: 7   Issue: 1   Pages: 664-674 Published: JAN 2017

**View Abstract**

Times Cited: 0
*(from Web of Science Core Collection)*

Usage Count

☐ 4. **Combined scanning probe microscopy and x-ray scattering instrument for in situ catalysis investigations**

By: Onderwaater, Willem G.; van der Tuijn, Peter C.; Mom, Rik V.; et al.
Conference: 21st Topical Conference on High-Temperature Plasma Diagnostics Location: Madison, WI Date: JUN 05-09, 2016
**REVIEW OF SCIENTIFIC INSTRUMENTS**   Volume: 87 Issue: 11   Article Number: 113705   Published: NOV 2016

**View Abstract**

Times Cited: 0
*(from Web of Science Core Collection)*

Usage Count

☐ 5. **Triggering chemical reactions by Scanning Tunneling Microscopy: From atoms to polymers**

By: den Boer, Duncan; Elemans, Johannes A. A. W.
**EUROPEAN POLYMER JOURNAL**   Volume: 83   Pages: 390-406   Published: OCT 2016

**Full Text from Publisher**    **View Abstract**

Times Cited: 1
*(from Web of Science Core Collection)*

Usage Count

☐ 6. **A Comparison of CO Oxidation by Hydroxyl and Atomic Oxygen from Water on Low-Coordinated Au Atoms**

By: van Spronsen, Matthijs A.; Weststrate, Kees-Jan; Juurlink, Ludo B. F.

Times Cited: 0
*(from Web of Science Core Collection)*

Usage Count

more options / values...

**Refine**

**Organizations-Enhanced** ▼

☐   LEIDEN UNIVERSITY (5)
☐   ADV RES CTR NANOLITHOG (4)
☐   UNIVERSITY OF KANSAS (3)
☐   HARVARD UNIVERSITY (3)
☐   NETHERLANDS ORGANIZATION
     APPLIED SCIENCE RESEARCH
     (2)

more options / values...

**Refine**

**Funding Agencies** ◀

**Open Access** ◀

**Authors** ◀

**View all options**

*For advanced refine options, use*

**Analyze Results**

---

ACS CATALYSIS   Volume: 6   Issue: 10   Pages: 7051-7058
Published: OCT 2016

**View Abstract**

☐   7.   **In situ observation of self-assembled hydrocarbon Fischer-Tropsch products on a cobalt catalyst**

By: Navarro, Violeta; van Spronsen, Matthijs A.; Frenken, Joost W. M.
NATURE CHEMISTRY   Volume: 8   Issue: 10   Pages: 929-934   Published: OCT 2016

**View Abstract**

Times Cited: **10**
*(from Web of Science Core Collection)*

**Usage Count**

☐   8.   **Tuning the Properties of Molybdenum Oxide on Al2O3/NiAl(110): Metal versus Oxide Deposition**

By: Mom, Rik V.; Rost, Marcel J.; Frenken, Joost W. M.; et al.
JOURNAL OF PHYSICAL CHEMISTRY C   Volume: 120   Issue: 35   Pages: 19737-19743   Published: SEP 8 2016

**View Abstract**

Times Cited: **0**
*(from Web of Science Core Collection)*

**Usage Count**

☐   9.   **Influence of the Central Metal Ion on the Desorption Kinetics of a Porphyrin from the Solution/HOPG Interface**

By: Bhattarai, Ashish; Marchbanks-Owens, Kevin; Mazur, Ursula; et al.
JOURNAL OF PHYSICAL CHEMISTRY C   Volume: 120   Issue: 32   Pages: 18140-18150   Published: AUG 18 2016

**View Abstract**

Times Cited: **0**
*(from Web of Science Core Collection)*

**Usage Count**

☐   10.   **Development of a reaction cell for in-situ/operando studies of surface of a catalyst under a reaction condition and during catalysis**

By: Nguyen, Luan; Tao, Franklin (Feng)
REVIEW OF SCIENTIFIC INSTRUMENTS   Volume: 87   Issue: 6   Article Number: 064101   Published: JUN 2016

**View Abstract**

Times Cited: **6**
*(from Web of Science Core Collection)*

**Usage Count**

☐   11.   **A versatile instrument for ambient pressure x-ray photoelectron spectroscopy: The Lund cell approach**

By: Knudsen, Jan; Andersen, Jesper N.; Schnadt, Joachim
SURFACE SCIENCE   Volume: 646   Special Issue: SI   Pages: 160-169   Published: APR 2016

**Full Text from Publisher**    **View Abstract**

Times Cited: **6**
*(from Web of Science Core Collection)*

**Usage Count**

☐   12.   **Activation of Cu(111) surface by decomposition into nanoclusters driven by CO adsorption**

By: Eren, Baran; Zherebetskyy, Danylo; Patera, Laerte L.; et al.
SCIENCE   Volume: 351   Issue: 6272   Pages: 475-478   Published: JAN 29 2016

**View Abstract**

Times Cited: **25**
*(from Web of Science Core Collection)*

**Highly Cited Paper**

**Usage Count**

☐   13.   **Atomistic details of oxide surfaces and surface oxidation: the example of copper and its oxides**

By: Gattinoni, Chiara; Michaelides, Angelos
SURFACE SCIENCE REPORTS   Volume: 70   Issue: 3   Pages: 424-447   Published: NOV 2015

**Full Text from Publisher**    **View Abstract**

Times Cited: **29**
*(from Web of Science Core Collection)*

**Usage Count**

☐   14.   **Combined STM and TPD Study of Rh(111) Under Conditions of High Oxygen Coverage**

By: Derouin, Jonathan; Farber, Rachael G.; Killelea, Daniel R.
JOURNAL OF PHYSICAL CHEMISTRY C   Volume: 119   Issue: 26   Special Issue: SI   Pages: 14748-14755   Published: JUL 2 2015

Times Cited: **7**
*(from Web of Science Core Collection)*

**Usage Count**

**View Abstract**

15. **High-pressure operando STM studies giving insight in CO oxidation and NO reduction over Pt(110)**

By: van Spronsen, M. A.; van Baarle, G. J. C.; Herbschleb, C. T.; et al.
CATALYSIS TODAY    Volume: 244   Pages: 85-95
Published: APR 15 2015

**Full Text from Publisher**    **View Abstract**

Times Cited: **11**
*(from Web of Science Core Collection)*

Usage Count

16. **The ReactorAFM: Non-contact atomic force microscope operating under high-pressure and high-temperature catalytic conditions**

By: Roobol, S. B.; Canas-Ventura, M. E.; Bergman, M.; et al.
REVIEW OF SCIENTIFIC INSTRUMENTS    Volume: 86
Issue: 3    Article Number: 033706   Published: MAR 2015

**View Abstract**

Times Cited: **4**
*(from Web of Science Core Collection)*

Usage Count

Select Page          🗗  ✉  5K

Save to Other File Formats        ▼        **Add to Marked List**

Sort by:   Publication Date -- newest to oldest    ▼            Page  1   of  1

Show:   50 per page   ▼

*16 records matched your query of the 37,941,506 in the data limits you selected.*

© 2017  **CLARIVATE ANALYTICS**        **TERMS OF USE**        **PRIVACY POLICY**        **FEEDBACK**

# Pseudogapped Fermi surfaces of $1T$-TaS$_2$ and $1T$-TaSe$_2$: A charge density wave effect

M. Bovet,[1] D. Popović,[2] F. Clerc,[3] C. Koitzsch,[3] U. Probst,[4] E. Bucher,[4] H. Berger,[5] D. Naumović,[1] and P. Aebi[3]

[1]*Département de Physique, Université de Fribourg, Pérolles, CH-1700 Fribourg, Switzerland*

[2]*Experimentalphysik, Universität des Saarlandes, D-66123 Saarbrücken, Germany*

[3]*Institut de Physique, Université de Neuchâtel, CH-2000 Neuchâtel, Switzerland*

[4]*Fachbereich Physik, Universität Konstanz, D-78457 Konstanz, Germany*

[5]*Institut de Physique Appliquée, EPFL, CH-1015 Lausanne, Switzerland*

(Received 26 September 2003; published 30 March 2004)

We report room temperature angle-resolved photoemission experiments on $1T$-TaS$_2$ and $1T$-TaSe$_2$ complemented by density-functional theory calculations. Fermi-surface mapping experiments in the charge-density wave (CDW) phase are similar for the two compounds and do not show symmetries due to the CDW-induced new Brillouin zones. However, the band structure a few eV below the Fermi level ($E_F$) displays a clear modulation that we relate, in both cases, to the CDW. At $E_F$, the spectral weight distribution reflects the band structure of the normal state, but no clear quasiparticle crossing is located. Near the zone center $\bar{\Gamma}$, CDW-split quasilocalized Ta $dz^2$ subbands are observed in the vicinity of $E_F$. For $1T$-TaS$_2$ and $1T$-TaSe$_2$, they are thermally populated slightly above $E_F$ and close to $E_F$, respectively. The observed behavior can be understood in terms of the CDW reconstructed, spectral function weighted band structure.

## I. INTRODUCTION

The pseudogap in high-temperature superconductors (HTS) is now regarded as a key property directly related to the mechanism behind superconductivity in these materials,[1] where an electronic instability drives the pseudogap and the remnant Fermi-surface (FS) behavior.[2] Recently, a pseudogap over large portions of the FS has been observed in angle-resolved photoemission (ARPES) experiments on the transition-metal dichalcogenide (TMD) $1T$-TaS$_2$ instead of a nesting induced partially removed FS in the charge-density wave (CDW) phase.[3] This new surprising property was questioned to be related to instabilities induced by the underlying Mott localization derived metal-insulator transition (MIT) (Ref. 4) at 180 K via fluctuations.[3] The isostructural $1T$-TaSe$_2$ with its identical CDW at RT appears to be the ideal candidate for further enlightening, as it does not exhibit a bulk MIT at lower temperatures. Very recent experiments, however, showed that $1T$-TaSe$_2$ exhibits a surface MIT.[5]

Even in the HTS, the origin of the pseudogap is still a topic of debate as to whether or not this pseudogap is a precursor of the actual gap in the electronic spectrum in the superconducting state below $T_c$.[6] Klemm[6] notices that the HTS pseudogap regime is strikingly similar to the one seen in TMD's and in some organic layered superconductors and proposes that the pseudogap in the HTS arises from CDW's and/or spin-density waves and not from superconducting fluctuations (or preformed pairs).

Despite their quite well-understood structural properties, studied by means of x-ray scattering,[7,8] the two $1T$-polytypes of the TaS$_2$ and TaSe$_2$ of the layered TMD's are also of strong interest in the debate on the mechanism behind the occurrence of the CDW, whose main feature is a starlike clustering (the so-called ''stars of David'') in the Ta plane [Fig. 1(c)].[9] The basic structure is sandwichlike: the hexagonal plane of Ta is sandwiched by two hexagonal S, respec-

tively, Se sheets leading to a quasi-two-dimensional (2D) material. The quasi-2D character of the Fermi surface has been used to explain the CDW formation,[9] which induces the starlike distortion in the Ta plane. However, the x-ray scattering results show a three-dimensional reconstruction of the lattice by the formation of the CDW also along the $c$ axis. In a previous publication,[10] we propose the necessary interplane coupling inbetween two sandwiches of $1T$-TaS$_2$ at RT to occur as a consequence of the *in-plane* CDW in the Ta layer. On the other hand, Horiba *et al.*[11] for $1T$-TaSe$_2$ conclude that the Fermi surface has three-dimensional character due to
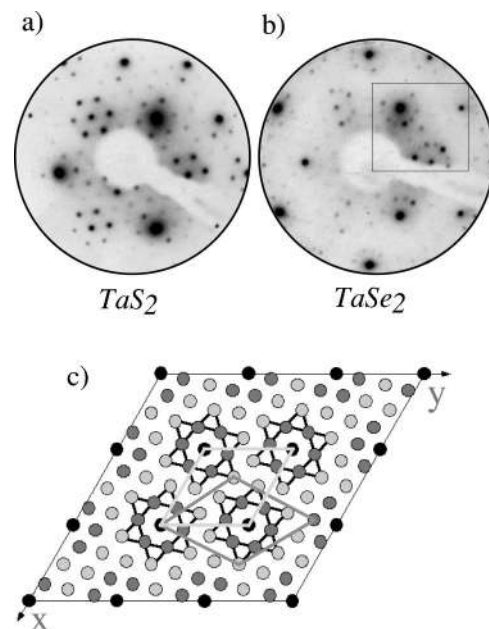


FIG. 1. Low-energy electron-diffraction patterns for $1T$-TaS$_2$ (a) and $1T$-TaSe$_2$ (b). In the Ta-plane, two CDW reconstructions may occur [inducing new superspots as emphasized with a square in (b)]; they are shown in (c). See text for more details.

a large charge transfer between Ta $5d$ and Se $4p$ orbitals. Last but not least, the debate on where to place a possible nesting vector on the FS contours, is still open. The structural evolution (induced by the CDW) with temperature $T$ of the two materials shows considerable differences reflected in drastic differences in the resistivity curves. Undistorted at high $T$, $1T$-TaS$_2$ has a first phase transition at 850 °C (Ref. 7) yielding an incommensurate (IC) CDW phase. Below 350 K, the so-called nearly commensurate (NC) phase consists of commensurate (C) domains (73 Å diameter in average, with the stars of David) separated by incommensurate domain walls;[7,12] the abrupt resistivity jump at 350 K is followed by a semiconductinglike temperature behavior the resistivity slightly increases with decreasing temperature. Below a MIT at 180 K the system enters the C phase, characterized by a resistivity with an order of magnitude higher but, paradoxically, with metalliclike slope. The $1T$-TaSe$_2$ with its single phase transition at 473 K gets into the commensurate CDW phase (with the same symmetry as $1T$-TaS$_2$) with a sudden increase in the resistivity but still with metallic temperature behavior.

In the present paper, we give a detailed comparison of the Fermi surfaces of $1T$-TaS$_2$ and $1T$-TaSe$_2$ as measured by ARPES. The photoemission experiments analysis is complemented by density-functional theory (DFT) band structure calculations for both samples. The article is organized as follows. In Sec. II the experimental and computational details are outlined. Fermi-surface mapping and band mapping experiments are presented in Secs. III and IV, respectively. In Sec. V the analysis puts forward the role of the thermal occupation of bands implying differences in transport properties of both materials. Finally, after presenting the band structure of the realistic CDW distorted lattice (Sec. VI), the article ends with a discussion of the nesting vector (Sec. VII) and conclusions (Sec. VIII).

## II. EXPERIMENT AND COMPUTATION

ARPES energy distribution curves (EDC's) and Fermi-surface mapping (FSM) measurements have been collected at RT in a modified VG ESCALAB Mk II spectrometer using monochromatized He I$\alpha$($h\nu = 21.2$ eV) photons.[13] The sequential motorized sample rotation has been outlined elsewhere.[14] The energy and angular resolution were 20 meV and $\pm 0.5°$, respectively. Pure $1T$-TaS$_2$ and $1T$-TaSe$_2$ samples were prepared by vapor transport[15,16] and cleaved *in situ* at pressures in the lower $10^{-10}$ mbar region. The accurate position of the Fermi level ($E_F$) has been determined on a polycrystalline copper sample. In some cases, the ARPES results have been normalized by the Fermi-Dirac function in order to bring to evidence states around the Fermi line. Cleanness and quality have been checked by x-ray photoelectron spectroscopy and by low-energy electron diffraction (LEED), respectively. Well-defined LEED superspots confirmed the presence of the CDW-induced reconstruction. X-ray photoelectron diffraction was used to determine the sample orientation *in situ* with an accuracy of better than 0.5°.

LEED results are shown in Figs. 1(a) and 1(b). Well-defined characteristic hexagonal spots of the basic structure are clearly present. Each of them is surrounded by those of the superstructure. For the $1T$-TaSe$_2$, however, more than one reconstruction is visible [Fig. 1(b), inset] due to two domains. Wilson *et al.*[9] performed electron micrographs of the Se alloy and also found different domains. They proposed dislocations in a single sandwich, i.e., twin boundaries formed by a Ta atom row separating $\alpha$ and $\beta$ superlattice domains, rotated by, respectively, $\pm 13.54°$ with respect to the *undistorted* basic structure.[9] However, they did not show evidence of two domains in $1T$-TaS$_2$, neither the recent literature does which states the same observations.[7,8]

Band structure calculations have been done using the WIEN package implementing the FLAPW method within the framework of DFT.[17] For the exchange-correlation potential the generalized gradient approximation was used.[18] We considered the photoemission process in assuming a free-electron final state without introduction of any matrix elements effects.[19]

## III. FERMI-SURFACE MAPPING

Since both compounds are isoelectronic ($d^1$ in the ionic picture) they are expected to give similar Fermi-surface maps. One has to keep in mind that an experimental FSM is not necessarily the actual FS, but a pattern reflecting the anisotropic distribution of the spectral weight of the electrons from the Fermi level. These patterns are shown in Figs. 2(a) and 2(b), mapped with respect to the conserved surface parallel component of the wave vector ($k_\parallel$). The first Brillouin zone (1BZ) has been drawn, as well as the crystallographic directions. The points of the images correspond to photoelectron intensities (gray scale, with high intensity in white) in an energy window around the Fermi level taken as a function of emission angle. The outer circle corresponds to grazing emission. The raw data shown in Fig. 2(a) has its high intensity in the 1BZ and is threefold and starlike. Its branches are more inequally weighted for the sulfide. At higher polar angles the intensity decreases but regains strength in the 2BZ (towards grazing emission). The features at high polar angles are difficult to distinguish as the gray scale has a limited dynamic range.

In order to enhance the information close to the grazing angles, the intensities have been normalized by the mean azimuthal value. In addition, mirror symmetry around the $\bar{\Gamma}$-$\bar{M}$ axis has been applied to recover the crystal symmetry. In our experiment this mirror symmetry is broken since the unpolarized light comes in along a non-high-symmetry direction. The consequent strong, orbital dependent polarization effect has been outlined, e.g., for copper in Ref. 21. The influence of polarized light on such photoemission experiments has also been discussed in the literature for the $1T$-TaS$_2$, but only for normal light incidence.[20]

DFT calculations for the *undistorted* structure in Fig. 2(c) compared to the experiments taken at RT in the CDW phase in Fig. 2(b) clearly give evidence for the $(1 \times 1)$, i.e., *unreconstructed* character of the electronic structure. In both cases, the simulation is a superposition of two three-ellipse-like flowers, one rotated by 120° with respect to the other.
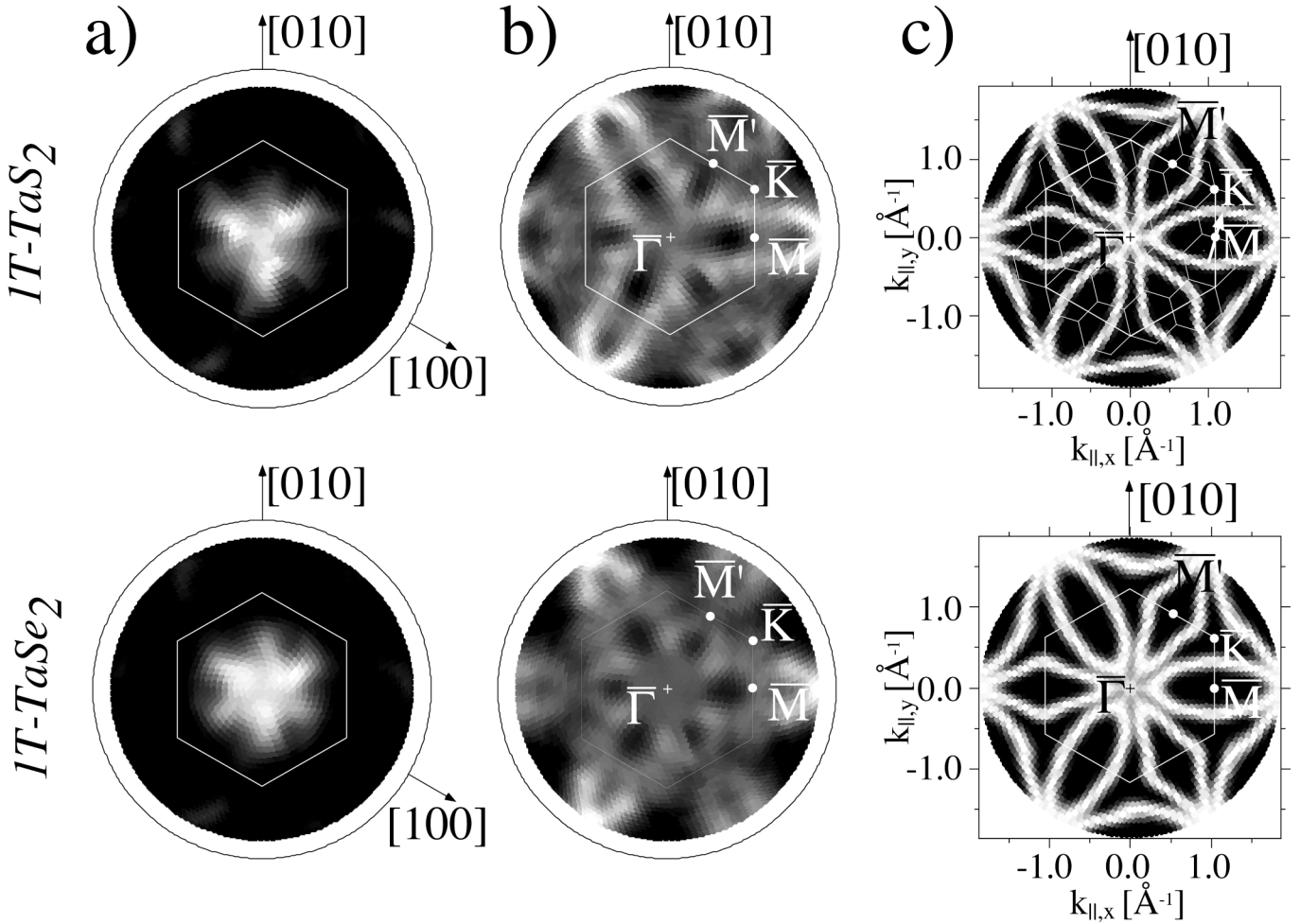
FIG. 2. Fermi-surface mapping with hexagonal unreconstructed hexagonal BZ's and high-symmetry points for both materials. Raw data (a) have been normalized by the mean azimuthal value (b). DFT simulations are given in (c). The $1T$-TaS₂ simulation has been added the CDW-induced reconstructed BZ's; a possible nesting vector is shown pointing across $\bar{M}$.

The fact that along $\bar{\Gamma}$-$\bar{M}'$ the ellipse gets a strong variation in going through the 1BZ gives a first indication for a weak $k_\perp$- dependence in the *unreconstructed* electronic structure of these quasi-2D materials. According to Ref. 20, the two flowers are subject to different selection rules in the photoemission process. The $\bar{\Gamma}$-$\bar{M}$ direction is preferred at $E_F$. Along $\bar{\Gamma}$-$\bar{M}'$, only the beginning of the ellipses is visible.

### IV. ENERGY DISTRIBUTION CURVES

FSM is ideally complemented by EDC's to figure out the role of the underlying band dispersion. The comparison of the experiment with the calculation for the *undistorted* structure, up to a binding energy of 2 eV, is the theme of Fig. 3 We focus on the $\bar{\Gamma}$-$\bar{M}$ direction. As outlined already in an early calculation,[22] one recognizes the Ta $5d$ band. In both, disulfide and diselenide, the band forms a small holelike pocket close to $\bar{\Gamma}$ followed by a large electronlike pocket around $\bar{M}$. For $1T$-TaS₂, there is practically no hybridization with the S $3p$. However, for $1T$-TaSe₂ at $\bar{\Gamma}$ and $\bar{M}$, the Se $4p$ orbitals get very close to the Ta band. Here, introduction

of spin-orbit coupling in the calculation (not shown here) even yields crossing bands. This DFT description illustrates that the Ta $5d$ and Se $4p$ wave functions overlap and hybridize, while in the disulfide the Ta $5d$ band is isolated and solely drives the electrical properties. And this hybridization[11] might play a crucial role in understanding the differences in transport properties of these two materials, as outlined in Secs. V and VIII. On the ARPES EDC's (Fig. 3) the reader immediately sees that the photoemission intensities, despite the superstructure as detected by x-ray diffraction and LEED, still keep the band dispersion of the $(1\times1)$ *undistorted* crystal.

We now begin to analyze in detail the spectral weight around the Fermi energy using the symmetrization procedure,[23,24] first along the high-symmetry directions $\bar{\Gamma}$-$\bar{M}$ and $\bar{\Gamma}$-$\bar{K}$, then on azimuthal EDC's measured at polar angles of 20° and 32° (see further on FSM of Fig. 5 for location in surface reciprocal space). The goal is to determine whether there is a pseudogap or a band (quasiparticle) crossing at the Fermi energy. The symmetrization method is a common practice in the cuprates to infer whether the spectral function
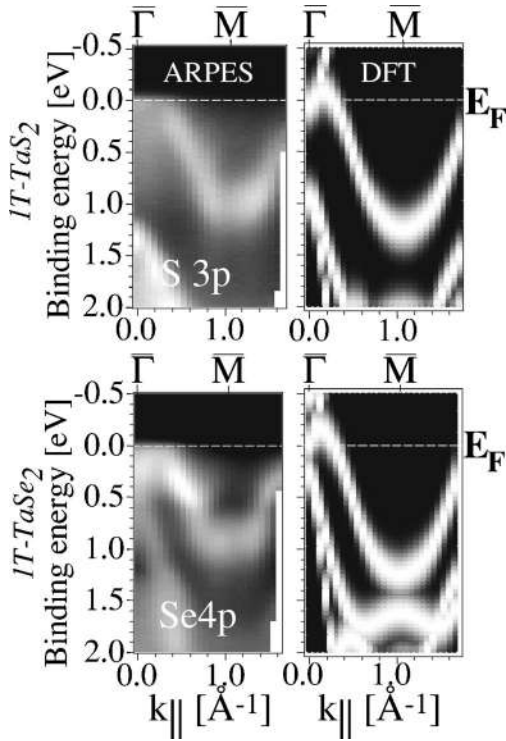
FIG. 3. ARPES and DFT energy distribution curves. See text for details.

peak crosses the chemical potential.[23,24] The idea of this symmetrization around $E_F$ (or $\omega=0$) is to remove the perturbative effect of the Fermi-Dirac distribution cuttoff with the intrinsic temperature dependence of the spectral function $A(k_F,\omega,T)$ and it is shown[24] to be efficient even for weakly dispersive bands at $E_F$. The photoemission intensities of a spectrum are symmetrized with respect to $E_F$ ($\omega=0$) and summed. In practice, $\vec{k}_F$ is then identified as the boundary in momentum space between where symmetrized data have a dip (local minimum) and where they exhibit a peak (local maximum) at $\omega=0$.[24] It is related to the fact that, when approaching $E_F$, the quasiparticle peak progressively brings spectral weight closer to it. As soon as it is not any more occupied (crossing has occurred), a dip is seen in the symmetrized data.

The measurements shown above, (Fig. 3), done on a large polar angle range (50°), show enhanced spectral weight at $E_F$ close to $\bar{\Gamma}$. The EDC's of Fig. 4 were all done along a high-symmetry direction crossing $\bar{\Gamma}$ (either $\bar{\Gamma}$-$\bar{M}$ or $\bar{\Gamma}$-$\bar{K}$). The spectra were taken every degree up to 1 eV binding energy. The spectrum plotted in bold has been measured at the normal ($\bar{\Gamma}$). Adjacent to the EDC's are the symmetrized curves. Along $\bar{\Gamma}$-$\bar{M}$ [Fig. 4(a)], the symmetrization for the disulfide leads to a peak, which gradually grows from 10° approaching the normal. Along the other direction [Fig. 4(b)], the scheme is the same, but starting from $\approx 16°$. We notice that no clear dip follows the peak, as it would be expected in order to be identified as a clearly crossing band. For the considered directions, the diselenide seems to be more pseudogapped as judged from the symmetrization peak
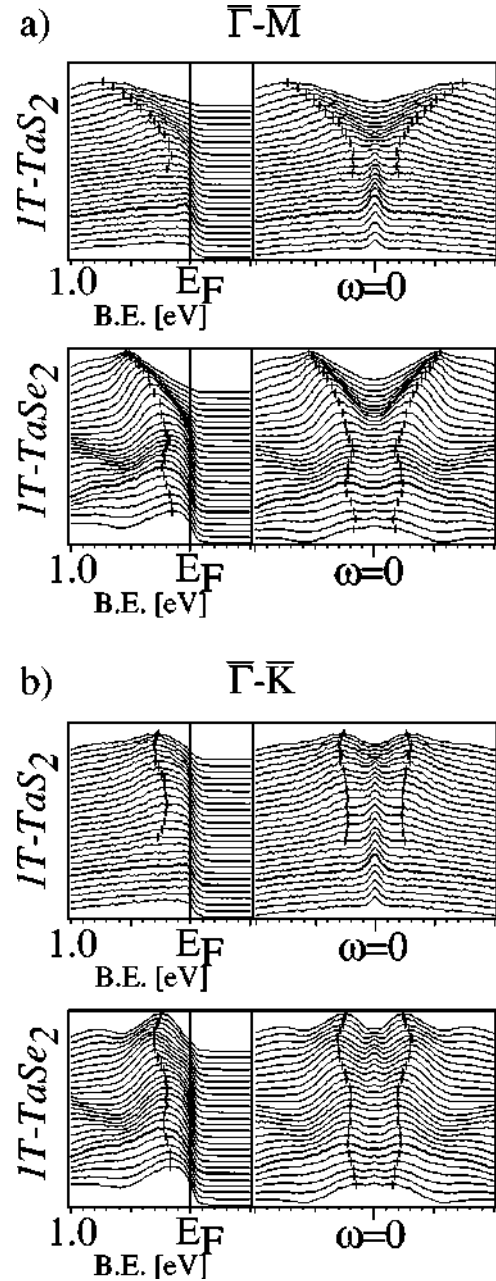


FIG. 4. On the left, spectra along two high symmetry directions, $\bar{\Gamma}$-$\bar{M}$ (a) and $\bar{\Gamma}$-$\bar{K}$ (b) across the normal emission (bold spectrum). Symmetrized data are shown on the right. See text.

in Fig. 4(a). Along $\bar{\Gamma}$-$\bar{K}$ in Fig. 4(b) the situation is similar and it is difficult to infer any crossing at the Fermi level. Nevertheless symmetrization peaks exist, confined in a circular region of about 20° centered at the normal. In the above discussions, the quasiparticle crossing was thought to occur starting from the occupied part of the band structure. It may be reasonable to envisage bands approaching $E_F$ from the unoccupied states, then only dispersing a few meV into the occupied part.

The EDC's displayed in Fig. 4 range up to $\approx 0.67$ Å$^{-1}$ for the $1T$-TaS$_2$ and 0.65 Å$^{-1}$ for $1T$-TaSe$_2$ in Fig. 3(a). In this range, the calculation proposes a regular crossing of the Ta

5d band, in contrast to the experiment. In Fig. 4, we put small bars on the peaks of the dispersing band. For the S alloy, the dispersion is as expected, except that the band surprizingly folds back to higher binding energy after having approached the Fermi level. Along the $\bar{\Gamma}$-$\bar{K}$ direction the dispersion is clearly oscillating. This modulation is even stronger for the diselenide. It indicates that the dispersion of the apparently *unreconstructed* band structure contains oscillating features due to the CDW.

We measured further EDC's but scanning azimuthal angles in order to probe the spectral weight at $E_F$ off normal but also away from the high-symmetry directions. Both samples clearly exhibit the same pseudogap. The 1T-TaSe₂ measurements in Fig. 5 (1T-TaS₂ measurements are not shown) do not give evidence for spectral weight comparable to the one mentioned at low polar angles (Fig. 4). Half a FSM—normalized by the mean azimuthal value—is shown as an orientation guide. The first EDC's [Fig. 5(a)] were taken at polar angle of 20° as pointed out by the white arrow on the FSM. The black arrow indicates the order in which the spectra have been collected. The symmetrized results do not have a peak at $\omega=0$, but the spectral weight is not zero. Therefore we have a pseudogap. The situation is very similar for the polar angle of 32° [Fig. 5(b)].

We simulated the EDC's of Fig. 5(a) with DFT [Fig. 5(c)] between the $\bar{\Gamma}$-$\bar{M}$ to the $\bar{\Gamma}$-$\overline{M'}$ directions. There is one band which is electronlike around the high-symmetry directions $\bar{\Gamma}$-$\bar{M}$ and $\bar{\Gamma}$-$\overline{M'}$. These pockets are recognizable in Fig. 5(a), but here two subbands disperse. These two flat subbands have also been measured by Horiba et al.[25] along the $\Gamma$ ALM plane and are explained as a consequence of the CDW formation according to the calculation of Smith et al.[26] They are also present at 32° [Fig. 5(b)] the first subband closer to $E_F$ seems to have decreased intensity with respect to the second one. The conclusions for 1T-TaS₂ are similar, with the difference that the two subbands are less marked or have the trend to form a single broad peak. But these less marked features are meaningful taking into account that the disulfide at RT is composed by C domains among IC domain walls (where the CDW phase is changing). Then the CDW features in the band structure have to be less pronounced and disturbed by the changing phase in the domain walls[7] of the incommensurations.

The calculation for the *undistorted* structure in Fig. 3 shows a clear crossing close to $\bar{\Gamma}$. But the experiment does not. We cannot, in conclusion, claim to observe a quasiparticle crossing the Fermi level despite the presence of the symmetrization peak close to the central region. The symmetrization peak shows angular dependence, and the pseudogap seems to grow with larger polar angle.

## V. THERMAL OCCUPATION AND TRANSPORT PROPERTIES

Before coming to an interpretation and a deeper understanding of the different subbands and the pseudogap via band structure calculations in Sec. VI, we proceed with a further analysis of states close to $E_F$. For analyzing intensi-
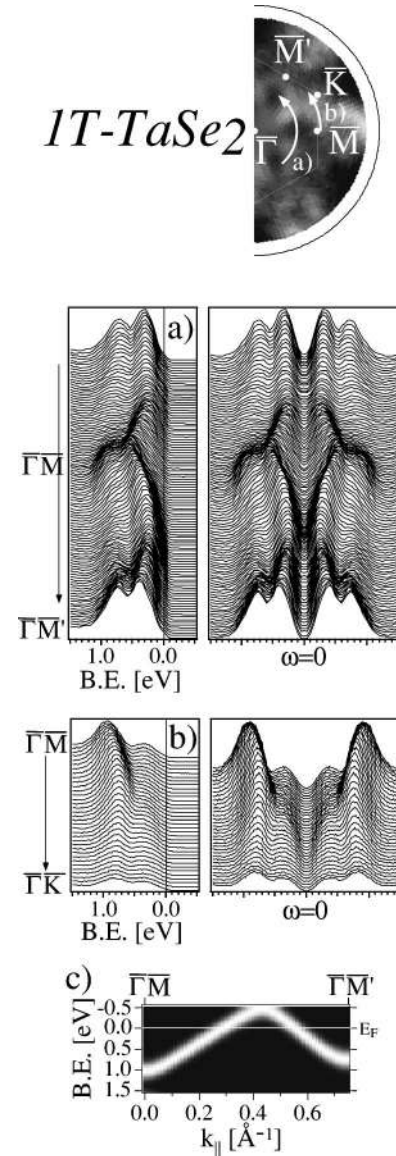


FIG. 5. Spectra taken along azimuthal angles on 1T-TaSe₂ for two polar angles, respectively, 20° (a) and 32° (b). Their corresponding location in surface reciprocal space is given with the arrows on the FSM. Both were symmetrized (b) and (e); we note here that, although no peak appears, at $\omega=0$, spectral weight is still present. It does not fall to zero. (c) Shows simulation for scanning at 20°.

ties in the vicinity of $E_F$, i.e., for states which are thermally excited, the spectra are divided by the Fermi-Dirac function (FD). In Fig. 6(a), the normal emission spectrum is shown. The spectra are cut at about 140 meV ($5k_BT$) above the chemical potential. The resulting FD normalized spectrum is represented by small crosses. In (b), the dispersion of peaks has been outlined by circles, which have been positioned by hand on the maxima of the spectral intensities. Both TMD's show a very flat dispersion close to zero binding energy in the polar angle range near $\bar{\Gamma}$. For 1T-TaS₂ the states lie slightly above the Fermi edge, whereas for 1T-TaSe₂, they are straddling $E_F$. This may be of importance for the transport properties; the disulfide needs thermal activation, like in
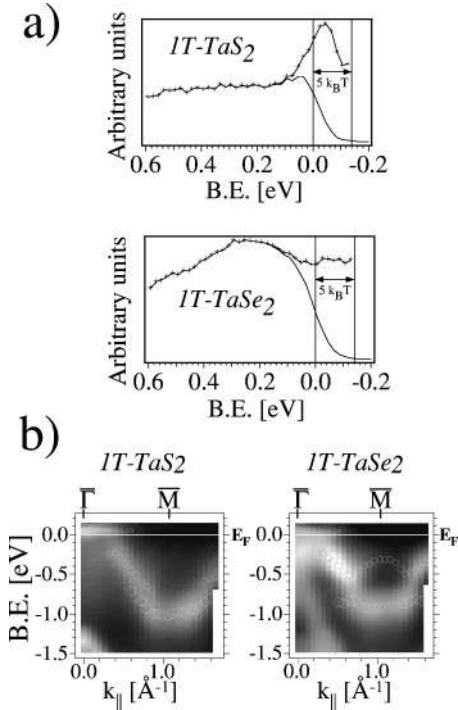
FIG. 6. Analysis of thermally excited states around $E_F$. Normal emission spectra are given in (a). The experimental spectrum is divided with the appropriate Fermi-Dirac function to reveal the thermally excited bands (crossed line). In (b), one sees the dispersion over the whole scanning range. Circular markers emphasize the splitting of the Ta band.

a semiconductor. The Se alloy has similar thermal occupation, but still with a band at $E_F$. Both samples, because of the CDW formation, have an increase in resistivity, however with intriguing different slopes as a function of $T$ at RT. The above photoemission considerations are here consistent with the semiconductinglike slope (negative) of the $1T$-TaS$_2$ and the metalliclike one (positive) of the $1T$-TaSe$_2$.

Figure 6(b) also shows the Ta $5d$ band on its full energy range. We placed on each local maxima of the spectra the circular markers. Both materials reveal, once more, a modulated dispersion with stronger intensities according to the $(1 \times 1)$ BZ. The Ta band appears clearly split, and the subbands tend to oscillate. This observation of fine modulated structures is more evident on the $1T$-TaSe$_2$. We see the first subband (at low binding energies) on the complete polar angle range, the second one is more flat.

## VI. REALISTIC RECONSTRUCTED BAND STRUCTURE OF $1T$-TaS$_2$

A deeper understanding of the subbands may be obtained via a DFT calculation (as illustrated in Fig. 7), now computing not only the basic hexagonal structure but by considering the atomic displacements of the atoms as induced by the CDW in the $1T$-TaS$_2$ and measured by means of x-ray scattering.[7] For the band structure calculation, an approximate commensurate ($\sqrt{13} \times \sqrt{13} \times 3$) superstructure was derived from the refined structural coordinates of the incom-

mensurate structure of the NC phase [notice that $\times 3$ in this ($\sqrt{13} \times \sqrt{13} \times 3$) superstructure means that the unit cell contains 3 TaS$_2$ sandwiches]. The bottom of this trigonal *distorted* unit cell contains the center of the "stars of David" as shown on Fig. 1(c). A detailed explanation is given in Ref. 10. For the DFT computation, only the first sandwich [as shown in Fig. 1(c)] around $z = 0$ was taken. The result is shown by dotted lines in Fig. 7(a) and is commented in detail in Ref. 10. The *reconstructed* band structure is plotted versus a path in the *unreconstructed* hexagonal reciprocal space. The correspondence between surface and bulk BZ's is illustrated in Fig. 7(b). In Fig. 7(e) both surface *reconstructed* (13.9° rotated hexagonal lattice, with positive rotation as observed on the LEED pattern) and *unreconstructed* (large hexagon) BZ's have been drawn with lines. A band character analysis indicates that the first seven subbands below the Fermi energy [Fig. 7(a)] are due to the Ta atoms. Thus the Ta $5d$ band is split by the CDW formation. We here emphasize the presence of the uppermost flat subband in the central plane of the 1BZ and its dispersion in $z$ along $\Gamma$-$A$. It moves off from the underlying subbands, and oscillates around $E_F$ at the border of the BZ (along $A-L$). This band has mostly $dz^2$ character.

Figure 7(c) shows the simulated EDC as issued from the *reconstructed* unit cell. A free-electron photoemission final state, as plotted in Fig. 7(d), is assumed to determine the $k$ points within the BZ. We can identify the six subbands, and the uppermost seventh subband straddling $E_F$ only coming down from $E_F$ after 1.5 Å$^{-1}$. It is a cut in the *reconstructed* ($r$) reciprocal space. The free-electron final state is shown up to 60°, the polar angle range we took for the simulation of the EDC [Fig. 7(d)]. (A thick line was chosen for the Fermi energy and a thin one for a binding energy of 2 eV.) At the normal, the measured $k$ points are closer to $A$ than to $\Gamma$, but reach the center of the BZ at 60°. This $z$ dispersion from $A$ to $\Gamma$ can be related to Fig. 7(a), in particular, when looking at the uppermost subband. It is the same dispersion as on the EDC [Fig. 7(c)]. Furthermore, according to the experimental bandwidth on the EDC (Fig. 3) (up to 1.3 eV), we have the confirmation that our photoemission experiments on the $1T$-TaS$_2$ probe the BZ off center plane. This would also practically not be affected by a slight change of our estimated inner potential (13 eV). It would just induce a small shift of the final state, which still would stay closer to $A$ than to $\Gamma$. And the same can be stated for the $1T$-TaSe$_2$, since the $c$-axis lattice constant is very similar. On the calculated EDC [Fig. 7(c)], the points at $E_F$ are exactly those plotted along $\bar{\Gamma}$-$\bar{M}$ on the *reconstructed* simulated FSM of Fig. 7(e). Just after $\bar{\Gamma}$ [going along $\bar{\Gamma}$-$\bar{M}$ in Fig. 7(c)], the Fermi line of the EDC is twice crossed by the flat subband. The crossing of this subband at $E_F$ forms the "flowers" paved FSM in Fig. 7(e). The "flowers" clearly follow the grid of the *reconstructed* higher BZ's, and [in Fig. 7(e)] we guess also the crossing of the seventh flat subband moving down when looking along $\bar{\Gamma}$-$\bar{M}$ in the *unreconstructed* 2BZ. As a matter of fact, this crossing is seen as a white circle close to the border of Fig. 7(e).

Experimentally we observed subbands and confirmed
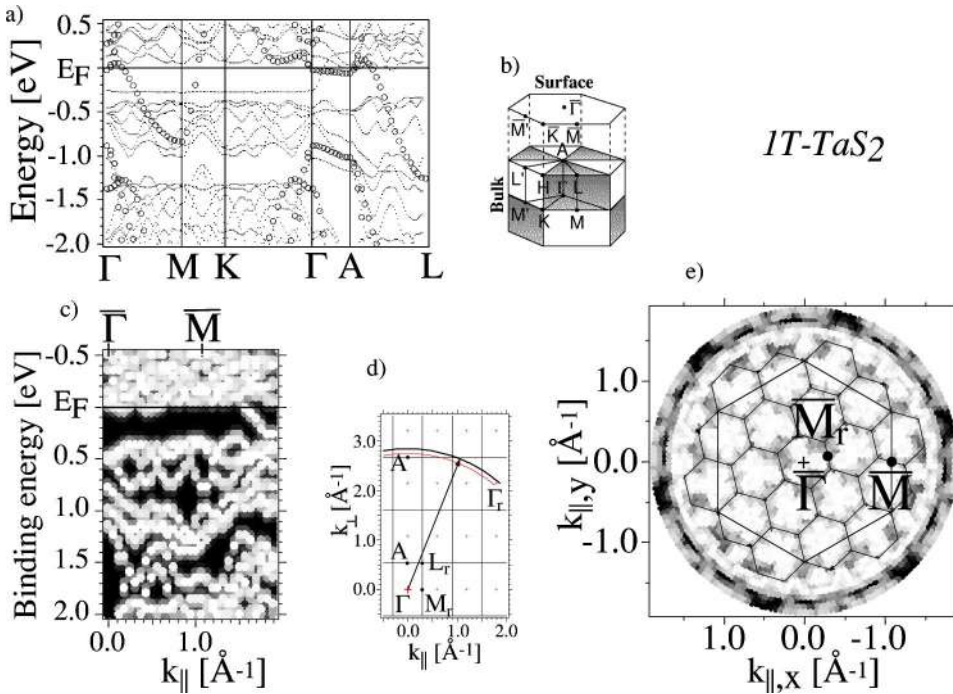
FIG. 7. Result from calculations for the *distorted* structure. (a) Band structure along high-symmetry lines, circular markers correspond to calculations for the undistorted structure. (b) Bulk surface BZ's correspondence. (c) Simulation of an EDC along $\bar{\Gamma}$-$\bar{M}$ for He I. (d) Cut in reciprocal space with free-electron final-state wave vector for He I. (e) Simulation of FSM with reconstructed BZ's.

theoretically the formation of subbands by the CDW. Despite the presence of flat subbands all over the BZ, the photoemission intensities are rather distributed according to the *unreconstructed* band structure (Figs. 2 and 3). For the 1$T$-TaS$_2$ the influence of the CDW induced new BZ's is not observed in the literature,[27–29] although at RT in the NC phase domains of $\approx 70$ Å size exist with a structure corresponding to the C phase.[7,12] We here state the same for the 1$T$-TaSe$_2$. Clearly, the calculations using the reconstructed structure do not reproduce the observed experimental intensity distributions displayed in Figs. 2(b) and 3. Certainly, the calculations using the *unreconstructed* structure [Figs. 2(c) and 3] fit much better. In order to understand this we need an important other ingredient.

Recently, Voit *et al.*[30] have modeled the spectral weight distribution of tight-binding electrons in a solid with competing periodic potentials as in the case of CDW superstructures. They show that the dispersion of the eigenvalues (band structure) follows the *reconstructed* BZ's, but the spectral weight (proportional to the photoemission intensity) is concentrated along the extended zone scheme dispersion of the *nonreconstructed* BZ, i.e., it follows the *unreconstructed* band structure. In Fig. 7(a), we plotted empty circles along the $(1 \times 1)$ dispersion of the disulfide. Accordingly, the experimental intensities are supposed to populate the underlying subbands following the unreconstructed bands and that is what we observed in the EDC's of Figs. 2–6.

Therefore, we are now able to obtain a detailed understanding of our measurements and of the electronic structure of these compounds. The CDW induces a profound reconstruction of the band structure. For a simple understanding, the formation of stars of 13 Ta atoms [Fig. 1(c)] (with one electron each, in an ionic picture) leads to seven subbands with two electrons per band except for the top one which is only half filled. The calculation of Fig. 7(a) where we see the

seven subbands along $\Gamma M K \Gamma$ between 0.2 and 1.0 eV binding energy confirms this view. The top-most seventh band (which is due to the star center Ta atom) crosses $E_F$ along $\Gamma$-$A$ confirming the partial occupation. Furthermore, considering the star of 13 Ta atoms being composed of the central atom surrounded by a first shell of 6, almost equivalent, nearest neighbors and a second shell of six, almost equivalent, next nearest neighbors we may group the subbands in three manifolds. Nearest and next nearest neighbors are represented by a manifold containing three subbands each and the third manifold only contains the top-most subband due to the star center atom. These three manifolds are clearly separated along $A - L$ as seen in Fig. 7(a) and also in the simulation [Fig. 7(c)]. The top-most manifold or subband is straddling $E_F$.

Going back to Fig. 6(b) we can identify the three manifolds with their intensity given by the spectral function following, according to Voit *et al.*,[30] the nonreconstructed band structure (see Fig. 3). In principle, the subband at $E_F$ is present all over the BZ. Its observation in ARPES, however, depends on its position with respect to $E_F$ (above or below while straddling $E_F$, see Figs. 7(a) and 7(c) and on the spectral function which favors the unreconstructed band structure.

In fact, the oscillating behavior of the top-most subband is displayed in Fig. 7(e) for the complete BZ. As a consequence we may explain our FSM experiments [Fig. 2(b)] in terms of the $(1 \times 1)$-unreconstructed FS [Fig. 2(c)] weighted with the oscillating behavior of the top-most subband. Furthermore this top-most subband has predominantly $dz^2$ character which explains the strong intensity drop via matrix elements for higher emission angles. This intensity drop (and therefore the matrix element effect) has been removed when going from Fig. 2(a) to Fig. 2(b), flattening the intensity plot.

The above is in accordance with our observations of a pseudogap. As mentioned above, the top-most subband is present all over the BZ. Even along $\Gamma MK\Gamma$ empty states are very close to $E_F$, everywhere. For this reason we are always finding spectral weight at $E_F$, whether it is originating from thermal occupation via the Fermi-Dirac distribution or whether states are truly below $E_F$. However, since these states are merely straddling $E_F$, we cannot observe a true crossing of a quasiparticle peak and hence experience a pseudogap behavior displaying an intensity distribution of the spectral weight according to the spectral function with $(1 \times 1)$ symmetry.

We complete the room-temperature considerations in this section with a brief speculation concerning the surface MIT recently found in $1T$-TaSe$_2$ at low temperature by Perfetti *et al.*[5] The new CDW-induced BZ's have lead to flattened backfolded bands, i.e., the CDW modulated electronic density has reduced the bandwidth W. This certainly reduces the $(W/U)$ parameter ($U$, the onsite Coulomb energy), which is crucial for understanding the activation of a Mott MIT.[5] In $1T$-TaS$_2$ at room temperature, the thermal occupation was proposed to act as in a semiconductor, which is confirmed by the semiconductinglike slope of the resistivity. As a consequence, there is a temperature where the thermal excitation is not sufficient anymore to create enough charge carriers. Possibly, it corresponds to the beginning of the Mott MIT. At this temperature, screening is lowered again (it was already decreased with the introduction of CDW induced new BZ's and corresponding backfolding of bands) and delivers the necessary favorable conditions for the Mott transition to develop for both bulk and surface.

On the other hand, for metallic $1T$-TaSe$_2$, the interplay $U$-$W$ is differently balanced due to the stronger overlap of Ta $5d$ and Se $4p$ derived bands. This hybridization tends to increase $W$, establishing unfavorable conditions for a phase transition. However, a reduced coordination number as it is the case at the surface, could be decisive to reduce $W$ specifically at the surface. This is proposed by Perfetti *et al.*[5] reporting such a surface MIT in the Se compound by comparing ARPES and dynamical mean-field theory calculation of the spectral function of a half-filled Hubbard model. Below this transition, however, there is still spectral weight remaining at $E_F$ with a possible contribution from the underlying bulk states. Two mechanisms would then explain the behavior, one as a consequence of the other. At room-temperature electron-phonon coupling is at work and the CDW modulated states are responsible for the RT pseudogap formation (see above). On top of the CDW-induced, reduced carrier density, as the temperature is lowered, electron-electron correlation sets in at the surface and leads to the transition.[5]

## VII. THE NESTING VECTOR

The distribution of the spectral weight follows the unreconstructed band dispersion. On the search for the origin of the CDW we are looking at the unreconstructed FS contours to find possble portions that are removed because of favorable nesting conditions. The unreconstructed Fermi-surface contours have an elliptic shape with rather flat sections close to the $\bar{M}$ point (Fig. 2). This offers the possibility to connect these flat parts of the contours on both sides of the $\bar{M}$ point according to a quasi-one-dimensional model with long parallel sections of the FS undergoing a Peierls transition. The length and direction of a possible nesting vector $\vec{q}_{CDW}$ appears favorable (see small white arrow in Fig. 2(c)). However, the idea behind the Peierls transition in a quasi-one-dimensional system is to bring the BZ boundary to lie on top of the flat parts of the FS contour. This is not happening in our case. We do not have a quasi-one-dimensional system but it is quasi-2D with threefold symmetry. Therefore, the system has to adopt a different strategy. By choosing a relatively long wavelength for the lattice distortion the new BZ's become relatively small, thus introducing a large number of new zones cutting the FS contours many times. Yet, this might not be enough to account for the elastic energy needed to distort the lattice. But there is another (favorable) consequence of enlarging the unit cell, namely the splitting of bands due to inequivalent positions of identical atoms, i.e., the splitting of the single Ta 5d band into seven subbands. In our case the system managed to lower six of the seven subbands (i.e., almost all) completely below $E_F$, certainly resulting in a major energy gain.

## VIII. CONCLUSIONS

We have shown that in addition to $1T$-TaS$_2$ also $1T$-TaSe$_2$ is pseudogapped. The CDW which has identical symmetry for the two compounds is found to be responsible. A detailed analysis of the band structure of both materials, as observed by photoemission with He $I\alpha$ radiation, reveals CDW split features which are confirmed by realistic *ab initio* DFT calculations, whose unit cell accounts for the atomic displacements due to the CDW formation. As a matter of fact, the CDW induced lattice distortion splits the Ta $5d$ band into subbands. It appears that only one of the subbands is close to $E_F$, the others being located below, herewith stabilizing the CDW structure. The subband close to $E_F$ is straddling the Fermi level and is responsible for the observed pseudogap behavior since it does not exhibit a clear quasiparticle crossing in the ARPES spectra but is creating persistent spectral weight at $E_F$. In addition, the spectral function is modulating the ARPES intensities according to the unreconstructed band structure, explaining the apparent absence of spectral features due to the new BZ's in FSM's and bandmapping experiments. As a consequence, this indicates that the pseudogap is not related to possible fluctuations of the underlying MIT as presumed previously.

[1] H. Ding, T. Yokoya, J.C. Campuzano, T. Takahashi, M. Randeria, M.R. Norman, T. Mochiku, K. Kadowaki, and J. Giapintzakis, Nature (London) **382**, 51 (1996); A.G. Loeser, Z.-X. Shen, D.S. Dessau, D.S. Marshall, C.H. Park, P. Fournier, and A. Kapitulnik, Science **273**, 325 (1996).

[2] F. Ronning, C. Kim, D.L. Feng, D.S. Marshall, A.G. Loeser, L.L. Miller, J.N. Eckstein, I. Bozovic, and Z.-X. Shen, Science **282**, 2067 (1998).

[3] Th. Pillo, J. Hayoz, H. Berger, M. Grioni, L. Schlapbach, and P. Aebi, Phys. Rev. Lett. **83**, 3494 (1999).

[4] P. Fazekas and E. Tosatti, Philos. Mag. B **39**, 229 (1979); Physica B **99**, 183 (1980).

[5] L. Perfetti, A. Georges, S. Florens, S. Biermann, S. Mitrovic, H. Berger, Y. Tomm, H. Höchst, and M. Grioni, Phys. Rev. Lett. **90**, 166401 (2003).

[6] R.A. Klemm, Physica C **348**, 839 (2000).

[7] A. Spijkerman, Jan L. de Boer, Auke Meetsma, Gerrit A. Wiegers, and Sander van Smaalen, Phys. Rev. B **56**, 13 757 (1997).

[8] G.A. Wiegers, J.L. de Boer, A. Meetsma, and S. van Smaalen, Z. Kristallogr. **216**, 45 (2001).

[9] J.A. Wilson, F.J. Di Salvo, and S. Mahajan, Adv. Phys. **24**, 196 (1975).

[10] M. Bovet, S. van Smaalen, H. Berger, R. Gaal, L. Forró, L. Schlapbach, and P. Aebi, Phys. Rev. B **67**, 125105 (2003).

[11] K. Horiba, K. Ono, J.H. Oh, T. Kihara, S. Nakazono, M. Oshima, O. Shiino, H.W. Yeom, A. Kakizaki, and Y. Aiura, Phys. Rev. B **66**, 073106 (2002).

[12] X.M. Wu and C.M. Lieber, Science **243**, 1703 (1989).

[13] Th. Pillo, L. Patthey, E. Boschung, J. Hayoz, P. Aebi, and L. Schlapbach, J. Electron Spectrosc. Relat. Phenom. **97**, 243 (1998).

[14] P. Aebi, J. Osterwalder, P. Schwaller, L. Schlapbach, M. Shimoda, T. Mochiku, and K. Kadowaki, Phys. Rev. Lett. **72**, 2757 (1994).

[15] B. Dardel, M. Grioni, D. Malterre, P. Weibel, Y. Baer, and F. Lévy, Phys. Rev. B **45**, 1462 (1992).

[16] B. Dardel, M. Grioni, D. Malterre, P. Weibel, Y. Baer, and F. Lévy, Phys. Rev. B **46**, 7407 (1992).

[17] P. Blaha, K. Schwarz, and J. Luitz, computer code WIEN97 (Karl-heinz Schwarz, Techn. Universität Wien, Austria, 1999), ISBN 3-9501031-0-4.

[18] J.P. Perdew, K. Burke, and M. Ernzerhof, Phys. Rev. Lett. **77**, 3865 (1996).

[19] Here, different values for both work function and inner potential were tested; however no relevant changes came out, as a consequence of the quasi-two-dimensional character of these materials.

[20] T. Matsushita, S. Imada, H. Daimon, T. Okuda, K. Yamaguchi, H. Miyagi, and S. Suga, Phys. Rev. B **56**, 7687 (1997).

[21] P. Aebi, J. Osterwalder, R. Fasel, D. Naumović, and L. Schlapbach, Surf. Sci. **307-309**, 917 (1994).

[22] H.W. Myron and A.J. Freeman, Phys. Rev. B **11**, 2735 (1975).

[23] M.R. Norman, H. Ding, M. Randeria, J.C. Campuzano, T. Yokoya, T. Takeuchi, T. Takahashi, T. Mochiku, K. Kadwaki, P. Guptasarma, and D.G. Hinks, Nature (London) **392**, 157 (1998).

[24] J. Mesot, M. Randeria, M.R. Norman, A. Kaminski, H.M. Fretwell, J.C. Campuzano, H. Ding, T. Takeuchi, T. Sato, T. Yokoya, T. Takahashi, I. Chong, T. Terashima, M. Takano, T. Mochiku, and K. Kadowaki, Phys. Rev. B **63**, 224516 (2001).

[25] K. Horiba, Kanta Ono, Han Woong Yeom, Yoshihiro Aiura, Osamu Shiino, Jin Ho Oh, Takayuki Kihara, Shinsuke Nakazono, Masaharu Oshima, and Akito Kakizaki, Physica B **284**, 1665 (2000).

[26] N.V. Smith, S.D. Kevan, and F.J. Di Salvo, J. Phys. C **18**, 3175 (1985).

[27] R. Claessen, B. Burandt, H. Carstensen, and M. Skibowski, Phys. Rev. B **41**, 8270 (1990).

[28] Th. Pillo, J. Hayoz, H. Berger, F. Lévy, P. Aebi, and L. Schlapbach, J. Electron Spectrosc. Relat. Phenom. **101-103**, 811 (1999).

[29] Th. Pillo, J. Hayoz, H. Berger, R. Fasel, L. Schlapbach, and P. Aebi, Phys. Rev. B **62**, 4277 (2000).

[30] J. Voit, L. Perfetti, F. Zwick, H. Berger, G. Margaritondo, G. Grüner, H. Höchst, and M. Grioni, Science **290**, 501 (2000).

# Spin-orbit splitting of the Shockley state in the Ag/Au(111) interface

H. Cercellier,[1] Y. Fagot-Revurat,[1] B. Kierren,[1] F. Reinert,[2] D. Popović,[2] and D. Malterre[1]

[1]*Laboratoire de Physique des Matériaux (UMR 7556), Université Henri Poincaré, Nancy I-B.P. 239,*
*F-54506 Vandœuvre-lès-Nancy, France*
[2]*Universität des Saarlandes, Fachrichtung 7.2-Experimentalphysik, D-66041 Saarbrücken, Germany*
(Received 15 July 2004; published 29 November 2004)

We have studied the modification of Au(111) surface state parameters with Ag deposition. We unambiguously evidence a continuous decrease in the spin-orbit splitting of the two surface state subbands upon increasing Ag coverage. An annealing leads to the formation of a chemically disordered Ag-Au alloy. This alloy formation is accompanied by an increase in the spin-orbit splitting. We established a quantitative correlation between the amplitude of this splitting and the relative amount of Au and Ag atoms probed by the surface state wave function proving the atomic character of the spin-orbit splitting. Control of the Ag-Au interface allows a continuous fine tuning of surface state properties; in particular, the $k$-dependent spin polarization.

The (111) surfaces of noble metals that present a $sp$ surface state (Shockley state) close to the L point of the Brillouin zone,[1] have been extensively studied by angle-resolved photoelectron spectroscopy (ARPES) in the last two decades.[2,3] This electronic state is a paradigm of two-dimensional electronic systems, and it has been used to study fundamental interactions such as electron-electron or electron-phonon interactions in solids.[4,5] Recently, the effect of spin-orbit interaction on the Shockley state has been evidenced.[6,7] In Au(111), this interaction yields a splitting of the Shockley band and the formation of two spin-polarized subbands.[8,9] A similar behavior is observed on the $d$-derived surface state in Li/W(110).[10,11] This splitting is, in principle, forbidden in centrosymmetric solids due to combined time reversal and inversion symmetries.[12,13] As an example, it appears in noncentrosymmetric semiconductors with blende structure such as GaAs,[14] but not in centrosymmetric semiconductors with diamond structure such as Ge.[15] The Au structure is centrosymmetric, but there is a breakdown of the inversion symmetry due the surface potential. However, it was shown that this surface potential cannot explain quantitatively the magnitude of the splitting, and it was suggested that atomic spin-orbit interaction plays an important role.[16] This atomic origin explains the large splitting observed on the surface state of Au (heavy metal and large spin-orbit interaction), whereas a vanishing one is observed in the case of Ag.[17] In this paper, we will show that this splitting can be continuously tuned by controlling the Ag/Au interface. Its evolution with Ag film thickness and with annealing leads us to the conclusion that the key parameter is the amount of Au atoms probed by the evanescent surface state. This result demonstrates that the spin-orbit coupling on the Shockley state has essentially an atomic origin.

The measurements were carried out in a UHV setup composed of a molecular-beam epitaxy chamber for the elaboration and characterization of the surfaces and a photoemission chamber with a high resolution Scienta SES 200 analyzer ($\Delta E < 5$ meV and $\Delta\theta < 0.5°$). Ag ultrathin films were prepared by molecular-beam epitaxy from a Knudsen cell [rate $\simeq 0.5$ monolayer (ML)/mn] on a Au(111) substrate with a miscut better than 0.1°. The sample was characterized by low energy electron diffraction and Auger electron spectroscopy. The substrate deposition temperature was 300 K to get a sharp Ag/Au(111) interface and a layer by layer growth, as actually claimed in the literature.[18–20] However, an alloying is observed with increasing temperature. All the ARPES measurements have been carried out at $T = 80$ K with He I ($h\nu = 21.22$ eV) or Ar I ($h\nu = 11.83$ eV) excitation energies. The measurement temperature has been chosen in order to minimize contamination and to avoid interdiffusion.

The photoemission spectra as a function of energy and momentum of the Shockley surface state of Au(111) substrate, a 0.5 ML, and a 1 ML Ag film, are reported in Fig. 1. The Au(111) spectrum exhibits a Shockley band whose energy at the center of the surface Brillouin zone ($\bar{\Gamma}$ point) is
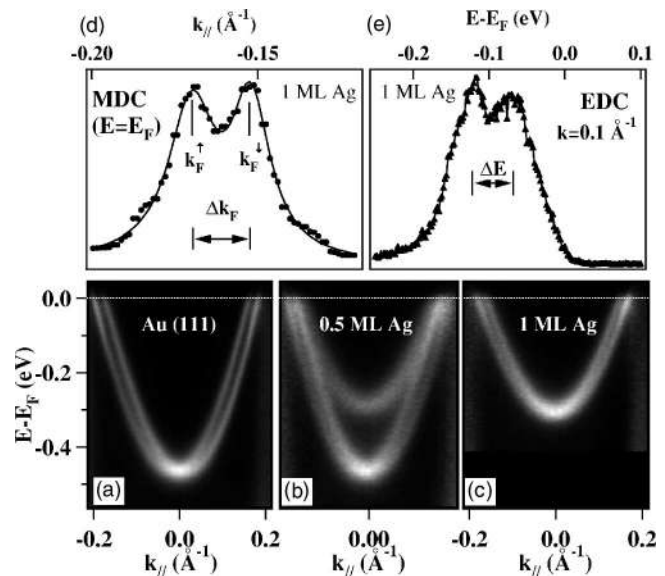


FIG. 1. ARPES intensity as a function of wave vector and energy for the Au(111) substrate (a), a 0.5 ML Ag film (b), and a 1 ML Ag film on Au(111) (c). Momentum distribution curves at $E_F$ (d) and energy distribution curve at $k = 0.1$ Å$^{-1}$ (e) for the 1 ML Ag film.

**70** 193412-1

$E_0 = E(\bar{\Gamma}) - E_F = -475$ meV, in good agreement with published data.[7] This band is split by spin-orbit interaction into two spin-polarized subbands. Due to the nearly free-electron-like character of the Shockley state, its Fermi surface is composed of two concentric circles in the first Brillouin zone.[7] The dispersion relations of these subbands can be written as

$$E(\vec{k}_\parallel) = \frac{\hbar^2 k_\parallel^2}{2m^*} \pm \alpha_R k_\parallel, \qquad (1)$$

where the Rasbha coefficient ($\alpha_R$) measures the magnitude of the spin-orbit interactions $H_{S.O} = \alpha_R(\vec{e}_z \times \vec{p}) \, \vec{\sigma}$ (Ref. 21) and $m^*$ is the electron effective mass. From a fitting procedure of the two dispersive subbands by parabolas, a value of $2\alpha_R^{Au} = 0.66 \pm 0.08$ Å eV can be estimated. This corresponds to a difference in Fermi momentum of the two subbands $\Delta k_F = |k_F^\uparrow - k_F^\downarrow| = 0.023 \pm 0.003$ Å$^{-1}$, as defined on the momentum distribution curves (MCD's) in Fig. 1(d), in perfect agreement with the previous published value.[17]

Similar spin-orbit split bands are also observed in the Ag/Au(111) system. This is illustrated in Figs. 1(b) and 1(c), where we report the respective photoemission intensities for 0.5 and 1 ML Ag films deposited on Au(111). For the 1 ML Ag film, the Shockley state at the $\bar{\Gamma}$ point is found to be shifted by 170 meV toward the Fermi energy ($E_0 = -305$ meV). This latter value can be understood as the surface state energy of Au(111) perturbed by a modified potential in the last layer due to Ag atoms. The various electronic parameters are also affected by the modification of the potential. Firstly, we observe a significant increase in the electron effective mass from 0.26 $m_0$ for the bare substrate to 0.33 $m_0$ for the 1 ML film. Secondly, the value of the splitting measured by the momentum separation ($\Delta k_F$) between the two subbands at $E_F$ is reduced by about 20% with respect to pure Au(111) surface. However, due to the very different effective mass, the energy between the two subbands at a given momentum [Fig. 1(d)] is significantly reduced (about 40%) with respect to Au(111). An interesting behavior is observed in the spectra of submonolayer films ($0 < \theta < 1$ ML). The normal emission spectra exhibit two spectral features at $E_0 = -475$ meV and $E_0 = -305$ meV, as shown in Fig. 1(b) for $\theta = 0.5$ ML. Upon increasing the Ag coverage, a balance of intensity of these two series of dispersive bands is observed. Such a behavior was previously observed in similar systems like Ag/Cu(111).[22,23] The two structures can be interpreted by surface states confined in the noncovered Au terraces ($E_0 = -475$ meV) and in the Ag islands ($E_0 = -305$ meV).[23,24] The Ag thickness dependence follows an exponential behavior, as already reported.[20]

In Fig. 2, we focus on the evolution of the MDC at the Fermi energy ($E_F$). This spectrum corresponds to a cut of the Fermi surface along a radial direction of the Brillouin zone. The solid lines represent an adjustment of the experimental spectra (with two lorentzians with the same width), which allows an estimation of the momentum spin-orbit splitting ($\Delta k_F$) at $E_F$. This figure shows that two contributions are resolved up to 3 ML films, whereas for larger thicknesses, only a broad feature is observed. Nevertheless, the anoma-
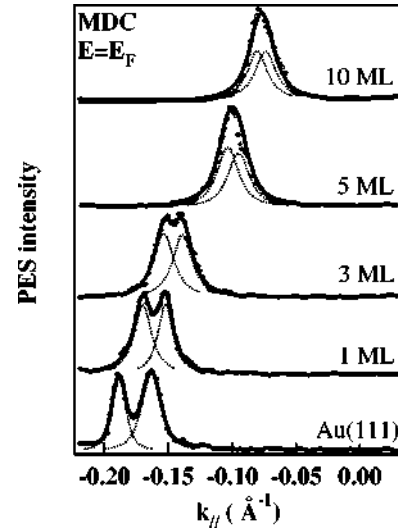


FIG. 2. MDC's taken at $E = E_F$. The dotted lines correspond to an adjustment with two lorentzians, which allows us to estimate the momentum splitting of the two subbands.

lous large width, larger than the experimental resolution, reveals a remaining spin-orbit induced band splitting of the surface state. From the Ag thickness dependence of $\Delta k_F$, the evolution of the Rashba coefficient can be obtained: $2\alpha_R$, equal to $0.66 \pm 0.08$ for Au(111), tends to $0.11 \pm 0.08$ in the limit of large Ag thickness, in agreement with the value obtained for Ag(111) single crystal $2\alpha_R \approx 0.06$.[17]

Auger spectroscopy indicates interdiffusion with increasing temperature. Figure 3(b) illustrates this alloying effect by showing the temperature dependence of the Au NVV Auger intensity for 1 and 3 ML films. The interfaces have been prepared at 100 K for the 1 ML film and 300 K for the 3 ML film. In both cases, upon increasing temperature, the Auger signal is at first nearly constant (with a slight negative slope) and then exhibits a large increase above a characteristic temperature. The negative slope is likely to be due to a smoothing of the Ag layer. This behavior is especially marked for the 1 ML because a deviation from a perfect layer by layer growth occurs due to the low preparation temperature (100 K). The strong increase in the Au Auger intensity above a characteristic temperature reveals segregation of Au atoms at the surface and the formation of a Ag—Au alloy. This characteristic temperature is thickness dependent since it is about 300 K for the 1 ML film and 450 K for the 3 ML film. The influence of the alloy formation on the electronic properties is evidenced in Fig. 3 by comparing the dispersion of the 3 ML Ag film surface state after an annealing at 510 K [Fig. 3(a)] and after an annealing at 570 K [Fig. 3(b)]. Two effects are clearly evidenced: first, a 200 meV energy shift to lower energy in the 570 K spectrum and second, a correlated increase in the splitting of the two spin-polarized subbands. The values of $E_0 = -410$ meV and $2\alpha_R = 0.5$ we obtained after the 570 K annealing are close to those observed in a pure Au(111) surface. This result suggests that the surface is essentially composed of Au atoms after such an annealing.

Figure 3(d) shows the annealing temperature dependence of the surface state energy at the $\bar{\Gamma}$ point ($-E_0$) and the
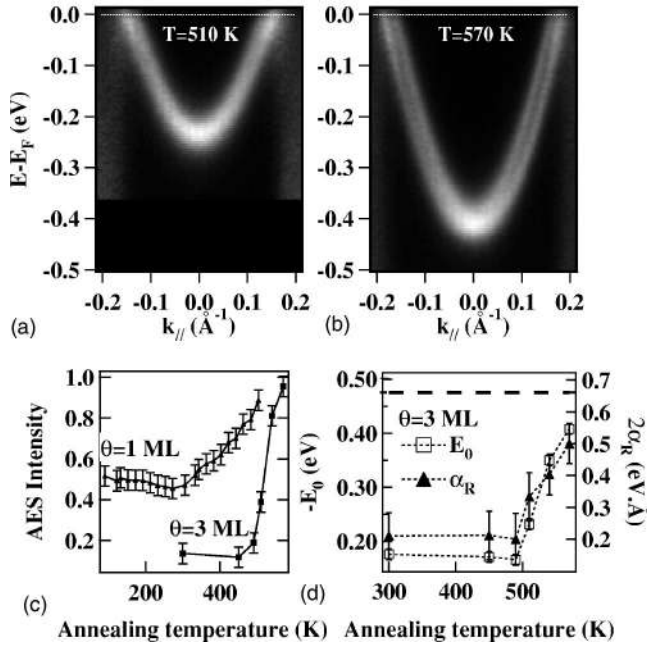
FIG. 3. Photoemission intensity as a function of energy and momentum for a 3 ML film after an annealing at 510 K (a) and at 570 K (b). (c) Annealing temperature dependence of the Au Auger intensity for a 1 and a 3 ML Ag film on Au(111), the spectra have been recorded with a time step of 30 s. (d) Annealing temperature dependence of the surface state energy at the $\bar{\Gamma}$ point and Rashba parameter [the horizontal dashed line represents values for the Au(111)].

Rashba coefficient for a 3 ML Ag film. Both quantities remain approximately constant for annealing temperatures smaller than 500 K and present a pronounced change above 500 K. Such dependences can be easily interpreted by the formation of a Au-rich alloy at the surface. What we would like to point out is the existence of very well-defined surface state dispersion in spite of the existence of an alloy, i.e., with chemical disorder, at the surface. This robustness of the Shockley surface state was previously observed at the (111) surface of a disordered $Cu_{0.9}Al_{0.1}$ alloy,[25] and is in agreement with theoretical predictions. Although the wave vector is not a good quantum number in chemically disordered alloys, coherent-potential-approximation calculations show that the spectral function exhibits well-defined peaks.[26]

It was proposed that atomic spin-orbit plays an important role in the formation of the two spin-polarized surface state subbands in Au(111).[16] As spin-orbit interactions are larger in Au atoms than in Ag ones, the Rashba parameter in Ag/Au(111) could be proportional to the amount of Au atoms probed by the Shockley state. In the direction normal to the surface, the wave function exhibits an evanescent shape as shown in Fig. 4(a). We have reported the solution of a one-dimensional Schrödinger equation simulating the potential of a 3 ML film according to the surface potential model proposed by Chulkov et al.[27] This figure shows that the surface state is mainly confined in the three Ag layers, but also extends slightly into the Au substrate. According to our assumption that the spin-orbit interaction is essentially atomic-like, the effective Rashba parameter can be expressed as the
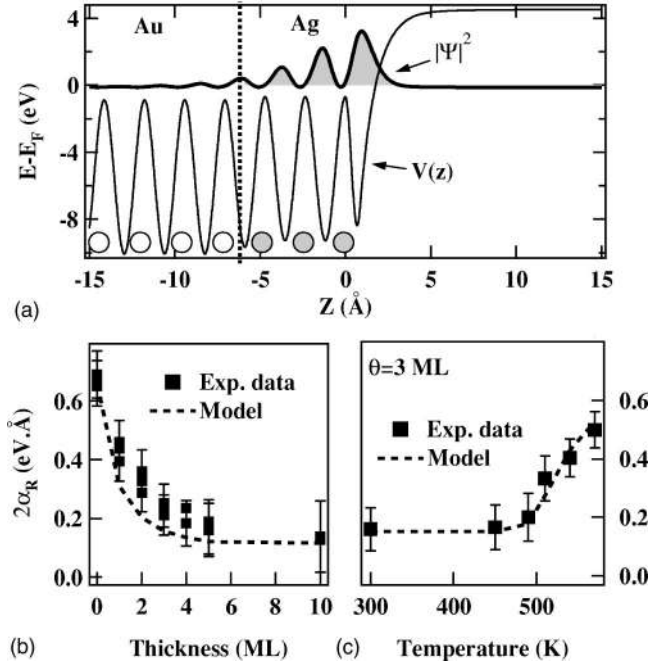


FIG. 4. (a) One-dimensional electronic potential and charge density ($|\Psi|^2$) of the Shockley state for a 3 ML Ag film (the white and gray circles represent the Au and Ag layers, respectively). (b) Experimental and simulated Rashba parameters for room temperature annealed Ag films. (c) Evolution of the Rashba parameter for a 3 ML film as function of annealing temperature.

mean value of the parameters of Au(111) ($\alpha_R^{Au}$) and Ag(111) ($\alpha_R^{Ag}$) surfaces weighted by the relative amount of Au atoms ($p^{Au}$) probed by the surface state:

$$\alpha_R = p^{Au}\alpha_R^{Au} + (1 - p^{Au})\alpha_R^{Ag}. \qquad (2)$$

The effect of the increase in the Ag film thickness is a large decrease in $p^{Au}$ probed by the Shockley state. By using Eq. (2) and the calculated wave functions for different film thicknesses, we can estimate the thickness dependence of the effective Rashba ($\alpha_R$) parameter [dotted line in Fig. 4(b)]. A good agreement is found with experimental results corroborating that the spin-orbit splitting is actually dominated by atomic interaction.

Annealing temperature dependence of the Rashba parameter confirms this interpretation. In order to obtain the $p^{Au}$ values after annealing in the disordered alloys, we have to calculate the relative amount of Au atoms in each layer. This is achieved in the framework of a simple one-dimensional diffusion model.[28] By taking $\nu_0 = 7 \times 10^{16}$ s$^{-1}$ for the diffusion rate and $E_A = 1.83$ eV for the energy barrier, we have calculated the concentration profile for 3 ML of Ag on Au(111) corresponding to the experimental conditions (temperature and duration of the annealing). This profile accounts for the Auger intensity dependence of Fig. 3(b). Therefore, from this profile and numerical solutions for the Shockley state, we can estimate the number of Au atoms ($p^{Au}$) probed by the Shockley wave function and the corresponding Rashba coefficient [Eq. (2)]. With increasing annealing temperature, the amount of Au atoms increases in the top layers

leading to an increase in the Rashba term. The good agreement with experimental data demonstrates that the spin-orbit splitting directly reflects the alloy composition close to the surface weighted by the Shockley wave function charge density.

Deposition of noble gases on Au(111) yields an increase in the spin-orbit splitting.[17] A similar increase was also observed on the *d*-derived surface state in Li/W(110) with increasing Li coverage.[10] However, in this system, the evolution of the splitting has been attributed to the modification of the the surface state extension. We take into account this

mechanism in Ag/Au(111) by calculating the wave function, but it has a minor influence.

In conclusion, we observed that a continuous decrease in the spin-orbit splitting of the *sp*-derived surface state occurs with deposing Ag on Au(111) substrate. On the contrary, the annealing of the interfaces leads to an increase in the splitting. Both dependences of the spin-orbit splitting can be simply correlated to the amount of Au atoms sampled by the surface state. This behavior confirms the fundamental role of the atomic spin-orbit interaction in the formation of spin-polarized surface state subbands and sheds additional light regarding the possibility of a fine tuning of the splitting.

[1] W. Shockley, Phys. Rev. **56**, 317 (1939).

[2] P.O. Gartland and B.J. Slagsvold, Phys. Rev. B **12**, 4047 (1975).

[3] S.D. Kevan, Phys. Rev. Lett. **50**, 526 (1983).

[4] R. Matzdorf, Surf. Sci. Rep. **30**, 153 (1998).

[5] N. Memmel, Surf. Sci. Rep. **32**, 91163 (1998).

[6] S. LaShell, B.A. McDougall, and E. Jensen, Phys. Rev. Lett. **77**, 3419 (1996).

[7] G. Nicolay, F. Reinert, S. Hüfner, and P. Blaha, Phys. Rev. B **65**, 033407 (2001).

[8] J. Henk, A. Ernst, and P. Bruno, Phys. Rev. B **68**, 165416 (2003).

[9] M. Muntwiler, M. Hoesch, V.N. Petrov, M. Hengsberger, L. Patthey, M. Shi, M. Falub, T. Greber, and J. Osterwalder, Physica B (in press).

[10] E. Rotenberg, J.W. Chung, and S.D. Kevan, Phys. Rev. Lett. **82**, 4066 (1999).

[11] M. Hochstrasser, J.G. Tobin, E. Rotenberg, and S.D. Kevan, Phys. Rev. Lett. **89**, 216802 (2002).

[12] M. Tinkham, *Group Theory and Quantum Mechanics* (McGraw-Hill, New York, 1964).

[13] C. Kittel, *Quantum Theory in Solids* (Wiley, New York, 1987).

[14] G. Dresselhaus, Phys. Rev. **100**, 580 (1955).

[15] R.J. Elliott, Phys. Rev. **96**, 280 (1954).

[16] L. Petersen and P. Hedegård, Surf. Sci. **459**, 49 (2000).

[17] F. Reinert, J. Phys.: Condens. Matter **15**, S693 (2003).

[18] Y. Borensztein, T. Lopez-Rios, and G. Vuye, Phys. Rev. B **37**, 6235 (1988).

[19] M.M. Dovek, C.A. Lang, J. Nogami, and C.F. Quate, Phys. Rev. B **40**, 11 973 (1988).

[20] A. Beckmann, M. Klaua, and K. Meinel, Phys. Rev. B **48**, 1844 (1993).

[21] E.I. Rashba, Sov. Phys. Solid State **2**, 1109 (1960).

[22] A. Bendounan, Y. Fagot-Revurat, B. Kierren, F. Bertran, V.Yu. Yurov, and D. Malterre, Surf. Sci. **496**, L43 (2002).

[23] A. Bendounan, H. Cercellier, Y. Fagot-Revurat, B. Kierren, V. Yu. Yurov, and D. Malterre, Phys. Rev. B **67**, 165412 (2003).

[24] A. Bendounan, H. Cercellier, B. Kierren, Y. Fagot-Revurat, V. Yu. Yurov, and D. Malterre, Europhys. Lett. **64**, 392 (2003).

[25] H. Asonen and M. Pessa, Phys. Rev. Lett. **46**, 1696 (1981).

[26] W.M. Temmerman, B.L. Gyorffy, and G.M. Stocks, J. Phys. F: Met. Phys. **8**, 2461 (1978).

[27] E.V. Chulkov, V.M. Silkin, and P.M. Echenique, Surf. Sci. **391**, 330 (1997); **437**, L1217 (1999).

[28] H. Cercellier, Ph.D. thesis, 2004.

# High resolution spectroscopic and microscopic signatures of ordered growth of ferrous sulfate in SO$_2$ assisted corrosion of Fe$_3$O$_4$(100)

D. Stoltz,[a)] A. Önsten, U. O. Karlsson, and M. Göthelid

*Materialfysik, MAP, KTH-Electrum, SE-16440 Kista, Sweden*

The authors present a high-resolution core-level photoemission study of a Fe$_3$O$_4$(100) surface exposed to 50 L (1 L=10$^{-6}$ mbar s) of H$_2$O and 50 L of SO$_2$. S 2$p$ core-level spectra reveal the presence of SO$_3$ and SO$_4$ species. An additional peak in the Fe 3$p$ core-level spectrum shows that they bond with iron from the substrate. Complementary scanning tunneling microscopy of the same surface demonstrates formation of a long-range ordered sulfate locked in the ($\sqrt{2} \times \sqrt{2}$)$R$45°-surface potential. © *2007 American Institute of Physics*. [DOI: 10.1063/1.2776854]

Corrosion denotes oxidation of a metal upon exposure to water and oxygen in the air and is commonly understood as deterioration of material properties and, in the case of iron, formation of rust. Pollutants such as SO$_2$ have been discovered to have an accelerating effect on corrosion.[1] The adsorption of sulfate/bisulfate anions from H$_2$SO$_4$ on noble metal surfaces, which are considered to be resistant to corrosion, was studied intensively in the past by means of scanning tunneling microscopy (STM) to reveal formation of a similar ($\sqrt{3} \times \sqrt{7}$) adlayer on top of Au(111),[2] Cu(111),[3] Pt(111),[4] Pd(111),[5] Rh(111),[6] Ru(111),[7] and Ir(111).[8] Slightly different overstructures were observed on Ag(111), Ag(100),[9] and Au(100).[10]

Contrary to noble metals, iron is known for extreme changes of its properties (weakening) due to oxidation. One way of corrosion protection of iron or steels is by the formation of protective iron oxide (Fe$_2$O$_3$ and Fe$_3$O$_4$) films. A previous study of sulfate on the hematite (Fe$_2$O$_3$) surface[11] has confirmed the presence of aqueous FeSO$_4^+$ complexes. It has also been discussed[11] that an outer-sphere adsorbate (defined as retaining at least one water molecule between the solute and the surface) cannot be seen by STM.

In this letter, we present a combined photoelectron spectroscopy (PES) and STM study of corrosion of Fe$_3$O$_4$(100). We proceed with dosing H$_2$O and SO$_2$ gases in ultrahigh vacuum conditions in order to imitate initial stages of atmospheric corrosion and avoid solutions which could stand in the way of obtaining atomic resolution of the adsorbate.

STM experiments have been performed in a constant current mode with a W tip at room temperature (RT) using a variable temperature STM from Omicron NanoTechnology. Positive bias means tunneling from occupied states. Photoemission experiments have been performed at RT using a Scienta R4000 parallel detection analyzer at beamline I511 at MAX-lab (Sweden). The experimental energy resolution was 45 meV at $h\nu$=280 eV and 30 meV at $h\nu$=170 eV. The position of the Fermi level ($E_F$) has been determined on a Ta foil. The FITXPS2 software[12] was used for core-level fits. WSXM 3.0 (Ref. 13) was used for the processing of STM images. The magnetite (Fe$_3$O$_4$) single crystal with (100) orientation was purchased from surface preparation laboratory and prepared according to Ref. 14. The low energy electron diffraction (LEED) pattern of the clean surface was sharp ($\sqrt{2} \times \sqrt{2}$)$R$45°. H$_2$O and SO$_2$ were dosed separately at room temperature during 10 min at total pressure of $8 \times 10^{-8}$ mbar, which corresponds roughly to 50 L (1 L=10$^{-6}$ mbar s). H$_2$O was dosed first.

Figure 1(a) shows a S 2$p$ core-level spectrum from a Fe$_3$O$_4$(100) surface covered with 50 L of H$_2$O and 50 L of SO$_2$. It can be decomposed into three spin-orbit split doublets [spin-orbit splitting of 1.2 eV, branching ratio of 0.5–0.6, and full width at half maximum (FWHM) of ~1 eV] with the binding energies of the first peaks at 161.3, 166.2, and 167.1 eV. The lowest binding energy doublet can be attributed to atomic sulfur (marked S in Fig. 1). Binding energy shifts of the other two doublets with respect to atomic S are thus 4.9 and 5.8 eV, which agrees very well with 4.7 and 5.6 eV shifts between S and SO$_3$ and S and SO$_4$ on a ZnO surface.[15] According to this, we also assign the two higher binding energy doublets in Fig. 1 to SO$_3$ and SO$_4$ species.

In Figs. 1(b) and 1(c), we present Fe 3$p$ core-level spectra in order to investigate bonding of SO$_x$ ($x$=3,4) species to the substrate. A spectrum from the clean surface is shown in Fig. 1(b). Upon exposure of clean Fe$_3$O$_4$(100) to water and sulfur dioxide, an additional component appears at lower binding energy (53.76 eV) in the Fe 3$p$ core level, as shown in Fig. 1(c). FWHM of this component is 3 eV, while the bulk Fe contribution is 3.8 eV wide. The Fe 3$p$ level is known to have a complex sextuplet structure.[16] Therefore, the peak fit presented in Fig. 1(c) should be understood more
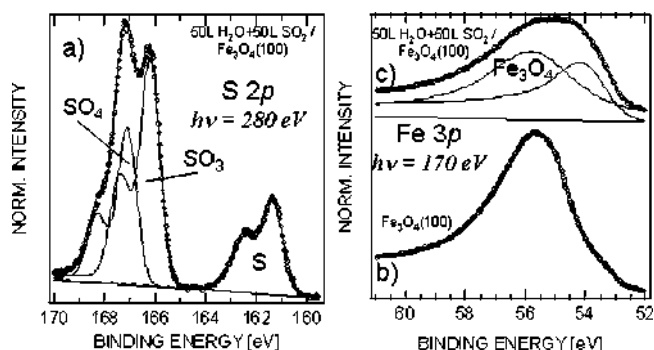


FIG. 1. (a) S 2$p$ and [(b) and (c)] Fe 3$p$ core-level spectra of 50 L H$_2$O and 50 L SO$_2$ covered [(a) and (c)] and clean (b) Fe$_3$O$_4$(100) taken at normal emission at RT.

a)Electronic mail: stoltz@physics.leidenuniv.nl
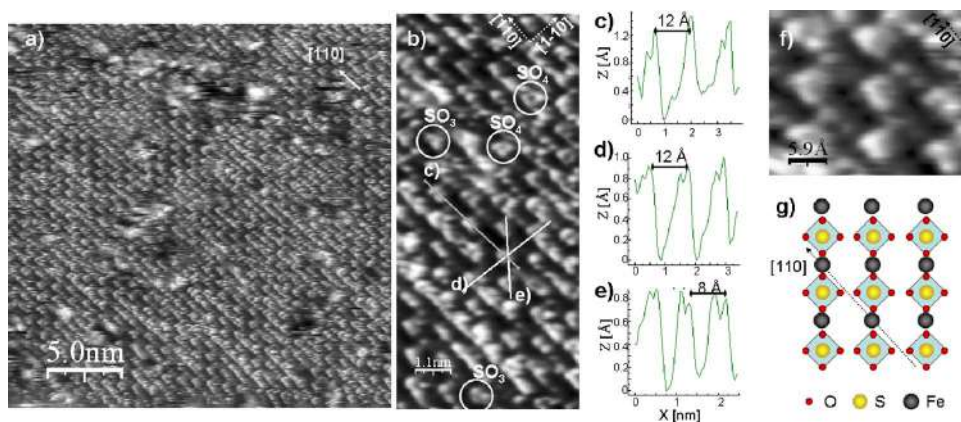
FIG. 2. [(a), (b), and (f)] STM image of a $Fe_3O_4(100)$ surface covered with 50 L $H_2O$ and 50 L $SO_2$, measured with a bias voltage of 1 V and a tunneling current of 0.2 nA at RT. [(c), (d), and (e)] Line profiles taken along indicated lines in (b). (g) Crystal structure of $FeSO_4$.

as a rough estimate. Nevertheless, it shows enhancement of a component closest to the $Fe^{2+}$ oxidation state.[17]

Figure 2(a) shows a $25 \times 25$ nm$^2$ area on a single $Fe_3O_4(100)$ terrace subject to 50 L of water and 50 L of sulfur dioxide. The surface is clearly ordered and the square-formed protrusions are constituting a rectangular network over the substrate. If we zoom in Fig. 2(a) and smoothen the image, we obtain the topographic map presented in Fig. 2(b). Both $SO_3$ and $SO_4$ are marked in the figure. $SO_3$ consists of three O atoms around a single S atom in trigonal planar configuration. $SO_4$ consists of four O atoms at the edges of an imaginary square: in a planar or in a tetrahedral arrangement. The S atom is either not visible in the tunneling conditions of Fig. 2 or situated underneath the oxygen atoms, as the STM images reveal intensity depletion in the centrum of the oxygen arrangement. Inspection of Fig. 2(a) reveals that the overlayer network predominantly consists of $SO_4$. $SO_3$ is sometimes found on $SO_4$ positions, substituting them in the sulfate network by borrowing one oxygen atom from the surface.

Line profiles shown in Figs. 2(c)–2(e) are typical for the overlayer network shown in Fig. 2(a). Line profiles shown in Figs. 2(c) and 2(d), taken along the [110] and [1$\bar{1}$0] directions, show that the $SO_4$ group repeats itself with a periodicity of 12 Å along these directions. At the same time, at 45° to them, the line profile in Fig. 2(e) shows a periodicity of 8 Å. These periodicities are the ones of the $(\sqrt{2} \times \sqrt{2})R45°$ reconstruction of the clean $Fe_3O_4(100)$ surface.[18–20] From these line profiles, we can also determine bond length between S and O in the $SO_4$ group. We get a value between 1.25 and 1.5 Å in the horizontal plane, which compares well with the observed[21] 1.49 Å in a tetrahedral anion.

Finally, a known crystal structure of bulk ferrous sulfate ($FeSO_4$) is presented in Fig. 2(g) and compared to the structure observed on our surface [Fig. 2(f)]. Between each two $SO_4$ groups, two atoms are visible in the [110] direction at a 3 Å separation. As positive bias values are used, we assume that these atoms are iron atoms from the substrate. One of them always appears higher than the other one [more intense in Fig. 2(f)]. As we are tunneling from the occupied states where the density of states of the $Fe^{2+}$ ions is larger than the one of the $Fe^{3+}$ ions,[20] the more intense Fe atoms in Fig. 2(f) should have 2+-oxidation state. As they are also participating in the sulfate adlayer, their z positions could be further modified. It is clear that the bonding of Fe to $SO_4$ group is a bit different than schematically shown in Fig. 2(g) due to bonding of Fe within the $Fe_3O_4$ crystal lattice. The adsorbate

structure observed here is very different from the possible $FeSO_3$ crystal structure.[22]

Slow oxidation of sulfur dioxide in water could proceed via a direct reaction,[1]

$$SO_2 + H_2O + \frac{1}{2}O_2 \rightarrow H_2SO_4, \tag{1}$$

where oxygen comes from the oxide surface. The $Fe^{3+}$-containing surface of $Fe_3O_4(100)$ would in that case act as a catalyst,[1] speeding up the reaction so that the reaction product, ferrous sulfate, is present at the surface after the deposition. Iron oxide surface already contains $Fe^{2+}$ and/or $Fe^{3+}$ ions. Therefore, formation of sulfate ions and finally ferrous sulfate is possible even without any promoters.[23] Noticing that iron in magnetite is already in its high oxidation states leads to another conclusion as well: there is no (further) oxidation/corrosion of the substrate, even though there is formation of $SO_4^{2-}$ ions and, consequently, a sulfate layer at the surface.

As regularly distributed $Fe^{3+}$ ions at the surface are governing the chemical reaction, the reaction product (ferrous sulfate) is also homogeneously and regularly distributed at the surface. As for another S-related species, $SO_3$, which is using photoemission detected in even higher abundance than $SO_4$, it should be noticed that it is a decomposition product of $SO_2$ at most surfaces at room temperature.[15,24–26] Its distribution is thus not bound to the long-range order of the substrate and it could be placed on those parts of the surface where long-range order of the sulfate is broken.

After deposition of water and sulfur dioxide on the surface of $Fe_3O_4(100)$, we still have a $(\sqrt{2} \times \sqrt{2})R45°$ LEED pattern. It is known that this reconstruction of the polar surface is characterized by enhanced stability.[27] In our case, an octahedral plane of the magnetite surface has been exposed to a chemically aggressive environment. Nevertheless, strongly oxidizing $SO_4^{2-}$ species in our experiment are trapped by the periodic surface stress or charge distribution of the $(\sqrt{2} \times \sqrt{2})R45°$ reconstruction. They bind to the substrate forming a $FeSO_4$ layer and the periodic potential of the $(\sqrt{2} \times \sqrt{2})R45°$ reconstruction stabilizes the ferrous oxide structure.

If the oxygen vacancy model[18,19] of the surface is assumed, $SO_4^{2-}$ species are being trapped in the periodic potential induced by the vacancy array. Oxygen vacancies on the $(\sqrt{2} \times \sqrt{2})R45°$-reconstructed $Fe_3O_4(100)$ surface are electron poor (virtual positive charge of +2) and should therefore

clearly be preferred by the $SO_4^{2-}$ species. On the other hand, if charge ordering on the surface[20] is invoked to explain the $(\sqrt{2} \times \sqrt{2})R45°$ reconstruction on the clean surface of $Fe_3O_4(100)$, the adsorption of $SO_3^{2-}$ species would be assumed in the vicinity of catalytic $Fe^{3+}$ dimers, whereas bonding of $SO_4^{2-}$ into sulfate could proceed via $Fe^{2+}$ in the similar fashion as it would in the oxygen vacancy model.

We have presented a combined high-resolution core-level PES and atomically resolved the STM study of a magnetite (100) surface under conditions of simplified initial atmospheric corrosion. We have found that $SO_3$ and $SO_4$ are present at the surface, but that $SO_4$ binds to the substrate to form ferrous sulfate. Ordering of the sulfate at the surface follows the $(\sqrt{2} \times \sqrt{2})R45°$ reconstruction of the polar magnetite surface, demonstrating extreme stability of this reconstruction even upon adsorption of chemically reactive species. Suitability of $Fe_3O_4(100)$ for corrosion protection is demonstrated through the reduction of the Fe-oxidation state upon exposure to water and sulphur dioxide.

[1] C. Leygraf, *Corrosion Mechanisms in Theory and Practice* (Dekker, New York, 2002), Chapter 15, pp. 529–532.

[2] G. J. Edens, X. Gao, and M. Weaer, J. Electroanal. Chem. **375**, 357 (1994).

[3] M. Wilms, P. Broekmann, C. Stuhlmann, and K. Wandelt, Surf. Sci. **416**, 121 (1998).

[4] A. M. Funtikov, U. Linke, U. Stimming, and R. Vogel, Surf. Sci. **324**, L343 (1995).

[5] L.-J. Wan, T. Suzuki, K. Sashikata, J. Okada, J. Inukai, and K. Itaya, J. Electroanal. Chem. **484**, 189 (2000).

[6] L.-J. Wan, S.-L. Jau, and K. Itaya, J. Phys. Chem. **99**, 9507 (1995).

[7] P.-C. Lu, C.-H. Yang, S.-L. Yau, and M.-S. Zei, Langmuir **18**, 754 (2002).

[8] L.-J. Wan, M. Hara, J. Inukai, and K. Itaya, J. Phys. Chem. B **544**, 93 (1999).

[9] M. Schweizer and D. Kolb, Surf. Sci. **544**, 93 (2003).

[10] M. Kleinert, A. Cuesta, L. Kibler, and D. Kolb, Surf. Sci. **430**, L521 (1999).

[11] C. M. Eggleston, S. Hug, W. Stumm, B. Sulzberger, and M. D. S. Afonso, Geochim. Cosmochim. Acta **62**, 585 (1998).

[12] D. L. Adams, FITXPS2 peak-fitting software (www.sljus.lu.se/download.html).

[13] Nanotec Electronica S. L., WSXM 3.0, 2006 (www.nanotec.es).

[14] K. Jordan, G. Mariotto, S. F. Ceballos, S. Murphy, and I. V. Shvets, J. Magn. Magn. Mater. **290**, 1029 (2005).

[15] J. A. Rodriguez, T. Jirsak, S. Chaturvedi, and M. Kuhn, Surf. Sci. **442**, 400 (1999).

[16] G. Rossi, F. Sirotti, N. Cherepkov, F. C. Farnoux, and G. Panaccione, Solid State Commun. **90**, 557 (1994).

[17] B. Sinković, P. D. Johnson, N. B. Brookes, A. Clarke, and N. V. Smith, Phys. Rev. Lett. **65**, 1647 (1990).

[18] F. C. Voogt, T. Fujii, P. J. M. Smulders, L. Niesen, M. A. James, and T. Hibma, Phys. Rev. B **60**, 11193 (1999).

[19] B. Stanka, W. Hebenstreit, U. Diebold, and S. A. Chambers, Surf. Sci. **448**, 49 (2000).

[20] G. Mariotto, S. Murphy, and I. V. Shvets, Phys. Rev. B **66**, 245426 (2002).

[21] D. W. J. Cruickshank, J. Chem. Soc. **1961**, 5486.

[22] G. Bugli and D. Carré, Acta Crystallogr., Sect. B: Struct. Sci. **36**, 1297 (1980).

[23] J. Weissenrieder, C. Kleber, M. Schreiner, and C. Leygraf, J. Electrochem. Soc. **151**, B497 (2004).

[24] H. Lu, E. Janin, M. E. Dávila, C. M. Pradier, and M. Göthelid, Vacuum **49**, 171 (1998).

[25] G. J. Jackson, S. M. Driver, D. P. Woodruff, N. Abrams, R. G. Jones, M. T. Butterfield, M. D. Crapper, B. C. C. Cowie, and V. Formoso, Surf. Sci. **459**, 231 (2000).

[26] J. A. Rodriguez, T. Jirsak, S. Chaturvedi, and J. Dvorak, J. Mol. Catal. A: Chem. **167**, 47 (2001).

[27] K. Jordan, S. Murphy, and I. V. Shvets, Surf. Sci. **600**, 5150 (2006).

# The role of steps in surface catalysis and reaction oscillations

Bas L. M. Hendriksen[1], Marcelo D. Ackermann[1,2], Richard van Rijn[1,2], Dunja Stoltz[1], Ioana Popa[2], Olivier Balmes[2], Andrea Resta[2], Didier Wermeille[2], Roberto Felici[2], Salvador Ferrer[2†] and Joost W. M. Frenken[1]*

**Atomic steps at the surface of a catalyst play an important role in heterogeneous catalysis, for example as special sites with increased catalytic activity. Exposure to reactants can cause entirely new structures to form at the catalyst surface, and these may dramatically influence the reaction by 'poisoning' it or by acting as the catalytically active phase. For example, thin metal oxide films have been identified as highly active structures that form spontaneously on metal surfaces during the catalytic oxidation of carbon monoxide. Here, we present _operando_ X-ray diffraction experiments on a palladium surface during this reaction. They reveal that a high density of steps strongly alters the stability of the thin, catalytically active palladium oxide film. We show that stabilization of the metal, caused by the steps and consequent destabilization of the oxide, is at the heart of the well-known reaction rate oscillations exhibited during CO oxidation at atmospheric pressure.**

Atomic steps on catalyst surfaces are often considered to be special, active sites for heterogeneous catalytic reactions[1]. They enable enhanced binding of reactant molecules[2–4] and exhibit enhanced activity for bond breaking[5–8] as a result of their reduced coordination. Catalytic nanoparticles contain a high density of steps and the steps may dominate their activity. Steps also play a key role in many other surface processes, for example as natural locations for crystal growth and erosion and as a source for mobile surface adatoms. Here, we show that steps on surfaces may play a role in catalysis not only by serving as active sites, but also by changing the stability of the catalytically active phase.

Recent experiments and theory suggest that oxides form on the surface of precious metal catalysts such as Ru, Pt, Pd and Rh during catalytic oxidation at atmospheric pressure while under oxygen-rich conditions[9–13]. Experiments performed under these conditions using _operando_ techniques, which simultaneously provide information on the state of the catalyst and on the reaction kinetics, indicate that these oxides are catalytically more active than the bare metal surfaces[10,11], although this is still subject to debate[14]. Such oxides form because at high oxygen pressures it is thermodynamically more favourable to incorporate oxygen atoms into the surface, thus creating oxygen-rich phases (oxides), than to form the low-coverage chemisorption structures typical for low oxygen pressures.

Whether a catalyst surface operating in an oxidizing mixture of reactants prefers a mere chemisorption structure or an oxide[13,15] depends upon the partial pressures of the reactants. The transition of the catalyst surface from the metal phase to the oxide phase dramatically changes the catalytic reaction mechanism. Whereas on the metal surface both reactants first adsorb and then react to form the product (the Langmuir–Hinshelwood mechanism), the more active oxidized surface serves as an intermediate product from which oxygen atoms are easily extracted by the other reactant (for example CO), after which the resulting oxygen vacancies are refilled with oxygen from the gas phase. This is similar to the Mars–Van Krevelen mechanism, in which gas molecules react with lattice oxygen from the metal oxide to form the product, and the redox process is completed by oxygen that diffuses through the oxide to fill up the oxygen vacancies caused by the reaction[16].

Previously, we have found that oscillations can occur in the reaction rate during CO oxidation under conditions under which both the oxide and metal phase can exist[17,18]. Spontaneous and self-sustained oscillations in the rate of CO oxidation have been extensively studied both at low pressures (for example, $1 \times 10^{-6}$ mbar) and at atmospheric pressure[19,20]. The low-pressure oscillations are due to atomic-scale restructuring of the surface of the catalyst (for example, Pt or Pd) or the formation of a subsurface oxygen layer, as was shown in the work of Ertl and colleagues[19]. In contrast, our earlier _in situ_ scanning tunnelling microscopy studies show that at atmospheric pressure the oscillations in the reaction rate are due to the spontaneous, periodic switching from a low-activity metal surface to a high-activity oxide surface[19,20]. In this Article we show that the density of steps on the catalyst surface (the 'roughness') can influence the stability of the metal and oxide phases. This has important implications for reactivity and, as shown, it is therefore the steps that regulate the self-sustained oscillations during CO oxidation on Pd(001) at atmospheric pressure.

## Results

Figure 1 shows that the rate of $CO_2$ production and CO pressure inside a flow reactor spontaneously oscillated under steady-state conditions with a constant feed of CO and $O_2$. The CO pressure oscillated in anti-phase with the $CO_2$ pressure as a result of variations in CO consumption in the reaction, which for a high rate is mass transfer limited[19]. Figure 1a presents surface X-ray diffraction (SXRD) data for the $(h,k,l) = (1,0,2)$ diffraction peak of Pd(001) during oscillating CO oxidation in a 17-ml flow cell, at 447 K and $P_{CO} = 25$ mbar and $P_{O_2} = 500$ mbar. (Details of the experiment

---

[1]Kamerlingh Onnes Laboratory, Leiden University, PO Box 9504, 2300 RA Leiden, The Netherlands, [2]European Synchrotron Radiation Facility, 6 rue Jules Horowitz, F-38043 Grenoble cedex, France; †Present address: CELLS – ALBA, Edifici Ciències Nord. Mòdul C-3 centra, Campus Universitari de Bellaterra, Universita Autònoma de Barcelona, 08193 Bellaterra, Spain. *e-mail: frenken@physics.leidenuniv.nl
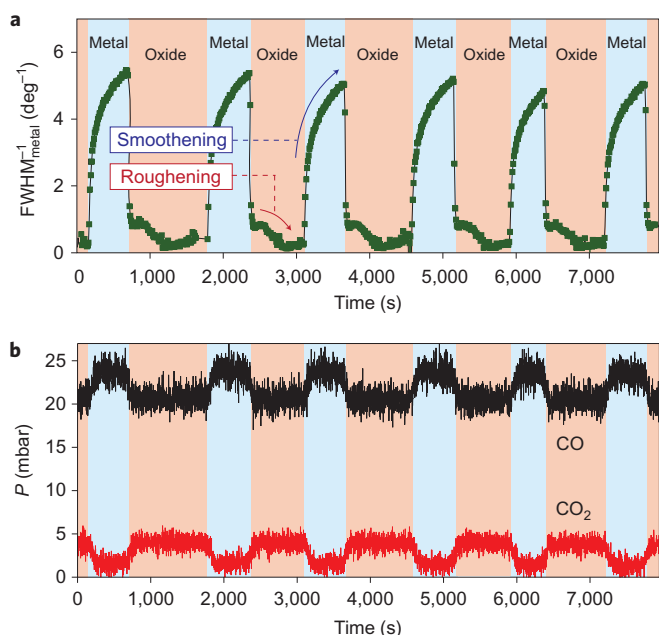
**Figure 1 | Spontaneous oscillations in the CO oxidation rate on Pd(001) as measured by SXRD and mass spectrometry.** Measurements were performed at a temperature of 447 K in a constant flow of a mixture of $CO/O_2/Ar$ gas with an oxygen pressure of 500 mbar, an argon pressure of 675 mbar and a CO pressure of 25 mbar flowing at 50 ml$_n$ min$^{-1}$. **a**, FHWM$_{metal}^{-1}$ (inversely proportional to the step density and a measure of the smoothness of the surface) of the diffraction peak at $(h,k,l) = (1,0,2)$. **b**, Partial pressure in the reactor of CO and $CO_2$ pressures as measured by mass spectrometry. At high CO partial pressures $P_{CO}$, the diffraction pattern shows that the surface structure is close to a bulk-like truncation of the Pd crystal (the reaction kinetics indicate that this metal surface is covered by a mixture of O atoms and CO molecules). At low $P_{CO}$, new diffraction peaks are found that correspond to a thin PdO(001) layer (for example, $(h,k,l) = (0.8,0.4,0.73)$; see Supplementary Fig. S1). The colours indicate whether the SXRD intensities identify the Pd(001) surface to have a metal structure (light blue) or to be covered by a thin oxide film (light red).

are provided in the Methods and the Supplementary Information, and the oscillatory variations in the SXRD signals and the partial pressures of the reactant and product gases may be observed in Supplementary Movies S1 and S2.)

In the low-reaction-rate phase ($P_{CO_2} = 2$ mbar) the $(h,k,l) = (1,0,2)$ diffraction peak had a high intensity, indicating that the surface was metallic. The inverse value of the full width of the diffraction peak at half maximum intensity, FWHM$_{metal}^{-1}$, increased with time during this part of each oscillation. In the metal phase, FWHM$_{metal}^{-1}$ is a direct measure of the smoothness of the surfaces in terms of the average terrace width or, equivalently, the inverse of the step density[21]. The increase in FWHM$_{metal}^{-1}$ therefore indicates that the surface became smoother through reductions in the step density until transition to the high-reaction-rate state occurred ($P_{CO_2} = 4.5$ mbar). At this stage the Pd(001) (1,0,2) diffraction peak has practically disappeared.

After the transition we observed a new diffraction peak at $(h,k,l) = (0.8,0.4,0.73)$ (Supplementary Fig. S1, Movie S2), which we have determined to correspond to the presence of a $1.9 \pm 0.5$-nm-thick PdO(001) film, similar to what has been found for Pd(001) in pure oxygen[22]. Additional, high-speed SXRD measurements revealed that this oxidation began with the abrupt appearance of an ultrathin surface oxide with well-known $\sqrt{5} \times \sqrt{5}$ periodicity[22], which was replaced (typically after 5 s) by the epitaxial, bulk-like PdO film. The diffracted PdO intensity increased over a

period of ~7 s, which probably indicates lateral closing of the bulk-like PdO layer.

After this ~7-s period, the oxide layer thickness exhibits a power-law growth ($L \propto t^p$) with an exponent of $p = 0.28$ (ref. 23). The transition to the high reaction rate coincided with the introduction of the $\sqrt{5} \times \sqrt{5}$ structure and remained unchanged as the PdO film formed. In the oxide phase the FWHM$_{metal}^{-1}$ of the weak diffraction peak that remained at (1,0,2) is a measure of the smoothness of the interface between the metal Pd(001) substrate and the PdO(001) film covering it. The fact that the FWHM$_{metal}^{-1}$ decreased with time shows that the interface became rougher. The evolution of the PdO(001) $(h,k,l) = (0.8,0.4,0.73)$ diffraction peak (that is, FWHM$_{oxide}^{-1}$) is shown in Supplementary Fig. S1 and Movie S2.

The observation from SXRD data of an increase in roughness of the oxide phase and the opposite behaviour in the metal phase is consistent with our high-pressure scanning tunnelling microscopy observations[17] (see Supplementary Information). Our interpretation is that during the Mars–Van Krevelen redox reaction a small fraction of the metal atoms in the oxide become sufficiently undercoordinated with oxygen to become mobile and diffuse out of their original positions until they are re-oxidized and immobilized on top of the oxide[9,10]. The lack of mobility of the oxide at the low operation temperature prevents the resulting roughness from decaying before further roughness is added by the same process. As a result, roughness gradually accumulates, approximately linearly with the total amount of generated $CO_2$. In the metallic phase, high surface mobility is observed and the reaction does not cause further increases in surface roughness, which therefore decays with time.

When we consider the timescales of the stages of an oscillation cycle it can be seen that the metal-to-oxide and oxide-to-metal transitions are practically 'instantaneous'. The ultrathin surface oxide appears within ~2 s and the PdO disappears exponentially with a typical timescale of ~6 s. However, the changes in roughness of
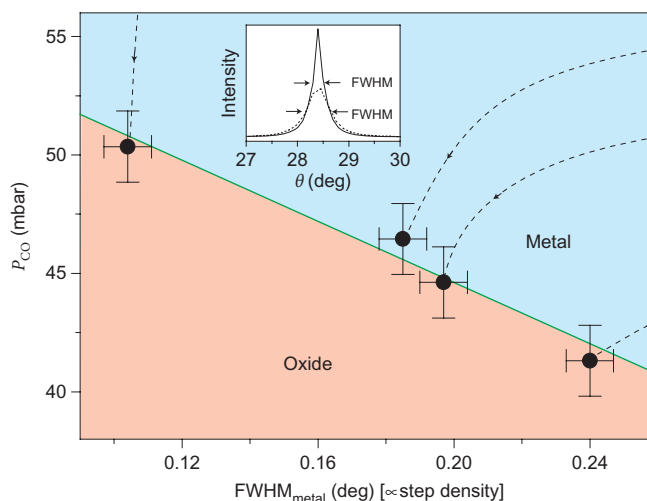


**Figure 2 | Stability diagram of the Pd(001) surface measured with SXRD.** Measurements were performed at a temperature of 460 K in a $CO/O_2$ gas mixture with a fixed oxygen partial pressure of $P_{O_2} = 0.48$ bar in a batch reactor. The parameter along the horizontal axis of the main figure is the FWHM$_{metal}$ of the diffraction peak on the metal surface with reciprocal coordinates $(h,k,l) = (1,0,0.2)$ immediately prior to the metal-to-oxide transition. This peak width is a sensitive measure of the density of steps on the metal surface. The trajectories of (FWHM$_{metal}$,$P_{CO}$) approaching the metal-to-oxide transition are indicated by the four dashed curves. The error margins reflect the maximum variations observed in the peak width and the CO pressure at the transition. The inset shows two diffraction peaks on a trajectory at different FWHM$_{metal}$.

both the metal and the oxide are slower processes. We therefore propose that variation in the roughness, that is the step density, induces both transitions and thereby regulates the oscillations to have periods on the order of 1,000 s.

To prove that the surface roughness is indeed responsible for inducing the phase transition we performed separate SXRD experiments in a 2-litre batch reactor that we pre-filled each time with
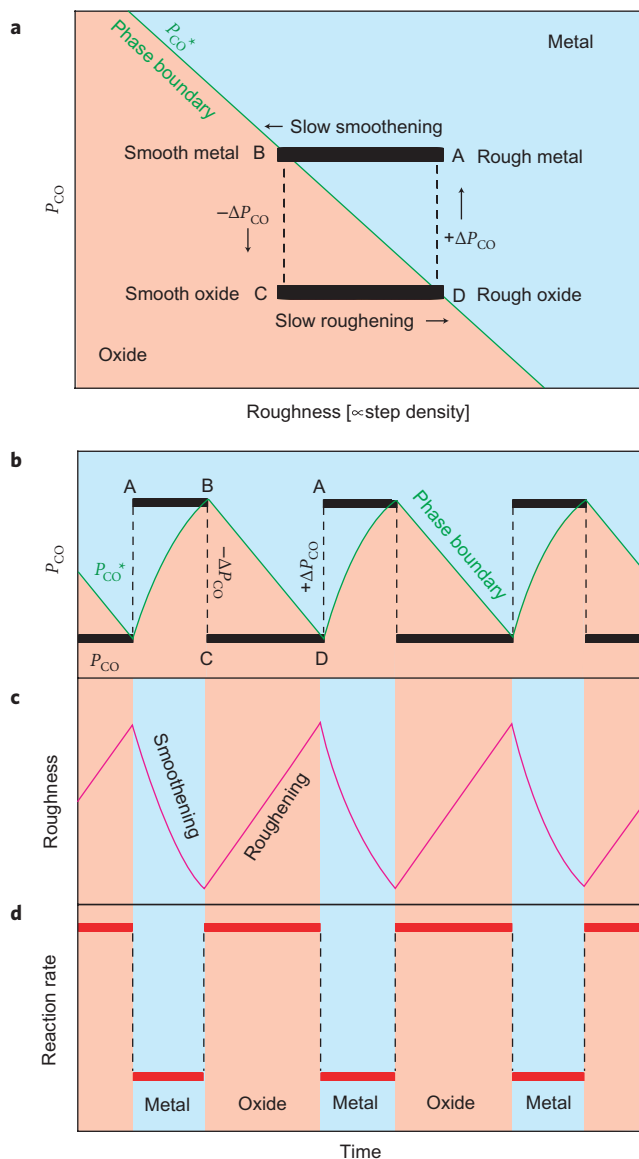


**Figure 3 | Generic model for the reaction rate oscillations.** Each cycle takes the surface through stages (**A**) rough metal, (**B**) smooth metal, (**C**) smooth oxide and (**D**) rough oxide, after which the next cycle starts again at (**A**). **a**, Metal-to-oxide stability diagram (cf. Fig. 2), in which the phase boundary is determined by the roughness and the CO partial pressure $P_{CO}^*$. For each cycle the surface crosses this boundary twice (at **B** and at **D**). **b–d**, Variations in roughness, $P_{CO}$, and reaction rate ($P_{CO_2}$) over three complete cycles. In the oxide phase, the surface becomes progressively rougher, whereas it becomes smoother in the metal phase (**b**). As can be read from **a**, these variations in roughness introduce corresponding variations in the $P_{CO}^*$ value of the metal-to-oxide transition, which are indicated by the green line in **b**. At points **B** and **D** in the cycle, this critical $P_{CO}^*$ value becomes equal to the actual CO pressure $P_{CO}$ (black lines in **b**) and the phase transition takes place. Because the reaction rate on the oxide is higher than that on the metal (**d**), the CO pressure in the reactor switches up or down by $\Delta P_{CO}$ every time the surface is reduced or oxidized (black lines in **b**).

a specific mixture of oxygen and CO. This mode of operation does not lead to spontaneous self-sustained oscillations, enabling us to separate the cause and effect of the oscillations. These experiments allow us to derive the stability diagram shown in Fig. 2, which shows the minimum partial pressure of CO at which the metal is stable against oxidation as a function of surface roughness, $FWHM_{metal}$. To use the roughness of the metal surface as a control parameter, we 'prepared' the surface in each experiment by keeping it in the metal phase for a different period of time (more time results in a smoother surface; lower $FWHM_{metal}$). In practice, this was done by starting each batch experiment at a different partial pressure of CO, at a fixed initial $O_2$ pressure. The details of this procedure are given in the Supplementary Information.

In each experiment, the two reactants were slowly converted to $CO_2$, thereby reducing the ratio between $P_{CO}$ and $P_{O_2}$. During this stage, the initially rough metal surface slowly became smoother, indicated by the decreasing FWHM of the (1,0,0.2) diffraction peak, which is nearly equivalent to the (1,0,2) peak of Fig. 1. The decrease in roughness continued until the metal-to-oxide transition took place, which was accompanied by a tenfold increase in the $CO_2$ production rate and the appearance of the diffraction peak at (0.8,0.4,0.73) of the PdO(001) film. We performed this procedure four times, each time for a different initial value of $P_{CO}$. This resulted in the four curves of $P_{CO}$ versus $FWHM_{metal}$ in Fig. 2. The lowest CO pressure in each curve, $P_{CO}^*$, indicates the conditions at which the metal-to-oxide transition took place. Figure 2 fully confirms our suspicion that roughness has a dramatic influence on the stability of the metal with respect to oxidation. The critical CO pressure $P_{CO}^*$ shows a one-to-one correspondence with the step density. A significantly more oxidizing $CO/O_2$ mixture is required to oxidize a rough surface than a smooth surface. From a kinetic point of view this is unexpected, because steps actually facilitate oxidation[24]; however, we argue below that it is in fact a thermodynamic effect.

## Discussion

Thermodynamically, the first-order metal-to-oxide transition of a smooth, step-free surface takes place when the free energies of the two competing structures, namely the metal surface with a chemisorbed layer of reactants and the oxide surface, are equal. The presence of steps shifts this balance, because steps on both phases cost different amounts of (free) energy. This shift can go either way, but there are two arguments why steps could work in favour of the metal phase and make it stable down to a lower CO pressure ($P_{CO}^*$). First, on many metal surfaces CO molecules adsorb significantly more strongly at steps than on terraces[2–4]. For a metal surface in contact with CO, this reduces the effective step free energy and, under special circumstances, can even lead to the spontaneous formation of steps[25]. We anticipate that this enhanced bonding effect is stronger for CO molecules than for O atoms adsorbed at steps on Pd(001) (ref. 26). We propose that this reduction in the effective step free energy by CO adsorption stabilizes a rough metal phase with respect to a rough oxide phase. Second, steps make the metal surface a bad template for the PdO(001) structure, because they necessarily lead to dislocations in the oxide. The effect of the step density on the metal-to-oxide transition is reminiscent of the role of steps in the phase transition from the $7 \times 7$ surface reconstruction to the $1 \times 1$ phase on Si(111), for which the transition temperature depends on step density[27].

The combination of all the experimental observations leads to a simple scenario for the self-sustained reaction oscillations (Fig. 3). Each cycle (**A**) $\rightarrow$ (**B**) $\rightarrow$ (**C**) $\rightarrow$ (**D**) $\rightarrow$ (**A**) contains the following four stages.

(1) (**A**) $\rightarrow$ (**B**) comprises a decrease in metal surface roughness. The cycle starts with a rough metal surface. The reaction follows the

Langmuir–Hinshelwood (gas adsorption and reaction) mechanism, resulting in a low reaction rate $R_{metal}$. In the metal phase the surface becomes smoother, shifting the conditions towards the metal-to-oxide phase transition ($P_{CO}^*$ increasing towards $P_{CO}$).

(2) (**B**) → (**C**) represents the metal-to-oxide transition. When the step density decreases enough and $P_{CO}^* = P_{CO}$, then the surface oxidizes. The reaction changes abruptly to the Mars–van Krevelen (oxide reduction and re-oxidation) mechanism with the high reaction rate $R_{oxide}$. Now that more CO is being consumed, $P_{CO}$ is reduced in the vicinity of the active surface by an amount $\Delta P_{CO}$, which further stabilizes the oxide. Note that in this description we do not distinguish between the observed oxide structures ($\sqrt{5} \times \sqrt{5}$ and PdO), as the reaction rate is equally high for both of them.

(3) (**C**) → (**D**) comprises an increase in oxide roughness. The Mars–van Krevelen reaction mechanism leads to a slow build-up of surface roughness. This, in turn, reduces $P_{CO}^*$ towards $P_{CO}$.

(4) (**D**) → (**A**) comprises the oxide-to-metal transition. When the oxide has become sufficiently rough that $P_{CO}^* = P_{CO}$, the system switches back to a (rough) metal surface. The reaction changes abruptly to the Langmuir–Hinshelwood mechanism, reducing the reaction rate to $R_{metal}$, and thus increasing $P_{CO}$ by $\Delta P_{CO}$, further stabilizing the metal phase. This restores the starting conditions and closes the cycle.

The period of the oscillation is determined by the magnitude of $\Delta P_{CO}$ and by the smoothening and roughening rates in the metal and oxide phases.

With the exception of the effect of the oxide roughness on the oxide-to-metal transition, all characteristics of this scenario are based on experimental observations. These characteristics include increasing and decreasing oxide and metal roughness respectively; the dependence of $P_{CO}^*$ on roughness; the different reaction mechanisms and rates; and the resulting changes in local $P_{CO}$.

We have also tested the scenario in a simple numerical calculation, in which we modelled the roughness evolution and the dependence of $P_{CO}^*$ on roughness with first-order differential equations. The results of the calculation, under steady-state conditions, are shown in Fig. 3 (for details of this calculation see Methods and Supplementary Information). Although the model is too crude to faithfully describe all details of the CO oxidation reaction on Pd(001), it fully captures the essence of the observed oscillations, such as the influence of $P_{CO}$ on the oscillation period and on the ratio between the metal and oxide parts of the oscillations.

Our observations and interpretation of the reaction oscillations are in disagreement with existing models for reaction oscillations during CO oxidation on Pt-group metals. We observed that the system oscillates between a metal surface with O and CO chemisorbed (low reaction rate) and the thin oxide layer (high reaction rate). The periodic transition between the metal and the oxide is caused by the formation and decay of roughness (steps). In contrast, at low pressures ($<1 \times 10^{-6}$ mbar), oscillations are caused by variations in the concentration of the chemisorbed reactants, periodically switching between two stable sates of Langmuir–Hinshelwood kinetics: a chemisorbed O-dominated (high reaction rate) and a CO-dominated metal surface (low reaction rate), coupled to adsorbate-induced restructuring of the metal surface or the insertion of subsurface oxygen species[19]. At atmospheric pressures—the regime discussed here—oxides play a role and, according to the widely accepted model proposed by Sales and colleagues, the switching between the chemisorbed O-dominated (high reaction rate) and CO-dominated (low reaction rate) metal surface is caused by the slow formation of a catalytically inactive oxide[20,28].

Based on our model and simple diffusion and reaction-rate considerations, we predict that the oscillation period should be a strong function of temperature, with higher temperatures leading to much shorter periods. Vicinal surfaces, which have high step densities by themselves, are expected to oxidize at lower CO pressures compared to low-index surfaces. In addition, the period of the metal phase of an oscillation cycle on a vicinal surface should be short, because the length over which atoms have to move to restore the initial (high) step density is short. Another important element is hidden in the design of the reactor and, in particular, in the flow resistance of the gas line between the CO pressure regulator and the reactor, because this resistance determines the strength $\Delta P_{CO}$ of the pressure variations. This quantity dictates how wide or narrow the window of pressures $P_{CO}$ is in which the system will exhibit spontaneous reaction oscillations, and also has a direct influence on the oscillation period. This aspect may be responsible for the large variation in oscillation behaviour found for the same reaction systems between different instruments or different research groups[20].

Our scenario presents a new mechanism for oscillatory oxidation reactions at atmospheric pressure. It is not specific for Pd(001); we have observed similar oscillations in CO oxidation on several other Pd and Pt surfaces (to be reported in future articles). Equivalent oscillation mechanisms, again involving the role of steps, may be at play in other catalytic reaction systems, including other oxidation reactions or reactions involving the formation of other surface species such as carbides, sulfides or nitrides.

The new role identified here for roughness in heterogeneous catalysis may serve as a specific target for future catalyst design, for example new structural promoters that inhibit the formation of steps or enhance surface mobility and thus increase the decay rate of the roughness.

## Methods

The SXRD experiments were performed at the ID03 beamline of the European Synchrotron Radiation Facility (ESRF) in two separate ultrahigh-vacuum, high-pressure set-ups. One was operated as a batch reactor with a volume of ~2 l, and the other contained a 17-ml flow reactor. Both reactors were equipped with beryllium windows to allow entry and exit of the X-rays. We used a focused beam of monochromatic, 17- or 20-keV X-rays, impinging on the surface at a grazing angle of typically 1°. All instruments were equipped with a gas manifold with pressure regulators and flow controllers with which the pressure, composition and flow rate of high-purity mixtures of $O_2$ and CO could be prepared. A quadrupole mass spectrometer was used for online analysis of gas composition in the reactor. In all experiments a mechanically polished, (001)-oriented Pd crystal was used that was prepared *in situ*, under ultrahigh-vacuum conditions. In each set-up, the temperature of the Pd was measured with a thermocouple and regulated to within $\Delta T = 2$ K. In the batch reactor only, the exothermic reaction led to a temperature increase higher than this when the surface switched from metal to oxide, but all measurements combined in Fig. 2 were taken in the metal phase and were not affected by this.

In the numerical model used to calculate the graphs shown in Fig. 3, each of the two phases of the surface, metal and oxide, was characterized by two rates, the reaction rate of CO oxidation and the rate of change of surface roughness (see Supplementary Information). The condition for the surface to be either in the oxide or the metal phase was $P_{CO} < P_{CO}^*(\rho)$ for the oxide and $P_{CO} > P_{CO}^*(\rho)$ for the metal, with $P_{CO}$ being the CO pressure in the reactor near the surface and $P_{CO}^*(\rho)$ the critical CO pressure at which the transition takes place, which depends on the roughness $\rho$ as $P_{CO}^*(\rho) = P_{CO}^*(0) - d\rho$. $P_{CO}^*(0)$ is the critical CO pressure for zero roughness, $d$ is a positive constant and the normalized roughness is $0 \le \rho < 1$. In the model the roughness increases in the oxide phase, proportional to the reaction rate. In the metal phase the roughness decays exponentially with time.

## References

1. Taylor, H. S. A theory of the catalytic surface. *Proc. R. Soc. Lond. A* **108,** 105–111 (1925).
2. Yates, J. T. Surface chemistry at metallic defect sites. *J. Vac. Sci. Technol. A* **13,** 1359–1367 (1995).
3. Hammer, B., Nielsen, O. H. & Nørskov, J. K. Structure sensitivity in adsorption: CO interaction with stepped and reconstructed Pt surfaces. *Catal. Lett.* **46,** 31–35 (1997).
4. Somorjai, G. A. *Introduction to Surface Chemistry and Catalysis* (Wiley, 1994).
5. Zambelli, T., Wintterlin, J., Trost, J. & Ertl, G. Identification of the 'active sites' of a surface-catalyzed reaction. *Science* **273,** 1688–1690 (1996).

6. Dahl, S. *et al.* Role of steps in N$_2$ activation on Ru(0001). *Phys. Rev. Lett.* **83,** 1814–1817 (1999).
7. Geerlings, J. J. C. *et al.* Fischer–Tropsch technology—from active site to commercial process. *Appl. Catal. A* **186,** 27–40 (1999).
8. Vang, R. T. *et al.* Controlling the catalytic bond-breaking selectivity of Ni surfaces by step blocking. *Nature Mater.* **4,** 160–162 (2005).
9. Over, H. *et al.* Atomic scale structure and catalytic reactivity of the RuO$_2$(110) surface. *Science* **287,** 1474–1476 (2000).
10. Hendriksen, B. L. M. & Frenken, J. W. M. CO oxidation on Pt(110): scanning tunneling microscopy inside a flow reactor. *Phys. Rev. Lett.* **89,** 046101 (2002).
11. Ackermann, M. D. *et al.* Structure and reactivity of surface oxides on Pt(110) during catalytic CO oxidation. *Phys. Rev. Lett.* **95,** 255505 (2005).
12. Lundgren, E. *et al.* Kinetic hindrance during the initial oxidation of Pd(100) at ambient pressures. *Phys. Rev. Lett.* **92,** 046101 (2004).
13. Reuter, K. & Scheffler, M. First-principles atomistic thermodynamics for oxidation catalysis: surface phase diagrams and catalytically interesting regions. *Phys. Rev. Lett.* **90,** 046103 (2003).
14. Gao, F., Wang, Y., Cai, Y. & Goodman D. W. CO oxidation on Pt-group metals from ultrahigh vacuum to near atmospheric pressures. 2. Palladium and platinum. *J. Phys. Chem. C* **113,** 174–181 (2009).
15. Rogal, J., Reuter, K. & Scheffler, M. CO oxidation at Pd(100): a first-principles constrained thermodynamics study. *Phys. Rev. B* **75,** 205433 (2007).
16. Mars, P. & Van Krevelen, D. W. Oxidation carried out by means of vanadium oxide catalysts. *Spec. Suppl. Chem. Eng. Sci.* **3,** 41–57 (1954).
17. Hendriksen, B. L. M., Bobaru, S. C. & Frenken, J. W. M. Oscillatory CO oxidation on Pd(100) studied with *in situ* scanning tunneling microscopy. *Surf. Sci.* **552,** 229–242 (2004).
18. Hendriksen, B. L. M., Bobaru, S. C. & Frenken, J. W. M. Bistability and oscillations in CO oxidation studied with scanning tunneling microscopy inside a reactor. *Catal. Today* **105,** 234–243 (2005).
19. Imbihl, R. & Ertl, G. Oscillatory kinetics in heterogeneous catalysis. *Chem. Rev.* **95,** 697–733 (1995).
20. Schüth, F., Henry, B. E. & Schmidt, L. D. Oscillatory reactions in heterogeneous catalysis. *Adv. Catal.* **39,** 51–127 (1993).
21. Robinson, I. K. Crystal truncation rods and surface roughness. *Phys. Rev. B* **33,** 3830–3836 (1986).
22. Stierle, A. *et al.* A surface X-ray study of the structure and morphology of the oxidized Pd(001) surface. *J. Chem. Phys.* **122,** 044706 (2005).
23. Wagner, C. The formation of thin oxide films on metals. *Corrosion Sci.* **13,** 23–52 (1973).
24. Klikovits, J. *et al.* Step-orientation-dependent oxidation: from 1D to 2D oxides. *Phys. Rev. Lett.* **101,** 266104 (2008).
25. Thostrup, P. *et al.* Adsorption-induced step formation. *Phys. Rev. Lett.* **87,** 126102 (2001).
26. Zhang, Y., Rogal, J. & Reuter, K. Density-functional theory investigation of oxygen adsorption at Pd(11N) vicinal surfaces (N=3,5,7): influence of neighboring steps. *Phys. Rev. B* **74,** 125414 (2006).
27. Williams, E. D. & Bartelt, N. C. Thermodynamics of surface morphology. *Science* **251,** 393–400 (1991).
28. Sales, B. C., Turner, J. E. & Maple, M. B. Oscillatory oxidation of CO over Pt, Pd and Ir catalysts: theory. *Surf. Sci.* **114,** 381–394 (1982).

## Author contributions
B.L.M.H. and J.W.M.F. conceived the new explanation for the oscillatory reaction and B.L.M.H. developed the corresponding numerical model. M.D.A. and I.P. performed the batch experiments. R.v.R., D.S., O.B., A.R. and D.W. performed the flow experiments. M.D.A., R.v.R. and B.L.M.H. analysed the data. R.F. and S.F. supervised the experiments and J.W.M.F. supervised the project. B.L.M.H., M.D.A., R.v.R. and J.W.M.F. co-wrote the paper. All authors discussed the results and commented on the manuscript.

## Additional information
The authors declare no competing financial interests. Supplementary information accompanies this paper at www.nature.com/naturechemistry. Reprints and permission information is available online at http://npg.nature.com/reprintsandpermissions/. Correspondence and requests for materials should be addressed to J.W.M.F.

# Water Adsorption on ZnO(0001): Transition from Triangular Surface Structures to a Disordered Hydroxyl Terminated phase

## Anneli Önsten,* Dunja Stoltz, Pål Palmgren, Shun Yu, Mats Göthelid, and Ulf O. Karlsson

*Materials Physics, Royal Institute of Technology KTH, Isafjordsgatan 22, S-164 40 Kista, Sweden*

*Received: January 18, 2010; Revised Manuscript Received: April 29, 2010*

We present room temperature scanning tunneling microscopy and photoemission spectroscopy studies of water adsorption on the Zn-terminated ZnO(0001) surface. Data indicates that the initial adsorption is dissociative leaving hydroxyl groups on the surface. At low water coverage, the adsorption occurs next to the oxygen-terminated step edges, where water is believed to bind to zinc cations leaving off hydrogen atoms to under-coordinated oxygen anions. When increasing the water dose, triangular terraces grow in size and pits diminish until the surface is covered with wide irregular terraces and a large number of small pits. Higher water exposure (20 Langmuir) results in a much more irregular surface. Hydrogen, which is produced in the dissociation reaction is believed to have an important role in the changed surface structure at high exposures. The fact that adsorbed water completely changes the structure of ZnO(0001) is an important finding toward the understanding of this surface at atmospheric conditions.

## Introduction

Interaction between water and metal oxides is important in fields as catalysis, corrosion, and geology. At normal air pressures, most metal surfaces are oxidized and all surfaces are covered with a water layer, whose thickness depends on the relative humidity of the air.[1] Even at ultrahigh vacuum (UHV) conditions ($<10^{-9}$ mbar), water and hydrogen are to some extent always present in the residual gas. It is thus highly probable that hydrogen or water unintentionally has participated in or influenced the surface reactions in many UHV studies. This has been proven to be the case in studies of, for example, clean ZnO[2] and TiO$_2$[3] single crystal surfaces. Water adsorption on oxides is thus of great interest both to understand fundamental surface reactions and to approach the state of surfaces at atmospheric conditions.

Zinc oxide surfaces have been the subject of numerous studies and their chemical and physical properties have been reviewed by Wöll.[2] One of the most important technological applications of zinc oxide surfaces is in the chemical industry where Cu/ZnO/Al$_2$O$_3$ catalysts are used in, for example, methanol synthesis.[4] Furthermore, gas sensing[5] and solar cells[6] are two possible applications of zinc oxide nanoparticles, whose large surface area strongly influence their properties. Since water is always present at ambient conditions, water adsorption on and reaction with ZnO is of importance in most of the applications of this material. Nevertheless, water is also known to have a direct role in, for example, the water gas shift reaction and in photochemical splitting of water, where a zinc oxide-based catalyst can be used.[4,7]

Because of the symmetry of the ZnO single crystal, it contains planes with only Zn cations or O anions in the [0001] direction. This stacking of layers with different polarity gives a nonzero dipole moment directed perpendicular to the (0001) plane. The (0001) and (000$\bar{1}$) surfaces terminating the crystal are thus denoted as "polar" and in ZnO they are Zn- and O-terminated, respectively. However, in the ionic model surfaces with a nonzero dipole moment have a diverging surface energy and

are thus not stable. Three possible stabilization mechanisms for polar surfaces have been suggested,[8] (i) charge transfer between the two opposite polar surfaces, (ii) formation of surface ion vacancies, which can lead to a change of the geometric positions of the surface ions, and (iii) adsorption of charged adparticles. As for ZnO, no consensus on a common mechanism for the two polar surfaces has yet been reached.[2] The more recent studies on ZnO(0001) suggest that depending on the surface preparation conditions, stabilization mechanisms (ii) or (iii) can be valid for this particular surface.[9−11]

When prepared in UHV with sputtering and annealing ($T = 500−700$ °C) cycles, the ZnO(0001) surface is covered with triangular islands and pits whose step edges are oxygen-terminated. This was initially shown in an STM study by Dulub et al.,[12] who suggested that triangular "magic" islands with size-dependent shapes give 25% of a monolayer of zinc ion vacancies, which could explain the stability of this surface. Later, Ostendorf et al.[13] found that higher annealing temperatures ($T \gtrsim 1030$ °C) give highly ordered step arrays partly covered with triangular islands and pits. They pointed out that all step edges are exclusively (10$\bar{1}$0) nanofacets, which, as they suggest, could contribute to the stabilization of the ZnO(0001) surface. In a newly published study by the same group, Torbrügge et al.[14] show evidence of local areas on the ZnO(0001) surface with a (1 × 3) reconstruction. Even though the areas with this reconstruction might only be localized to certain spots of the surface, the authors suggested that one third rather than one fourth of the surface Zn ions should be removed to stabilize the surface. They also observed that at places where the reconstruction was incomplete, adsorbates, which they interpreted as hydrogen, were present.

In addition to stabilization of ZnO(0001) through surface reconstructions, hydroxide stabilized ZnO(0001)−OH surfaces have been obtained through wet chemical etching. This was reported on in two AFM studies by Valtiner et al.[10,11] The hydroxide layer was shown to have a well ordered ($\sqrt{3} \times \sqrt{3}$)R 30° structure in a pH range of 5.5−11.[11] The fact that different surface preparation conditions can result in different stabilization of this polar surface is confirmed by a density functional theory

---

* To whom correspondence should be addressed. E-mail: onsten@kth.se.

(DFT) study by Kresse et al.[9] In the latter study, triangular structures, OH termination and condensated water were found to be stable in different regions of oxygen and hydrogen chemical potentials. Yet, the adsorption of OH groups on the surface covered with triangular structures was found to be energetically unstable. The transition from the triangularly structured surface to the OH-terminated surface is thus unclear.

There are several studies on water adsorption on ZnO-(0001).[15−19] Casarin et al[17] showed by means of local DFT calculations that molecular adsorption of water is favored on the perfect ZnO(0001) surface. However, their model did not include the large density of step edges that later has been shown to exist on the ZnO(0001) surface.[12,20,21] The only experimental study at UHV conditions on water adsorption on the zinc terminated polar ZnO surface that has been found by the authors is a combined ultraviolet photoemission spectroscopy (UPS) and temperature-programmed desorption (TPD) study from 1983.[15] In this study, water was believed to be in its molecular form at room temperature on both the zinc- and oxygen-terminated polar ZnO surfaces and on ZnO(10$\bar{1}$0). This conclusion was partly based on the UPS measurements in which only one molecular orbital was visible due to interference from the Zn 3d peak. However, hydroxyl groups are usually differentiated from molecular water by the presence of two instead of three peaks associated with molecular orbitals in the valence band spectrum.[22] The one-peak spectrum they obtained could thus not suffice to identify the adsorbed specie. Furthermore, they emphasized that the only desorption product they observed was molecular water. This can however not exclude dissociation, since water adsorption is mostly reversible on metal oxides.[22] The conclusion drawn in the UPS-TPD study could thus be questioned. Moreover, water has later been shown to adsorb dissociatively on ZnO(000$\bar{1}$)[23] and partly dissociatively on ZnO-(10$\bar{1}$0).[24,25]

Most of the studies on ZnO single crystal surfaces are performed in UHV chambers on sputtered and annealed samples and the surface structures thus obtained are interesting to study from a fundamental point of view. However, to understand surface reactions on these surfaces at more realistic conditions it is important to introduce water, since all surfaces are covered with a water layer at atmospheric conditions. Water dissociation, which often is favored at oxide surfaces, leaves OH-groups and hydrogen atoms on the surface. In bulk zinc oxide, the role of hydrogen has been shown to be particularly important, since it is one of the most common impurities in this material.[26,27] It has been suggested that hydrogen could be at least partially responsible for the n-type conductivity in undoped zinc oxide single crystals.[28] Furthermore, in a recent theoretical study of hydrogen adsorption on ZnO(0001), the H(1 × 1) surface is shown to be metallic.[29] An earlier study[16] predicts that hydrogen adsorption on the O-terminated ZnO(000$\bar{1}$) surface results in a metallic surface while OH groups make the zinc-terminated ZnO(0001) surface nonmetallic. These properties could have vast effects on the reactivity of this surface. Therefore when having the intention to better understand, for example, catalytic reactions on ZnO surfaces, it could actually be more relevant to study the water covered surface than the clean surface. Also surface and subsurface defects are important and affect the reactivity. However, to use water-covered surfaces as model systems in, for example, theoretical calculations we need to learn more about these surface structures.

In the present study, room temperature adsorption of H$_2$O on ZnO(0001) has been studied with scanning tunneling microscopy (STM) and photoemission spectroscopy (PES).

Sites, mechanism, and products of adsorption are discussed. This study points out the importance of taking water and hydrogen into account when studying zinc oxide surfaces and takes us one step closer an understanding of the ZnO(0001) surface at ambient conditions.

## Experimental Details

The high resolution PES measurements were performed at beamline I511 at MAX-lab in Lund, Sweden. A description of the experimental setup can be found elsewhere.[30] The base pressure in preparation and analysis chambers was 3 × 10$^{-10}$ mbar. The spectra were acquired at grazing incidence at an angle of approximately 80° off-normal incidence and at normal emission. The photon energy was chosen to 619 eV giving an experimental energy resolution of 130 meV. The binding energy was referenced to the Fermi level, which was measured at a grounded tantalum foil in electrical contact with the sample.

The STM measurements were performed in a UHV system, which consists of an analysis chamber that houses an Omicron VT-STM and a preparation chamber that is equipped with LEED, a sputter gun and annealing equipment. The STM measurements were performed in constant current mode and at room temperature. A mechanically cut Pt−Ir tip was used as STM probe. The base pressure in both chambers was below 1 × 10$^{-10}$ mbar.

The ZnO crystals were purchased from Surface Preparation Laboratory and were cleaned through Ar$^+$ sputter (1 keV) and annealing (600−700 °C) cycles until a distinct (1 × 1) LEED pattern was obtained. In the PES measurements, no contaminants except for a small amount of the sputter gas Argon were detected on the clean samples. In the PES preparation chamber, the sample was heated by running a current through a thin Ta foil attached at the backside of the sample. The heating method that was used in the STM experiment was electron bombardment and the sample was mounted on a Ta sample holder. The annealing temperature was measured with a pyrometer and was found to be ∼600 °C in the PES chamber and ∼700 °C in the STM chamber. The pyrometer was focused on the Ta foil or sample holder and an emissivity value ($\varepsilon = 0.3$) characteristic for Ta was used, as the sample is expected to have a high transparency toward IR radiation. Because of heat losses, the annealing temperature of the actual sample is expected to be somewhat lower than the temperature measured on the sample holder.

Deionized water was cleaned by five freeze and thaw cycles and was dosed through a leak valve. The purity of the water vapor was checked by means of mass spectrometry. Prior to the PES measurements, the influence of the photon beam on H$_2$O was studied by recording many succeeding short spectra from the same spot of the sample. To avoid effects caused by the beam, special precautions were taken. The spectra were acquired by changing the spot for beam exposure and several measurements were added to give the final spectra.

## Results and Discussion

**PES.** To get chemical information about whether water adsorption on ZnO(0001) is molecular or dissociative, the water-exposed surface has been investigated with PES. In Figure 1, O 1s spectra acquired from a clean and water-exposed (5 L water) ZnO(0001) surface are shown. These spectra are decomposed into one and two Voigt components, respectively, whose Lorentzian line width is 0.33 eV for both components and the Gaussian linewidths are given in the figure. The main peak, which is located at 530.9 eV in both spectra can be
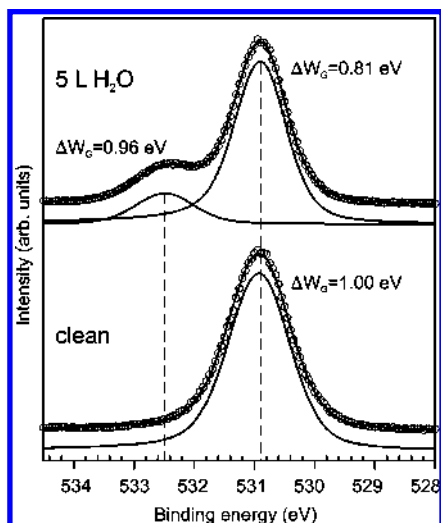
**Figure 1.** O 1s core level spectra ($h\nu = 619$ eV) acquired at room temperature of clean and water exposed (5 L) ZnO(0001). The spectra are decomposed into one or two Voigt components, whose Gaussian widths ($\Delta W_G$) are given in the figure.

**TABLE 1: Binding Energies ($E_{Bin}$) for O 1s Components (approximate values) in PES Studies of Water Exposed Single Crystal Metal Oxide Surfaces**

| | $E_{Bin}$ (eV) | | | $\Delta E_{Bin}$ (eV) | | | |
|---|---|---|---|---|---|---|---|
| oxide surface | O | OH | $H_2O$ | O–OH | O–$H_2O$ | $T$ (K) | ref |
| $Al_2O_3$(100) | 531.5 | | 533.5 | | 2.0 | 100 | 31 |
| $\alpha$-$Cr_2O_3$(0001) | 531.5 | 532.4 | 534.0 | 0.9 | 2.5 | 250 | 32 |
| $\alpha$-$Cr_2O_3$(0001) | 530.8 | 531.4 | | 0.6 | | 300 | 33 |
| $Fe_3O_4$(111) | 530.0 | 532.1 | | 2.1 | | 180 | 34 |
| $TiO_2$(110) | 530.6 | 532.2 | | 1.6 | | 300 | 35 |
| $TiO_2$(110) | 530.2 | | 532.9 | | 2.7 | 100 | 36 |
| $V_2O_3$(111) | 530.0 | 531.3 | 533.2 | 1.3 | 3.2 | 180–600 | 31 |
| ZnO(000$\bar{1}$) | 531.6 | 533.7 | | 2.1 | | 100 | 23 |

assigned to bulk and surface oxygen in zinc oxide. In the spectrum recorded from the water dosed surface, there is a peak located at 532.5 eV, which is shifted from the main peak with 1.6 eV and this is assigned to hydroxyl groups. This is verified by a study by Valtiner et al,[10] who treated ZnO(0001) in electrolyte solutions with or without a subsequent heat treatment in the presence of water vapor. Both surfaces (with and without heat treatment) gave a PES spectrum with an additional peak shifted with 1.7 eV from the bulk O 1s peak. They assigned the additional peak to hydroxidic oxygen, which was confirmed by a time-of-flight secondary ion mass spectroscopy (ToF-SIMS) measurement. The conclusion that the adsorption is dissociative is also confirmed by earlier PES studies in the literature on water adsorption on single crystal oxide surfaces[23,31–37] (see Table 1), in which dissociative and molecular adsorption gives an O 1s component that is shifted with 0.6–2.1 eV respective 2.0–3.2 eV relative to the main O 1s peak. The identity of the adsorbate has been confirmed with at least one additional experimental technique in all these studies.

It can be noted that the Gaussian width of the main curve fit component is larger for the clean surface ($\Delta W_G = 1.00$) than for the water dosed surface ($\Delta W_G = 0.81$). The large width of the main peak from the clean surface could be explained by the great number of surface defects, for example, step edges and subsurface defects of ZnO(0001). Small shifts between different types of O sites and the relatively large width of the O 1s spectrum in general could explain why different contributions cannot be resolved but just broaden the spectrum. When the sample is exposed to water, many of the O sites contributing

to the width of the main peak prior to adsorption will bind to hydrogen and will then contribute to the hydroxyl peak alone.

**STM.** STM images of the clean and water exposed ZnO(0001) surface are shown in Figures 2–3. We begin with discussing the effects of water adsorption on a small scale level. Starting with Figure 2, it gives a closer look on the details in the clean and water exposed (2–5 L) surface.

The clean surface, presented in Figure 2a, is characterized by triangular islands and pits of various sizes and their orientation is rotated by 180° when comparing triangles on two terraces separated by a single step. This is typical for the ZnO(0001) surface annealed at intermediate temperatures of 600–700 °C and there is no sign of step-bunching occurring at higher temperatures[13] in the presented images. The average single step height is found to be 2.7 Å corresponding well with half the *c*-axis value for the wurtzite unit cell amounting to 5.21 Å.[38] Taking a closer look at the surface (see Figure 2a1), small protrusions about 10–15 Å in size appear. The surface density of the protrusions is 0.4 nm$^{-2}$. They seem to be more densely packed at the borders of larger triangles. However, most of them show no mutual order, but are randomly distributed on the surface. Ostendorf et al.[13] mention in their AFM study of ZnO(0001) that "the terraces normally appear to be rough and covered with blurry protruding features". Similar protrusions were also present in the first high-resolution STM images of the ZnO(0001) surface taken by Dulub et al.[12] The authors did not mention these features, but instead they state that their surface is covered with a large number of pits, which are separated by in average 8 Å. The pits appeared round, which they suggested could be a tip broadening effect. Dulub et al. mention that the smallest triangular islands observed have an edge length of 16 Å, which is the smallest island size allowed in their model and comparable to the size of the small protrusions shown in Figure 2a1. However, the origin of the protrusions mentioned here was not properly discussed in either the study by Dulub et al.[12] or by Ostendorf et al.[13] Therefore, we tentatively assign these features with no mutual order to small triangles, whose shape is too small to be resolved with the tip used but nevertheless having step edges that are oxygen-terminated.

After 2 L water exposure, depicted in Figure 2b, the number of triangular islands and pits has decreased significantly compared to the clean surface. The triangular islands appear to have grown in size and merged to larger terraces. After water adsorption, the step edges are no longer straight but obtain a cauliflower-like shape (see Figure 2b2). The pits have diminished and the smallest pits are no longer triangular but have an irregular shape. The protruding features that cover the terraces of the clean surface have grown larger and the terraces are covered with a mix of these large protrusions and small irregular pits (see Figure 2b1). After 5 L water exposure, shown in Figure 2c, almost all triangular islands have merged and form irregularly shaped terraces. The terraces are characterized by a large number of small pits (see Figure 2c1) with no apparent lateral order, but with hints of a triangular shape. The surface density of such pits is 0.2 nm$^{-2}$.

Water dissociation on oxides is believed to require strong bonding between the oxygen in the molecule and a cation site on the surface, as well as a short distance between this cation site and an anion site on the substrate, thus enabling hydrogen bonding to the surface that will weaken the O–H bond in the molecule.[22] The only anions exposed on the ZnO(0001) surface are the oxygen ions at step edges. It is thus likely that water adsorption and dissociation takes place next to step edges of
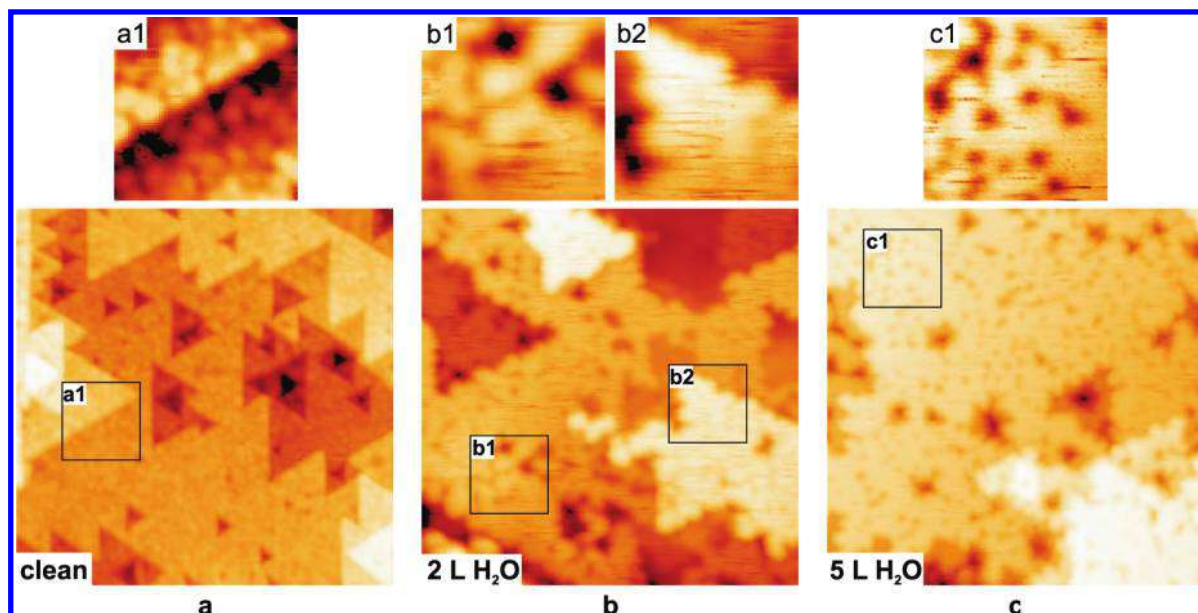
**Figure 2.** 50 nm × 50 nm STM images (a−c) of clean and water exposed ZnO(0001). The enlarged insets have the size 10 nm × 10 nm. Tunneling parameters are (+3.0 V, 0.04 nA) for panel a and (+2.0 V, 0.04 nA) for panels b and c.
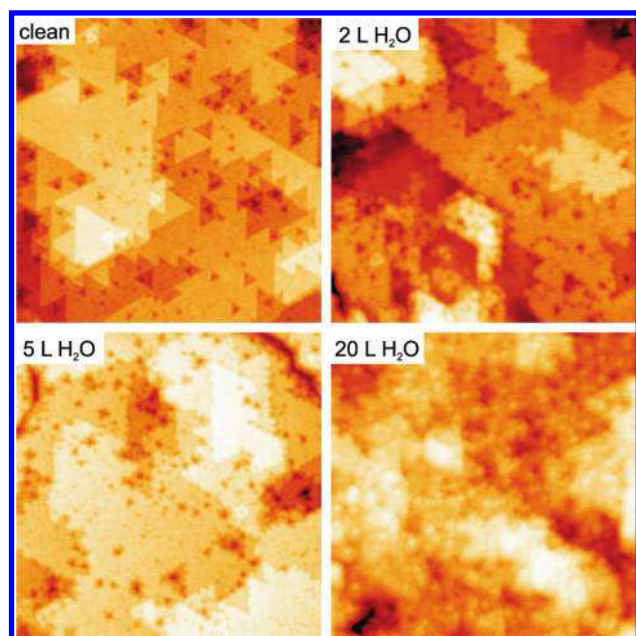


**Figure 3.** 100 nm × 100 nm STM images (+3.0 V,0.04 nA) of clean and water exposed ZnO(0001). The bottom right image (20 L H$_2$O) is acquired with the double scan speed (400 nm/s) compared to the other images (200 nm/s) in this figure, explaining the somewhat lower resolution.

the triangular islands and pits, which are also what the STM images in Figure 2 show. As a suggestion, water molecules could initially adsorb on zinc sites next to step edges involving bonds to 1−3 zinc cations. Water dissociation could then occur by leaving hydrogen to the step edge oxygen anions, giving OH-terminated step edges. When the hydrogen acceptors at the step edges are occupied, it is unclear how the subsequent dissociation occurs. One possibility could be that step edge hydrogen atoms are rather mobile and move to zinc sites on the terrace leaving place for new hydrogen atoms to adsorb. Previous He-atom scattering measurements[39] have shown that hydrogen form a (1 × 1) overlayer on ZnO(0001) at low hydrogen coverages. According to DFT calculations by Kresse et al.,[9] the most favorable site for hydrogen atoms on ZnO(0001)

is atop Zn atoms. However, the same calculations show that the reactivity of hydrogen atoms is so high that they can reduce zinc oxide to metallic zinc leaving OH groups on the surface. This would require oxygen atoms that migrate from subsurface layers, a process that would lead to a decreased surface and subsurface order. They also predict that the most favorable site for OH adsorption is the hollow site, where the oxygen atom in the hydroxyl group binds to three zinc atoms. Yet, dissociative adsorption of water at step edges differ significantly from the adsorption of OH groups at terrace sites. Moreover, the resolution of the STM images obtained in the present study does unfortunately not suffice to be able to predict the exact adsorption site for water.

The surface morphology on an overall scale is visualized in Figure 3, where overview images are presented that reveal how the clean ZnO(0001) surface evolves upon adsorption of 2, 5, and 20 L water. Noticeable is the transition from the triangular features found on the clean surface to the more disordered surface found after 20 L H$_2$O deposition. For the lower doses, 2 and 5 L, the triangles are still clearly visible but at 20 L, only hints of them still remain. At 20 L exposure, there are no longer any distinct terraces but the whole surface seems rough and disordered. The surface irregularities appear in a large variety of shapes and forms. Clearly, the effect of water adsorption has a large influence on the surface morphology.

Adsorbed hydrogen could as suggested by Kresse et al.[9] urge a mass transport of oxygen from subsurface to surface layers, which will lead to more disordered terraces. The increased irregularity found for the 20 L dose could thus be caused by hydrogen that is left from the dissociation process. Becker et al. showed by comparing He-atom reflectivity and LEED measurements that hydrogen adsorption on ZnO(0001) creates a large number of defects that are concentrated to the top few layers of the surface. They also observed with PES that both Zn−H and OH species were present on the ZnO(0001) surface after exposure to hydrogen. At that time they believed that no oxygen atoms are exposed in this surface and used this fact to conclude that H atoms must penetrate the surface to subsurface layers to form OH groups leading to the breaking of Zn−O bonds and a consequent disordering of the surface layer. Now,

it is well-known that the UHV-annealed surface contain triangular pits and islands that are oxygen terminated[12] and oxygen atoms are thus exposed in contrast to their assumption. It should be noted, however, that in the study by Becker et al., the samples were not only cleaned by sputtering and annealing in UHV as in many other studies of ZnO(0001)[12–14] but they were also annealed in oxygen. It is not impossible that this results in a different (0001) surface and/or subsurface structure due to a larger oxygen content in the crystal. In addition, Becker et al. also made ion scattering spectroscopy (ISS) measurements at an angle of incidence of 40°, which showed a significant increase of the relative intensity of O atoms compared to Zn atoms upon hydrogen adsorption. It thus appears as if the conclusion by Becker et al. that hydrogen restructures the surface and subsurface layers might still hold. Nevertheless, it is unclear whether the increased irregularity at 20 L water exposure in the present study is caused by O atoms moving to the surface as suggested by Kresse et al.[9] or by H atoms moving to subsurface layers as suggested by Becker et al.[39] Having in mind the increased amount of O observed by the latter group, hydrogen adsorption could also urge a transport of Zn interstitials from surface to subsurface regions. Moreover, it is quite probable that more than one of these processes is at play. To better understand the effect water and hydrogen has on ZnO surfaces and their reactivity, it is important to investigate the interaction between these species and different surface and subsurface defects. Experimentally, this can be done by studying adsorption on samples prepared with various sample preparation techniques.

## Conclusions

Scanning tunneling microscopy and photoemission spectroscopy have been used to study the interaction between water and ZnO(0001). Water is shown to adsorb dissociatively leaving hydroxyl groups on the surface. The adsorption appears to occur along step edges of the triangular pits and islands that are characteristic of the clean surface. Step edges become irregular upon exposure to water and as the water dose is increased, terraces grow in size while pit sizes diminish. At higher coverage (20 Langmuir) the surface disorder has increased considerably and guided by earlier studies, we suggest that hydrogen created in the dissociation process is responsible for this. Water thus induces a complete restructuring of the surface. This is a significant finding for the understanding of the structure of ZnO(0001) at ambient conditions, being relevant in fields as catalysis and corrosion.

## References and Notes

(1) Leygraf, C. *Atmospheric Corrosion*; Wiley: New York, 2000.
(2) Wöll, C. *Prog. Surf. Sci.* **2007**, *82*, 55.
(3) Wendt, S.; Schaub, R.; Matthiesen, J.; Vestergaard, E. K.; Wahlström, E.; Rasmussen, M. D.; Thostrup, P.; Molina, L. M.; Lægsgaard, E.; Stensgaard, I.; Hammer, B.; Besenbacher, F. *Surf. Sci.* **2005**, *598*, 226.
(4) Spencer, M. S. *Top. Catal.* **1999**, *8*, 259.
(5) Eriksson, J.; Khranovskyy, V.; Söderlind, F.; Käll, P.-O.; Yakimova, R.; Lloyd Spetz, A. *Sens. Actuators, B* **2009**, *137*, 94.
(6) Redmond, G.; Fitzmaurice, D.; Graetzel, M. *Chem. Mater.* **1994**, *6*, 686.
(7) Steinfeld, A. *Int. J. Hydrogen Energy* **2002**, *27*, 611.
(8) Noguera, C. *J. Phys.: Condens. Matter* **2000**, *12*, R367.
(9) Kresse, G.; Dulub, O.; Diebold, U. *Phys. Rev. B* **2003**, *68*, 245409.
(10) Valtiner, M.; Borodin, S.; Grundmeier, G. *Phys. Chem. Chem. Phys.* **2007**, *9*, 2406.
(11) Valtiner, M.; Borodin, S.; Grundmeier, G. *Langmuir* **2008**, *24*, 5350.
(12) Dulub, O.; Diebold, U.; Kresse, G. *Phys. Rev. Lett.* **2003**, *90*, 016102.
(13) Ostendorf, F.; Torbrügge, S.; Reichling, M. *Phys. Rev. B* **2008**, *77*, 041405(R).
(14) Torbrügge, S.; Ostendorf, F.; Reichling, M. *J. Phys. Chem. C* **2009**, *113*, 4909.
(15) Zwicker, G.; Jacobi, K. *Surf. Sci.* **1983**, *131*, 179.
(16) Wander, A.; Harrison, N. M. *J. Chem. Phys.* **2001**, *115*, 2312.
(17) Casarin, M.; Maccato, C.; Vittadini, A. *Surf. Sci.* **1997**, *377*, 587.
(18) Martins, J. B. L.; Moliner, V.; Andrés, J.; Longo, E.; Taft, C. A. *J. Mol. Struct. (Theochem)* **1995**, *330*, 347.
(19) Martins, J. B. L.; Andrés, J.; Longo, E.; Taft, C. A. *Int. J. Quantum Chem.* **1996**, *57*, 861.
(20) Dulub, O.; Boatner, L. A.; Diebold, U. *Surf. Sci.* **2002**, *519*, 201.
(21) Diebold, U.; Koplitz, L. V.; Dulub, O. *Appl. Surf. Sci.* **2004**, *237*, 336.
(22) Henderson, M. A. *Surf. Sci. Rep.* **2002**, *46*, 5.
(23) Kunat, M.; Gil Girol, S.; Burghaus, U.; Wöll, C. *J. Phys. Chem. B* **2003**, *107*, 14350.
(24) Dulub, O.; Meyer, B.; Diebold, U. *Phys. Rev. Lett.* **2005**, *95*, 136101.
(25) Meyer, B.; Rabaa, H.; Marx, D. *Phys. Chem. Chem. Phys.* **2006**, *8*, 1513.
(26) Monakhov, E. V.; Kuznetsov, A. Y.; Svensson, B. G. *J. Phys. D: Appl. Phys.* **2009**, *42*, 153001.
(27) Jagadish, C.; Pearton, S. J. *Zink Oxide Bulk, Thin Films and Nanostructures*; Elsevier: Amsterdam, 2006.
(28) Hofmann, D. M.; Hofstaetter, A.; Leiter, F.; Zhou, H.; Henecker, F.; Meyer, B. K.; Orlinskii, S. B.; Schmidt, J.; Baranov, P. G. *Phys. Rev. Lett.* **2002**, *88*, 045504.
(29) Sanchez, N.; Gallego, S.; Cerdá, J.; Muñoz, M. C. *Phys. Rev. B* **2010**, *81*, 115301.
(30) Denecke, R.; Väterlein, P.; Bässler, M.; Wassdahl, N.; Butorin, S.; Nilsson, A.; Rubensson, J.-E.; Nordgren, J.; Mårtensson, N.; Nyholm, R. *J. Electron Spectrosc. Relat. Phenom.* **1999**, *101*, 971.
(31) Abu Haija, M.; Guimond, S.; Uhl, A.; Kuhlenbeck, H.; Freund, H.-J. *Surf. Sci.* **2006**, *600*, 1040.
(32) Henderson, M. A.; Chamber, S. A. *Surf. Sci.* **2000**, *449*, 135.
(33) Maurice, V.; Cadot, S.; Marcus, P. *Surf. Sci.* **2001**, *471*, 43.
(34) Joseph, Y.; Ranke, W.; Weiss, W. *J. Phys. Chem. B* **2000**, *104*, 3224.
(35) Wang, L.-Q.; Baer, D. R.; Engelhard, M. H.; Shultz, A. N. *Surf. Sci.* **1995**, *344*, 237.
(36) Hugenschmidt, M. B.; Gamble, L.; Campbell, C. T. *Surf. Sci.* **1994**, *302*, 329.
(37) Ozensoy, E.; Szanyi, J.; Peden, C. H. F. *J. Phys. Chem. B* **2005**, *109*, 3431.
(38) Wyckoff, R. W. G. *Crystal Structures*; Wiley: New York, 1963; Vol. 1.
(39) Becker, T.; Hövel, S.; Kunat, M.; Boas, C.; Burghaus, U.; Wöll, C. *Surf. Sci. Lett.* **2001**, *486*, L502.

# Role of Defects in Surface Chemistry on Cu₂O(111)

Anneli Önsten,* Jonas Weissenrieder, Dunja Stoltz, Shun Yu, Mats Göthelid, and Ulf O. Karlsson

Materials Physics, Royal Institute of Technology KTH, S-164 40 Kista, Sweden

**S** *Supporting Information*

**ABSTRACT:** High-resolution photoemission spectroscopy and scanning tunneling microscopy (STM) have been used to investigate defects on Cu₂O(111) and their interaction with water and sulfur dioxide (SO₂). Two types of point defects, i.e., oxygen and copper vacancies, are identified. Copper vacancies are believed to be the most important defects in both water and SO₂ surface chemistry. Multiply coordinatively unsaturated oxygen anions (O$_{MCUS}$) such as oxygen anions adjacent to copper vacancies are believed to be adsorption sites for both water and SO₂ reaction products. Water adsorption at 150 K results in both molecular and dissociated water. Molecular water leaves the surface at 180 K. At 300 K and even more at 150 K, SO₂ interacts with oxygen sites at the surface forming SO₃ species. However, thermal treatment up to 280 K of Cu₂O(111)/SO₂ prepared at 150 K renders only SO₄ on the surface.
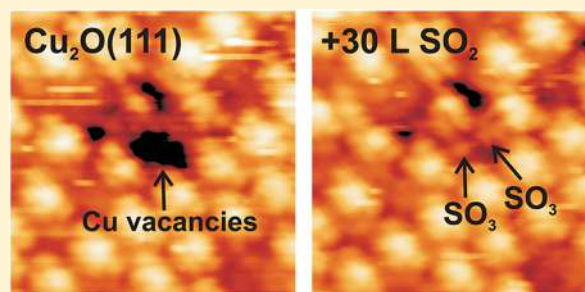
## INTRODUCTION

Cuprous oxide (Cu₂O) is a p-type semiconductor with a band gap of ~2.2 eV[1,2] and has potential future applications in solar energy conversion,[3–5] photocatalytic splitting of water for hydrogen generation,[6–9] and electrode material in lithium ion batteries.[10] Cu₂O and Cu⁺ ions have important roles in the functioning of Cu-based catalysts,[11,12] which are used in, e.g., the water–gas shift reaction for production of hydrogen[13,14] and for methanol synthesis.[12] Moreover, Cu₂O is one of the most abundant initial corrosion products of copper.[15] Studying the surface chemical properties of Cu₂O is thus important to understand chemical processes taking place at copper surfaces.

The O-terminated Cu₂O(111) surface has been found to be one of the most energetically stable Cu₂O surfaces.[16–18] The (111) surface is also an imperfect cleavage plane of Cu₂O, implying that cleaving leaves a surface dominated by the (111) surface.[19] Schulz and Cox[20] studied (111) surfaces with both (1 × 1) and (√3 × √3)R30° periodicity using X-ray and ultraviolet photoelectron spectroscopies and low-energy electron diffraction (LEED). They assigned the (√3 × √3)R30° reconstruction to the removal of one-third of the surface oxygen anions. In a later study, Önsten et al. confirmed the conclusion that the reconstruction is based on oxygen vacancies.[21]

The atomic structure of Cu₂O(111) has been the focus of a few theoretical studies.[11,16–18,22–24] Bulk terminated Cu₂O-(111) contains four different species, namely, coordinatively saturated copper and oxygen ions (Cu$_{CSA}$ and O$_{CSA}$) and coordinatively unsaturated ions (Cu$_{CUS}$ and O$_{CUS}$). Soon et al. have theoretically predicted that the most stable configuration of this surface in a wide range of oxygen chemical potentials is Cu₂O(111)-Cu$_{CUS}$.[16,17] This configuration contains a surface (coordinatively unsaturated) Cu vacancy. Önsten et al. investigated this surface by means of scanning tunneling

microscopy (STM) and LEED but could not confirm the existence of Cu$_{CUS}$ vacancies in the surface structure.[21] The STM images were later reinterpreted in a simulation by Li et al.[23]

The surface chemical properties of Cu₂O(111) have been investigated in theoretical studies with various molecules such as H₂O,[25,26] H₂S,[26] NO,[27–29] CO,[16,27,30,31] N₂O,[32] and benzatriazole.[33] However, many of these studies are based on bulk-terminated models of this surface and not the most stable Cu₂O(111)-Cu$_{CUS}$ configuration proposed by Soon et al.[11,17] Unambiguous determination of the correct surface structure is especially important since Cu$_{CUS}$ has been reported as the most reactive surface site for several molecules.[28,32–34] It is thus important to investigate the general surface configuration as well as surface defects for a better understanding of the chemical properties of this surface.

Here we present STM and high-resolution photoemission spectroscopy (PES) studies of Cu₂O(111) and its interaction with water and sulfur dioxide. We discuss different types of defects and suggest defect sites where surface reactions take place.

## EXPERIMENTAL DETAILS

The photoemission measurements were performed at beamline I511 at MAX-lab in Lund, Sweden. The beamline is undulator based giving photon energies in the range of 100–1200 eV, and the energy was selected by a modified SX-700 monochromator. The end station analysis chamber was equipped with a rotatable Scienta R-4000 electron analyzer. In connection to this chamber, there was a preparation chamber, which housed a

LEED apparatus, a sputter gun, annealing equipment, leak valves, and a quadrupole mass spectrometer. The samples were heated by running a current through a thin Ta foil attached to the back of the sample. The cooling was administered by a continuous flow of liquid nitrogen in the tubes of the manipulator. The temperature was measured with a type K thermocouple that was attached to a Ta foil in close contact with the sample. The base pressure in the analysis chamber was $2 \times 10^{-10}$ mbar. The incoming photon beam was directed at an angle of approximately 80° from the sample surface normal. A more detailed description of the experimental setup can be found elsewhere.[35] All spectra except one in Figure 1 were
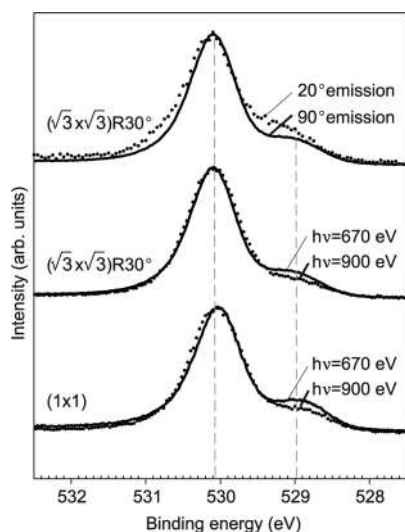


**Figure 1.** O 1s core level spectra from clean $Cu_2O(111)$ surfaces. The spectra have been recorded using different photon energies ($h\nu$) and emission angles as marked out in the figure.

collected in normal emission. The experimental energy resolutions were ~140 meV for O 1s spectra ($h\nu = 670$ eV) and ~50 meV for S 2p spectra ($h\nu = 260$ eV). All spectra were normalized to the background on the lower energy side of the photoelectron line. The binding energy was referenced to the Fermi level, which was measured at a tantalum foil in electrical contact with the sample. After a Shirley-type background subtraction, some of the spectra were numerically fitted with Voigt (Gaussian−Lorentzian) functions.

Recording of several succeeding short spectra from the same spot of the sample showed that the $SO_3$ species formed at RT were almost unaffected by the photon exposure used to collect our spectra. Only a small amount of beam-induced desorption was observed (4% per collected S 2p spectrum). To minimize any photon-induced reaction, spectra were acquired by adding several subsequent measurements from the same surface but from different spots.

The STM experiments were performed in an ultrahigh vacuum system, which consists of an STM chamber that houses an Omicron VT-STM and a preparation chamber that is equipped with a LEED apparatus, a sputter gun, and annealing equipment. The sample was mounted on a tantalum plate, which was heated through electron bombardment. The STM measurements were performed in constant current mode at room temperature. Both mechanically cut Pt−Ir tips and electrochemically etched W-tips were used as STM probes. The base pressure in the STM chamber was $1 \times 10^{-10}$ mbar.

The $Cu_2O(111)$ crystal was purchased from Surface Preparation Laboratory (The Netherlands) and is a natural crystal. No impurities were detected except for potassium (K) that was discovered to be inhomogenously distributed over the sample surface. When collecting photoemission spectra, only the parts of the sample surface where no K was detected were probed. The $Cu_2O(111)$ samples were cleaned through sputtering, annealing in $O_2$ ($2 \times 10^{-6}$ mbar) at 870−970 K, and annealing in UHV at 820−970 K until no carbon was detected and a $(1 \times 1)$ or a $(\sqrt{3} \times \sqrt{3})R30°$ LEED pattern was obtained. The $SO_2$ gas was purchased from Sigma-Aldrich (99.9% purity). Both water (Millipore purity) cleaned by pump−freeze cycles and $SO_2$ were dosed through leak valves, and the purity of the gases was confirmed by mass spectrometry.

## ■ RESULTS AND DISCUSSION

**$Cu_2O(111)$ Surface Defects.** Experimental studies have shown evidence of two types of $Cu_2O(111)$ surface terminations obtained after different sample preparations.[21] Oxygen vacancies can form a $(\sqrt{3} \times \sqrt{3})R30°$ reconstruction but are also present to a varying extent on $(1 \times 1)$-terminated surfaces, as shown by STM (see Supporting Information).

In Figure 1, O 1s spectra from $(1 \times 1)$ and $(\sqrt{3} \times \sqrt{3})R30°$ terminated $Cu_2O(111)$ are shown. The dominating peak, located at 530.0−530.1 eV is assigned to oxygen in the oxide (bulk and surface oxygen). The peak at 528.9−529.0 eV is shifted 1.1−1.2 eV from the main peak. Harmer et al.[19] observed a similar low energy peak in the O 1s spectrum from fractured crystalline $Cu_2O$ and assigned it to undercoordinated oxygen. In mineral cuprite, the (111) surface is expected to be an imperfect cleavage plane, meaning that cleaving leaves a surface dominated by the (111) surface.

To investigate whether the low binding energy (BE) O 1s component can be related to the surface, the O 1s line has been measured using two different photon energies (670 and 900 eV) and two different emission angles (90° and 20°) as shown in Figure 1. The photoelectron mean free paths are approximately 6.5 and 10.0 Å when using photon energies 670 and 900 eV, respectively. These values are obtained from the so-called universal curve (mean free path versus electron energy).[36] The more surface sensitive photon energy 670 eV gives a relatively larger low BE O 1s component compared to the photon energy 900 eV. Furthermore, the more surface-sensitive lower emission angle gives a more pronounced low BE O 1s component. The O 1s spectra in Figure 1 thus show that the low BE O 1s peak is dominated by surface oxygen anions. We will see in the subsection "$SO_2$ Adsorption" that the low BE O 1s component completely disappears upon adsorption of 10 L of $SO_2$ at 150 K. This shows that the latter peak could indeed be considered as a pure surface component.

The relatively low intensity of the low BE peak (at most 19% of the total O 1s peak area as seen in Table 1 in the Supporting Information) indicates that it should not represent all surface oxygen anions. At a fully $(\sqrt{3} \times \sqrt{3})R30°$ reconstructed surface, which is the most oxygen-deficient surface, one-third of the surface oxygen anions are missing. The minimum "coverage" of surface oxygen anions should then be two-thirds of a monolayer, which is too much to represent the small low BE O 1s peak. The coverage of oxygen anions representing the low BE peak is estimated to around 0.2 monolayers (see Supporting Information). Moreover, STM images in the Supporting Information reveal that protrusions are replaced

by depressions at some places on the $(1 \times 1)$-terminated surface. The depressions are interpreted as one or several copper vacancies since the protrusions are assigned to copper cations.[21,23] These pits cover ~5% of the $(1 \times 1)$-terminated $Cu_2O(111)$ surface area and could be related to the low BE peak. The low BE peak would thus represent surface oxygen anions adjacent to copper vacancies. Surface oxygen anions adjacent to copper vacancies have more than one broken bond. Therefore, these oxygen sites are hereafter referred to as $O_{MCUS}$, where the index MCUS refers to "multiply coordinatively unsaturated". $O_{MCUS}$ anions could be found not only adjacent to copper vacancies but also next to steps or kinks at the surface.

**$H_2O$ Adsorption.** Water adsorption on $Cu_2O(111)$ has been studied by means of photoemission spectroscopy. The sample was cleaned with annealing in oxygen, giving a $(1 \times 1)$ LEED pattern with weak $\sqrt{3}$ spots prior to adsorption. No water was observed to adsorb at room temperature. O 1s spectra obtained at 150 K from clean and 1 L of water exposed $Cu_2O(111)$ are shown in Figure 2a and b, respectively. The
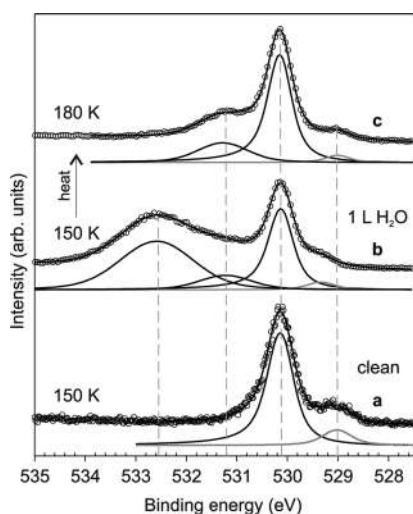


**Figure 2.** O 1s core level spectra ($h\nu$ = 670 eV) from clean (a) and $H_2O$ exposed (b,c) $Cu_2O(111)$. Water adsorption was performed at 150 K (b), and the water layer was then heated to 180 K (c).

spectrum in Figure 2c shows how the O 1s spectrum evolves upon heating the water layer to 180 K. Binding energies, peak areas, and $OH/H_2O$ coverages for the spectra are shown in Table 1. The peak area is given in percentage of the total O 1s peak area. The coverage estimations are based on calculations using the electron mean free path at the specific photoelectron energy used and the relative area of an O 1s component compared to the total O 1s peak area.

When the $Cu_2O(111)$ surface is exposed to 1 L of water, two new O 1s peaks appear at 531.2 and 532.6 eV. The two peaks are shifted from the main oxygen peak by 1.1 and 2.5 eV, respectively, to higher binding energy. These shifts are typical for hydroxyl groups (1.1 eV) and molecular water (2.5 eV) on single crystal oxide surfaces.[37−44] Already at 180 K, the molecular water has left the surface, which indicates that all molecular water adsorbed to the surface at 150 K is physisorbed. The $O_{MCUS}$ component shifts by 0.3 eV to higher binding energy upon adsorption of 1 L of water at 150 K. However, when the physisorbed water layer is desorbed, the $O_{MCUS}$-related O 1s peak shifts back to its value on the clean surface. This indicates that the relatively small shift is due to weak interaction between the undercoordinated surface oxygen anions and physisorbed water. Possibly, this interaction is hydrogen bonding between water molecules and oxygen sites. Moreover, water adsorption leads to a decrease of the intensity of the $O_{MCUS}$ peak. Atomic hydrogen created by water dissociation likely adsorbs on undercoordinated oxygen sites. However, a significant part of the $O_{MCUS}$ peak is still left after adsorption of 1 L of water, which indicates that there are at least two types of oxygen anions contributing to the $O_{MCUS}$ component. Water dissociation on oxide surfaces normally occurs when there is a strong bond between the oxygen in the water molecule and a cation site on the surface.[45] In addition, there is usually a bond between the hydrogen in the molecule and a nearby situated anionic site at the surface.[45] This will result in a weaker O−H bond, which enables bond breaking.[45] Water dissociation on $Cu_2O(111)$ probably occurs when oxygen in the water molecule binds to a surface copper cation and hydrogen in the molecule binds to a nearby located $O_{MCUS}$ anion. This should give around 2 OH groups per $O_{MCUS}$ anion. As seen in Table 1, an OH coverage of 0.25 ML is accompanied by a decrease of the $O_{MCUS}$ surface sites with 0.08 ML (0.12−0.04 ML). It thus appears as if around ~3 OH groups are formed per $O_{MCUS}$ site. This indicates that one-third of water dissociation on $Cu_2O(111)$ appears at oxygen sites other than $O_{MCUS}$ sites.

**$SO_2$ Adsorption.** $SO_2$ adsorption was performed both at room temperature and at 150 K. In Figure 3, O 1s spectra from clean and $SO_2$-exposed $Cu_2O(111)$ are shown. Binding energies, Gaussian widths, and relative areas of the O 1s spectral components and coverages are given in Table 2. The Lorentz width has been fixed to 0.4 eV for all O 1s components. Peak area is given in percentage of the total O 1s peak area. The coverage estimations are based on calculations using the electron mean free path at the specific photoelectron energy used and the relative area of an O 1s component compared to the total O 1s peak area. The $SO_x$ related peak is assumed to originate from $SO_2$ binding to one oxygen anion forming $SO_3$. The sample was cleaned with annealing in oxygen, giving a $(1 \times 1)$ LEED pattern with weak $\sqrt{3}$ spots prior to adsorption.

**Table 1. O 1s Spectral Components for Clean and Water-Exposed $Cu_2O(111)$**

|  | $H_2O$ | main O 1s | | O 1s ($O_{MCUS}$) | | | O 1s (OH) | | | O 1s ($H_2O$) | |
|---|---|---|---|---|---|---|---|---|---|---|---|
| $T$ | dose[a] | $E_{Bin}$[b] | $E_{Bin}$ | area | cov.[c] | $E_{Bin}$ | area | cov.[c] | $E_{Bin}$ | area | cov.[c] |
| (K) | (L) | (eV) | (eV) | (%) | (ML)[d] | (eV) | (%) | (ML)[d] | (eV) | (%) | (ML)[d] |
| 150 | - | 530.1 | 529.0 | 13 | 0.12 | - | - | - | - | - | - |
| 150 | 1 | 530.1 | 529.3 | 4 | 0.03 | 531.2 | 11 | 0.10 | 532.6 | 52 | 0.85 |
| 180 | 1 | 530.1 | 529.0 | 5 | 0.04 | 531.3 | 24 | 0.25 | - | - | - |

[a]Water exposure is performed at 150 K. [b]Bulk O 1s lines have been aligned with Figure 2b. [c]Coverage. [d]Monolayer.
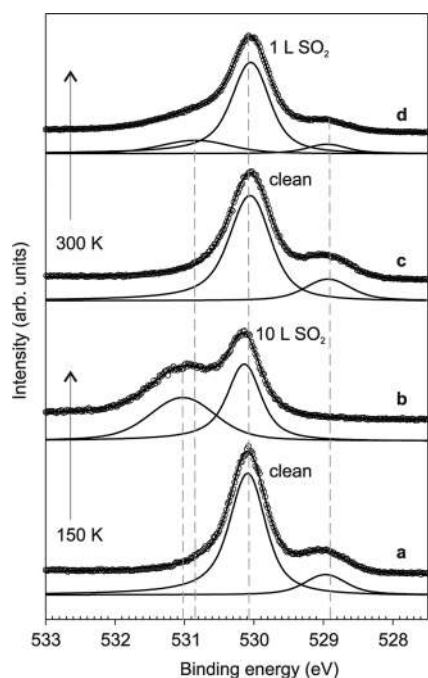
**Figure 3.** O 1s core level spectra ($h\nu$ = 670 eV) from clean (a and c) and SO$_2$ exposed (b and d) Cu$_2$O(111) at 150 K (a,b) and 300 K (c,d).

At room temperature, SO$_2$ saturation was observed to appear at a dose of about 1 L, meaning that no difference in the spectra was observed at higher SO$_2$ doses. SO$_2$ adsorption gives an additional O 1s component shifted with 0.8 eV to larger binding energy. This component can be assigned to SO$_x$ species, and it has a large Gaussian width (0.95 eV) compared to the main peak (0.4 eV). Adsorption at room temperature leads to a significant decrease of the O$_{MCUS}$ peak area to less than half of its initial value indicating that SO$_2$ adsorbs at and binds to O$_{MCUS}$ sites. In fact, the relative integrated intensity of the SO$_x$ related peak (18%) is almost twice as large as the decrease of the relative integrated intensity of the O$_{MCUS}$ peak upon SO$_2$ adsorption at room temperature (19−8 = 11%), as can be seen in Table 2. This suggests that every SO$_2$ molecule, which contains two oxygen atoms, adsorbs on an O$_{MCUS}$ site. When the O$_{MCUS}$ atom in the surface binds to a SO$_2$ molecule forming SO$_3$, the BE of this oxygen atom is shifted to a BE close to that of the O 1s main peak. The discussion above gives evidence that SO$_2$ binds to one surface oxygen anion in the surface forming SO$_3$. This conclusion is confirmed by the fact that the binding energies of the S 2p photoelectron lines in Figure 6 clearly indicate that SO$_3$ species are formed.

It can be noted that a small O$_{MCUS}$ O 1s component still remains after room-temperature SO$_2$ adsorption. This suggests that the O$_{MCUS}$ peak consists of at least two components, one that disappears upon adsorption and one that remains. Since the peak does not change position when it decreases in size, the two components must be very closely situated in binding energy. Another possibility is that there is only one O$_{MCUS}$ site and that repulsive adsorbate−adsorbate interactions prevent SO$_3$ formation on all O$_{MCUS}$ adsorption sites at 300 K. The present authors find the interpretation with two types of O$_{MCUS}$ sites somewhat more credible since the O$_{MCUS}$ peak area decreases to half of its initial value upon both OH group saturation at 180 K and SO$_3$ saturation at 300 K. This favors the interpretation with two types of O$_{MCUS}$ sites since OH−OH and SO$_3$−SO$_3$ interactions should be different due to the different properties of OH and SO$_3$ surface species.

Interestingly, the O$_{MCUS}$ peak is no longer distinguishable after exposure of 10 L of SO$_2$ at 150 K (see Figure 3b). The size of the SO$_x$ related O 1s peak is larger, but its binding energy shift from the main peak of 0.9 eV is approximately the same compared to the SO$_x$ peak that evolves upon room-temperature adsorption. Moreover, exposure of 20 L of SO$_2$ gives the same O 1s spectrum as upon exposure of 10 L of SO$_2$. This implies that no SO$_2$ multilayer is formed at this temperature. According to our estimations, 0.4 monolayer (ML) SO$_3$ is formed at 150 K. By comparing the SO$_3$ coverage to the coverage of O$_{MCUS}$ anions at 150 K (0.16 ML), it becomes clear that SO$_2$ adsorbs on both types of O$_{MCUS}$ sites as well as other oxygen sites at 150 K.

Valence band spectra from clean Cu$_2$O(111)-(1 × 1) and from this surface exposed to 10 L of SO$_2$ at 150 K are shown in Figure 4. The spectra are normalized to the Cu 3d peak height. The features in the region 1−4 eV are primarily Cu 3d derived, while the features in the region 6−7.5 eV have a more pronounced O 2p character. A detailed discussion of the spectrum obtained from the clean Cu$_2$O(111) surface can be found elsewhere.[17,46,47] Adsorbate (SO$_x$) induced contributions appear at 5−7.5 eV and 8.5−10.5 eV. These contributions can be ascribed to emission from adsorbed SO$_x$ since the spectrum from gas-phase SO$_2$ contains three peaks at 6, 7, and 10 eV, respectively.[48] Moreover, the valence band spectra from compounds such as LiSO$_3$ also contain features in the mentioned regions.[49] Another effect of SO$_2$ adsorption on the valence band is a reduced intensity in the regions 0−1.5 eV and 4.0−4.5 eV (see arrows in Figure 4). Soon et al.[17] identified states for oxygen atoms with unsaturated bonds around a copper vacancy in the bulk Cu$_2$O structure by first-principles calculations based on density functional theory. These electronic states had the largest contribution to the valence band states around 0−1.5 eV and around 4−5 eV. Consequently, the reduced intensity in these two regions

**Table 2. O 1s Spectral Components for Clean and SO$_2$ Exposed Cu$_2$O(111)**

| | SO$_2$ | main O 1s | | O 1s (O$_{MCUS}$) | | | | O 1s (SO$_x$) | | | |
|---|---|---|---|---|---|---|---|---|---|---|---|
| $T$ | dose | $E_{Bin}$ | $\Delta E_G$ | $E_{Bin}$ | $\Delta E_G$ | area | cov.$^a$ | $E_{Bin}$ | $\Delta E_G$ | area | cov.$^a$ |
| (K) | (L) | (eV) | (eV) | (eV) | (eV) | (%) | (ML)$^b$ | (eV) | (eV) | (%) | (ML)$^b$ |
| 150 | - | 530.1 | 0.35 | 529.0 | 0.47 | 17 | 0.16 | - | - | - | - |
| 150 | 10 | 530.1 | 0.31 | - | - | - | - | 531.0 | 0.89 | 50 | 0.4 |
| 300 | - | 530.0 | 0.45 | 528.9 | 0.55 | 19 | 0.18 | - | - | - | - |
| 300 | 1 | 530.0 | 0.39 | 528.9 | 0.45 | 8 | 0.07 | 530.8 | 0.95 | 18 | 0.09 |

$^a$Coverage. $^b$Monolayer.
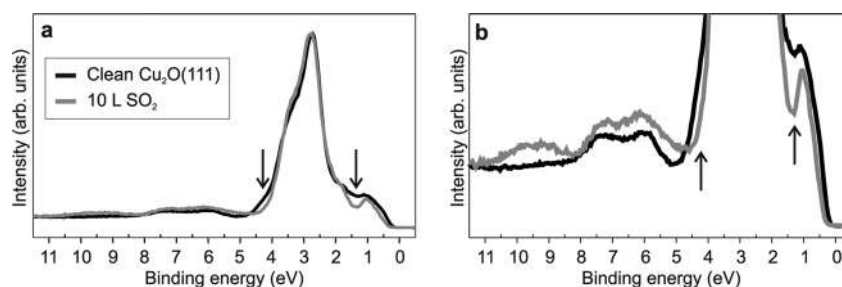
**Figure 4.** Valence band spectra ($h\nu$ = 143 eV) of clean $Cu_2O(111)$ (black line) and this surface exposed to 10 L of $SO_2$ (gray line). Both spectra are recorded at 150 K.

upon $SO_2$ adsorption could give further evidence that $SO_2$ adsorbs on oxygen anions adjacent to copper vacancies. This is based on the assumption that electronic states for surface oxygen atoms with unsaturated bonds around a copper vacancy are located in about the same valence band regions as the corresponding bulk states.

Additional evidence for the suggestion that $SO_2$ molecules adsorb on $O_{MCUS}$ sites is given by the STM images in Figure 5.
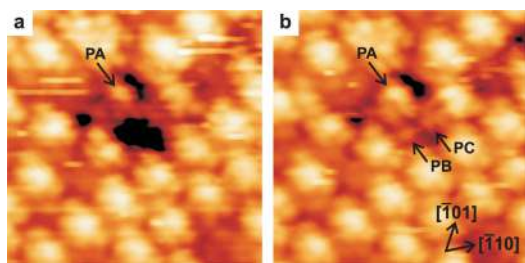


**Figure 5.** 59 Å × 59 Å STM image (1.0 V, 0.05 nA) of (a) clean and (b) $SO_2$ exposed (30 L of $SO_2$) $Cu_2O(111)$.

Figure 5a was recorded from the clean surface, and Figure 5b was recorded from the same spot of the surface after exposure to 30 L of $SO_2$ at room temperature. Significant changes can be observed at sites of one or more copper vacancies after $SO_2$ adsorption. The protrusion PA grows larger upon adsorption. Moreover, adsorption gives rise to two new protrusions PB and PC, marked out in Figure 5b. The distance between PB and PC is around 6 Å. When assuming a lattice constant of 4.2696 Å for $Cu_2O$,[50] the nearest-neighbor distance between copper ions in the same plane is 3.02 Å, and the distance between two nearest oxygen ions in the (111) surface plane is 6.04 Å. Hence, the distance between PA and PB in the STM image is close to the distance between two nearest oxygen anions in the (111) plane. It is thus likely that PA and PB represent two adsorbed $SO_2$ molecules (or $SO_3$ groups), which bind to two different oxygen anions, and that each of these oxygen anions is connected to at least one copper vacancy.

In Figure 6a–g, S 2p spectra from $SO_2$-exposed $Cu_2O(111)$ are shown. Figure 6a is obtained from a surface exposed to 1 L of $SO_2$ and mostly consists of one S 2p component located at 166.3 eV. This binding energy is typical for $SO_3$ species on oxide surfaces[51−55] and for sulfite compounds (e.g., $NaSO_3$).[56] A small component at 168.0 eV, assigned to $SO_4$, has also improved the curve fitting slightly. As already mentioned, a dose of 1 L of $SO_2$ saturates the surface at room temperature and at the $SO_2$ pressure ($4 \times 10^{-9}$ mbar) used in this study. The S 2p spectrum in Figure 6b is acquired from a surface exposed to 10 L of $SO_2$ at 150 K and $8 \times 10^{-8}$ mbar and is also
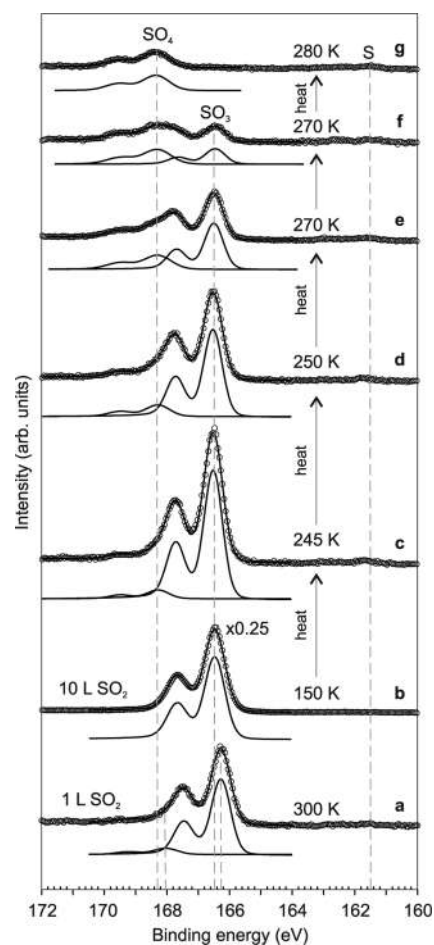


**Figure 6.** S 2p core level spectra ($h\nu$ = 260 eV) from $SO_2$-exposed $Cu_2O(111)$. (a) Both adsorption and measurement are performed at 300 K. (b) Obtained from a surface at 150 K exposed to 10 L of $SO_2$. (c−e) Spectra obtained after heating this surface (the heating temperature is given for every spectrum in the figure).

a $SO_2$-saturated surface. The area of this peak is about four times larger but only shifted with 0.2 eV to higher binding energy compared to the spectrum obtained at room temperature. The factor four between $SO_2$ coverages at 150 K and at room temperature is in agreement with the coverage estimations in Table 2, which are based on O 1s spectra. Thus, $SO_2$ appears to form $SO_3$ species through interaction with oxygen sites in the $Cu_2O(111)$ surface. At room temperature, $SO_2$ adsorbs on approximately half of the $O_{MCUS}$ sites forming 0.1 monolayer (ML) of $SO_3$. At 150 K, $SO_2$ adsorbs on both types of $O_{MCUS}$ sites (giving about 0.2 ML) and on the same amount of other oxygen sites (0.2 ML)

giving in total 0.4 ML of $SO_3$. The additional $SO_3$ species (0.3 ML) formed at 150 K are more loosely bound to the surface than the $SO_3$ species formed at room temperature.

When heating the $SO_2$-exposed surface at 150 K to higher temperatures, the $SO_3$-related S 2p line starts to shrink at 210 K, and at 250 K its intensity is just somewhat larger than the S 2p line in Figure 6a obtained after room-temperature exposure of $SO_2$. At the same time as the intensity of this peak decreases, a new peak appears at 168.3 eV, and its intensity increases slowly but continuously. The binding energy of this component and its shift from the $SO_3$-related component are typical for $SO_4$ species on oxide surfaces[51,52,54,55,57] and for sulfate compounds (e.g., $NaSO_4$).[56] At 280 K, all $SO_3$ species either have desorbed or are forming bonds with oxygen sites in the surface giving $SO_4$ species. The coverage of $SO_4$ species (2% of a monolayer) is significantly lower than the coverage of $SO_3$ upon $SO_2$ adsorption at room temperature. However, the latter $SO_4$ coverage is clearly larger than the $SO_4$ coverage upon $SO_2$ adsorption at room temperature. The low coverage shows that $SO_4$ formation should appear at defects such as $O_{MCUS}$.

$SO_4$ could form on $Cu_2O(111)$ either through $SO_2$ bonding to two O sites in the surface or through $SO_2$ disproportionation and oxygen vacancy formation ( $SO_{2,gas} + 2O_{oxide} \rightarrow 2SO_{3,ads} \rightarrow SO_{2,gas} + SO_{4,ads} + O_{vac}$). In both cases, the reaction requires two closely located surface oxygen sites. Since the S–O bond distance in the free $SO_2$ molecule is around 1.43 Å and the nearest-neighbor distance between two oxygen anions in the $Cu_2O(111)$ surface plane is 6.04 Å, the two oxygen sites involved in $SO_4$ formation should not be situated in the same surface plane. Instead, the two oxygen sites involved in the formation of the $SO_4$ molecule should be one oxygen anion in the outer surface layer and one of the neighboring oxygen anions in the second oxygen layer from the surface. In the bulk oxide structure, the distance between the latter two types of oxygen anions is around 3.7 Å. Furthermore, formation of a $SO_4$ molecule most probably involves oxygen sites next to a copper vacancy. It should be noted that every Cu cation is connected to two oxygen anions, where one is in the topmost surface layer and the other in the second oxygen layer. Therefore, the removal of a copper ion in the topmost Cu layer gives one $O_{MCUS}$ ion in the topmost layer and one O anion with one broken bond ($O_{CUS}$) in the second layer. It is very likely that the latter oxygen sites are the ones involved in $SO_4$ formation.

Then remains the question why $SO_3$ is formed at room temperature while $SO_4$ is formed when adsorbing at 150 K and heating to 280 K (approximately room temperature). One possible explanation for this could be that $SO_2$ adsorption on $O_{CUS}$ sites in the second oxygen layer might be possible only at temperatures lower than room temperature when adsorption is performed at low $SO_2$ pressures ($p = 10^{-8} - 10^{-7}$ mbar) in UHV conditions. Adsorption at lower temperature will thus enable $SO_2$ interaction with two oxygen sites, or in the case of $SO_2$ disproportionation, it will enable interaction between two $SO_{3,ads}$. $SO_4$ may form at room temperature at higher $SO_2$ pressures due to different kinetics. However, more experimental as well as theoretical studies are needed to find the exact reaction pathway and kinetics for the $SO_3$ to $SO_4$ conversion on $Cu_2O(111)$.

We hope that the work presented here will stimulate studies, theoretical as well as experimental, which further investigate $Cu_2O$ surfaces and their chemical properties.

## CONCLUSIONS

The $Cu_2O(111)$ surface has been investigated with high-resolution photoemission and scanning tunneling microscopy (STM). Although oxygen vacancies are the most prominent defects in STM images, copper vacancies are shown to be more important in both $H_2O$ and $SO_2$ surface chemistry. The O 1s spectrum of the clean surface contains, in addition to the main O 1s component, a component shifted from the main peak with 1.1–1.2 eV to lower energy. We tentatively assign this component to surface oxygen anions with more than one broken bond, i.e., surface oxygen anions at a copper vacancy, a step, or a kink. This component appears as being a sum of at least two components representing two types of multiply undercoordinated oxygen anions ($O_{MCUS}$). $O_{MCUS}$ anions are shown to be adsorption sites for both hydrogen from dissociated water and for $SO_2$ forming $SO_3$. Copper vacancies are thus important in the stabilization of both OH and $SO_3$ species on the $Cu_2O(111)$ surface. No water adsorbs at room temperature, but adsorption of 1 Langmuir water (1 L = $10^{-6}$ Torr s) at 150 K gives a fraction of a monolayer dissociated water and a layer of molecular water. At 180 K, molecular water desorbs, and only hydroxyl groups remain. At room temperature, $SO_2$ interacts with one of the two types of $O_{MCUS}$ sites. At 150 K, $SO_3$ species are formed to a much larger extent than at RT, and both types of $O_{MCUS}$ sites and other oxygen sites are involved. These $SO_3$ species start to desorb at 210 K, and $SO_4$ species start to appear. When heating up to 280 K, a continuous desorption of $SO_3$ species appears simultaneously with a slow increase of the amount of $SO_4$ species until only $SO_4$ species remain on the surface. We suggest that $SO_4$ forms through $SO_2$ interaction with two oxygen sites connected to the same copper vacancy (an $O_{MCUS}$ in the topmost oxygen layer and a singly coordinatively unsaturated oxygen anion ($O_{CUS}$) in the second oxygen layer). $SO_2$ interaction with $O_{CUS}$ sites in the second topmost oxygen layer might be enabled by low temperature and possibly by higher $SO_2$ pressure.

## ASSOCIATED CONTENT

**Ⓢ Supporting Information**

Additional experimental details. This material is available free of charge via the Internet at http://pubs.acs.org.

## AUTHOR INFORMATION

**Corresponding Author**

*E-mail: onsten@kth.se. Phone: +46 (0)87904162. Fax: +46 (0)87527782.

**Notes**

The authors declare no competing financial interest.

## ACKNOWLEDGMENTS

## REFERENCES

(1) Nikitine, S.; Grun, J. B.; Sieskind, M. Etude spectrophotometrique de la serie jaune de $Cu_2O$ aux basses temperatures. *J. Phys. Chem. Solids* **1961**, *17*, 292–300.

19362

dx.doi.org/10.1021/jp3112217 | *J. Phys. Chem. C* 2013, 117, 19357–19364

(2) Uihlein, C.; Fröhlich, D.; Kenklies, R. Investigation of exciton fine structure in Cu₂O. *Phys. Rev. B* **1981**, *23*, 2731−2740.

(3) Rai, B. Cu₂O solar cells: A review. *Sol. Cells* **1988**, *25*, 265−272.

(4) Musa, A.; Akomolafe, T.; Carter, M. Production of cuprous oxide, a solar cell material, by thermal oxidation and a study of its physical and electrical properties. *Sol. Energy Mater. Sol. Cells* **1998**, *51*, 305−316.

(5) Jeong, S.; Mittiga, A.; Salza, E.; Masci, A.; Passerini, S. Electrodeposited ZnO/Cu₂O heterojunction solar cells. *Electrochim. Acta* **2008**, *53*, 2226−2231.

(6) Hara, M.; Kondo, T.; Komoda, M.; Ikeda, S.; Shinohara, K.; Tanaka, A.; Kondo, J.; Domen, K. Cu₂O as a photocatalyst for overall water splitting under visible light irradiation. *Chem. Commun.* **1998**, *3*, 357−358.

(7) Nian, J.-N.; Hu, C.-C.; Teng, H. Electrodeposited p-type Cu₂O for H₂ evolution from photoelectrolysis of water under visible light illumination. *Int. J. Hydrogen Energy* **2008**, *33*, 2897−2903.

(8) Paracchino, A.; Laporte, V.; Sivula, K.; Grätzel, M.; Thimsen, E. Highly active oxide photocathode for photoelectrochemical water reduction. *Nat. Mater.* **2011**, *10*, 456−461.

(9) Sun, S.; Song, X.; Sun, Y.; Deng, D.; Yang, Z. The crystal-facet-dependent effect of polyhedral Cu₂O microcrystals on photocatalytic activity. *Catal. Sci. Technol.* **2012**, *2*, 925−930.

(10) Morales, J.; Sanchez, L.; Bijani, S.; Martinez, L.; Gabaz, M.; Ramos-Barrado, J. R. Electrodeposition of Cu₂O? An Excellent Method for Obtaining Films of Controlled Morphology and Good Performance in Li-Ion Batteries. *Electrochem. Solid State Lett.* **2005**, *8*, A159−A162.

(11) Soon, A.; Todorova, M.; Delley, B.; Stampfl, C. Surface oxides of the oxygen-copper system: Precursors to the bulk oxide phase? *Surf. Sci.* **2007**, *601*, 5809−5813.

(12) Solomon, E. I.; Jones, P. M.; May, J. A. Electronic structures of active sites on metal oxide surfaces: definition of the copper-zinc oxide methanol synthesis catalyst by photoelectron spectroscopy. *Chem. Rev.* **1993**, *93*, 2623−2644.

(13) Vissokov, G. P. Plasma-chemical preparation of nanostructured catalysts for low-temperature steam conversion of carbon monoxide: properties of catalysts. *Catal. Today* **2004**, *89*, 213−221.

(14) Vissokov, G. P. Plasma-chemical preparation of nanostructured catalysts for low-temperature steam conversion of carbon monoxide: catalytic activity. *Catal. Today* **2004**, *89*, 223−231.

(15) Leygraf, C.; Graedel, T. *Atmospheric Corrosion*; Wiley: New York, 2000.

(16) Soon, A.; Todorova, M.; Delley, B.; Stampfl, C. Thermodynamic stability and structure of copper oxide surfaces: A first-principles investigation. *Phys Rev. B* **2007**, *75*, 125420.

(17) Soon, A.; Cui, X.-Y.; Delley, B.; Wei, S.-H.; Stampfl, C. Native defect-induced multifarious magnetism in nonstoichiometric cuprous oxide: First-principles study of bulk and surface properties of Cu₂−δO. *Phys. Rev. B* **2009**, *79*, 035205.

(18) Islam, M. M.; Diawara, B.; Maurice, V.; Marcus, P. Bulk and surface properties of Cu₂O: A first-principles investigation. *J. Mol. Struct. Theochem* **2009**, *903*, 41−48.

(19) Harmer, S. L.; Skinner, W. M.; Buckley, A. N.; Fan, L.-J. Species formed at cuprite fracture surfaces; observation of O 1*s* surface core level shift. *Surf. Sci.* **2009**, *603*, 537−545.

(20) Schulz, K. H.; Cox, D. F. Photoemission and low-energy-electron-diffraction study of clean and oxygen-dosed Cu₂O(111) and (100) surfaces. *Phys. Rev. B* **1991**, *43*, 1610−1621.

(21) Önsten, A.; Göthelid, M.; Karlsson, U. O. Atomic structure of Cu₂O(111). *Surf. Sci.* **2009**, *603*, 257−264.

(22) Islam, M. M.; Diawara, B.; Maurice, V.; Marcus, P. First principles investigation on the stabilization mechanisms of the polar copper terminated Cu₂O(111) surface. *Surf. Sci.* **2009**, *603*, 2087−2095.

(23) Li, C.; Wang, F.; Li, S. F.; Jia, Y. Stability and electronic properties of the O-terminated Cu₂O(111) surfaces: First-principles investigation. *Phys. Lett. A* **2010**, *374*, 2994−2998.

(24) Li, M.; Zhang, J.; Zhang, Y.; Zhang, G.; Wang, T. Density functional theory calculations of surface properties and H2 adsorption on the Cu₂O(111) surface. *Appl. Surf. Sci.* **2011**, *257*, 10710−10714.

(25) Nygren, M. A.; Pettersson, L. G. M. H₂O interaction with the polar Cu₂O(100) surface: A theoretical study. *J. Phys. Chem.* **1996**, *100*, 1874−1878.

(26) Casarin, M.; Maccato, C.; Vigato, N.; Vittadini, A. A theoretical study of the H₂O and H₂S chemisorption on Cu₂O(111). *Appl. Surf. Sci.* **1999**, *142*, 164−168.

(27) Duan, Y.; Zhang, K.; Xie, X. Theoretical studies of CO and NO on CuO and Cu₂O(110) surfaces. *Surf. Sci.* **1994**, *321*, L249−L254.

(28) Fernández-García, M.; Conesa, J. C.; Bagus, P. S.; Rubio, J.; Illas, F. Bonding geometry and mechanism of NO adsorbed on Cu₂O(111): NO activation by Cu⁺ cations. *J. Chem. Phys.* **1994**, *101*, 10134−10139.

(29) McClenaghan, N. D.; Hu, P.; Hardacre, C. A density functional theory study of the surface relaxation and reactivity of Cu₂O(100). *Surf. Sci.* **2000**, *464*, 223−232.

(30) Bredow, T.; Pacchioni, G. Comparative periodic and cluster ab initio study on Cu₂O(111)/CO. *Surf. Sci.* **1997**, *373*, 21−32.

(31) Bredow, T.; Márquez, A. M.; Pacchioni, G. Analysis of electronic contributions to the vibrational frequency of CO/Cu₂O(111). *Surf. Sci.* **1999**, *430*, 137−145.

(32) Sun, B.-Z.; Chen, W.-K.; Wang, X.; Lu, C.-H. Comparative periodic and cluster ab initio study on Cu₂O(111)/CO. *Appl. Surf. Sci.* **2007**, *253*, 7501−7505.

(33) Jiang, Y.; Adams, J. B.; Sun, D. Benzotriazole Adsorption on Cu₂O(111) Surfaces: A First-Principles Study. *J. Phys. Chem. B* **2004**, *108*, 12851−12857.

(34) Scarano, D.; Bordiga, S.; Lamberti, C.; Spoto, G.; Ricchiardi, G.; Zecchina, A.; Areán, C. O. FTIR study of the interaction of CO with pure and silica-supported copper(I) oxide. *Surf. Sci.* **1998**, *411*, 272−285.

(35) Denecke, R.; Väterlein, P.; Bässler, M.; Wassdahl, N.; Butorin, S.; Nilsson, A.; Rubensson, J.- E.; Nordgren, J.; Mårtensson, N.; Nyholm, R. Beamline I511 at MAX II, capabilities and performance. *J. Electron Spectrosc. Relat. Phenom.* **1999**, *101−103*, 971−977.

(36) Hüfner, S. *Photoelectron Spectroscopy*; Springer: New York, 2003.

(37) Haija, M. A.; Guimond, S.; Uhl, A.; Kuhlenbeck, H.; Freund, H.-J. Adsorption of water on thin V₂O₃(0001) films. *Surf. Sci.* **2006**, *600*, 1040−1047.

(38) Henderson, M. A.; Chamber, S. A. HREELS, TPD and XPS study of the interaction of water with the a-Cr₂O₃(001) surface. *Surf. Sci.* **2000**, *449*, 135−150.

(39) Maurice, V.; Cadot, S.; Marcus, P. Hydroxylation of ultra-thin films of a-Cr₂O₃(0001) formed on Cr(110). *Surf. Sci.* **2001**, *471*, 43−58.

(40) Joseph, Y.; Ranke, W.; Weiss, W. Water on FeO(111) and Fe₃O₄(111): Adsorption Behavior on Different Surface Terminations. *J. Phys. Chem. B* **2000**, *104*, 3224−3236.

(41) Wang, L.-Q.; Baer, D. R.; Engelhard, M. H.; Shultz, A. N. The adsorption of liquid and vapor water on TiO₂(110) surfaces: the role of defects. *Surf. Sci.* **1995**, *344*, 237−250.

(42) Hugenschmidt, M. B.; Gamble, L.; Campbell, C. T. The interaction of H₂O with a TiO₂(110) surface. *Surf. Sci.* **1994**, *302*, 329−340.

(43) Peng, X. D.; Barteau, M. A. Characterization of oxide layers on Mg(0001) and comparison of H₂O adsorption on surface and bulk oxides. *Surf. Sci.* **1990**, *233*, 283−292.

(44) Ozensoy, E.; Szanyi, J.; Peden, C. H. F. Interaction of Water with Ordered θ-Al₂O₃ Ultrathin Films Grown on NiAl(100). *J. Phys. Chem. B* **2005**, *109*, 3431−3436.

(45) Henderson, M. A. The interaction of water with solid surfaces: fundamental aspects revisited. *Surf. Sci. Rep.* **2002**, *46*, 1−308.

(46) Ghijsen, J.; Tjeng, L. H.; van Elp, J.; Eskes, H.; Westerink, J.; Sawatzky, G. A.; Czyzyk, M. T. Electronic structure of Cu₂O and CuO. *Phys. Rev. B* **1988**, *38*, 11322−11330.

(47) Bruneval, F. Exchange and correlation in the electronic structure of solids from silicon to cuprous oxide: GW approximation and beyond. *PhD Thesis*, Ecole Polytechnique, Palaiseau, France; 2005.

(48) Fujimori, A.; Saeki, M.; Kimizuka, N.; Taniguchi, M.; Suga, S. Photoemission satellites and electronic structure of $Fe_2O_3$. *Phys. Rev. B* **1986**, *34*, 7318−7328.

(49) Prins, R. Intensities in the X-ray photoelectron spectra and electronic structures of the oxyanions of Si, P, S, Cl, Mn, and Cr. *J. Chem. Phys.* **1974**, *61*, 2580−2591.

(50) *Handbook of Chemistry and Physics*, 74th ed.; Lide, D. R., Ed.; CRC Press: Boca Raton, FL, 1993/94.

(51) Rodriguez, J. A.; Liu, P.; Pérez, M.; Liu, G.; Hrbek, J. Destruction of $SO_2$ on Au and Cu Nanoparticles Dispersed on MgO(100) and $CeO_2$(111). *J. Phys. Chem. A* **2010**, *114*, 3802−3810.

(52) Rodriguez, J. A.; Jirsak, T.; Chaturvedi, S.; Kuhn, M.; González, L.; Maiti, A. Studies on the Behavior of Mixed-Metal Oxides and Desulfurization: Reaction of $H_2S$ and $SO_2$ with $Cr_2O_3$(0001), MgO(100), and $Cr_xMg_{1−x}O$(100). *J. Am. Chem. Soc.* **2010**, *122*, 12362−12370.

(53) Stoltz, D.; Önsten, A.; Karlsson, U. O.; Göthelid, M. High resolution spectroscopic and microscopic signatures of ordered growth of ferrous sulfate in $SO_2$ assisted corrosion of $Fe_3O_4$(100). *Appl. Phys. Lett.* **2007**, *91*, 093107.

(54) Rodriguez, J. A.; Jirsak, T.; Freitag, A.; Larese, J. Z.; Maiti, A. Interaction of $SO_2$ with MgO(100) and Cu/MgO(100): Decomposition reactions and the formation of $SO_3$ and $SO_4$. *J. Phys. Chem. B* **2000**, *104*, 7439−7448.

(55) Rodriguez, J. A.; Jirsak, T.; Chaturvedi, S.; Dvorak, J. Chemistry of $SO_2$ and $NO_2$ on ZnO(0001)-Zn and ZnO powders: changes in reactivity with surface structure and composition. *J. Mol. Catal. A: Chem.* **2001**, *167*, 47−57.

(56) Lindberg, B. J.; Hamrin, K.; Johansson, G.; Gelius, U.; Fahlman, A.; Nordling, C.; Siegbahn, K. Molecular Spectroscopy by Means of ESCA. *Phys. Scr.* **1970**, *1*, 28−298.

(57) Rodriguez, J. A.; Liu, G.; Jirsak, T.; Hrbek, J.; Chang, Z.; Dvorak, J.; Maiti, A. Activation of gold on titania: Adsorption and reaction of $SO_2$ on $Au/TiO_2$(110). *J. Am. Chem. Soc.* **2002**, *124*, 5242−5250.

**19364**

dx.doi.org/10.1021/jp3112217 | *J. Phys. Chem. C* 2013, 117, 19357−19364

# Oxidation of Al–Pd–Mn quasicrystal surfaces

D. Popović *, D. Naumović, M. Bovet, C. Koitzsch, L. Schlapbach, P. Aebi

*Institut de Physique, Université de Fribourg, Pérolles, CH-1700 Fribourg, Switzerland*

## Abstract

The oxidation of both, quasicrystalline and crystalline surfaces of an icosahedral Al–Pd–Mn quasicrystal cut perpendicular to its five-fold axis and of Al(1 1 1) has been studied by means of X-ray photoelectron spectroscopy, ultraviolet photoemission spectroscopy, low-energy electron diffraction and X-ray photoelectron diffraction. The oxidation of the elements of the alloy is quantified and compared for the different phases and Al(1 1 1). The quasicrystalline surface is found to react less with oxygen than the crystalline surface and more rapidly compared to Al(1 1 1). The observed behaviour is discussed in terms of the termination of the corresponding surfaces. © 2001 Elsevier Science B.V. All rights reserved.

*Keywords:* Oxidation; Alloys; Aluminum; Photoelectron spectroscopy

## 1. Introduction

Quasicrystals are well-ordered metal alloys with no translational symmetry. This unusual property attracts the attention of fundamental research. On the other hand, quasicrystals offer some interesting features for applications, such as low coefficient of friction, low surface energy, high electrical resistivity and hardness, but low thermal conductivity [1–3]. The possibilities for applications have initiated the investigation of the oxidation of quasicrystal surfaces.

Both, crystalline (c-) and quasicrystalline (qc-) surfaces can be prepared on the bulk icosahedral (i-) Al–Pd–Mn quasicrystal by specific sputtering and annealing treatment [4,6]. From previous

work [7–9] it is known that the qc-Al–Pd–Mn surfaces oxidise in a two-step process (chemisorption of oxygen followed by oxide formation), forming a thin, passivating and spatially inhomogeneous oxide layer. The oxidation resembles that of elemental Al. Thin oxide layers (5 Å) form under ultra-high vacuum (UHV) conditions. Thicker layers grow (up to 100 Å) if the oxygen exposure is performed in a more aggressive environment [8,9]. Previous work [7–9] also reported that Al is the only element to oxidise and segregate at the surface whereas the other elements of the alloy appear to oxidise only in the presence of water [8–10]. Saturation of the oxidation process is reported at exposures around 50 L [7] or 80 L [8,10,11] (1 Langmuir (L) = $10^{-6}$ Torr s) and oxidation is pressure dependent [12]. Low-energy electron diffraction (LEED) spots disappear at 20–25 L [7], indicating the destruction of the long-range order. The surface energy and the friction

* Corresponding author. Tel.: +41-26-300-9088; fax: +41-26-300-9747.

*E-mail address:* dunja.popovic@unifr.ch (D. Popović).

coefficient of the oxidised quasicrystalline surface are lower than for Al-oxide and make quasicrystals attractive for surface coating applications [2].

In the c-surface, oxidation of Mn [11] and Pd [10] occurs as well. It is reported that Al enrichment of the surface is weaker in the c-phase than in the qc-phase [10], but that the oxidation is stronger [3]. Larger amounts of aluminium and almost all manganese at the surface are oxidised and thicker oxides are formed [3,10].

The study of oxidation has also been performed on other quasicrystals, such as Al–Cu–Fe [10,11, 13–15].

Upon exposure to oxygen, elemental Al forms a protective, passivating, amorphous oxide layer [16,17]. The LEED pattern disappears at exposures of the order of 1000 L for the close-packed (1 1 1) face and at one order of magnitude smaller exposures for (1 1 0) and (0 0 1) faces [16,18,19]. The latter immediately develop bulk-like oxide films, because of their more open geometry, whereas the (1 1 1) face goes through a two-step oxidation (chemisorption of oxygen followed by oxide formation) [16,20,21]. In a high-resolution synchrotron-radiation study five different peaks appear in the Al 2p X-ray photoelectron spectroscopy (XPS) line of the Al(1 1 1) surface exposed to oxygen [16]. The substrate core levels shift due to the charge transfer between oxygen atoms and the substrate [22]. Two peaks in the valence band of Al(1 1 1) appear at 7.1 and 9.8 eV below the Fermi edge, related to the O 2p orbitals perpendicular ($\sigma$) and parallel ($\pi$) to the surface, respectively [19]. The transformation of the second peak into a continuum of states signalises the formation of the oxide [23]. The oxidation of Al(1 1 1) is a pressure-dependent process [24] and differences exist between oxidation in pure oxygen or water [20,25].

The aim of this work is to quantify the differences between the oxidation of quasicrystalline and crystalline surfaces of i-Al–Pd–Mn in pure oxygen and to characterise the changes upon exposures to oxygen using different techniques, i.e., XPS, X-ray photoelectron diffraction (XPD), ultraviolet photoemission spectroscopy (UPS) and LEED. The Al–Pd–Mn qc-surface is Al-rich [26,27] and, in order to examine the similarities with the oxidation of Al, an Al(1 1 1) crystal was used in the oxidation experiments for comparison.

## 2. Experimental

The i-Al–Pd–Mn quasicrystal ingot has been grown using the Czochralsky method in CECM–CNRS, Vitry-sur-Seine, France. It has been polished with diamond paste and oriented with its five-fold axis normal ($\pm 3°$) to the surface. Its stoichiometry was determined to be $Al_{70.3}Pd_{21.4}Mn_{8.3}$. The shape of the sample is a half disk, 2 mm thick and more than 10 mm in diameter. The qc-surface is a bulk-terminated icosahedral surface prepared by sputtering and annealing [6]. The c-surface can be interpreted as five domains of a cubic bcc Al–Pd crystalline alloy oriented perpendicularly to its [1 1 3] direction [5] and is prepared on the i-Al–Pd–Mn by $Ar^+$ sputtering without annealing [6].

Contamination-free surfaces were obtained by successive cycles of $Ar^+$ sputtering at 0.5–1.5 kV and annealing during approximately 15 min. The annealing temperature was controlled with a pyrometer. For the qc-Al–Pd–Mn surface the annealing temperature was 620°C and for Al(1 1 1) 500 °C. For c-Al–Pd–Mn the surface was not annealed [6]. The cleanliness of the surface was checked with UPS [22] and cleaning cycles were repeated until no features on the position of O 2p derived states were observed. LEED was used to check the surface ordering for the qc-surface and Al(1 1 1). Compositions were determined with cross-section corrected XPS core-level peak areas. The XPD patterns served for near-surface geometrical structure analysis. [1] Oxidations have been performed at $1 \times 10^{-8}$ mbar for exposures smaller than 10 L; $5 \times 10^{-8}$ mbar for medium exposures and $7 \times 10^{-8}$ mbar for exposures larger than 100 L.

---

[1] The emitted photoelectron wave from a chosen core-level scatters at the surrounding atoms and interferes with the directly emitted wave to give an interference pattern as a function of emission angle. This strongly anisotropic angular distribution of photoelectrons then gives the possibility to obtain a basic picture of the local, real-space environment of the emitter, due to the "forward focusing" phenomenon. (For a detailed review on XPD, see e.g., Ref. [28].)

Oxygen was supplied by back-filling the preparation chamber through a leak valve. The exposure values in units of Langmuirs are not calibrated to the sensitivity of the pressure gauge.

The experimental set-up represents an extended version of the Vacuum Generators ESCALAB Mk II spectrometer, operating with a base pressure in the low $10^{-10}$ mbar region. XPS, XPD and UPS have been performed in the analysis chamber, equipped with a twin-anode X-rays source, an ultraviolet (UV) lamp with monochromator [29] and a hemispherical electron-energy analyser with a three-channeltron detection system. A motorised manipulator allows sample rotation with two degrees of freedom. All the measurements were carried out at room temperature. XPS and XPD (not shown) were performed with Mg K$\alpha$ ($hv = 1253.6$ eV) radiation. The spectra have been measured with a pass energy of 50 eV corresponding to an energy resolution (Mg K$\alpha$ source and analyser) of approximately 1 eV. Normal emission or 45° off-normal emission was used for the X-ray spectra, as will be indicated. The 45° off-normal geometry is more surface sensitive. For technical reasons the Al(1 1 1) surface has only been measured at normal emission. In order to have a quantitative comparison, some of the experiments on Al–Pd–Mn have been performed at normal and 45° off-normal emission. Monochromatised He I radiation ($hv = 21.2$ eV) was used in UPS. All UPS measurements were performed at normal emission. LEED patterns (not shown) were recorded with normal incidence and electron energies of 60 eV.

## 3. Results and discussion

### 3.1. XPS

The compositions for the clean surfaces of the qc- and the c-phase are determined by XPS to be 68.5% Al, 27% Pd and 4.5% Mn and 58.8% Al, 36.7% Pd and 4.5% Mn, respectively. The qc-phase displays the characteristic features of the quasicrystals: five-fold symmetry (as seen from XPD) and a pseudogapped Fermi edge (as seen from UPS), while the crystalline surface has a metallic character (as seen from UPS) [4,6]. The core-level lines of Al and Mn in the qc-phase lie close to their positions in the elemental samples, while the Pd lines are 2 eV shifted towards higher binding energies compared with the ones of elemental Pd [8,9]. The lines of Al and Mn are at the same positions for the qc- and the c-surface of Al–Pd–Mn, while the positions of Pd lines at the c-surface are less shifted towards higher binding energies (<1 eV shift) than in the qc-phase. This is consistent with the reported changes from pure elements to the alloy [8,9]. In the valence band of the alloy, the Pd 4d derived feature is at 4.3 eV below the Fermi edge for the qc-surface, but at 3.7 eV binding energy in the crystalline phase, and the shift is in the same direction as described for the core-levels.

Changes of the core-level spectral lines upon exposure to oxygen are presented in Fig. 1a–d. The vertical arrows indicate oxygen exposure values, A corresponding to 0, 10, 35, 75, 110 L at 45° off-normal emission and B to 0, 20, 75, 150, 225, 300, 375 L at normal emission (sequences from bottom to top). For graphs with results of the qc-phase, exposure to 8400 L at 45° off-normal emission is presented by spectra in grey. The results of a quantitative analysis are shown in Fig. 2.

In Fig. 1a oxidation-induced changes characteristic for the Al 2p emission appear in the spectra of c-, qc-Al–Pd–Mn and Al(1 1 1) surfaces. A second peak appears and grows as a shoulder on the higher binding-energy side of the initial Al 2p peak, which decreases in intensity due to oxygen coverage. The Al 2s peak shows the same behaviour (not shown). As can be seen from the growth in intensity of the shoulder with oxygen exposure, Al oxidises less in Al(1 1 1) (Fig. 1a, bottom) than in qc-Al–Pd–Mn (Fig. 1a, middle), but less in qc-Al–Pd–Mn than in c-Al–Pd–Mn (Fig. 1a, top). Spectra presented in Fig. 1a are taken at 45° off normal for c-Al–Pd–Mn, where the measurement is more surface sensitive and at normal emission for qc-Al–Pd–Mn and Al(1 1 1), but the same conclusions follow from the examination of spectra taken at 45° off-normal emission (not shown) for both Al–Pd–Mn surfaces. In addition, exposures B consist of significantly higher doses than exposures A.

The Al 2p line has been fitted by a linear combination of the metallic emission peak, a Gaussian representing the appearing oxygen-related peak
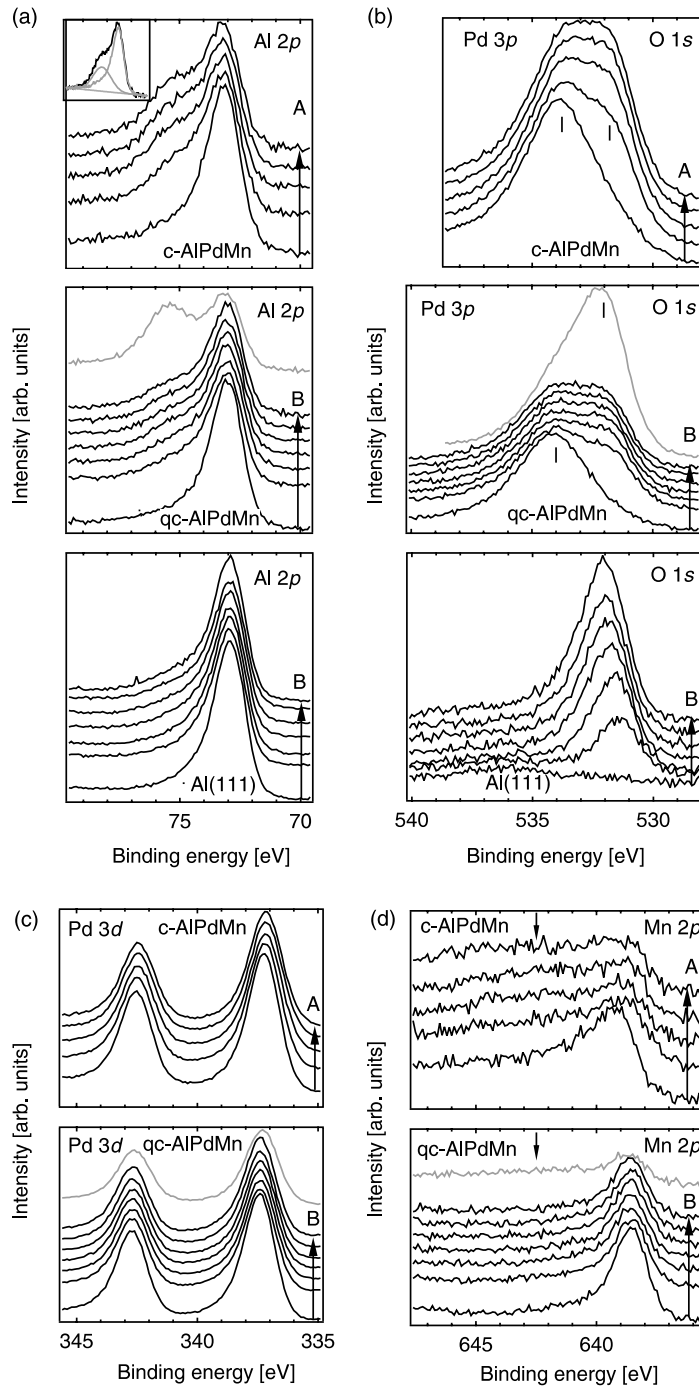
Fig. 1. XPS spectra of (a) Al 2p, (b) Pd $3p_{3/2}$ and O 1s, (c) Pd 3d and (d) Mn $2p_{3/2}$ core-level emission from qc-, c-Al–Pd–Mn and Al(1 1 1). The arrows are indicating oxygen exposure values: A: 0, 10, 35, 75, 110 L at 45° off-normal emission and B: 0, 20, 75, 150, 225, 300, 375 L at normal emission (sequences from bottom to top). Exposure of 8400 L is performed at 45° off-normal emission and presented in grey. The inset shows a typical fitting in the case of Al 2p (c-Al–Pd–Mn at 110 L of $O_2$ exposure).
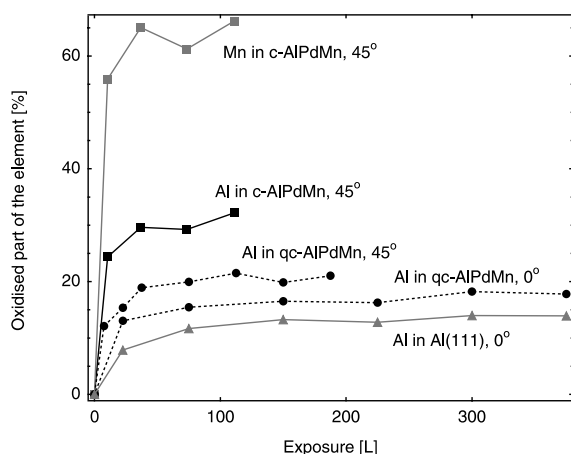
Fig. 2. Percentages of oxidised Al (Mn) in total amount of Al (Mn) atoms. Surfaces as indicated. The Al(1 1 1) surface has only been measured at normal emission and results on Al–Pd–Mn at both normal and 45° off-normal emission are presented in order to have a quantitative comparison with both c-Al–Pd–Mn and Al(1 1 1).

and a linear function, representing the linear background of the fitted spectrum (the inset in Fig. 1a presents a result for oxidised c-Al–Pd–Mn). The Al 2p peak of the clean surface has an asymmetrically-broadened form, characteristic for metals [22,30]. The linear-background subtracted spectrum of the clean surface was used to represent the metallic substrate emission. The underlying idea that its shape remains unchanged during the oxidation, has been also applied in other fitting procedures [25,31].

For the estimation of the growth of the oxygen/oxide layer the investigation of the O 1s peak was performed (Fig. 1b). O 1s and Pd 3p$_{3/2}$ are energetically very close (Fig. 1b, top and middle) and each spectrum was fitted with the metallic Pd 3p$_{3/2}$ peak, a Gaussian shape for O 1s and a linear background. The linear-background subtracted spectrum of the clean surface was used as Pd 3p$_{3/2}$ peak in the fitting. O 1s spectra on the Al(1 1 1) surface (Fig. 1b, bottom) were fitted with a Gaussian function and a linear background. All parameters used in the fitting procedures throughout this work were variable.

Concerning the Pd 3d lines, it is known from previous work [8] that, upon oxidation, elemental palladium 3d lines broaden and shift towards

higher binding energies. The position of the palladium lines in the qc-surface is already shifted by 2 eV towards higher binding energies with respect to the position of elemental palladium, and according to Ref. [9] the expected oxidation-induced shift is towards lower binding energies for the qc-surface.

In Fig. 1c we observe a decrease of the total intensity of the Pd 3d line of the Al–Pd–Mn surfaces with increasing exposures to oxygen. This signalises that, due to the growing coverage of the oxygen/oxide, the Pd signal from the alloy declines. A shift, smaller than 0.2 eV, towards lower binding energies can be noticed, more pronounced in the crystalline phase. According to Ref. [9], this is expected for the oxidised surface, but is not in agreement with reported results [8], where a shift of 0.1 eV towards higher binding energies is measured. We observe no changes of the spectral-line widths or asymmetries. The latter indicates that the palladium density of states near the Fermi level does not change significantly and that there is consequently no change of the environment related to oxygen bonding [32]. The Pd 3d shift could also indicate a change of environment due to the oxidation of other elements in the alloy. If palladium oxidises, the proportions of this effect are quite weak: a small shift is observed, but no spectral-line broadening. This is in agreement with the previously found inertness of pure metallic palladium [8]. The changes of Pd lines in qc- and c-Al–Pd–Mn surfaces are comparable and the claim of oxidation in one case would have to apply to the other as well, contrary to the reported oxidation of Pd only in the c-phase [10].

Mn in qc-Al–Pd–Mn does not oxidise for exposures up to 375 L, the metallic emission simply decreases, like in the case of Pd (Fig. 1d, bottom). The spectra along the B arrow all show absence of features on the higher binding-energy side of the metallic peak (Fig. 1d, bottom). Line shifts or changes in the line shape have not been noticed. In c-Al–Pd–Mn Mn oxidises to a very high extent: the metallic Mn line declines in intensity and another peak grows on its high binding-energy side from the lowest exposures (Fig. 1d, top, arrow points at the oxygen-induced peak). The same analysis procedure as described for Al 2p (Fig. 2) was applied in this situation.

Spectra in grey (Fig. 1) show that upon exposure of qc-Al–Pd–Mn to 8400 L of oxygen, Al oxidises to a great extent (Fig. 1a, middle), O 1s peak grows correspondingly (Fig. 1b middle), signs of oxidation of Mn are visible (Fig. 1d, bottom) and Pd 3d shifts more than for the moderate exposures (Fig. 1c, bottom). Mn has been considered not to oxidise at all under UHV at room temperature and not even after exposure to air (if not very humid) [8–10]. We show unambiguously that oxidation of Mn happens even in UHV at room temperature, for extremely large exposures (Fig. 1d, bottom, spectrum in grey). The arrow points at the oxygen-related feature appearing in the same way as for the c-surface (Fig. 1d, top). Note, that the spectral shape in the region of the arrow changes from a downward to an upward curvature upon oxidation.

In Fig. 2 we present how the percentage of the element which is oxidised, within the probing depth, changes with exposure. The percentage of the element which is oxidised is calculated as the ratio of the oxidation-induced shoulder area and the total peak area. Quantitative analysis (Fig. 2) confirms our observations of the changes visible in the raw spectra (Fig. 1). More than 50% of Mn oxidises in the c-Al–Pd–Mn, exceeding percentages of oxidised Al in both Al–Pd–Mn phases. Al also oxidises more in the crystalline than in the quasicrystalline phase. Finally, Al oxidises more in the alloy than in Al(1 1 1), a fact that is not merely a consequence of our probing depth. The Al density in the volume probed with XPS of the Al(1 1 1) surface is homogeneous. The structure of the qc-surface of Al–Pd–Mn is described in the model by Gierer et al. [26,27], which is based on the bulk structure proposed by Boudard et al. [33] and de Boissieu [34]. In the profile of the qc-surface in this model, there are four different types of layers and three of them contain aluminium. Within the first 5 Å there are eight layers and only one of them without aluminium. This distribution continues down to 20 Å depth, which means that the distribution of Al is also homogeneous at this scale, as in the bulk of the quasicrystal. The same holds for the c-Al–Pd–Mn, since its periodic structure guarantees uniform distribution of atoms of different elements on the scale of the order of 10 Å

(mean free path of XPS) or more. The fact that we do not probe only the topmost Al-rich layer of the qc-surface and that all the surfaces have a uniform composition at the relevant depth scale, enables the comparison of the quantity of oxidised Al among the different surfaces examined.

The XPD pattern taken at the oxygen $KL_{23}L_{23}$ Auger transition line (not shown) does not display any anisotropy. This confirms the formation of a disordered oxide. XPD patterns of the clean c-surface show anisotropy characteristic for its specific structure [6]. Upon exposure to oxygen, these patterns become blurred for the Al and Pd emission, but visible up to the highest exposures. No image anisotropy is seen for the Mn emission on the crystalline surface after 110 L oxygen exposure, which is consistent with the high degree of oxidation of this element in the crystalline phase.

The alloy composition (Fig. 3) has been calculated to yield 100% for Al, Pd and Mn, while the percentage of O adds to that. Surface segregation of Al occurs in both Al–Pd–Mn phases (Fig. 3a) and segregation of Mn occurs in c-Al–Pd–Mn (Fig. 3b). The contribution of Pd is decreasing in both phases (Fig. 3c), as well as Mn in the quasicrystalline phase (Fig. 3b). The compositions of the clean qc-Al–Pd–Mn and c-Al–Pd–Mn are different, but relative changes are stronger in the crystalline phase (Fig. 3). The percentage of Pd (Fig. 3c), for instance, changes by less than 10% in the quasicrystalline phase subjected to exposures up to 375 L; for the crystalline phase this change is 15% for exposure of 110 L. It is known that the diffusivity of specific elements in the quasicrystals is at least one order of magnitude smaller than the diffusivities of elemental samples of its components [35]. The diffusivity in the crystalline phase is also larger than the one of the quasicrystalline phase [36]. This is consistent with the noticed line-position changes in these phases from the beginning of Section 3.1, suggesting that the properties of the crystalline phase are between the ones of the quasicrystal and the elemental crystals. Thus we observe stronger segregation in the c-Al–Pd–Mn than in the qc-Al–Pd–Mn. Both percentages of Al and Mn have increased in the crystalline surface during the oxidation process, but the relative increase of Mn is larger. The heats of formation of
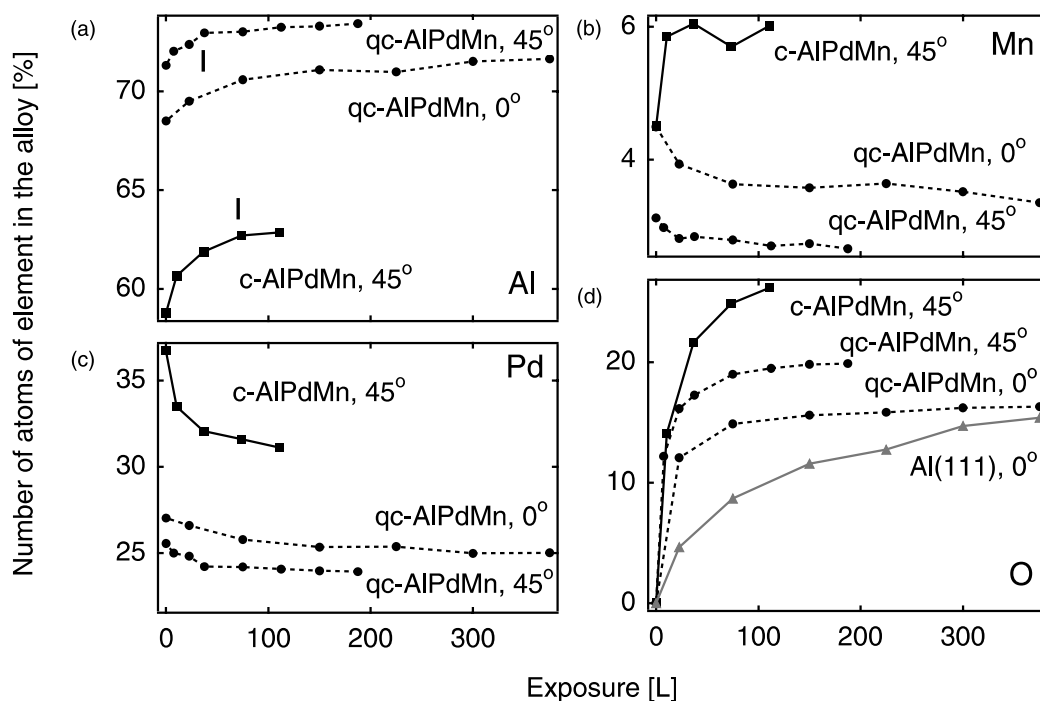
Fig. 3. Number of atoms of (a) Al, (b) Mn, (c) Pd and (d) O in oxidised surfaces. Percentages of the first three add up to 100. Percentage of O is given in addition of the clean sample 100% and as the percentage of clean sample total atoms. Markers are indicating the saturation points: 40 L for the qc-Al–Pd–Mn and 75 L for the c-Al–Pd–Mn. Surfaces as indicated.

the bulk oxides of Al and Mn are $-1676$ to $-1657$ kJ/mol for $Al_2O_3$ and $-1388$ kJ/mol for $Mn_3O_4$, respectively, much larger than $-85$ kJ/mol for PdO [37]. This explains why both Al and Mn strongly oxidise and segregate at the surface, contrary to the behaviour observed in the quasicrystalline phase.

It is important to notice that a layer-by-layer compositional structure as in the case of the qc-surface, with the exponential decay of XPS sensitivity with depth in the substrate, would not show any significant surface segregation effect if only a coverage of oxygen (lower than 15 Å, which is the case in our experiment) is added on top. This goes along with the discussed homogeneous distribution of the elements on the scales of the order of 20 Å and the XPS mean free paths that are certainly above 5 Å. The observed XPS intensity changes can only be explained by significant segregation, i.e. diffusion of Al, which is confirmed by the observed Al-oxide formation. It is difficult to conclude

whether diffusion of Al only from the topmost two layers of the qc-surface into the oxygen overlayer is sufficient to give the observed rate of Al-segregation, or whether the diffusion of atoms from deeper layers in the qc-surface is needed.

The increasing percentage of oxygen, added to exceed the 100% of the clean-sample composition, is shown in Fig. 3d. The amount of oxygen in the crystalline phase is the largest. The oxygen percentage in Al(1 1 1) grows slower and remains below the one in qc-Al–Pd–Mn, approaching the value at which the quasicrystal has saturated. A calculation of the sticking coefficient for the clean surface [2] gives a six times larger value for the quasicrystal than for Al(1 1 1).

The composition changes in Al–Pd–Mn saturate approximately around 75 L in the crystalline

---

[2] The determination of the sticking coefficient is described in Ref. [38].

and around 40 L in the quasicrystalline phase (Fig. 3), consistent with the previous results [7–9]. The saturation values are marked in Fig. 3a, where it is best seen.

The positions of oxygen-related peaks are shifting towards higher binding energies with increasing exposures, as determined from the fitting procedure. The Pd 3d doublet shifts towards lower binding energies. In both, qc-Al–Pd–Mn and Al(1 1 1) the final position of O 1s is 532 eV and that of the Al 2p shoulder is 75.2 eV, in agreement with the literature values for $Al_2O_3$ on Al(1 1 1) [20,25]. Shifts of the Al and Mn oxygen-induced shoulders are more pronounced in the crystalline phase, consistent with the larger oxygen uptake in this phase.

## 3.2. UPS

Upon exposure to oxygen O 2p derived features appear in the valence band region of Al(1 1 1) and the Al–Pd–Mn surfaces (Fig. 4a–c). They consist of one main peak, around 7 eV binding energy, and a shoulder on the higher binding-energy side, at approximately 9 eV below the Fermi edge, in agreement with the literature values for oxygen on Al(1 1 1) [19]. The palladium feature in the valence band of Al–Pd–Mn surfaces (∼4 eV binding energy) becomes attenuated with increasing exposure (Fig. 4a and b). Fig. 4 shows that the structure of the O 2p peak is slightly different for different

surfaces: it grows narrower on Al(1 1 1) (Fig. 4c), broader on qc-Al–Pd–Mn (Fig. 4b) and even broader on c-Al–Pd–Mn (Fig. 4a). This is probably related to the number of peaks involved in the oxygen structure and their corresponding parameters. The Fermi level intensity of the surfaces investigated decreases with the exposure.

For a quantitative analysis, the clean-surface valence band was subtracted from every valence band spectrum and the area of the oxygen feature (peak 1, positive) and the area which is taken away from the palladium feature (peak 2, negative) were calculated (Fig. 4d). Oxygen grows more and palladium declines more in the crystalline than in the quasicrystalline phase (Fig. 4d). The changes of the peak areas with exposure are monotonic and consistent for both peaks. Therefore the conclusion about the more pronounced oxygen-induced changes in the crystalline phase is feasible, regardless of possible photon intensity variations for spectra taken at different exposures. Furthermore, the changes in the valence band approach saturation at the same exposures, as in XPS.

## 3.3. Sensitivity to photon irradiation

Another important point to notice is that X-rays and UV light promote the oxidation of the surfaces studied in this work. This has been tested by exposing the given surface to X-rays, UV light
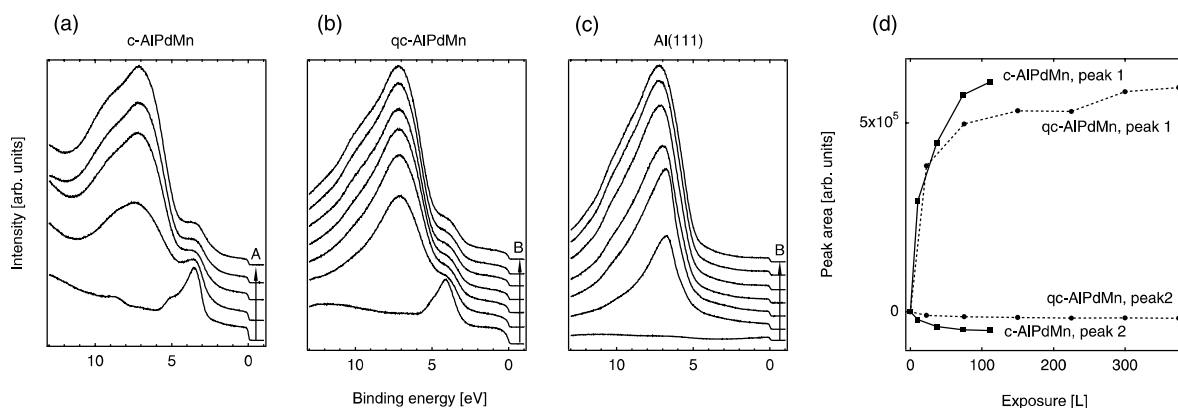


Fig. 4. UPS spectra of (a) c-, (b) qc-Al–Pd–Mn and (c) Al(1 1 1). The arrows are indicating oxygen exposure values, A: 0, 10, 35, 75, 110 L and B: 0, 20, 75, 150, 225, 300, 375 L (sequences from bottom to top, measured at normal emission). Peak area analysis is presented in (d).

or just by leaving it in UHV for approximately 1 h. Tests have been performed on the clean surfaces, on the surfaces oxidised with 15 L of oxygen and on the highly oxidised quasicrystalline surface exposed to 8400 L of oxygen. UPS was used to detect the quantity of oxygen present on the surface before and after the treatment, since it is more sensitive than XPS.

All surfaces examined show stronger changes after photon irradiation than by merely keeping them in UHV. A similar result for Al(1 1 1) has already been reported [39]. On the qc-surface all these changes are stronger than on both the c-Al–Pd–Mn and the Al(1 1 1) surfaces.

The described effects are more pronounced at the surfaces previously exposed to oxygen. This is illustrated in Fig. 5 for the qc-surface. Upon exposure to UV light during 1 h the valence band spectrum of the clean qc-surface (bottom) changes less than the one of the oxidised surface (top). In the extreme case of 8400 L exposure the effects are of the same magnitude as for the ones oxidised with 15 L of oxygen.

It has been suggested by Cabrera and Mott [39] that an increased oxidation in the presence of the UV light can be associated with the ejection of the electrons from the metal to the adsorbed oxygen which increases the field across the oxide film.
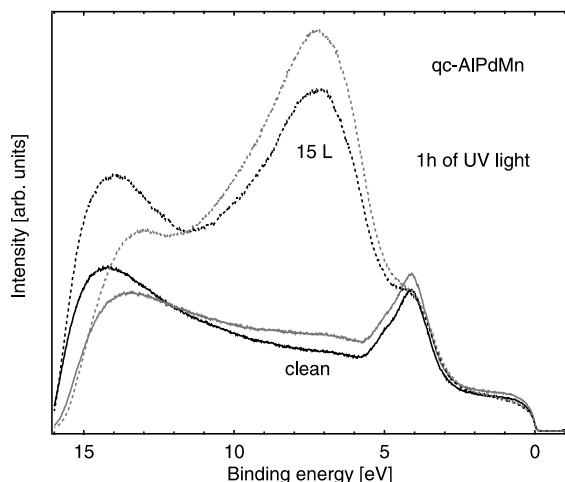
They conclude that it is necessary that the thickness of the oxide layer is larger than 10 Å for this effect to prevail the tunnelling of the electrons back to the metal. In the case of the quasicrystalline surface, this thickness is certainly not exceeded [7,8]. The observed phenomenon could be explained by an increase of diffusivity induced by photon irradiation. On the other hand, the stronger reaction of the previously oxidised surfaces, by comparison to the clean ones, is along the conclusions from Cabrera and Mott [39], where photoelectrons promote the reaction with oxygen across the existing oxide layer.

### 3.4. LEED

The LEED pattern of Al(1 1 1) consists of three stronger and three weaker spots in hexagonal symmetry. LEED images of qc-Al–Pd–Mn are fivefold symmetric. The clean-surface diffraction spots decline in intensity upon exposure to oxygen until they disappear completely (not shown). No new structure is observed. The disappearance of the diffraction pattern occurs between 7 and 25 L exposure on qc-Al–Pd–Mn, consistent with the results of others [7]. At 75 L exposure only three spots of the six-dots pattern on Al(1 1 1) remain visible. The obliteration of the pattern was not achieved with exposures up to 375 L, but the development of the intensities suggests that it may be expected around 1000 L.

### 4. Conclusion

Our results can be interpreted in terms of the layer-by-layer surface composition of quasicrystalline Al–Pd–Mn proposed by Gierer et al. [26,27]. The topmost layer of the quasicrystalline Al–Pd–Mn is Al-rich and therefore Al oxidises first. A passivating layer of Al-oxide forms on top and acts as a barrier between oxygen and other elements of the alloy. Mn is present at the surface only in traces, and together with the passivating Al-oxide, this is the reason why we do not observe oxidation of Mn up to very high exposures. Perhaps better statistics, i.e., higher photon flux, would reveal that Mn is slightly oxidised even at



Fig. 5. UPS valence band spectra of the qc-Al–Pd–Mn before (black) and after (grey) 1 h of exposure to UV light. Full lines stand for clean, dashed for surfaces exposed to 15 L of oxygen.

low exposures. Pd appears deeper below the surface and the measurements imply that it is either slightly oxidised or that it reacts to the changes of the environment which is oxidising. The quasicrystalline surface termination plays an important role in the oxidation process. The diffusivities of the elements in the quasicrystal are much smaller than in the elemental samples [35], and so the topmost layer composition determines which elements are oxidising. Some previous works [40,41] suggested that a reduced density of states near the Fermi level might be responsible for less available electrons and thus limited reactivity of quasicrystals. We observe stronger oxidation of the quasicrystal, than of elemental aluminium, which does not relate to their respective densities of states near the Fermi level.

The crystalline phase of the Al–Pd–Mn alloy reacts more with oxygen than the quasicrystalline. The oxidation process saturates at approximately 40 L on the quasicrystalline surface and at 75 L on the crystalline, in both XPS and UPS. There are several factors influencing the observed behaviour. The structure of the crystalline phase is periodic and there is no Al-dense surface layer, which makes all elements available at the surface for oxidation. The morphology of the surface created in the sputtering treatment is rough, favouring rapid and penetrating oxidation. Finally, the diffusivities of the elements are larger than in the quasicrystalline phase. The weak reaction of Pd here can be attributed to its inherent inertness [8]. However, the crystalline phase is less sensitive to UV light or X-rays than the quasicrystalline. This could be the consequence of the photon-induced increase of diffusivities in the quasicrystalline surface.

The quasicrystalline surface is more reactive and more sensitive than Al(1 1 1). The saturation of the oxidation seems to be the same for both surfaces, but the highly reactive Al–Pd–Mn surface achieves this state almost immediately, while the process lasts longer for Al(1 1 1). This suggests that the quasicrystal, in the reactivity, is situated between the Al(1 1 1) surface and other, more reactive, low-index Al faces. Thus, the geometry of the quasicrystalline surface appears more open than the densely packed Al(1 1 1) surface, consis-

tent with the results for the *i*-Al–Pd–Mn surface by Gierer et al. [26,27] and less open than other low-index Al faces.

Upon oxidation the quasicrystals show a particular behaviour such as selective oxidation of their components and formation of a passivating layer, desirable for applications. Furthermore, the observations of the oxidation process allow us to draw conclusions about the quasicrystals surface properties, and to compare them with other materials which are well known.

## Acknowledgements

## References

[1] C. Janot, Quasicrystals: A Primer, second ed., Oxford University Press, Cambridge, 1994.
[2] J.-M. Dubois, Phys. Scr. T 49 (1993) 17.
[3] C.J. Jenks, P.A. Thiel, Langmuir 14 (1998) 1392.
[4] D. Naumović, P. Aebi, L. Schlapbach, C. Beeli, T.A. Lograsso, D.W. Delaney, Phys. Rev. B 60 (1999) R16330.
[5] B. Bolliger, M. Erbudak, A. Hensch, D.D. Vvedensky, Mat. Sci. Eng. A 294–296 (2000) 859.
[6] D. Naumović, P. Aebi, L. Schlapbach, C. Beeli, Mat. Sci. Eng. A 294–296 (2000) 882.
[7] S.-L. Chang, W.B. Chin, C.-M. Zhang, C.J. Jenks, P.A. Thiel, Surf. Sci. 337 (1995) 135.
[8] S.-L. Chang, J.W. Anderegg, P.A. Thiel, J. Non-Cryst. Solids 195 (1996) 95.
[9] P.J. Pinhero, S.-L. Chang, J.W. Anderegg, P.A. Thiel, Phil. Mag. B 75 (1997) 271.
[10] C.J. Jenks, P.J. Pinhero, S.-L. Chang, J.W. Anderegg, M.F. Besser, D.J. Sordelet, P.A. Thiel, in: A.I. Goldman, D.J. Sordelet, P.A. Thiel, J.M. Dubois (Eds.), Proceedings of the Conference, New Horizons in Quasicrystals: Research and Applications, World Scientific, Singapore, 1997, p. 157.
[11] C.J. Jenks, P.J. Pinhero, T.E. Bloomer, J.W. Anderegg, P.A. Thiel, in: S. Takeuchi, T. Fujiwara (Eds.), Proceed-

ings of the 6th International Conference on Quasicrystals, World Scientific, Singapore, 1998, p. 761.

[12] P.A. Thiel, A.I. Goldman, C.J. Jenks, in: Z.M. Stadnik (Ed.), Physical Properties of Quasicrystals, Springer, Berlin, 1999, p. 327.

[13] B.I. Wehner, U.Köster, in: A.I. Goldman, D.J. Sordelet, P.A. Thiel, J.M. Dubois (Eds.), Proceedings of the Conference, New Horizons in Quasicrystals: Research and Applications, World Scientific, Singapore, 1997, p. 152.

[14] D. Rouxel, M. Gavatz, P. Pigeat, B. Weber, in: A.I. Goldman, D.J. Sordelet, P.A. Thiel, J.M. Dubois (Eds.), Proceedings of the Conference, New Horizons in Quasicrystals: Research and Applications, World Scientific, Singapore, 1997, p. 173.

[15] M. Gavatz, D. Rouxel, D. Claudel, P. Pigeat, B. Weber, in: S. Takeuchi, T. Fujiwara (Eds.), Proceedings of the 6th International Conference on Quasicrystals, World Scientific, Singapore, 1998, p. 765.

[16] C. Berg, S. Raaen, A. Borg, J.N. Andersen, E. Lundgren, R. Nyholm, Phys. Rev. B 47 (1993) 13063.

[17] S.M. Bedair, H.P. Smith Jr., J. Appl. Phys. 42 (1971) 3616.

[18] I.P. Batra, L. Kleinman, J. Electron Spectrosc. Rel. Phenom. 33 (1984) 2175.

[19] S.A. Flodstrom, C.W.B. Martinsson, R.Z. Bachrach, S.B.M. Hagström, R.S. Bauer, Phys. Rev. Lett. 40 (1978) 907.

[20] C.F. McConville, D.L. Seymour, D.P. Woodruff, S. Bao, Surf. Sci. 188 (1987) 1.

[21] H.F. Brune, J. Wintterlin, J. Trost, G. Ertl, J. Wiechers, R.J. Behm, J. Chem. Phys. 99 (1993) 2128.

[22] S.A. Flodstrom, R.Z. Bachrach, R.S. Bauer, S.B.M. Hagström, Phys. Rev. Lett. 37 (1976) 1282.

[23] W. Eberhardt, F.J. Himpsel, Phys. Rev. Lett. 42 (1979) 1375.

[24] R.Z. Bachrach, G.V. Hansson, R.S. Bauer, Surf. Sci. 109 (1981) L560.

[25] H.D. Ebinger, J.T. Yates Jr., Phys. Rev. B 57 (1998) 1976.

[26] M. Gierer, M.A. Van Hove, A.I. Goldman, Z. Shen, S.-L. Chang, C.J. Jenks, C.-M. Zhang, P.A. Thiel, Phys. Rev. Lett. 78 (1997) 467.

[27] M. Gierer, M.A. Van Hove, A.I. Goldman, Z. Shen, S.-L. Chang, P.J. Pinhero, C.J. Jenks, J.W. Anderegg, C.-M. Zhang, P.A. Thiel, Phys. Rev. B 57 (1998) 7628.

[28] C. S. Fadley, in: R.T. Bachrach (Ed.), Synchrotron Radiation Research: Advances in Surface Science, vol. 1, Plenum, New York, 1990.

[29] Th. Pillo, L. Patthey, E. Boschung, J. Hayoz, P. Aebi, L. Schlapbach, J. Electron. Spectrosc. Rel. Phenom. 97 (1998) 243.

[30] S. Doniach, M. Šunjić, J. Phys. C 3 (1970) 285.

[31] B.R. Strohmeier, Surf. Interf. Anal. 15 (1990) 51.

[32] L. Schlapbach, S. Hüfner, S. Büchler, T. Riesterer, J. Less-Common Met. 130 (1987) 301.

[33] M. Boudard, M. de Boissieu, C. Janot, G. Heger, C. Beeli, H.U. Nissen, H. Vincent, R. Ibberson, M. Audier, J.M. Dubois, J. Phys. C 4 (1992) 10149.

[34] M. de Boissieu, unpublished.

[35] P. Archambault, C. Janot, MRS Bulletin 22 (11) (1997) 48.

[36] J.M. Dubois, S.S. Kang, P. Archambault, B. Colleret, J. Mater. Res. 8 (1) (1993) 38.

[37] D.W. Wagman, W.H. Evans, V.B. Parker, R.H. Schumm, I. Halow, S.M. Bailey, K.L. Churney, R.L. Nutall, J. Phys. Chem. Ref. Data 11 (Suppl. 2) (1982) 392.

[38] H. Lüth, Surfaces and Interfaces of Solids, Springer, Germany, 1993.

[39] N. Cabrera, N.F. Mott, Rep. Prog. Phys. 12 (1948) 163.

[40] A.I. Goldman, J.W. Anderegg, M.F. Besser, S.-L. Chang, D.W. Delaney, C.J. Jenks, M.J. Kramer, T.A. Lograsso, D.W. Lynch, R.W. McCallum, J.E. Shield, D.J. Sordelet, P.A. Thiel, American Scientist 84 (1996) 230.

[41] B.I. Wehner, U. Köster, in: S. Takeuchi, T. Fujiwara (Eds.), Proceedings of the 6th International Conference on Quasicrystals, World Scientific, Singapore, 1998, p. 773.

# ANGLE-SCANNED PHOTOEMISSION ON YbH$_x$: RELEVANCE FOR SWITCHABLE MIRRORS

J. HAYOZ, C. KOITZSCH, D. POPOVIĆ, M. BOVET,

D. NAUMOVIĆ and P. AEBI*

*Institut de Physique, Université de Fribourg, Pérolles,*

*CH-1700 Fribourg, Switzerland*

Yttrium, lantanum and rare earth elements can be loaded with hydrogen inducing a metal–insulator transition and giving rise to optical switching from reflecting to transparent. We present angle-scanned photoemission experiments characterizing thin YbH$_x$ films grown on W(110) at room temperature. Hydrogen loading is performed in an ultrahigh-vacuum-compatible high pressure (1 bar) reaction cell. Via full-hemispherical X-ray photoelectron diffraction and low energy electron diffraction, it is demonstrated that these films grow well-ordered and single-crystalline. Ultraviolet photoemission reveals a gap for the dihydride phase confirming a transition from reflecting to transparent as seen by visual inspection. Ion implantation through additional H+ sputtering allows one to increase the hydrogen content to $x \approx 2.4$.

## 1. Introduction

The switchable optical properties of some metal hydrides[1] and also their hydrogen storage capabilities are of strong interest with respect to applications. Mostly trivalent elements such as Y and La have been used to induce optical switching at room temperature (RT) and with hydrogen pressures of the order of 1 bar. In Y, for instance, the metallic dihydride phase is loaded with hydrogen where, at $x \approx 2.85$ H atoms per formula unit, the material turns transparent. However, the physics behind putting hydrogen into a material is still not well understood. With hydrogen a proton and an electron are added to the metal host. This results in doping the host material and the understanding of doping is one of today's central problems in solid state physics. It has been realized that state-of-the-art *ab initio* local density approximation calculations do not reproduce the optical gap necessary to explain the transparent state in the tryhydride phase.[2] Other models, based on strong electron correlations, have been proposed to explain the metal–insulator transition.[3,4] There is an interesting and appealing connection between these models and the Zhang–Rice singlett[5] in high temperature superconductors (HT$_c$'s). Hydrogen is suggested to be present in the form of H$^-$, one electron taken from the metal host. The two electrons on H$^-$ are correlated but with drastically different radii around the proton. One electron is strongly bound to the proton whereas the other overlaps heavily with the metal d-states of the neighboring atoms. The two electrons form a singlett analogous to holes in the HT$_c$'s. On the other hand, very recent GW calculations[6,7] demonstrate the formation of a sufficient gap to explain the metal–insulator transition without the need for strong electron correlations.

Indeed, detailed angle-resolved photoemission (ARPES) experiments are needed to favor one or the other model. However, practically all previous work on metal hydrides has been done on polycrystals and/or on samples that are capped with a protective Pd layer. In order to perform ARPES experiments, uncapped single crystalline material is needed. Furthermore, preparation has to take place *in situ* since Y, La and the rare earth used so far are extremely reactive. It is therefore important to explore how to prepare single crystalline hydrid films and to

---

*Corresponding author.
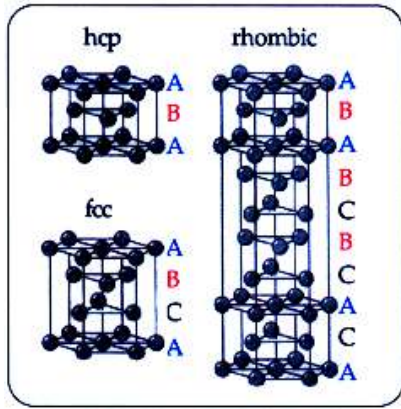
Fig. 1.  Possibilities of close-packed layer stacking. Indicated are the sequences for hexagonal close-packed (hcp) face-centered cubic (fcc) and rhombic structures with characteristic layers A, B and C (from Ref. 10).

characterize them with respect to both the geometrical and the electronic structure. Recently, we were able to prepare thin, single crystalline Y films on W(110) and to load them with hydrogen.[8,9] The W(110) surface represents a quasihexagonal template inducing the growth of close-packed layers. Different sequences are possible (see Fig. 1) between the purely face-centered (fcc) and hexagonal close-packed (hcp) stacking with ABCABC... and ABAB... layers, respectively. The rhombic structure, for instance, can be viewed as a mixture of fcc and hcp stacking.

Since it is necessary to apply significant H partial pressures [compared to ultrahigh vacuum (UHV)] in order to reach the different hydride phases, we constructed a UHV-compatible high pressure (1 bar) cell.[9]

Here we present results on the preparation and characterization of thin single crystalline Yb films. Up to now switching to the transparent state has been induced in trivalent materials while increasing hydrogen pressure between the dihydride and the trihydide phase. Yb is divalent and the localized 4f electrons have a similar binding energy to the valence bandwidth, giving rise to an unstable 4f configuration.

The expectation is that it may be possible to have a reversed behavior for Yb thin films, i.e. the dihydride insulating and transparent and the transformation into the mirror (metallic) state induced by either reducing or increasing the hydrogen concentration.

We find that thin Yb films grown at RT on W(110) are single-crystalline and of hcp structure. Hydrogen loading is more difficult than for Y. Upon exposure to 1 bar of hydrogen the dihydride phase is formed exhibiting a characteristic gap in the valence band spectrum. Ion implantation via $H^+$ sputtering increases the near surface hydrogen concentration, $x$, to $x \approx 2.4$ and the spectra are indicative for a mixed valent phase which is reported to be metallic again.[11]

## 2.  Experimental

The experiments were performed in a VG ESCALAB Mk II spectrometer with a base pressure $\leq 5 \cdot 10^{-11}$ mbar. The sample stage is modified for motorized sequential angle-scanned data acquisition over $2\pi$ solid angle.[12,13] $MgK_a$ (1254.6 eV) and $SiK_a$ (1740 eV) radiation is used for X-ray photoelectron spectroscopy (XPS) and X-ray photoelectron diffraction (XPD). The data acquisition mode to collect full-hemispherical XPD data is described in detail elsewhere.[14] Ultraviolet photoemission measurements were performed with monochromatized HeI$\alpha$ (21.2 eV) and He II (40.8 eV) radiation. The setup of the plasma discharge lamp with monochromator is presented in Ref. 15. The W(110) surface was prepared in UHV by flashing to 2500 K. After flashing, the W crystal was left in UHV for at least 5 h to reach room temperature. Yb was then evaporated by resistive heating of a Ta basket. Approximately 200-Å-thick films were grown within 30 min. The coverage was monitored with a quartz crystal oscillator. During deposition the pressure did not exceed $10^{-9}$ mbar. For all the films presented below the oxygen contamination as measured with XPS was below the detection limit and the W signal was not detectable anymore. In order to vary the H concentration, deposition was done under $H_2$ partial pressure and the films were exposed to 1 bar purified $H_2$. Details of the hydrogen pressure cell are presented elsewhere.[9] Briefly, highest purity $H_2$ for all hydrogen treatments of the films was produced via permeation through a Ag–Pd filter tube where the downstream side never comes in contact with non-UHV environment.

## 3.  Results and Discussion

Figure 2 displays XPD patterns for differently prepared films. The XPD patterns allow a very
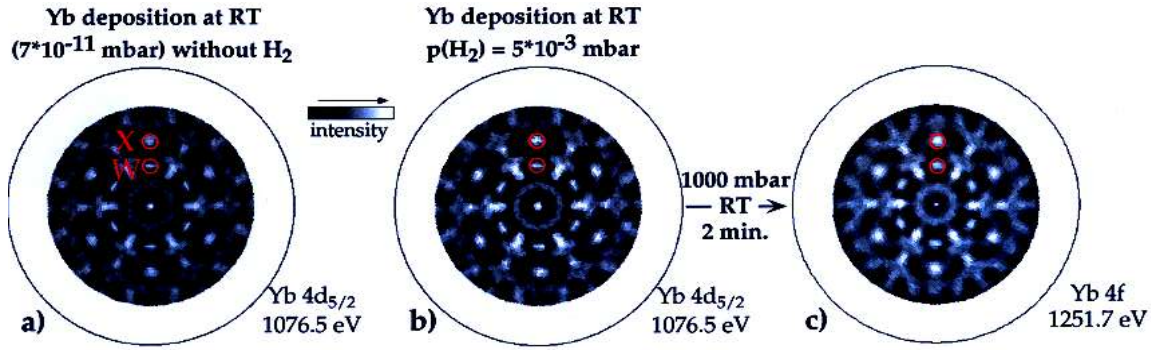
Fig. 2. Photoelectron diffraction patterns (sixfold-symmetry-averaged) for (a) a 200-Å-thick Yb film deposited on W(110) at room temperature (RT); (b) same as (a) but deposition under $5 \times 10^{-3}$ mbar H$_2$ partial pressure; (c) same as (a) but deposited under $10^{-6}$ mbar H$_2$ partial pressure and subsequently exposed to 1000 mbar H$_2$. Photoelectron kinetic energies and deposition conditions are labeled. Points X and W mark specific forward focusing maxima.

simple interpretation in the case, such as here, of photoelectron kinetic energies above approximately 500 eV.[16] Photoelectrons leaving the emitter atom are strongly focused in the forward direction by the neighboring atoms. The measured intensities are therefore strongly enhanced along densely packed atomic rows and crystallographic planes. In this energy regime, the so-called forward focusing is only weakly dependent on the atomic number $Z$ of scatterer atoms. Furthermore, it was shown in Ref. 13 based on a large data set that the final-state scattering produces patterns that are virtually independent of the initial state angular momentum.

Due to the limited mean free path of photoelectrons, the angular intensity distribution measured in the forward focusing regime is characteristic of the near surface crystallography. Via comparison with angular distributions taken from known structures, the identification of unknown systems is possible.[17]

The intensity of the Yb $4d_{5/2}$ and $4f$ photoemission lines have been measured as a function of emission angle and mapped stereographically in a linear gray scale representation (Fig. 2). High and low intensities are drawn in white and black, respectively. Normal emission corresponds to the center of the plot whereas emission parallel to the surface, i.e. 90° polar emission angle, is indicated by the outer circle.

For the measurement shown in Fig. 2(a), Yb was deposited in UHV at RT, whereas for Fig. 2(b) the film was deposited at RT but under a H$_2$ partial pressure of $5 \times 10^{-3}$ mbar. The patterns of the two films look very similar and can be identified as Yb lay-

ers with hcp stacking. The XPD pattern of close-packed layers with fcc stacking, as found in the case of YH$_2$ (not shown), is distinctly different.[8] The finding of hcp stacking for Yb deposition on W(110) at RT is in contradiction to the fcc stacking reported by Weschke *et al.*[18] The reason might be that Yb exhibits a transition from hcp to fcc below RT,[19,20] and therefore is intrinsically unstable with respect to different stackings. Note also that single crystalline Yb films deposited at RT on saphire (11–20) exhibit fcc stacking (not shown).

An additional exposure to 1 bar of H$_2$ applied to a film grown under $10^{-6}$ mbar H$_2$ partial pressure results in a pattern such as shown in Fig. 2(c). The contrast is slightly degraded but the intensity distribution is still very similar. Differences are due to a roughening of the film (see below) and also to an admixture of non-hcp stacking, i.e. a rhombic structure. From bulk polycrystals it is known that Yb forms a nonmetallic, rhombic dihydride phase.[11] Since photoelectrons have a finite escape depth, several layers are sampled and the exact stacking sequence, i.e. the amount of ABC stacking admixture, cannot be identified with precision. In addition the situation is complicated by the presence of differently oriented domains. However, the measurement clearly indicates strong hcp stacking character.

The distinct high intensity features in Fig. 2, labeled W and X, originate from close-lying emitter–scatterer directions characteristic of the stacking. The corresponding emission angles are determined by the $c/a$ ratio, where $a$ and $c$ are the in- and out-of-
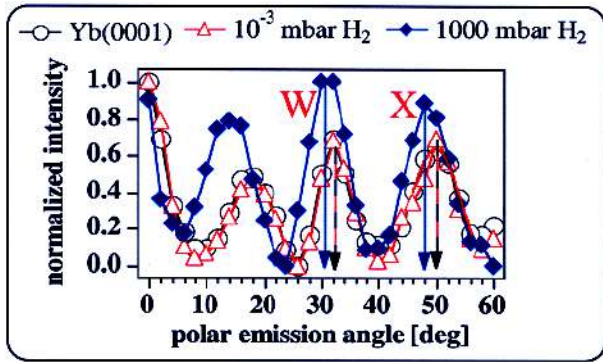
Fig. 3.   Polar scans across characteristic forward focusing maxima indicated in Fig. 2. The maxima shift for the different films, indicating a change in interlayer spacing.

plane lattice constants, respectively. A closer analysis, shown in Fig. 3, manifests a decreased emission angle and therefore an increased $c/a$ ratio for the 1 bar $H_2$ exposed film [Fig. 2(c)]. The increase of $c/a$ amounts to roughly 8%.

In order to get information on the in-plane lattice constant, $a$, and consequently on the interlayer expansion, and also on the long range order quality of the films, we performed LEED experiments. Figure 4(a) shows the diffraction spots of the Yb film deposited at RT in UHV, recorded for a primary electron energy of 80 eV. The spots are sharp and well defined, indicative of a well-ordered film. In Fig. 4(b) we display the pattern for a Yb film deposited under a $H_2$ partial pressure of $5 \times 10^{-3}$ mbar. The film remains equally well ordered. For an exposure

to 1 bar $H_2$, however, a certain loss of long range order is observed in Fig. 4(c). The distance between the diffraction spots (marked by a white arrow in Fig. 4) gives a measure for the in-plane distance. Going from Fig. 4(a) to 4(b), no change is observed. In Fig. 4(c), however, the distance between the diffraction spots slightly increases, indicating a decrease of the in-plane lattice constant by approximately 2%.

Together with the result for the $c/a$ ratio from XPD (8% increase) we find an interlayer expansion of approximately 6excellent agreement with the expansion of 6%, reported for $YbH_2$.[10] Therefore, XPD and LEED together give evidence for the formation of the dihydride. The films stay single-crystalline (XPD) but there is a certain loss of long range order (LEED). Note that a similar treatment applied to Y films already induces the trihydride phase.[9]

The next step is to consider the photoemission spectra of the Yb 3d emission line which is susceptible to the valence of Yb. The removal of a 3d electron in the divalent case results in a single line, which is only broadened by lifetime and instrumentals effects. For trivalent Yb the hole in the 4f shell (induced through the promotion of a 4f electron into the valence band) together with the 3d hole created by the photoemission process results in a rather broad multiplet structure. Figure 5 displays the spectra of the different films. Labeled with (a) and (b) are films deposited in UHV and under a $H_2$ partial pressure of $5 \times 10^{-3}$ mbar, respectively. No significant differences are noticed. The two ticks mark a bulk and surface plasmon/band transition[11,21] and are not
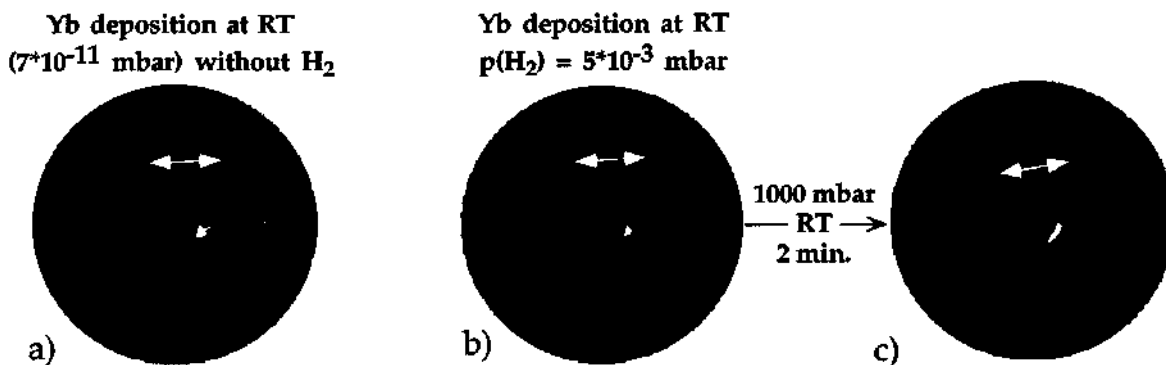


Fig. 4.   Low energy electron diffraction pattern ($E_0 = 80$ eV) for (a) a 200-Å-thick Yb film deposited on W(110) at room temperature (RT); (b) same as (a) but deposition under $5 \times 10^{-3}$ mbar $H_2$ partial pressure; (c) same as (a) but deposited under $10^{-6}$ mbar $H_2$ partial pressure and subsequently exposed to 1000 mbar $H_2$. White arrows indicate the distance between two diffraction spots indicative of in-plane lattice constant changes.
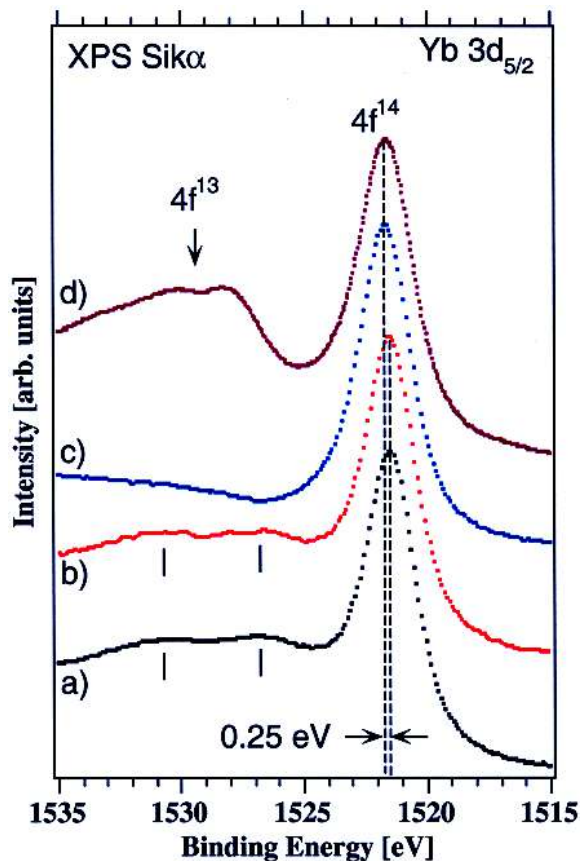
Fig. 5. SiK$\alpha$ excited Yb3d$_{5/2}$ photoemission line for (a) a 200-Å-thick Yb film deposited on W(110) at room temperature (RT); (b) same as (a) but deposition under $5 \times 10^{-3}$ mbar H$_2$ partial pressure; (c) same as (a) but deposited under $10^{-6}$ mbar H$_2$ partial pressure and subsequently exposed to 1000 mbar H$_2$; (d) a 200-Å-thick Yb film deposited on sapphire (11–20) at RT and subsequently H$^+$-sputtered.



Fig. 6. Normal emission photoemission spectra of 200-Å-thick Yb films grown on W(110) at room temperature. (*Bottom*) Pure Yb measured with HeI radiation, (*middle*) Yb film deposited under $10^{-6}$ mbar H$_2$ and subsequently exposed to 1000 mbar H$_2$, measured with HeI, (*top*) same as (*middle*) but measured with HeII radiation.

present anymore in the dihydride [spectrum (c)] which is insulating (see below). For spectrum (c) the film has been exposed, in addition to deposition under $10^{-6}$ mbar H$_2$, to 1 bar H$_2$ for 2 min. The spectrum is very similar to spectra of polycrystalline samples with a concentration of $x = 2.0$.[11,21,22] These polycrystalline samples have been calibrated very carefully with volumetric methods by dissolving them in dilute HCl.[11] Therefore, the films corresponding to spectrum (c) are close to YbH$_2$ confirming our findings with XPD and LEED. Spectrum (d) represents a film deposited on sapphire (11–20) and, in addition, has been sputtered with H$^+$ (4.5 keV, 60 $\mu$A) for 5 min. The split shoulder at higher binding energy

is characteristic of f$^{13}$ final state multiplets and therefore of a mixed valent phase. A comparison with data taken on polycrystalline samples[11,21,22] indicates that we reached approximately YbH$_{2.4}$, a composition reported to be metallic.[11] The film of spectrum (d), however, becomes completely disordered, as seen from XPD and LEED (not shown).

In order to access the electronic structure directly, valence band spectra have been recorded. Figure 6 shows normal emission data taken with HeI ($h\nu = 21.2$ eV) (two bottommost spectra) and HeII ($h\nu = 40.8$ eV) (topmost spectrum) radiation. For Yb metal (bottommost spectrum) with a 4f$^{14}$ ground state configuration, 4f$^{13}$ photoemission final state doublets are observed, split into 4f$_{7/2}$ and 4f$_{5/2}$ lines. Each line consists of two components due to contributions from bulk and surface atoms separated

by the so-called surface core level shift.[23] The sharp peak close to zero binding energy (Fermi level) is the well-known surface state present on many close-packed rare earth surfaces.[24] For the film which is evaporated under a $H_2$ partial pressure of $10^{-6}$ mbar and subsequently exposed to 1 bar of $H_2$ (center and top spectrum) the electronic states near the Fermi level completely disappeared, indicating the opening of the gap and the metal–insulator transition. A visual inspection of a film prepared under the same conditions on (transparent) sapphire indicates that it becomes transparent. Thus, the YbH2 films are insulating and transparent.

In addition, the surface-induced splitting of the 4f states has disappeared but the binding energy positions of the maxima are centered at the surface-shifted core levels. This behavior can be attributed to a roughening of the surface induced by the loading of the film under 1 bar of $H_2$. A variety of different Yb surface atom environments are created with different core level shifts, leading to the broadening. This broadening is consistent with the loss of long range order as observed by LEED in Fig. 4(c).

Furthermore a broad feature has appeared at about 5.5 eV binding energy. This feature can be attributed to hydrogen-induced states since the HeII spectrum taken on the same films (topmost spectrum) shows a strong relative weight increase of the f-states with respect to the 5.5 eV maximum. Therefore it is not of 4f character, for example induced through a valence change. It is also not a fingerprint of oxygen contamination since it would also have appeared in the O 1s XPS and O-contaminated films exhibit a valence band feature centered at 6 eV.

## 4.   Conclusions

In summary, we have demonstrated that Yb, at RT, grows with hcp stacking on W(110). Loading with 1 bar of $H_2$ results in the dihydride as indicated by the increased interlayer spacing, the comparison with published XPS data of polycrystalline samples and the opening of the gap in the normal emission valence band spectra. Deposition under a $H_2$ partial pressure of $5 \times 10^{-3}$ mbar almost does not induce changes, clearly indicating that hydrogenation of Yb is more difficult than for example for Y. Ion implantation via $H^+$ sputtering results in a mixed valent $YbH_x$ phase with $x \approx 2.4$, which is metallic again. Therefore Yb

definitely offers the possiblity of inducing a metal–insulator transition via both H content increase and decrease.

The formation of the dihydride phase results in a considerable roughening of the surface manifested in broadened LEED spots and an increased intensity and broadening of the surface component of the 4f lines.

## References

1. J. N. Huiberts, R. Griessen, J. H. Rector, R. J. Wijngaarden, J. P. Dekker, D. G. de Groot and N. J. Koemann, *Nature* **380**, 231 (1996).
2. P. J. Kelly, J. P. Dekker and R. Stumpf, *Phys. Rev. Lett.* **78**, 1315 (1997).
3. R. Eder, H. F. Pen and G. A. Sawatzky, *Phys. Rev.* **B56**, 10115 (1997).
4. K. K. Ng *et al.*, *Phys. Rev. Lett.* **78**, 1311 (1997).
5. F. C. Zhang and T. M. Rice, *Phys. Rev. Lett.* **37**, 3759 (1988).
6. T. Miyake, F. Aryasetiawan, H. Kino and K. Terakura, *Phys. Rev.* **B61**, 16491 (2000).
7. P. van Gelderen, P. A. Bobbert, P. J. Kelly and G. Brocks, *Phys. Rev. Lett.* **85**, 2989 (2000).
8. J. Hayoz, S. Sarbach, Th. Pillo, E. Boschung, D. Naumovic, P. Aebi and L. Schlapbach, *Phys. Rev.* **B58**, R4270 (1998).
9. J. Hayoz, Th. Pillo, M. Bovet, A. Züttel, St. Guthrie, G. Pastore, L. Schlapbach and P. Aebi, *J. Vac. Sci. Tech.* **A18**(5), 2417 (2000).
10. P. Vajda, in *Handbook on the Physics and Chemistry of Rare Earths*, eds. K. A. Gschneider and L. Eyring, Vol. 20 (Elsevier, Amsterdam, 1995).
11. S. Büchler, PhD thesis, Swiss Federal Institute of Technology, Switzerland (1989).
12. J. Osterwalder, T. Greber, A. Stuck and L. Schlapbach, *Phys. Rev.* **B47**, 13764 (1991).
13. D. Naumović, A. Stuck, T. Greber, J. Osterwalder and L. Schlapbach, *Phys. Rev.* **B47**, 7462 (1993).
14. R. Fasel, P. Aebi, J. Osterwalder, L. Schlapbach, R. G. Agostino and G. Chiarello, *Phys. Rev.* **B50**, 14516 (1994).
15. Th. Pillo, L. Patthey, E. Boschung, J. Hayoz, P. Aebi and L. Schlapbach, *J. Electr. Spectrosc. Relat. Phenom.* **97**, 243 (1998).
16. C. S. Fadley, in: R. T. Bachrach, ed., *Synchrotron Radiation Research: Advances in Surface Science*, Vol. 1 (Plenum, New York, 1990).

17. Th. Pillo, J. Hayoz, P. Schwaller, H. Berger, P. Aebi and L. Schlapbach, *Appl. Phys. Lett.* **75**, 1550 (1999).

18. E. Weschke, A. Yu. Grigoriev, C. Schüssler-Langeheine, C. Mazumdar, R. Meier, S. Vandré, S. Ram, L. Kilian, G. Kaindl and C. Sutter, *Phys. Rev. Lett.* **83**, 584 (1999).

19. E. Bucher, P. H. Schmidt, A. Jayaraman, K. Andres, J. P. Maita, K. Nassau and P. D. Dernier, *Phys. Rev.* **B2**, 3911 (1970).

20. F. X. Kayser, *Phys. Rev. Lett.* **25**, 662 (1970).

21. S. Büchler, R. Monnier and L. Degiorgi, L. Schlapbach, *Zeitschrift für Physikalische Chemie Neue Folge* **163**, 579 (1989).

22. S. Büchler, L. Schlapbach, R. Monnier and L. Degiorgi, *Journal de Physique, Suppl. 12* **48**, C9–947 (1987).

23. G. Kaindl, A. Höhr, E. Weschke, S. Vandré, C. Schüssler-Langeheine and C. Laubschat, *Phys. Rev.* **B51**, 7920 (1995).

24. M. Bodenbach, A. Höhr, C. Laubschat, G. Kaindl and M. Methfessel, *Phys. Rev.* **B50**, 14446 (1994).

# High-resolution photoemission on Ag/Au(111):
## Spin-orbit splitting and electronic localization of the surface state

D. Popović,[1,2] F. Reinert,[3,*] S. Hüfner,[1] V. G. Grigoryan,[4] M. Springborg,[4] H. Cercellier,[5,6] Y. Fagot-Revurat,[5] B. Kierren,[5] and D. Malterre[5]

[1]*FR 7.2 Experimentalphysik, Universität des Saarlandes, 66123 Saarbrücken, Germany*
[2]*Department of Physics, Karlstad University, 65188 Karlstad, Sweden*
[3]*Experimentelle Physik II, Universität Würzburg, 97074 Würzburg, Germany*
[4]*Physikalische Chemie, Universität des Saarlandes, 66123 Saarbrücken, Germany*
[5]*Laboratoire de Physique des Matériaux, Université Henri Poincaré, Nancy I, Boîte Postale 239, 54506 Vandœuvre-lés-Nancy, France*
[6]*Institut de Physique, Université de Neuchâtel, CH-2000 Neuchâtel, Switzerland*

We present a detailed photoemission study of the surface state dispersion in 0–10 ML thin Ag films on Au(111). The dispersion of the *L*-gap Shockley-type surface state changes monotonically from the one of Au towards the one of Ag with increasing layer thickness indicating an extension of the wave function into the solid. High resolution photoemission (PES) enables an insight into decreasing spin-orbit splitting of the surface state in Ag-covered-Au(111). The photoemission data have been well reproduced by *ab initio* band structure calculations using the WIEN2K code. The dependence of the binding energy on the increasing silver film thickness is indicative of the localization of the surface state at the surface by comparing it with the calculated electron density of the surface state. Measurements on 10 ML Ag/Au(111) reveal the *d*-band states of Ag, but one still observes *sp*-related quantum well states of silver within the projected *sp*-band gap of gold.

Shockley-type surface states in the *L* gap of noble metal (111) surfaces provide a suitable model system for electronic states in two dimensions. Since high-resolution photoelectron spectroscopy (PES) has enabled a precise investigation of the intrinsic line width and the spin-orbit (SO) splitting of the surface state on Au(111),[1,2] it has become increasingly interesting to study in which way adsorbates influence it. The deposition of noble gases like Xe, Kr, or Ar in a monolayer regime shows a decrease in surface state binding energy and an increase in spin-orbit splitting up to 30% with respect to the value of pure Au(111).[3] Thin epitaxial films of other noble metals on Au(111) lead to different phenomena due to the existence of an own surface state at the respective (111) surface. The energetic positions of surface and bulk states determine the binding energies of the observed states in thin films in the vicinity of the Fermi level.[4,5]

Ag/Au(111) is an intermetallic system, exhibiting parallel epitaxy due to a very small lattice mismatch (0.2%, $a_{Au}$ =4.0782 Å, $a_{Ag}$=4.0853 Å). Two peculiarities of Au(111) as a substrate are the so-called herringbone reconstruction of the topmost surface layer (visible also in PES,[6] its influence on the Ag film growth is discussed elsewhere[7]) and the spin-orbit splitting of the Shockley state.[1,2] The Shockley-state in Au(111) exists in the inverted *sp*-band gap due to the boundary conditions at the surface.[8] Quantum-well states in intermetallic systems are confined within the same projected *sp* bulk band gap.[9] Complementary to that, the projected band gap and the valence band carry information about the bulk or the substrate. The interesting question of probing deep interfaces, has been investigated in the past by observing the quantum-well states[9] or core-level shifts.[10] We show in this paper that the projected band structure of gold is still visible in the data after 10 ML of silver have been evaporated and

when the *d* band of silver is already completely formed. The changes of the surface state are in accordance with the slower development of the *sp* bands with layer thickness. Whereas the *d* band develops together with the film, the surface state and the quantum well states offer information about the film thickness and the projected band gap enables a direct visualization of the substrate.

The photoemission experiments have been performed with a SCIENTA SES 200 analyzer in the angular mode in the UHV chamber with the base pressure $5 \times 10^{-11}$ mbar. The energy resolution is $\Delta E$=3.5 meV, the angular resolution $\Delta \theta \approx \pm 0.15°$.[11,12] The measurements have been performed with a monochromatized GAMMADATA VUV lamp at a photon energy of $h\nu$=21.2 eV (He I) at the sample temperature 20–30 K (Saarbrücken, SB) or with a nonmonochromatized UVS-300 SPECS discharge lamp at the photon energy of $h\nu$=11.83 eV (Ar I) and the sample temperature of 80 K (Nancy, N). The measuring time was approximately 15 min for one data set of the complete occupied surface state.

The surface of the Au(111) was prepared by repeated cycles of Ar⁺ sputtering and subsequent annealing up to 700 °C (SB) or 350 °C (N). Ag films were evaporated at room temperature with triple-evaporator Omicron EFM 3T ($I_e$=17 mA, flux=1 $\mu$A, HV=690 V), at evaporation rate of 0.3 Å/min (SB) or by a Knudsen cell at evaporation rate of 0.5 ML/min (N) in the high $10^{-10}$ mbar pressure range. The coverage was determined by a quartz-microbalance and checked by STM (N).[7]

Band structure calculations have been performed using the WIEN2K package implementing the FLAPW (full-potential linearized augmented plane-wave) method within the framework of density functional theory (DFT).[14] For the exchange-correlation potential the generalized gradient ap-
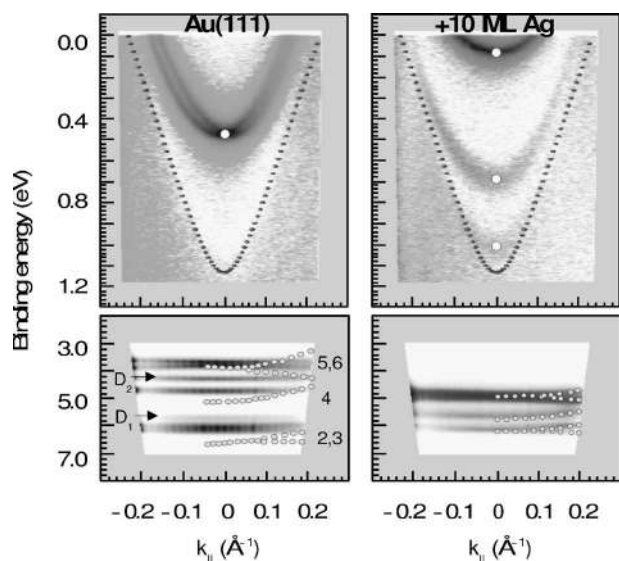
FIG. 1. Top: Surface state (lower binding energy) and quantum well states (higher binding energies) along $\bar{\Gamma}\bar{K}$ marked by white dots for Au(111) and 10 ML Ag/Au(111). Band-structure calculations of the Au $sp$ gap have been shifted to fit the measured binding energy for the pure Au(111) and are shown as black circles. Bottom: valence band; 2-6 are valence bands of the Au(111), $D_1$ and $D_2$ are the surface resonances. White dots represent band-structure calculations for pure Au (left) and Ag (right) by Smith (Ref. 13). The measurements have been taken with He I at $T=20$ K.

proximation (GGA) was used.[15] A basis set of 1600 LAPWs and a 100 $k$-points mesh in the irreducible Brillouin zone have been used. SO-coupling was included in a second variational step. The surface was modeled by a periodic slab of 23 Au and correspondingly from one to six Ag layers on the each Au surface, separated by 20 bohr of vacuum. For smaller slabs, the interaction of the two confining surfaces, both via the "bulk" and via the "vacuum,"[16] leads to an artificial splitting of the surface state. For a seven-layer slab this splitting is much larger than the SO splitting of the Au(111) surface state. The size of the system, i.e., 23 layers and 20 bohr vacuum, is chosen in order to reduce the artifact below 1 meV at $k=0$, which is two orders of magnitude smaller than the SO splitting at $E_F$ ($>100$ meV). The slab thickness exceeds both decay lengths of the surface state in Au(111) (3.6 ML) and Ag(111) (12 ML).[17] Finally, allowing for struc-

tural relaxation did not lead to changes observable within our experimental uncertainty.

Figure 1 shows surface and bulk valence band states for Au(111) (left) and 10 ML Ag/Au(111) (right) over a wide binding energy (BE) range, from the Fermi level down to 7 eV. The upper panels show the surface states with their band minima marked with white circles: The first two quantum well states (at 688 and 1048 meV BE for a silver covered surface) and, with higher intensity, the Shockley state (at 479 meV BE left and 84 meV BE right). The surface and quantum well states shift towards lower binding energies with increasing silver coverage within the limits of the projected bulk band gap of Au(111). The gap is visible in Fig. 1 as the light area. The black circles indicate the dispersion of the uppermost calculated bulk band, shifted by 120 meV towards $E_F$, to match with the experimental position. The projected band gap of Au does not change with coverage. On the other hand, the calculated "band gap minimum" is the bulk mode with the lowest binding energy. This corresponds for a couple of monolayers to the lowest quantum well state of the Ag film.

The lower panels in Fig. 1 show the energy range of the $4d$ and $5d$ bands of Ag and Au, respectively. Contributions for the Au(111) surface (left) are identified according to Refs. 18 and 19 and overlayed by the band-structure calculations from Ref. 13. The bulk bands are denoted by numbers 2–6, whereas $D_1$ and $D_2$ are surface resonances. The valence band of 10 ML Ag/Au(111) corresponds perfectly to the overlayed band-structure calculations of pure Ag taken from the Ref. 13. Both calculations for silver and gold are taken from the Ref. 13 along $\Gamma$K direction, and He I radiation should correspond to $k_\perp$ in the vicinity of $\Gamma$.[20,21] However, the measurement paths on Au and Ag are differently displaced from $\Gamma$, which leads to different agreement between the calculation and the measurement for Au and Ag. The number and the splitting of the Au-bands are observed experimentally, their BEs are somewhat overestimated. One sees by comparison with the measurements that due to the small sampling depth of PES (at He I $\sim$5–10 Å)[22] the Au-bands are absent for 10 ML Ag/Au(111) and that the measured valence band corresponds completely to the one of bulk silver. Although the $d$ bands are already the ones of bulk silver, the upper panel for the 10 ML system still shows the $L$ gap of the Au(111) substrate lying $\approx$30 Å below the surface. The projected $sp$-band structure of Ag will evolve from the quantum-
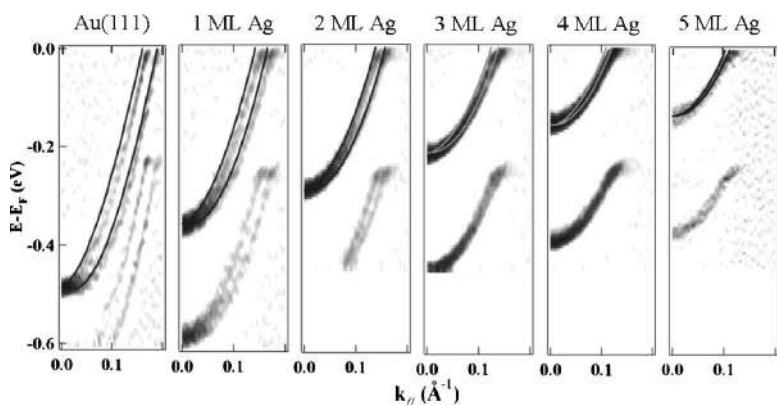


FIG. 2. Surface state dispersion changes with silver coverage taken with Ar I. The grey-scale maps represent the second derivative of the measured intensity. The calculations of the Shockley state (black lines) have been shifted for each coverage to fit the measured binding energies. The replica at higher BEs is due to the Ar satellite.

TABLE I. Binding energy (BE), effective mass, and spin-orbit splitting (SOS) of the surface state for the corresponding coverages of Ag on Au(111) as obtained from the band-structure calculations (superscript th) and as measured (superscript exp).

| Surface | BE$^{th}$(meV) | BE$^{exp}$(meV) | $m^*/m_e^{th}$ | $m^*/m_e^{exp}$ | SOS$^{th}(\Delta k_{\parallel})$(Å$^{-1}$) | SOS$^{exp}(\Delta k_{\parallel})$(Å$^{-1}$) |
|---------|------------|-------------|-------------|-------------|----------------------------|-----------------------------|
| Au(111) | 429 | 487 | 0.23 | 0.26 | 0.030 | 0.023 |
| +1 ML Ag | 409 | 305 | 0.28 | 0.33 | 0.023 | 0.019 |
| +2 ML Ag | 334 | 222 | 0.32 | 0.34 | 0.019 | 0.015 |
| +3 ML Ag | 274 | 184 | 0.35 | 0.38 | 0.014 | 0.013 |
| +4 ML Ag | 235 | 158 | 0.36 | 0.40 | 0.011 | 0.013 |
| +5 ML Ag | 223 | 98 | 0.36 | 0.41 | 0.009 | 0.010 |
| +6 ML Ag | 194 | 77[a] | 0.37 | | 0.007 | <0.010 |
| Ag(111) | 178 | 64 | 0.37 | 0.42 | 0.004 | <0.010 |

[a]Measured at 90 K (Refs. 7 and 24).

well states and reach the position of the Ag $sp$-gap BE minimum after several tens of monolayers, according to the previously reported "slower" development of the $sp$ bands of the adsorbate by comparison with the $d$ bands.[23] This is related to the highly localized character of the $d$ bands and, contrary to that, free-electron-like character of the extended $s$ states, which are thus sensitive to the projected gap and quantum-well boundaries.

The evolution of the surface state with Ag coverage is depicted in Fig. 2. The gray-scale maps represent the second derivative of the measured intensity. The replica of the surface state, appearing at higher binding energies, is due to the Ar satellite. With increasing Ag layer thickness one can clearly observe a shift of the surface state towards the Fermi level and a decrease of the spin-orbit splitting. A fit of the dispersion by two parabolas allows a more detailed analysis and yields the values for the maximum binding energy, the effective mass and the SOS given in Table I). Obviously all



FIG. 3. Ag-coverage dependent surface state binding energy: Experimental data using He I (shaded squares) and Ar I (white squares) radiation, band-structure calculations (triangles) and electron density of the surface state (see the inset) distributed over discrete numbers of monolayers (circles and line) both scaled between the binding energies of clean Ag(111) and Au(111) as reference points. The inset shows NFE calculations of the surface-state electron density perpendicular to the surface by Beckmann (Ref. 25) for 12 ML Ag/Au(111).

three parameters show a monotonous change from the values of pure Au(111) towards the values of Ag(111).

The black lines in Fig. 2 represent the result of our band structure calculations. Because the exact position of the Fermi level is often a problem in DFT results, it was necessary to shift the calculated surface state dispersions in energy to the position of the experimental result (values are given in Table I). The calculated effective masses and the spin-orbit splitting are in agreement with the experimental values.

Figure 3 presents the dependence of the measured and calculated BEs on the Ag film thickness. The squares represent the results of several measurements, obtained with different film preparation techniques and using He I or Ar I radiation. Thus, one gets insight into the data spread which could originate from different surface preparations or coverage calibrations. In spite of the observed differences, the BEs of all measured surface states agree reasonably well. Beside the measurements, the *ab initio* band structure calculations of the surface state are presented (triangles), scaled linearly between the two reference points at 0 ML [clean Au(111)] and 20 ML [for which we take the parameters of the clean Ag(111) surface]. The calculated binding energies (triangles) reproduce very well the changes of the measured binding energy with the Ag coverage.

The observed changes in surface state dispersion can be explained by closer inspection of the electron density as a function of the distance from the surface. The inset in Fig. 3 displays the result of a nearly free electron approximation for the electron density of a Au(111) surface covered by 12 ML of Ag.[25] Because the decay length is of the order of the overlayer thickness, the displayed electron density represents roughly the one of pure Ag(111). The plot shows that more than 80% of the surface state electrons are localized within the first 5 MLs. The electron density distribution can be used to illustrate the dependence of the BE on the layer thickness. If we use the electron density, integrated over the Ag overlayer thickness, as a weighting factor for the binding energies of pure Au(111) and Ag(111), we get the solid line in Fig. 3. The good agreement shows, that the surface state properties of the overlayer system can be decomposed in contributions from the two components. It demonstrates the exponential development of the Ag contribution in the BE of the surface state, which is related to the silver contribution to the total

number of atoms within the decay length of the surface state. It describes the measured binding energies perfectly.

We have presented high-resolution photoemission data of the *L*-gap Shockley states for 0–10 epitaxially grown ML of silver on Au(111). The Shockley state exhibits gradual changes with the layer thickness and the values of the relevant surface state parameters, describing the band dispersion, evolve from the ones of gold into the ones of silver. High-resolution photoemission has enabled the direct observation of the decrease of the spin-orbit splitting of the surface state with silver coverage. Good agreement is achieved between *ab initio* band structure slab-layer calculations embedded in the WIEN2K code and the photoemission data: The surface state band parameters are well reproduced by the theory, except for the value of the Fermi level, which is too high in the calculations. However, the relative shifts depending on the overlayer thickness are described by the calculations and can intuitively be explained by the distribution of the electron density decaying into the crystal volume. Whereas the localized *d*-bands are already bulk-like for 10 ML, the *sp* gap of the system is still the one of the substrate,

thus influencing the surface state which forms within the gap, even if the coverage thickness exceeds the photoelectron mean free path significantly. On the other hand, the good agreement of the slab-layer calculations with the experiment shows that this method is able to reproduce details of the surface electronic structure and can therefore be used to investigate interface systems theoretically. Furthermore, the characteristic changes of the surface state due to modifications of the surface and thus induced different changes of the *d* or *sp* bands, together with the possibility of a numerical reproduction by *ab initio* methods make the surface related states capable of providing important information about surface processes and interfaces.

*Electronic address: reinert@physik.uni-wuerzburg.de

[1] F. Reinert, J. Phys.: Condens. Matter **15**, S693 (2003).

[2] G. Nicolay, F. Reinert, S. Hüfner, and P. Blaha, Phys. Rev. B **65**, 033407 (2001).

[3] F. Forster, G. Nicolay, F. Reinert, D. Ehm, S. Schmidt, and S. Hüfner, Surf. Sci. **532-535**, 160 (2003).

[4] A. Bendounan, Y. Fagot-Revurat, B. Kierren, F. Bertran, V. Yu. Yurov, and D. Malterre, Surf. Sci. **496**, L43 (2002).

[5] A. Bendounan, H. Cercellier, Y. Fagot-Revurat, B. Kierren, V. Yu. Yurov, and D. Malterre, Phys. Rev. B **67**, 165412 (2003).

[6] F. Reinert and G. Nicolay, Appl. Phys. A: Mater. Sci. Process. **78**, 817 (2004).

[7] H. Cercellier, Y. Fagot-Revurat, B. Kierren, D. Malterre, and F. Reinert, Surf. Sci. **566**, 520 (2004).

[8] W. Shockley, Phys. Rev. **56**, 317 (1939).

[9] T. Miller, A. Samsavar, G. Franklin, and T.-C. Chiang, Phys. Rev. Lett. **61**, 1404 (1988).

[10] T. Hsieh, T. Miller, and T.-C. Chiang, Phys. Rev. B **33**, 2865 (1986).

[11] F. Reinert, G. Nicolay, S. Schmidt, D. Ehm, and S. Hüfner, Phys. Rev. B **63**, 115415 (2001).

[12] G. Nicolay, F. Reinert, S. Schmidt, D. Ehm, P. Steiner, and S. Hüfner, Phys. Rev. B **62**, 1631 (2000).

[13] N. Smith, Phys. Rev. B **9**, 1365 (1974).

[14] P. Blaha, K. Schwarz, G. K. H. Madsen, D. Kvasnicka, and J. Luitz, WIEN2K, *An Augmented Plane Wave+Local Orbitals Program for Calculating Crystal Properties* (Karlheinz Schwarz, Techn. Universität Wien, Austria, 2001), ISBN 3-9501031-1-2.

[15] J. P. Perdew, K. Burke, and M. Ernzerhof, Phys. Rev. Lett. **77**, 3865 (1996).

[16] N. Takeuchi, C. T. Chan, and K. M. Ho, Phys. Rev. B **43**, 13899 (1991).

[17] T. C. Hsieh and T. Chiang, Surf. Sci. **166**, 554 (1986).

[18] J. Nelson, S. Kim, W. Gignac, R. Williams, J. Tobin, S. Robey, and D. Shirley, Phys. Rev. B **32**, 3465 (1985).

[19] R. Paniago, R. Matzdorf, and A. Goldmann, Europhys. Lett. **26**, 63 (1994).

[20] P. Wehner, R. Williams, S. Kevan, D. Denley, and D. Shirley, Phys. Rev. B **19**, 6164 (1979).

[21] K. Mills, R. Davis, S. Kevan, G. Thornton, and D. Shirley, Phys. Rev. B **22**, 581 (1980).

[22] S. Hüfner, *Photoelectron spectroscopy* (Springer-Verlag, Germany, 2003), 3rd ed.

[23] J. G. Tobin, S. W. Robey, L. E. Klebanoff, and D. A. Shirley, Phys. Rev. B **35**, 9056 (1987).

[24] H. Cercellier, Y. Fagot-Revurat, B. Kierren, F. Reinert, D. Popović, and D. Malterre, Phys. Rev. B **70**, 193412 (2004).

[25] A. Beckmann, M. Klaua, and K. Meinel, Phys. Rev. B **48**, 1844 (1993).

# A high-resolution core-level study of Ni-catalyzed absorption and desorption of hydrogen in Mg-films

S.E. Stoltz [a,*], D. Popović [b]

[a] MAX-lab, Lund University, Box 118, SE-221 00 Lund, Sweden
[b] Material and Semiconductor Physics, KTH-Electrum, SE-164 40 Kista, Sweden

## Abstract

Ultra-thin magnesium and magnesium–nickel films grown on Mo(1 1 0) under ultra-high vacuum (UHV) conditions are hydrogenated at room temperature with atomic H and studied by high-resolution core-level photoelectron spectroscopy (PES). For the Mg-film a layer of hydride is formed at the Mg/Mo interface and a sub-mono layer of hydride is formed at the surface, while an intermediate region remained non-hydrogenated. For the Mg–Ni-film a thick layer of surface hydride was detected, showing that Ni enhances formation of Mg-hydride at the surface. During the heat-up of the hydrogenated Mg–Ni-film hydrogen desorption started at 400 K.
© 2007 Elsevier B.V. All rights reserved.

## 1. Introduction

The change to a renewable energy source in moving vehicles is no longer only an environmental issue, but an economic matter and a scientific challenge as well. Hydrogen is a perfect fuel, but its safe storage is an unsolved problem. Materials which can absorb hydrogen are being extensively studied because their implementation reduces the potential danger related to high-pressure vessels in moving vehicles (for a review see e.g. [1]). One of them is Mg(MgH$_2$), which has good weight to absorbing capacity ratio, but is nevertheless only scarcely studied by means of photoelectron spectroscopy (PES). Sprunger and Plummer report about surface hydride formation upon hydrogen deposition on a Mg single crystal at low temperature [2] and its irreversible transition to a chemisorbed and desorbing hydrogen at the surface upon annealing [3]. They notice that the hydride formation is facilitated by pre-dissociation of H$_2$. The techniques that they implement are

X-ray photoelectron spectroscopy (XPS), electron energy loss spectroscopy (EELS) and thermal desorption spectroscopy (TDS). On the other hand, Ostenfeld et al. [4] have investigated hydrogenation of ultra-thin Mg-films on a Mo(1 1 1) substrate, as Mg-films appear to be more appropriate than single crystals considering the scientific questions and future application issues. The techniques that they implement are XPS, low energy ion scattering spectroscopy (LEISS) and temperature programmed desorption (TPD). Their study focuses on the influence of Mg-film thickness, its deposition temperature or the atomic/molecular hydrogen used for the hydrogenation to the formation of the hydride. They conclude that the formation of magnesium hydride with H$_2$ is only possible when evaporating Mg in a hydrogen background at temperatures below 363 K [4].

In this paper, we investigate a more appropriate material candidate for hydrogen storage by synchrotron light based high-resolution core-level PES. Considering parameter space attractive for mobile hydrogen storage (1–10 bar, 0–100 °C) [1], Mg compounds have been preferred to pure Mg, first of all Mg–Ni alloys. Theoretical studies [6] show

that Mg–Ni has relatively low hydride formation energy. Here we present a comparative PES study of hydrogen absorbtion and desorption in ultra-thin Mg and Mg–Ni films grown on Mo(110). Our investigation reveals different mechanisms of hydride formation in these two films never reported before and more desirable properties of Mg–Ni-film in terms of applications.

## 2. Experimental

The Mo(110) crystal was cleaned by Ar ion sputtering (1 keV) followed by annealing at 1300 K and flash up to maximum of 1400 K. The photoelectron spectra were measured at beamline I311 at the MAX-lab synchrotron radiation facility in Lund, Sweden. This beamline which includes a modified SX-700 plane grating monochromator and a Scienta SES-200 electron energy analyzer is well suited for high-resolution electron spectroscopy at high-photon energies (up to $hv = 1500$ eV). The base pressure in the vacuum chamber was in the low $10^{-10}$ mbar range. The experimental energy resolution was 600 meV for spectra measured with $hv = 810$ eV, 200 meV for spectra measured with $hv = 350$ eV and 50 meV for spectra measured with $hv = 150$ eV. FITXPS2 software [10] was used for core-level fits.

Mg was evaporated from a Ta-boat heated by a tungsten filament. Ni was evaporated from a Ni rod at +1250 V which was e-bombarded from a hot filament at zero potential. In two different experiments, dissociated hydrogen was deposited on a Mg-film and on a Mg–Ni-film. Atomic H was produced with a hot tungsten filament ~5 cm from the sample. The sample was actually exposed to a mixture of H and $H_2$, but it is the H exposure which is relevant for the experiment as it will be discussed in the next section. The deposition was done at room temperature and the pressure in the preparation chamber was $1 \times 10^{-5}$ mbar for 5 min.

In the first experiment the Mo(110) surface was contaminated with small remains of C in spite of several oxygen treatments up to 1250 K, yielding nevertheless almost $1 \times 1$ low energy electron diffraction (LEED) pattern (very weak additional spots were seen). However, these impurities do not induce any conceptual changes. A 36 Å thick unordered Mg-film was evaporated on the Mo crystal at an evaporation rate of 2.4 Å/min. After the evaporation the LEED pattern disappeared. The derivation of the nominal thickness of the deposited films is explained in the next section.

In the second experiment no impurities are seen in PES and the LEED pattern was a sharp $1 \times 1$. A 16 Å thick unordered Mg–Ni-film was evaporated in 7 min at a rate of 2.3 Å per minute and the LEED pattern disappeared. The Ni to Mg ratio in the film was 1:4.6 in the upper half of the film and slightly higher close to the Mo crystal, as will be determined in the next section of this paper. Minor oxygen impurities appeared after the H dosing. The crystal was eventually heated-up and the Mg 2p peak was moni-

tored by PES. The temperatures given during the warmup of the Mg–Ni-film were obtained by means of a infrared thermometer, with error less than 5%.

## 3. Results

The thicknesses of the Mg and Mg–Ni-films are calculated according to the inelastic mean free path (see Ref. [8]) from core-level intensities of the Mo 3d (substrate) and the Mg 2p (adsorbate) peaks as formulated in the following equation:

$$\frac{I_{\text{adsorbate}}}{I_{\text{substrate}}} = \frac{\lambda_{\text{adsorbate}} \sigma_{\text{adsorbate}} (1 - e^{-t/\lambda_{\text{adsorbate}}})}{\lambda_{\text{substrate}} \sigma_{\text{substrate}} e^{-t/\lambda_{\text{substrate}}}}, \qquad (1)$$

where $I$ is intensity of core-level peaks, $\lambda$ is mean free path, $\sigma$ is the photoionization cross-section and $t$ is the thickness of the film. Mean free path values from the universal curve and cross-sections from Ref. [9] are used. All beamline and analyser parameters were identical for all compared peaks and changes in the radiation flux have been taken into account. The thicknesses were determined to be 36 Å for the Mg-film and 16 Å for the Mg–Ni-film. Consistent results are obtained when film thickness was determined from the attenuation of the Mo 3d signal before and after Mg or Mg–Ni deposition. The difference between the universal curve and the actual mean free path causes an uncertainty of about 20%. Formation of islands is excluded due to the very low-intensity of the Mo 3d peak after the Mg or Mg–Ni deposition.

The proportions of Mg and Ni in the Mg–Ni-film were found by comparing Mg 2p and Ni 3p core-level spectra measured at different settings (810 eV at normal emission, 350 eV at normal emission and at a polar emission angle $\theta = 60°$). In the upper half of the film there is ~17–18% of Ni and slightly more close to the Mo crystal.

Fig. 1a shows Mg 2p spectra from the Mg-film before (dashed line) and after H deposition (full line) and Fig. 1b shows Mg 2p spectra from the Mg–Ni-film before (dashed line) and after H deposition (full line). The peak at high-BE is attributed to Mg-hydride [3] and Fig. 1 clearly shows that the Mg-film is either poorly hydrogenized or that the hydride is lying deeper from the surface. Mg in the Mg–Ni-film is much more hydrogenated than Mg in the Mg-film. Another hydride formation characteristics (not shown here and visible only in pure Mg-films) are disappearance of the Mg surface plasmon loss peak at 57.0 eV and attenuation of the Mg bulk plasmon at 60.3 eV.

In Fig. 1a the spin–orbit splitting of the Mg 2p peak is clearly visible, while this is not the case in Fig. 1b due to the Mg–Ni interaction influenced broadening of the Mg 2p level in the Mg–Ni-film. Mg–Ni interaction also causes both the bulk peak and the hydride peak to appear at lower BEs for the Mg–Ni-film, which indicates that Ni donates electrons to Mg (chemical shift). While bulk Mg signal originates from all Mg atoms, it will be shown later that the hydride signal originates predominantly from those
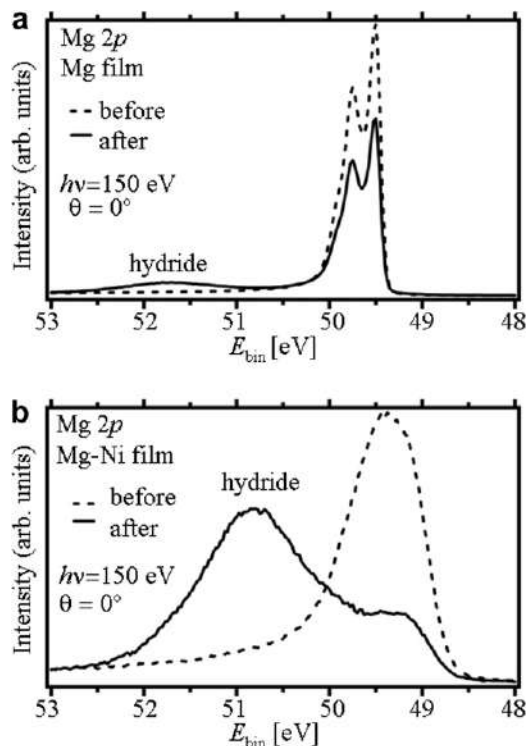
Fig. 1. Mg 2p spectra measured with 150 eV photon energy before (dashed lines) and after H deposition (full lines) on the Mg-film (a) and the Mg–Ni-film (b).
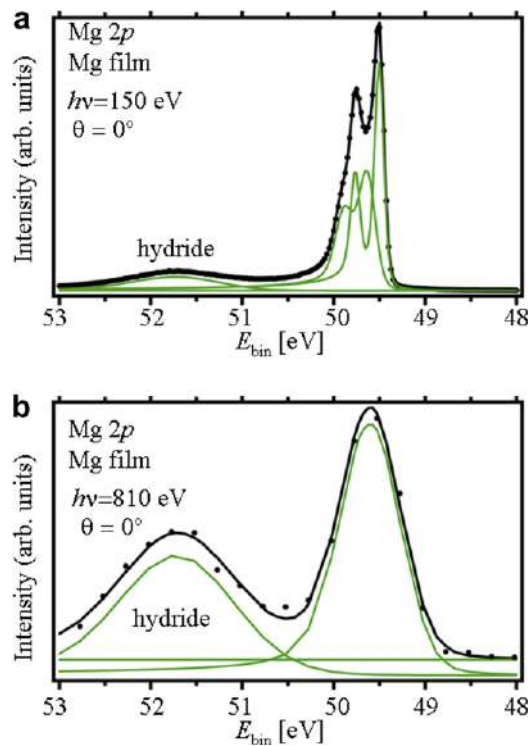


Fig. 2. The data points (dots) of Mg 2p spectra together with a fitted curve (full line) from the hydrogenated Mg-film: (a) Normal emission spectrum measured with $hv = 150$ eV is fitted with three spin–orbit doublets. (b) Normal emission spectrum measured with $hv = 810$ eV is fitted with two peaks.

Table 1
Results from fit of the Mg 2p core-level spectra from the hydrogenated Mg-film

| $hv$ (eV) | $\theta$ (°) | $\lambda \cos\theta$ (Å) | $I_{bulk}$ | $I_{surface}$ | $I_{hydride}$ |
|---|---|---|---|---|---|
| 150 | 60 | 2.75 | 23.6 | 48.8 | 27.6 |
| 350 | 60 | 3.9 | 32.1 | 37.9 | 30.6 |
| 150 | 0 | 5.5 | 41.8 | 42.8 | 15.4 |
| 350 | 0 | 7.8 | 58.5 | 21.1 | 20.4 |
| 810 | 0 | 11.5 | 52.5[a] | | 47.7 |

The table shows intensities of bulk, surface and hydride peaks, in percents of total emission.

[a] The surface and bulk components are not resolved in the $hv = 810$ eV spectrum. Therefore we give the total emission of these peaks (52.5).

Mg atoms which are surrounded by Ni. The hydride peak is therefore subject to a larger chemical shift than the bulk peak. The effects of the hydrogenation are visible in the Ni 3p level as well (not shown), which reveals that Ni takes part in the hydride formation.

We also tried to form hydride in the Mg–Ni-film by $H_2$ exposure. No hydride was formed in this way, as noticed in the previous studies in the case of a Mg-film [4]. This indicates that in order to produce large amounts of hydride, one would have to use atomic hydrogen. Luckily, atomization of $H_2$ is not an unsolved problem for the applications: in Ref. [7] for instance, a Pd layer was used to dissociate $H_2$.

In Fig. 2 we present core-level fits of Mg 2p spectra of the hydrogenated Mg-film measured at normal emission with different photon energies: 150 eV in (a) and 810 eV in (b). The core-level fit in Fig. 2a reveals that the Mg peak from the Mg-film contains two spin–orbit doublets. The high-BE doublet is more surface sensitive and is attributed to surface atoms. The shift between the surface and the bulk peak is 0.1 eV. A low-intensity peak at the high-BE side (2 eV shift) is attributed to Mg hydride. The hydride peak increases when higher excitation energy (which probes deeper) is used (Table 1), and with a photon energy of 810 eV the intensity of the hydride peak and the metallic Mg peak are about the same (Fig. 2b). Unfortunately, the increased photon energy implies worse energy resolution (see Section 2) and the components of the Mg 2p peak are not resolved in Fig. 2b. In spectra measured at $\theta = 60°$ the hydride peak also increases (Table 1).

This indicates a thick layer of hydride bordering to the Mg/Mo interface and a sub-monolayer of hydride at the surface, while an intermediate region remains non-hydrogenated as schematically presented in Fig. 3a. Reduction of the surface to bulk Mg 2p component ratio between the clean and the hydrogenized surface is in agreement with this model.

The Mg 2p level from the Mg–Ni-film is broader and the inclusion of a spin–orbit split in the fitting procedure is not obvious. A fit shown in Fig. 4 reveals that the Mg 2p level can be fitted with three peaks. These are a Mg–Ni peak at 49.1 eV (marked 1 in Fig. 4) which originates from Mg bonded to Ni, a Mg peak at 49.6 eV (2) originating from Mg which is not bonded to Ni and
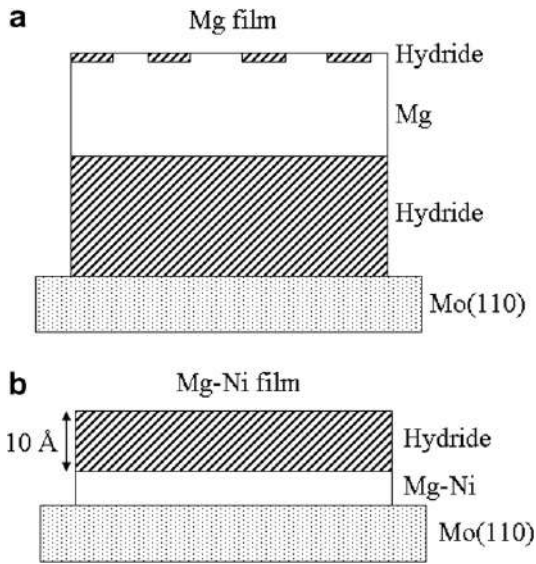
Fig. 3. Schematic representation (not to scale) of the hydrogenated Mg-film (a) and the hydrogenated Mg–Ni-film (b) on Mo(1 1 0) surface.

a hydride peak at ~50.9 eV (3). Peaks 1 and 2 are already present in the Mg 2p spectrum of the clean Mg–Ni surface. Upon hydride formation they experience H-induced chemical shifts similar to the Ni induced one described with Fig. 1. The binding energy of the hydride peak varies from 50.8 eV to 51.0 eV. This indicates that at least two hydride components are present in this peak. As they are not resolved, we keep one component (3 in Fig. 4) for all our fits.

One of those two components originates from the very surface, while the other one originates from bulk hydride. Their relative contributions in peak 3 in Fig. 4 change with photon energy and angle-induced surface sensitivity changes. As they have slightly different binding energies the total binding energy of component 3 is also changing.

In Fig. 4 the Mg 2p spectra after H deposition are fitted with these peaks and a summary of how the intensities change with $hv$ and $\theta$ is given in Table 2. The hydride peak increases with lower photon energy and with an increased $\theta$. This indicates that hydride is formed at the surface. The simplest model is that down to a certain depth, $d$, the Mg–Ni-film is hydrogenated and between the hydride and the crystal a layer of non-hydrogenated Mg–Ni-film remains, as schematically shown in Fig. 3b.

The thickness of the hydride layer is calculated using the equation:

$$\frac{I_{\text{Hydride}}}{I_{\text{Mg–Ni}}} = \frac{1 - e^{-d/\lambda}}{e^{-d/\lambda} - e^{-t/\lambda}}, \tag{2}$$

where $I_{\text{Hydride}}$ and $I_{\text{Mg–Ni}}$ are intensities of photoemission peaks. The total thickness of the film is $t$ and the term $e^{-t/\lambda}$ compensates for finite thickness of the film. The thickness of the hydride layer $d$ is found by solving the equation. The Mg peak (at 0 eV) is not included in these calculations, because we believe that it originates from Mg atoms which are not bonded to Ni and these atoms play a minor role in the hydrogenation of the Mg–Ni-film. Also, by excluding
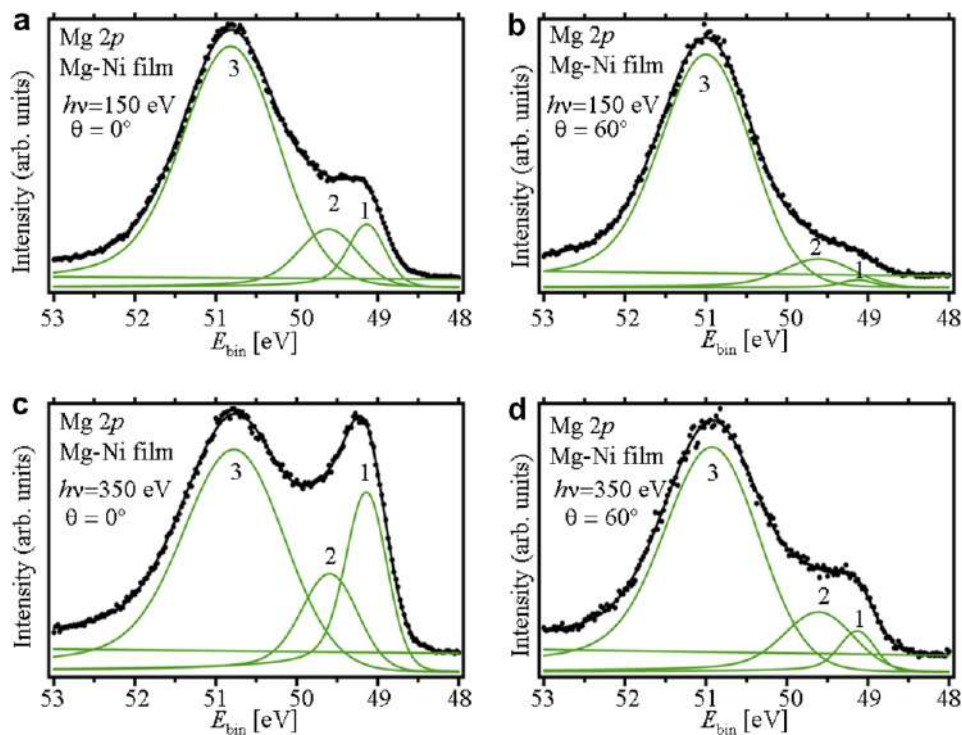


Fig. 4. The data points (dots) of Mg 2p spectra from hydrogenated Mg–Ni-film together with a fitted curve (full line). Measurements were taken at (a) $hv = 150$ eV and $\theta = 0°$, (b) $hv = 150$ eV and $\theta = 60°$, (c) $hv = 350$ eV and $\theta = 0°$ and (d) $hv = 350$ eV and $\theta = 60°$.

Table 2
Results from fit of the Mg 2p core-level spectra from the hydrogenated Mg–Ni-film

| $h\nu$ (eV) | $\theta$ (°) | $\lambda\cos\theta$ (Å) | $I_{\text{Mg–Ni}}$ (1) | $I_{\text{Mg}}$ (2) | $I_{\text{hydride}}$ (3) |
|---|---|---|---|---|---|
| 150 | 60 | 2.75 | 1.1 | 8.4 | 90.5 |
| 350 | 60 | 3.9 | 5.5 | 15.4 | 79.1 |
| 150 | 0 | 5.5 | 8.4 | 12.1 | 79.5 |
| 350 | 0 | 7.8 | 21.0 | 15.6 | 63.3 |

The table shows intensities of Mg–Ni (1), Mg (2) and hydride peak (3), in percents of total emission.

this peak a more consistent result in terms of hydride thickness (d) was found. The universal curve is used to find the mean free path parameter, $\lambda$, which is corrected by a factor of $\cos\theta = 0.5$, for spectra obtained at $\theta = 60°$. The mean value of $d$ thus obtained is 10.0 Å (standard deviation = 1.4 Å).

The hydrogenated Mg–Ni-film was finally heated. Mg 2p spectra recorded at different temperatures are shown in Fig. 5a. They reveal a general trend of the hydride films upon annealing: the hydride peak at the higher BEs (~51 eV) is disappearing and Mg peak is recovering to the state it has in a pure Mg–Ni-film. The measurements have been performed with a photon energy of 150 eV and each spectrum took 15 s to measure. A contour graph which displays all these spectra is shown in Fig. 5b. The
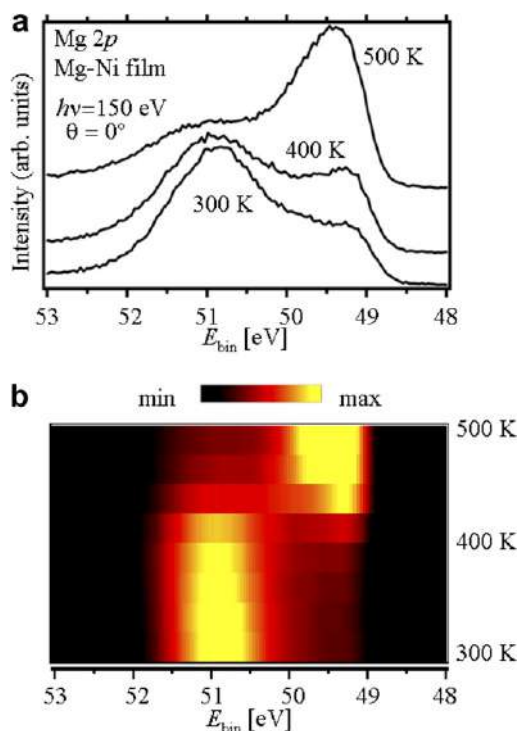


Fig. 5. Mg 2p spectra from the hydrogenated Mg–Ni-film measured with 150 eV photon energy during warm-up (a) at selected temperatures or (b) over the entire temperature range from 300 K to 500 K (contour-plot representation with high-intensity in yellow and low-intensity in black). (Yellow hot is changed to gray scale in the printed version.)

temperature raise was 1.8 K/s, which is similar to Ref. [4] (3 K/s). The intensity map in Fig. 5 shows that at 400 K the hydride peak rapidly decreases in intensity and a peak corresponding to non-hydrogenated Mg–Ni-film appears. At higher temperature this peak starts to dominate the spectrum and reaches its maximum intensity at 500 K. The integrated intensity of the Mg 2p spectrum shows a small increase at around 450 K, probably due to surface segregation of Mg atoms [11]. After warming to temperatures above 500 K the intensity of the Mg 2p peak drastically decreases. The interpretation is that the hydrogen desorption starts at 400 K, and that the Mg–Ni-film is destroyed at 550 K. However, the temperature raise in this experiment was quite swift. Therefore about 20% of the hydride content remained in the film when Mg segregation started (see topmost spectrum in Fig. 5a).

## 4. Discussion

According to our high-resolution PES study the Mg-film on Mo(110) develops a sub-monolayer of hydride at the surface and a much thicker hydride layer bordering the Mg/Mo interface, while an intermediate region remains non-hydrogenated. This can explain two peaks seen in temperature programmed desorption spectra Ref. [4]. Mo plays a significant role for the Mg-film hydrogenation, as is clear from the enhanced hydride formation in Mg close to the Mg/Mo interface. We conclude that both Ni and Mo enhance the hydride formation in Mg. However Ni enhances the hydride formation more strongly, which is why the hydride forms at the surface and not at the Mg–Ni/Mo interface.

Ni is a catalyst for formation of surface and sub-surface hydride, which is clear from the stronger hydride intensity in core-level spectra from Mg–Ni compared to Mg-films. Sprunger and Plummer achieved Mg hydrogenation at low temperatures [2,3]. We have accomplished a ~10 Å thick layer of surface hydride by room-temperature H-deposition on the Mg–Ni-film, which is clearly an advantage if applications are considered. For the Mg–Ni we do not find any indication of hydride formation close to the Mg–Ni/Mo interface. The hydride formation is thus totally determined by the geometrical distribution of Ni, which proves to be a better catalyst than a neighboring Mo crystal. During warm-up the hydrogen desorbs from the Mg–Ni-film well before the film is irreversibly changed by Mg-segregation on top and Ni-segregation at the bottom, which would be followed by desorption of the Mg-film. This is why Mg–Ni-films are better candidate for hydrogen storage than Mg-films, in which hydrogen desorbs simultaneously with Mg. [4]. In Ref. [5] it is shown that a multilayer capping of MgO also gives this effect, but it also enhances the desorption temperature. In our study we have the same difference between hydrogen desorption and film destruction. However, as our films contain much less oxygen, this temperature difference in our experiment can be assigned to the Ni content in the film.

## 5. Conclusion

In this paper, we present a comparative high-resolution PES study of two potential candidates for the hydrogen storage materials: Mg and Mg–Ni. Our chemically-shifted core-level components-analysis shows that Ni acts as a catalyst for the Mg-hydride formation and influences both the magnitude of the hydride building as well as its distribution within the Mg-film. Under the influence of Ni a thick surface hydride layer is formed, which furthermore can be desorbed from the film, leaving it unchanged. Different effects of mixed Ni or interfacing Mo on the hydride film geometry opens the possibilities for structural hydrogen storage.

## Acknowledgements

## References

[1] L. Schlapbach, A. Züttle, Nature 414 (2001) 773.
[2] P.T. Sprunger, E.W. Plummer, Chemical Physics Letters 187 (1991) 559.
[3] P.T. Sprunger, E.W. Plummer, Surface Science 307–309 (1993) 118.
[4] C.W. Ostenfeld, J.C. Davies, T. Vegge, I. Chorkendorff, Surface Science 584 (2005) 17.
[5] C.W. Ostenfeld, I. Chorkendorff, Surface Science 600 (2005) 1363.
[6] T. Vegge, L.S. Hedegaard-Jensen, J. Bonde, T.R. Munter, J.K. Norskov, Journal of Alloys and Compounds 386 (2005) 1.
[7] E. Johansson, C. Chacon, C. Zlotea, Y. Andersson, B.J. Hjörvarsson, Physics of Condensed Matter 16 (2004) 7649.
[8] S. Hüfner, Photoelectron Spectroscopy, third ed., Springer-Verlag, 2002, p. 12.
[9] J.J. Yeh, I. Lindau, Atomic Data and Nuclear Data Tables 32 (1985) 1.
[10] D.L. Adams, fitXPS2 Peak-fitting software. www.sljus.lu.se/download.html.
[11] P. Stefanov, Vacuum 47 (1995) 1107.

# Surface resonance on the $(6\sqrt{3} \times 6\sqrt{3})$–$R30°$-reconstructed 5 ML Au on $(\sqrt{3} \times \sqrt{3})$–$R30°$-4H–SiC(0001)

D. Stoltz [a,*], S.E. Stoltz [b], L.S.O. Johansson [c]

[a] *Materialfysik, MAP, KTH-Electrum, SE-16440 Kista, Sweden*
[b] *MAX-Lab, Lund University, SE-22100 Lund, Sweden*
[c] *Department of Physics, Karlstad University, SE-65188 Karlstad, Sweden*

## Abstract

In this paper we present evidence for a surface resonance on the $(6\sqrt{3} \times 6\sqrt{3})$–$R30°$-reconstruction obtained on 5 monolayers (ML) of Au deposited on the $(\sqrt{3} \times \sqrt{3})$–$R30°$-4H–SiC(0001) and subsequently annealed. We use synchrotron radiation-based angle resolved photoelectron spectroscopy to show that this resonance has no $k_\perp$-dispersion, but a parabolic-like $k_\parallel$-dispersion of 0.4 eV around $\Gamma$. Its electronic localization in the $(6\sqrt{3} \times 6\sqrt{3})$–$R30°$ surface reconstruction is documented by comparison with the $(2\sqrt{3} \times 2\sqrt{3})$–$R30°$ structure, obtained at a slightly lower annealing temperature after 5 ML Au deposition on the $(\sqrt{3} \times \sqrt{3})$–$R30°$-4H–SiC(0001) substrate.
© 2007 Elsevier B.V. All rights reserved.

*Keywords:* Gold; Silicon carbide; Surface electronic phenomena; Surface resonance; Surface structure; Synchrotron radiation angle resolved photoelectron spectroscopy; Low energy electron diffraction (LEED)

## 1. Introduction

Since the early studies of the valence band structure of Au(111) by Smith [1–3] and Stöhr et al. [4] the positions of the direct transitions from the uppermost d-band have been established. Later measurements of Courths et al. [5] and Kevan and Gaylord [6] have shown that the valence band of Au(111) contains features dispersionless with the change of photon energy. One of them is a well-known Shockley-type surface state (SS in Fig. 1), which appears in the L-gap of all noble metal (111) surfaces. The others were shown by Paniago et al. [7] to be herringbone reconstruction related surface resonances (D1, D2 in Fig. 1). The existence of yet another surface resonance (S in Fig. 1) was discussed by Zimmer and Goldmann [8].

The electronic structure changes if thin films of Au are observed instead of bulk Au(111). Reconstruction related resonances (D1, D2) can appear there [9] and the shoulder S develops with the Au coverage on W(110) [9], Si(111)-$2 \times 1$ [10] or cleaved Si(111) [11], which questions its relation to the surface potential. On the other hand, a new dispersionless state related to the surface potential appears for ∼2 ML Au/W(110), although it is not identified as a surface resonance [9]. Surface resonances are states degenerate with the bulk bands, which is why they are rather difficult to identify experimentally. They can disperse in $k_\parallel$, but not in $k_\perp$. One very good example of surface resonances is presented by Courths [12] in the ordered alloy Cu$_3$Au(111).

In this paper we present evidence for a reconstruction related surface resonance in $(6\sqrt{3} \times 6\sqrt{3})$–$R30°$ surface of 5 ML Au on $(\sqrt{3} \times \sqrt{3})$–$R30°$-4H–SiC(0001) by inspection of its $k_\parallel$- and $k_\perp$-dispersion, as well as the comparison with the valence band of a different reconstruction at the same Au coverage.

## 2. Experimental

The experiments have been performed at the beamline 33 at the MAX-lab synchrotron in Lund. Beamline 33 is

---

* Corresponding author. Tel.: +46 739 757305.
*E-mail address:* dunjap@kth.se (D. Stoltz).
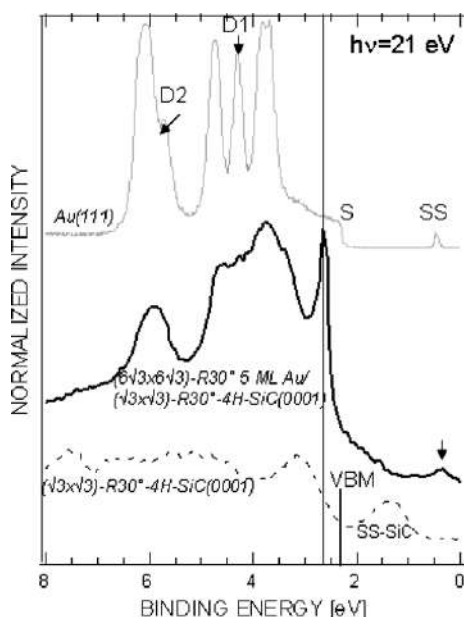
Fig. 1. Normal emission valence band of $(\sqrt{3} \times \sqrt{3})$–$R30°$-4H–SiC(0001) (dashed), $(6\sqrt{3} \times 6\sqrt{3})$–$R30°$ 5 ML Au on $(\sqrt{3} \times \sqrt{3})$–$R30°$-4H–SiC-(0001) (black bold line) and Au(111) (grey; taken from Fig. 1 in Ref. [16] at normal emission). The reconstructions are marked. All spectra are measured with photon energy of 21 eV. Au(111) was measured at 20 K, the rest at 100 K.

bending magnet based and allows for photon energies in the range between 15 eV and 200 eV. The end station is an angle resolving VG analyzer (ARUPS 10), which was used in this study with angular resolution of $\pm 2°$ and energy resolution of $\leqslant 100$ meV. The detector is rotatable in two angular degrees of freedom: in the horizontal and in the vertical plane. The sample is also rotatable around two axis: the polar and the azimuthal axis. The polar angle was set to give an incidence angle of the light of 45°. The azimuthal orientation of the sample was monitored by low energy electron diffraction (LEED). The base pressure of the analysis chamber was $4 \times 10^{-11}$ mbar, while that of the preparation chamber was in the lowest $10^{-10}$ mbar region.

The 4H–SiC(0001) wafer with 8° miscut in the $[11\bar{2}0]$ direction was purchased from Cree. It is high quality (low micropipe) N-type wafer polished on both sides. Precleaning was performed in methanol and by HF (5%) etching before the introduction in the UHV-chamber. In situ preparation started with outgassing at $T < 600$ °C. A well ordered (3 × 3) surface was obtained after 30 min anneal of the sample at 800 °C in ~2 ML/5 min Si flux [13–15]. The $(\sqrt{3} \times \sqrt{3})$–$R30°$-reconstruction was obtained by annealing the sample for additional 30 min at 1000 °C with no Si flux [13–15]. For temperature reading a pyrometer was used, with the emissivity 0.85 [15] and accuracy better than 10°.

Two ends of the sample were clamped onto two electrically isolated parts of the sample holder. Heating of the sample was achieved by running a current through the sam-

ple. Because of the different contact resistances a temperature gradient of ~50° develops over the sample. This was also visible by eye at the anneal temperatures at which the sample glows. This temperature gradient might have led to the onset of $(6\sqrt{3} \times 6\sqrt{3})$–$R30°$-reconstruction at the highest temperature end of the sample.

Five monolayers of gold were deposited on the $(\sqrt{3} \times \sqrt{3})$–$R30°$ surface of 4H–SiC(0001) from a W-filament carrying a piece of gold at ~0.5 ML/min. Deposited film was post-annealed at 650–700 °C (due to the already mentioned temperature gradient) during 5 min. The same emissivity value has been used for the pyrometer readings as in the case of the clean surface. The appearance and the quality of the reconstructions was checked by low energy electron diffraction (LEED). The sample was then cooled with liquid nitrogen for the photoelectron spectroscopy measurements. Prepared film consists predominantly of unreacted gold, which is expected to grow with (111) orientation following the hexagonal substrate with ~6% lattice mismatch. Film structure and morphology will be discussed in more detail elsewhere. The Au coverage was estimated from the core-level intensities.

Fermi level correction has been performed according to Fermi edge measurements on a tantalum foil under the same experimental conditions as in the Au/SiC experiment. The intensities have been calibrated with respect to the synchrotron ring current and the number of sweeps.

## 3. Results and discussion

Fig. 1 presents the development of the valence band (VB) with gold coverage. Spectrum from the $(\sqrt{3} \times \sqrt{3})$–$R30°$-4H–SiC(0001) is shown at the bottom with the dashed line. Surface state characteristic for this surface is clearly visible at 1.3 eV binding energy in agreement with Ref. [17]. With the deposition of gold the electronic structure changes from the one of SiC, towards the one of Au (grey spectrum on the top, measured with angular resolution of $\pm 0.15°$ and energy resolution of $\leqslant 3.5$ meV [16]). At ~5 ML of gold, the d-bands of gold are almost fully developed. D1 and D2 mark herringbone reconstruction related surface resonances in Au(111) [7] which are not expected to appear on our sample. Surface state of SiC is being replaced by a surface state at the binding energy close to that of the SS in pure gold (see arrow at the bold spectrum). Its appearance suggests that the gold has (111) orientation, as this is the only crystallographic direction in Au exhibiting projected band gap around the $\Gamma$ point (normal emission) [18] and thus allowing for the appearance of the surface states there.

A sharp peak at 2.6 eV binding energy (marked by a long vertical line in Fig. 1) appears at 5 ML Au on $(\sqrt{3} \times \sqrt{3})$–$R30°$-4H–SiC(0001) with $(6\sqrt{3} \times 6\sqrt{3})$–$R30°$-reconstruction (bold line). In the Au bandstructure, this feature lies clearly on the occupied side of the projected sp-gap (parabolic with minimum at ~1.13 eV at $\Gamma$ [16]), as well as at the higher binding energy side of the last VB

features (the shoulder S at ~2 eV). Furthermore, it lies energetically below the SiC valence band maximum (VBM, ~2.3 eV [17], marked on the SiC spectrum in Fig. 1). This all suggests that this state lies within the bulk bands of both substrate and adsorbate.

However, this sharp peak in the valence band of the $(6\sqrt{3} \times 6\sqrt{3})$–$R30°$-reconstructed 5 ML Au on $(\sqrt{3} \times \sqrt{3})$–$R30°$-4H–SiC(0001) has two-dimensional character. In Fig. 2 its photon energy dependent dispersion is presented in the photon energy range between 17 eV and 25 eV. All spectra were measured at normal emission. The lack of $k_\perp$-dispersion, as can be seen from its constant binding energy at different photon energies, confirms its two-dimensionality. Although it is two-dimensional, this state cannot be a true surface state, because it does not lie within any of the relevant gaps defined by SiC and Au.

In Fig. 3 a dispersion of this sharp VB peak in the $\Gamma K$ direction of the substrate is presented. The emission angle is indicated on the right side. The angular region which was investigated is between −10° and 15°, where this state disappears. We see that apart from the clear intensity change, a downwards parabolic-like dispersion (marked by ticks) around $\Gamma$ can be seen. The bandwidth of this state in this angular region is thus ~0.4 eV.

As we have shown that this state is two-dimensional and therefore not a bulk state, but that it is degenerate with the bulk states, it can be only a surface resonance (SR). For the quantum well state (QWS) one would rather expect much less intense and, in case of Au/SiC interface [19], a much broader peak, which would have to lie at the lower binding energy side of the SiC valence band maximum. To investigate this issue more thoroughly, we present a VB scan over the sample at normal emission in Fig. 4. The sample has been exposed to 5 ML of Au and post-annealed. As described earlier, the anneal temperature has a gradient of ~50 °C over the sample. The anneal temperatures corresponding to each measured spectrum are stated on the left. On the right side, the measured LEED patterns are shown. We see that the high-anneal-temperature side of the sample reconstructed to give $(6\sqrt{3} \times 6\sqrt{3})$–$R30°$ structure, while the low-anneal-temperature side of the sample reconstructed to give $(2\sqrt{3} \times 2\sqrt{3})$–$R30°$ structure. The identical $(6\sqrt{3} \times 6\sqrt{3})$–$R30°$-LEED pattern as shown here has been shown to correspond to a mixture of reconstructions on pure 6H–SiC(0001), which is still called $(6\sqrt{3} \times 6\sqrt{3})$–$R30°$ for practical reasons [20–23]. However, the $(6\sqrt{3} \times 6\sqrt{3})$–$R30°$-reconstruction on pure SiC has very different valence band structure than what we report here and no $k_\perp$-dispersionless features [24].
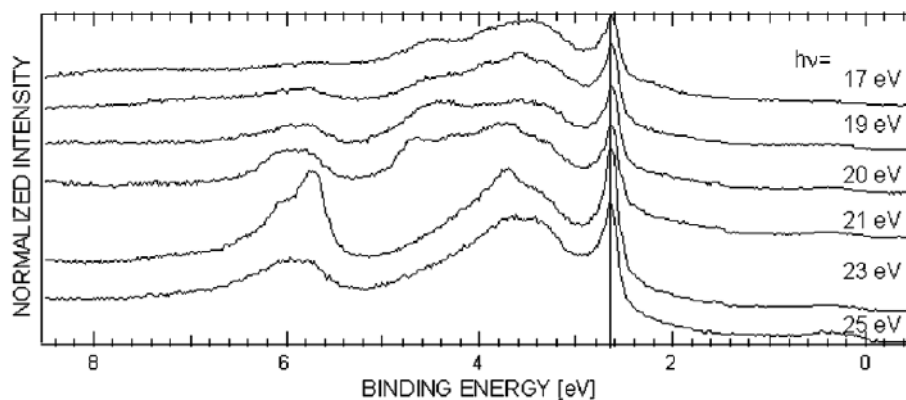


Fig. 2. Photon energy scan of the $(6\sqrt{3} \times 6\sqrt{3})$–$R30°$ 5 ML Au on $(\sqrt{3} \times \sqrt{3})$–$R30°$-4H–SiC(0001). Photon energies are marked on the right. All spectra are measured at normal emission at 100 K.
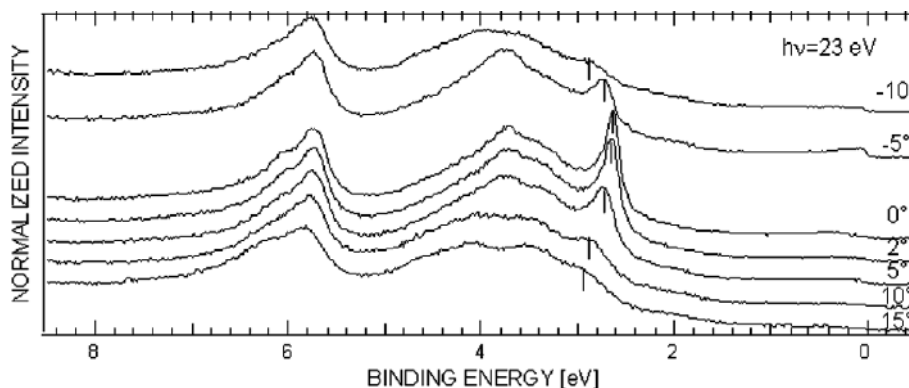


Fig. 3. Valence band dispersion of the $(6\sqrt{3} \times 6\sqrt{3})$–$R30°$-reconstructed 5 ML Au on $(\sqrt{3} \times \sqrt{3})$–$R30°$-4H–SiC(0001) in the $\Gamma K$ direction of the substrate. Emission angles are marked on the right. All spectra are measured with photon energy of 23 eV at 100 K.
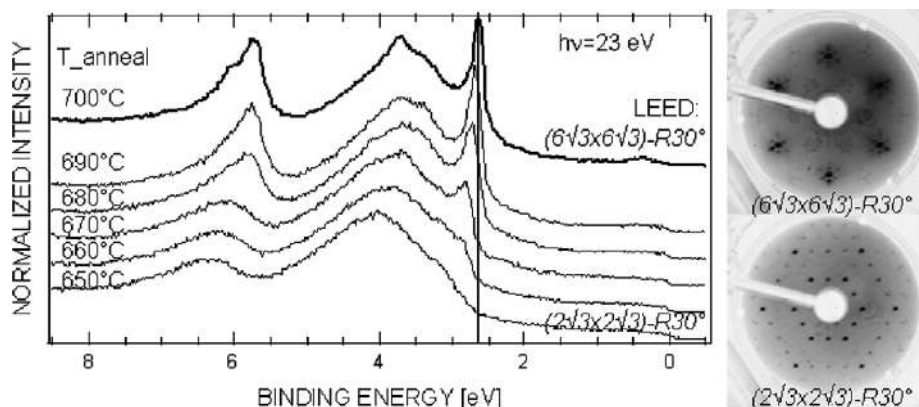
Fig. 4. Valence band scan across the 5 ML Au on $(\sqrt{3} \times \sqrt{3})$–$R30°$-4H–SiC(0001) surface with photon energy of 23 eV at normal emission at 100 K. The annealing temperature is marked on the left and the reconstruction seen by LEED is shown on the right. LEED beam energy was 113 eV.

The sharp peak at 2.6 eV is present in the $(6\sqrt{3} \times 6\sqrt{3})$–$R30°$, but not in the $(2\sqrt{3} \times 2\sqrt{3})$–$R30°$-reconstruction on the same surface. This is another indicator that this state is not a QWS. Both parts of the sample were exposed to the same amount of Au and the annealing temperature difference of ∼50 °C cannot contribute to significantly flatter surface and therefore appearance of the QWS only on one part of the surface. Core-level measurements indicate slightly more Au (∼6 ML) at the $(2\sqrt{3} \times 2\sqrt{3})$–$R30°$-reconstructed surface. This is an even stronger indication that the sharp peak at 2.6 eV is not a QWS. If it was a QWS, it would have to be visible at the $(2\sqrt{3} \times 2\sqrt{3})$–$R30°$-reconstructed surface as well. Furthermore, the disappearance of the sharp peak with the change of reconstruction indicates that this peak is clearly reconstruction related, i.e. a surface resonance.

## 4. Conclusions

We identify a surface resonance on $(6\sqrt{3} \times 6\sqrt{3})$–$R30°$-reconstructed 5 ML Au on $(\sqrt{3} \times \sqrt{3})$–$R30°$-4H–SiC-(0001). We show that this state is degenerate with bulk bands, but that it has a two-dimensional character. It exists between −10° and +15° along $\Gamma K$ direction of the substrate and its dispersion is shown to be parabolic-like around $\Gamma$ with 0.4 eV bandwidth. Its presence is directly related to the surface reconstruction. Our investigations of films with 1–5 ML Au deposited on the $(\sqrt{3} \times \sqrt{3})$–$R30°$-4H–SiC-(0001) surface show that the reconstruction formation is very sensitive to the annealing temperature. It is therefore important to notice that the surface resonance observed here is characteristic for 700 °C post-anneal temperature, but probably not for 5 ML of Au deposited.

## Acknowledgements

## References

[1] N. Smith, Phys. Rev. B 9 (1974) 1365.
[2] N. Smith, Phys. Rev. B 3 (1971) 1862.
[3] N. Smith, Phys. Rev. B 5 (1972) 1192.
[4] J. Stöhr, G. Apai, P.S. Wehner, F.R. McFeely, R.S. Williams, D. Shirley, Phys. Rev. B 14 (1976) 5144.
[5] R. Courths, H.-G. Zimmer, A. Goldmann, H. Saalfeld, Phys. Rev. B 34 (1986) 3577.
[6] S.D. Kevan, R.H. Gaylord, Phys. Rev. B 36 (1987) 5809.
[7] R. Paniago, R. Matzdorf, A. Goldmann, Europhys. Lett. 26 (1994) 63.
[8] H.-G. Zimmer, A. Goldmann, Surf. Sci. 115 (1986) 115.
[9] H. Knoppe, E. Bauer, Phys. Rev. B 48 (1993) 5621.
[10] M. Iwami, T. Terada, H. Tochihara, M. Kubota, Y. Murata, Surf. Sci. 194 (1988) 115.
[11] I. Braicovich, C.M. Garner, P.R. Skeath, C.Y. Su, P.W. Chye, I. Lindau, W.E. Spicer, Phys. Rev. B 20 (1979) 5131.
[12] R. Courths, M. Lau, T. Scheunemann, H. Gollisch, R. Feder, Phys. Rev. B 63 (2001) 195110.
[13] K. Heinz, J. Bernhardt, J. Schardt, U. Starke, J. Phys.: Condens. Mat. 16 (2004) S1705.
[14] U. Starke, J. Schardt, M. Franke, Appl. Phys. A – Mater 65 (1997) 587.
[15] R. Ostendorf, K. Wulff, C. Benesch, H. Merz, H. Zacharias, Phys. Rev. B 70 (2004) 205325.
[16] D. Popović, F. Reinert, S. Hüfner, V.G. Grigoryan, M. Springborg, H. Cercellier, Y. Fagot-Revurat, B. Kierren, D. Malterre, Phys. Rev. B 72 (2005) 045419.
[17] L.I. Johansson, F. Owman, P. Mårtensson, Surf. Sci. 360 (1996) L478.
[18] P. Heimann, H. Miosga, H. Neddermeyer, Phys. Rev. Lett. 42 (1979) 801.
[19] C. Virojanadara, L.I. Johansson, Surf. Sci. 600 (2006) 436.
[20] F. Owman, P. Mårtensson, Surf. Sci. 369 (1996) 126.
[21] F. Owman, P. Mårtensson, J. Vac. Sci. Technol. B 14 (1996) 933.
[22] Y. Marumoto, T. Tsukamoto, M. Hirai, M. Kusaka, M. Iwami, T. Ozawa, T. Nagamura, T. Nakata, Jpn. J. Appl. Phys. 34 (1995) 3351.
[23] L. Li, I.S.T. Tsong, Surf. Sci. 351 (1996) 141.
[24] L.I. Johansson, F. Owman, P. Mårtensson, C. Persson, U. Lindefelt, Phys. Rev. B 53 (1996) 13803.

# A high-resolution core-level photoemission study of the Au/4H-SiC(0001)-($\sqrt{3} \times \sqrt{3}$) interface

**D Stoltz[1], S E Stoltz[2] and L S O Johansson[3]**

[1] Materialfysik, MAP, KTH-Electrum, SE-16440 Kista, Sweden
[2] MAX-Lab, Lund University, SE-22100 Lund, Sweden
[3] Department of Physics, Karlstad University, SE-65188 Karlstad, Sweden

E-mail: dunjap@kth.se

**Abstract**

We present a systematic study of different reconstructions obtained after deposition of Au on the ($\sqrt{3} \times \sqrt{3}$)-R30°-4H-SiC(0001) surface. For 1–2 monolayers (ML) Au and annealing temperature $T_{anneal} \sim 675$ °C, a $3 \times 3$ reconstruction was observed. For 4 ML Au and $T_{anneal} \sim 650$ °C, a ($2\sqrt{3} \times 2\sqrt{3}$)-R30° reconstruction appeared, while 5 ML Au annealed at 700 °C reconstructed to give a ($6\sqrt{3} \times 6\sqrt{3}$)-R30° pattern. From the Si 2p and Au 4f core-level components, we propose interface models, depending on the amount of Au on the surface and the annealing temperature. For 1–4 ML Au annealed at 650–675 °C, gold diffuses under the topmost Si into the SiC and forms a silicide. An additional Si component in our Si 2p spectra is related to the interface between the silicide and SiC. For 5 ML Au annealed at 700 °C, silicide is also formed at the surface, covering unreacted Au on top of the SiC substrate. The interface Si component is also observed in the Si 2p spectra of this surface. The key role in Au/$\sqrt{3}$-4H-SiC(0001) interface formation is played by diffusion and the silicon-richness of the surface.

## 1. Introduction

Au on Si has been one of the most interesting systems for both applications in electronic devices and fundamental studies of interface formation and diffusion in the past decades. It has been clear since the earliest studies that strong interdiffusion of both Au in Si and Si in Au drives a complex interface formation in Au/Si [1, 2]. In the case of Si(111) as a substrate, the result is silicide ($Au_3Si$) at the surface covering some unreacted gold on top of the Si substrate [3, 4]. In contrast, Au on a Si(100) surface gives a silicide embedded between the Si at the surface and the bulk Si sample [5].

The interest in the Au/SiC interface has been growing during the past decade, as SiC started replacing Si in high-temperature, high-speed, high-power and high-voltage sensor

and electronic devices [6]. Investigations of Au/4H-SiC(000$\bar{1}$) reveal silicide at the surface, covering unreacted gold on top of the SiC sample [7], which is very similar to the interface formation between gold and Si(111). On the surface of 4H-SiC(0001), more silicon-rich ($3 \times 3$, ($\sqrt{3} \times \sqrt{3}$)-R30°) or more carbon-rich reconstructions (($6\sqrt{3} \times 6\sqrt{3}$)-R30°) can be obtained after different surface preparations [8], and they can serve as substrates for gold deposition. Studies of gold deposition on the $3 \times 3$ surface show the appearance of several different reconstructions depending on the post-anneal temperature [9]. For the ($2\sqrt{3} \times 2\sqrt{3}$)-R30° reconstruction, an interface consisting of Si at the surface followed by silicide layer followed by SiC has been proposed [9]. This is clearly different than the observed Au/4H-SiC(000$\bar{1}$) interface, but essentially the same as the one for Au/Si(100). A similar interface has been seen in $3 \times 3$-reconstructed Au on ($\sqrt{3} \times \sqrt{3}$)-R30°-4H-SiC [9].

In this paper we present a systematic study of different reconstructions obtained after deposition of Au on the ($\sqrt{3} \times \sqrt{3}$)-R30° SiC surface. We correlate coverages and post-annealing temperatures with different reconstructions. Using synchrotron radiation based photoelectron spectroscopy we analyse the emission angle dependence of the intensities of different core-level components, to obtain information about their surface character or bulk character. Finally, we propose models for interfaces, depending on the amount of Au on the surface and the annealing temperature.

## 2. Experimental details

The experiments were performed at beamline 33 at the MAX-lab synchrotron in Lund. Beamline 33 is bending magnet based, and it allows for photon energies in the range between 15 and 200 eV. The end station is an angle-resolving VG analyser (ARUPS 10), which was used in this study with angular resolution of $\pm 2°$ and energy resolution of $\leqslant 100$ meV. The detector is rotatable in two angular degrees of freedom: in the horizontal and in the vertical plane. The sample manipulator is also rotatable around two axes: the polar axis and the azimuthal axis. The polar angle was set to give an incidence angle of the light of 45°. The azimuthal orientation of the sample was monitored by low-energy electron diffraction (LEED). The base pressure of the analysis chamber was $4 \times 10^{-11}$ mbar, while that of the preparation chamber was in the lowest $10^{-10}$ mbar region.

The 4H-SiC(0001) wafer with 8° miscut in the [11$\bar{2}$0] direction was purchased from Cree. It is a high-quality (low micropipe) n-type wafer polished on both sides. Precleaning was performed in methanol and by HF (5%) etching before the introduction in the UHV chamber. *In situ* preparation started with outgassing at $T < 600$ °C. A well-ordered $3 \times 3$ surface was obtained after 30 min anneal of the sample at 800 °C in $\sim$2 ML 5 min$^{-1}$ Si flux [8, 10, 11]. The ($\sqrt{3} \times \sqrt{3}$)-R30° reconstruction (short $\sqrt{3}$) was obtained by annealing the sample for an additional 30 min at 1000 °C with no Si flux [8, 10, 11]. For temperature reading a pyrometer was used, with the emissivity 0.85 [11]. The temperature gradient over the sample was $\sim$50 °C, which might have led to the onset of ($6\sqrt{3} \times 6\sqrt{3}$)-R30° reconstruction at the highest-temperature end of the sample.

Gold was deposited on the ($\sqrt{3} \times \sqrt{3}$)-R30° surface from a W filament carrying a Au piece at $\sim$0.5 ML min$^{-1}$. Deposited films were post-annealed at 650–700 °C (due to the already-mentioned temperature gradient) for 5 min. The same emissivity value has been used for the pyrometer readings as in the case of the clean surface. The appearance and the quality of the reconstructions was checked by LEED. The sample was then cooled with liquid nitrogen for the photoelectron spectroscopy measurements. The Au coverages were estimated from the core-level intensities and quartz microbalance measurements.

Fermi level correction was performed according to the Fermi edge measurements on a tantalum foil under the same experimental conditions as in the Au/SiC experiment. The
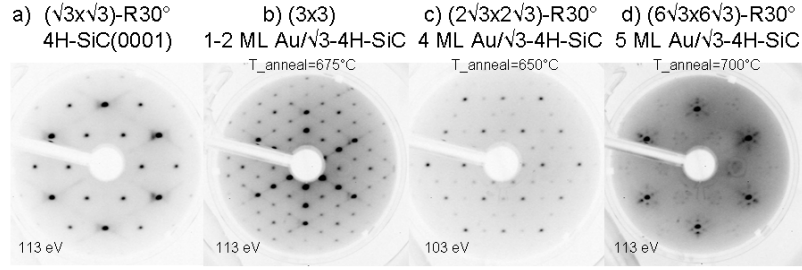
**Figure 1.** LEED patterns of (a) $(\sqrt{3} \times \sqrt{3})$-R30°-4H-SiC(0001) (short $\sqrt{3}$-4H-SiC); (b) $(3 \times 3)$ 1–2 ML Au/$\sqrt{3}$-4H-SiC; (c) $(2\sqrt{3} \times 2\sqrt{3})$-R30° 4 ML Au/$\sqrt{3}$-4H-SiC; (d) $(6\sqrt{3} \times 6\sqrt{3})$-R30° 5 ML Au/$\sqrt{3}$-4H-SiC. The post-anneal temperatures applied on the sample after gold deposition are marked on top. The LEED beam energy is marked in the lower-left corner.

**Table 1.** Acronyms used throughout this paper for different surfaces.

| Surface | Reconstruction | $T_{anneal}$ (°C) | Acronym |
|---|---|---|---|
| 4H-SiC(0001) | $(\sqrt{3} \times \sqrt{3})$-R30° | — | $\sqrt{3}$-4H-SiC |
| 1 ML Au/$\sqrt{3}$-4H-SiC | $3 \times 3$ | 675 | 1 ML Au-$3 \times 3$ |
| 2 ML Au/$\sqrt{3}$-4H-SiC | $3 \times 3$ | 675 | 2 ML Au-$3 \times 3$ |
| 4 ML Au/$\sqrt{3}$-4H-SiC | $(2\sqrt{3} \times 2\sqrt{3})$-R30° | 650 | 4 ML Au-$2\sqrt{3}$ |
| 5 ML Au/$\sqrt{3}$-4H-SiC | $(6\sqrt{3} \times 6\sqrt{3})$-R30° | 700 | 5 ML Au-$6\sqrt{3}$ |

intensities were calibrated with respect to the synchrotron current and the number of sweeps. The FITXPS2 software [12] was used for core-level fits.

## 3. Results

In figure 1(a) the LEED pattern of the substrate SiC surface, which was used for all gold depositions, is shown. It depicts the $(\sqrt{3} \times \sqrt{3})$-R30° reconstruction on the 4H-SiC(0001) ($\sqrt{3}$-4H-SiC). In figures 1(b)–(d) three different surface reconstructions are shown, which can be obtained by depositing and post-annealing gold on the $\sqrt{3}$-4H-SiC. In figure 1(b) a $3 \times 3$ reconstruction characteristic for small Au coverages (1–2 ML) and post-annealing temperatures of 675 °C (see figure 2) is presented. The one shown in the image was obtained for 2 ML Au. This reconstruction has been reported in similar conditions in [9]. In figure 1(c) a $(2\sqrt{3} \times 2\sqrt{3})$-R30° (short $2\sqrt{3}$) reconstruction is shown. It appears for coverages of 4–5 ML and post-anneal temperatures of 650 °C (see figure 2). The one shown in the image was obtained for 4 ML Au. On the other hand, the $(6\sqrt{3} \times 6\sqrt{3})$-R30° reconstruction (short $6\sqrt{3}$) is characteristic for 2–5 ML of Au on $\sqrt{3}$-4H-SiC post-annealed at 700 °C (see figure 2). The pattern shown in the image was obtained for 5 ML Au. A certain role for appearance of this reconstruction is played by the slightly higher annealing temperature of the 4H-SiC(0001) at one part of the sample, which may induce onset of $(6\sqrt{3} \times 6\sqrt{3})$-R30° reconstruction already on the pure substrate. We have not, however, observed the $6\sqrt{3}$ LEED pattern prior to gold deposition. Between these three reconstructions badly defined LEED patterns have been observed in figure 2 (shaded area). These will not be considered in further analysis. Acronyms which will be used for different coverages, instead of the full names describing the substrate, adsorbate and the reconstruction, are summarized in table 1.

The LEED patterns in figures 1(a)–(c) correspond exactly to the given reconstruction. In contrast, an identical $6\sqrt{3}$ LEED pattern as shown in figure 1(d) has been shown to correspond
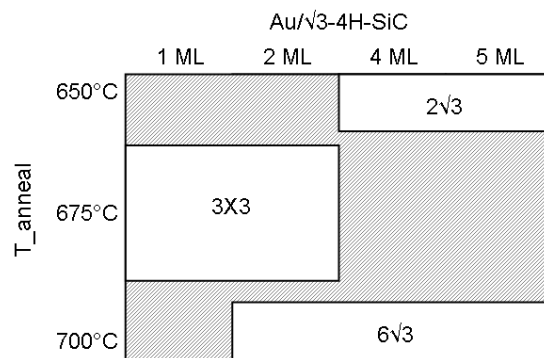
Au/√3-4H-SiC



**Figure 2.** Schematic representation of gold coverage and anneal temperature dependent reconstructions on Au/√3-4H-SiC.

to a mixture of reconstructions on pure 6H-SiC(0001) [13–16]. Scanning tunnelling microscopy (STM) studies [13] show the presence of $5 \times 5$ and $6 \times 6$ patterns superimposed on to $(2.1\sqrt{3} \times 2.1\sqrt{3})$-R30°, with or without the $\sqrt{3}$ structure. Comparison with our LEED pattern reveals that $\sqrt{3}$ spots are not present in our case.

In figure 3, Si 2p core levels at normal emission (NE) and 45° off normal for 1, 2 ML Au-$3 \times 3$ and 4 ML Au-$2\sqrt{3}$ are presented. The spectra correspond to the LEED patterns shown in figures 1(b) and (c). All spectra can be decomposed into three spin–orbit split doublets[4]. The doublet with the highest binding energy (dashed grey line) corresponds to SiC. At low coverages it is very similar to the Si 2p core level of the $\sqrt{3}$-4H-SiC surface (not shown), but it experiences a chemical shift of $-0.7$ eV upon Au exposure. Its intensity decreases with Au coverage, as expected.

The second doublet (bold grey line) is rather broad for all investigated coverages (total width of ∼0.5 eV) and exhibits a $-0.8$ eV shift with respect to the SiC peak in Au/√3-4H-SiC. This is the same as reported for silicide on Au/4H-SiC(000$\bar{1}$) [7] and for silicide on Au/4H-SiC(0001)-($3 \times 3$) [9]. We also assign this doublet to the silicide.

The third doublet (grey line) is sharper than the previous ones (total width of ∼0.3 eV) and has a binding energy at $-1.1$ eV from the SiC peak. For the lowest coverages it shows angular behaviour of a surface component, i.e. it increases in intensity at higher emission angles. At higher coverages, it shows angular-dependent intensity typical for an interface component. Due to its low width we attribute it to the Si at the surface or at the interface between Au–Si and SiC.

In figure 4, Au 4f core levels at normal emission for 1, 2 ML Au-$3 \times 3$ and 4 ML Au-$2\sqrt{3}$ are presented. Only one spin–orbit split doublet is resolved in all Au 4f spectra. All spectra are thus fitted consistently with similar parameters for this doublet[5]. The binding energies are shifted by ∼0.54 eV towards the higher binding energies compared to reference values for pure gold (84/87.7 eV). The doublets are relatively broad (total width ∼0.9 eV), but the inclusion of another doublet is not supported by the spectral shape. This suggests that there is only one chemical species of Au, which according to the silicide component in the Si 2p spectra and according to the shift of the measured Au spectrum with respect to the bulk Au binding energies can only be attributed to the silicide.

---

[4] Si 2p spin–orbit split doublets were fitted with following parameters: 0.61 eV spin–orbit splitting, 0.5 branching ratio, 0.06–0.08 eV Lorentzian width and variable Gaussian width, 0.04–0.17 asymmetry parameter.
[5] Au 4f spin–orbit split doublets were fitted with following parameters: 3.67 eV spin–orbit splitting and 0.07–0.25 asymmetry parameter.
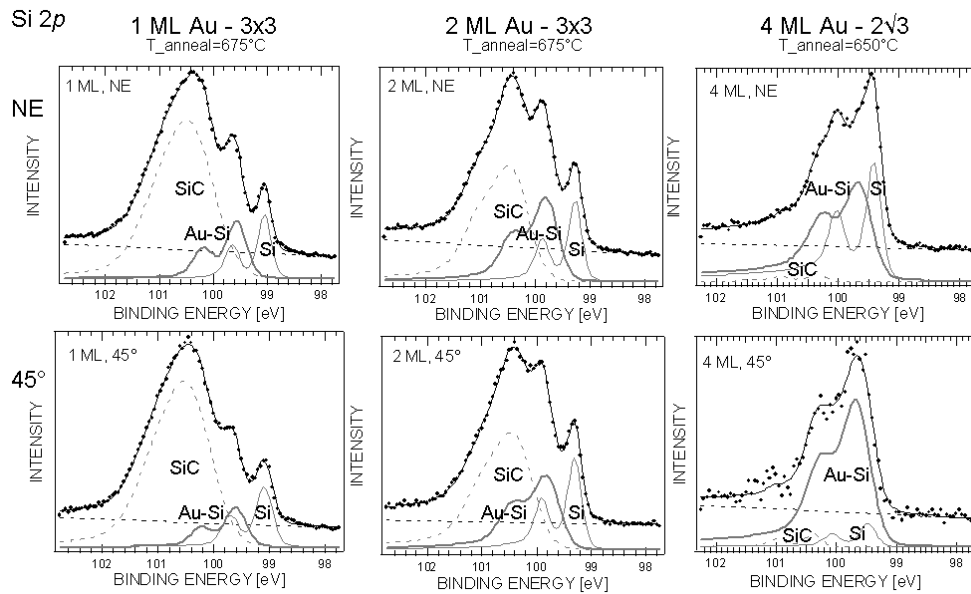
**Figure 3.** Si 2p core-level measurement (dots) and fit (black line) consisting of three spin–orbit split doublets (grey) and a linear background (dashed black line) at normal emission (NE) and 45° off normal for 1, 2 ML Au-3 × 3 (annealed at 675 °C) and 4 ML Au-2$\sqrt{3}$ (annealed at 650 °C). All spectra were measured with photon energy of 130 eV.
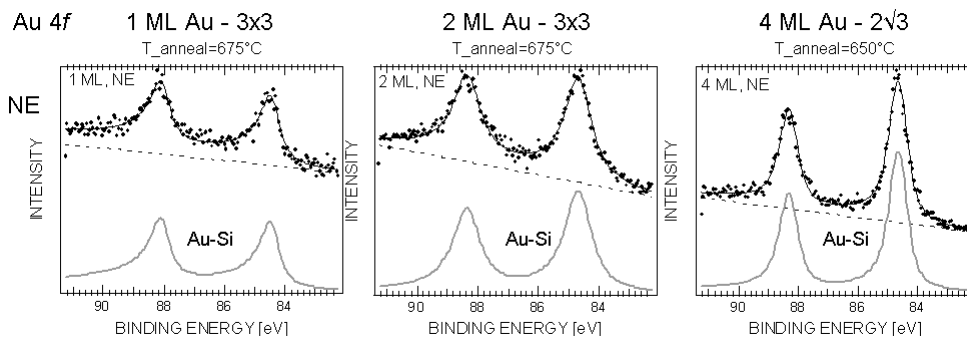


**Figure 4.** Au 4f core level measurement (dots) and fit (black line) consisting of one spin–orbit split doublet (grey) and a linear background (dashed black line) at normal emission (NE) for 1, 2 ML Au-3 × 3 (annealed at 675 °C) and 4 ML Au-2$\sqrt{3}$ (annealed at 650 °C). All spectra were measured with photon energy of 130 eV.

In figure 5, both Si 2p and Au 4f core levels at normal emission and 45° off normal for 5 ML of Au/$\sqrt{3}$-4H-SiC annealed at 700 °C are presented. This surface shows the 6$\sqrt{3}$ reconstruction from figure 1(d). As mentioned earlier, this reconstruction may be triggered by the slightly higher annealing of the clean SiC at that part of the sample, and thus the induced onset of the 6$\sqrt{3}$-SiC reconstruction. This was not seen by LEED, but some similarities between 5 ML Au-6$\sqrt{3}$ and 6$\sqrt{3}$-SiC exist in core levels. The Si 2p core level in figure 5 at NE covers similar binding energies as the one of the 6$\sqrt{3}$-SiC in figure 3(a) of [17].
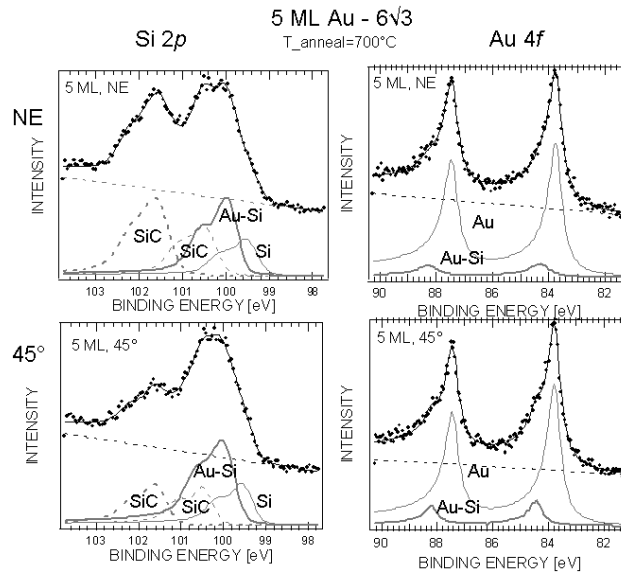
**Figure 5.** Si 2p and Au 4f core-level measurement (dots) and fit (black line) consisting of spin–orbit split doublets (grey) and a linear background (dashed black line) at normal emission (NE) and 45° off normal for 5 ML Au-$6\sqrt{3}$ annealed at 700 °C. All spectra were measured with photon energy of 130 eV.

However, the electronic structure of the $6\sqrt{3}$ reconstruction on pure or gold-covered SiC is very different [18].

Our spectrum can be decomposed in four spin–orbit split doublets. Two of them (dashed grey lines) show bulk character. While one of them (dashed grey line) is at the same binding energy as the SiC component seen at 1–4 ML of Au, the second bulk-like peak (bold dashed grey line) appears at ∼1 eV higher binding energy than the SiC peak. This peak is similar to the one observed in [17] for $6\sqrt{3}$-SiC, with a shift of 0.6 eV towards higher binding energies. Therefore, we also attribute it to the onset of $6\sqrt{3}$ reconstruction (slightly higher annealing temperature) on the clean SiC [17].

The most pronounced doublet (bold grey line) is a surface component (see off normal emission) and is attributed to the silicide. At its lower binding energy side a surface peak due to interface Si is seen (grey line). Their binding energy shifts are similar to the ones on the previously discussed surfaces (−0.5 and −0.9 eV). The width of the silicide peak is still ∼0.6 eV, while the width of the Si peak is now ∼0.6 eV. This suggest less well-defined coordination of interface Si, contrary to the sharp Si peak at 1–2 ML Au originating from the well-ordered surface atoms.

In the Au 4f spectra in figure 5, two different doublets can be clearly resolved. The higher binding energy one (bold grey line) is at approximately the same binding energy as the doublet in 1–4 ML Au, and it has a similar width of ∼0.85 eV. It has been assigned to the silicide and at 5 ML it has a surface character. On the lower binding energy side a much more intense doublet is observed (grey line). Its binding energy is 83.8/87.4 eV, very close to the reference Au values (84/87.7 eV) and its width is ∼0.68 eV. This doublet is assigned to a thick layer of unreacted gold below the surface. The shift between the two doublets is ∼0.65 eV, similar to that in [3, 7, 9].
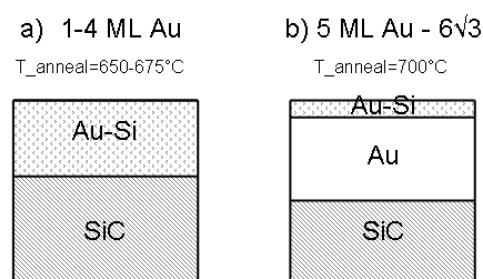
**Figure 6.** Schematic representation (not to scale!) of interface formation for (a) 1–4 ML Au annealed at $T_{anneal} = 650$–$675\,°C$ and (b) 5 ML Au-$6\sqrt{3}$ annealed at $T_{anneal} = 700\,°C$.

## 4. Discussion

In figure 6, models for the Au/$\sqrt{3}$-4H-SiC interface have been proposed based on the core-level results presented in previous figures. In these models, only SiC, Au–Si and Au have been taken into account, for simplicity. All the interface or surface Si components have been left out. For 1–4 ML and annealing at 650–675 °C (figure 6(a)), gold diffuses under the surface and forms a silicide layer. An additional component in the Si 2p spectra suggests that an interfacial Si layer develops between the surface silicide and buried SiC. In figure 6(b) the interface of 5 ML Au-$6\sqrt{3}$ annealed at 700 °C is shown. Silicide is at the surface, but underneath it is unreacted Au. Below them is SiC, which contributes with two bulk-like peaks to the Si 2p lineshape.

　　With increasing amount of gold, an increasingly large layer of silicide is formed at the surface at annealing temperatures of 650–675 °C. While the annealing temperature is crucial for the reconstruction at the surface, variations between 650 and 675 °C do not seem to play a role for interface formation. Both diffusion of gold and silicon is relevant for the silicide formation. As the surface that we measured was always liquid nitrogen cooled after preparation, we made sure that the diffusion was stopped and that we were looking at the non-changing system. For a bit higher annealing temperatures (700 °C), gold aggregation replaces silicide formation. Specific interface formation at 5 ML Au-$6\sqrt{3}$ is also related to the $6\sqrt{3}$ reconstruction. At the clean SiC surface, this reconstruction is carbon-rich. Higher annealing temperatures lead to silicon depletion at the surface and this depletion can be responsible for smaller amount of Si available for silicide formation.

　　Finally, photoelectron spectroscopy from a well-ordered surface is not free of photoelectron diffraction effects. These could influence the core-level intensity changes at 45° emission angle, which were used in this study. It is therefore important to notice that identification of the surface components in our spectra has been done based on the core-level shifts, peak widths and comparisons with the literature. The core-level spectra recorded at 45° emission angle agree very well with these findings. However, one conclusion could be affected by photoelectron diffraction. The placement of silicide on the surface within the interface model for 5 ML Au-$6\sqrt{3}$ annealed at 700 °C (figure 6(b)) was based on the observation that the silicide component in the Au 4f core level becomes stronger at 45°. If this was influenced by the photoelectron diffraction, the order of Au and Au–Si would simply change in figure 6(b): Au would be lying on top, while silicide would be at the interface between Au and SiC. In the absence of photoelectron diffraction data, we leave figure 6(b) as it is, because it is in good agreement with already reported interfaces of Au/Si(111) [3, 4] or Au/4H-SiC(000$\bar{1}$) [7].

## 5. Conclusions

A systematic study of different reconstructions obtained after deposition of Au on the ($\sqrt{3} \times \sqrt{3}$)-R30°-4H-SiC(0001) is presented. For 1–2 ML Au and $T_{anneal} \sim 675\,°C$ a $3 \times 3$-

reconstruction was observed. For 4 ML Au and $T_{anneal} \sim 650\,°C$, a $(2\sqrt{3} \times 2\sqrt{3})$-R30° reconstruction appeared, while 5 ML Au annealed at $700\,°C$ reconstructed to give a $(6\sqrt{3} \times 6\sqrt{3})$-R30° pattern. From the Si 2p and Au 4f core-level components, we propose interface models, depending on the amount of Au on the surface and annealing temperature. For 1–4 ML Au annealed at 650–675 °C, gold diffuses under the topmost Si into the SiC and forms a silicide. An additional Si component in our Si 2p spectra is related to the interface between the silicide and SiC. For 5 ML Au annealed at 700 °C, silicide is also formed at the surface, covering unreacted Au on top of the SiC substrate. An interface Si component is also observed in the Si 2p spectra of this surface. Diffusion and silicon-richness of the surface are determining factors behind this interface formation.

## Acknowledgments

## References

[1] Braicovich I, Garner C M, Skeath P R, Su C Y, Chye P W, Lindau I and Spicer W E 1979 *Phys. Rev.* B **20** 5131
[2] Sarkar D K, Bera S, Dhara S, Nair K G M, Narasimhan S V and Chowdhury S 1997 *Appl. Surf. Sci.* **120** 159
[3] Molodtsov S L, Laubschat C, Kaindl G, Shikin A M and Adamchuk V K 1991 *Phys. Rev.* B **44** 8850
[4] Yeh J-J, Hwang J, Bertness K, Friedman D J, Cao R and Lindau I 1993 *Phys. Rev. Lett.* **70** 3768
[5] Haruyama Y, Kanda K and Matsui S 2004 *J. Electron Spectrosc. Relat. Phenom.* **137–140** 97
[6] O'Connor J R and Smiltens J (ed) 1960 *Silicon Carbide—A High Temperature Semiconductor* (Oxford: Pergamon)
[7] Virojanadara C and Johansson L I 2005 *Surf. Sci.* **585** 163
[8] Heinz K, Bernhardt J, Schardt J and Starke U 2004 *J. Phys.: Condens. Matter* **16** S1705
[9] Virojanadara C and Johansson L I 2006 *Surf. Sci.* **600** 436
[10] Starke U, Schardt J and Franke M 1997 *Appl. Phys.* A **65** 587
[11] Ostedorf R, Wulff K, Benesch C, Merz H and Zacharias H 2004 *Phys. Rev.* B **70** 205325
[12] Adams D L 2001 fitxps2 peak-fitting software www.sljus.lu.se/download.html version 2.12
[13] Owman F and Mårtensson P 1996 *Surf. Sci.* **369** 126
[14] Owman F and Mårtensson P 1995 *J. Vac. Sci. Technol.* B **14** 933
[15] Marumoto Y, Tsukamoto T, Hirai M, Kusaka M, Iwami M, Ozawa T, Nagamura T and Nakata T 1995 *Japan. J. Appl. Phys.* **34** 3351
[16] Li L and Tsong I S T 1996 *Surf. Sci.* **351** 141
[17] Johansson L I, Owman F and Mårtensson P 1996 *Surf. Sci.* **360** L483
[18] Stoltz D, Stoltz S E and Johansson L S O 2007 *Surf. Sci.* http://dx.doi.org/10.1016/j.susc.2007.04.078

# Spectroscopic evidence for reversible hydrogen storage in unordered Mg$_5$Ni$_1$ thin films

**S E Stoltz**[1] **and D Stoltz**[2]

[1] MAX-lab, Lund University, Box 118, SE-221 00 Lund, Sweden
[2] Kamerlingh Onnes Laboratory, Leiden University, PO Box 9504, 2300 RA Leiden,
The Netherlands

E-mail: Sven.Stoltz@maxlab.lu.se

## Abstract

Thin magnesium–nickel films grown on Mo(110) under ultra-high vacuum conditions were hydrogenated with atomic H and studied by high-resolution core-level photoelectron spectroscopy (PES) and thermal desorption spectroscopy (TDS). We show spectroscopic evidence for reversible hydrogen storage and clear evidence that no Mg segregation or desorption occurs when hydrogen is desorbed from the film. During the heat-up of the hydrogenated Mg$_5$Ni$_1$ film (0.7 K s$^{-1}$) TDS shows that hydrogen desorption starts at 350 K and reaches its maximum at 420 K. Mg desorption starts at 450 K. The stability of the storage can be enhanced by cooling.

(Some figures in this article are in colour only in the electronic version)

## 1. Introduction

Hydrogen-absorbing materials are of great interest for potential applications as hydrogen storage in moving vehicles (for a review see e.g. [1]). One of them is Mg (MgH$_2$), which has a good weight to absorption capacity ratio. Photoemission studies of the hydrogenation of Mg single crystals have been done by Sprunger and Plummer [2, 3]. Hydrogen absorption and desorption have been further studied on thin Mg films by Ostenfeld *et al* [4], as they are experimentally easier to handle and more relevant for applications. However, the bonds between Mg and H are too strong in pure Mg. For reaching the parameter space needed for mobile hydrogen storage regarding compressibility, desorption temperature and reusability [1], Mg compounds have been preferred to pure Mg, primarily Mg–Ni alloys. The hydrogen is stored in a hydride phase; in this case the hydrogen atoms are chemically bonded to Mg. Theoretical studies [5] show that Mg–Ni has relatively low hydride formation energy. Nevertheless, hydrogen absorption in Mg–Ni alloys has only rarely been studied by means of photoelectron spectroscopy (PES).

Our previous comparative study [6] of the hydrogenation of both Mg and Mg–Ni films revealed different mechanisms of hydride formation, and we found that Mg–Ni is more desirable for applications than Mg. For the Mg film a layer of hydride was found to form

at the Mg/Mo interface (due to the catalytic properties of Mo) and a sub-monolayer of hydride at the surface, while the intermediate region remained non-hydrogenated. For the Mg–Ni film a thick layer of surface hydride was detected, showing that Ni enhances the formation of Mg-hydride at the surface. Ni was thus found to act as a catalyst for the Mg-hydride formation and to influence both the magnitude of hydrogenation and its distribution within the Mg film. Under the influence of Ni a thick surface hydride layer was formed, which furthermore could be desorbed from the film.

In this paper we present a study based on PES and thermal desorption spectroscopy (TDS) of hydrogen absorption and desorption in thin Mg–Ni films grown on Mo(110). We focus on the reversibility of hydrogenation, i.e. the possibility to hydrogenize and dehydrogenize a Mg–Ni film, without altering the host material. This capability is crucial for hydrogen storage, and in this paper we show spectroscopic evidence for it.

## 2. Experimental details

The photoelectron spectra were measured at beamline I311 at the MAX-lab synchrotron radiation facility in Lund, Sweden. This beamline has a modified SX-700 plane grating monochromator and a Scienta SES-200 electron energy analyser and is therefore well suited for high-resolution electron spectroscopy at high photon energies (up to $h\nu = 1500$ eV). The base pressure in the vacuum chamber was in the low $10^{-10}$ mbar range. The experimental energy resolution was 600 meV for spectra measured with $h\nu = 810$ eV, 200 meV for spectra measured with $h\nu = 350$ eV, and 50 meV for spectra measured with $h\nu = 150$ eV. The FitXPS2 software [7] was used for core-level fits.

The Mo(110) crystal was cleaned by Ar-ion sputtering (3 keV) followed by annealing at 1300 K. Surface cleanliness was checked by PES and surface ordering by low-energy electron diffraction (LEED), which showed a sharp $1 \times 1$ pattern. Mg was evaporated from a Ta boat heated by a tungsten filament, and Ni was evaporated from a Ni wire which was wound around a tungsten filament. A 17 Å thick unordered Mg–Ni film was evaporated in 40 min at a rate of $\sim 0.4$ Å min$^{-1}$. The Ni to Mg ratio in the film was 1:5. After the evaporation the LEED pattern disappeared and $\sim 2\%$ of oxygen contamination was detected by PES.

The Mg–Ni film was hydrogenized using atomic H, which was disassociated on a hot tungsten filament $\sim 5$ cm from the sample. The sample was actually exposed to a mixture of H and $H_2$, but it is the H exposure which is relevant for the experiment because $H_2$ will not be absorbed [6]. By using a tungsten filament to disassociate $H_2$ we circumvented the use of an additional surface layer (e.g. Pd to disassociate $H_2$ [8]). This is a big experimental advantage, because PES is a surface-sensitive technique. Hydrogen was dosed for 5 min at the preparation chamber pressure of $1 \times 10^{-5}$ mbar at room temperature.

The Mg–Ni film was both charged and discharged with hydrogen. The hydrogen charging is described above and the discharge was done by heating. The sample was heated up by running a constant current through the tungsten wire holding the Mo(110) crystal (substrate) while the hydrogenated Mg–Ni film was pointed towards a mass spectrometer (MKS, MicroVision Plus) to monitor the hydrogen ($m/e = 2$) and magnesium ($m/e = 24$) signals (i.e. no linear programming). The sample was $\sim 15$ cm from the mass spectrometer. The temperature was measured with a K-type (Cr/Al) thermocouple.

## 3. Results and discussion

The thicknesses of the Mg and Mg–Ni films were estimated from the attenuation of the Mo 3d (substrate) signal according to the following equation (see [9]):
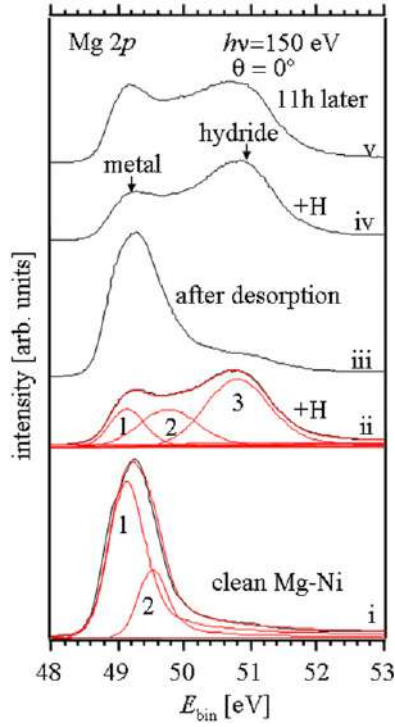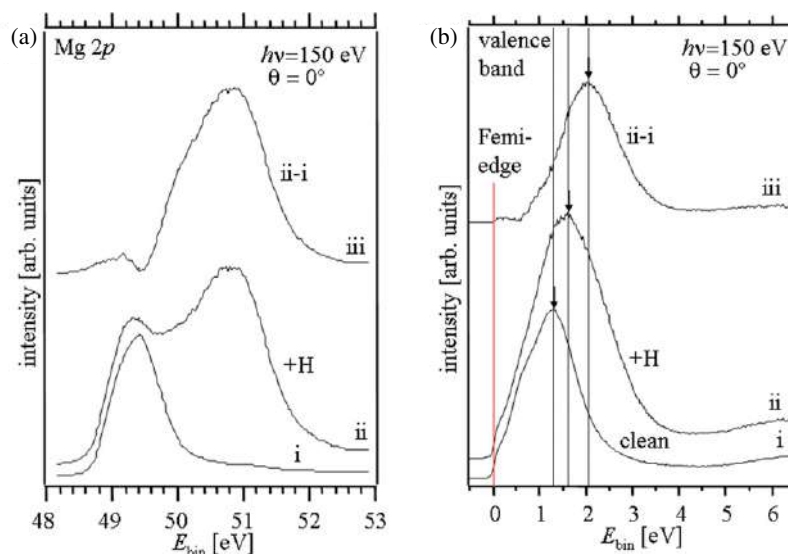
**Figure 1.** Mg 2p spectra from a clean Mg–Ni film (i), after H deposition (ii), after $H_2$ desorption (iii), after H redeposition (iv) and 11 h later (v). The spectra were measured at normal emission with a photon energy of 150 eV.

$$\frac{I_{\text{after}}}{I_{\text{before}}} = e^{-t/\lambda}, \tag{1}$$

where $I$ is intensity of Mo 3d peaks before and after evaporation of the Mg–Ni film, $\lambda$ is the inelastic mean free path and $t$ is the thickness of the film. Mean free path values from the universal curve were used. The thickness of the film was found to be 17 Å (the estimated error is less than 20%). All beamline and analyser parameters were identical for the measurements used for this evaluation, and changes in the radiation flux have been taken into account.

The proportions of Mg and Ni in the Mg–Ni film were found by comparing Mg 2p and Ni 3p core-level spectra and taking photoemission cross-sections [10] into account, as formulated in the following equation:

$$\frac{\text{Ni}_{\text{conc.}}}{\text{Mg}_{\text{conc.}}} = \frac{I_{\text{Ni 3p}}/\sigma_{\text{Ni 3p}}}{I_{\text{Mg 2p}}/\sigma_{\text{Mg 2p}}}, \tag{2}$$

where $I$ is intensity in core-level peaks and $\sigma$ is the photoemission cross-section. Because of the similar kinetic energy of photoelectrons from Mg 2p and Ni 3p, the mean free paths, $\lambda$, were approximately the same and did not have to be included in equation (2). The Ni to Mg ratio in the film was found to be 1:5 (estimated error ~10%). To check the Ni to Mg ratio in the whole film we measured spectra at different settings (810 eV at normal emission, 350 eV at normal emission and at a polar emission angle $\theta = 60°$) and used equation (2). The same Ni to Mg ratio was obtained through the whole film (1:5).

All beamline and analyser parameters were identical for all compared peaks, and changes in the radiation flux have been taken into account (the Mg 2p peak and the Ni 3p peak were measured in the same spectrum).

Figure 1 shows the Mg 2p spectrum during two cycles of hydrogen being stored in and emptied from a Mg–Ni film. The clean Mg 2p spectrum (spectrum (i) in figure 1) changes

**Table 1.** Results from fit of the Mg 2p core-level spectra from figure 1. The spectra were measured with a photon energy of 150 eV at normal emission. The table shows the intensities of the Mg–Ni (peak 1), Mg (peak 2) and hydride peak (peak 3), as a percentage of the total emission.

| Spectra | (i) | (ii) | (iii) | (iv) | (v) |
|---|---|---|---|---|---|
| $I_{\text{Mg–Ni}}$ (peak 1) | 73% | 17% | 70% | 14% | 19% |
| $I_{\text{Mg}}$ (peak 2) | 27% | 28% | 21% | 25% | 29% |
| $I_{\text{Hydride}}$ (peak 3) | — | 55% | 14% | 62% | 52% |

when the film becomes hydrogenated in such a way that metallic emission decreases, while the hydride peak at the higher binding energy increases (spectrum (ii) in figure 1), in accordance with [6]. When the hydrogenated film was warmed up, $H_2$ left the sample and the hydride peak decreased. During the absorption/desorption cycles the heating was stopped at 420 K. Furthermore, it was possible to refill the sample again with hydrogen (see spectrum (iv) in figure 1). This is spectroscopic evidence for reusable hydrogen storage in Mg–Ni films. At these conditions (ultra-high vacuum (UHV) and room temperature) a slow dehydrogenation of the hydrogenated Mg–Ni film was detected. This is clear from spectrum (v) in figure 1 measured 11 h after spectrum (iv).

The Mg 2p spectra in figure 1 were analysed with a peak-fitting software [7]. The Mg 2p level from the Mg–Ni film was broad and the inclusion of a spin–orbit split in the fitting procedure was not obvious. We showed that it is possible to fit the Mg 2p level with three peaks [6]. These peaks are a Mg–Ni peak at 49.1 eV with a full width at half maximum (FWHM) of 0.65 eV (marked 1 in figure 1), a Mg peak at 49.6 eV with a FWHM of 1.0 eV (marked 2 in figure 1) and a hydride peak at $\sim$50.8 eV with a FWHM of 1.2 (marked 3 in figure 1). Peak 1 originates from Mg bonded to Ni, peak 2 originates from Mg which is not bonded to Ni, and peak 3 originates from Mg bonded to hydrogen atoms. The deconvolution is shown for spectra (i) and (ii) in figure 1. Peak 1 and peak 2 were already present in the Mg 2p spectrum of the clean Mg–Ni film (spectra (i) and (iii) in figure 1), while peak 3 is significant only on hydrogenated surfaces (spectra (ii), (iv) and (v) in figure 1). For the clean or dehydrogenated surface (spectra (i) and (iii) in figure 1), peak 2 was at 49.5 eV and less wide. This is caused by a different surrounding i.e. metal and not hydride. The intensities of peaks 1, 2 and 3 were obtained by core-level fitting of all five spectra presented in figure 1 and are summarized in table 1.

By comparing the intensities of fitted core-level peaks corresponding to metal (peak 1 in figure 1) and hydride (peak 3 in figure 1), the thickness of the hydride layer was found to be $\sim$8 Å (peak 2 should not be included while calculating the thickness of the hydride layer; this is further explained in [6]). In the photoelectron spectrum measured at a polar angle of 60°, (not shown) the hydride peak is stronger; this confirmed that the hydride was on top of the metal. During the absorption/desorption cycles the heating was stopped at 420 K. At this temperature, most of the hydrogen had desorbed from the film, but Mg segregation and desorption had not yet started, in accordance with [6]. The Mg 2p core-level spectrum after hydrogen desorption (spectrum (iii) in figure 1) is very similar to the one of the clean surface (spectrum (i) in figure 1). But core-level fits revealed emission from the hydride peak (compare spectra (i) and (iii) in table 1). But this hydride peak (peak 3 in spectrum (iii) in figure 1) is not surface sensitive, and therefore the remnant of the hydride seemed to be homogeneously distributed in the film. It is possible that with a slower temperature rise the dehydrogenation would be more complete. In the case of oxidation, peak 3 in spectrum (iii) could be a core-level shift from MgO. However, this can be excluded, because we had about the same amount of oxygen impurities ($\sim$2–3%) on the surface as on the clean film, and the clean film showed no MgO emission (spectrum (i) in figure 1). Also this peak (peak 3 in spectrum (iii)) was not surface
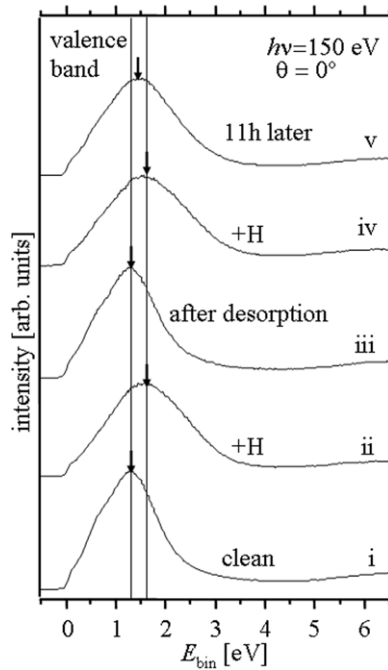
**Figure 2.** Valence band spectra from a clean Mg–Ni film (i), after H deposition (ii), after $H_2$ desorption (iii), after H redeposition (iv) and 11 h later (v). The spectra were measured at normal emission with a photon energy of 150 eV.

**Table 2.** Peak position and FWHM of the peak in the valence band (figure 2).

| Spectra | (i) | (ii) | (iii) | (iv) | (v) |
|---|---|---|---|---|---|
| Peak position (eV) | 1.31 | 1.59 | 1.28 | 1.56 | 1.47 |
| FWHM (eV) | 1.42 | 1.93 | 1.40 | 1.97 | 1.82 |

sensitive, which one would have expected for oxygen impurities. In spectrum (iv) in figure 1 the hydride peak is larger than in spectrum (ii) of the same figure. This is because the film was already partly hydrogenated when the H deposition started. Table 1 can also help to quantify hydride losses from the hydrogenated film over time. Spectrum (v) in figure 1 was measured 11 h after spectrum (iv) in the same figure, and according to table 1 the hydride peak had lost 10% of its intensity. This desorption at room temperature is related to UHV conditions, because a vacuum environment pulls out hydrogen from the film, while the surrounding of $H_2$ stabilizes the hydride. Therefore, this would not be an issue in future applications with a surrounding pressure of 1–10 bar [1].

Figure 2 shows the valence band spectra during the same two cycles of hydrogenation of the Mg–Ni film shown in figure 1. The spectra are dominated by a (mainly Ni 3d) peak centred at ∼1.5 eV below the Fermi energy. This peak shifts towards higher binding energy and increases in width when the film is hydrogenated. The peak positions and the values of full width half maxima (FWHMs) are compiled in table 2. Spectrum (i) in figure 2 (clean) is very similar to spectrum (iii) in the same figure (after H desorption). And spectrum (ii) in figure 2 (after the first H deposition) is very similar to spectrum (iv) in the same figure (after the second deposition). After 11 h (spectrum (v) in figure 2) the peak had shifted to an intermediate position, due to a slow dehydrogenation of the hydrogenated Mg–Ni film. This confirms that valence band changes are in agreement with the observations of the core levels. The peak in the valence band shifted towards higher binding energies because of new states in the hydrogenated parts of the film. In the hydrogenated film (spectrum (ii) and spectrum (iv) in figure 2) the

**Figure 3.** (a) Mg 2p spectra from a clean Mg–Ni film (i), after H deposition (ii) and the Mg 2p level from a completely hydrided Mg–Ni film (iii), constructed from a linear combination (subtraction) of (i) and (ii). (b) Valence band spectra from a clean Mg–Ni film (i), after H deposition (ii) and the valence band from a completely hydrided Mg–Ni film (iii), constructed from a linear combination (subtraction) of (i) and (ii).

valence band peak becomes broader. This is because the film is not completely hydrogenated and the peak is a superposition of contributions from both hydrogenated and metallic parts of the film.

We to constructed a hypothetical spectrum from a fully hydrogenated Mg–Ni film by a linear combination. In figure 3(a) the Mg 2p spectra before (i) and after (ii) hydrogenation (same as in figure 1) are combined to construct a Mg 2p spectrum from a completely hydrogenated Mg–Ni film (spectrum (iii) in figure 3). Spectrum (iii) is found by taking (iii) = (ii) − (i), where (i) is the flux normalized spectrum of the clean Mg–Ni film multiplied by 0.30 and (ii) is the flux normalized spectrum after the hydrogenation. The same procedure was used for the valence bands in figure 3(b), i.e. the spectrum before hydrogenation was multiplied by the same factor (0.30) before a hypothetical valence band spectrum of a completely hydrogenated Mg–Ni film (spectrum (iii) in figure 3(b)) was constructed by subtraction ((iii) = (ii) − (i)). For the Mg 2p spectrum the factor 0.30 was found by eliminating the metallic peak (peak 1). For the valence band, the factor 0.30 was found by having very low emission close to the Fermi edge in the valence band spectrum.

When the Mg–Ni film was hydrogenated the environment changed also for Mg atoms which were not directly bonded to hydrogen; therefore the metal peak before (see spectrum (i) in figure 3(a)) and after (see spectrum (ii) in figure 3(a)) hydrogenation are a bit different and cannot be completely subtracted from each other. This is why spectrum (iii) in figure 3(a) shows some irregularities in the lineshape. The hydride peak has a shoulder on the low binding energy side which originates from Mg atoms not bonded to Ni atoms (peak 2 in figure 1 and table 1).

The peak in the valence band of the completely hydrogenated Mg–Ni film (spectrum (iii) in figure 3(b)) is shifted further towards higher binding energies. The binding energy of the peak is 2.0 eV and the FWHM becomes 1.4 eV. The emission at the Fermi level disappeared and a
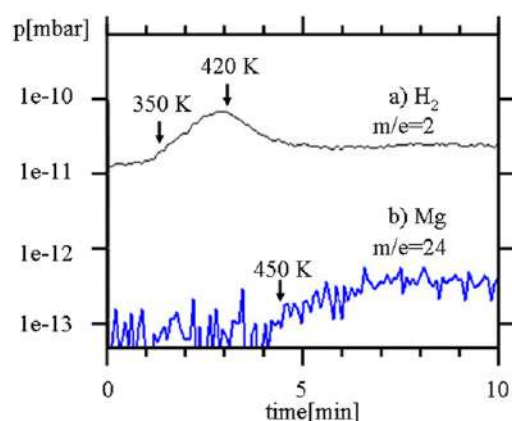
**Figure 4.** TDS spectra of (a) $H_2$ ($m/e = 2$) and (b) Mg ($m/e = 24$). The temperature of the sample was raised by a constant current of 7.5 A through the tungsten wire which held it.

gap of 0.7 eV opened up. This peak is more narrow than the peak in the spectrum from the hydrogenated film (figure 3(b) (ii) FWHM = 1.9 eV) which consisted of contributions from two (unresolved) peaks (metal and hydride). The previously reported optical band gap for a hydrogenated alloy with this Ni to Mg ratio (1:5) is 3.2 eV [8]. But the optical band gap is between the valence band maximum (lowest binding energy) and the lowest unoccupied states, while the gap we observed (0.7 eV) is between the valence band maximum and the Fermi level.

Figure 4 shows TDS spectra from (a) $H_2$ ($m/e = 2$) and (b) Mg ($m/e = 24$) during the final heat-up. We were probing $m/e = 2$ and not $m/e = 1$ because, despite the fact that hydrogen is stored as atomic H, it desorbs in its molecular form. Figure 4(a) shows that at 350 K the $H_2$ signal started to increase, and it reached its maximum signal at 420 K after 3 min. When desorbing hydrogen (from spectrum (ii) to spectrum (iii) in figures 1 and 2) we stopped there. Up to this point the temperature rise was almost linear (0.7 K s$^{-1}$). Figure 4(b) shows that at 450 K the Mg signal starts to rise, which indicates that Mg desorption has started.

When heating up a Mg–Ni film, Mg segregation could occur. This is a known problem with Mg–Ni alloys [11], and we have therefore performed a detailed comparison of spectra from the clean film and spectra from the film after hydrogen desorption. We have measured Mg 2p and Ni 3p spectra at different photon energies and angles before and after the first cycle of hydrogen absorption–desorption. The Ni to Mg intensity ratio from core levels remained unchanged for all spectra ($h\nu = 810$ eV at normal emission, $h\nu = 350$ eV at normal emission and $h\nu = 350$ eV at 60°), which showed that no segregation occurred. This means that it is possible to desorb hydrogen while leaving the film intact, because the hydrogen desorbs from the Mg–Ni film well before segregation sets in or before the film is irreversibly changed by desorption. This is why Mg–Ni films are better candidates for hydrogen storage than Mg films, in which hydrogen desorbs simultaneously with Mg [4].

Figure 5 presents live spectra (time-resolved) from a film with a Ni to Mg ratio of 1:4 at room temperature (figure 5(a)) and at LN$_2$-temperature (figure 5(b)). Each contour plot comes from 12 spectra measured over 3 min for 15 s each. The spectral intensity is shown by a yellow hot (grey) colour scale. The difference between figures 5(a) and (b) became very clear. While the film underwent a fast dehydrogenation at room temperature, it was totally stable at liquid-nitrogen temperature.

The stability of the hydrogenated film was not only dependent on the environment, but also on the Ni to Mg ratio in the film. By increasing the Ni content in the film from 1:5 to 1:4 one gets a much faster spontaneous dehydrogenation at room temperature, as shown in figure 5(a). The low binding energy metallic peak is recovered, while the hydride peak disappeared already
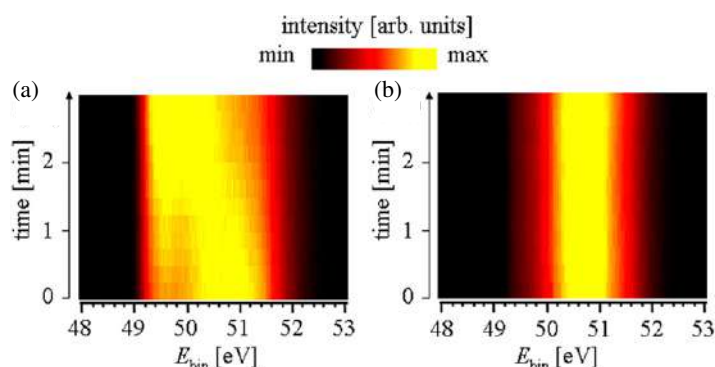
**Figure 5.** Mg 2p spectra from a more Ni-rich hydrogenated Mg–Ni film measured with 150 eV photon energy at (a) room temperature or (b) liquid-nitrogen temperature. The spectra are represented by a contour plot with high intensity in yellow and low intensity in black. The yellow hot colour scale is changed to greyscale in the printed version.

after a couple of minutes under the beam. However, spontaneous desorption or instability under the beam can be stopped by cooling the sample to liquid-nitrogen temperature, as shown in figure 5(b). While this experiment was performed at liquid-nitrogen temperature, which was the only one lower than room temperature which could be achieved under stable conditions at our beamline, some preliminary investigations showed that significantly higher temperatures would suffice to stabilize the hydrogenated film, presumably around 0 °C.

## 4. Conclusion

In this paper we have presented a high-resolution photoemission and thermal desorption study of the reversible hydrogenation of Mg–Ni films. We showed spectroscopic evidence for reversible hydrogen storage in a $Mg_5Ni_1$ film. We also showed that stored hydrogen can be desorbed from the Mg–Ni film without Mg segregation or desorption. Hydrogen desorption was found to start at 350 K, and it reached its maximum at 420 K at 0.7 K s$^{-1}$ heating rate. And by following the Mg signal from the mass spectrometer we found that Mg desorption started at 450 K for this film. Spontaneous hydrogen desorption at room temperature was shown to depend on the Mg:Ni ratio in the film, and could be stopped by cooling.

## Acknowledgments

## References

[1]  Schlapbach L and Züttle A 2001 *Nature* **414** 353
[2]  Sprunger P T and Plummer E W 1991 *Chem. Phys. Lett.* **187** 559
[3]  Sprunger P T and Plummer E W 1994 *Surf. Sci.* **307–309** 118
[4]  Ostenfeld C W, Davies J C, Vegge T and Chorkendorff I 2005 *Surf. Sci.* **584** 17
[5]  Vegge T, Hedegaard-Jensen L S, Bonde J, Munter T R and Norskov J K 2005 *J. Alloys Compounds* **386** 1
[6]  Stoltz S E and Popović D 2007 *Surf. Sci.* **601** 1507
[7]  Adams D L, fitXPS2 Peak-fitting software www.sljus.lu.se/download.html
[8]  Johansson E, Chacon C, Zlotea C, Andersson Y and Hjörvarsson B J 2004 *J. Phys.: Condens. Matter* **16** 7649
[9]  Hüfner S 2002 *Photoelectron Spectroscopy* 3rd edn (Berlin: Springer) p 12
[10] Yeh J J and Lindau I 1985 *At. Data Nucl. Data Tables* **32** 1
[11] Stefanov P 1995 *Vacuum* **47** 1107

# Tunneling evidence for spatial location of the charge-density-wave induced band splitting in 1*T*-TaSe₂

D. Stoltz,[1,*] M. Bielmann,[2] M. Bovet,[3] L. Schlapbach,[2] and H. Berger[4]

[1]*Materialfysik, MAP, KTH-Electrum, SE-16440 Kista, Sweden*
[2]*Swiss Federal Lab for Materials Science and Technology (EMPA), CH-8600 Dübendorf, Switzerland*
[3]*Institut de Physique, Université de Neuchâtel, CH-2000 Neuchâtel, Switzerland*
[4]*Institut de Physique Appliquée, EPF, 1015 Lausanne, Switzerland*

We present the atomically resolved room temperature scanning-tunneling microscopy study of bias dependent images of charge density waves (CDWs) in 1*T*-TaSe₂. With the help of angle-resolved photoemission of the CDW-split Ta $d_{z^2}$ band in 1*T*-TaSe₂, we determine the electronic location of Ta $d_{z^2}$ subbands on inequivalent atoms of the reconstructed Ta plane. We thus demonstrate the atomic origin of the CDW-formation related effects observed in the band structure of this material.

The charge-density-wave (CDW) formation has been one of the most popular topics of the last decades due to interest in the mechanism behind the interplay of the complex structural and electronic changes. One of the convenient hosts of the CDWs are the layered transition metal dichalcogenides (TMDs) of the 1*T* type. The quasi-two-dimensionality of these materials allows straightforward interpretations of the band mapping in terms of the mapping of the initial bands of the crystal and it promises conditions for the Fermi surface nesting—one of the most popular mechanisms proposed to be responsible for the CDW formation. Furthermore, recent investigations reveal similar mechanisms behind the electronic instability driven pseudogap in high-temperature superconductors[1,2] and the pseudogapped Fermi surface in 1*T*-TMDs: TaSe₂ and TaS₂.[3,4]

The advantage of studying 1*T*-TaSe₂ originates from the fact that it is in commensurate CDW phase already at room temperature (RT). Scanning-tunneling microcopy (STM) on this compound has revealed so far the CDW wavelength $\lambda_{CDW}=12.6$ Å (Ref. 5) and the image of the CDW reconstruction,[6–10] stating that the atomic modulation gives minor contribution to the overall *z* deflection, which is dominated by the CDW. Kim *et al.*[6] were the first to apply scanning-tunneling spectroscopy (STS) to investigate fingerprints of the CDW-reconstructed band structure.

In this Brief Report, we present atomically resolved RT STM measurements on 1*T*-TaSe₂ in its CDW phase. By tuning the bias voltage of the STM image, we tunnel into different CDW-split subbands of the Ta $d_{z^2}$ band. These subbands are identified by band mapping. We demonstrate that they are spatially located on three groups of inequivalent atoms by visualizing those atoms when tunneling at a bias voltage same as the subband binding energy.

STM experiments on 1*T*-TaSe₂ have been performed in a UHV system equipped with a UHV atomic force microscopy/STM scanning probe microscope from Omicron NanoTechnology operating at RT described elsewhere.[11] The images were taken in a constant height mode. Bias voltages are given with respect to the sample, i.e., positive bias means tunneling from occupied states. Band-mapping experiments have been performed using Vacuum Generators ESCALAB

Mk II spectrometer at room temperature with monochromatized He I ($h\nu=21.2$ eV) photons[12] by means of computer controlled sequential sample rotation.[13] The energy and angular resolution were 20 meV and 0.5°, respectively. The accurate position of the Fermi level ($E_F$) has been determined on a polycrystalline copper sample. Surface reconstruction was checked by low energy electron diffraction. X-ray photoelectron diffraction was used to determine the sample orientation *in situ* with an accuracy of better than 0.5°. Samples of 1*T*-TaSe₂ have been prepared from the elements by reversible chemical reaction with iodine as a transport agent, between 950° (hot zone) and 900° (cold zone).[14] They were cleaved *in situ* at pressures in the lower $10^{-10}$ mbar region.

Figure 1 shows experimental results obtained, implementing angle-photoemission spectroscopy along the $\bar{\Gamma}\bar{M}$ (a) and $\bar{\Gamma}\bar{K}$ (b) directions and up to a binding energy of 2 eV. Spectra cover the range between (a) 0° and 50° or (b) −5° and 20°
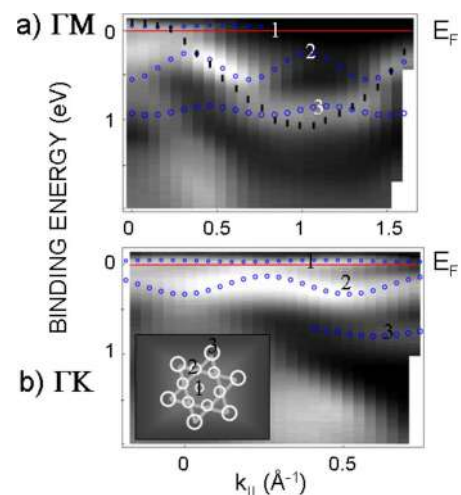


FIG. 1. (Color online) Band mapping along (a) $\bar{\Gamma}\bar{M}$ and (b) $\bar{\Gamma}\bar{K}$ of the cleaved 1*T*-TaSe₂ with a photon energy of 21.2 eV at RT. Dark circles represent the band splitting and folding with the new periodicity. Black markers highlight the schematic position of the unreconstructed band. High intensity in white.

in a given polar direction (converted to $k_\parallel$ in the image). The images depict dispersion of the Ta $d_z^2$ band, which exhibits a large electronlike pocket around the $\bar{M}$ point. At the higher binding energies, the Se $4p$ band appears energetically close to the Ta $d_z^2$ band primarily in the vicinity of $\bar{\Gamma}$ point.

Figure 1 shows that the Ta $d_z^2$ band [expected to disperse along ticks in Fig. 1(a)] is instead split into three subbands (circles). According to the Star-of-David model[15] of the $(\sqrt{13} \times \sqrt{13})R13.54°$ reconstruction in the Ta plane [Fig. 1(b), inset], the three subband manifolds are expected in the CDW phase. The formation of the stars breaks the hexagonal symmetry of the undistorted lattice and introduces three types of inequivalent atomic positions: the atom in the center (1), the six atoms constituting the first hexagon around it (2), and the six atoms constituting the outmost hexagon of the starlike cluster (3). These groups are assumed to correspond to different subband manifolds of the CDW-split Ta $d_z^2$ band [marked also as 1, 2, and 3 in Figs. 1(a) and 1(b)]. As the bands within the manifolds are not resolved, we will continue addressing the subband manifolds just as subbands.

The photoemission intensities follow the unreconstructed band structure[16] and thus highlight the three new subbands along the $1 \times 1$ dispersion:[4] high intensity of bands 1, 2, and 3 in Fig. 1(a) is mainly along the ticks marking the unreconstructed band. The new subbands are furthermore clearly backfolding: circles in Figs. 1(a) and 1(b) are following periodic functions with the periodicity of the new, reconstructed BZ and they describe the measured dispersion of the subbands astonishingly well. Both the band splitting and the backfolding of the subbands are CDW-related effects. A splitting of the Ta $d$ band into oscillating subbands was confirmed by the *ab initio* band-structure calculations for the similar material—$1T$-TaS$_2$ (Ref. 4) with the CDW-induced atomic positions.

The periodic lattice distortion introduced by the CDW lock-in can be visualized by an STM. Figure 2 shows (a) 7 $\times$ 7 nm$^2$, (b) 8 $\times$ 6 nm$^2$, and (c) 7 $\times$ 6.6 nm$^2$ of the *in situ* cleaved $1T$-TaSe$_2$ surface measured with different bias voltages and a tunneling current of 1.2 nA.

Figure 2(a) at a bias voltage of 0.4 eV (tunneling from the occupied states) shows arrays of white flowerlike patterns. Their periodicity is $\sim$12 Å, which corresponds to the diameter of one star drawn schematically in Fig. 1(b) (inset) and reproduced on the left side of Fig. 2. The periodic repetition of this pattern confirms the presence of the charge density waves. If we look at Fig. 1, the 0.4 eV binding energy corresponds mainly to the second subband. It is thus clear that by tunneling from the occupied states of one of the subbands, we achieve highest intensity on those atoms that electronically contribute to the chosen band. The resolution of Fig. 2(a) allows us to assign this subband to the first six atoms surrounding the central atom of the reconstruction (see arrows). It is clear from the image that the central atom as well as the outer six atoms are much less intense than the inner hexagon.

Figure 2(b) at a bias voltage of 0.2 V (tunneling from the occupied states) shows similar CDW pattern as in Fig. 2(a). In this image, the central atoms of the Star of David start to become the most intense, while the hexagon formed by the
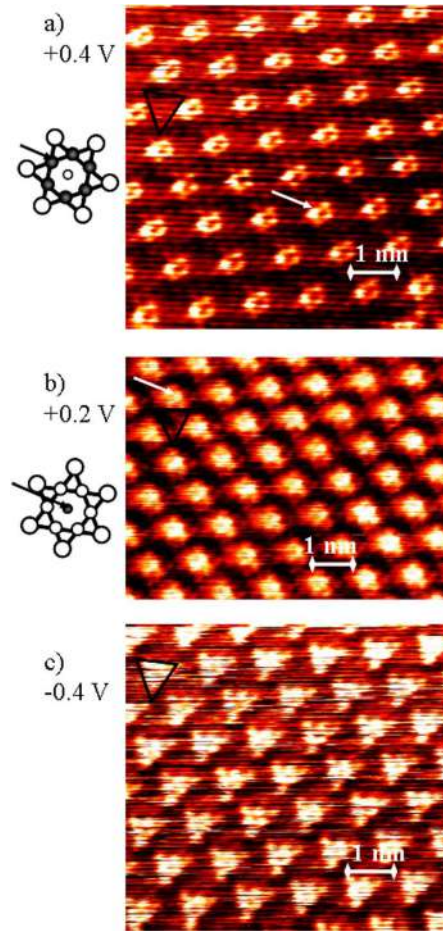


FIG. 2. (Color online) STM images of the cleaved $1T$-TaSe$_2$ surface taken at RT with 1.2 nA and (a) 0.4 V, (b) 0.2 V, and (c) $-0.4$ V. Images are (a) 7 nm, (b) 8 nm, and (c) 7 nm wide. High intensity in white.

first six atoms around the central one is still visible but much less intense than in Fig. 2(a). This can be explained by the correlation between the tunneling current and the electronic structure. The topmost subband is lying closest to 0.2 eV, which explains the intensity enhancement at the central atom (see arrows). However, even subband 2 contributes to the total intensity at this binding energy, which is why we see atoms of the first hexagon around the central atom, although less intense. Consequently, the outmost atomic hexagon in the Star of David is electronically responsible for the Ta $d_z^2$ subband with the largest binding energy.

Finally, in Fig. 2(c), a bias voltage of $-0.4$ V has been implemented to obtain the image. The image is dominated by triangularly shaped groups of atoms which still have the periodicity of the CDW-induced superstructure. There are several possible explanations for this. The lowest lying unoccupied bands are of $d_{x^2-y^2}$, $d_{xy}$ character and should also undergo splitting due to the CDW [see calculations for TaS$_2$ (Ref. 4)]. If tunneling occurs into these bands, the spatial distribution of high intensity in the STM image should reveal their symmetry. Another possibility is that tunneling outside the Ta $d_{z^2}$ band leaves most of the Star-of-David atoms in low intensity [dark areas in Fig. 2(c)], enhancing most out-

most atoms [compare triangles marked in Figs. 2(a)–2(c)]. This would be similar to the contrast reversal reported earlier in purple potassium molybdenum bronze.[17] In one previous study,[9] images with similar triangular atomic groups have been reported and explained by the changes in the electronic structure of the tip. In our study, these images have appeared only at a bias of −0.4 V.

Sacks *et al.*[18] have made an attempt to resolve the STM images of the CDW materials (such as $2H$-NbSe$_2$) by considering CDW effects on the band structure and thus on the tunneling. They state that several bands define the Fermi surface and that it will thus be tunneled from them all. Band degeneracy is taken to originate from band folding, while band splitting is disregarded. In our study we start from the band-mapping data which show energetically localized subbands of the Ta $d_{z^2}$ band and which are interpreted in agreement with the band-structure calculations. Both band splitting and backfolding have influence on the formation of such subbands. Tunneling occurs thus primarily from a subband, in which the binding energy is the same as the bias.

In $1T$-TaSe$_2$ at room temperature, the slope of the temperature-dependent resistivity is metallic. Although $1T$-TaSe$_2$ does not show any metal-insulator transitions (MIT) at low temperatures, the surface MIT in $1T$-TaSe$_2$ has been recently reported at 200–250 K.[19,20] The CDW-induced band-structure changes lead to reduced bandwidth ($W$) and reduced $W/U$ ($U$ measures electron-electron interaction), which trigger a Mott-type transition.[19] Our measurements were performed at room temperature, in the electron-phonon interaction determined CDW ground state, which is also according to our STS measurements (not shown) metallic.

On the search for the driving mechanism of the CDW, the idea of the Peierls transition in a quasi-one-dimensional system has many times been considered even for a quasi-two-dimensional system such as $1T$-TaSe$_2$. However, this system is quasi-two-dimensional with threefold symmetry and the Peierls transition is not very likely. If we consider energetics of the CDW transition, the CDW-induced band splitting leads to new subbands which are energetically lower than the original Ta $5d$ band of the unreconstructed lattice.[4] The energy gained in this way can be used for elastic lattice distortion.

Our STM results support this idea. The conduction charge would be equally distributed over all Ta atoms in the unreconstructed lattice. Upon CDW transition, small changes in the atomic positions of all Ta atoms lead to periodic lattice distortion. In the CDW phase, we see that the conduction charge is mainly located on the central atom of the Star-of-David cluster, meaning that only 1 out of 13 atoms is contributing to the topmost band, which straddles the Fermi level. This can explain the resistivity jump related to the CDW transition in a rather obvious way. More than that, the stability of the CDW phase and the compensation of the lattice distortion energy clearly originate from the energetically lowered bands, which are spatially located on the remaining 12 atoms of the Star-of-David cluster and which are completely filled.

To conclude, band mapping of $1T$-TaSe$_2$ along $\bar{\Gamma}\bar{M}$ and $\bar{\Gamma}\bar{K}$ reveals CDW-induced splitting and folding of the Ta $d_z^2$ band into three subbands. Tunneling from separate subbands allows direct visualization of the atoms contributing to CDW-split electronic states. We thus assign the atoms of the Star-of-David cluster to the Ta $d_z^2$ subbands as follows: the topmost subband is electronically located on the central atom, the outer hexagon is the principal charge carrier of the second subband, and the outmost hexagon is thus related to the third subband. The relevance of this result is discussed in terms of driving mechanisms for CDW formation: as the conduction band has weight only on 1 out of 13 atoms in the CDW phase, all remaining atoms contribute to the formation of the energetically lowered bands, which could energetically compensate the lattice distortion.

*stoltz@physics.leidenuniv.nl

[1] H. Ding, T. Yokoya, J. C. Campuzano, T. Takahashi, M. Randeria, M. R. Norman, T. Mochiku, K. Kadowaki, and J. Giapintzakis, Nature (London) **382**, 51 (1996).

[2] A. G. Loeser, Z.-X. Shen, D. S. Dessau, D. S. Marshall, C. H. Park, P. Fournier, and A. Kapitulnik, Science **273**, 325 (1996).

[3] T. Pillo, J. Hayoz, H. Berger, M. Grioni, L. Schlapbach, and P. Aebi, Phys. Rev. Lett. **83**, 3494 (1999).

[4] M. Bovet, D. Popović, F. Clerc, C. Koitzsch, U. Probst, E. Bucher, H. Berger, D. Naumović, and P. Aebi, Phys. Rev. B **69**, 125117 (2004).

[5] C. G. Slough, W. W. McNairy, R. V. Coleman, B. Drake, and P. K. Hansma, Phys. Rev. B **34**, 994 (1986).

[6] J.-J. Kim, W. Yamaguchi, T. Hasegawa, and K. Kitazawa, Phys. Rev. B **50**, 4958 (1994).

[7] B. Giambattista, A. Johnson, R. V. Coleman, B. Drake, and P. K. Hansma, Phys. Rev. B **37**, 2741 (1988).

[8] G. Raina, K. Sater, U. Müller, N. Venkateswaran, and J. Xhie, J. Vac. Sci. Technol. B **9**, 1039 (1990).

[9] W. Han, R. A. Pappas, E. R. Hunt, and R. F. Frindt, Phys. Rev. B **48**, 8466 (1993).

[10] B. Giambattista, C. G. Slough, W. W. McNairy, and R. V. Coleman, Phys. Rev. B **41**, 10082 (1990).

[11] P. Ruffieux, O. Gröning, P. Schwaller, L. Schlapbach, and P. Gröning, Phys. Rev. Lett. **84**, 4910 (2000).

[12] T. Pillo, L. Patthey, E. Boschung, J. Hayoz, P. Aebi, and L. Schlapbach, J. Electron Spectrosc. Relat. Phenom. **97**, 243 (1998).

[13] P. Aebi, J. Osterwalder, P. Schwaller, L. Schlapbach, M. Shimoda, T. Mochiku, and K. Kadowaki, Phys. Rev. Lett. **72**, 2757

(1994).

[14] B. Dardel, M. Grioni, D. Malterre, P. Weibel, Y. Baer, and F. Levý, Phys. Rev. B **45**, 1462 (1992).

[15] J. A. Wilson, F. J. D. Salvo, and S. Mahajan, Adv. Phys. **24**, 117 (1975).

[16] J. Voit, L. Perfetti, F. Zwick, H. Berger, G. Margaritondo, G. Grüner, H. Höchst, and M. Grioni, Science **290**, 501 (2000).

[17] P. Mallet, K. M. Zimmermann, P. Chevalier, J. Marcus, J. Y. Veuillen, and J. M. Gomez Rodriguez, Phys. Rev. B **60**, 2122

(1999).

[18] W. Sacks, D. Roditchev, and J. Klein, Phys. Rev. B **57**, 13118 (1998).

[19] L. Perfetti, A. Georges, S. Florens, S. Biermann, S. Mitrović, H. Berger, Y. Tomm, H. Höchst, and M. Grioni, Phys. Rev. Lett. **90**, 166401 (2003).

[20] S. Colonna, F. Ronci, A. Cricenti, L. Perfetti, H. Berger, and M. Grioni, Phys. Rev. Lett. **94**, 036405 (2005).

ELSEVIER

# Scanning tunneling microscopy of Fe- and O-sublattices on $Fe_3O_4(1\,0\,0)$

D. Stoltz*, A. Önsten, U.O. Karlsson, M. Göthelid

*Materialfysik, MAP, KTH-Electrum, SE-16440 Kista, Sweden*

## Abstract

We present scanning tunneling microscopy of an octahedral (B) plane terminated $(\sqrt{2} \times \sqrt{2})R45°$-reconstructed surface of a natural magnetite (1 0 0) crystal. Implementing a W-tip we achieve the same resolution on Fe rows as was reported in the past either with the use of antiferromagnetic tips or on magnetite ($Fe_3O_4$) films. We show images of Fe or O sublattices of $Fe_3O_4$ with atomic resolution.
© 2007 Elsevier B.V. All rights reserved.

## 1. Introduction

Magnetite ($Fe_3O_4$) has been the subject of intensive studies by the scientific community during the last decades due to its potential for spin electronics applications, its metal–insulator transition (Verwey transition) at ~125 K [1] and its interesting reconstructions at room temperature [2]. It is an inverse spinel material with a unit cell ($a = 8.3963$ Å) containing 32 $O^{2-}$ anions and 24 $Fe^{2+}$ and $Fe^{3+}$ cations. There are eight $Fe^{3+}$ cations in tetrahedral sites, eight $Fe^{3+}$ cations in octahedral sites and eight $Fe^{2+}$ cations in octahedral sites. In the (1 0 0) direction of the magnetite crystal layers of tetrahedrally coordinated $Fe^{3+}$ cations (A-layers) and layers of octahedrally coordinated $Fe^{2+}$ and $Fe^{3+}$ cations and $O^{2-}$ anions (B-layers) alternate. The separation between neighboring planes (A–B) is 1.05 Å, while the separation between planes of the same type (A–A or B–B) is 2.10 Å. B-plane cations form rows that run along the [1 1 0], [1 $\bar{1}$ 0], [1 0 1], [1 0 $\bar{1}$], [0 1 1] and [0 1 $\bar{1}$] directions, the rows being 90°-rotated in successive octahedral planes [3,4].

A $(\sqrt{2} \times \sqrt{2})R45°$-reconstruction has been observed by several groups on natural/synthetic single crystals and thin films grown by molecular beam epitaxy (MBE) and is generally accepted as a signature of a clean surface [3–7]. A surface preparation procedure for obtaining A-, B- or mixed termination of the surface has been given recently by Ceballos et al. [4]. The first explanation of the $(\sqrt{2} \times \sqrt{2})R45°$-reconstructed B-surface of $Fe_3O_4(0\,0\,1)$ originates from electrostatic considerations of Voogt et al. [8] and scanning tunneling microscopy (STM) results of Stanka et al. [3] on $Fe_3O_4$ films on MgO(0 0 1). They have proposed that charge compensation is achieved by an array of oxygen vacancies accompanied by a change in the valence state of the Fe. Contrary to that, Mariotto et al. [9] and Shvets et al. [10] have attributed the $(\sqrt{2} \times \sqrt{2})R45°$-reconstruction on $Fe_3O_4(1\,0\,0)$ to charge ordering of Fe cations in octahedral positions, and not to an ordered array of vacancies as proposed by previous studies.

While Stanka et al. [3,11] have succeeded to obtain atomic resolution of Fe-rows using a W-tip, Jordan et al. [12], Mariotto et al. [9,13] and Shvets et al. [10] argue that antiferromagnetic MnNi-tips are necessary for obtaining the same resolution. One important difference is that the study of Stanka was performed on a 5000 Å thick film of $Fe_3O_4$, while the other group used synthetic and natural crystals.

In this paper, we present a STM study of a contaminant-free B-terminated magnetite surface of a natural crystal, prepared as described in Ref. [4]. A W-tip was used for imaging. Our images of iron-rows show the same

---

*Corresponding author. Tel.: +31 71 527 8407.
*E-mail address:* stoltz@physics.leidenuniv.nl (D. Stoltz).

resolution as the images obtained with antiferromagnetic tips. For the first time, oxygen at this surface has been imaged. Atomic resolution is achieved on both Fe- and O-rows using negative bias voltage.

## 2. Experimental

STM experiments have been performed in a UHV system equipped with a variable temperature (VT)-STM from OMICRON NanoTechnology. Images were taken in a constant current mode with a W-tip. Bias voltages are given with respect to the sample, i.e. positive bias means tunneling from occupied states. The sample was kept at room temperature. WSxM 3.0 [14] was used for processing of STM images.

The natural magnetite ($Fe_3O_4$) single crystal of (1 0 0) orientation was purchased from Surface preparation laboratory. It was cleaned in ethanol and dried in $N_2$ before it was introduced in the UHV-chamber. *In situ* preparation consisted of long time (7–13 h) outgassing up to a temperature of $T \sim 720\,°C$ (measured with a pyrometer with the emissivity 0.63). A clean surface was achieved by repeating the following preparation cycle [12] several times: (i) sputter with $Ar^+$ for 15 min (min) at 1 kV, (ii) anneal at $720\,°C$ in $2.3 \times 10^{-6}$ mbar $O_2$ for 30 min and (iii) continue annealing at $720\,°C$ in UHV for 2–7 h. According to previous study [4], principal differences between natural crystals and films of magnetite originate from contaminants (sulphur, potassium and calcium) and defects.

## 3. Results

Fig. 1 presents the low energy electron diffraction (LEED) pattern of the $Fe_3O_4$(1 0 0) natural single crystal surface which was cleaned as described in the previous section. It shows the $(\sqrt{2} \times \sqrt{2})R45°$-reconstruction. This reconstruction appears quite early in the cleaning process— already after the first preparation cycle. However, surfaces investigated by STM have been prepared by several preparation cycles.
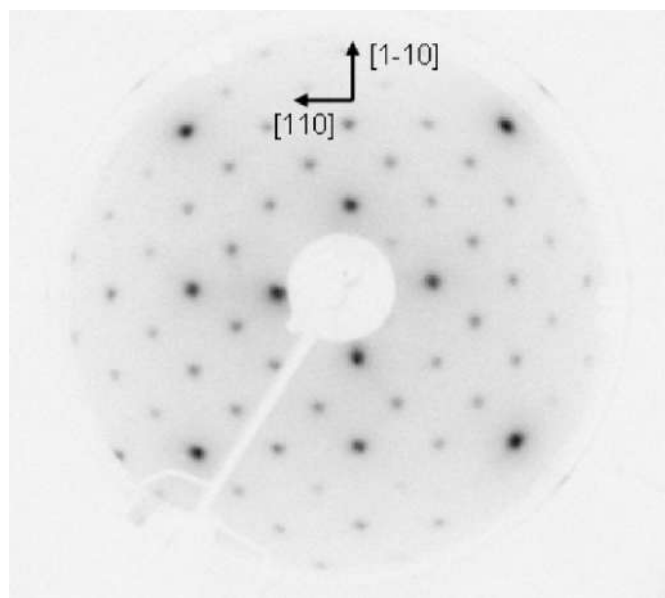
Fig. 2 shows a representative STM image of a $Fe_3O_4$(1 0 0) surface with a LEED pattern as shown in Fig. 1. The step edge directions lie along the [1 1 0] and [1 $\bar{1}$ 0] crystallographic axes. The step heights are integer multiples of 2.1 Å, which corresponds to the separation between two crystallographic planes of same type (A–A or B–B). Monoatomic steps equal to 1.05 Å were never observed, ruling out the possibility of both tetrahedral and octahedral atomic planes coexisting on the surface. This result is in agreement with earlier STM results on $Fe_3O_4$(0 0 1) using both nonmagnetic and magnetic tips [9].

The higher resolution and smaller scale image presented in Fig. 3a reveals atomic structure on Fe rows running along the [1 1 0] crystallographic axis. A zoom into this structure is presented in Fig. 3b. Fe rows are separated by 6 Å and consist of atoms at 3 Å distance. This is typical for the octahedral (B) plane of $Fe_3O_4$(0 0 1). As already stated, we do not observe any A–B steps on the surface, which is why we conclude to an octahedral surface termination. It is worth mentioning that the topography maps from Figs. 3a,b have been subject to mirror-transformation and rotation in order to be directly comparable with other results from the literature (see Fig. 3 from Ref. [12]).

Jordan et al. [12] have also investigated a B-terminated plane of $Fe_3O_4$(0 0 1) with a MnNi and a W-tip. The



Fig. 1. LEED image taken with an incident electron beam energy of 90 eV showing the $(\sqrt{2} \times \sqrt{2})R45°$ reconstruction of the clean $Fe_3O_4$(1 0 0) surface.
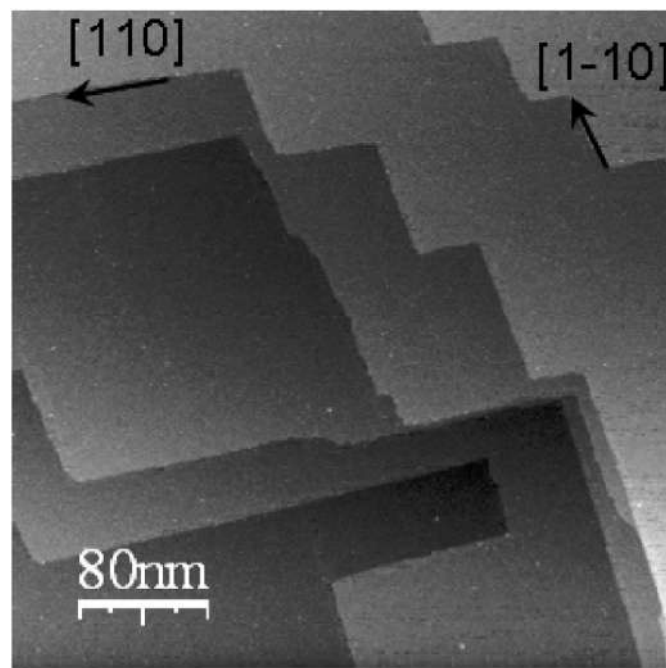


Fig. 2. STM image of a $(\sqrt{2} \times \sqrt{2})R45°$-reconstructed $Fe_3O_4$(1 0 0) surface taken with a bias voltage of 1.4 V and a tunneling current of 0.26 nA. The size of the image is 200 nm × 200 nm.

authors conclude that twice better resolution is achievable if an antiferromagnetic MnNi tip is used, because W-tips do not distinguish between the Fe-dimers which are
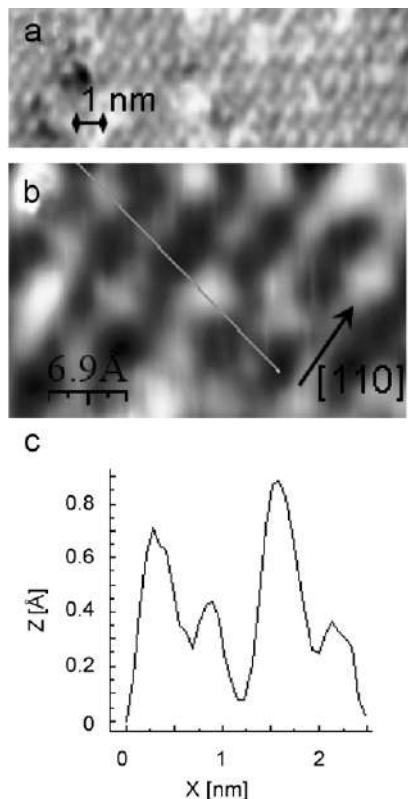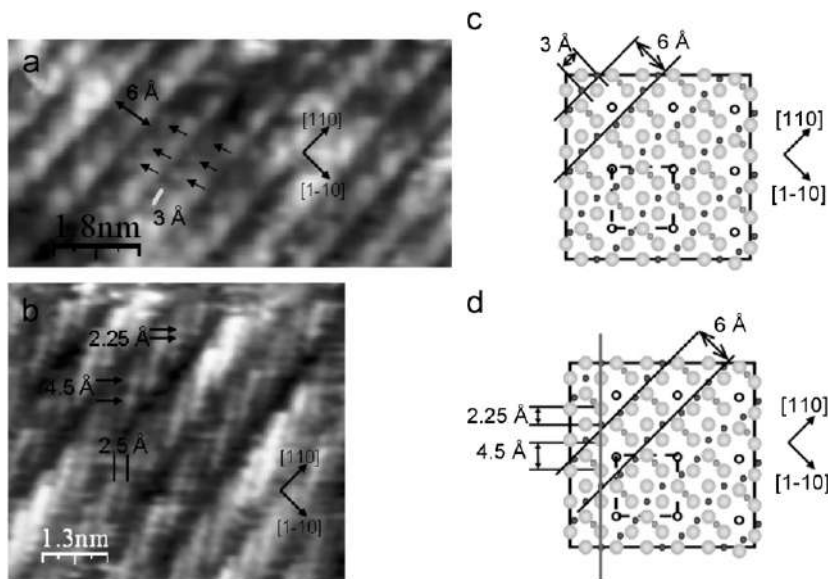


Fig. 3. (a, b) STM images of a $(\sqrt{2} \times \sqrt{2})R45°$-reconstructed $Fe_3O_4(1\,0\,0)$ surface taken with a bias voltage of 1 V and a tunneling current of 0.25 nA with a W-tip. (c) Line profile along [1 $\bar{1}$ 0] direction (marked in b).

presumably formed on the surface [12]. By comparison of our Fig. 3b with Fig. 3 in Ref. [12] we can conclude that our W-tip has enabled the same resolution in the imaging of the magnetite surface as the MnNi tip has in the case of Jordan et al. [12]. Our observations from topography maps in Figs. 3a,b can be confirmed by inspection of line profile along the [1 $\bar{1}$ 0] direction presented in Fig. 3c. While only a 12 Å periodicity was observed earlier using a W-tip (Fig. 3 from Ref. [12]), two shorter periodicities have been measured with an antiferromagnetic MnNi-tip (Fig. 3 from Ref. [12]) which were assigned to the dimer formation at the surface. Our measurement with a W-tip (Fig. 3c) reveals here, as well as in the topography image, the same resolution and the same periodicities of 5 and 7 Å as in the previous results with a MnNi-tip.

In Figs. 4a,b we see another image of the same surface achieved with different tunneling parameters. While the previous STM images were obtained using a positive bias voltage, as in most previous studies, the STM scan presented in Figs. 4a,b was obtained using a negative bias voltage, i.e. tunneling into unoccupied states. Figs. 4a,b are part of the same scan, but a spontaneous tip change led to differences between them. In Fig. 4a atomic rows in the [1 1 0] direction are visible. Their periodicity in the [1 $\bar{1}$ 0] direction is ~6 Å. Within this distance along the [1 $\bar{1}$ 0] direction one iron row and two oxygen rows are expected according to the oxygen vacancy model of this surface [15] (see schematic representation in Fig. 4c). As the image shown in Fig. 4a reveals only one row per 6 Å in the [1 $\bar{1}$ 0] direction, we assign it, in consistence with our previously shown data, as well as those from the literature, to iron rows on the magnetite (1 0 0) surface.



Fig. 4. (a,b) STM image of a $(\sqrt{2} \times \sqrt{2})R45°$-reconstructed $Fe_3O_4(1\,0\,0)$ surface taken with a bias voltage of $-0.8$ V and a tunneling current of 0.2 nA. (c,d) Schematic representation of the oxygen vacancy model of a $(\sqrt{2} \times \sqrt{2})R45°$-reconstructed $Fe_3O_4(0\,0\,1)$ surface. Large silver circles represent oxygen atoms and small dark gray circles represent octahedral $Fe^{2+}$. Small grey circles represent tetrahedral $Fe^{3+}$ below the surface. Empty circles are oxygen vacancies, which are positioned on top of octahedral Fe from the second layer under the surface and which constitute the $(\sqrt{2} \times \sqrt{2})R45°$-reconstructed unit cell (dashed square).

Iron rows are imaged with atomic resolution. They contain Fe atoms at a separation of $\sim 3$ Å (see arrows in Fig. 4a). Between the iron rows, double oxygen rows should appear. However, they are not as well resolved as the iron rows. The only difference between Figs. 3a,b (taken with a positive bias voltage) and Fig. 4a (taken with a negative bias voltage) is that more corrugation on O-atoms is visible in Fig. 4a.

In Fig. 4b we present the same scan as shown in Fig. 4a before a spontaneous tip change. Atomic resolution in this image is achieved along O rows at $45°$ angle from the Fe-rows. The direction of these "rows" in Fig. 4b is marked by a vertical line in Fig. 4d. The rows are separated horizontally by 2.25 Å. Along each row, we see characteristic spacings of 2.25 and 4.5 Å, which correspond very well to the atomic structure of this surface (see markings in Figs. 4b,d).

Vertical rows of oxygen atoms are cut by dark areas along the [1 1 0] direction. These "dark rows" correspond to missing Fe-rows, as can be seen when comparing Figs. 4a,b. As distances typical for oxygen atoms appear in Fig. 4b, it is certain that we are tunneling into oxygen atoms. In that case, not-tunneling into Fe would make these rows appear dark in Fig. 4b. This also demonstrates that a spontaneous tip change can lead from tunneling into Fe to tunneling into O at negative bias values.

## 4. Discussion

Different tips have been used for STM imaging of magnetite (0 0 1) surfaces in the past. Atomically resolved images of Fe rows have been obtained with W-tips only on magnetite films of various thicknesses. Stanka et al. [3] present STM images of Fe-rows on a 5000 Å thick epitaxial film of $Fe_3O_4(0 0 1)$ grown by oxygen-plasma assisted molecular-beam epitaxy on MgO(0 0 1). Subagyo et al. [16] have used similar samples and also show zigzag Fe-rows in accordance with the oxygen vacancy model. Larger difficulties appear when imaging of a natural or synthetic crystal is attempted. A W-tip proved unable of atomic resolution imaging of $Fe_3O_4(1 0 0)$ [12]. Instead, a MnNi-tip [12,9,13] or even a Fe-tip [17] was used, although the latter one gave no better results regarding the atomic resolution.

We show that a W-tip is capable of delivering atomic resolution images on a natural magnetite crystal. However, our W-tip was subject to an unusual treatment, due to another experiment. It was subject to sulfur dioxide and water exposures and was only cleaned by high-voltage pulses during scanning. This could have affected the electronic structure of the tip, but atomic resolution does not necessarily have to be a consequence of this. In the oxygen vacancy model [8] or the Jahn–Teller stabilized model [18] of the clean $Fe_3O_4(0 0 1)$ surface, the $(\sqrt{2} \times \sqrt{2})R45°$-reconstruction is explained without invoking Fe-dimer formation [9]. According to these models, atomic imaging of the $Fe_3O_4(0 0 1)$ surface should be

possible with a W-tip. And even within the charge-ordering model [9], it is not clear that the dimer formation should be an obstacle for obtaining atomic resolution with a W-tip. We have also noticed that better STM images were achieved after increased number of cleaning cycles. Finally, the investigation of our experimental findings suggests that no clear fingerprints of oxygen vacancies are present, but that different corrugations and periodicities in Fig. 3c speak in favor of the charge-ordering model.

Scanning tunneling spectroscopy (STS) results [19] reveal a band-gap of 0.2 eV on the (0 0 1) surface of magnetite, consistent with our own STS and valence-band photoemission measurements (not shown). This is a rather small gap, but it still makes the surface semiconducting at room temperature. However, tunneling at various different bias voltages is possible and we have collected images at both positive and negative values of bias voltage, unlike some previous reports claiming that no stable tunneling current could be obtained under negative bias conditions [4].

Photoelectron spectroscopy of the valence band of magnetite reveals both O 2p and Fe 3d states [20–25]. The Fe 3d states are closer to the Fermi level than the O 2p states (centered at 7.3 eV [23]) and the intensity contribution closest to the Fermi level is thus of the octahedral-$Fe^{2+}$-character [20–22]. Accordingly, mostly octahedrally coordinated $Fe^{2+}$-atoms have been resolved by tunneling from occupied states in the past.

Band-structure calculations [26] confirm that $d_{t2g}$ and $d_{eg}$ states of Fe cations with both valencies contribute the most to the empty states in the vicinity of the Fermi level as well. Although the iron and oxygen contributions can be identified, O 2p–Fe 3d hybridization is considerable in $Fe_3O_4$ [23]. This overlapping or hybridization of the iron and oxygen states in the valence band could be considered responsible for tunneling possibilities into both oxygen and iron atoms. The reason why we are the first to resolve oxygen on the magnetite surface could thus lie in the changed electronic structure of our tip (as discussed earlier), but also in the general fact of existing O 2p–Fe 3d hybridization (which could allow tunneling into both O and Fe by tunneling into any valence band state). It is also possible that the O 2p empty states lie closer to the Fermi level than the occupied O 2p states do, thus making it more probable to tunnel into O using a negative bias voltage.

## 5. Conclusions

We present STM scans on a $(\sqrt{2} \times \sqrt{2})R45°$-reconstructed $Fe_3O_4(1 0 0)$ surface using a W-tip. The resolution achieved compares with the previous studies where an antiferromagnetic tip was used. We discuss this in terms of exposure of our tip to sulfur dioxide and water, but more importantly in terms of imaging of the surface as described by different $(\sqrt{2} \times \sqrt{2})R45°$-surface models. We also show imaging of Fe or O sublattices with atomic resolution at a negative bias voltage.

**Acknowledgments**

**References**

[1] D.J. Huang, H.-J. Lin, J. Okamoto, K.S. Chao, H.-T. Jeng, G. Guo, C.-H. Hsu, C.-M. Huang, D.C. Ling, W.B. Wu, C.S. Yang, C.T. Chen, Phys. Rev. Lett. 96 (2006) 096401.
[2] N. Spiridis, J. Barbasz, Z. Łodziana, J. Korecki, Phys. Rev. B 74 (2006) 155423.
[3] B. Stanka, W. Hebenstreit, U. Diebold, S.A. Chambers, Surf. Sci. 448 (2000) 49.
[4] S.F. Ceballos, G. Mariotto, K. Jordan, S. Murphy, C. Seoighe, I.V. Shvets, Surf. Sci. 548 (2004) 106.
[5] N. Spiridis, B. Handke, T. Slezak, J. Barbasz, M. Zajac, J. Haber, J. Korecki, J. Phys. Chem. B 108 (2004) 14356.
[6] G. Mariotto, S.F. Ceballos, S. Murphy, N. Berdunov, C. Seoighe, I.V. Shvets, Phys. Rev. B 70 (2004) 035417.
[7] G. Mariotto, S. Murphy, N. Berdunov, S.F. Ceballos, I.V. Shvets, Surf. Sci. 564 (2004) 79.
[8] F.C. Voogt, T. Fujii, P.J.M. Smulders, L. Niesen, M.A. James, T. Hibma, Phys. Rev. B 60 (1999) 11193.
[9] G. Mariotto, S. Murphy, I.V. Shvets, Phys. Rev. B 66 (2002) 245426.
[10] I.V. Shvets, G. Mariotto, K. Jordan, N. Berdunov, R. Kantor, S. Murphy, Phys. Rev. B 70 (2004) 155406.
[11] L. Zhang, M. Kuhn, U. Diebold, Surf. Sci. 371 (1997) 223.
[12] K. Jordan, G. Mariotto, S.F. Ceballos, S. Murphy, I.V. Shvets, J. Magn. Magn. Mater. 290 (2005) 1029.
[13] G. Mariotto, S.F. Ceballos, S. Murphy, I.V. Shvets, J. Appl. Phys. 93 (2003) 7142.
[14] Nanotec Electronica S. L. WSxM 3.0, ⟨www.nanotec.es⟩, 2006.
[15] K. Jordan, S. Murphy, I.V. Shvets, Surf. Sci. 600 (2006) 5150.
[16] A. Subagyo, K. Sueoka, Jpn. J. Appl. Phys. 44 (2005) 5447.
[17] J.M.D. Coey, I.V. Shvets, R. Wiesendanger, H.-J. Güntherodt, J. Appl. Phys. 73 (1993) 6742.
[18] R. Pentcheva, F. Wendler, H.L. Meyerheim, W. Moritz, N. Jedrecy, M. Scheffler, Phys. Rev. Lett. 94 (2005) 126101.
[19] K. Jordan, A. Cazacu, G. Manai, S.F. Ceballos, S. Murphy, I.V. Shvets, Phys. Rev. B 74 (2006) 085416.
[20] K. Wandelt, Surf. Sci. Rep. 2 (1982) 1.
[21] T. Fujii, F.M.F. de Groot, G.A. Sawatzky, F.C. Voogt, T. Himba, K. Okada, Phys. Rev. B 59 (1999) 3195.
[22] R.J. Lad, V.E. Henrich, Phys. Rev. B 39 (1989) 13478.
[23] S.F. Alvarado, M. Erbudak, P. Munz, Phys. Rev. B 14 (1976) 2740.
[24] S. Vasedevan, M.S. Hedge, C.N.R. Rao, J. Solid State Chem. 29 (1979) 253.
[25] S.G. Bishop, P.C. Kemeny, Solid State Commun. 15 (1974) 1877.
[26] H.-T. Jeng, G.Y. Guo, Phys. Rev. B 65 (2002) 09442.

Mats Göthelid, Michael Tymczenko, Winnie Chow, Sareh Ahmadi, Shun Yu, Benjamin Bruhn, Dunja Stoltz,

Henrik von Schenck, Jonas Weissenrieder, and Chenghua Sun

---

**Articles you may be interested in**

Site-dependent charge transfer at the Pt(111)-ZnPc interface and the effect of iodine
J. Chem. Phys. 140, 174702 (2014); 10.1063/1.4870762

Interface electronic states and molecular structure of a triarylamine based hole conductor on rutile Ti O 2 ( 110 )
J. Chem. Phys. 128, 184709 (2008); 10.1063/1.2913245

A diagonal cut through the SiC bulk unit cell: Structure and composition of the 4 H - Si C ( 1 1 ‾ 02 ) surface
Appl. Phys. Lett. 92, 061902 (2008); 10.1063/1.2839384
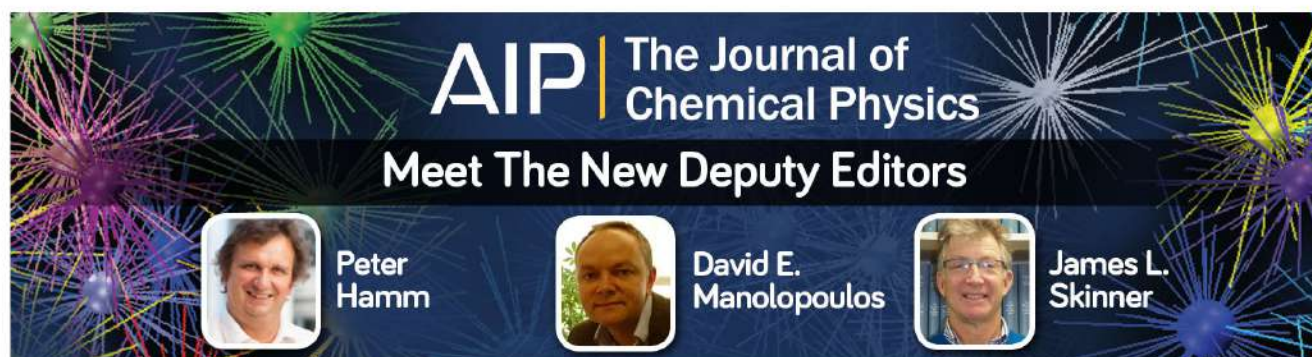
Oxygen adsorption on Mo(112) surface studied by ab initio genetic algorithm and experiment
J. Chem. Phys. 126, 234710 (2007); 10.1063/1.2743427

Determination of iodine adlayer structures on Au(111) by scanning tunneling microscopy
J. Chem. Phys. 107, 585 (1997); 10.1063/1.474419

---

# Surface concentration dependent structures of iodine on Pd(110)

Mats Göthelid,[1,a)] Michael Tymczenko,[1] Winnie Chow,[1] Sareh Ahmadi,[1] Shun Yu,[1] Benjamin Bruhn,[1] Dunja Stoltz,[1] Henrik von Schenck,[1] Jonas Weissenrieder,[1] and Chenghua Sun[2,a)]

[1]*Materialfysik, ICT Electrum 229, Kungliga Tekniska Högskolan (KTH), S-164 40 Kista, Sweden*
[2]*Australia Institute for Bioengineering and Nanotechnology, The University of Queensland, QLD 4072, Australia*

We use photoelectron spectroscopy, low energy electron diffraction, scanning tunneling microscopy, and density functional theory to investigate coverage dependent iodine structures on Pd(110). At 0.5 ML (monolayer), a c(2 × 2) structure is formed with iodine occupying the four-fold hollow site. At increasing coverage, the iodine layer compresses into a quasi-hexagonal structure at 2/3 ML, with iodine occupying both hollow and long bridge positions. There is a substantial difference in electronic structure between these two iodine sites, with a higher electron density on the bridge bonded iodine. In addition, numerous positively charged iodine near vacancies are found along the domain walls. These different electronic structures will have an impact on the chemical properties of these iodine atoms within the layer. © *2012 American Institute of Physics.* [http://dx.doi.org/10.1063/1.4768165]

## INTRODUCTION

Palladium is one important transition metal used in both homogeneous and heterogeneous catalysis. Organo-halides are often used to form reactive carbon fragments,[1] which leave a halogen coordinated to the catalyst metal. Depending on the coordination site and charge transfer between surface and adsorbate, the surface halide may act as a catalyst poison[2] or as a key factor in controlling chemical selectivity.[3] This effect on selectivity is related to the strength of the palladium-halide interaction and the surface bond geometry. Moreover, halogens are used to etch metals[4] and semiconductors[5] and a fundamental understanding of halogen surface properties is crucial. Iodine/iodide is often used as redox couple in dye sensitized solar cells (the Grätzel cell).[6] It was recently reported that the concentration of iodine in the electrolyte affects the output from the solar cell.[6] The results were discussed in terms of ionic mobility of tri-iodide, chemical availability, recombination losses, and light absorption interference with the dye.[6] However, the iodine chemistry on the metal electrode was not discussed in detail. In order to gain a broader understanding of iodine chemistry, structures, and charge transfer processes, we have studied iodine sub-monolayer structures on various metals (Pd, Pt, Au, Cu, Zn) using scanning tunneling microscopy (STM), photoelectron spectroscopy (PES), and density functional theory (DFT). Here, we report an investigation of iodine-induced structures on Pd(110).

Iodine was previously studied on Pd(110) where two ordered structures were found: c(2 × 2) at 0.5 ML (monolayer) iodine coverage and a flat quasi-hexagonal (q-hex) structure at higher coverage.[7] A similar scenario was observed for iodine on Cu(110), where the quasi hexagonal phase was observed at ∼0.67 ML co-existing with an ordered CuI phase.[8]

The quasi hexagonal phase was explained by a compression of the iodine layer along the ⟨−110⟩ direction.[8] The idea of the formation of a compressed quasi hexagonal phase was earlier proposed by Bardi and Rovida from their work on Ag(110)-I,[9] and by Erley for Cl on Pd(110).[10] One possible iodine adsorption site in the c(2 × 2) structure is the four fold hollow position as proposed in Refs. 7–9. On Ag(110), it was instead proposed from density functional theory (DFT) that short bridge adsorption is preferred over top, hollow, and long bridge, in order of decreasing preference.[11] What are the electronic and chemical properties of iodine sitting in different sites? We find that iodine occupies hollow sites up to 0.5 ML coverage and then gradually also fills long bridge sites. The electronic properties differ significantly in these two sites, and consequently their chemical properties.

## EXPERIMENTAL METHODS

The photoemission experiments were performed at beam line I511, at MAX-lab, in Lund, Sweden. The beam line is undulator based using a modified SX-700 monochromator.[12] The photoemission spectra were recorded in normal emission with a Scienta SES200 electron spectrometer.[13] Pd $3d_{5/2}$ spectra were acquired at 405 eV and 453 eV photon energies. The I4d core level spectrum was recorded at 134 eV. The total experimental resolution was ca. 40 meV for the I4d and 120 meV for the Pd3d spectra. STM experiments were done in a RHK 3500 UHV STM using cut PtIr tips in constant current mode.

The sample was prepared in preparation chambers connected to the photoemission and STM chambers via gate valves. These chambers are equipped with low energy electron diffraction (LEED) optics, Ar-ion sputter gun, and sample heating. The samples were mounted on Ta-sample holders. Sample temperatures were measured with chromel-alumel thermocouples, spot-welded on the side of the sample or by a

---
a)Authors to whom correspondence should be addressed. Electronic addresses: gothelid@kth.se and c.sun1@uq.edu.au.
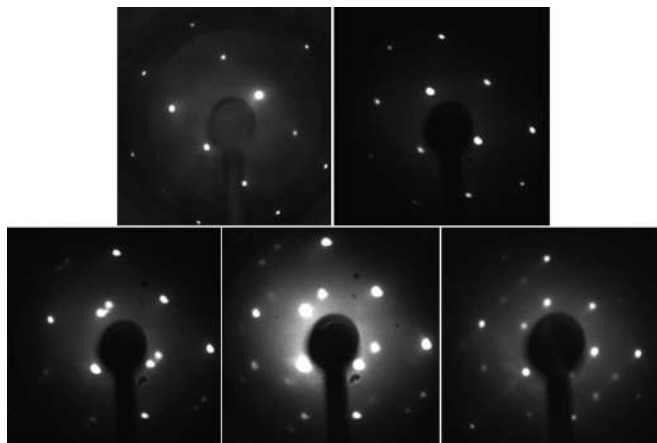
FIG. 1. LEED patterns from the (1 × 1) (upper left) at 95 eV and c(2 × 2) (upper right) at 78 eV. Lower row are photographs from the quasi-hexagonal structure at 72 eV and 66 eV, respectively, and finally a (3 × 2) pattern in the low right hand picture. The (0,0) spot is the spot just low-left of the electron gun.
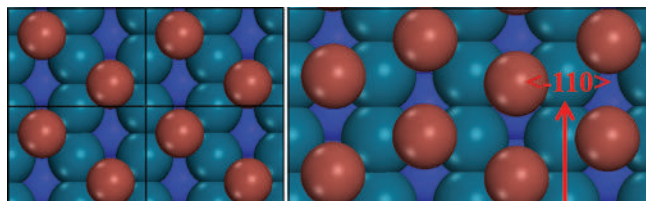


FIG. 2. Optimized structure models at different iodine coverage; green balls represent Pd and red balls represent iodine. The left hand figure is the c(2 × 2) structure at 0.5 ML coverage and the right hand figure is a 3 × 2 structure at 0.67 ML iodine coverage. Iodine atoms are shown as red spheres, and palladium atoms at the top and second layers are shown as cyan and blue spheres, respectively.

pyrometer. The Pd(110) sample was prepared by argon sputtering and oxygen treatment at high temperatures ($P_{O2}$ = 2–5 × $10^{-7}$ Torr, 530 °C), followed by flashing to 830 °C in order to obtain a clean and well-ordered surface. The cleanliness of the surface was checked by PES and LEED.

Iodine was deposited onto the surface at room temperature from an electrochemical cell, consisting of an AgI pellet heated to ~100 °C.[14] Exposures were measured in $\mu$A.minute, i.e., the ionic current going through the cell (10 $\mu$A in this case) times the duration of the evaporation. On Pd(110) deposition of 200 $\mu$A.min, $I_2$ at room temperature resulted in the q-hex structure, which transformed to c(2 × 2) after annealing at 350 °C. The iodine coverage on the c(2 × 2) surface was estimated to be 0.52 ± 0.03 ML from the I4d intensity compared to the Pd(111)-I ($\sqrt{3}$x$\sqrt{3}$)R30° surface with 0.33 ML coverage.[15] The coverage in the quasi hexagonal structure cannot be accurately determined using this method due to photoelectron diffraction effects that renders different results at different photon energies. However, based on the previous study on Cu(110)-I[8] and our STM, we believe that the q-hex coverage is close to 2/3 ML.

## COMPUTATIONAL METHODS

Spin-polarized density functional theory (DFT) calculations have been performed within the generalized-gradient approximation (GGA),[16] with the plane-wave basis (cutoff energy: 380 eV) and the exchange-correlation functional of Perdew-Burke-Ernzerhof (PBE),[17,18] as implemented in the Vienna *ab initio* simulation package (VASP).[19,20] Total energy and maximum force are converged to $10^{-4}$ eV and 0.05 eV/Å, respectively, and the k-space is sampled by a Monkhorst-Pack mesh with the distance between any neighboring k-points less than 0.025/Å. Atomic populations are analyzed based on the Bader approach,[21] and Mulliken analysis[22] has also been carried out using another plane-wave DFT code–CASTEP[23] and similar results are obtained. Pd(110) is modeled by slab models (11 Pd layers, with a

thickness of 14.30 Å) for two supercells, (2 × 2) and (3 × 2), based on which five coverages $\theta$ for iodine adsorption have been investigated with $\theta$ = 1/6, 1/4, 1/2, 2/3, and 1 monolayer (ML). The use of a (3 × 2) cell is motivated by the fact that this is one possible structure following compression in the ⟨−110⟩ direction. It was also occasionally observed in LEED.

## RESULTS AND DISCUSSION

Representative LEED pictures are shown in Figure 1 below. The original (1 × 1) pattern is shown in the top left image while a picture from the c(2 × 2) structure is displayed in the top right hand picture. The two lower images from the q-hex structure were recorded at different electron energies. At increasing energy, the spots in the centre of the zone split and move apart. A similar behavior was observed for Cu(110)-I[8] and was interpreted as a compression of the iodine layer in the ⟨−110⟩ direction. This compression resulted in a non-uniform domain wall structure with a quasi hexagonal atomic structure. Occasionally, we also observed a (3 × 2) LEED pattern. This pattern was only observed irregularly, but it proves that the (3 × 2) structure indeed exists.

Our theoretical calculations were first done in order to find the energetically most stable structures at different iodine coverage. At low coverage, iodine prefers to stay at the hollow site, and with increasing coverage, iodine starts occupying bridge sites. In Figure 2 optimized geometries for $\theta$ = 1/2 ML and $\theta$ = 2/3 ML are present, corresponding to c(2 × 2) and (3 × 2) patterns. Adsorption energies and atomic population (AP) for iodine adsorbed at different sites are given in shown in Table I. As indicated by the adsorption energies, hollow sites offer stronger adsorption capacity because each iodine at hollow site bonds with five Pd atoms.

In Figure 3, we present atomically resolved STM images from Pd(110)-I c(2 × 2), recorded at 4 mV tunnel bias and 0.2 nA tunnel current. The atomically resolved structure is in

TABLE I. Calculated adsorption energies and atomic populations (Bader analysis) for iodine in hollow and bridge positions on the c(2 × 2) and (3 × 2) structures.

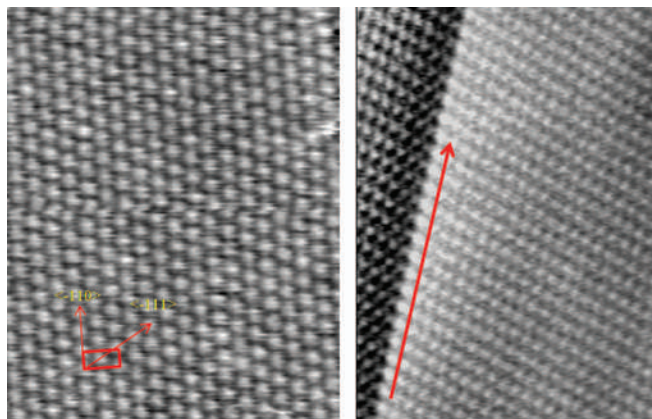|  | $E_{ads}$ hollow (eV) | $E_{ads}$ bridge (eV) | $AP_I$ hollow (e) | $AP_I$ bridge (e) |
|---|---|---|---|---|
| c(2 × 2) | 3.33 |  | 7.01 |  |
| (3 × 2) | 3.26 | 2.96 | 7.01 | 7.10 |

FIG. 3. Atomically resolved STM images from the Pd(110)-I c(2 × 2) phase together with atomic structure models. Atomic distances are 5.5 Å in ⟨−110⟩ and 4.8 Å in ⟨−111⟩. The long red arrow points along ⟨−110⟩.

splendid agreement with the atomic model in Figure 2(a). In Figure 3(a), a (2 × 2) unit cell has been added together with crystallographic directions. The atomic distances are 5.50 Å in the ⟨−110⟩ direction and 4.76 Å along the ⟨−111⟩ direction, which is the shortest distance between iodine. The height corrugation is 0.2 Å. Figure 3(b) contains two terraces separated by a step running along the ⟨−111⟩ direction. The atomic corrugation in this image is ∼ 0.1 Å.

Figure 4 was recorded at an intermediate coverage with the c(2 × 2) phase in the lower left and upper right corners co-existing with the compressed phase in the central part of the image. While the c(2 × 2) structure nicely follows the terrace edges, the compressed phase comprise domain walls rotated away from the terrace edge direction. The angle between the two arrows, **a** and **b**, in the image is ∼30°. From the LEED pattern and the discussion in Ref. 8, the compression should be in the ⟨−110⟩ direction. The angle between ⟨−110⟩ and ⟨−111⟩ is 35°, in fair agreement with the measured angle in the image. Furthermore, the atomic lines perpendicular to the step edges are still straight, in agreement with a unidirectional compression. A close look at the wave structure, along arrow **b**, gives that the lines are not perfectly straight, but has local variations. This is similar to observations on Cu(110)-I.[8] The corrugation is believed to originate in a compression of the iodine layer, which shifts iodine away from the hollow position into long bridge.[8] The long bridge and hollow (and transitions between them) are the only available sites if the c(2 × 2) structure is compressed along ⟨−110⟩. On Cu(110), c(8 × 2) structures were observed, including domain walls with locally higher iodine coverage. In order to relieve strain on the iodine, there is a shift of the domain walls out of phase along the short end of the unit cell. In our case, we do not observe a c(8 × 2) ordering, but we do observe a large number of vacancies in the structure, which also relieve the local pressure.

Figure 5 was recorded from the fully developed q-hex phase, where the atomic structure is resolved between the domain walls. The structure resembles the c(2 × 2) structure, but the atomic distances are compressed and it also contains defects around which the distances are different. Atoms near defects appear higher, due to an increased density of electronic states near the Fermi level. Interestingly, the domain
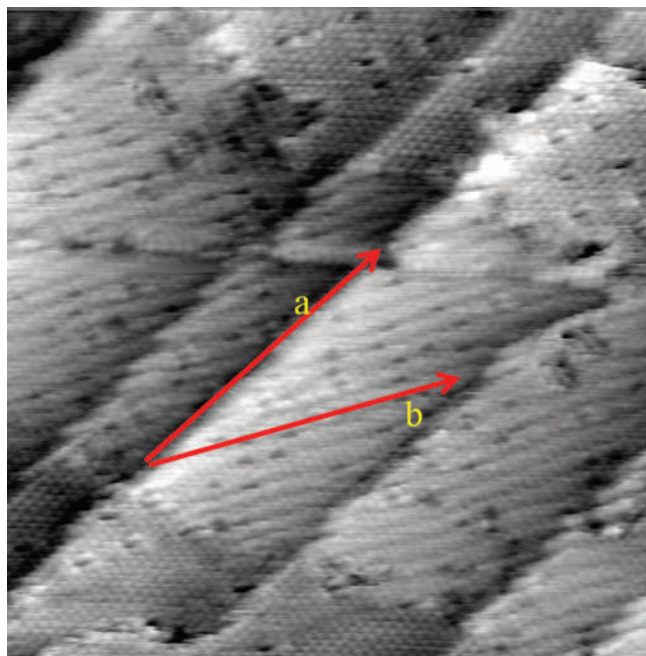


FIG. 4. STM image of mixed the c(2 × 2) and q-hex phases.

walls appear brighter on defects rich areas. Furthermore, the atomic distances are different in areas with different amounts of defects. These observations suggest that the iodine over-layer is rather flexible, both in terms of atomic geometry and electronic structure. Our model in Fig. 2(b) is made of equal amounts of hollow and long bridge adsorbed iodine. The model is not exactly representing the structure observed in the STM image, but by compressing the c(2 × 2) structure along ⟨−110⟩, the only possible atomic positions for iodine are hollow, long bridge and transitions between them. We believe that a model with hollow and long bridge will represent this system fairly well.

## CORE LEVEL SPECTROSCOPY

Electronic structure variations are reflected in site dependent core level binding energies. $Pd3d_{5/2}$ spectra from Pd(110) (1 × 1) and Pd(110)-I c(2 × 2) are presented in Figure 6; the two upper spectra from (1 × 1) and the two lower spectra from c(2 × 2). Photon energies are indicated in connection to respective spectra. We present two different line profile
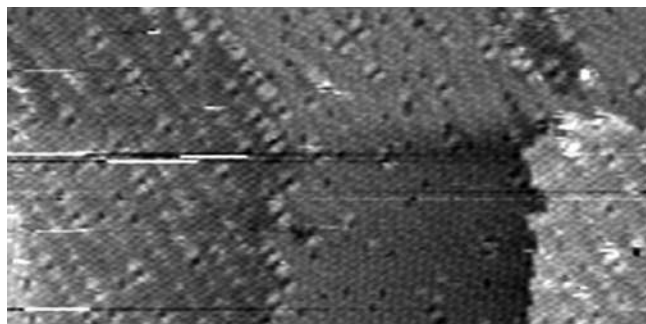


FIG. 5. STM image from the q-hex phase, recorded at 4 mV negative tip bias.
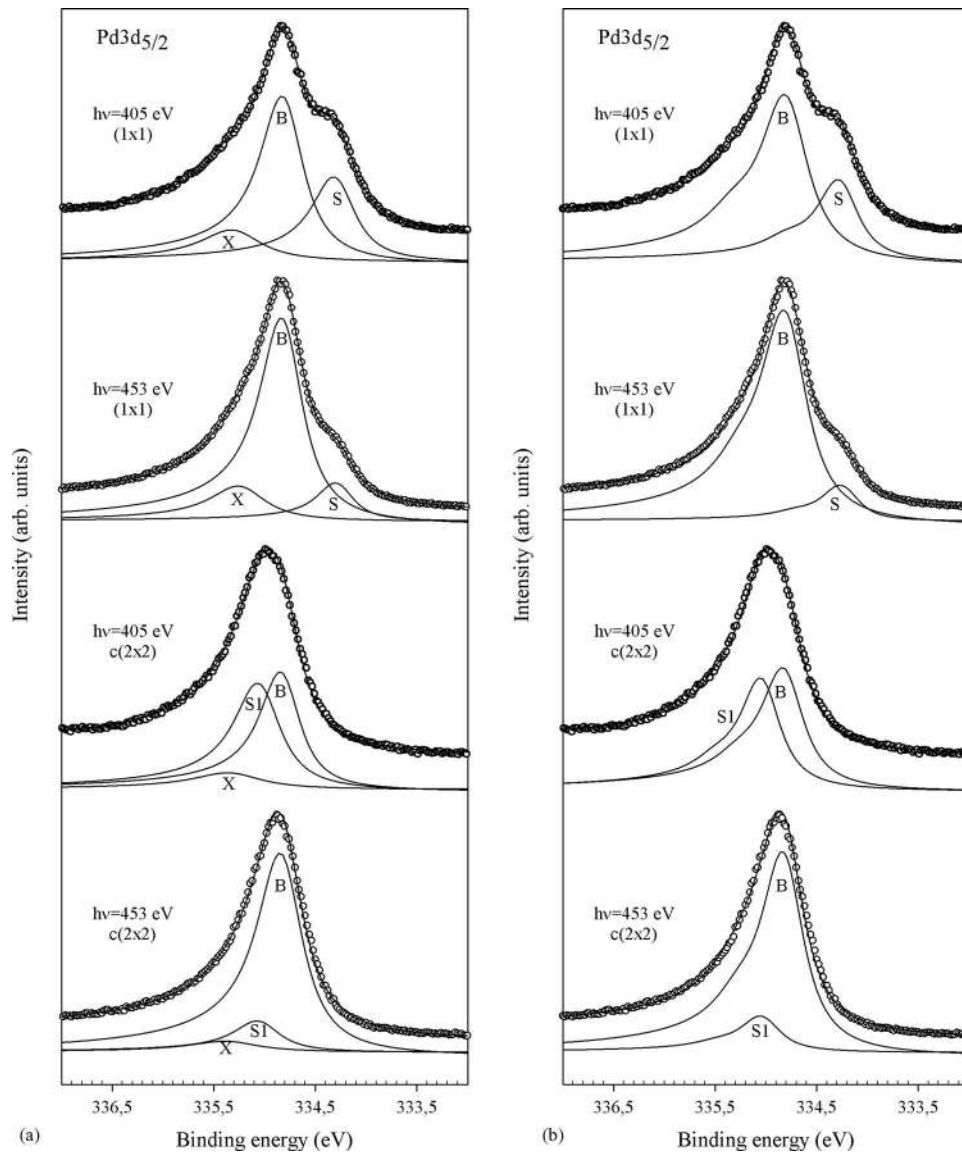
FIG. 6. Pd3d$_{5/2}$ core level spectra recorded at 405 eV and 453 eV photon energies from the (1 × 1) and c(2 × 2)-I structures. Numerical fitting of the spectra were done using two different methods; (a) with Doniach-Sunjic lines and in (b) with a built-in loss feature.

analyses giving the same result: a surface core level shift $0.52 \pm 0.02$ eV to lower binding energy on the clean surface and a $0.22 \pm 0.02$ eV shift to higher binding energy on the c(2 × 2)-I surface.

Curve fitting using Doniach-Sunjic line profiles[24] has failed to properly describe the Pd3d core level spectrum, in particular on the high binding energy side, due to the rapidly varying density of states around the Fermi level.[25–27] For this reason, very few fitted high resolution spectra from clean palladium surfaces are found in the literature. Close inspection often reveals a small "hump" in spectra at very high resolution.[26–29] This apparent problem disappears upon adsorption, since many adsorbates induce core level shifts on that side of the spectrum, and therefore fitted spectra are much more often seen after adsorption.

In the left-hand figure, we present results of a fit where, in addition to the bulk and surface contributions, an extra component X has been introduced. With this component added,

stable and reproducible fits of all four spectra are obtained using exactly the same line profile for all components: Gaussian width 0.15 eV, Lorentzian width 0.41 eV, and asymmetry parameter 0.13. The X component is shifted 0.51 eV from the bulk peak position and the relative intensity is 15% independent of photon energy. On the clean unreconstructed surface, the surface component is identified from the reduced intensity on the low binding energy side in the 453 eV spectrum in which the electron mean free path can be expected to be longer than at 405 eV photon energy.[26] The surface to bulk intensity is 0.51 in the top-most spectrum and 0.16 in the 453 eV spectrum. Having a surface shift to lower binding energy is in good agreement with previous reports on this and other low index Pd surfaces.[26–31]

After the formation of the c(2 × 2) structure, new spectra were recorded. They are presented in the two lower panels of Figure 6. We again use three components to reproduce the experimental spectra: bulk (B), surface (S1), and extra (X).
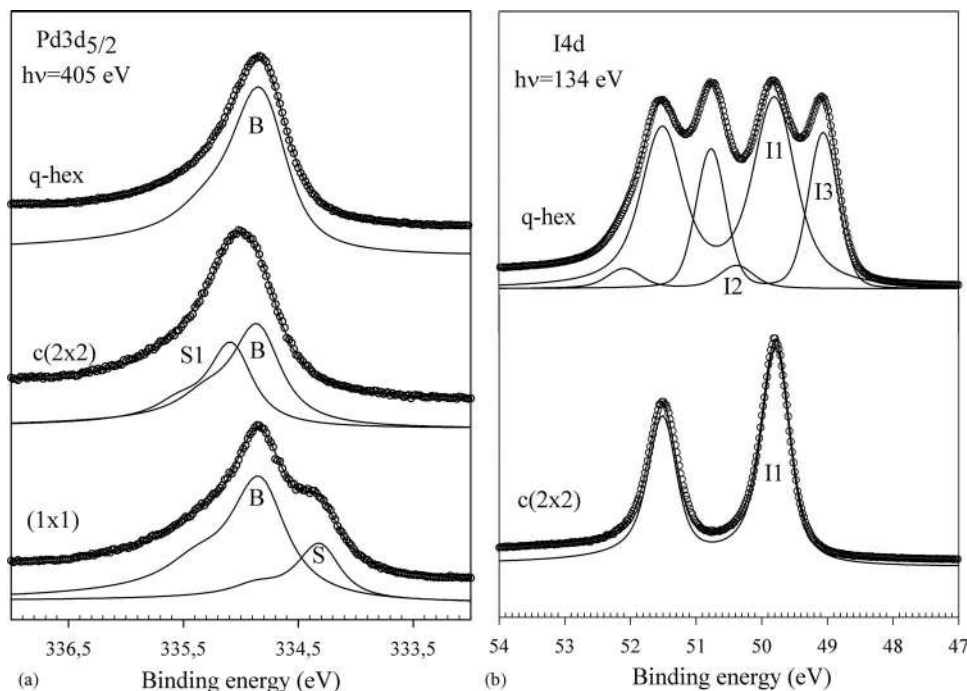
FIG. 7.  (a) Pd3d$_{5/2}$ and (b) I4d core level spectra recorded from the $(1 \times 1)$, $c(2 \times 2)$-I, and quasi hexagonal (q-hex) structures.

The need for the surface peak is seen on the width and shape around the peak maximum of the spectrum. Again, the surface contribution is identified from the variation in relative intensity between the two photon energies. Here, the surface to bulk ratio is 0.94 at 405 eV photon energy, while it is 0.16 at 453 eV. The iodine induced surface core level shift is 0.22 $\pm$ 0.02 eV to higher binding energy, while the X peak remains on the same 0.52 eV from the bulk peak. It has a lower intensity in this structure.

An alternative method to extract surface core level shifts in these spectra is based on the idea of Nyholm *et al.*[26] who identified Pd3d surface and bulk contributions from Pd(100) by using a subtraction procedure utilizing the adsorption of hydrogen to take out the surface core level shift on that surface. We applied a similar analysis of the Pd(111) $(1 \times 1)$ and Pd(111)-I $(\sqrt{3}x\sqrt{3})$ surfaces.[15] The resulting surface core level shift and relative intensities compared very well with other literature (see Ref. [15]). Here, we apply a similar method to the Pd(110) surface with and without iodine in a $c(2 \times 2)$ structure. The model function is a main line and a "built-in" loss feature in each component, the relative intensity, and energy separation from the main peak is adjusted in the fit. The separation was optimized to be the same 0.47 eV in all four spectra and the relative intensity is 11% of the host peak. The results are presented in Figure 6(b). The surface core level shift on the clean surface is 0.53 $\pm$ 0.02 eV. At 405 eV photon energy, the surface to bulk intensity ratio is 0.49 while it is 0.17 at 453 eV. Analyzing Pd3d from the $c(2 \times 2)$-I structure reveals a 0.22 eV surface core level shift to higher binding energy compared to the bulk. The surface-to-bulk ratio is 0.91 and 0.16, respectively. Thus, the energy shifts and relative intensities are practically the same in the two methods of analysis, except for the X-component. Each component in a fit should represent separate chemical or electronic species on

the surface; i.e., atoms in different sites or bonding configurations. We believe that the X-component does not represent a group of atoms on the surface, but reflects excitations across the Fermi level made by the outgoing photoelectron, and the fit using built in loss is a better representation.

Pd3d spectra recorded from three surfaces; $(1 \times 1)$, $c(2 \times 2)$, and quasi hexagonal, are presented in Figure 7. The difference between $(1 \times 1)$ and $c(2 \times 2)$ is rather large, as already seen in Figure 6. The surface shifted component on the unreconstructed surface (S) is replaced for a new component (S1) on the $c(2 \times 2)$. The shift to higher binding energy in $c(2 \times 2)$ indicates a slightly oxidative effect of iodine on Pd. Unexpectedly, the S/B ratio is larger on $c(2 \times 2)$ than on $(1 \times 1)$, both structures hold 1 ML of chemically shifted surface Pd atoms. However, at 453 eV (Figure 6), the ratios are closer. This indicates significant photoelectron diffraction effects.

Spectral changes between $c(2 \times 2)$ and quasi-hexagonal are not directly obvious. However, the surface shifted component in the $c(2 \times 2)$ phase has disappeared as seen in the curve fit. We kept the line profile the same in all spectra except for the position and the width. The single component in the q-hex phase is slightly broader, but in all other respects it has the same line profile. The binding energy also coincides with the bulk binding energy on the $(1 \times 1)$ and $c(2 \times 2)$ surfaces. Thus, we conclude that Pd3d from q-hex is nicely fit with one single component. This finding may seem surprising at first since there still is one monolayer of Pd atoms beneath the iodine layer. One possible explanation is that the compact iodine layer adapts several slightly different adsorption geometries that render small but slightly different surface shifts, leading to broadening rather than clear components.

The I4d spectra recorded from the Pd(110)-I $c(2 \times 2)$ and quasi hexagonal surfaces at $h\nu = 134$ eV are presented

in Figure 7. One single component at 51.51 eV is sufficient to reproduce the experimental c(2 × 2) spectra, which supports a single chemisorption site on the surface. The spectrum from the quasi hexagonal phase is spectacularly different incorporating three components. We take I1 to represent iodine in hollow sites, the same as in the c(2 × 2) phase. The remaining two components are, based on the relative intensities, tentatively assigned to; iodine near defects (I2) and iodine in bridge sites (I3). The chemical shift between I1 and I3 is 0.89 eV and indicates that there is a rather serious electronic difference between the two sites. We calculated the chemical shift from the (3 × 2) model giving a 0.80 eV energy separation, in good agreement with our experiment. Thus, although the model does not perfectly represent the actual atomic structure on the surface, it captures the main features of our core level spectra and we believe that hollow and long-bridge adsorption sites are most common on this surface.

Typically, a shift to lower binding energy is interpreted as being due to a more electron rich environment, while a shift to higher binding energy is typical for oxidation, i.e., a reduced electron density on those atoms. Such interpretation is perhaps over simplified; one has to take final state effects into account. What happens when the photoelectron has left? The positive core hole attracts the surrounding electron cloud, and the more available those electrons are in terms of density and mobility the better screened is the hole. A poorer screening leads to a higher apparent binding energy and better screening leads to lower binding energy. Our observation thus suggests that bridge bonded atoms have access to more electrons, either in the initial and/or the final state, which agrees well with the calculated atomic populations shown in Table I.

This discussion would also suggest that the iodine responsible for the I2 component has a reduced electron density. STM indicated a fair amount of defects, atomic vacancies in the iodine layer. Neighboring atoms appear higher in the empty state STM image. A majority of those defects are located on the domain walls, which can be associated with the bridge site iodine. Thus, from the combined core level and STM results, we suggest that vacancies appear more frequently on the bridge site, and neighboring atoms are charge positively. The relative I1/I3 intensity indicates a higher occupation of hollow than bridge sites. This is in line with the removal of some bridge bonded iodine and also a core level shift on neighboring atoms (to I2), both reducing the I3 intensity.

The different geometrical and electron densities on atoms within the iodine monolayer will translate to different chemical properties and charge transfer abilities. Our findings demonstrate the importance of both surface structure and surface concentration of iodine on the properties and performance of a monolayer. It also shows that I4d core level spectroscopy can be a useful tool to identify chemical differences within an iodine layer.

## CONCLUSIONS

We have used core level PES, LEED, STM, and DFT to investigate iodine induced c(2 × 2) and quasi hexagonal structures on Pd(110). Two adsorption sites dominate; hollow and long-bridge, with a higher electron density on bridge bonded iodine, leading to a large chemical shift I4d spectra as observed both experimentally and theoretically. Moreover, the surface layer hosts a number of vacancies, preferentially at the bridge-bonded sites, that are charged positively. These variations within the iodine layer underline the importance of surface structure and surface density on chemical and electronic properties.

[1] J. P. Collman, L. S. Hegedus, J. R. Norton, and R. G. Finke, *Principles and Applications of Organo-transition Metal Chemistry*, 2nd ed. (University Science Books, Mill Valley, CA, 1987).

[2] M. P. Kiskinova, *Poisoning and Promotion in Catalysis based on Surface Science Concepts and Experiments*, Studies in Surface Science and Catalysis (Elsevier, 1992).

[3] W. Cabri and I. Candiani, Acc. Chem. Res. **28**, 2 (1995).

[4] E. Dona, M. Cordin, C. Diesl, E. Bertel, C. Franchini, R. Zucca, and J. Redinger, J. Am. Chem. Soc. **131**, 2827 (2009).

[5] W. Simpson and J. A. Yarmoff, Annu. Rev. Phys. Chem. **47**, 527 (1996).

[6] Ze Yu, M. Gorlov, J. Nissfolk, G. Boschloo, and L. Kloo, J. Phys. Chem. **114**, 10612 (2010).

[7] W. F. Themesgen, J. B. Abreu, R. J. Barriga, E. A. Lafferty, M. P. Soriaga, K. Sashikata, and K. Itaya, Surf. Sci. **385**, 336 (1997).

[8] B. V. Andryushechkin, K. N. Eltsov, and V. M. Shevlyuga, Surf. Sci. **584**, 278 (2005).

[9] U. Bardi and G. Rovida, Surf. Sci. **128**, 145 (1983).

[10] W. Erley, Surf. Sci. **114**, 47 (1982).

[11] H. R. Tang, W. N. Wang, Z. H. Li, W. L. Dai, K. N. Fan, and J. F. Deng, Surf. Sci. **450**, 133 (2000).

[12] R. Denecke, P. Väterlein, M. Bässler, N. Wassdahl, S. Butorin, S. A. Nilsson, J. E. Rubensson, J. Nordgren, N. Mårtensson, and R. Nyholm, J. Electron Spectrosc. Relat. Phenom. **101–103**, 971 (1999).

[13] N. Mårtensson, P. Baltzer, P. Brühwiler, J-O. Forsell, A. Nilsson, A. Stenborg, and B. Wannberg, J. Electron Spectrosc. Relat. Phenom. **70**, 117 (1994).

[14] N. D. Spencer, P. J. Goddard, P. W. Davies, M. Kitson, and R. M. Lambert, J. Vac. Sci. Technol. A **1**, 1554 (1983).

[15] M. Göthelid, H. von Schenck, J. Weissenrieder, B. Åkermark, A. Tkatchenko, and M. Galvan, Surf. Sci. **600**, 3093 (2006).

[16] W. Kohn and L. J. Sham, Phys. Rev. **140**, A1133–A1138 (1965).

[17] J. P. Perdew, K. Burke, and M. Ernzerhof, Phys. Rev. Lett. **77**, 3865 (1996).

[18] G. Kresse and D. Joubert, Phys. Rev. B **59**, 1758 (1999).

[19] G. Kresse and J. Furthmüller, Phys. Rev. B **54**, 11169 (1996).

[20] G. Kresse and J. Furthmüller, Comput. Mater. Sci. **6**, 15 (1996).

[21] R. F. W. Bader, S. G. Anderson, and A. J. Duke, J. Am. Chem. Soc. **101**, 1389 (1979).

[22] R. S. Mulliken, J. Chem. Phys. **36**, 3428 (1962).

[23] S. J. Clark, M. D. Segall, C. J. Pickard, P. J. Hasnip, M. J. Probert, K. Refson, and M. C. Payne, Z. Kristallogr **220**, 567 (2005).

[24] See, for example, O. Björneholm, A. Nilsson, H. Tillborg, P. Bennich, A. Sandell, B. Hernnäs, C. Puglia, and N. Mårtensson, Surf. Sci. **315**, L983 (1994) and references therein; S. Doniach and M. Sunjic, J. Phys. **C3**, 285 (1970).

[25] G. K. Wertheim and P. H. Citrin, *Photoemission in Solids I*, in Topics in Applied Physics, edited by M. Cardona and L. Ley (Springer, 1978).

[26] R. Nyholm, M. Qvarford, J. N. Andersen, S. L. Sorensen, and C. Wigren, J. Phys. Condens. Matter **4**, 277 (1992).

[27] S. Surnev, M. Sock, M. G. Ramsey, F. P. Netzer, M. Wiklund, M. Borg, and J. N. Andersen, Surf. Sci. **470**, 171 (2000).

[28] J. N. Andersen, M. Qvarford, R. Nyholm, S. L. Sorensen, and C. Wigren, Phys. Rev. Lett. **67**, 2822 (1991).

[29] A. J. Jaworowski, R. Ásmundsson, P. Uvdal, and A. Sandell, Surf. Sci. **501**, 74 (2002).

[30] M. G. Ramsey, F. P. Leisenberger, F. P. Netzer, A. J. Roberts, and R. Raval, Surf. Sci. **385**, 207 (1997).

[31] J. N. Andersen, D. Hennig, E. Lundgren, M. Methfessel, R. Nyholm, and M. Scheffler, Phys. Rev. B **50**, 17525 (1994).

# SO$_2$ interaction with Zn(0001) and ZnO(0001) and the influence of water

Anneli Önsten *, Dunja Stoltz, Pål Palmgren, Shun Yu, Thomas Claesson, Mats Göthelid, Ulf O. Karlsson

*Materials Physics, Royal Institute of Technology KTH, S-164 40 Kista, Sweden*

## ABSTRACT

Photoelectron spectroscopy has been used to study room temperature adsorption of sulfur dioxide on clean and water exposed (0001) surfaces of zinc and zinc oxide. Water has no significant effect either on clean or on SO$_2$ exposed Zn(0001) at the low water pressures used ($p < 10^{-7}$ mbar). In the case of the zinc-terminated ZnO(0001) surface, however, water adsorbs dissociatively and OH groups are shown to have a considerable effect on SO$_2$ surface reactions. A strong oxidation reaction occurs between Zn(0001) and SO$_2$ giving various sulfur containing species. On ZnO(0001), SO$_2$ interacts mainly with oxygen sites giving SO$_3$ or SO$_4$ species. It is shown that the ZnO(0001) sample preparation procedure can have large effects on surface chemical and physical properties. Samples cleaned by four different preparation procedures are investigated, namely sputtering only and sputtering followed by annealing at 450 °C, 530 °C and 600–650 °C. Annealing at 600 °C leads to a transition from a partly OH-terminated surface to a triangularly structured surface free from OH groups. Adsorption of SO$_2$ on the latter surface leads to a decreased surface conductivity, which hampers photoemission measurements. Water is shown to block SO$_2$ adsorption sites on both 450 °C and 530 °C annealed samples. On the latter sample, SO$_2$ reduction has been observed to a small extent on the clean surface and to a larger extent when the surface is prehydroxylated. Here, we speculate that water, similar to hydrogen, generates surface zinc clusters on ZnO(0001). Zinc clusters could enable charge transfer to the antibonding LUMO of the SO$_2$ molecule and subsequent dissociation.

© 2012 Elsevier B.V. All rights reserved.

## 1. Introduction

Zinc is well known for its use in corrosion protecting layers on steel (galvanization). At atmospheric conditions, zinc reacts immediately with air to form a layer of zinc oxide and in a humidified atmosphere, a layer of zinc hydroxide is subsequently formed [1]. A protective film of zinc carbonate is then formed [1]. This layer is only stable in a small pH range and gaseous pollutants such as sulfur dioxide or particles that acidify the water layer covering the surface can highly influence the degradation of zinc.

The interest in zinc oxide as a material has got an extensive upswing in the literature the latest decade, mostly because of its semiconducting and optical properties. Zinc oxide surfaces are very useful in catalysis and gas sensing. One of the most important technological applications of zinc oxide surfaces is in the chemical industry, where Cu/ZnO/Al$_2$O$_3$ catalysts are used in e.g. methanol synthesis and in the water gas shift reaction for production of hydrogen.

Sulfur dioxide (SO$_2$) is an aggressive pollutant that is mostly created in the combustion of fuels derived from coal and oil, since these fuels usually contain a small amount of sulfur containing impurities. When water is present in the atmosphere, SO$_2$ forms acid rain, which is known to cause environmental problems and to accelerate corrosion. There is consequently a need of developing efficient methods for the

removal or destruction of SO$_2$ (DeSOx). Moreover, metal oxides such as CaO and ZnO are often used as sorbents in SO$_2$ removal processes. In industry, SO$_2$ is useful in e.g. the manufacture of sulfuric acid, but it can also cause problems due to its poisoning effect on catalysts [2]. Research on the interaction between SO$_2$ and solid surfaces is thus of large interest to get a fundamental understanding of surface reactions in various fields such as catalysis, corrosion and DeSOx processes.

A large amount of studies focus on the interaction of SO$_2$ with single crystal surfaces. It has been found that SO$_2$ dissociates either partly or completely on most metal surfaces with the exceptions of Ag and Au [3,4]. When coming to the more inert oxide surfaces, the reaction is very much dependent on the type of oxide and on the sample preparation procedure [5,6], which influence the amount of surface defects. Generally, SO$_2$ can either react with oxygen sites of the oxide, forming SO$_3$ and SO$_4$ species or interact with metal sites. S–O bond breaking leading to SO$_2$ dissociation has been shown to occur only at metal sites of an oxide surface [5,7]. S–O bond cleavage demands charge transfer from the surface to the antibonding LUMO of the SO$_2$ molecule [5]. Since the charge density at metal sites on oxide surfaces usually is too low, SO$_2$ dissociation is not favored on these surfaces.

Most studies on the reaction of SO$_2$ with single crystal surfaces have been performed in ultrahigh vacuum (UHV). At atmospheric conditions, the air that surrounds a surface has a large amount of constituents and SO$_2$ represents only a very small part of all gases (0.3–65 ppb) [1]. Furthermore, at normal air pressures, most surfaces are covered with a water layer. The thickness of this layer depends on the relative humidity

of the air [1]. Even at UHV conditions ($<10^{-9}$ mbar), water and hydrogen are to some extent present in the residual gas. It has been shown in UHV studies of ZnO [8] and TiO$_2$ [9] surfaces that what was believed to be "clean" surfaces, actually contained OH or H species. It is quite likely that water or hydrogen has unintentionally participated in many surface science studies. Coadsorption with water is thus of great importance both to understand fundamental surface reactions and to approach the state of the surface under atmospheric conditions.

In the present study, room temperature adsorption of SO$_2$ on clean and water exposed Zn(0001) and ZnO(0001) surfaces has been studied with photoelectron spectroscopy (PES). We compare these results to previous studies on SO$_2$ adsorption on polycrystalline zinc [10,11] and on ZnO(0001) [12] and discuss differences with respect to our results. The influences of sample preparation and water adsorption on the surface structure and SO$_2$ chemistry are also discussed in detail.

## 2. Experimental details

All PES measurements were performed at beamline I511 at MAX-lab in Lund, Sweden. The beamline is undulator based giving photon energies in the range of 100–1200 eV and the energy is selected by a modified SX-700 monochromator. The end station analysis chamber is equipped with a rotatable Scienta R-4000 electron analyzer. In connection to this chamber is a preparation chamber which houses Low Energy Electron Diffraction (LEED) apparatus, sputter and annealing equipment as well as leak valves and a quadrupole mass spectrometer. A more detailed description of the experimental set-up can be found elsewhere [13].

All experiments were performed at room temperature and the base pressure in both chambers was below $2 \cdot 10^{-10}$ mbar. The spectra were acquired at grazing incidence at an angle of approximately 80° off-normal and at normal emission. The experimental energy resolutions were 30–40 meV for S 2p spectra ($h\nu = 260$ eV), 130–150 meV for O 1s spectra ($h\nu = 619$ eV) and 11–14 meV for VB spectra ($h\nu = 113$ eV). All core level spectra were normalized to the background intensity at the low-binding energy side of the core level line and the binding energy was referenced to the Fermi level, which was measured on a grounded tantalum foil in electrical contact with the sample. After a Shirley-type background subtraction, some of the spectra were numerically fitted with Voigt (Gaussian–Lorentzian) functions. A small asymmetry ($\alpha < 0.03$) was allowed in order to improve the fittings.

The Zn(0001) crystal was purchased from Surface Preparation Laboratory and cleaned by cycles of argon ion bombardment (500 eV) and "annealing" in vacuum at room temperature (30 min–3 h) until no signals of oxygen or carbon was detected with XPS. The $1 \times 10 \times 10$ mm$^3$ sized ZnO crystal was purchased from Surface Preparation Laboratory (SPL) and was cut into three $1 \times 3 \times 10$ mm$^3$ sized samples. These three equivalent samples, named sample A, B and C were used in this study. According to information received from SPL, the ZnO crystal was produced with the flame fusion method. The ZnO(0001) samples were cleaned through Ar$^+$ sputter (1 keV) and annealing cycles until no carbon was detected and a ($1 \times 1$) LEED pattern was obtained. The samples were heated by running a current through a thin Ta foil attached at the backside of the sample. For samples A and B, the Ta foil was thin (0.03 mm) and 1 mm wide and parallel to the long side (10 mm) of the sample, while for sample C, the foil was thicker (~0.1 mm) and as wide as the sample. When annealing, the major part of the IR radiation from the filament was transmitted through the samples. Therefore a pyrometer would measure the temperature of the foil and not the sample. For samples A and B, it is likely that the filament temperature was significantly higher than the temperature of the sample. The maximum annealing temperatures for these samples have therefore been estimated from a plot of the temperature, measured with a pyrometer as a function of the filament current. This plot was obtained when measuring the temperature of an opaque TiO$_2$ sample, using the same heater setup as in the present study. The estimated

annealing temperatures for sample A is 450 °C and for B it is 530 °C. For sample C, the temperature reading obtained with a pyrometer (600–650 °C) is close to the sample temperature, since the foil cover the whole backside of the sample and is in close contact with the sample.

The de-ionized water was cleaned by several freeze and thaw cycles. The SO$_2$ gas used for the measurements on sample A and on the Zn(0001) sample was purchased from Air Liquide (99.9% purity) while the gas used for sample B was purchased from Sigma-Aldrich (99.9% purity). Both the water and the SO$_2$ gas were dosed through leak valves and the purity of the gases was confirmed by means of mass spectrometry. A very small amount of CO and/or N$_2$ was detected in the gases.

When recording many succeeding short spectra from the same spot of the Zn(0001) sample, photon beam induced dissociation of SO$_2$ was observed, while the photon beam only induced desorption of SO$_2$ on ZnO(0001). When acquiring the spectra on ZnO(0001), sample B, the beam was scanned over the sample and the scan speed was adjusted to avoid beam damage. The spectra taken on Zn(0001) and ZnO(0001), samples A and C, were acquired without scanning but the position for beam exposure was changed and several measurements on the same core level were added to give the final spectra. To verify that the surface chemistry observed was not induced by the photon beam, an S 2p spectrum of the 50 L (1 L = $10^{-6}$ Torr s) SO$_2$ covered Zn(0001) surface was recorded with a Mg anode X-ray source from our home-lab, whose photon intensity is much lower than the synchrotron beam used at MAX-lab. Due to the lower resolution, the width of the S 2p spectrum obtained with the homelab XPS system was much larger, but overall the spectrum showed the same relative intensities as the one recorded at MAX-lab.

## 3. Results

### 3.1. Zn(0001)

The results from SO$_2$ adsorption and coadsorption with water on Zn(0001) are plotted in Figs. 1–4. Here, the term coadsorption does not denote the simultaneous adsorption of two species, but two subsequent dosings. The dosings presented here are 5 L and 50 L SO$_2$ and 50 L SO$_2$ followed by 50 L H$_2$O. The clean surface was also exposed to water, but no adsorption was observed at room temperature. This is in agreement with an earlier study [14] where 100 L water was adsorbed at 77 K and all water desorbed when the Zn(0001) crystal was heated to 180 K. However, when the sample was preexposed to oxygen and then exposed to water at 77 K, hydroxyl groups were still present on the surface at ~500 K. The same type of behavior has been observed on Cu(111) [15–17].

Four spin-orbit split doublets are clearly visible in each of the S 2p spectra in Fig. 1 and their binding energies and relative area in percentage of the whole S 2p spectrum are listed in Table 1. The components can be attributed to sulfur or zinc sulfide (ZnS), SO$_2$ bound to zinc sites in the surface, SO$_3$ species or zinc sulfite (ZnSO$_3$) and SO$_4$ species or zinc sulfate (ZnSO$_4$) according to an earlier study on SO$_2$ adsorption on polycrystalline zinc [10]. Compared to the spectra obtained from the polycrystalline sample [10], the Gaussian broadenings of the core level peaks from the Zn(0001) surface are smaller, which facilitates curve fitting. In the curve fitting procedure, the Lorentzian widths of the S 2p spectral components are fixed to 0.09 eV, which is close to the width that has been estimated from the core hole lifetime (0.06 eV) [18]. All other curve fitting parameters used in the core-level analysis are given in the figure caption of Fig. 1.

The O 1s spectra shown in Fig. 2 can easily be deconvoluted into two components with a fixed Lorentzian width of 0.35 eV. Other curve fitting parameters are given in the figure caption of Fig. 2. The component at a ~530.2 eV binding energy is assigned to ZnO while the component at ~532.0 eV is assigned to ZnSO$_x$ [10]. The higher dose of SO$_2$ gives
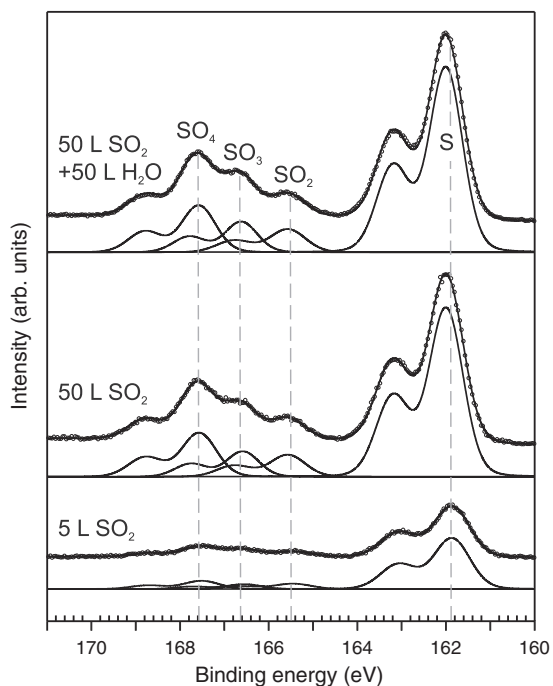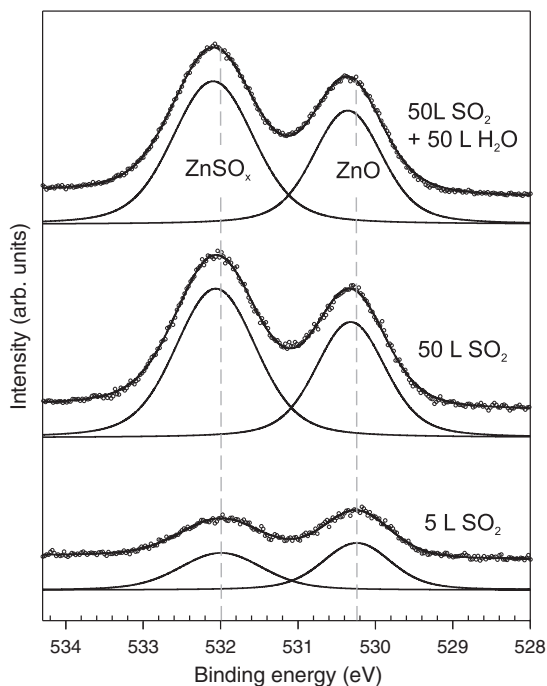
**Fig. 1.** S 2*p* core level spectra (*hv* = 260 eV) of SO₂ adsorbed on Zn(0001). In the uppermost spectrum, adsorption of 50 L SO₂ is followed by 50 L H₂O. Each of the spectra is decomposed into four components. The curve fitting components have spin-orbit splits of 1.17–1.21 eV, branching ratios of 1.95–2.25 eV and Gaussian widths of 0.80–0.91 eV.

a 0.1 eV shift of both O 1*s* peaks to higher binding energies. No O 1*s* line appears upon exposure of 5 L water.

By using SO$_x$/S peak area ratios in S 2*p* spectra and SO$_x$/S ratios in O 1*s* spectra, the relative amounts of reaction products formed when exposing Zn(0001) to SO₂ have been calculated and are shown in Table 2.



**Fig. 2.** O 1*s* core level spectra (*hv* = 619 eV) of SO₂ adsorbed on Zn(0001). In the uppermost spectrum, adsorption of 50 L SO₂ is followed by 50 L H₂O. Each of the spectra is decomposed into two components. The Gaussian width is 0.92–0.95 eV for the component at ~530.2 and 1.13–1.15 eV for the component at ~532.0 eV.
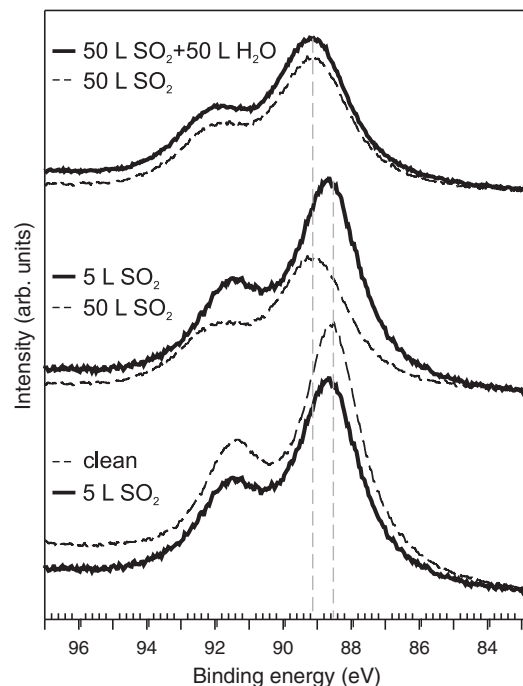


**Fig. 3.** Zn 3*p* core level spectra (*hv* = 204 eV) of clean and SO₂ exposed Zn(0001). One of the uppermost spectra is acquired from a surface exposed to 50 L SO₂ followed by 50 L H₂O.

Clear changes of both the Zn 3*p* spectrum in Fig. 3 and of the valence band spectrum in Fig. 4 are revealed upon adsorption of SO₂. At the clean surface, the Zn 3*p*$_{3/2}$ peak is situated at a 88.6 eV binding energy. Upon SO₂ exposure, the Zn 3*p* peak shifts to higher binding energies and is broadened, which could be due to an extra Zn 3*p* component that appears at the high binding energy side. At the higher SO₂ dose (50 L) the Zn 3*p* peak is located at 89.2 eV, which means that it is shifted as much as ~0.6 eV compared to the same peak from the
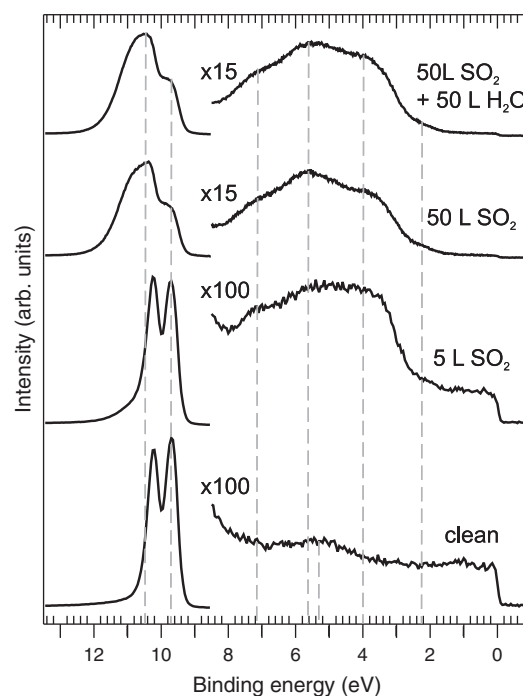


**Fig. 4.** Valence band spectra (*hv* = 113 eV) of clean and SO₂ exposed Zn(0001). The uppermost spectrum is acquired from a surface exposed to 50 L SO₂ followed by 50 L H₂O. The spectra are normalized at 13 eV.

**Table 1**
Binding energies and relative areas for spectral components from SO₂ exposed Zn(0001) and polycrystalline Zn [10].

| Core level | Adsorbate specie | $E_{Bin}$ (eV) | | Peak area, Figs. 2–3 (%) | | |
|---|---|---|---|---|---|---|
| | | | | 5 L | 50 L | 50 L SO₂+ |
| | | Poly [10] | Zn(0001) | SO₂ | SO₂ | 50 L H₂O |
| S $2p_{3/2}$ | S | 162.0 | 161.9 | 74.0 | 65.0 | 64.3 |
| | SO₂ | 165.8 | 165.5 | 8.0 | 8.8 | 8.8 |
| | SO₃ | 166.8 | 166.6 | 6.7 | 9.5 | 10.6 |
| | SO₄ | 167.7 | 167.6 | 11.3 | 16.7 | 16.3 |
| O 1s | O | 530.5 | 530.2 | 50.8 | 40.0 | 40.8 |
| | SO$_x$ | 531.5 | 532.0 | 49.2 | 60.0 | 59.2 |

clean surface. From our measurements on the ZnO(0001) surface we deduced a Zn $3p_{3/2}$ binding energy of 89.2–89.6 eV depending on surface preparation. The highest dose of SO₂ thus gives a Zn $3p$ peak that is in the same binding energy region as zinc oxide. This indicates a complete oxidation of one or a few atomic layers of the Zn(0001) crystal.

The valence band spectrum of zinc has in earlier studies [19] been shown to consist of a sharp $3d$-peak located at about 10 eV below the Fermi level and a wide and flat region at the top of the valence band, which is Zn $4sp$ derived. In the spectrum from the clean surface in Fig. 4, the Zn $3d$ peak has a well-resolved spin orbit splitting and the Zn $3d_{5/2}$ peak is located at a binding energy of 9.7 eV. In addition, there is one distinct Zn $4sp$ related feature at around 5.3 eV. Dramatic changes in the Zn $3d$ peak appear after the 50 L dose, which is due to a strong oxidation of the sample and formation of ZnO, ZnS and ZnSO$_x$. Furthermore, SO₂ adsorption introduces several new features, which are located at the approximate binding energies 2.2, 4.0, 5.6 and 7.2 eV respectively. It is difficult to associate the peaks with certain orbitals, since they are probably a mix of orbitals from Zn, ZnO, ZnS and ZnSO$_x$ compounds and molecular SO$_x$ orbitals. At the higher SO₂ coverage, all the SO₂ related features have grown stronger, but compared to the lower dose, the relative intensity of the feature at ~5.6 eV is higher. Since the ZnSO$_x$/ZnO ratio (x = 3,4) has been shown to be larger for the 50 L SO₂ dose (see Table 1), one can speculate that this feature is related to ZnSO$_x$ species.

As already mentioned, no water adsorption was observed on the clean Zn(0001) surface at room temperature. Moreover, the effects of water on the SO₂ preexposed surface, as shown in Figs. 1–4 are so small that they are probably within the limits of the experimental uncertainty. Thus, no significant effect of water on the surface chemistry has been observed at the low water pressures used in this study ($<2 \cdot 10^{-7}$ Torr).
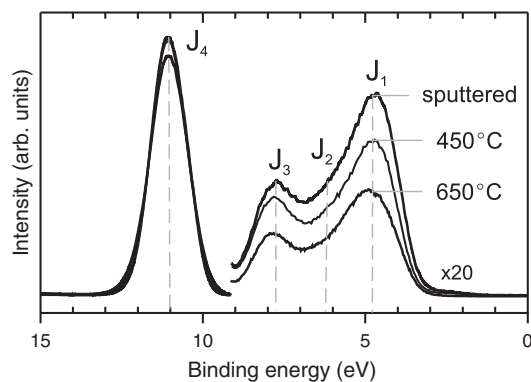
### 3.2. ZnO(0001)

#### 3.2.1. Effect of sample preparation and water exposure

Sample preparation method and annealing temperature can have vast effects on structure and properties of metal oxide surfaces. In Fig. 5, valence band spectra from ZnO(0001) samples with three different sample preparations are shown, namely sputtering alone and sputtering with subsequent annealing at 450 and 650 °C respectively. The spectra are normalized with respect to the Zn $3d$ peak area. This type of normalization does not give correct quantitative information.

**Table 2**
Proportion of reaction products upon SO₂ adsorption on Zn(0001).

| SO₂ dose | Reaction products (%) | | | | | Atoms (%) | |
|---|---|---|---|---|---|---|---|
| (L) | ZnO | ZnS | SO$_{2,ads}$ | ZnSO₃ | ZnSO₄ | O | S |
| 5 | 45.6 | 40.3 | 4.4 | 3.6 | 6.1 | 62.2 | 37.8 |
| 50 | 43.0 | 37.0 | 5.0 | 5.4 | 9.6 | 65.4 | 34.6 |



**Fig. 5.** Valence band spectra ($h\nu = 113$ eV) of clean ZnO(0001) surfaces. Observe that the right part in the spectra is magnified 20 times. The upper spectrum comes from a sample that has been sputtered for 60 min at normal incidence.

Nevertheless, it facilitates the comparison of the intensity in O $2p$ and Zn $3d$ dominated regions. Three distinct features are present at binding energies 4.8, 7.8 and 11.1 eV. The asymmetry of the peak at 4.8 eV also indicates that a weaker feature is present at a binding energy of 6 eV. The four features have been named J₁–J₄ as in the study of Ranke et al. [20] and are marked out in the valence band spectra. The sharp Zn $3d$ peak is represented by J₄, while J₁–J₃ are mainly O $2p$ derived with a small contribution from Zn $4sp$ orbitals [20]. The Zn $4s$ electrons are mainly contributing to the J₃ feature [20]. It can be noted from Fig. 5 that the higher the annealing temperature, the higher is the Zn $3d$/O $2p$ ratio.

LEED measurements revealed ($1 \times 1$)-terminations for all studied surfaces. In general, sputtering alone gives a disordered surface with a very weak LEED pattern while it becomes clearer upon annealing at 450–530 °C. The most distinct pattern was obtained when annealing at 600–650 °C.

In an earlier study by our group, water exposure has been shown to completely change the surface structure of ZnO(0001) [21]. Similar STM images as reported in this earlier study are shown in Fig. 6. Images from ZnO(0001) cleaned with sputtering and annealing at 600–700 °C and this surface exposed to 5 L of water are shown in Fig. 6a and b respectively. The clean surface consists of triangular structures. Water adsorbs on step edges in an uneven fashion making step edges irregular. As the water dose increases, the triangular islands grow and pits diminish. At a dose of 20 L, a very irregular surface structure appears (see Önsten et al. [21]).

O 1s spectra acquired from clean and water exposed samples are displayed in Fig. 7. Three different types of clean surfaces are represented in the figure, one that is sputtered to induce defects (a) and the other two are sputtered and annealed at 450 °C (c) and 600 °C (f) respectively. Each spectrum is decomposed into two Voigt functions, whose Lorentzian linewidth is 0.33–0.35 eV. The binding energy and Gaussian width of each component as well as the relative area and coverage of the high binding energy component are listed in Table 3.

All O 1s spectra contain a peak, which is located at 530.9–531.0 eV and it can be assigned to bulk and surface oxygen in zinc oxide. The width of this peak shows a tendency to decrease with increasing annealing temperature. Surface oxygen is presumably concentrated to step edges [22].

For clean surfaces, a small peak is also located at a ~532.3 eV binding energy for the 450 °C annealed sample and ~532.6 eV for the sputtered surface. The latter peak can be attributed to hydroxyl groups since it is shifted from the bulk O 1s peak with around 1.3–1.6 eV, which is characteristic for hydroxyl species on oxides (see Table 1 in [21]). Moreover, no other contaminants like carbon or nitrogen have been detected. The O 1s spectrum from the sample that has been annealed at 600 °C has been fitted with one peak only.
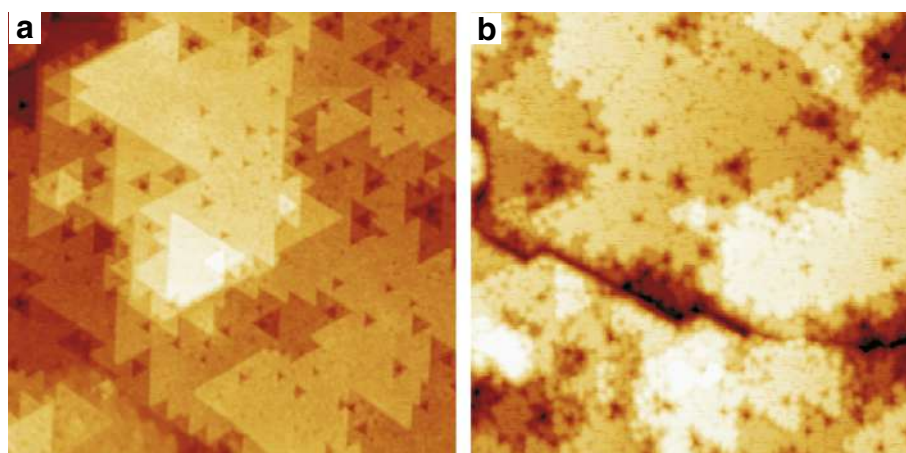
**Fig. 6.** 100 nm × 100 nm STM images (+3.0 V, 0.04 nA) of clean (a) and 5 L water exposed (b) ZnO(0001).
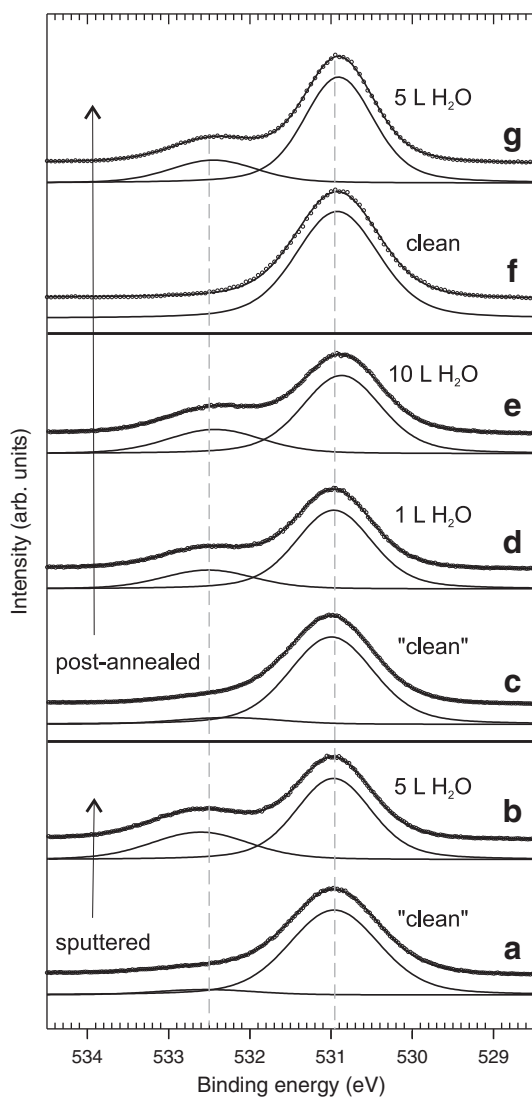


**Fig. 7.** O 1s core level spectra ($h\nu = 619$ eV) from clean and water exposed ZnO(0001) surfaces at room temperature. Spectrum a is obtained from a sample that has been sputtered for 60 min at normal incidence. Sample preparation annealing temperatures are 450 °C for spectra c–e and 600 °C for f–g. Full lines show decomposition of the spectra into two components. Binding energies and Gaussian widths of the components are given in Table 3.

Consequently, there is something inherently different between the 600 °C annealed sample compared to the other samples.

When exposing the samples to water, the high energy O 1s component grows stronger and shifts to somewhat higher energy for the 450 °C post-annealed surface (532.4–532.6 eV). The binding energy shift of 1.5–1.6 eV with respect to the bulk O 1s peak indicates that the water adsorption is predominantly dissociative. We earlier suggested that water adsorbs at zinc sites close to oxygen terminated step edges and that dissociation occurs when the water molecules leave off hydrogen species to oxygen sites at step edges. Water exposure leads to a decreased width of the main O 1s peak. This effect of water has been explained in an earlier study by our group on water adsorption on ZnO(0001) [21]. The larger width of the main O 1s peak for the clean surface could be due to the large number of defects giving various types of O sites. When the O sites bind to hydrogen giving OH groups, they will contribute to the hydroxyl peak alone and the width of the main peak will thus decrease.

A rough estimation of the hydroxyl coverage can be made from the O 1s spectra in Fig. 7 by using a relation based on Lambert–Beer absorption law [23,24]:

$$\frac{I_{ads}}{I_{ads}+I_{sub}} = 1-\exp^{-d/l}. \tag{1}$$

The above relation assumes normal emission for photoelectrons, since all spectra in this study were collected in this mode. $I_{ads}$ and $I_{sub}$ are the peak areas of the normalized O 1s peaks for the adsorbate and substrate respectively. $l$ represents the photoelectron mean free path and $d$ is the adsorbate layer thickness. The mean free path is obtained from the universal curve of mean free path versus photoelectron energy

**Table 3**
Binding energies (E$_{Bin}$), Gaussian linewidths (ΔE$_G$), relative areas and coverages of curve fitted O 1s components from clean and water exposed ZnO(0001) surfaces.

| T$_a$[a] | H$_2$O dose | Bulk O 1s | | OH O 1s | | | |
|---|---|---|---|---|---|---|---|
| | | E$_{Bin}$ | ΔE$_G$ | E$_{Bin}$ | ΔE$_G$ | Area | Cov. |
| (°C) | (L) | (eV) | (eV) | (eV) | (eV) | (%) | (ML) |
| – | – | 531.0 | 1.11 | 532.6 | 1.25 | 6 | 0.15 |
| – | 5 | 531.0 | 0.90 | 532.6 | 1.23 | 30 | 0.75 |
| 450 | – | 531.0 | 1.03 | 532.3 | 1.22 | 8 | 0.20 |
| 450 | 1 | 531.0 | 0.91 | 532.5 | 1.13 | 22 | 0.55 |
| 450 | 10 | 530.9 | 0.95 | 532.4 | 1.17 | 26 | 0.65 |
| 530 | – | 530.8 | 0.93 | 532.3 | 1.12 | 8 | 0.20 |
| 600 | – | 530.9 | 0.96 | – | – | – | – |
| 600 | 5 | 530.9 | 0.81 | 532.4 | 1.06 | 21 | 0.53 |

[a] The samples are sputtered or sputtered and post-annealed at a certain annealing temperature (T$_a$).

[23] and its value is assumed to be the same for the adsorbate layer as for the substrate. When the spectra in Fig. 7 were collected, the photon energy used was 619 eV and the binding energy for the O 1$s$ peak is 531–532 eV, which gives a kinetic energy of 87–88 eV for the photo-electrons. This gives an approximate $l$ value of 4.5 Å [23]. $d$ is first set to the thickness of a monolayer of OH-groups to obtain the expected in-tensity ratio at a coverage of 1 ML. To obtain an approximate value of the coverage, the relative area of the OH related peak is then compared to the calculated value for one monolayer of OH. The monolayer thick-ness is estimated as the sum of the Zn–OH distance (1.95 Å [25]) and half of the distance between outermost zinc and oxygen atomic layers (0.35 Å [22]) giving in total 2.3 Å. Zn–OH bonds are thus assumed to be perpendicular to the surface. Surface relaxation has not been taken into account and an OH monolayer is defined as one OH-group per sur-face Zn cation. The calculated coverages are shown in Table 3 and are around 0.5 monolayer (ML) for water exposed (1–10 L) surfaces. A somewhat higher coverage is observed on the sputtered surface com-pared to the post-annealed ones.

### 3.2.2. SO₂ on clean and water exposed ZnO(0001)

S 2$p$ spectra for SO₂ exposed surfaces are shown in Figs. 8–9. These spectra are recorded from samples that before SO₂ exposure have been cleaned either with sputtering alone or with sputtering and subse-quent annealing at 450 °C (Fig. 8) or 530 °C (Fig. 9). Adsorption is made both on clean and water exposed surfaces and in one case (Fig. 9f), water exposure is made after SO₂ adsorption. It should be noted that the spectra in Fig. 8 are collected using another photon energy than the one in Fig. 9 (see figure captions). The implication of this is a more inclining background intensity in the spectra collected at 204 eV, shown in Fig. 8 compared to the spectra collected at 260 eV, shown in Fig. 9. The surface sensitivity is about the same for the two photon ener-gies used. Annealing at 600–650 °C gave a sharper LEED pattern than when annealing at 450–530 °C. Unfortunately, however, we found that when exposing samples annealed at 600–650 °C to SO₂, it was im-possible to record spectra from these samples due to severe charging
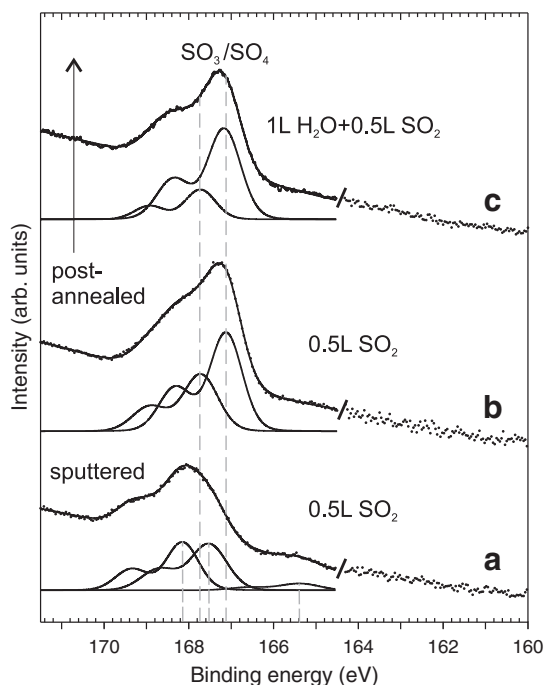


**Fig. 8.** S 2$p$ core level spectra ($hv = 204$ eV) of SO₂ adsorbed on clean and water exposed ZnO(0001). Each of the spectra consists of two measurements recorded in subsequent bind-ing energy regions and they are separated with a dash (/) in the figure. The decomposition of the SO₃/SO₄ peaks into two components is shown in full lines. Spectrum a is obtained from a sample that has been sputtered for 60 min at normal incidence prior to SO₂ exposure. Spectra b–c are obtained from samples that have been cleaned by sputtering and annealing at 450 °C.
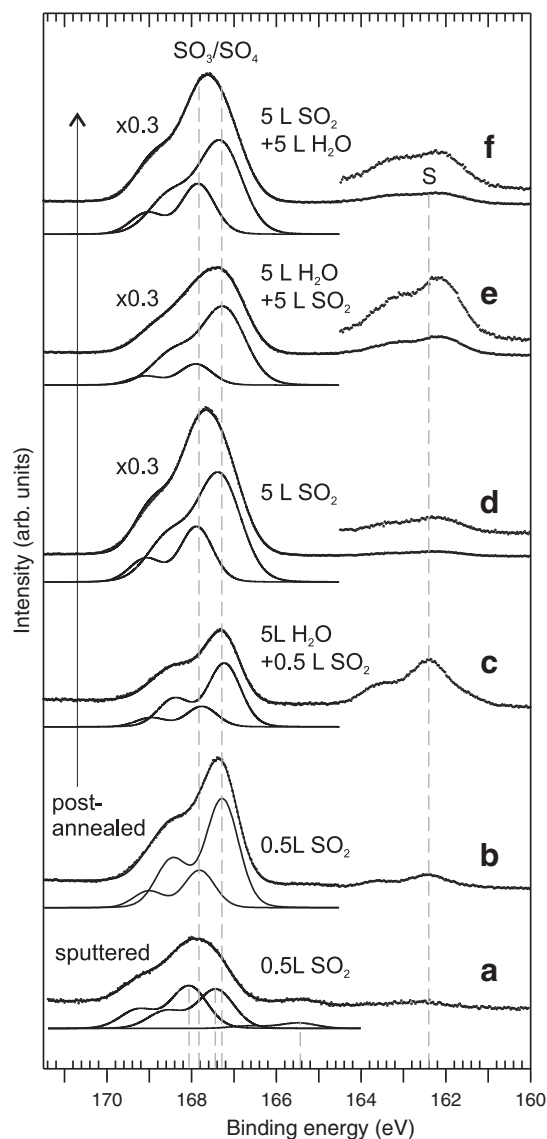


**Fig. 9.** S 2$p$ core level spectra ($hv = 260$ eV) of SO₂ and H₂O followed by a dose of SO₂ on ZnO(0001). The SO₃/SO₄ peaks have been decomposed into two components. Observe that the intensities in spectra d–f are multiplied with 0.3. The low binding energy regions of spec-tra d–f are also shown with initial (normalized) intensities. Spectrum a is obtained from a sample that has been sputtered for 30 min at 45° incidence prior to SO₂ exposure. Spectra b–f are acquired from samples that have been cleaned by sputtering and annealing at 530 °C.

effects. These charging effects appeared mostly upon SO₂ exposure, to some extent on water exposed surfaces (not observed when measuring the O 1$s$ spectra in Fig. 7), while it was not observed on clean samples.

All S 2$p$ spectra contain a dominant peak at 167.1–168.0 eV. In the spectra from the 530 °C annealed sample (Fig. 9), an additional peak ap-pears at lower binding energy (162.0–162.4 eV), which can be assigned to atomic sulfur adsorbed on zinc sites (see Table 4). The high binding energy peak is shifted from the low binding energy sulfur peak with 4.8–5.6 eV, a shift that is typical for SO₃ and/or SO₄ species (see Table 4). The peaks are relatively wide, which is probably due to low sample conductivity, which results in poor screening of the core hole. Another possibility is that the large width is caused by several closely situated components associated with different adsorption configura-tions and/or sites. By means of curve fitting, the SO$_x$ related S 2$p$ peaks have been shown to consist of at least two components. If fitting with two components, they are located at 167.2 ± 0.1 eV and 167.8 ± 0.1 eV for the post-annealed surfaces. For the sputtered surfaces, these components are shifted with approximately 0.2 and 0.4 eV to

**Table 4**
Binding energies ($E_{Bin}$) and binding energy shifts ($\Delta E_{Bin}$) for S $2p_{3/2}$ lines measured with photoemission for different $SO_2$ adsorption products on single crystal metal and metal oxide surfaces.

| Sample surface | $E_{Bin}$ (eV) | | | | | $\Delta E_{Bin}$ (eV) $(E_{Bin} - E_{Bin,S})^a$ | | | T (K) | Ref. |
|---|---|---|---|---|---|---|---|---|---|---|
| | S | SO | $SO_2$ | $SO_3$ | $SO_4$ | $SO_2$ | $SO_3$ | $SO_4$ | | |
| Ag(110) | – | – | 165.4 | 166.1 | 167.9 | – | – | – | 300 | [26] |
| Ag(110)–p(2×1)–O | – | – | 165.4 | 166.1 | 167.9 | – | – | – | 240–570 | [27] |
| Ag(111) | – | – | – | 165.5 | 167.3 | – | – | – | 230–700 | [28] |
| Cu(111) | 160.2 | 165.2 | 164.1 | – | – | – | – | – | 170–450 | [29] |
| Ni(111) | 162.0 | – | – | 166.7 | – | – | 4.7 | – | 300 | [30] |
| Ni(100) | 161.3 | – | – | 165.9 | – | – | 4.6 | – | 300 | [28] |
| Pt(110) | 161.0 | – | 163.7/164.6 | 165.2 | 166.0 | 2.7/3.6 | 4.2 | 5.0 | 140 | [31] |
| Pt(111) | 161.5 | – | 164.0/164.8 | – | 166.5 | 2.5/3.3 | – | 5.0 | 85–418 | [32] |
| Ru(0001) | 161.4 | 162.8 | 164.3/164.8 | 165.6 | 166.4 | 2.9/3.4 | 4.2 | 5.0 | 88 | [33] |
| $CeO_2$(111) | – | – | – | 166.9 | 168.2 | – | – | – | 150 | [34] |
| $Cr_2O_3$(0001) | 161.9 | – | 164.5 | 166.3 | 168.2 | 2.6 | 4.4 | 6.3 | 100–450 | [35] |
| $Fe_3O_4$(100) | 161.3 | – | – | 166.2 | 167.1 | – | 4.9 | 5.8 | 300 | [36] |
| MgO(100) | – | – | – | 166.3 | 168.4 | – | – | – | 300 | [37] |
| $TiO_2$(110) | 162 | – | – | – | 167.5 | – | – | 5.5 | 300–600 | [38] |
| ZnO(0001) | 161.7 | – | 165.0 | 166.5 | – | 3.4 | 4.8 | – | 100–600 | [12] |
| ZnO(0001) | – | – | – | 166.4 | – | – | – | – | 110–150 | [39] |
| ZnO poly | – | – | 165.8 | 166.8 | 168.2 | – | – | – | 100 | [10] |
| compounds [b] | 162.0 | – | – | 166.7 | 169 | – | 4.7 | 7 | 300 | [40] |

[a] $E_{Bin,S}$ is the binding energy for the atomic sulfur (S) component.
[b] Sulfur containing compounds such as sulfides (e.g. NaS), sulfites (e.g. $NaSO_3$) and sulfates (e.g. $NaSO_4$).

higher binding energy. The Lorentzian width is fixed to 0.08 eV, the spin-orbit split is $1.19 \pm 0.01$ eV and the branching ratio is $2.29 \pm 0.06$. Also the low binding energy peaks consist of at least two components each but no curve fitting components are shown in the figures and all of them can be assigned to atomic sulfur adsorbed on different sites.

When a sputtered and therefore defect-rich surface is exposed to 0.5 L $SO_2$ (Figs. 8a and 9a), a peak appears at 167.9–168 eV for which the two components are approximately equal. Furthermore, there is a small peak at 165.4–165.5 eV, which appears only on sputtered surfaces. This peak could be attributed to $SO_2$ that is chemisorbed on zinc sites on the oxide [10]. Both the line profile and the binding energy of the peaks in the spectra from the sputtered surfaces agree well with earlier PES measurements on $SO_2$ exposed polycrystalline zinc oxide [10]. The spectra in Figs. 8a and 9a come from samples that have been subjected to different sputtering treatments. In Fig. 8a, the sputtering was made at normal incidence for 60 min., while in Fig. 9a sputtering was made at 45° incidence for 30 min. The former treatment is more destructive and has potential for creating a larger amount of defects. Despite this, the two spectra mentioned have a very similar lineshape. The only difference is a small shift (~0.2 eV) towards higher binding energy for Fig. 8a compared to Fig. 9a.

Exposing post-annealed surfaces to 0.5 L $SO_2$ (Figs. 8b and 9b) gives an S 2p peak at somewhat lower energy, namely at ~167.3 eV and this peak is dominated by the lower BE $SO_3/SO_4$ component. The area of the higher binding energy (BE) component is approximately the same as on the sputtered surface. The total area of the $SO_x$ peak is thus larger for the post-annealed surfaces compared to the sputtered surfaces, which have been exposed to the same $SO_2$ dose. However when studying the O 1s spectra (see description of Fig. 10 below), it appears as if $SO_x$ coverages are approximately equal. The peak intensity differences between sputtered and post-annealed samples could be explained by different background intensities and show that one cannot rely fully on intensities for quantitative estimations. When comparing Figs. 8b and 9b, the $SO_x$ peak is quite similar. The major difference between these spectra is that there is a sulfur related peak at ~162.4 eV in Fig. 9b but not in Fig. 8b.

When the $SO_2$ exposure is increased to 5 L on the 530 °C annealed sample (Fig. 9d), both $SO_x$ peaks grow larger and the width of the low BE $SO_x$ peak increases significantly. The larger peak width could be due to new types of adsorption sites and/or adsorption geometries of the molecules that appear at higher exposures. In contrast to this,

the peak assigned to atomic sulfur at lower binding energy does not increase significantly but the shape of the peak changes. The sites where $SO_2$ dissociation takes place initially are thus saturated already at the lower dose of $SO_2$ and the chemical environment around the adsorption sites changes upon increased $SO_2$ exposure.

Water is shown to have two main effects on $SO_2$ surface chemistry on ZnO(0001). First, less $SO_3/SO_4$ forms on water preexposed surfaces (Figs. 8c, 9c and e) than on clean surfaces (Figs. 8b and 9d), implying that water blocks some $SO_2$ adsorption sites on ZnO(0001). The second effect, which has only been observed on the 530 °C annealed sample, is that the amount of atomic sulfur increases significantly on the water
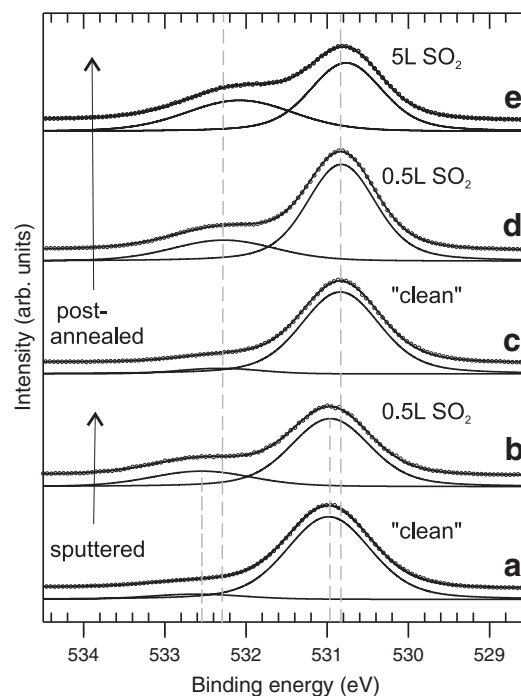


**Fig. 10.** O 1s core level spectra ($h\nu = 619$ eV) of $SO_2$ on ZnO(0001). The sample preparation annealing temperature prior to adsorption was 530 °C. Spectrum a is obtained from a sample that has been sputtered for 30 min at 45° incidence. Each spectrum is decomposed into two components.

**Table 5**
Binding energies ($E_{Bin}$), Gaussian linewidths ($\Delta E_G$), relative areas and coverages of curve fitted O 1s components from $SO_2$ exposed ZnO(0001) surfaces.

| $T_a$[a] | $SO_2$ dose | Bulk O 1s | | $SO_x (x=3)$[b] O 1s | | | |
|---|---|---|---|---|---|---|---|
| | | $E_{Bin}$ | $\Delta E_G$ | $E_{Bin}$ | $\Delta E_G$ | Area | Cov. |
| (°C) | (L) | (eV) | (eV) | (eV) | (eV) | (%) | (ML) |
| – | 0.5 | 530.9 | 1.02 | 532.5 | 1.30 | 22 | 0.15 |
| 530 | 0.5 | 530.8 | 0.80 | 532.3 | 1.28 | 23 | 0.15 |
| 530 | 5 | 530.8 | 0.85 | 532.1 | 1.37 | 39 | 0.3 |

[a] The samples are cleaned by sputtering or sputtering and post-annealing. $T_a$ is the annealing temperature.
[b] Although the (x=4) possibility cannot be excluded, the coverage calculations are based on (x=3).

preexposed surface. Water is shown to have the same but weaker effect when the water dosing is performed after the $SO_2$ dosing (Fig. 9f).

In Fig. 10, O 1s spectra for clean and $SO_2$ exposed ZnO surfaces are shown. The spectra from the $SO_2$ exposed samples contain two distinct peaks where the main peak (530.8–531.0 eV) is attributed to bulk and surface oxygen in the ZnO sample and the peak shifted with 1.3 eV from the main peak is assigned to $SO_x$ species. Binding energies, Gaussian widths, relative area for the high energy component and $SO_x$ coverages are listed in Table 5. The approximate coverage of $SO_x$ species can be estimated with the same formula (1) used for the OH coverage estimations. When estimating monolayer thickness, we first make an assumption that each $SO_2$ molecule binds to one oxygen anion at a defect (e.g. a step) in the otherwise Zn-terminated surface as suggested by Rodriguez et al. [12]. This coordination gives an $SO_3$-like species. Here it should be noted that interpretation of the S 2p spectra does not exclude $SO_4$ formation but due to the lack of literature values on bond lengths in $SO_4$ on ZnO(0001), we could not make calculations based on $SO_4$ formation. Chaturvedi et al. [10] has made ab initio self-consistent field calculations on the most stable configurations and binding parameters for different coordinations of $SO_2$ adsorbed on ZnO(0001) polar surfaces. They obtained an S−O bond distance of 1.41 Å and an O−S−O angle of 119 ° for $SO_2$ adsorbed a-top an oxygen site in the ZnO(0001) surface. By using the latter configuration and assuming that the surface is situated half-way between terminating Zn-cations and the closest oxygen anions and that the bond is perpendicular to the surface, the thickness of a monolayer of $SO_x$ can be estimated to 1.8 Å. It should be noted that the spectra from the clean surfaces contain an OH related peak in the same region as the $SO_x$ related peak. Therefore, the area of the high binding energy peak from the clean surface has been subtracted from the $SO_x$ related peak prior to coverage calculations. It could be questioned whether it is correct to use the same values for monolayer thickness for the sputtered surface, where the surface coordination is quite different from the annealed sample. This demonstrates that the coverage calculations are only rough estimations and to obtain more exact values, coverage calibrations and/or other types of measurements have to be made.

## 4. Discussion

### 4.1. $SO_2$ chemistry on Zn(0001)

$SO_2$ adsorption leaves four types of species on Zn(0001) at room temperature, namely atomic sulfur, $SO_2$ bonding via S to Zn, $SO_3$, and $SO_4$ species. The same types of species have been found on $SO_2$ exposed polycrystalline zinc by Chaturvedi et al. [10] and they observed that an increased $SO_2$ dose leads to a higher $SO_x$/S ratio. They argued that $SO_2$ dissociation is the thermodynamically most favorable reaction but it demands metal sites that enable charge transfer from the sample to the lowest unoccupied molecular orbital of $SO_2$. This charge transfer leads to an S−O bond weakening and a subsequent dissociation [5]. When most of the zinc sites where $SO_2$

dissociation occurs are covered with O and S species, $SO_2$ molecules starts to react with O sites to a larger extent, which gives a more extensive formation of $SO_3$ species. An increase in $SO_x$/S ratio with increasing $SO_2$ dose is also observed in the present study. In both studies, gas doses have been measured by recording the gas pressure and the time for which the sample has been subjected to this gas pressure. Since different pressure readings can be obtained by different pressure gauges one cannot assume that spectra with the same gas dose can be compared. When comparing S 2p spectra in the two studies, the spectrum from the 5 L exposed surface has a very similar lineshape to the spectra from the 0.9 L and 1.9 L exposed polycrystalline Zn surfaces [10]. If the $SO_2$ chemistry would be the same for the two types of surfaces, a dose of 10–20 L $SO_2$ in the study by Chaturvedi et al. would give a similar spectrum as for the 50 L dose in the present study. However, a dose of 12 L $SO_2$ (the largest dose shown) in the polycrystalline Zn study gives an S 2p spectrum with a much higher $SO_3$/S peak area ratio. Since our studies of photon beam induced effects (see Experimental details) have revealed that the beam stimulates dissociation of $SO_3$ and not of $SO_2$ or $SO_4$, the first guess would be that a more intense photon beam in the present study could be responsible for the lower $SO_3$/S ratio measured on Zn(0001). However, we have taken precautions to avoid beam induced $SO_3$ dissociation. This has been accomplished through a stepwise change of the sample spot exposed. In addition, a measurement with 50 L $SO_2$ has been remade by means of our home-lab XPS (see Experimental details) and the same relative S 2p intensities were found with these measurements. Consequently, it appears as if $SO_3$ formation is favored on the polycrystalline sample compared to the single crystalline (0001) sample.

An $SO_2$ molecule contains double the amount of oxygen atoms compared to sulfur atoms. If all the adsorption products stay on the surface, the ratio between the number of oxygen to sulfur atoms should still be 2. By using the relative areas of the components in the S 2p and O 1s spectra, O/S atom ratios can be obtained. Since an $SO_x$/S ratio can be obtained from an S 2p spectrum and an $SO_x$/O ratio can be obtained from an O 1s spectrum, there is no need to use cross sections in the ratio calculations. In the present study, the O/S ratios are 1.6 and 1.9 for 5 and 50 L $SO_2$ respectively (see Table 2). This means that there are oxygen atoms missing, which could be due to a recombination of oxygen atoms giving gaseous $O_2$ molecules ($2O_{ads} \rightarrow O_{2,gas}$). In contrast to this, adsorption of 7 L $SO_2$ on polycrystalline Zn gives an O/S ratio of nearly 5 (estimated from Figs. 1 and 2 in Chaturvedi et al. [10]). Chaturvedi et al. suggested that a significant part of the $SO_2$ dissociation on polycrystalline Zn is partial ($SO_{2,gas} \rightarrow SO_{gas} + O_{ads}$), which could explain the excess of oxygen atoms. An O/S atomic ratio of 5 means that only 25% of the $SO_2$ gas reacting with the surface gives the complete dissociation reaction ($SO_{2,gas} \rightarrow S_{ads} + 2O_{ads}$). This indicates that the (0001) surface is superior to the polycrystalline surface when it comes to complete dissociation. One explanation for this difference could be that atoms and molecules more easily diffuse on the (0001) surface giving more access to Zn sites where complete dissociation occurs. This diffusion difference could also explain why $SO_3$ formation, which is much less exothermic than dissociation seems to occur to a larger extent on polycrystalline Zn. By comparing the spectra for the 50 L $SO_2$ exposed (0001) surface in Figs. 1–2 with the respective spectra for 7 L $SO_2$ exposed polycrystalline sample, the O 1s spectra show an $SO_x$/O peak area ratio that is approximately the same while the S 2p spectra reveal a much higher $SO_x$/S ratio [10]. We tentatively suggest this to be due to a higher coverage of adsorbed O on the polycrystalline surface. Moreover, $SO_3$ formation is favored on this surface due to more available sites for this process ($O_{ads}$).

An alternative reaction to get the reaction products S, $SO_3$ and $SO_4$ as observed upon $SO_2$ exposure of Zn(0001) could be $SO_2$ disproportionation. Disproportionation of $SO_2$ involves interaction between adsorbed $SO_2$ on the surface and simultaneous reduction and oxidation of S in the

SO$_2$ molecule (e.g. $3SO_{2,ads} \rightarrow S_{ads} + 2SO_{3,ads}$). However, our results do not give any information on whether the reaction products were formed by interaction and charge exchange between the surface and adsorbates or between adsorbates. Therefore we have based our conclusions on the earlier experimental and theoretical (ab-initio self-consistent-field calculations) studies by Chaturvedi et al. [10].

### 4.2. ZnO(0001) sample preparation effects

Metal oxide surfaces contain a large number of defects and the types and amount of defects can have a strong impact on surface catalytic properties. Furthermore, by exposing an oxide sample to different treatments, one can influence its surface chemical structure and properties. Reduced oxides can e.g. have different catalytic properties compared to stoichiometric oxides.

ZnO(0001) is a zinc terminated polar surface and a perfect bulk-like termination is unstable according to the simple ionic model, since it would be associated with a dipole moment per surface unit cell leading to a diverging electrostatic potential and infinite surface energy [41]. However, the ionic model is oversimplified and the surface energy for polar surfaces is not infinite, although polar surfaces are generally less favorable than non-polar surfaces due to the dipole moment normal to the surface [42,43]. Therefore, quenching of the dipole moment of polar surfaces occurs through so called 'stabilization mechanisms' [43]. Moreover, recent studies show that one has to take into account atomic relaxations in order to understand stabilizations of polar surfaces [44]. It has been shown that the ZnO(0001) surface can be stabilized by various reconstructions [22,45–47] or adsorption of atoms or molecules [46,48,49,47,43]. In addition, it has been shown that surface donors can create downward band-bending leading to an electron accumulation layer on ZnO(0001) [50]. What types of donors, who give this effect is still under discussion [51–53]. One termination that has been studied in detail by e.g. Dulub et al. [22] is the triangularly structured $(1 \times 1)$ ZnO(0001) surface obtained by sputtering and annealing at 500–700$\pm$C in UHV. This termination is associated with triangular islands and pits that have oxygen decorated step edges. In the present study, the samples have been cleaned by sputtering alone or sputtering and annealing. Furthermore, the annealing temperature has been varied in order to investigate its effect on surface properties.

Sputtering gives rise to an irregular surface with a large number of defects, which is illustrated by the weak LEED pattern and the large width of the bulk oxygen O 1$s$ peak (see Fig. 7 and Table 3). What types of defects are created is not known but it is likely that sputtering increases the surface step density. Since the step edges of the terraces are oxygen terminated, this would result in an increased number of oxygen anions in the outermost surface layer. The valence band spectra in Fig. 5 agree with such a statement, since the O 2$p$/Zn 3$d$ intensity ratio is higher on sputtered surfaces compared to post-annealed surfaces. Three other possible explanations for the higher O 2$p$/Zn 3$d$ intensity ratio for the sputtered surface have been found by the authors. Firstly, the crystal can be reduced upon post-annealing. Secondly, the Ar$^+$ ion sputter yield of zinc has been predicted to be more than two times higher than that for oxygen [54]. Preferential sputtering of zinc cations in ZnO could thus be expected, even though it is far from certain. Sputtering of CdO has e.g. been shown to induce a reduction of the crystal [55,56], although Cd has the same predicted sputter yield as Zn [54]. Thirdly, photoelectron diffraction effects could influence the O 2$p$/Zn 3$d$ intensity ratio. However, this possibility has not been investigated further.

Annealing has two main effects on the surface. Firstly, it induces an oxygen deficiency in the crystal that increases with annealing temperature. Secondly, the width of the main O 1$s$ peak decreases with annealing temperature up to ~530 °C, which implies that the surface order increases and the number of defects decreases. However annealing in vacuum also creates defects related to oxygen deficiency.

Based on our data, it is not possible to judge whether these defects are oxygen vacancies or zinc interstitials or both. It is quite likely that these defects are present in the whole crystal rather than concentrated only to the surface but our data do not confirm this assumption.

Point defects in bulk zinc oxide have been the subject of a large amount of studies. The three most commonly discussed point defects, which also have lowest formation energies are oxygen vacancies, zinc vacancies and zinc interstitials [57]. Oxygen vacancies or zinc interstitials have earlier been suggested to give rise to the intrinsic n-doping that most zinc oxide crystals exhibit. However, both DFT calculations and experimental measurements have shown that these defects could not explain the n-type doping in ZnO [57]. Oxygen vacancies have been shown to be deep donors while zinc interstitials are not expected to be stable in n-type ZnO [58,57]. It is an established fact that hydrogen, at least partially, can be responsible for the n-type doping [59]. When growing crystals, it is very hard to completely avoid hydrogen to be incorporated in the crystal and all ZnO crystals contain hydrogen to some extent. Several types of hydrogen have been found, e.g. H bound in an oxygen vacancy (H$_O$) [60], H incorporated in the crystal at the Zn–O bond centered site (H$_{BC}$) [60], two hydrogen species bound to a zinc vacancy (V$_{Zn}$H$_2$) [61] and H$_2$ complexes or so-called "hidden hydrogen" [62,63]. Both H$_O$ and H$_{BC}$ have been identified as n-type donors [60].

Hence, when increasing the annealing temperature, not only will the number of oxygen vacancies and/or zinc interstitials increase but at certain temperatures, different types of hydrogen will be annealed out from the crystal. Since hydrogen often acts as an electron donor in ZnO, a change of the hydrogen content in the crystal can influence its conductivity and surface charge density, which influences surface chemical properties. According to the literature, H$_{BC}$, H$_O$ and V$_{Zn}$ H$_2$ leave the crystal at 190 °C [60], 500 °C [64,65] and 600 °C [61] respectively. In addition, transformation of H$_2$ complexes to atomic hydrogen happens at ~400 °C [62].

The O 1$s$ spectra in Fig. 7 reveal that all clean surfaces annealed at 530 °C or lower contain hydroxyl groups to some extent. We tentatively interpret this as hydrogen bound to oxygen in the crystal, i.e. not only surface hydroxyl. In addition, other types of hydrogen are probably present in the crystal, although we cannot detect them with photoemission. Annealing at 600 °C gives an O 1$s$ spectrum that consists of one component only and no hydroxyl related peak. This indicates that hydrogen bound to oxygen has left the crystal. According to the literature, hydrogen that leaves a ZnO crystal at 600 °C could be V$_{Zn}$H$_2$ and this type of hydrogen defect does indeed involve O–H bonds [61]. Moreover, it has been shown in the studies of ZnO(0001) by the present authors, that a temperature of 600 °C ($\pm$ 50 °C) is needed in order to get a LEED pattern with maximum sharpness and good STM images of a flat surface with triangular structures. This indicates that this temperature is needed to get a transition from a partly OH-terminated surface to a triangularly structured surface. As mentioned earlier, the bulk-terminated polar ZnO(0001) surface is energetically unfavorable and different mechanisms exist to quench the dipole moment associated with this surface, such as the adsorbtion of OH groups. Annealing at 600 °C, leads to desorption of OH groups and to structural changes in order to obtain another surface termination, which reduces the dipole.

An interesting effect that was observed only on samples annealed at 600–650 °C was sample charging problems in the photoemission measurements. This effect was interesting, since it appeared only after SO$_2$ exposure and is a result of the well-known gas-sensing properties of ZnO [66–68], as further discussed in the end of Section 4.3. Two reasons for why the decrease of conductivity upon SO$_2$ adsorption was observed only on samples annealed at 600–650 °C could be found by the authors. Firstly, the structure and properties of the 600–650 °C annealed surface is different. This surface is more well-ordered, as compared to the other studied surfaces and is covered by triangular structures, as shown in STM images. This surface termination and the electronic structure

associated with it might lead to other adsorbate induced charge transfer processes and chemical reaction paths upon $SO_2$ adsorption. Secondly, the initial conductivity of the clean samples that have been annealed at 600–650 °C might be lower than that of the other samples. This could be due to hydrogen dopants leaving the crystal when annealing at this temperature. $V_{Zn}H_2$ hydrogen that has been observed to leave the ZnO crystal at 600 °C has not been identified as a donor. A more probable reason for the decreased conductivity could be that $H_O$ has left the crystal. Lavrov observed a leave-off temperature of ~500 °C for $H_O$, while our study could indicate that it is left in the temperature range 530 °C<T≤600 °C. The difference in temperature readings could be due to different sample heating and temperature measurement equipment and methods.

### 4.3. $SO_2$ chemistry on ZnO(0001)

The adsorption of $SO_2$ on the polar surfaces of ZnO has been investigated with photoemission in two earlier studies made by Rodriguez et al. [12,39]. They showed that $SO_3$ was formed on both surfaces but in larger extent on the oxygen terminated surface. Small amounts of atomic sulfur were also observed. Furthermore, they concluded that $SO_2$ mainly adsorbs on oxygen sites and that formation of sulfur is hindered due to a low charge density at zinc sites. Since the zinc terminated ZnO(0001) surface is primarily terminated by zinc ions, they suggested that $SO_2$ adsorbs on the oxygen terminated step edges. Rodriguez et al. [12] found an S $2p_{3/2}$ binding energy of ~166.5 eV and a shift from the atomic sulfur peak of ~4.8 eV, which they assign to $SO_3$ species. In addition, they confirm this assignment with X-ray absorption near-edge spectroscopy (XANES) measurements.

In the present study, the S $2p$ binding energies for low $SO_2$ doses (0.5 L) adsorbed on post-annealed surfaces show similar binding energy shifts (~4.9 eV) but higher binding energies (167.1–167.4 eV) than in the studies by Rodriguez et al. This indicates that we have $SO_3$ species on the surface. However, at higher $SO_2$ doses (5 L) the binding energy shift increases to 5.5 eV, which is more typical for $SO_4$ species. Moreover, the two S $2p$ components are shifted by 0.5 eV only and should thus not be associated to $SO_3$ and $SO_4$ species respectively. Our final conclusion is that our data do not unambiguously reveal whether we have $SO_3$ or $SO_4$ species.

A clear difference between the S $2p$ spectra shown in this work compared to the ones presented by Rodriguez et al. [12] is that the widths of the peaks are larger in the present study. A first guess would be that this difference is due to a more defective surface with a larger variety of adsorption sites in the present study. However, when looking more closely into the results from the two studies, it becomes evident that the interpretation of this difference is not that straightforward. Here, S $2p$ spectra (Figs. 8–9) from $SO_2$ exposed sputtered and post-annealed surfaces differ quite a lot, both in binding energy and line profile. Contrary to this, Rodriguez et al. presented S $2p$ spectra from $SO_2$ exposed sputtered surfaces, which appeared to have approximately the same peak width as post-annealed surfaces. Therefore, it is more probable that the difference in peak width between the two studies is due to a higher conductivity in the crystal used by Rodriguez et al. caused by a larger density of defects and/or impurities that contribute to the n-type doping. Furthermore, the large S $2p$ peak widths in the present study are most likely due to limited screening of the core hole in the photoemission measurements. A higher conductivity of the sample of Rodriguez et al. compared to the samples in the present study might be due to different manufacturing methods/conditions of the crystals and/or different sample preparation procedures and sample histories.

There is another discrepancy between the two studies that concerns the $SO_2$ chemistry of sputtered versus post-annealed surfaces. In the earlier study by Rodriguez et al. [12], the sputtered surface is more reactive towards $SO_2$ compared to the post-annealed surface.

Moreover, there was no considerable difference between the binding energy and line shape of the S $2p$ peaks from the two types of surfaces. In the present study, however, the reactivity of the sputtered and post-annealed surfaces are approximately equal while the S $2p$ line shape and binding energy differ significantly. A different effect of sputtering could be due to (i) differing sputtering procedures and/or (ii) different sample morphologies prior to sputtering. We note that the wide S $2p$ peak from the sputtered surface in the present study has very similar lineshape and binding energy to that from $SO_2$ exposed polycrystalline zinc oxide in a study by Chaturvedi et al. [10]. It is thus most likely that the sputtered surface reported here is much rougher than in the earlier study. However, there is another point, which is hard to explain based on differing sputtering procedures and that is that sputtering gives higher $SO_2$ reactivity in the study by Rodriguez et al. but the same effect is not observed in the present study. Actually, higher reactivity of the sputtered surface is expected, since sputtering should give more terraces and steps and thus more oxygen adsorption sites where $SO_2$ can form $SO_3$ [12]. However, this is not what we observe in the present study, indicating that there is another factor related to initial sample morphology, which influences the formation of $SO_3/SO_4$ groups. The sample morphology prior to sputtering could differ due to different manufacturing methods/conditions of the crystals and/or different sample preparation procedures and sample histories. These morphological differences could involve the amount of defects and dopants present in the samples. It could be that certain types of defects are needed to stabilize $SO_3/SO_4$ formation. Thus if the ZnO(0001) surface in the present study contain too few defects of this type, this might be the limiting factor for $SO_3/SO_4$ formation instead of exposed oxygen sites. Oxygen vacancies have shown to play a pivotal role in the stabilization of $SO_3$ and $SO_4$ species on $TiO_2(110)$ [69]. One could speculate that oxygen vacancies or perhaps oxygen vacancies combined with hydrogen dopants could have a similar role on the ZnO(0001) surface. However, the stabilization mechanism should be different due to the inherent differences between the two oxides.

When comparing the $SO_2$ chemistry on samples annealed at 450 and 530 °C, it is shown that a small amount of $SO_2$ is reduced to atomic sulfur on the latter sample but none on the former sample. S–O bond breaking and a subsequent $SO_2$ dissociation occurs through charge transfer from the surface to the S–O antibonding LUMO in the molecule [5]. On metal oxide surfaces, the charge density on metal sites is usually too low, which explains why $SO_2$ normally does not dissociate on these surfaces. By creating occupied metal states above the valence band, one can increase the charge density on metal sites and therefore also the probability of S–O bond breaking [70]. This can be done e.g. by the introduction of oxygen vacancies or doping with alkali metals [70]. The enhanced oxygen deficiency observed when increasing the annealing temperature from 450 to 530 °C could thus explain why $SO_2$ dissociation occurs only on the 530 °C annealed sample, although to a small extent. The increase in oxygen deficiency indicates a larger number of oxygen vacancies and/or zinc interstitials that could give rise to the states above the valence band maximum of the oxide. If these defects are oxygen vacancies, they might be combined with hydrogen. However, since this type of hydrogen specie is not detectable with PES, we could not prove the presence of such species.

Simultaneous formation of reduced species (atomic S) and oxidized species ($SO_3$ and $SO_4$) could also be due to $SO_2$ disproportionation. Disproportionation of $SO_2$ involves interaction between adsorbed $SO_2$ on the surface and simultaneous reduction and oxidation of S in the $SO_2$ molecule (e.g. $3SO_{2,ads} \rightarrow S_{ads} + 2SO_{3,ads}$). However, our results do not give any information on whether the reaction products were formed by interaction and charge exchange between the surface and adsorbates or between adsorbates. Therefore we have based our conclusions on the earlier theoretical (ab-initio self-consistent-field calculations) and experimental studies by Chaturvedi et al. [10] and Rodriguez et al. [12].

SO$_2$ adsorption on a ZnO(0001) sample annealed at 600–650 °C is shown to induce a lower surface conductivity. This is demonstrated by the severe charging problems that occur in the PES measurements after SO$_2$ exposure. The decrease in surface conductivity is a result of the well-known gas-sensing properties of ZnO [66–68]. It thus appears as if SO$_2$ adsorption leads to an increase of the resistivity of the outer surface layers of ZnO(0001). In contrast to this, SO$_2$ adsorption decreases the resistivity of ZnO powder [67] and tetrapods [68]. However, our results are not contradicted by these measurements, since polar surfaces can have very different properties compared to other surfaces. Two reasons for why this lowering in conductivity is observed upon SO$_2$ adsorption only on samples annealed at 600–650 °C have been found by the authors. One reason concerns a lower conductivity of the clean sample and the other deals with changed surface structure and chemistry. A more detailed discussion about this is found in the last paragraph of Section 4.2.

### 4.4. Impact of H$_2$O on ZnO(0001) and its SO$_2$ chemistry

In an earlier study [21] we have shown that water adsorbs dissociatively at the oxygen terminated step edges of ZnO(0001). When increasing the water dose, the triangular islands grow and pits diminish in size. At the highest water dose investigated (20 L), the surface was highly disordered. Due to lack of atomic resolution in the STM images, they do not give enough information to determine the exact adsorption mechanism.

In general, water dissociation on oxides is believed to be initiated by strong bonding between the oxygen atom in the water molecule and a cationic site in the surface and bonding of hydrogen to a nearby anionic site [71]. Assuming that this adsorption mechanism holds for ZnO(0001), water would adsorb at zinc sites next to step edges so that hydrogen could bind to the oxygen-terminated step edges. It is unclear, however, how the dissociation proceeds when all oxygen anions at step edges are occupied by hydrogen species. One could speculate that hydrogen diffuses into the bulk or sub-surface layers or it binds to the outmost zinc cations. However, if hydrogen binds to Zn cations, it cannot be present in the form of a proton but more likely uncharged or negatively charged. Formation of uncharged hydrogen upon water adsorption could explain why a higher dose of water (20 L) appears to destroy the surface order of ZnO(0001) in a similar way as hydrogen. In a study by Becker et al. [72], hydrogen has shown to form a H(1 × 1) overlayer on ZnO(0001), where H binds to Zn sites. At larger hydrogen doses, the surface order was destroyed, which the authors explained with OH bond formation, which was confirmed in a recent DFT study [73]. Thus, hydrogen appears to be able to penetrate the ZnO(0001) surface to subsurface layers, where it forms OH groups, which destroy the surface order [73]. Moreover, total energy calculations showed that the H(1 × 1) covered ZnO(0001) surface is favorable and leads to strong H–Zn bonds and a metallic surface [74]. In contrast to this, a recent synchrotron-radiation angle-resolved photoelectron spectroscopy study [79] showed that the hydrogen exposed ZnO(0001) surface is semiconducting, while hydrogen exposed ZnO(10$\bar{1}$0) and ZnO(000$\bar{1}$) surfaces are metallic. Furthermore, the latter study indicated that hydrogen etches the ZnO(0001) surface leading to the formation zinc clusters(ZnO + H → OH + Zn), which was confirmed by real-time monitoring spectroscopic ellipsometry studies [75]. Another DFT study, which was combined with atomistic thermodynamics showed that a monolayer H coverage was very favorable on the triangularly structured ZnO(0001) surface, since both zinc atoms and step edge oxygen atoms were protonated [76]. Evidently, although there are similarities between water and hydrogen adsorption, one cannot equate them, since hydrogen formation in water dissociation is accompanied with OH group formation.

The effects of preadsorbed water on the SO$_2$ chemistry of ZnO(0001) can teach us something about how water influences the properties of this surface. Preadsorbed water is shown to have two main effects on

SO$_2$ adsorption. First, hydrogen species formed when water dissociates are shown to block oxygen anion adsorption sites leading to less SO$_3$/SO$_4$ formation. Since both water dissociation and SO$_3$/SO$_4$ formation involves oxygen anion sites at step edges, this behavior is quite expected. The second effect of water has only been observed on the 530 °C annealed sample upon exposure to 5 L water. On this sample, the amount of atomic sulfur formed is much higher on the water exposed surface compared to the clean surface. This indicates that water exposure increases the charge density on zinc sites, since SO$_2$ dissociation requires charge transfer from the surface to the S–O antibonding LUMO of SO$_2$ [5]. An increased charge density on cation sites is not expected. If anything, water mostly has an oxidizing rather than reducing effect. There have been a few studies where water has shown to have a reducing effect on oxide surfaces [77,66,71]. However, here we suggest that the increase in charge density on zinc sites is due to the formation of zinc clusters at the surface. These zinc clusters could be formed when hydrogen atoms formed in the water dissociation starts to move to sub-surface layers, where they form OH groups and destroy the surface and subsurface order.

Once again, it should be noted that the increase in charge density on zinc sites upon water exposure is only observed on the 530 °C annealed ZnO(0001) sample. The same behavior is not observed on the 450 °C annealed sample, although it should be noted that the water dose studied was 1 L for the latter sample as compared to 5 L for the 530 °C annealed sample. Consequently, this might implicate that there is a minimum dose of water, which is needed in order to obtain zinc clusters on the surface. Moreover, it could be that defects connected to the higher oxygen deficiency in the 530 °C annealed ZnO(0001) sample, such as oxygen vacancies are needed in order for zinc clusters to form.

Sulfuric acid-like species (H$_x$SO$_4$) have been suggested as a reaction product upon coadsorption of water and SO$_2$ in an earlier study on polycrystalline zinc [11]. Ali Audi and Sherwood [78] found that sulfate (SO$_4^{2-}$) and bisulfate (HSO$_4^-$) ions can be distinguished by using their valence band photoemission spectra. They observed that the separation between two distinct peaks situated in the 9–15 eV binding energy region was typically ~4 eV for sulfate and ~3 eV for bisulfate. In the present study, however, the very intense Zn 3$d$ peak is situated in the middle of this region and SO$_x$ related peaks are difficult to distinguish.

### 4.5. Surface chemical properties of Zn(0001) versus ZnO(0001)

It is well known, e.g. in the field of corrosion that zinc forms zinc hydroxide in the presence of water. However, the (0001) surface of zinc as well as the (111) surface of copper has a very low reactivity towards water. Early valence band and core level spectroscopy measurements have shown that water does not stay adsorbed on these surfaces at room temperature [14–16]. In the case of zinc, this is quite unexpected, since the reaction between Zn and water to form ZnO is exothermic by ~120 kJ/mol [71]. The low reactivity towards water has been explained by kinetic limitations. It has been shown that preadsorbed oxygen lowers the water dissociation barrier and enables hydroxylation on Zn(0001). This is in agreement with our studies since no water is adsorbed on Zn(0001) while it easily reacts with ZnO(0001). However, no apparent changes are observed upon water adsorption on Zn(0001) that has been oxidized by SO$_2$. In accordance with this, the effects of water on SO$_2$ exposed ZnO(0001) (see Fig. 9f) are small at least when it comes to SO$_3$/SO$_4$ species. Water has a larger impact on the amount of atomic sulfur species formed on ZnO(0001) that has been preexposed to SO$_2$. Moreover, when water exposure precedes SO$_2$ exposure, it blocks adsorption sites, hindering SO$_3$/SO$_4$ formation.

When comparing the SO$_2$ surface chemistry on Zn(0001) and ZnO(0001), there are two clear differences. Firstly, more atomic sulfur is formed on the Zn(0001) surface, which is evidently due to the sample being a metal with high charge density, which enables charge transfer to the antibonding LUMO of the molecule. Secondly, SO$_2$

species binding to Zn cations are present on Zn(0001), to some extent on sputtered ZnO(000$\bar{1}$) but no such species have been observed on ZnO(0001). It thus appears as if SO$_2$ species are formed on metallic Zn sites and on undercoordinated Zn cations.

Although the SO$_2$ and water chemistry on Zn(0001) can be complex, the results from ZnO(0001) appear to be even more cryptic and do partly conflict with the earlier study on SO$_2$ adsorption on ZnO(0001) [12]. Henrich and Cox have stated in their well-known book "Surface Science of Metal Oxides" that "the chemisorption behavior of ZnO is extremely complicated". The reason for their statement is that the results obtained on this subject often contradict each other and do not agree with the simple models used. Furthermore, Henrich and Cox speculated that the reason for these discrepancies might partly explain the useful catalytic and gas sensing properties of the material. In a recent study, Valtiner et al. [47] showed by combining diffraction experiments and density-functional theory calculations that many different but energetically favorable reconstructions can exist for a certain stoichiometry. The latter study showed that vibrational-entropy contributions have a large impact on the final ZnO(0001) surface structure. This implicates that sample preparation conditions and especially annealing temperature has large impact on surface structure.

Here, we have tried to elucidate some factors that can explain why many studies on ZnO surface are contradicting. We believe that the manufacturing method of a ZnO single crystal or thin film can highly influence the types and amounts of defects initially present in the sample. Especially hydrogen and a combination of point defects and hydrogen could be responsible for discrepancies between different studies, since hydrogen is hard or impossible to detect with many experimental techniques used in surface science. Moreover, different sample surface preparation procedures can be responsible for conflicting results. As mentioned by Valtiner et al. [47], one of the most important factors that influence stoichiometry and defects could be the annealing temperature. An increased annealing temperature leads to a more extensive oxygen deficiency and a higher amount of oxygen vacancies and/or zinc interstitials. What could be just as important as the creation of defects related to oxygen deficiency, is that at certain temperatures, different types of hydrogen are evaporated out of the ZnO sample. Since some types of hydrogen species could serve as n-type donors in the n-type ZnO sample, the conductivity and charge density of the crystal can be modified when crossing certain temperatures. This could in its turn influence surface chemical properties. Another important factor is that Zn ions in ZnO have only one stable oxidation state, namely Zn$^{2+}$. This implies that formation of oxygen vacancies do not introduce cations with other oxidation states as in many transition metal oxides. Instead, oxygen vacancies give higher n-type conductivity in the bulk or if the vacancies are situated on the surface, an accumulation layer can be formed. If the band bending is large enough, a surface metallic state, also called a two-dimensional electron gas, can be created. This can have vast effects on e.g. surface chemical properties.

Zinc oxide surfaces are of high technological importance and the material is promising for new future applications. To get a better understanding of the chemical and physical properties of these surfaces, it is important to investigate the effects of sample manufacturing and cleaning procedures on the surface stoichiometry and structure. Moreover, it is essential to understand the interaction between surface and subsurface/bulk regions.

## 5. Conclusions

High Resolution Photoelectron Spectroscopy studies of sulfur dioxide adsorption on clean and water exposed (0001) surfaces of zinc and zinc oxide at room temperature are presented. Water exposure leaves Zn(0001) unaltered while hydroxyl groups are formed on the zinc-terminated surface ZnO(0001), confirming the well-known importance of oxygen in the interaction between zinc and water. Zn(0001) is highly reactive to SO$_2$ and a dose of 50 L (1 L = 10$^{-6}$ Torr s) gives a

completely oxidized surface that consists of various sulfur containing compounds. When comparing to an earlier study on polycrystalline zinc [10], the complete dissociation of SO$_2$ to atomic sulfur and oxygen is shown to be much more efficient. The SO$_2$ surface chemistry on ZnO(0001) is influenced by sample preparation. SO$_3$/SO$_4$ species are the most abundant reaction products on all samples. No SO$_2$ dissociation appears at room temperature on a sample, which has been annealed to ~450 °C prior to the adsorption. A small amount of atomic sulfur appears upon SO$_2$ exposure on a sample that has been annealed to ~530 °C. The higher annealing temperature gives a higher oxygen deficiency due to the creation of zinc interstitials and/or oxygen vacancies, possibly combined with hydrogen species. This could give a higher charge density at metal sites on the oxide surface, which would facilitate charge transfer to the S–O antibonding orbital of the molecule and a subsequent SO$_2$ dissociation. Annealing at 600–650 °C gives a triangularly structured surface free from OH groups. SO$_2$ adsorption on the latter surface leads to a decreased surface conductivity, which hampers photoemission measurements. The decreased surface conductivity has importance for understanding ZnO gas sensing properties. Preadsorbed water has two major effects on SO$_2$ chemistry. First, water tends to decrease SO$_3$/SO$_4$ formation by blocking step edge oxygen adsorption sites. The second effect appears only on samples annealed to ~530 °C and involves a more extensive SO$_2$ dissociation on the prehydroxylated surface compared to the clean surface. This effect indicates that water increases the charge density at surface Zn cations. We suggest that the observed disordering of the ZnO(0001) surface upon water adsorption leads to zinc cluster formation. The increased charge density at zinc clusters compared to zinc cations would facilitate charge transfer to the SO$_2$ molecule and subsequent dissociation. The final conclusion of the work on ZnO(0001) is that sample manufacturing and preparation can have vast effects on surface chemical and physical properties. One important factor influencing surface and bulk properties is the annealing temperature. Increased annealing temperature gives both an improved surface order and an increased number of oxygen vacancies. Moreover, at certain temperatures different types of hydrogen species are annealed out from the crystal. Since some species are shallow donors, this can have large impact on the properties of the surface.

## References

[1] C. Leygraf, Atmospheric Corrosion, Wiley, New York, 2000.
[2] C.H. Bartholomew, Appl. Catal., A 212 (2001) 17.
[3] J. Haase, J. Phys. Condens. Matter 9 (1997) 3647.
[4] H.-W. Wassmuth, J. Ahner, M. Höfer, H. Stolz, Prog. Surf. Sci. 42 (1993) 257.
[5] J.A. Rodriguez, T. Jirsak, L. González, J. Evans, M. Pérez, A. Maiti, J. Chem. Phys. 115 (2001) 10914.
[6] K.E. Smith, V.E. Henrich, J. Vac. Sci. Technol., A 7 (1989) (1967).
[7] J.A. Rodriguez, J.M. Ricart, A. Clotet, F. Illas, J. Chem. Phys. 115 (2001) 454.
[8] C. Wöll, Prog. Surf. Sci. 82 (2007) 55.
[9] S. Wendt, R. Schaub, J. Matthiesen, E.K. Vestergaard, E. Wahlström, M.D. Rasmussen, P. Thostrup, L. Molina, E. Laegsgaard, I. Stensgaard, B. Hammer, F. Besenbacher, Surf. Sci. 598 (2005) 226.
[10] S. Chaturvedi, J.A. Rodriguez, T. Jirsak, J. Hrbek, J. Phys. Chem. B 102 (1998) 7033.
[11] T. Jirsak, J.A. Rodriguez, Langmuir 16 (2000) 10287.
[12] J.A. Rodriguez, T. Jirsak, S. Chaturvedi, J. Dvorak, J. Mol. Catal. A: Chem. 167 (2001) 47.
[13] R. Denecke, P. Väterlein, M. Bässler, N. Wassdahl, S. Butorin, A. Nilsson, J.-E. Rubensson, J. Nordgren, N. Mårtensson, R. Nyholm, J. Electron Spectrosc. Relat. Phenom. 101 (1999) 971.
[14] C.T. Au, M.W. Roberts, A.R. Zhu, Surf. Sci. 115 (1982) L117.
[15] C.T. Au, M.W. Roberts, Chem. Phys. Lett. 66 (1979) 340.

[16] C.T. Au, M.W. Roberts, Chem. Phys. Lett. 74 (1980) 472.
[17] S. Yamamoto, K. Andersson, H. Bluhm, G. Ketteler, D.E. Starr, T. Schiros, H. Ogasawara, L.G.M. Pettersson, M. Salmeron, A. Nilsson, Phys. Chem. C 111 (2007) 7848.
[18] M.O. Krause, J.H. Oliver, J. Phys. Chem. Ref. Data 8 (1979) 329.
[19] L. Ley, S.P. Kowalczyk, F.R. McFeely, R.A. Pollak, D.A. Shirley, Phys. Rev. B 8 (1973) 2392.
[20] W. Ranke, Solid State Commun. 19 (1976) 685.
[21] A. Önsten, D. Stoltz, P. Palmgren, S. Yu, M. Göthelid, U.O. Karlsson, J. Phys. Chem. C 114 (2010) 11157.
[22] O. Dulub, U. Diebold, G. Kresse, Phys. Rev. Lett. 90 (2003) 016102.
[23] S. Hüfner, Photoelectron Spectroscopy, Springer, New York, 2003.
[24] Y. Joseph, W. Ranke, W. Weiss, J. Phys. Chem. B 104 (2000) 3224.
[25] R.W.G. Wyckoff, Crystal Structures, John Wiley & Sons, 1963.
[26] D.A. Outka, R.J. Madix, G.B. Fisher, C. DiMaggio, J. Phys. Chem. 90 (1986) 4051.
[27] A.R. Alemozafar, X.-C. Guo, R.J. Madix, N. Hartmann, J. Wang, Surf. Sci. 504 (2002) 223.
[28] A.R. Alemozafar, R.J. Madix, Surf. Sci. 592 (2005) 141.
[29] M. Polcik, L. Wilde, J. Haase, Phys. Rev. B 57 (1997) 57.
[30] A. Galtayries, C. Cousi, S. Zanna, P. Marcus, Surf. Interface Anal. 36 (2004) 997.
[31] P. Zebisch, M. Stichler, P. Trischberger, M. Weinelt, H.-P. Steinrück, Surf. Sci. 371 (1997) 235.
[32] M. Polcik, L. Wilde, J. Haase, B. Brena, G. Comelli, G. Paolucci, Surf. Sci. 381 (1997) L568.
[33] F. Hennies, A. Föhlisch, W. Wurth, P. Feulner, A. Fink, D. Menzel, J. Chem. Phys. 127 (2007) 154709.
[34] J.A. Rodriguez, P. Liu, M. Pérez, G. Liu, J. Hrbek, J. Phys. Chem. A 114 (2010) 3802.
[35] J.A. Rodriguez, T. Jirsak, S. Chaturvedi, M. Kuhn, L. González, A. Maiti, J. Am. Chem. Soc. 122 (2010) 12362.
[36] D. Stoltz, A. Önsten, U.O. Karlsson, M. Göthelid, Appl. Phys. Lett. 91 (2007) 093107.
[37] J.A. Rodriguez, T. Jirsak, A. Freitag, J.Z. Larese, A. Maiti, J. Phys. Chem. B 104 (2000) 7439.
[38] J.A. Rodriguez, G. Liu, T. Jirsak, J. Hrbek, Z. Chang, J. Dvorak, A. Maiti, J. Am. Chem. Soc. 124 (2002) 5242.
[39] J.A. Rodriguez, T. Jirsak, S. Chaturvedi, M. Kuhn, Surf. Sci. 442 (1999) 400.
[40] B.J. Lindberg, K. Hamrin, G. Johansson, U. Gelius, A. Fahlman, C. Nordling, K. Siegbahn, Phys. Scr. 1 (1970) 286.
[41] F. Bertaut, C.R. 246 (1979) 3447.
[42] P.W. Tasker, J. Phys. C 12 (1979) 4977.
[43] G. Kresse, O. Dulub, U. Diebold, Phys. Rev. B 68 (2003) 245409.
[44] J.V. Lauritsen, S. Porsgaard, M.K. Rasmussen, M.C.R. Jensen, R. Bechstein, K. Meinander, B.S. Clausen, S. Helveg, R. Wahl, G. Kresse, F. Besenbacher, ACS Nano 5 (2011) 5987.
[45] F. Ostendorf, S. Torbrügge, M. Reichling, Phys. Rev. B 77 (2008) 041405(R).
[46] S. Torbrügge, F. Ostendorf, M. Reichling, J. Phys. Chem. C 113 (2009) 4909.
[47] M. Valtiner, M. Todorova, G. Grundmeier, J. Neugebauer, Phys. Rev. Lett. 103 (2009) 065502.
[48] M.J. Lyle, O. Warschkow, B. Delley, C. Stampfl, Phys. Rev. B 82 (2010) 165401.
[49] M. Valtiner, S. Borodin, G. Grundmeier, Phys. Chem. Chem. Phys. 9 (2007) 2406.
[50] M.H. Allen, C.H. Swartz, T.H. Myers, T.D. Veal, C.F. McConville, S.M. Surbin, Phys. Rev. B 81 (2010) 075211.
[51] D.C. Look, B. Claflin, H.E. Smith, Appl. Phys. Lett. 92 (2008) 122108.
[52] B.J. Brillson, Y. Dong, D. Doutt, D.C. Look, Z.-Q. Fang, Physica B 404 (2009) 4768.
[53] B.J. Coppa, C.C. Fulton, P.J. Hartlieb, R.F. Davis, B.J. Rodriguez, B.J. Shields, R.J. Nemanich, J. Appl. Phys. 95 (2004) 5856.
[54] D. Briggs, M.P. Seah, Practical Surface Analysis by Auger and X-ray Photoelectron Spectroscopy, Wiley, 1983.
[55] K.S. Kim, W.E. Baitinger, J.W. Amy, N. Winograd, J. Electron Spectrosc. Relat. Phenom. 5 (1974) 351.
[56] G.V. Kamanov, The Oxide Handbook, IFI/Plenum, New York, 1973.
[57] A. Janotti, C.G. Van de Walle, Rep. Prog. Phys. 72 (2009) 126501.
[58] A. Janotti, C.G. Van der Walle, J. Cryst. Growth 287 (2006) 58.
[59] E.V. Monakhov, A.Y. Kuznetsov, B.G. Svensson, J. Phys. D: Appl. Phys. 42 (2009) 153001.
[60] E.V. Lavrov, F. Herklotz, J. Weber, Phys. Rev. B 79 (2009) 165210.
[61] E.V. Lavrov, J. Weber, F. Börrnert, C.G. Van de Walle, R. Helbig, Phys. Rev. B 66 (2002) 165205.
[62] G.A. Shi, M. Saboktakin, M. Stavola, S.J. Pearton, Appl. Phys. Lett. 85 (2004) 5601.
[63] E.V. Lavrov, F. Herklotz, J. Weber, Phys. Rev. Lett. 102 (2009) 185502.
[64] G.A. Shi, M. Stavola, S.J. Pearton, M. Thieme, E.V. Lavrov, J. Weber, Phys. Rev. B 72 (2005) 195211.
[65] A. Janotti, C.G. Van der Walle, Nat. Mater. 6 (2009) 44.
[66] V.E. Henrich, P.A. Cox, The Surface Science of Metal Oxides, Cambridge University Press, 1994.
[67] N. Tamaekong, C. Liewhiran, A. Wisitsoraat, S. Phanichphant, Sensors 10 (2010) 7863.
[68] O. Lupan, L. Chow, G. Chai, Sens. Actuators, B 141 (2009) 511.
[69] A.J. Limb, O. Bikondoa, C.A. Muryn, G. Thornton, Angew. Chem. Int. Ed. 46 (2007) 549.
[70] J.A. Rodriguez, T. Jirsak, L. Gonzalez, J. Evans, M. Pérez, A. Maiti, J. Chem. Phys. 115 (2001) 10914.
[71] M.A. Henderson, Surf. Sci. Rep. 46 (2002) 1.
[72] T. Becker, S. Hövel, M. Kunat, C. Boas, U. Burghaus, C. Wöll, Surf. Sci. Lett. 486 (2001) L502.
[73] K. Nishidate, M. Hasegawa, Phys. Rev. B 86 (2012) 035412.
[74] N. Sanchez, S. Gallego, J. Cerdá, C. Muñoz, Phys. Rev. B 81 (2010) 115301.
[75] G. Bruno, M.M. Giangregorio, G. Malandrino, P. Capezzuto, I.L. Fragalá, M. Losurdo, Adv. Mater. 21 (2009) 1700.
[76] M. Valtiner, M. Todorova, J. Neugebauer, Phys. Rev. B 82 (2010) 165418.
[77] R.L. Kurtz, R. Stockbauer, T.E. Madey, E. Román, Surf. Sci. 218 (1989) 178.
[78] A. Ali Audi, P.M.A. Sherwood, Surf. Interface Anal. 29 (2000) 265.
[79] K. Ozawa, K. Mase, Phys. Rev. B 83 (2011) 125406.

# The ReactorSTM: Atomically resolved scanning tunneling microscopy under high-pressure, high-temperature catalytic reaction conditions

C. T. Herbschleb, P. C. van der Tuijn, S. B. Roobol, V. Navarro, J. W. Bakker, Q. Liu, D. Stoltz, M. E. Cañas-Ventura, G. Verdoes, M. A. van Spronsen, M. Bergman, L. Crama, I. Taminiau, A. Ofitserov, G. J. C. van Baarle, and J. W. M. Frenken

## Articles you may be interested in

Design of a new reactor-like high temperature near ambient pressure scanning tunneling microscope for catalysis studies
Rev. Sci. Instrum. **84**, 034101 (2013); 10.1063/1.4792673

A new scanning tunneling microscope reactor used for high-pressure and high-temperature catalysis studies
Rev. Sci. Instrum. **79**, 084101 (2008); 10.1063/1.2960569

Small-volume, ultrahigh-vacuum-compatible high-pressure reaction cell for combined kinetic and in situ IR spectroscopic measurements on planar model catalysts
Rev. Sci. Instrum. **76**, 123903 (2005); 10.1063/1.2140449

A high pressure, high temperature, scanning tunneling microscope for in situ studies of catalysts
Rev. Sci. Instrum. **71**, 3777 (2000); 10.1063/1.1290043

The "Reactor STM": A scanning tunneling microscope for investigation of catalytic surfaces at semi-industrial reaction conditions
Rev. Sci. Instrum. **69**, 3879 (1998); 10.1063/1.1149193
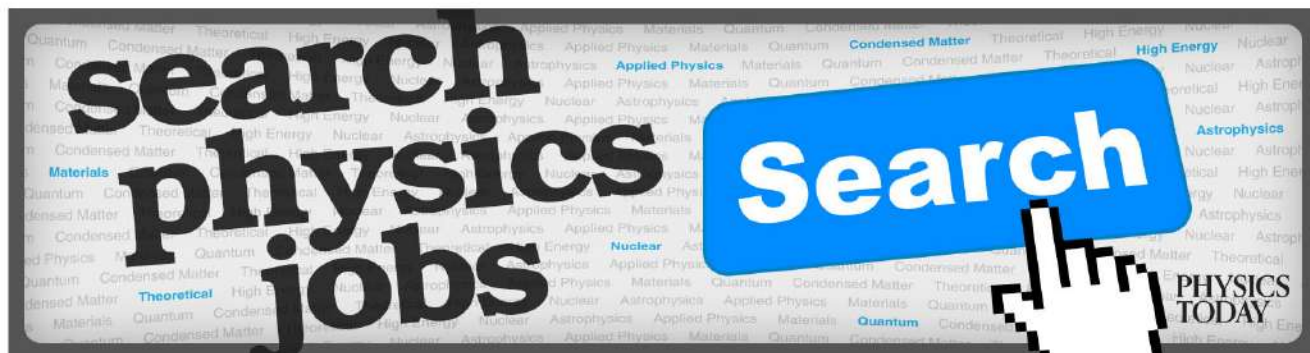
# The ReactorSTM: Atomically resolved scanning tunneling microscopy under high-pressure, high-temperature catalytic reaction conditions

C. T. Herbschleb,[1,a)] P. C. van der Tuijn,[1] S. B. Roobol,[1] V. Navarro,[1] J. W. Bakker,[1] Q. Liu,[1,b)] D. Stoltz,[1,c)] M. E. Cañas-Ventura,[1,d)] G. Verdoes,[1,e)] M. A. van Spronsen,[1] M. Bergman,[1] L. Crama,[1] I. Taminiau,[1,f)] A. Ofitserov,[2] G. J. C. van Baarle,[2] and J. W. M. Frenken[1,g)]

[1]Huygens-Kamerlingh Onnes Laboratory, Leiden University, P.O. box 9504, 2300 RA Leiden, The Netherlands
[2]Leiden Probe Microscopy B.V., J.H. Oortweg 21, 2333 CH Leiden, The Netherlands

To enable atomic-scale observations of model catalysts under conditions approaching those used by the chemical industry, we have developed a second generation, high-pressure, high-temperature scanning tunneling microscope (STM): the ReactorSTM. It consists of a compact STM scanner, of which the tip extends into a 0.5 ml reactor flow-cell, that is housed in a ultra-high vacuum (UHV) system. The STM can be operated from UHV to 6 bars and from room temperature up to 600 K. A gas mixing and analysis system optimized for fast response times allows us to directly correlate the surface structure observed by STM with reactivity measurements from a mass spectrometer. The *in situ* STM experiments can be combined with *ex situ* UHV sample preparation and analysis techniques, including ion bombardment, thin film deposition, low-energy electron diffraction and x-ray photoelectron spectroscopy. The performance of the instrument is demonstrated by atomically resolved images of Au(111) and atom-row resolution on Pt(110), both under high-pressure and high-temperature conditions. © *2014 Author(s). All article content, except where otherwise noted, is licensed under a Creative Commons Attribution 3.0 Unported License.* [http://dx.doi.org/10.1063/1.4891811]

## I. INTRODUCTION

Much of our current knowledge of the precise mechanisms underlying chemical reactions at catalyst surfaces is derived from experiments under ultra-high vacuum (UHV) or high vacuum (HV) conditions. The discrepancy with respect to the typical working conditions of practical catalysts comes from the fact that many surface-sensitive techniques such as low-energy electron diffraction (LEED), Auger electron spectroscopy (AES), and X-ray photoelectron spectroscopy (XPS) cannot be combined easily with the environment to which a catalyst would normally be exposed, for example, in the three-way catalyst of a car or in catalytic processes in the petrochemical industry. Moreover, the UHV provides a clean and easily controllable environment for accurate experiments.[1,2] Although such low-pressure model studies have contributed extensively to our fundamental understanding of catalysts, recent investigations at high gas pressures have yielded new insights that go beyond the mere extrapolation of the low-pressure results.[3–6] This difference is often referred to as the "pressure gap."[7] Recently, several surface analysis techniques have been adapted to more realistic conditions. Examples are transmission electron microscopy (TEM),[8] surface X-ray diffraction (SXRD),[9] scanning tunneling microscopy (STM),[10–14] and atomic force microscopy (AFM).[15]

Scanning tunneling microscopy is one of the few atomically sensitive surface-science techniques that do not introduce fundamental problems or limitations when bridging the pressure gap. It can operate in the full range from UHV to high pressures of, e.g., 1 bar and beyond, and from cryogenic temperatures to temperatures well above 1000 K.[16,17] With its capability to image surfaces with atomic resolution, the STM holds the promise to determine the detailed dependence of the structure of model catalyst surfaces on various gas environments, to identify the active sites for catalytic reactions and to elucidate the role of possible promoters, all under the relevant, high-pressure, high-temperature conditions of the catalytic processes of interest. The weakness of the local tip-surface interaction provides confidence that in most cases this interaction will not significantly affect the structure and the properties of the catalyst. These advantageous properties of the technique go hand in hand with a demanding combination of technical difficulties. The main difficulty is the imaging stability of the instrument in terms of the drift and noise resulting from temperature and pressure variations and the presence of a gas flow. In addition, to desire to detect reaction products in the gas mixture adds additional constraints on the volume of the high-pressure cell versus the surface area of the model catalyst sample.

---

a)Present address: ASM Europe BV, Versterkerstraat 8, 1322 AP Almere, The Netherlands.
b)Present address: Carbon-Biotechnology Ltd., Xiangyun Road No. 6, 203000 Wujin Jingfa district, Changzhou, Jiangsu, China.
c)Present address: Royal Institute of Technology (KTH), Electrum 229, Isafjordsgatan 22, 16440 Kista, Sweden.
d)Present address: Evonik Industries AG, Paul-Baumann-Straße 1, 45772 Marl, Germany.
e)Present address: Christaan van der Klaauw Astronomical Watches, Businesspark Friesland-West 47, 8447 SL Heerenveen, The Netherlands.
f)Present address: Infinite Potential Laboratories, 485 Wes Graham Way, Ontario N2L 0A7, Canada.
g)Author to whom correspondence should be addressed. Electronic mail: frenken@physics.leidenuniv.nl. Present address: Advanced Research Center for Nanolithography, P.O. Box 41883, 1009 DB Amsterdam, The Netherlands.

In this paper we present the design and performance of the ReactorSTM. The setup combines an STM, partly integrated in a small flow cell, with a UHV system that is equipped with standard surface preparation techniques, such as ion bombardment and metal deposition. The ReactorSTM enables us to study the surface structure of a catalyst in combination with simultaneous mass spectrometry and thereby directly correlate structural changes with chemical activity. We start this paper with a discussion of the concept and the specifications of the instrument, followed by a description of the actual design and performance.

## II. CONCEPT

Figure 1 summarizes the concept of the ReactorSTM. It consists of a small reactor volume with inert walls, inside a UHV system. The reactor is connected to two thin gas lines, one serving as the gas inlet and the other as the exhaust. The inlet is connected to a gas system which controls the flow, mixing ratio and pressure of the reactant gasses. The exhaust is connected to a mass spectrometer for analysis of the composition of the gas flow that leaves the reactor. Of the scanning tunneling microscope, only the STM tip and the tip holder are exposed to the gasses inside the reactor. Two flexible o-rings seal off the reactor volume from the UHV. The lower o-ring separates the reactor on the lower side from all other STM components, such as the piezo element that is used to actuate the motion of the tip; these components stay in UHV, while the pressure in the reactor can be as high as several bar. In this way, the reactor volume is kept small, which lowers the detection limit of reaction products, makes the refresh rate of the gas in the reactor high and the response time to changes in the reactivity short. It also ensures that most of the vulnerable components of the STM are not exposed to high pressures of aggressive gasses. The upper o-ring, against which the sample surface is pressed, is used to seal the reactor on the upper side from the surrounding UHV environment. The sample is radiatively heated from the rear, i.e., the upper side.

The architecture of a small high-pressure cell inside a UHV system is radically different from early high-pressure STM designs,[11–13] in which a UHV chamber is backfilled with gas, and it goes significantly further than the current state of the art,[14] by keeping the piezo element outside of the high-pressure volume. This has important additional advantages leading to unequalled imaging performance, especially at elevated temperatures.

First of all, this design avoids convective heat transport via the gas phase from the sample to the scanner. Small differences in temperature, for example, between the hot sample and the cooler piezo element, can result in significant convective motion in the gas. Test measurements for a typical STM configuration have shown this type of heat transport to be erratic and to change magnitude on a timescale of a few seconds. This resulted in severe, erratic drifting distortions in the STM images on the same timescale. Without the presence of gas around the piezo element, such distortions are avoided completely. In addition, the limited heat transport also minimizes the total heating power, thereby further reducing thermal drifting of the scanner. Without convection, the drift is not erratic in nature and can be coped with routinely. Finally, this design allows for a much smaller reaction volume, which reduces the residence time of the gas, needed to reach a measurable concentration of reaction products, which makes it possible to operate the reactor in flow rather than batch mode.

Similar to other high-pressure STM designs, this configuration makes it straightforward to combine the high-pressure experiments with UHV techniques. Ultrahigh vacuum is a prerequisite for high-quality sample preparation, involving ion sputtering, metal deposition, vacuum annealing, et cetera, and for the application of traditional, sensitive surface analysis techniques, such as low-energy electron diffraction (LEED), Auger electron spectroscopy (AES) and X-ray photoelectron spectroscopy (XPS). UHV is also important to avoid contamination of the freshly prepared samples during their transfer to the high-pressure environment. This naturally leads to a configuration with a high-pressure cell that can be sealed off inside a UHV system. We have chosen to combine all required functionalities into a multi-chamber UHV setup, of which one chamber contains the high-pressure cell, integrated with the STM.

## III. SPECIFICATIONS

In order to approach industrial conditions during our STM measurements, we need to operate the STM with the sample surface exposed to a controllable gas flow at pressures beyond 1 bar. A meaningful time resolution in the reactivity measurements that matches high imaging rates, requires the gas flow to be high enough to refresh the reactor volume within a few seconds. For a small reactor, with a volume in the order of 1 ml, this requirement translates into a flow of typically 10 $ml_n$/min. In addition to high pressures, industrial conditions imply high temperatures. How high depends very much on the specific catalytic process at hand. The window of typical conditions starts at 400 K and runs up to much higher temperatures, such as 1000 K and above. Although we have developed a variable temperature (UHV) STM that routinely images surfaces at sample temperatures of 1000 K and above,[17] for the ReactorSTM we prioritize gas response times and accurate reactivity measurements over temperature range.
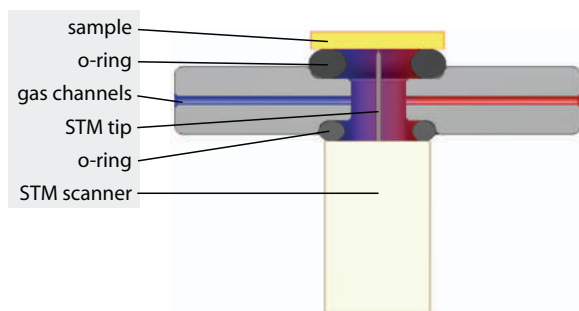


FIG. 1. Conceptual drawing of the ReactorSTM. The STM tip is contained within a small high-pressure volume, while the STM scanner is not exposed to the gasses. The sample forms one side of the reactor while the other reactor walls are chemically inert. Two polymer o-rings seal off the high-pressure volume from the UHV system around it.

Therefore we limit ourselves to 600 K, a temperature that is achievable with elastomer seals, allowing a more compact design.

STM imaging with high resolution, resolving the atomic structure at a catalyst surface, requires a stable STM with a short mechanical loop between the tip and the specimen surface, an effective vibration isolation system, good temperature stability to suppress thermal drift, and a low electronic noise level. The total noise level should not exceed a fraction of the atomic corrugation, i.e., in the images it should typically remain below 0.01 nm, both along the surface plane and perpendicular to it. To image rapid processes at the surface, under reaction circumstances, high-speed scanning is also needed. Our target here is to acquire one image per second. In order to correlate the observed surface structure with measurements of the reaction rate, it is necessary to operate the STM simultaneously with a mass spectrometer, in our case a quadrupole mass spectrometer (QMS). The complete gas detection system should have a response time in the order of seconds. This involves leading part of the exhaust gas line of the reactor volume to the QMS without creating a large dead volume, and without influencing the control over pressure and flow in the reactor.

An integral part of the ReactorSTM is a dedicated gas handling system that produces gas flows through the reactor volume with flow rates corresponding to a residence time of gas in the reactor ranging from seconds to minutes, and, independently, a range of total pressures below and above 1 bar. In order to explore the effect of the gas composition, the gas system should make it possible to generate mixtures of gasses. We have chosen for mixtures of up to four gasses plus a carrier gas. For the investigation of the effect of composition, the gas system should be able to vary the mixing ratios over a wide range, for which we have chosen a maximum value of 100:1. Short response times require the volume of the gas system to be minimal. For the same reason, dead volumes cannot be tolerated. A very interesting type of measurement is to follow the response of the catalyst to a sharp pulse of a different gas composition. One of the requirements for such experiments in combination with the sensitive STM observations is that such pulses do not lead to significant variations in total flow and total pressure. Cleanliness of the gas composition makes it important that the entire gas system can be baked out, in our case to 343 K. Finally, the gas system should be fully computer controlled and interfaced with the STM control and data acquisition system, which is necessary for time synchronization purposes.

The requirements that directly affect the STM configuration can be summarized as follows:

- *Imaging resolution:* atomic resolution (*z*-resolution below 0.01 nm) on close-packed metal surfaces under high-pressure, high-temperature conditions, e.g., at 1 bar and 450 K.
- *Imaging rate:* 1 or more images per second (images of $256 \times 256$ pixels, e.g., 5 nm $\times$ 5 nm).
- *Gas pressure in the reactor:* beyond 1 bar.
- *Ratio between partial pressures of different gasses in gas mixture:* up to 100:1.

- *Refresh time constant gas mixture in reactor:* down to 5 s.
- *Gas flow rate through the reactor:* up to 10 ml$_n$/min.
- *Time delay for gas mixture between gas handling system and reactor:* less than 5 s.
- *Time delay for gas mixture between reactor and mass spectrometer:* less than 5 s.
- *Temperature range of the catalyst:* room temperature up to 600 K
- *Thermal drift:* below 1 µm/h (piezo range) in *z*-direction; below 50 nm/min along *x,y*.

## IV. DESIGN

In this section we discuss the general architecture of the UHV system and provide a more detailed description of the ReactorSTM and gas handling system.

### A. UHV system

Figure 2 shows the configuration of the UHV system. It consists of three chambers[18] separated by valves.[19] From left to right, these chambers are the XPS chamber, the preparation chamber, and the STM chamber. Sample holders can be placed in different positions and orientations in each of these chambers, required to face each of the installed preparation and analysis tools. The sample holders can be transported between the chambers by means of a rack and pinion transfer rod.[18] A sample load-lock system mounted on the XPS chamber makes it possible to quickly introduce and export sample holders without the need to break the main vacuum. Each of the three chambers is pumped separately by an ion pump in combination with a Ti sublimation pump.[20] Additionally, the
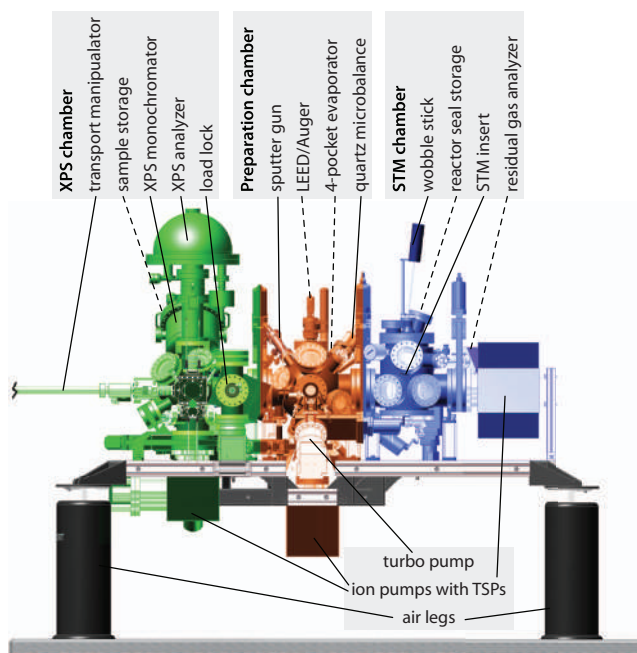


FIG. 2. Schematic drawing of the UHV system showing the three chambers with the equipment for sample preparation and characterization. Dashed lines point to components that are not visible.

preparation chamber is equipped with a chemically resistant turbo-molecular pump,[21] which is used to evacuate the system after it has been vented and to continuously pump the high gas flows that are sometimes required during preparation of model catalyst surfaces. To reach UHV, the vacuum system can be baked to 425 K, by means of two heating fans and a bake-out tent that encloses the entire system. During STM operation, the turbo-molecular pump is always off, in order to avoid the coupling of its mechanical vibrations into the STM. To minimize the influence of external mechanical vibrations, the entire, three-chamber combination is mounted on a stiff frame that is supported by air legs.[22]

The main component of the STM chamber is the high-pressure STM itself, which is mounted on the bottom flange, including all its electrical connections and gas lines. On the top flange of the chamber, a seal library has been installed together with a wobble stick. This combination makes it possible to easily replace the seal that separates the high pressure inside the reactor from the UHV of the STM chamber, as described in Sec. IV B.

The preparation chamber houses a manipulator, which can translate and rotate the sample surface, to face each of the instruments on the chamber. These include an ion gun[23] for sputter cleaning of the surface, an e-beam evaporator[24] for metal deposition, for example, to obtain thin metal films or supported nano-particles, and a combined LEED/AES system[25] for quick inspection of the periodicity, crystal quality, and cleanliness of the surface. A gas manifold with Ar, $O_2$, $H_2$, or other gasses is connected to the preparation chamber via automated all-metal leak valves.[26] Using a valve and separate pumping connection, the LEED/AES system can be sealed off from the rest of the preparation chamber, which is particularly useful during sample preparation steps that involve significant pressures of aggressive gasses, such as $O_2$ or $H_2S$.

The XPS chamber is dominated by the X-ray source and the hemispherical energy analyzer of the XPS setup,[27] which can be used for inspection of the surface chemical composition prior to and after high-pressure experiments. The chamber is made out of Mu-metal to shield the XPS from external magnetic fields. The chamber also contains a sample library that can store two additional sample holders.

## B. STM configuration

Figure 3(a) shows a schematic cross section of the combination of the sample holder and the reactor with STM scanner. With the sample holder placed on the STM, a small, 0.5 ml reactor volume is defined. This reactor volume is sealed off from the surrounding UHV by two elastomer rings. The upper seal is clamped between the catalyst sample and the STM body. It is a custom-made Kalrez[28] ring that is vulcanized onto a stainless steel holder, which enables us to exchange these seals using a wobble stick without breaking the vacuum. The lower seal is a Viton O-ring between the STM body and the top part of the scan actuator. Both rings are chemically rather inert, especially the Kalrez, which is in direct contact with the active catalyst surface. The Kalrez seal is specified for operation up to 600 K and this limits the operating temperature of the STM.

The STM body is made out of Zerodur,[29] a type of glass that has a low thermal expansion coefficient, which minimizes the thermal drifting of the STM during temperature changes. An additional advantage of this material is that it is chemically inert, which is necessary since the upper surface of the STM body forms one of the walls of the high-pressure cell.

The hat-shaped sample is held in position in the sample holder by a molybdenum spring. It is electrically isolated from the other components of the sample holder. A filament, mounted behind the sample, enables sample heating either by thermal radiation or by electron bombardment. A sapphire shield thermally isolates the filament from the rest of the sample holder. A type K thermocouple is laser-spot-welded to the sample, for accurate temperature measurement. The sample holder has a 5-pin connector that provides separate



(a)

**high pressure reactor volume**
single crystal sample
kalrez o-ring
zerodur body with gas channels
viton o-ring
reactor wall

**sample holder**
sapphire spacer
heating filament
sample clamp
sample mounting screws
isolation ceramics
spacer legs

**scanner with integrated coarse approach**
STM tip
sliding tip-holder
electrical shielding
ceramic spacers
tip-holder guidance tracks
magnet
piezo tube

(b)

**scanner/reactor**
sample holder
reactor body
opening/closing bellow

**vibration isolation**
spring suspension
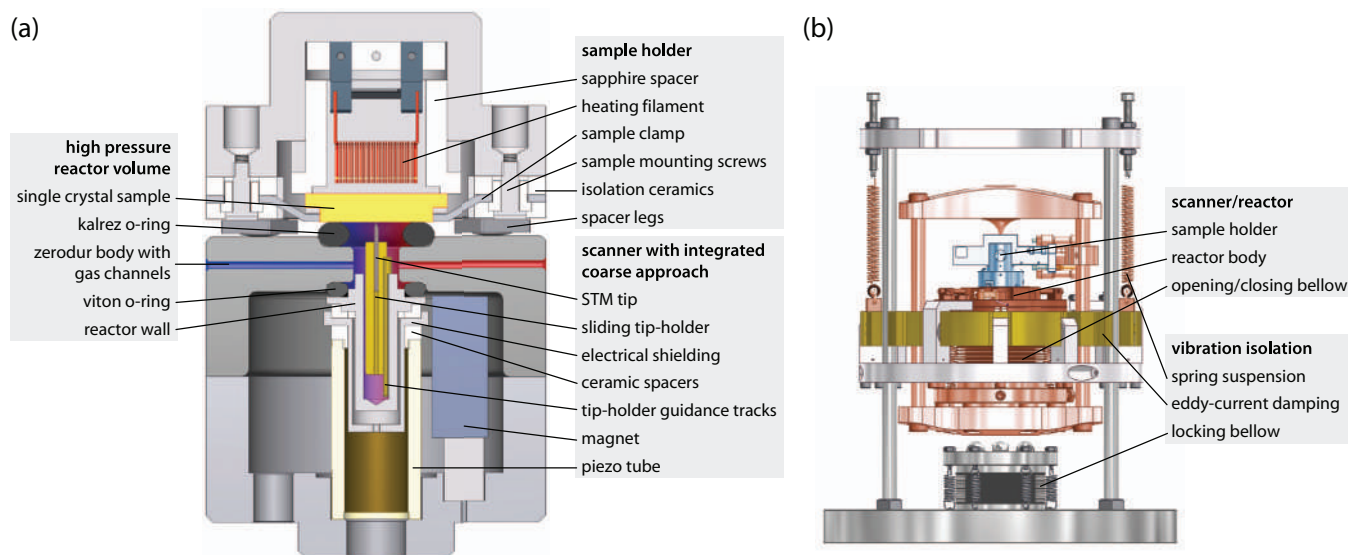eddy-current damping
locking bellow

FIG. 3. Detailed schematic of (a) the scanner and reactor and (b) the insert with vibration isolation, mounted on a CF-200 flange.

contacts to the filament, the thermocouple and the sample. The latter connection is used either to ground the sample, e.g., for ion sputtering, electron bombardment, XPS, LEED, and AES, or to provide a bias voltage for STM and STS measurements. Two versions have been constructed of the sample holder body, one out of Zerodur[29] and the other out of Invar, a low-expansion steel. In both cases, a low-expansion material was used, again to minimize thermal drift. The brittleness of Zerodur established a practical disadvantage, which made us prefer the Invar version. Fortunately, XPS spectra acquired on samples clamped in the Invar holder did not indicate noticeable changes in the spectrum due to the magnetic character of the Invar.

The sample holder is strongly pressed against the top of the STM body, so that it makes hard mechanical contact via three adjustable screws. In this way a short and stiff mechanical loop is established between the sample and the tip, which is essential for high-quality STM imaging. After a sample has been mounted in its sample holder, the length of the three screws is adjusted such that with the screws in contact with the scanner body, the Kalrez ring is compressed to 80% of its original thickness. This situation provides a reliable, leak-tight seal, enabling to maintain UHV in the STM chamber, even when the reactor volume is exposed beyond atmospheric pressure.

Two thin silica-coated capillaries run up from gas feedthroughs on the bottom flange (see below) and connect to the reactor volume via channels in the Zerodur STM body. One is used as the supply line of gasses into the reactor; the other serves as the exhaust line.

A single piezotube is used for both the coarse approach and the fine scanning motion. The STM tip is clamped in a steel holder, which is pulled against two steel rails by a SmCo magnet[30] that is glued on a separate support. The three steel parts, tip holder, and rails are gold-plated in order to ensure chemical inertness and to optimize the stick-slip behavior of the holder along the rails (see below). The magnetic force, determined by the distance between the tip holder and the magnet, is tuned via the size, shape, and location of the magnet, in such a way that the maximum acceleration that can be generated along the length axis by the EBL2 piezo element[31] is high enough to overcome the static friction force between the tip holder and the rails. In this way, the same piezo element used for STM scanning is also used to inertially translate the tip holder up or down along the rails, which makes it possible to perform a controlled approach- or disengage motion over several mm distance. The electrical connection to the tip that is necessary to measure the tunneling current is established via the tip holder and the rails and the aluminum tube in which the rails are clamped. We have selected aluminum as the material for this tube, since this tube is in contact with the reactive gas mixture and aluminum is inert for the catalytic reactions under investigation. Electrical shielding is provided by an additional hat-shaped aluminum piece. The two aluminum parts are electrically isolated from each other and from the piezo tube by two insulating Macor[32] rings. The piezo element is glued to a titanium base, which has a thermal expansion coefficient that compensates the expansion of the piezo tube during temperature changes.

The backbone structure in Figure 3(b) is used to combine the complete STM assembly with vibration isolation and the necessary electrical connections and gas capillaries on a single CF-200 flange. In spite of its complexity, the STM assembly is a compact unit that is mounted relatively easily from below into the SPM chamber of the UHV system. The STM portal that holds the STM body, the Kalrez seal, and the sample holder, is suspended by a set of springs that is combined with an eddy current damping system, in order to isolate the STM from external, mechanical vibrations. The two silica-coated capillaries are each connected to a gas feedthrough on the bottom flange. Both are wound as soft springs around the portal to minimize coupling of external mechanical vibrations via the gas lines into the STM.

Two features are essential to facilitate easy and reliable transfer of sample holders into and out of the STM portal. First of all, during sample transfer activities, the spring suspension should be disarmed by mechanically locking the STM portal to the backbone structure. This makes it possible to exert forces on the portal for pushing in or pulling out sample holders. Second, the system should enable one to generate a force up to 100 N to mechanically press the sample and sample holder against the reactor body, thereby compressing the kalrez seal by 20% and closing the reactor volume with respect to the UHV chamber; also the opposite should be possible, pulling sample and sample holder away from the reactor body. Once the reactor is closed, it should remain closed, also when the STM portal is unlocked and suspended from the springs. These two actions are achieved by means of the controlled inflation of two bellows. When the upper bellow is inflated, the sample and sample holder are pressed against the reactor body and the reactor volume is sealed off from the surrounding UHV. When the lower bellow is inflated, the STM portal is locked to the backbone structure. The upper bellow is connected via a capillary to a gas feedthrough, and the lower one is directly connected to a feedthrough. The capillary of the upper bellow is again wound as around the portal, to minimize mechanical vibrations.

The STM is controlled by fast analog/digital SPM control electronics[33] capable of video-rate STM imaging.[34]

## C. Gas supply and analysis system

As motivated above, a gas system was required that can mix various gasses over wide ranges in composition, with separate control over the gas flow rate of each individual component in the mixture and the total pressure of the gas flow with a short response time, in the order of a few seconds or less. The latter requirement necessitates a configuration with small total volume and without dead or badly refreshed gas volumes. Another requirement was that it should be possible that during STM imaging the partial gas pressures, flow rates and total pressure can be changed, without having to interrupt imaging. This means that no unwanted effects such as pressure bursts, with possible tip crash as result, can be tolerated. Fortunately, for applications in, e.g., gas chromatography (GC) and high-performance liquid chromatography, a wide range of components is commercially available with extremely low dead volumes, such as tubing, connection pieces, filters, and several
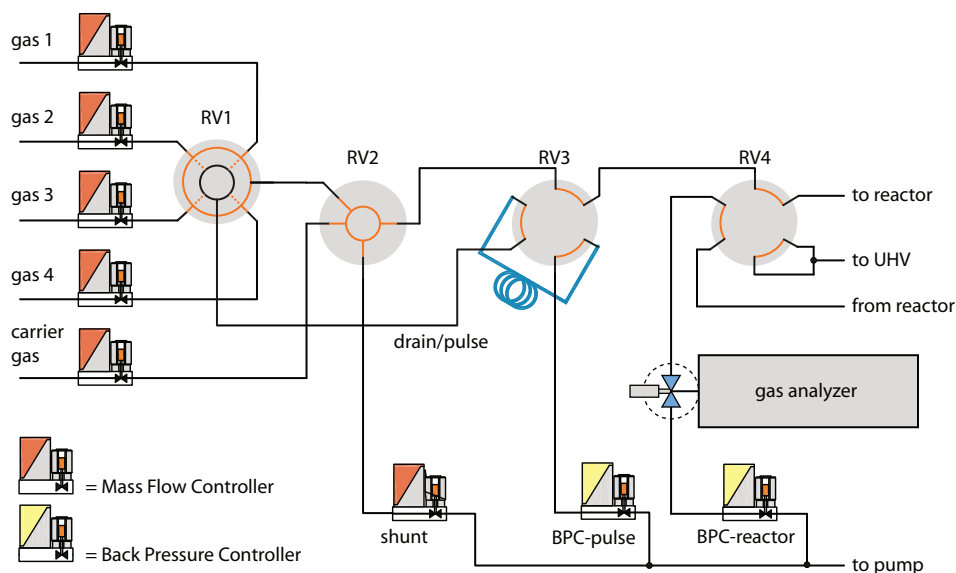
FIG. 4. Manifold for gas mixing and analysis. Up to four gasses plus a carrier gas can be mixed by a computer controlled manifold, consisting of rotating valves (RV1-4), several mass flow controllers (MFCs), and two back pressure controllers (BPCs). A continuous sampling gas analyzer[37] provides high time-resolution gas analysis.

types of valves, including rotating valves. In our gas system a special role is played by a custom-modified version of a GC valve. The crucial element is a rotor with a conical polymer surface that contains an engraved pattern. This rotor is pressed inside a metal body, to ensure a leak-tight seal. By rotation of the rotor the engraved pattern can be made to access and interconnect different channels, drilled in a symmetric, radial pattern in the metal body. This can be used to obtain different flow paths, depending on the rotor position. Note that it is possible to engrave the rotor such that no dead volume is enclosed in this valve at any time, also not in the channels that are not in use. For the specific needs of our gas system, we have produced rotors with several custom engraving patterns.

To separately control the composition, the flow rate, and the total pressure inside the reactor, we have employed a combination of mass flow controllers (MFCs) and back pressure controllers (BPCs) from Bronkhorst Hi-Tech[35] with a flow rate of 0–10 ml$_n$/min and pressure range of 0–6 bars, respectively.

In our gas system the outer diameter of the stainless steel tubing is chosen to be 1/16 in. The choice of the inner diameter of the tubing is a trade-off between very small volumes that would reduce the total internal volume of the system thereby optimizing the response time, and larger volumes to minimize the pressure drop over the gas lines for a given flow rate to reduce the difference in the pressure measured by the BPC and the actual pressure inside the reactor. We chose 0.5 mm inner diameter for the tubing between the MFCs and the reactor, since for that part of the system the response time is the most important parameter and a certain pressure drop between the MFCs and the reactor can be tolerated. For the section\ between the reactor and the BPC, the pressure drop should be minimal in order to relate the BPC reading to the reactor pressure; for this section of the tubing an inner diameter of 0.75 mm was chosen.

Using these components, we have adopted the architecture schematically shown in Figure 4. The high purity gases gas 1–4, in our implementation $O_2$, CO, NO, and $H_2$, are supplied from lecture bottles with reducing valves. To prevent particles from entering the gas system, particle filters are placed between the reducing valves and the MFCs. Each of the gasses flows through a MFC, which determines the flow rate of that gas. The rotating valve RV1 is the "mixing valve" and can select any combination of the maximally four gas flows that arrive at its input. The flow exiting the mixing valve and entering the "selector valve" (RV2) is the sum of the selected gas flows. The engraving pattern of the mixing valve is such that those gases that are not selected are not "stored" in the valve, but leaving the valve via the line indicated as "drain/pulse." Via the loop and the pulse BPC, the not selected gases are pumped away. The role of this BPC is crucial, since it allows one to, prior to the addition of a certain gas to the flow to the reactor, stabilize the flow pressure of that gas flow to match the current reactor pressure. After this stabilization, RV1 can be switched to add the extra gas flow to the reactor flow, without detrimental effects on the STM-imaging.

RV2 directs the flow via RV3 towards the STM reactor volume. The second output of RV2 is connected to the shunt MFC and enables one to split off a part of the flow by sending it via the shunt line to the pump. This makes it possible to reach extremely low flow rates through the reactor, without the need for extreme (and inaccurate) settings for the MFC's. A second inlet of RV2 is connected to a carrier gas MFC and allows for having very small partial pressures of a certain mixture in the reactor while still having a large total pressure. It also ensures that for very small flows of a mixture, a flow of carrier gas can be added to have a good response time to a change of settings.

Before the gas flows to the reactor, it passes the "pulse valve" (RV3). In addition to the regular gas flow from the selector, RV3 also receives input from the pulse/drain line,

connected to RV1, which it stores in a small gas loop with a total volume which is selected to be 0.5 ml, equal to the reactor volume. The pressure of the gas in that loop can be controlled by the "pulse BPC." In the orientation of RV3 shown in Figure 4, the gas flow from RV2 is passed down to RV4 and the not-selected gasses from RV1 are sent via the loop volume and the pulse BPC towards the pump. RV3 can be rotated rapidly into a position in which the extra volume of the gas loop is inserted into the flow path of the regular gas mixture. This generates a well-defined pulse of the gas that was initially stored in the loop. The configuration of this valve with the gas loop is such that, in case both the pulse and reactor BPC have the same set point, the pulse only provides a short variation in the gas composition, while it does not change the total pressure or the total gas flow. Therefore the pulse can be applied during STM imaging without having to retract the tip.

The final rotating valve, RV4, is a rotating 6-way valve that has two positions. The first position, shown in Figure 4, is for high-pressure STM experiments. In this position, the prepared mixture is directed towards the reactor. The flow exiting the reactor is sent via RV4 towards the gas analyzer. After passing by the gas analyzer, the flow is finally directed via RV4 towards a BPC that controls the reactor pressure independently from the total gas flow. The BPC is connected directly to the pump that generates the flow through the reactor. The two other connections of RV4 are connected to the main UHV chamber. In the second position of RV4, both the inlet and outlet lines of the reactor are connected to the UHV via RV4. This ensures that the sample is protected as good as possible from degassing of the capillaries and reactor wall when the reactor has been closed but no gas exposure is desired yet, for example, during coarse approach. Another role of the second position of RV4 is that it connects the gas stream leaving RV3 directly to the BPC of the reactor, via the gas analyzer. In this way the gas composition can be tested by QMS or GC analysis prior to exposing the sample to the gas. It also allows keeping the gas system clean by having always a flow through most of the lines, even when the reactor is open to the UHV.

The gas analyzer is placed before the BPC to make it independent of the varying flow impedance of the BPC. However this means that the analyzer must operate in the full pressure range of 0–6 bars and can only consume a small fraction of the gas flow. In addition, the requirement of at most 5 s delay between gas leaving the reactor and being analyzed places a tight restriction on the internal volume of the analyzer. A T100 gas analyzer[36] is used, which is based on a QMS. This analyzer has a 5 μl inlet volume and a typical gas consumption of less than 1 $\mu l_n$/min, and it is tunable for operation across the desired pressure range. If response time is not an issue for the experiment, then the internal volume of the analyzer is no longer restricted, and this system can be replaced by or complemented with any other gas analysis method, including gas chromatography and infrared spectroscopy.

All valves of the gas supply system are controlled by a PC. LabView and Python programs have been written to continuously log the valve settings and BPC/MFC read-outs. The Python software also allows programming of sequences of actions.

## V. PERFORMANCE

In this section we present the essential aspects of the performance of the complete ReactorSTM setup. After a brief summary of the vacuum and gas flow behavior, we turn to the STM imaging performance under vacuum and high-pressure conditions, at room temperature and at elevated temperatures.

### A. UHV system and gas manifold

The three chambers of the UHV system routinely reach a base pressure of in the range of $10^{-10}$ mbar after a bakeout of 48 h at 400 K. The operation of the bellows used to open and close the reactor and to lock the spring suspension system of the STM did not have any effect on the pressure in the UHV system. In practice, an absolute pressure of approximately 4 bars in the bellow that closes the reactor results in a sufficiently large closing force to compress the Kalrez seal and establish a rigid coupling between the surface of the Zerodur reactor body and the three adjustment legs on the sample holder. With that closing force, we can operate the reactor at pressures up to 6 bars, while the leak rate from the reactor into the UHV chamber typically results in a slight raise of pressure to the $10^{-9}$ mbar range. Eventually, after longer use, seals have been observed to degrade, leading to a modest increase of the UHV pressure when having high pressures inside the reactor.

The performance of the modified rotating GC valves over time was evaluated during use. After having been rotated a few hundred times, they were still found to exhibit a low leak rate in the order of $10^{-9}$ mbar l/s. Setting a new position of these rotating valves takes 0.1–1 s, depending on the travel the rotor has to make. The possible momentary interruption of the gas flows, caused by the rotation of the valve rotors, is sufficiently buffered by the volume of the gas lines and only modestly affects the STM imaging. The time response of the gas system is illustrated in Figure 5 by a typical time-trace of the gas analyzer during a CO oxidation experiment. In this experiment, we switched from a 50% CO flow to a 50% $O_2$
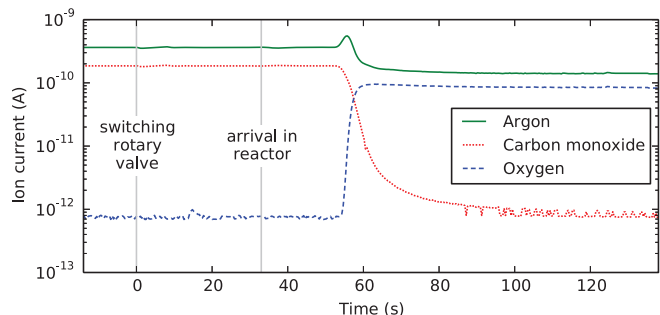
FIG. 5. Gas mixing response at 1 bar, 2 $ml_n$/min total flow, as detected by the mass spectrometer. Replacing CO by $O_2$ starting from a 1:1 mixture of Ar and CO, using rotary valve RV1 (Figure 4). The arrival of the gasses in the reactor at T = 33 s has been deduced from thermal drift in the STM images. The transition time of the $O_2$ introduction is 5 s. The spike in the Ar signal is an increase in partial pressure caused by the momentary interruption of the CO and $O_2$ flows during the movement of the rotary valve. Note that the Ar flow is not interrupted since it enters the manifold via RV2, neither is there an effect on the total pressure.

flow with argon as carrier gas at a pressure of 1 bar. At a modest flow of 2 ml$_n$/min, it takes 33 s for the gas to reach the reactor and another 20 s to reach the mass spectrometer. These delays scale linearly with flow, so an improvement of a factor 10 can easily be gained with higher flows. The switch from the O$_2$ to the CO atmosphere is completed within approximately 5 s, indicating the low intermixing of the gases in the gas lines, the reactor, and the sampling valve.

## B. STM

A first series of test measurements was performed to establish the imaging resolution and high-speed performance of the STM in "UHV-mode." In this mode, the ReactorSTM is fully operational but we leave out the Kalrez seal between sample and reactor, so that the reactor is pumped via the UHV chamber. The presence or absence of this seal has no

influence on the imaging performance, but makes a significant difference for the pressure to which the sample (and the tip) are exposed. Thus, the "UHV-mode" enables us to judge the imaging performance, unperturbed by gasses. Figure 6 demonstrates that the imaging resolution of the ReactorSTM is comparable to that of other, typical UHV-STM setups, i.e., not compromised by the special, high-pressure-flow-reactor configuration with the capillaries, the bellows, the Zerodur, and the stick-slip tip holder for coarse approach. Atomic resolution is obtained routinely, not only on graphite (panels (a) and (b)) but also on the close-packed Au(111) surface (panels (c) and (d)). The *z*-resolution is estimated to be 10 pm (panel (e)). Note that we have measured atomically resolved images at frame rates up to 4 images/s with only mild image distortions (panel (b)), which is favorable for acquiring movies of dynamic phenomena.

The thermal behavior of the ReactorSTM setup was characterized by ramping the sample temperature from 410 K to 460 K over the course of 3 h, while imaging the surface continuously with the STM. From the comparison of the images over this 3-h time window, we deduce that the average displacement was ∼25 nm/K parallel to the surface and ∼8 nm/K perpendicular to the surface. The lateral drift component was uniform and small enough to be accommodated comfortably by routine drift correction techniques and over the full 50 K temperature window, both drift components added up to no more than approximately one third of the full range of the piezo scanner.

The influence of the total reactor pressure on the STM imaging was explored by scanning the Au(111) surface while ramping the reactor pressure from 0 bar up to 3 bars and back to 0 bar. This resulted in reversible displacements below 300 nm parallel to the surface (i.e., below 100 nm/bar) and below 400 nm perpendicular to the surface (below 133 nm/bar). Over this wide pressure range, the mechanical distortions of the ReactorSTM setup are thus modest enough to remain well within the range of the piezo scanner.

The full performance of the ReactorSTM is illustrated in Figure 7, in which atomic resolution is demonstrated on Au(111) at a high sample temperature of 378 K and an O$_2$
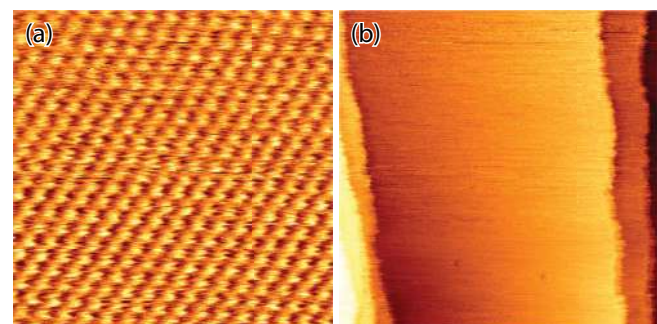


FIG. 6. Four atomically resolved STM images obtained with the ReactorSTM in "UHV mode" at room temperature. (a) and (b) Highly oriented pyrolithic graphite (HOPG), 8.0 nm × 8.0 nm (512 × 512 pixels) at 8.7 s/image, and 2.9 nm × 2.9 nm (512 × 512 pixels) at 2.6 s/image, both imaged with a tunneling voltage of V$_t$ = 0.40 V and a tunneling current of I$_t$ = 0.46 nA. (c) and (d) Au(111) surface, 23 nm × 23 nm (512 × 512 pixels, V$_t$ = 0.10 V, I$_t$ = 0.12 nA), and 4.6 nm × 4.6 nm (512 × 512 pixels, V$_t$ = 0.12 V, I$_t$ = 0.10 nA). The zig-zag pattern in (c), which is also present as a modulation in height and in lateral position in (d) is due to the well-known "herringbone reconstruction" on Au(111). (e) Height line from an atomically resolved Au(111) image, providing an estimate of the *z*-noise of 10 pm peak-to-peak for a bandwidth of 5 kHz.



FIG. 7. Two STM images obtained with the ReactorSTM on Au(111) in a flow of 10 ml/min of O$_2$ at a pressure of 1.2 bars and at a sample temperature of 378 K. (a) Small-area image showing atomic resolution, 4.4 nm × 4.4 nm, taken with a tunneling voltage of V$_t$ = 0.22 V and a tunneling current of I$_t$ = 0.20 nA, corrected for drift by shearing the image horizontally over 21°, then cropped. (b) Larger-area image, V$_t$ = 0.24 V, I$_t$ = 0.24 nA, 75 nm × 75 nm, showing step fluctuations.
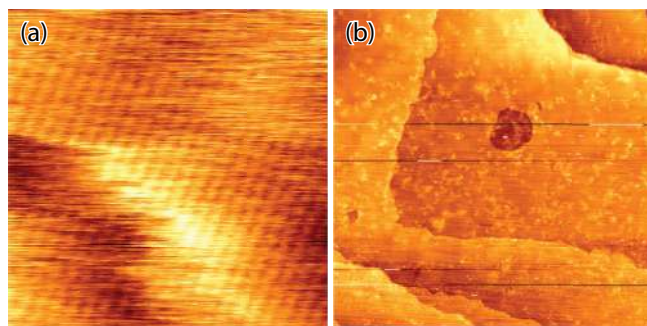
FIG. 8. Two STM images obtained with the ReactorSTM under high-pressure high-temperature conditions. (a) The Pt(110) surface, showing atomic rows with a vague signature of the individual atoms, 7.5 nm × 7.5 nm, imaged in a flow of 1 bar of CO at a sample temperature of 433 K, imaged with a tunneling voltage of $V_t = -0.04$ V and a tunneling current of $I_t = -0.08$ nA, (b) A 318 nm × 318 nm area of the Co(0001) surface, imaged under conditions for the Fischer-Tropsch (FT) synthesis of hydrocarbon molecules from a 1:2 mixture of CO and $H_2$ known as syngas. The total pressure is 1.2 bars, consisting of 200 mbar syngas and 1000 mbar Ar, and the temperature is 500 K. Imaged with a sample bias of $V_t = 1.05$ V and a tunneling current of $I_t = 0.15$ nA.

flow at a high pressure of 1.2 bars (panel (a)). The large-scale image of panel (b) shows the dynamic behavior of the atomic steps at this elevated temperature.[37] Note that the herringbone reconstruction that is clearly present in Figure 6 and characteristic for the clean Au(111) surface is absent in the images of Figure 7. We have not investigated systematically whether this lifting of the reconstruction is caused by the high-temperature exposure to the high $O_2$ pressure or by the presence of a trace impurity in the $O_2$ flow, such as water. We note that the images of Figure 7 have been obtained while three turbo-molecular pumps of the UHV system were running at full speed. Although this has introduced a minor vibrational signature in Figure 7(a), the effect is sufficiently modest, not to wash out the atomic resolution.

In Figure 8, we provide two STM images of catalytically more relevant situations. Panel (a) shows the Pt(110) surface at a temperature of 433 K in a flow of 1 bar of CO, taken in the course of an experiment dedicated to the catalytic oxidation of CO.[3,38–46] The distance between the atom rows shows that the CO has lifted the (1 × 2) reconstruction, characteristic of the clean surface. The atomic periodicity can be recognized vaguely in the atomic rows. The high temperature and the presence of the CO lead to rapid fluctuations in the position of the atomic step between the upper left and lower right parts of the image, which make the appearance of that step in the image extremely jagged. Similarly, large excursions can be recognized in the upper left corner of the image from a step with an average position to the left of the imaged area. In panel (b), we show the Co(0001) surface under conditions for the Fischer-Tropsch (FT) synthesis of hydrocarbon molecules from a flow at 200 mbar of a 1:2 ("syngas") mixture of CO and $H_2$ at a sample temperature of 500 K. The structures formed on the terraces and accumulating along the steps, have formed in the course of the FT reaction on this surface, and remain to be identified and further characterized.

STM tips require special attention when operating in catalytic conditions. Etched tungsten tips that traditionally per-

form well in ultrahigh vacuum are vulnerable for interaction with reactive gasses, such as water and oxygen. Tip oxidation compromises the imaging resolution under catalytically relevant conditions. Adsorption-enhanced diffusion of tip atoms can result in frequent changes in the shape and sharpness of the tip apex. In addition, the tip itself can be catalytically active and distort the reactivity measurements, although this effect is expected to be modest due to the small surface area and the lower temperature of the tip compared to the sample. Most results presented in this paper have been obtained with mechanically cut platinum-iridium tips. First tests with gold-coated metal tips give some hope that it may be possible to combine sharp, conductive tips with chemical inertness.

From the performance tests and the examples given in this section, we conclude that the ReactorSTM described in this paper fully meets the specifications given in Sec. III. It is the first STM capable of imaging catalytically interesting surfaces with atomic resolution under reaction conditions: high temperatures *and* high pressures of flowing gas mixtures. During imaging, the temperature of the catalyst, the flow rate, total pressure, and composition can all be changed over wide ranges, without the necessity to interrupt the imaging. Mass spectrometry of the gas that flows out of the reactor enables us to quantitatively correlate the catalytic performance of the model catalyst with the detailed structural information in the STM images, with a time resolution down to a few seconds.

## VI. OUTLOOK

At present, the ReactorSTM is being used in the investigation of a growing variety of catalytic reaction systems. Examples are oxidation/reduction reaction, Fischer-Tropsch synthesis, and hydro-desulphurization. The observation in many of these cases of surface restructuring into high-gas-pressure-specific configurations should be taken as a justification *a posteriori* for the development of this special-purpose scanning tunneling microscopy setup for "the other side" of the pressure gap.

We close this paper by addressing several aspects that may further add to the performance of this microscope. The maximum sample temperature of 600 K and the maximum gas pressure of 6 bars are just within the range of industrial conditions. A higher operating temperature will require a different sealing material than Kalrez. We are in the process of replacing several of the components of the gas handling system in order to make the microscope suitable for a maximum pressure of 20 bars.

A highly relevant modification of our microscope that we are currently developing is that of a non-contact ReactorAFM version, as well as a version that combines the two functionalities, STM and nc-AFM. The two resulting forms of this microscope will enable us to also bridge the material gap and perform high-pressure, high-temperature observations on non-conductive surfaces, such as oxide supports and supported metal nanoparticles. This will take us beyond the geometry of extended, flat single-crystal metal surfaces and bring us closer to the geometry of practical catalysts.

## ACKNOWLEDGMENTS

[1] M. Bowker, *The Basis and Applications of Heterogeneous Catalysis* (Oxford Chemistry Primers, 1998).

[2] G. A. Somorjai, *Introduction to Surface Chemistry and Catalysis* (Wiley, New York, 1993).

[3] B. L. M. Hendriksen, M. F. Chang, M. A. J. Klik, and J. W. M. Frenken, Phys. Rev. Lett. **89**, 046101 (2002).

[4] M. D. Ackermann, T. M. Pedersen, B. L. M. Hendriksen, O. Robach, S. C. Bobaru, I. Popa, C. Quiros, H. Kim, B. Hammer, S. Ferrer, and J. W. M. Frenken, Phys. Rev. Lett. **95**, 255505 (2005).

[5] X. Su, P. S. Cremer, Y. Ron Shen, and G. A. Somorjai, J. Am. Chem. Soc. **119**, 3994 (1997).

[6] R. Westerström, J. Gustafson, A. Resta, A. Mikkelsen, J. N. Andersen, E. Lundgren, N. Serianr, F. Mittendorfer, M. Schmid, J. Klikovits, P. Varga, M. D. Ackermann, J. W. M. Frenken, N. Kasper, and A. Stierle, Phys. Rev. B **76**, 155410 (2007).

[7] H. Over and M. Muhler, Prog. Surf. Sci. **72**, 3 (2003).

[8] J. F. Creemer, S. Helveg, G. H. Hoveling, S. Ullmann, A. M. Molenbroek, P. M. Sarro, and H. W. Zandbergen, Ultramicroscopy **108**(9), 993 (2008).

[9] R. van Rijn, M. D. Ackermann, O. Balmes, T. Dufrance, H. Gonzalez, H. Isern, L. Petit, V. A. Sole, D. Wermeille, R. Felici, A. Geluk, E. De Kuyper, and J. W. M. Frenken, Rev. Sci. Instrum. **81**, 014101 (2010).

[10] P. B. Rasmussen, B. L. M. Hendriksen, H. Zeijlemaker, H. G. Ficke, and J. W. M. Frenken, Rev. Sci. Instrum. **69**, 3879 (1998).

[11] B. L. Weeks, C. Durkan, H. Kuramochi, M. E. Welland, and T. Rayment, Rev. Sci. Instrum. **71**(10), 3777 (2000).

[12] E. Lægsgaard, L. Österlund, P. Thostrup, P. B. Rasmussen, I. Stensgaard, and F. Besenbacher, Rev. Sci. Instrum. **72**(9), 3537 (2001).

[13] M. Rößler, P. Geng, and J. Wintterlin, Rev. Sci. Instrum. **76**(2), 023705 (2005).

[14] F. Tao, D. Tang, M. Salmeron, and G. A. Somorjai, Rev. Sci Instrum. **79**, 084101 (2008).

[15] S. B. Roobol, M. E. Cañas-Ventura, M. Bergman, M. A. van Spronsen, W. Onderwaater, P. C. van der Tuijn, R. Koehler, A. Ofitserov, G. J. C. van Baarle, and J. W. M. Frenken, "The ReactorAFM: Non-Contact Atomic Force Microscope operating under high-pressure and high temperature catalytic conditions" (unpublished).

[16] C. J. Chen, *Introduction to Scanning Tunneling Microscopy* (Oxford University Press, 1993).

[17] M. S. Hoogeman, D. Glastra van Loon, R. W. M. Loos, H. G. Ficke, E. de Haas, J. J. van der Linden, H. Zeijlemaker, L. Kuipers, M. F. Chang, M. A. J. Klik, and J. W. M. Frenken, Rev. Sci. Instrum. **69**, 2072 (1998).

[18] VG Scienta.

[19] UHV gate valve series 10, VAT Inc.

[20] VacIon Plus 150/300 StarCell Combination Pump, Agilent Technologies.

[21] Turbo-molecular pump TPH 261PC in combination with DUO 20 MC, Pfeiffer Vacuum.

[22] Pneumatic Vibration Isolators, Newport Corporation.

[23] Model IG70, OCI Vacuum Micro-engineering.

[24] Mini e-beam evaporator EGCO4, Oxford Applied Research.

[25] SpectaLEED, Omicron NanoTechnology GmbH.

[26] ALV, Leiden Probe Microscopy B.V.

[27] Focus 500 x-ray source, Phoibos 100 analyzer, 2D CCD detector, Flood gun FG15/40, SPECS Surface Nano Analysis GmbH.

[28] Custom part, DuPont.

[29] Zerodur, Schott.

[30] SmCo magnet, IBS Magnet.

[31] EBL #2, EBL Products.

[32] Corning Inc.

[33] Video Rate SPM Controller, Leiden Probe Microscopy B.V.

[34] M. Rost, L. Crama, P. Schakel, E. van Tol, G. van Velzen-Williams, C. Overgauw, H. ter Horst, H. Dekker, B. Okhuijsen, M. Seynen, A. Vijftigschild, P. Han, A. J. Katan, K. Schoots, R. Schumm, W. van Loo, T. H. Oosterkamp, and J. W. M. Frenken, Rev. Sci. Instrum. **76**, 053710 (2005).

[35] F-201CV EL-flow and P-702CV EL-press, Bronkhorst High-Tech B.V.

[36] T100 gas analyzer, Leiden Probe Microscopy B.V.

[37] L. Kuipers, M. S. Hoogeman, J. W. M. Frenken, and H. van Beijeren, Phys. Rev. B **52**(15), 11387 (1995).

[38] M. Kim, M. Bertram, M. Pollmann, A. von Oertzen, A. S. Mikhailov, H. H. Rotermund, and G. Ertl, Science **292**, 1357 (2001).

[39] S. Ladas, R. Imbihl, and G. Ertl, Surf. Sci. **197**, 153 (1988).

[40] H. P. Bonzel and R. Ku, J. Vac. Sci. Technol. **9**, 663 (1972).

[41] H. P. Bonzel and R. Ku, Surf. Sci. **33**, 91 (1972).

[42] A. von Oertzen, A. S. Mikhailov, H. H. Rotermund, and G. Ertl, J. Phys. Chem. B **102**, 4966 (1998).

[43] S. Ladas, R. Imbihl, and G. Ertl, Surf. Sci. **198**, 42 (1988).

[44] C. E. Wartnaby, A. Stuck, Y. Y. Yeo, and D. A. King, J. Chem. Phys. **102**, 1855 (1995).

[45] E. Vlieg, I. K. Robinson, and K. Kern, Surf. Sci. **233**, 248 (1990).

[46] Q. Ge and D. A. King, J. Chem. Phys. **111**, 9461 (1999).

# Fingerprinting substitution sites in Pb,Dy-Bi$_2$Sr$_2$Ca$_1$Cu$_2$O$_{8+\delta}$ using X-ray Photoelectron Diffraction

D. Popović[1,a], M. Bovet[2], H. Berger[3], and P. Aebi[2]

[1] FR 7.2 Experimentalphysik, Universität des Saarlandes, 66123 Saarbrücken, Germany
[2] Institut de Physique, Université de Neuchâtel, 2000 Neuchâtel, Switzerland
[3] Institut de Physique Appliquée, EPF, 1015 Lausanne, Switzerland

**Abstract.** The substitution sites of Pb and Dy dopants in the cuprate-type high temperature superconductor Bi$_2$Sr$_2$Ca$_1$Cu$_2$O$_{8+\delta}$ are determined by a direct comparison of the angle-scanned X-ray photoelectron diffraction (XPD) patterns. We demonstrate the power of XPD as a fingerprinting tool and conclude that Pb occupies Bi sites and Dy the Ca sites. The presence of the incommensurate lattice modulation is not visible in XPD, probably due to a Pb-induced, reduced modulation amplitude.

## 1 Introduction

The discovery of high temperature superconductors has triggered numerous studies of the details of their geometrical structure. The superconducting Bi$_2$Sr$_2$Ca$_1$Cu$_2$O$_{8+\delta}$ (Bi2212, $T_c$ = 85 K) is the most extensively studied bismuth-containing superconductor. It has a layered structure and an incommensurate superlattice modulation with the period of 25.8 Å along the $b$ axis. This modulation has been subject of many studies, both at the surface [1–3] and in the bulk [4–6].

Many different materials have been used to dope the pure Bi2212 in order to influence the charge around the Cu-O planes believed to be responsible for superconductivity or to modify the structure. In this context the question about the influence of dopants on the modulation is interesting as well. Pb substitution of Bi in Bi2212 has led to many studies [7–9], because sufficient Pb doping inhibits the modulation.

For the determination of the effects of dopants on the charge distribution it is very important to know what site the dopant atom is occupying and whether it is distributed homogeneously substituting mainly one element of the host compound or clustering together. Chemical knowledge can help to suggest the occupation site, but it remains difficult to prove it unambiguously.

X-ray photoelectron diffraction (XPD) [7,10–12] proves to be the method of choice for substitution site identification. We want to mention that this method may also be applied to other complex compounds, for instance

[a] e-mail: `d.popovic@mx.uni-saarland.de`

minerals. In a previous study, Pillo et al. [11] have investigated Pb,Y-Bi2212 and demonstrated the power of the XPD method for investigating the substitution sites by a direct comparison of diffraction patterns. They find that Pb and Y occupy the Bi and Ca sites of the host material, respectively, and show that the lattice modulation is present again for Y-Pb-Bi2212 although it is absent in Pb-Bi2212 for similar Pb contents.

Here, the occupation sites of Pb,Dy-Bi2212 are studied. XPD is capable of providing the information about the substitution sites and we demonstrate that Pb occupies the Bi sites and Dy the Ca sites. The lattice modulation is not apparent in the XPD patterns as it is the case for pure Bi2212 [12] probably due to a Pb induced, reduced modulation amplitude.

## 2 Experimental

The experimental set-up represents an extended version of the Vacuum Generators ESCALAB Mk II spectrometer, operating with a base pressure in the low $10^{-10}$ mbar region. The spectrometer is equipped with a hemispherical electron-energy analyzer with a three-channeltron detection system. A motorized manipulator allows sample rotation with two degrees of freedom [13,14]. The angular resolution was better than 1° full cone acceptance. All the measurements were carried out at room temperature.

X-ray photoelectron spectroscopy (XPS) and XPD were performed with Mg $K\alpha$ ($h\nu$ = 1253.6 eV) or Si $K\alpha$ ($h\nu$ = 1740 eV) radiation. The spectra have been

measured with a pass energy of 100 eV corresponding to an energy resolution of approximately 1 eV.

In XPD, the emitted photoelectron wave from a chosen core-level scatters at the surrounding atoms and interferes with the directly emitted wave to give an interference pattern as a function of emission angle. For photoelectrons emitted with kinetic energies above approximately 500 eV, this strongly anisotropic angular distribution of photoelectrons gives the possibility to obtain a basic picture of the local, real-space environment of the emitter [14], due to the "forward focusing" phenomenon along the emitter-scatterer axis (for review see Ref. [15]). Prominent intensity maxima in full hemispherical XPD patterns (diffractograms) can often be immediately identified with near-neighbor directions. The photoelectron angular distribution is, to a first approximation, a forward-projected image of the atomic structure around the photoemitters. Its sensitivity to local order and chemical species makes XPD a powerful technique for surface structural investigations. XPD can be used to characterize near surface structure [16], substitution sites [11], film growth [17–19] and even phase transitions [20].

A typical XPD diffractogram consists of intensity at a given core level binding energy for about 5500 angular settings $(\theta, \phi)$ of photoelectron emission angles $\theta$ (polar) and $\phi$ (azimuthal). Measured intensities are represented in a stereographic projection (see Fig. 1). The center of each plot represents normal emission and the outer circle corresponds to grazing emission, $\theta = 90°$. Along each imaginary circle with the center in the center of the plot, theta is constant and phi varies from 0° to 360°. The intensity is represented in a grey-scale plot, with high intensity in white.

Diffractograms presented in this paper are background corrected, i.e., a smooth polar angle dependent background has been subtracted in order to flatten the images and to enhance the contrast.

The samples were grown from nonstoichiometric systems consisting of solute and flux which form a high temperature solution [21]. The single crystals are $2 \times 3$ mm$^2$ large and less than 0.5 mm thick. They were mounted onto the sample holder with silver epoxy. For the measurements the crystals were cleaved in situ at a pressure in the lower $10^{-10}$ mbar region, yielding clean mirrorlike surfaces with (001) orientation. The cleanness was checked by XPS.

## 3 Results and discussion

The near surface composition of the Pb,Dy-Bi2212 was determined by XPS. The Pb:Bi ratio is found to be 0.15. This is below the critical value of about 0.25 for removing the modulation [8,9]. The Dy:Ca ratio is 1.1, showing that large quantities of Ca have been substituted. It is know that XPS results considering composition are not necessarily the same as the ones obtained by other techniques, however the ratios are mostly relevant. Furthermore, they will be used here for comparison with our previous study, which has been performed using the same technique.
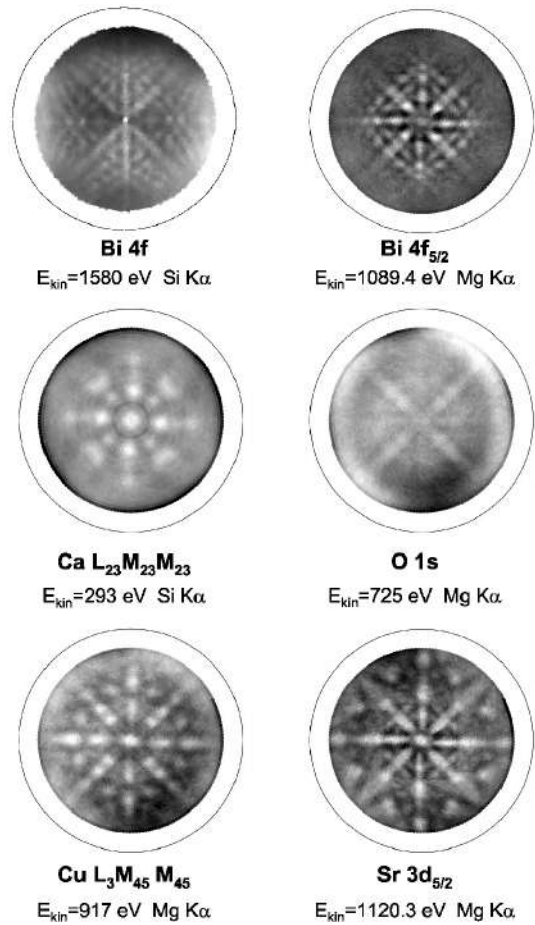


**Fig. 1.** Shown are measurements on the core levels or Auger transitions (Ca and Cu) of elements present in pure Bi2212: Bi 4f (top right), Ca $L_{23}M_{23}M_{23}$, O 1s, Cu $L_3M_{45}M_{45}$ and Sr $3d_{5/2}$. Measurements have been performed with Si-$K\alpha$ radiation (1740 eV) on Pb-Bi2212 for Ca and on Bi2212 for Bi (top left) [12] and with Mg-$K\alpha$ radiation (1253.6 eV) on Pb,Dy-Bi2212 for all the others. Background corrected data (see text) are shown as a linear gray scale plot in stereographic projection.

In Figure 1 we present a set of XPD patterns showing emission from the atomic species of the host material Bi2212: Ca, Bi, O, Cu and Sr. One observes a clear fourfold symmetry of all patterns (except for Fig. 1 (top left) taken from [12] for comparison). This is in contrast to the previous work of Osterwalder et al. [12], where the strong modulation along the b axis in pure Bi2212 causes a considerable deviation from the fourfold symmetry, i.e., where the XPD diffractograms become two-fold symmetric, clearly distinguishing between the crystals a and b axis, as can be seen by comparing the Bi 4f-diffractograms in Figure 1 (top left and right). Modulation is present in our system as well, (as confirmed by low energy electron diffraction (LEED), not shown) but apparently with a weaker amplitude as for the pure Bi2212.

On the other hand, the four-fold symmetry is consistent with the previously published data of Pillo et al. [11]

where the Pb and Y doped Bi2212 has been studied. The concentration of Pb in their crystal (0.27) was large enough to cause the disappearance of the modulation in Pb-Bi2212. However, doping with Y *re*-introduced the modulation, although weaker than the one of the pure Bi2212. In our case the concentration of Pb is well below 0.25 and the modulation is present (because of lack of Pb), as evidenced by LEED, which lets us conclude that Dy can not have a strong influence on reestablishing the modulation. In both studies the modulation appears in LEED images for two different reasons and is in both studies not strong enough to change the XPD-measurements. The overall fine structure in the XPD images is identical for both crystals.

We can conclude that the intensity of the modulation in our system is diminished and probably does not exceed in amplitude the one of Pb,Y-Bi2212, which is significantly smaller than the one for pure Bi2212, but larger than zero. It is very likely that the cause for the reduction of the modulation amplitude is the presence of Pb. Its concentration, however, is not large enough to totally remove the modulation.

The kinetic energies of all the measured core levels or Auger lines are in the vicinity of each other, except for Ca. The measurement of the Ca diffractogram was difficult due to the overlap of the core level lines of the different elements and the small concentration of Ca. In order to obtain a measurement with better statistics, we have investigated Ca in Pb-Bi2212, where it is present in a larger quantity. The Auger transition was the only available emission line for Ca, where, at the same time an emission line of Dy was available close by (within some 100 eV kinetic energy distance). Low kinetic energies (less than approximately 500 eV) are known for the shorter inelastic mean free paths and diminished electron wave anisotropy leading to forward focusing peaks. For a direct comparison of XPD patterns, using XPD as a fingerprinting technique without a detailed understanding of the different interference features, it is therefore important to choose similar kinetic energies.

The structure of the presented diffractograms is quite complicated, but the images are distinctly different from each other. Therefore, instead of trying to understand the details of the fine structure due to interference and forward focusing, the individual patterns can be used as a fingerprint for the respective local real-space environment of the corresponding element, i.e., for the crystallographic site, as previously suggested [11]. Thus, we do not proceed with the structural analysis which can be performed using the measured patterns, but rather use them for the identification method, which demands only the measurements of the diffractograms of the dopants. A comparison with the fingerprints leads directly to the identification of the substitution site. In this sense, the diffractograms in Figure 1 represent characteristic fingerprints for the local real space environment of the different elements and therefore for the different sites.

In Figure 2, the XPD of the dopants, i.e., emission patterns from Pb $4f_{7/2}$ and Dy $3d_{5/2}$ are presented in the
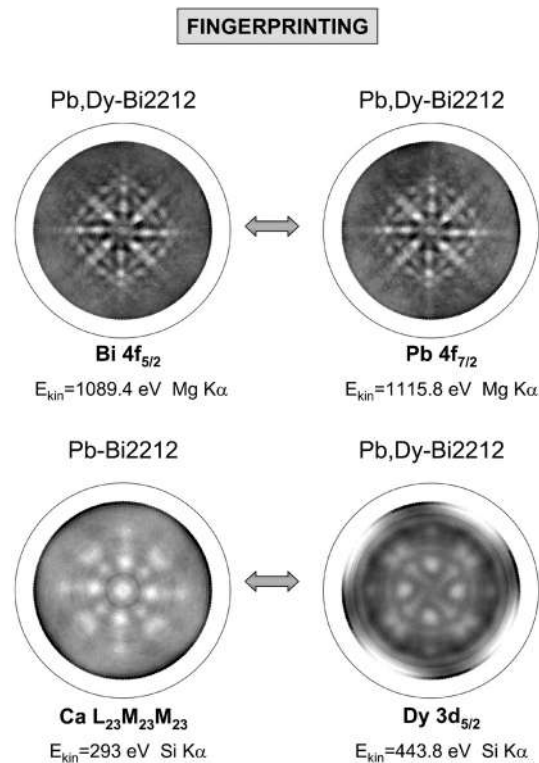


**Fig. 2.** Fingerprinting: direct comparison of the XPD patterns of Bi $4f_{5/2}$ with Pb $4f_{7/2}$ and Ca $L_{23}M_{23}M_{23}$ (Auger transition) with Dy $3p_{3/2}$. All data are background normalized (see text). In addition, the Dy diffractogram has been four-fold symmetrized.

right column. On the left side in Figure 2, the most similar diffraction patterns to the ones on the right side have been chosen among the XPD data of the host material presented in Figure 1. One observes a striking coincidence of the Pb pattern with the one of Bi and of the Dy pattern with the one of Ca. Pb and Bi diffractograms are taken at approximately 1000 eV. In this kinetic energy region forward focusing effects are dominant and we could say that we are comparing projected real-space images of the two elements. Dy and Ca are, on the other hand, measured at lower kinetic energies. This means that the diffractograms are not necessary dominated by the forward focusing effects, and that one can probably not resolve directly the atomic structure from forward focusing directions. However, these lower energies do not hinder fingerprinting, i.e. substitution site identification. From the identical appearance of the two patterns at the similar energies, we can conclude about identical local environments, i.e., chemical sites. We can conclude unequivocally, that Pb and Dy dopant atoms occupy Bi and Ca sites, respectively.

In this study, a simple case of a single element substitution has been treated. By no means the applicability area of the fingerprinting method is limited to single site substitution. Multiple site substitution would lead to a pattern which is a linear combination of the diffraction patterns of those host elements, which are being substituted. One

would accordingly simulate the measured XPD-pattern of the dopant as a linear combination of the patterns of the host in order to determine quantitatively which sites have been substituted and to which extent. This wide range of application possibilities makes fingerprinting one of the most comfortable methods for the investigations of doping and element substitution, as long as the detection limit of XPS (typically a few percent) is respected.

## 4 Conclusion

We have shown that XPD represents a direct tool to determine substitution sites of dopants, even in very complex materials with many constituents with low concentrations. It is demonstrated that XPD can, for these purposes, be used at low kinetic energies – the presence of forward focusing is not a requirement for the fingerprinting. In Pb and Dy doped Bi2212 we have demonstrated that the Pb atoms occupy the Bi sites and the Dy atoms the Ca sites. The substitution sites are similar to the previously published case of Pb,Y-Bi2212 [11]. The modulation along the crystal $b$ axis is present, according to the composition of Pb,Dy-Bi2212. However, the four-fold symmetry of all the XPD patterns indicates that the lattice modulation is weaker than in pure Bi2212, which is assigned to the Pb doping.

## References

1. P.A.P. Lindberg, Z.-X. Shen, B.O. Wells, D.B. Mitzi, I. Lindau, W.E. Spicer, A. Kapitulnik, Appl. Phys. Lett. **53**, 2563 (1988)
2. M.D. Kirk, J. Nogami, A.A. Baski, D.B. Mitzi, A. Kapitulnik, T.H. Geballe, C.F. Quate, Science **242**, 1673 (1988)
3. C.K. Shih, R.M. Feenstra, J.R. Kirtley, G.V. Chandrashekhar, Phys. Rev. B **40**, 2682 (1989)
4. T. Siegrist, S.A. Sunshine, L.F. Schneemeyer, D.W. Murphy, R.J. Cava, B. Batlogg, R.B. van Dover, R.M. Fleming, S.H. Glarum, S. Nakahara, R. Farrow, J.J. Krajewski, S.M. Zahurak, J.V. Waszczak, J.H. Marshall, P. Marsh, L.W. Rupp Jr., W.F. Peck, Phys. Rev. B **38**, 893 (1988)
5. Y. Le Page, W.R. McKinnon, J.-M. Tarascon, P. Barboux, Phys. Rev. B **40**, 6810 (1989)
6. A. Yamamoto, M. Onada, E. Takayama-Muromachi, F. Izumi, T. Ishigaki, H. Asano, Phys. Rev. B **42**, 4228 (1990)
7. P. Schwaller, P. Aebi, H. Berger, C. Beeli, J. Osterwalder, L. Schlapbach, J. Electron Spectrosc. Relat. Phenom. **76**, 127 (1995)
8. N. Fukushima, M. Yoshiki, Phys. Rev. B **50**, 2696 (1994)
9. N. Fukushima, H. Niu, S. Nakamura, S. Takeno, M. Hayashi, K. Ando, Physica C **159**, 177 (1989)
10. P. Schwaller, P. Aebi, J. Osterwalder, L. Schlapbach, M. Shimoda, T. Mochiku, K. Kadowaki, Phys. Rev. B **48**, 6732 (1993)
11. T. Pillo, J. Hayoz, P. Schwaller, H. Berger, P. Aebi, L. Schlapbach, Appl. Phys. Lett. **75**, 1550 (1999)
12. J. Osterwalder, P. Aebi, P. Schwaller, L. Schlapbach, M. Shimoda, T. Mochiku, K. Kadowaki, Appl. Phys. A **60**, 247 (1995)
13. P. Aebi, J. Osterwalder, P. Schwaller, L. Schlapbach, M. Shimoda, T. Mochiku, K. Kadowaki, Phys. Rev. Lett. **72**, 2757 (1994)
14. J. Osterwalder, T. Greber, A. Stuck, L. Schlapbach, Phys. Rev. B **44**, 13764 (1991)
15. C. Fadley, *Synchrotron Radiation Research: Advances in Surface Science*, edited by R.T. Bachrach (Plenum, New York, 1990), Vol. 1
16. R. Fasel, P. Aebi, R. Agostino, D. Naumović, J. Osterwalder, A. Santaniello, L. Schlapbach, Phys. Rev. Lett. **76**, 4733 (1996)
17. R. Fasel, P. Aebi, L. Schlapbach, J. Osterwalder, Phys. Rev. B **52**, R2313 (1995)
18. J. Hayoz, T. Pillo, R. Fasel, L. Schlapbach, P. Aebi, Phys. Rev. B **59**, 15975 (1999)
19. J. Hayoz, C. Koitzsch, D. Popović, M. Bovet, D. Naumović, L. Schlapbach, P. Aebi, Surf. Rev. Lett. **9**, 235 (2002)
20. J. Hayoz, S. Sarbach, T. Pillo, E. Boschung, D. Naumović, P. Aebi, L. Schlapbach, Phys. Rev. B **58**, R4270 (1998)
21. P. Almeras, H. Berger, G. Margaritondo, Solid State Commun. **87**, 425 (1993)

# Investigation of surface structure related features in the multiple-scattering simulations of photoelectron diffraction of 3C–SiC(0 0 1)-$c(4 \times 2)$

D. Stoltz[a,*], S.E. Stoltz[b], S.M. Widstrand[c], L.S.O. Johansson[c]

[a]*Materialfysik, MAP, KTH-Electrum, SE-16440 Kista, Sweden*
[b]*MAX-Lab, Lund University, SE-22100 Lund, Sweden*
[c]*Department of Physics, Karlstad University, SE-65188 Karlstad, Sweden*

## Abstract

In this paper we have conducted a systematic study of the photoelectron diffraction (PED) effects from the 3C–SiC(0 0 1)-$c(4 \times 2)$ surface by means of multiple-scattering calculations. Two models have been proposed to describe this surface: alternately up and down dimers (AUDD) [P. Soukiassian, F. Semond, L. Douillard, A. Mayne, G. Djuradin, L. Pizzagalli, C. Joachim, Phys. Rev. Lett. 78 (1997) 907], based on the scanning tunneling microscopy data, and missing-row asymmetric-dimer (MRAD) [W. Lu, P. Krüger, J. Pollmann, Phys. Rev. Lett. 81 (1998) 2292], based on the total energy pseudopotential calculations. By calculating PED patterns from different emitters in these two models, we show that the surface structure induced features are visible even in total emission diffraction patterns. For the overall diffractogram a scatterer properties of the first layer under the surface become crucial due to the backscattering at low kinetic energies. This layer is Si-layer in the MRAD model, but C-layer in the AUDD model. While this causes clear differences between the diffraction patterns of the AUDD and the MRAD models, it is shown to diminish the differences between the PED patterns of the AUDD and the other models which consist of only one monolayer of Si on top.

## 1. Introduction

The studies of SiC have been triggered by its more desirable properties for the applications, but nevertheless similar structure and reconstructions as the ones of the Si surfaces. SiC is being widely implemented in the short-wavelength optoelectronic devices (green, blue and violet diodes, ultraviolet photodetectors), transistors and transistor memory cells [1]. Interface formation between SiC and other materials, which is highly relevant for the applications, depends primarily on the properties of the silicon–carbides surface reconstruction. And several different reconstructions can be obtained on the 3C–SiC(0 0 1) (3C stands for the cubic SiC polytype) surface by diminishing the Si/C ratio: $(1 \times 1)$, $(3 \times 2)$, $(5 \times 2)$, $c(4 \times 2)$, $c(2 \times 2)$. Another surface reconstruction, $(2 \times 1)$, is shown to be a defective phase of $c(4 \times 2)$ [2,3], enabling the only known reversible surface phase transition $c(4 \times 2) \leftrightarrow (2 \times 1)$ in a semiconducting compound [2].

The similarity of the $(2 \times 1)$ reconstructions on 3C–SiC(0 0 1) and on Si(1 0 0) has made 3C–SiC(0 0 1) very popular for surface studies. However, the $c(4 \times 2)$ reconstruction of the Si(0 0 1) surface is not similar to the one of the 3C–SiC(0 0 1). This reconstruction has thus been intensively studied and two structural models have been proposed to describe it: the alternately up and down dimers (AUDD) [4] and the missing-row asymmetric-dimer

---

*Corresponding author.

  *E-mail address:* dunjap@kth.se (D. Stoltz).

(MRAD) [5] models. The latter was based on total energy pseudopotential calculations and some comparison with the available scanning tunneling microscopy (STM)-data. It suggests that on top of the surface Si-layer another 0.5 ML of Si exists and forms asymmetric dimers. The AUDD model was based on the STM measurements and supported later by core-level investigations [6] and the observations of the reversible phase transition from the $c(4 \times 2)$ to the $(2 \times 1)$ surface [2,3]. Within this model the surface is terminated by a single Si-layer which forms rows of symmetric dimers that are displaced vertically alternating up and down.

Until now many different proofs have been shown in favor of one or the other model describing the $c(4 \times 2)$ surface. There are four independent experimental studies supporting the AUDD model: STM data [4], core-level spectroscopy [6], STM and ARUPS [2], hydrogenation studies [7]. The MRAD is supported by pseudopotential calculations [5], early core-level studies [9] and the same STM data, as the AUDD [4].

In the present paper, we report structural investigation of the 3C–SiC(0 0 1)-$c(4 \times 2)$ surface by means of a powerful surface structure investigation method—multiple-scattering calculations of the PED angular intensity distributions. In this way, we are in a position to determine the nature of the contributions from the two competing models of the 3C–SiC(0 0 1)-$c(4 \times 2)$ surface to the diffraction patterns or the photon energy scans. Our calculations reveal where the most prominent differences between the models can be seen in the PED patterns and what is causing them. The systematic study of the MRAD, the AUDD and some other models than AUDD with surface terminated by only one Si monolayer reveals the relationship between the backscattering dominated diffraction patterns and surface termination in terms of Si coverage.

## 2. Calculations

Whereas a PE-diffractogram at kinetic energies above 500 eV is a stereographic projection of the atomic positions (for review see Ref. [10]), at lower kinetic energies more isotropic electron scattering occurs, which requires multiple-scattering analysis methods [11,12]. But multiple-scattering effects are also restricted by the decrease of the inelastic mean-free path to only a few Å. We have used the free software MSCD developed by Chen and Van Hove [11] for the multiple-scattering calculations of the PED-patterns.

We have been running our calculations with Rehr–Albert approximation order 2 and multiple-scattering order 8 on a cluster with the radius 8 Å and depth 7 Å. The $\theta$-range and step were 0–76 or 90°/2° and $\varphi$-range and step were 0–357°/3°. The incident angle of the light was 55° and polarization was linear, chosen with respect to our experimental study.

The bulk 3C–SiC(0 0 1) structure is zinc-blende. The lattice constants used for the presented calculations were experimental value of $a_0/\sqrt{2} = 3.08$ [4] for the AUDD model and theoretical $a_0/\sqrt{2} = 3.068$ [13] for the MRAD model. This difference turned out to be irrelevant. Clusters containing ~100 atoms have been used for the calculations presented in this paper in order to minimize the time of the calculations. This was necessary because the extension of our systematic study required some 150 calculations. Larger cluster has been used for some selected calculations (217 instead of 90 atoms; not shown) and they reveal even more fine structure than the presented ones, but are consistent with all conclusions of this paper.

## 3. Results

Two structural models have been proposed to describe the 3C–SiC(0 0 1)-$c(4 \times 2)$ surface: the AUDD [4] and the MRAD [5] models. They are presented from top and side view in Fig. 1, with Si atoms in grey and C atoms shaded and a bit smaller. Only the Si atoms from the topmost layer are presented with black and white circles. Within the AUDD model the surface is terminated by a single Si-layer (Fig. 1b) which forms rows of symmetric dimers that are displaced vertically alternating up and down, as can be seen in Fig. 1a. The black dimers in Fig. 1a and b are 0.1 Å below the white ones [4]. A unit cell of the $c(4 \times 2)$ reconstruction is chosen in one of many possible ways and marked by a rhomb.

Contrary to the AUDD surface termination, the MRAD model suggests that on top of the surface Si-layer (grey circles in Fig. 1c marked 3–6 in Fig. 1d; this is the layer which consists of up and down dimers in the AUDD model) another 0.5 ML of Si exists and forms asymmetric dimers (black and white circles). This asymmetry refers to both unequal lateral displacements of the two dimer-atoms from the centrum of the underlying Si network (grey circles in Fig. 1c), but also to the differences in the $z$-position of these two atoms, $z$ measuring the distance perpendicular to the surface, as can be seen in Fig. 1d. The black atoms in Fig. 1c and d are 0.544 Å below the white ones [5]. Despite these significant structural differences, both models have the same $c(4 \times 2)$ symmetry, which is also in the case of MRAD marked by one possible choice of a unit cell.

The numbers in Fig. 1b and d stand for inequivalent atoms used for the calculations and will be referred to in the following. The second and the third layer in the MRAD model as counted from the surface are having four inequivalent atoms each. This is because of the reconstruction induced small changes in the atomic positions of the underlying layers. If this is neglected, the last three layers in Figs. 1b and d are same.

In Fig. 2 we show multiple-scattering simulations of the PED using the MRAD model of the 3C–SiC(0 0 1)-$c(4 \times 2)$ surface at the kinetic energy of a Si 2p core level excited with the photon energy of 200 eV. In PED, the emitted photoelectron wave from a chosen core-level (Si 2p) scatters at the surrounding atoms and interferes with the directly emitted wave to give an interference pattern as a
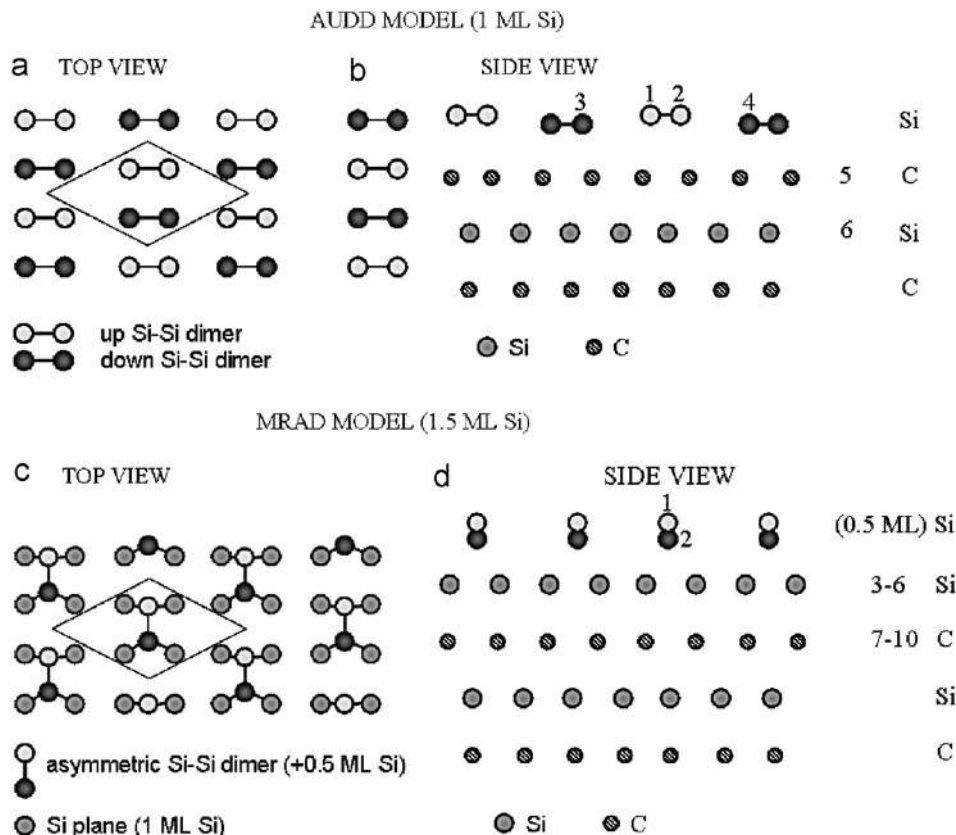
Fig. 1. Schematic representation (not to scale!) of the two models of the 3C–SiC(0 0 1)-$c(4 \times 2)$ surface: (a) top and (b) side view of alternately up and down dimers (AUDD) [4] and (c) top and (d) side view of missing-row asymmetric-dimer (MRAD) [5]. Surface termination in terms of Si coverage is given in brackets for both models.
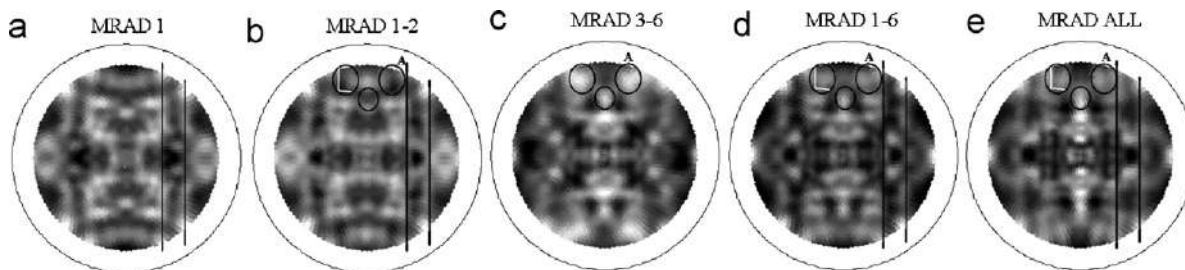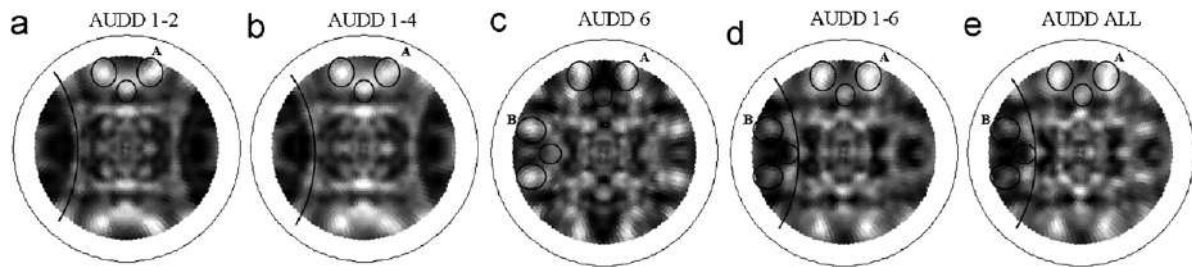


Fig. 2. MSCD calculations of the Si 2p diffractograms from the different (marked on top) inequivalent Si atoms in the MRAD model. (a) 1 corresponds to the topmost atom in the asymmetric dimer. (b) 2 corresponds to the second atom in the asymmetric dimer. 1–2 cover the topmost 0.5 ML of Si consisting of asymmetric dimers. (c) 3–6 cover the entire underlying Si-layer. (d) 1–6 is thus total 1.5 ML Si at the surface in the MRAD model. (e) ALL stands for emission from all Si atoms within the cluster. Linear grey-color scheme is used, with high intensity in white and low intensity in black. Photon energy used for the calculation was 200 eV.

function of emission angle $(\theta, \varphi)$. Intensities are represented in a stereographic projection. The center of the plot represents normal emission $(\theta = 0°)$ and the outer circle corresponds to grazing emission, $\theta = 90°$. Along each imaginary circle with the center in the center of the plot, $\theta$ is constant and $\varphi$ varies from $0°$ to $360°$ when moving anti-clockwise ($\varphi = 90°$ on the top). Horizontal direction is identical to the horizontal direction of the schematic representations of models in Fig. 1. The intensity is represented in a linear grey-color scheme, with high intensity in white and low intensity in black. In order to flatten the

images, to enhance and correct absolute intensities, for each polar angle the intensities at different azimuthal angles have been divided by the average intensity at that polar angle. The result is an image with high anisotropy at all emission angles.

The MRAD model is not symmetric with respect to the horizontal axes. It is "asymmetric", as its name says, and as we have already discussed in Fig. 1. It is, however, possible that the real surface consists of two different domains with equal distributions. Therefore we show in this paper 2-fold symmetrized MRAD calculations.

Fig. 3. MSCD calculations of the Si 2p diffractograms from the different (marked on top) inequivalent Si atoms in the AUDD model. 1–4 (b) cover the topmost 1 ML of Si consisting of up (1–2) (a) and down (3–4) dimers. (c) 6 is the Si-layer beneath the surface. (d) 1–6 denotes inequivalent Si emitters numbered 1, 2, 3, 4 and 6. The carbon layer 5 is not emitting. (e) ALL stands for emission from all Si atoms in the cluster. Linear grey-color scheme is used, with high intensity in white and low intensity in black. Photon energy used for the calculation was 200 eV.

While the experimental PED patterns are measured at a certain kinetic energy, which corresponds to the contribution from a certain bulk or surface component in the Si 2p core level, these different contributions are simulated in our calculations by different choice of the emitters. The kinetic energy is kept constant because changing it over the span of Si 2p peak does not change the calculations. Fig. 2 shows MSCD calculations from various inequivalent atoms (their numbers are written above each diffractogram and correspond to the numbers from Fig. 1d) in the MRAD model.

The first and the second inequivalent atom correspond to the up (white in Fig. 1b and d) and the down (black in Fig. 1b and d) atoms in the asymmetric dimers. Whether one observes the emission from the topmost atoms (Fig. 2a) or from the entire dimers (Fig. 2b) does not seem to play a role: Fig. 2a and b are very alike. It is important to notice that the emission from the topmost atoms in any model contributes to the diffraction pattern mostly via backscattering. Forward scattering is possible only from the lower dimer to the upper dimer and would still contribute only at the very grazing emission angles, due to the small height differences in the topmost layer. It is thus mostly backscattering effects that we see in the diffraction patterns from the topmost layers.

The greatest difference between the AUDD and the MRAD models lies in the extra Si-halflayer which is incorporated in the MRAD model. Inequivalent atoms of the full Si-layer underneath this extra 0.5 ML are denoted by numbers 3–6 (see Fig. 1d). When the emission from this layer (Fig. 2c) is added with the emission from the topmost (extra) halflayer, the result (Fig. 2d) resembles the total emission (Fig. 2e). This is visible in the development of the high-intensity features in the regions encircled by ellipses A, but also in the contrast at lower polar angles. Surface emission Figs. 2a and b show no high intensity in angular region A. They contain instead a prominent intensity depletion marked by the white line. High intensity in this region in the total emission (Fig. 2e) obviously originates from the Si-layer (3–6) or similar bulk layers. The intensity minimum appears when the topmost Si atoms (1–2) are added in Fig. 2d and persists even in the total emission. This means that the intensity depletion marked

by the white line in region A is a fingerprint of surface emission.

Another surface feature in the total emission are straight high-intensity lines marked in Fig. 2. They appear in the topmost 0.5 ML Si (1–2), but are not visible in the bulklike emission from the Si-underlayer (3–6). As they are present in Figs. 2d and e, we conclude that they are another surface-related feature visible in total emission.

In Fig. 3 simulations at the kinetic energy of a Si 2p core level excited with the photon energy of 200 eV from various inequivalent atoms (their numbers are written above each diffractogram and they correspond to the numbers from Fig. 1b in the AUDD model) are presented. The first and the second inequivalent atom emission (Fig. 3a) corresponds to the up dimer (white in Fig. 1a), while the first to fourth inequivalent atom emission (Fig. 3b) corresponds to both up and down dimers (white and black in Fig. 1a). Whether one observes the emission from the up or from both up and down dimers does not seem to play a role (Fig. 3a and b are very alike). This is similar to the MRAD model, where emission from the up atom in the dimer is very similar to the emission from the entire dimer. It is also the same for both models that the emission from the topmost layers is dominated by backscattering. However, the very patterns of the surface emission from the MRAD calculations are not similar to the ones of the AUDD calculations. This will be discussed in detail with the next figure.

Prominent high-intensity lines are visible in surface emissions of the AUDD model as well. However, they look like more round arcs in the case of AUDD, as marked in Fig. 3. They appear in Fig. 3a and b and stay visible as the low background intensity up to the total emission PED pattern in Fig. 3e. As for the region marked by ellipses A, it shows unsplit high intensity in emissions from all components. This is thus another fingerprint of the surface emission, which is visible in the total emission and which is different for the AUDD and the MRAD. As for the high-intensity features in ellipses B, they come from the non-surface silicon: they appear in Fig. 3c. Nevertheless, they appear only in the AUDD model, as can be seen in both emission from this Si component or in the total emission.

The next full Si-layer is separated from the topmost one by a layer of carbon in the AUDD model and is described by the inequivalent atom 6. (Carbon layer is described by the inequivalent atom 5, see Fig. 1b.) The emission from this layer (Fig. 3c), or from this layer and the topmost layer together (Fig. 3d) resembles already the total emission (Fig. 3e), similarly to the previously stated in the case of the MRAD model. Only in the case of the MRAD model that means that the emission from the topmost 1.5 ML of Si gives bulklike signal. In the case of the AUDD model it is the emission from the topmost 1 ML of Si with the emission from the first underlying 1 ML of Si. The letter is separated from the former one by one monolayer of C. This is obviously an important issue in understanding the differences between the AUDD and the MRAD features in PED, because Si and C have different scattering properties. This will become even more clear with the next image.

As any determination of the surface structure would preferably rely on the differences in the surface emission, we compare in Fig. 4 angular PE-intensity distributions of the MRAD (a) and AUDD (b) models from selected inequivalent Si atoms at the surface calculated at the kinetic energy of a Si 2p core level excited with the photon energy of 200 eV. These diffractograms have already been shown in Figs. 2b and 3a up to the polar angle of $\theta = 76°$. Here we present the calculations up to the maximal grazing emission of $\theta = 90°$. Same grey scale is preserved as in Figs. 2b and 3a, in order to avoid confusion. This has diminished the intensity of the otherwise strong grazing emission features, which would make the rest of the image appear dark if an individual scale was used.

The emission from the two topmost inequivalent Si atoms in both models is chosen for this figure, which correspond to the topmost 0.5 ML of Si in the MRAD (the dimers, black and white circles in Fig. 1b) or only top dimers in the AUDD (up dimers, white circles in Fig. 1a). In the case of the AUDD choosing only top dimers corresponds also to only 0.5 ML. To justify such a

selection, we have shown that calculations of the emission from the up dimers in the AUDD or from both up and down dimers almost do not differ from each other (Fig. 3a and b). Similarly, the emission from the topmost atom in the MRAD is very similar to the emission from the whole topmost asymmetric dimer (Fig. 2a and b). And the inclusion of any other Si-layers among the emitters in both models would render the image bulklike. Furthermore, the surface component in the Si 2p core-level spectra is attributed to the up dimers in the AUDD [6] or to the asymmetric dimers in the MRAD [5].

Fig. 4 shows that the grazing emission anisotropy of the diffractograms of the two models is very similar. Lower polar angles reveal more clear differences between the two models. Most of the features, as well as the intensity contrast or the background intensity are quite different. High-intensity lines of the AUDD pattern show rounded forms, as marked in Fig. 4b by arc. In the MRAD pattern, more straight lines are present, as marked in Fig. 4a. However, in both of them there appears a rectangular shape at lower polar angles—only with different orientation. Within this rectangle four prominent features with intensity depletion in centrum can be noticed in the corners in the case of MRAD (Fig. 4a, arrow A), whereas three vertical maxima are placed to the left and to the right of the centrum of the AUDD diffractogram (Fig. 4b, white arrows). These are the most obvious differences between the two models and they appear at relatively low polar angles. The only high-intensity feature at higher polar angles which is different for the AUDD and the MRAD models is marked by an arrow B in Fig. 4a. It is very strong in the case of the MRAD, but not present at all in the case of the AUDD. It also shows intensity depletion in its centrum. Unfortunately, none of these features are clearly present in the total emissions from different models (see Figs. 2e and 3e).

As already mentioned with the two previous figures, the emission from the topmost atoms in both models contains mostly backscattered intensity. Emitters in Fig. 4a are the asymmetric dimers of the MRAD model. As depicted in Fig. 1d, photoelectrons from these atoms would back-scatter in the first line from the underlying Si atoms (3–6). In the case of the AUDD, emitters in Fig. 4b are the top dimers. As shown in Fig. 1b these are placed at the nearly same plane as the down dimers. The backscattering of photoelectrons from the up to the down dimers would thus contribute only at the grazing emission. At lower polar angles, one would expect the underlying carbon layer (5) to be of much stronger influence to the diffraction patterns. The differences that we observe between the PED patterns of the two models in Fig. 4 are thus dominated by the different structure and scattering properties of the first underlying layer, which is Si in the case of the MRAD and C in the case of the AUDD. It is important to notice that this crucial difference is introduced by an extra monolayer of Si on top of the MRAD model. If the MRAD was terminated by a single Si-layer, photoelectrons from the
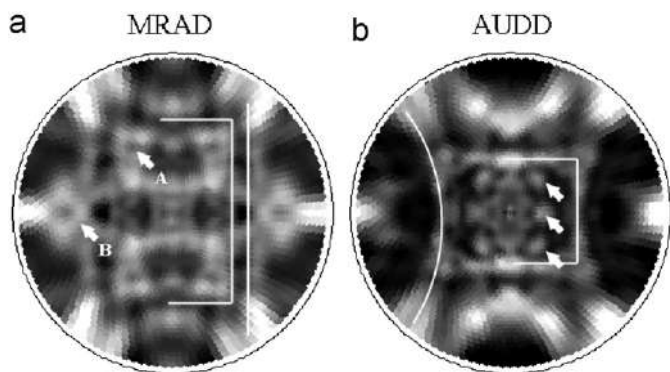


Fig. 4. MSCD calculations of the Si 2p diffractograms from the topmost Si atoms: topmost extra 0.5 ML of Si consisting of asymmetric dimers in the MRAD model (1–2) (a) and up dimers in the AUDD model (1–2) (b). Linear grey-color scheme is used, with high intensity in white and low intensity in black. Photon energy used for the calculation was 200 eV.
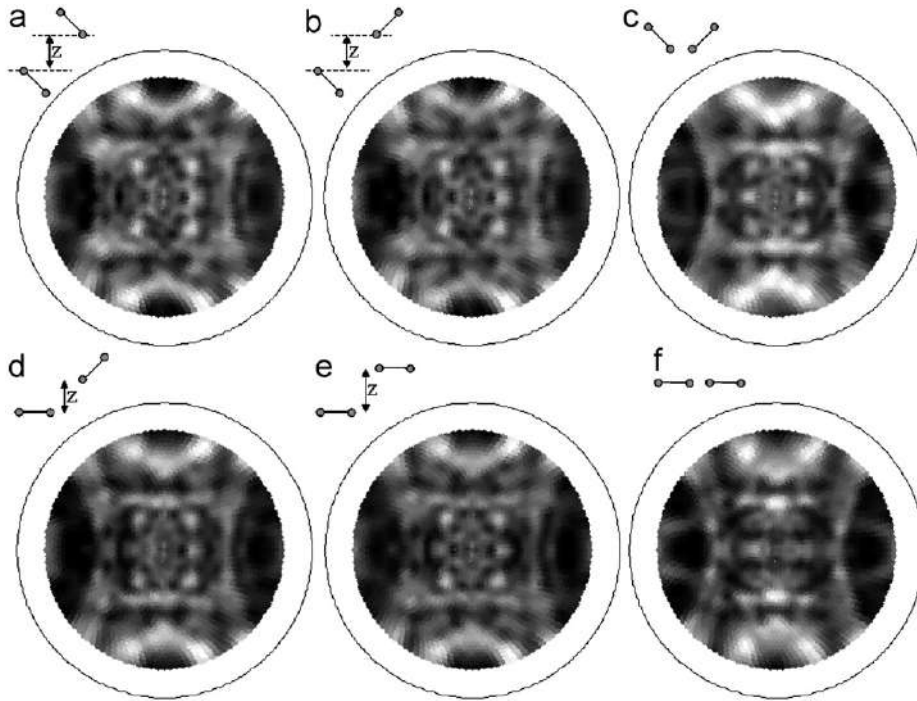
Fig. 5. MSCD calculations of the Si 2p diffractograms from the variations of the AUDD model. Schematic representation (not to scale!) of the topmost Si-layer of the calculated model is given on top. Emitters are the topmost dimers (a, b, d, e) or one of the dimers (c, f). Linear grey-color scheme is used, with high intensity in white and low intensity in black. Photon energy used for the calculation was 200 eV.

topmost atoms would also be backscattered from the underlying C-layer, as in the case of the AUDD.

As the thickness of the silicon termination of the surface appears to be crucial for the different PED patterns of MRAD and AUDD, we have investigated some variations of the AUDD model and present the MSCD calculations of them together with their schematic geometric arrangements in Fig. 5. Calculations are done at the kinetic energy of a Si 2p core-level excited with the photon energy of 200 eV. Emitters are the same as in Fig. 4: the topmost dimers in Figs. 5a, b, d, e or one of the dimers in Figs. 5c and f. The original AUDD model has the same geometry as depicted in Fig. 5e, but in Fig. 5e, the vertical separation between the up and down dimers ($z$) is doubled (from 0.1 to 0.2 Å). Contrary to that, the same separation is zero in Fig. 5f, which thus corresponds to the $(2 \times 1)$ reconstruction according to the AUDD model [6]. If we compare them to the original AUDD-model calculation from Fig. 3a, we will not see any change in the main features or the contrast distribution, except for some washing out of the three intensity maxima to the left and to the right from the normal emission (see white arrows in Fig. 4b) in the case of $(2 \times 1)$ reconstruction (Fig. 5f). The fine differences are certainly beyond the quality of any measured diffractogram. Furthermore, we have tried to impose some more drastic changes to the AUDD model, by making the up dimers asymmetric (Fig. 5d) or both dimers asymmetric in three different ways (Fig. 5a–c), with the dimer height 0.1 Å and $z = 0.1$ Å. Note that Fig. 5c corresponds to a similar $c(4 \times 2)$ reconstruction of the Si(0 0 1) surface. The rough
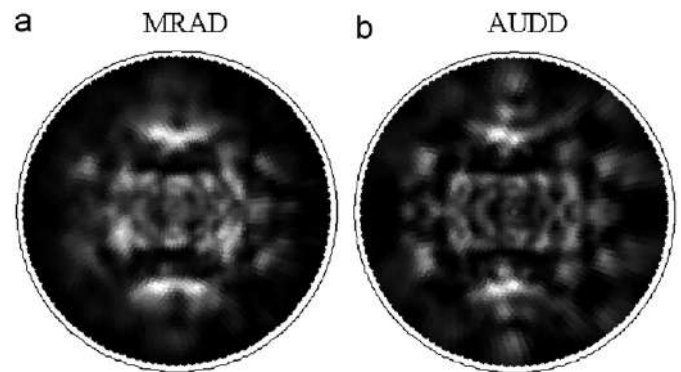


Fig. 6. MSCD calculations of the C 1s emission from the C-layer closest to the surface in (a) the MRAD (7–10) and (b) the AUDD (5) model. Linear grey-color scheme is used, with high intensity in white and low intensity in black. Photon energy used for the calculation was 300 eV. No background correction was implemented.

symmetry of the patterns as well as the flow of the main lines or the intensity distribution do not seem to be significantly altered with respect to the original AUDD calculations. This points out the difficulty of differentiating the AUDD model from any other model with the 1 ML Si termination of the surface and shows that the power of PED in differentiating between the MRAD and the AUDD lies precisely in their different Si surface coverages.

One remaining question is if there is any other way than the PED patterns used here to see the differences between the two models better. Fig. 6 shows calculated PE-intensity angular distributions of the MRAD (a) and AUDD (b)

models from the carbon layer closest to the surface at the energy of the C 1s emission. Photon energy used for the calculation was 300 eV. With the MSCD-determined binding energy of C 1s, the resulting kinetic energy of the calculation is ~50 eV, which is half of the kinetic energy for the Si 2p calculations. Carbon calculations have been performed up to the grazing angles ($\theta = 90°$). The carbon layer is lying on top of the bulk structure in both models and is covered by Si-terminated surface in both models. Only the thickness of the Si termination is slightly different: 1.5 ML in the MRAD model or 1 ML in the AUDD model.

The patterns in Fig. 6a and b are very similar. The only noticeable difference between the two patterns is the washed out intensity at higher polar angles (the outer ring) in the MRAD simulation. This is a consequence of the extra 0.5 ML Si on the surface in this model. This thicker Si coverage induces thicker barriers for the photoelectrons leaving the carbon layer at higher polar angles. As the AUDD model is characterized by a surface termination consisting of a single Si-layer, the grazing emission area of the pattern appears less disturbed. In Fig. 6 we show calculations with no background correction. This correction normally enhances the grazing emission features, yielding high anisotropy at all emission angles. We have left it out in Fig. 6 in order to see the intensity differences in the grazing emission in two models due to different Si coverages.

Apart from diffractograms, photon energy scans (e-scans) are also a powerful tool in the surface structure determination. They are easier to collect experimentally, but are not as rich with information as the diffraction patterns. In Fig. 7

we present calculated e-scans for the MRAD and the AUDD models. They are calculated for the Si 2p emission and represented as a graph of photoemission wave vector dependent Chi-values. Chi values have been calculated within the MSCD package as Chi = $(I - I_0/I_0)$, where $I_0$ stands for the smooth intensity background and $I$ for the intensity [11]. Wave vector has been calculated in $Å^{-1}$ as $0.512331\sqrt{E_{kin}(eV)}$ [11].

Fig. 7a shows substantial differences between the e-scans of the two models at the polar angle $\theta = 45°$ and azimuthal angle $\varphi = 0°$. This azimuthal angle corresponds to the horizontal axes in Fig. 1. If we thus observe the photoemission at $45°$ between the horizontal and the vertical axes in Fig. 1b and d, the outgoing photoelectrons will have different variation of the intensities with photon energy for the two models. However, the differences tend to become smaller as the wave vector, i.e. photon energy becomes larger than $7Å^{-1}$ (not shown).

If the azimuthal angle is changed to $\varphi = 90°$ (Fig. 7b), which corresponds to the vertical axes in Fig. 1a and c, the differences between the two models become invisible. This shows that $\varphi = 0°$ reveals better the differences between the models. Furthermore, both calculations for $\varphi = 90°$ and $270°$ are shown for the MRAD in Fig. 7b. It is clear that these two directions are not equivalent by symmetry as they are in the AUDD model. The MRAD e-scan along $\varphi = 90°$ differs more from the AUDD one than the MRAD e-scan along $\varphi = 270°$. The most prominent difference arises around $5.5 Å^{-1}$, i.e. ~220 eV photon energy. This is, however, still not sufficiently strong to enable successful differentiation between the AUDD and the MRAD



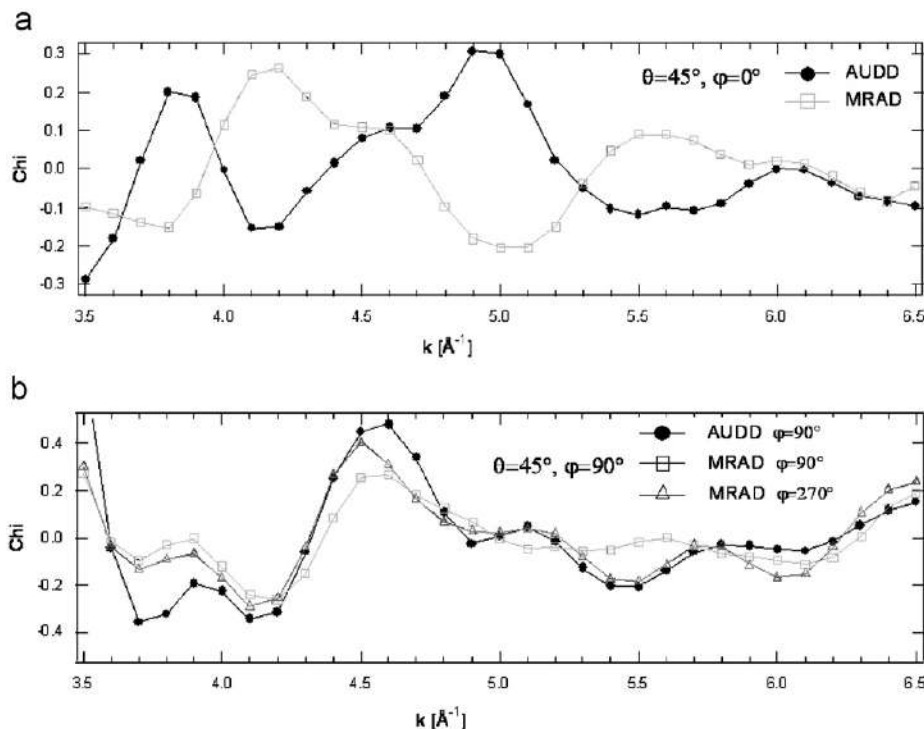Fig. 7. MSCD calculations of the e-scans at Si 2p emission of the AUDD and the MRAD models at $\theta = 45°$ and (a) $\varphi = 0°$ or (b) $\varphi = 90°$.

predictions, if a comparison with the experimental e-scan in this direction should be made.

## 4. Discussion

The development of the MRAD model [5] was directly related to the early core-level studies suggestion [9] about more than one layer of Si on the top of the 3C–SiC(0 0 1)-$c(4 \times 2)$ surface, inspired most of all by an anomalously large binding energy shift of the S1 component ($-1.4$ eV) in the Si 2p spectrum. The earliest core-level studies [14] (energy resolution 0.4 eV) suggested that there is about 1 ML of excess Si at the surface, the pseudopotential calculations [5] discovered a total energy minimum for extra 0.5 ML of Si. However, the most recent core-level investigation [6] (energy resolution better than 150 meV) interprets different surface and bulk contributions in the Si 2p core-level according to the 1 ML Si termination of the AUDD surface model.

One of the powerful structural techniques which can be implemented to solve the dilemma between the two models is PED at low kinetic energies. When excited by low photon energy synchrotron light, the outgoing photoelectrons experience enhanced backscattering and diminished mean-free path. This can be used to study the emission from the topmost layers due to the backscattering from the underlying layer. This underlying layer is a Si-layer in the MRAD, but a C-layer in the AUDD model, and they have different scattering properties. This factor obviously plays a more crucial role than the precise surface structure in deciding which model gives more appropriate description of the 3C–SiC(0 0 1)-$(4 \times 2)$ surface. This is obvious because the changes in the calculated diffractograms when varying drastically the geometry of the top Si-layer from the one of AUDD are minor compared to the differences between the calculated diffractograms of the AUDD and the MRAD models.

It is very challenging to collect data with good enough statistics to be able to extract diffractogram on the surface-related feature S1 [6]. The challenge is not defined only by the low intensity of this component in the Si 2p spectrum, but also by the presence of multiple overlapping components which would have to be used consistently for the Si 2p fits at all angular settings. It is therefore important that we show in this paper that some important features of the surface emission are preserved in the total emission diffraction patterns. Furthermore, a measured diffractogram on the surface-related feature S1 would not reveal more about the origin of this component, as emission from different surface emitters yields very similar images within one model. That means that even a very demanding PED experiment could not confirm that the S1 component is, for instance, related to the up dimers only and not both up and down dimers of the AUDD model. Similarly, it would not be able to tell if this peak is due to the up atom or entire asymmetric dimer of the MRAD model. And finally, it is not realistic to expect that it could be assigned to only one of the various 1 Si ML models.

We show that contrary to the usual expectations, the experimental investigations at grazing emission, emission of carbon underlayer or e-scans at horizontal tilt angles would not be useful for determination of the better model of the 3C–SiC(0 0 1)-$(4 \times 2)$ surface. We suggest that new *ab initio* calculations will be needed to explain the experimental support of the AUDD model and to give a complete explanation of the measured 3C–SiC(0 0 1)-$c(4 \times 2)$ electronic structure [3].

## 5. Conclusions

We show a systematic multiple-scattering study of the PED from the AUDD and the MRAD models of the 3C–SiC(0 0 1)-$(4 \times 2)$ surface. Our calculations demonstrate the choice of parameters which is optimal for PED-related comparative study of the two models. Surface-related diffraction features in the diffractograms are shown to persist even when all atoms are emitters. The backscattering of the photoelectrons appears to be dominant in differentiating the two models, as the layer underneath the topmost atoms is Si in the MRAD, but C in the AUDD. This is more crucial than the very surface structure, whose drastic changes induce only minor modifications of the diffraction pattern.

## References

[1] P.A. Ivanov, V.E. Chelnokov, Semiconductors 29 (1995) 1003.
[2] V.Y. Aristov, L. Douillard, O. Fachoux, P. Soukiassian, Phys. Rev. Lett. 79 (1997) 3700.
[3] L. Duda, L.S.O. Johansson, B. Reihl, H.W. Yeom, S. Hara, S. Yoshida, Phys. Rev. B 61 (2000) R2460.
[4] P. Soukiassian, F. Semond, L. Douillard, A. Mayne, G. Djuradin, L. Pizzagalli, C. Joachim, Phys. Rev. Lett. 78 (1997) 907.
[5] W. Lu, P. Krüger, J. Pollmann, Phys. Rev. Lett. 81 (1998) 2292.
[6] V.Y. Aristov, H. Enriquez, V. Derycke, P. Soukiassian, Phys. Rev. B 60 (1999) 16553.
[7] S.M. Widstrand, L.S.O. Johansson, K.O. Magnusson, M.I. Larsson, H.W. Yeom, S. Hara, S. Yoshida, Surf. Sci. 479 (2001) 247.
[9] M.L. Shek, Surf. Sci. 349 (1996) 317.
[10] C. Fadley, in: R.T. Bachrach (Ed.), Synchrotron Radiation Research: Advances in Surface Science, vol. 1, Plenum Press, New York, 1990.
[11] Y. Chen, M.A.V. Hove, ⟨http://electron.lbl.gov/mscdpack/mscdpack.html⟩.
[12] Y. Chen, F.J.G. de Abajo, A. Chaseé, R.X. Ynzunza, A.P. Kaduwela, M.A.V. Hove, C.S. Fadley, Phys. Rev. B 58 (1998) 13121.
[13] M. Sabisch, P. Krüger, A. Mazur, M. Rohlfing, J. Pollmann, Phys. Rev. B 53 (1996) 13121.
[14] V.M. Bermudez, J.P. Long, Appl. Phys. Lett. 66 (1994) 475.

ELSEVIER

# X-ray photoelectron diffraction investigation of the cleavage plane in $1T$-transition metal dichalcogenides

D. Stoltz[a],*, S.E. Stoltz[b]

[a]*Materialfysik, MAP, KTH-Electrum, 16440 Kista, Sweden*
[b]*MAX-Lab, Lund University, 22100 Lund, Sweden*

## Abstract

We present a detailed study of the three members of the $1T$-transition metal dichalcogenides: $TiSe_2$, $TaSe_2$ and $TaS_2$ by means of the X-ray photoelectron diffraction combined with single-scattering simulations. Our simulations of different surface terminations and their comparison with the measured diffraction patterns allow to determine that the cleavage occurs within the van der Waals gap. Single-scattering calculations are shown to simulate very well the measured diffractograms on these compounds.
© 2007 Elsevier B.V. All rights reserved.

## 1. Introduction

The latest studies of the layered $1T$-transition metal dichalcogenides (TMDs) $TaSe_2$, $TaS_2$ and $TiSe_2$ have mostly been focused on the electronic properties of their charge density wave phases. All three compounds are charge density wave materials and the ground state in the charge density wave phase of the first two compounds is directly related to the appearance of the pseudogap at the Fermi level [1]. The fact that the pseudogap at the Fermi level was recently also considered to be a precursor of the high-temperature superconductivity in the Bi-containing compounds [2,3] makes an important relationship between the cuprates and structurally simpler layered materials, TMDs. As most of the investigation methods of the charge density waves in TMDs implement photoemission, questions about the surface termination become important for both structural investigations and electronic structure interpretations.

TMDs are compounds with the general formula $MC_2$, where $M$ stands for transition metal of the group IVb (Ti),

Vb (Ta) or VIb, and $C$ stands for chalcogen (S, Se). They are further divided into structural subgroups ($1T, 2H, \ldots$), where number denotes the number of the coupled $CMC$ sandwiches and the letter stands for the (trigonal, hexagonal,…) symmetry. In all structural subgroups, hexagonally packed atomic planes are being stacked into $CMC$ sandwiches separated by the van der Waals (vdW) gap. This layered structure makes TMDs very interesting for the problems of strongly correlated materials, in particular because of the similarity with the high-temperature superconductors. It causes anisotropic electronic properties, which make also $1T$-TMDs quasi-2D systems. The preparation technique of these materials, cleaving perpendicular to the surface normal ([0 0 1]), relies upon this structure as well.

In spite of the fact that the surface preparation of the TMDs is most commonly cleavage perpendicular to the surface normal, experimental evidence of the surface termination of samples prepared by this technique, to our knowledge, does not exist. It is expected that the cleavage occurs within the vdW gap. However, it proves very difficult or impossible to determine the element occupying the topmost surface layer by means of scanning tunneling microscopy (STM), core-level-background analysis

*Corresponding author. Tel.: +46 87904154.
  *E-mail address:* dunjap@kth.se (D. Stoltz).

(QUASES or similar) or X-ray photoelectron spectroscopy (XPS). Tunneling in STM can also be achieved in the non-surface layers, which makes it difficult to determine the surface termination. XPS or XPS background analysis are not efficient either, because there are many atomic layers of both metal and chalcogen within the mean-free path of the photoelectrons.

In the present paper, we report structural investigation of the 1T-surfaces by means of a powerful surface structure investigation method, X-ray photoelectron diffraction (XPD). We implement this technique with the use of motorized sample rotation and automatized data collection. Complementary to the measurements, we simulate the measured diffraction patterns by means of single-scattering (SS) calculations. In this way, we are in position to investigate the termination of the surface.

## 2. Experimental aspects

The experimental set-up represents an extended version of the vacuum generators ESCALAB Mk II spectrometer, operating with a base pressure in the low $10^{-10}$ mbar region. The spectrometer is equipped with a hemispherical electron-energy analyzer with a three-channeltron detection system. A motorized manipulator allows sample rotation with two degrees of freedom [4]. XPD was performed with Mg K$\alpha$ ($h\nu = 1253.6$ eV) radiation incident at the sample surface at 54° with respect to the normal emission direction. The spectra have been measured with a pass energy of 100 eV corresponding to an energy resolution of approximately 1 eV. The angular resolution was better than 1° full cone acceptance. All the measurements were performed at room temperature.

In XPD, the emitted photoelectron wave from a chosen core-level scatters at the surrounding atoms and interferes with the directly emitted wave to give an interference pattern as a function of emission angle. For photoelectrons emitted with kinetic energies above approximately 500 eV, this strongly anisotropic angular distribution of photoelectrons gives the possibility to obtain a basic picture of the local, real-space environment of the emitter, due to the "forward focusing" phenomenon along the emitter–scatterer axis (for review see Ref. [5]). Prominent intensity maxima in full hemispherical XPD patterns (diffractograms) can often be immediately identified with near-neighbor directions. The photoelectron angular distribution is, to a first approximation, a forward-projected image of the atomic structure around the photoemitters. Its sensitivity to local order and chemical species makes XPD a powerful technique for surface structural investigations. It can be used to characterize film growth [6–8], phase transitions [9], substitution sites [10,11] and orientation of the adsorbed molecules [12].

A typical diffractogram consists of intensity at a given core-level binding energy for about 5500 angular settings ($\theta, \varphi$) of photoelectron emission angles $\theta$ (polar) and $\varphi$ (azimuthal). Measured intensities are represented in a stereographic projection (see Fig. 3–5). The center of each plot represents normal emission and the outer circle corresponds to grazing emission, $\theta = 90°$. Along each imaginary circle with the center in the center of the plot, $\theta$ is constant and $\phi$ varies from 0° to 360°. The intensity is represented in a linear gray-scale plot, with high intensity in white. Diffractograms presented in this paper are intensity-normalized in the following way: for each polar angle the intensities at different azimuthal angles have been divided by the average intensity at that polar angle [13]. Absolute intensities have thus been corrected and the result is an image with high intensity at all emission angles.

Samples of 1T-TaS$_2$ and 1T-TaSe$_2$ have been grown from the elements by reversible chemical reaction with iodine as a transport agent, between 950° (hot zone) and 900° (cold zone) [14]. TiSe$_2$ was grown at 500 °C with ICl$_3$ as a transport agent in the presence of a slight Se excess [15]. The single crystals are $2 \times 3$ mm$^2$ large and less than 0.5 mm thick. They were mounted onto the sample holder with silver epoxy and cleaved *in situ* at a pressure in the lower $10^{-10}$ mbar region, yielding clean mirror-like surfaces with (0 0 0 1) orientation. The cleanness was checked by XPS.

## 3. Calculations

An often used technique to prove the geometrical interpretation of XPD patterns are single-scattering calculations (SSC) [16–18]. This method proved to give good qualitative agreement with the measurements, especially in the overlayer systems, where the multiple scattering is expected to be much reduced. The SSC are performed within the "spherical wave model" [17], as described in detail in Ref. [18].

We have performed simulations of the XPD patterns using SSC program [19] on clusters containing $\sim 1700-1900$ metal and chalcogen atoms within the lateral radius of 20 Å and the total height of $\sim 30$ Å, i.e. six repeated 1T-sandwiches of chalcogen–metal–chalcogen planes. Emitters have been chosen up to the full cluster depth in all calculations. The partial-wave scattering phase shifts were calculated with the MUFPOT program [20], which is based on the muffin–tin potential approximation [21], with the wave functions taken from Ref. [22]. All the calculations have been performed at room temperature with uncorrelated Debye–Waller factor.

The inelastic effects are described in the SSC formalism by an exponential decay of wave amplitude [18]. Empirical studies lead to conclusions that mean-free path values in the SSC correspond to the half of the values known from the literature [23,24]. According to this result, we have used the mean-free path value $\sim 10$ Å, which corresponds to $\sim 20$ Å, which is within the range of the mean-free paths measured on different elements or compounds at 1000 eV kinetic energy [25,26].

One way to judge quantitatively about the quality of the fit between the simulation and the experimental photoelectron
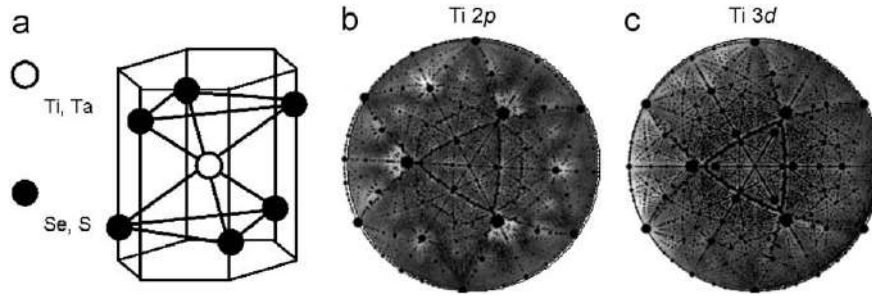
Fig. 1. (a) Schematic representation of the 1T-structure. On the right: stereographic projection of all the possible forward focusing directions in the 1T-TiSe$_2$ cluster (black dots, size increases closer to the surface)superimposed on the XPD data (linear gray-scale with high intensity in white and low in black) for Ti (b) and Se (c). Measured up to apolar angle of $\theta = 88°$.

diffraction is by means of *R*-factor based on the space of the multipole coefficients [27]. Our calculations show that *R*-factor values are not reliable, probably due to over-emphasis of the strength of the forward focusing peaks by the SSC leading to neglecting of the interference details, the shape of the forward focusing peaks or any (fine) structure at all. *R*-factor will therefore not be used.

1T-TMDs are of CdI$_2$ structural type with the space group $D_{3d}^3$ (P$\bar{3}$ml). The metal atoms have the octahedral coordination within this structural type, as is shown in Fig. 1(a). The lattice constants of 1T-compounds which have been used for the calculations are $a = 3.346$ Å, $c = 5.860$ Å for TaS$_2$, $a = 3.477$ Å, $c = 6.272$ Å for TaSe$_2$ and $a = 3.535$ Å, $c = 6.004$ Å for TiSe$_2$ [28].

## 4. Results

In Fig. 1(b, c) the stereographic projections of the possible forward focusing directions for Ti (b) and Se (c) are presented in black dots. They were calculated on the described cluster up to the polar angle of 90° according to the geometrical structure of the 1T-TiSe$_2$. Larger points correspond to the scatterers closer to the emitter. Under-neath are XPD measurements on Ti 2p (kinetic energy of 798.2 eV) and Se 3d (kinetic energy of 1200 eV) core-levels in 1T-TiSe$_2$. Trigonal symmetry is dominant and consis-tent with the crystal symmetry of the 1T-family. The patterns of Ti and Se are similar.

The most prominent "triangle" in the images is a clear fingerprint of trigonal symmetry. It is furthermore related to the most important features in the diffraction patterns of 1T-TMDs. Its sides lie along the Kikuchi bands, which originate from the deeper layers of the 1T-structure. These bands are also visible experimentally and they exist due to the forward focusing within the close packed crystal planes [29]. The vertices of the triangle are strong forward focusing maxima. They have complex structure due to the multiple forward focusing possibilities for the emission from the second 1T-sandwich beneath the surface. They are represented by the largest dot in the calculation of the scattering directions, as well as by the strongest intensity in the measured diffraction patterns.
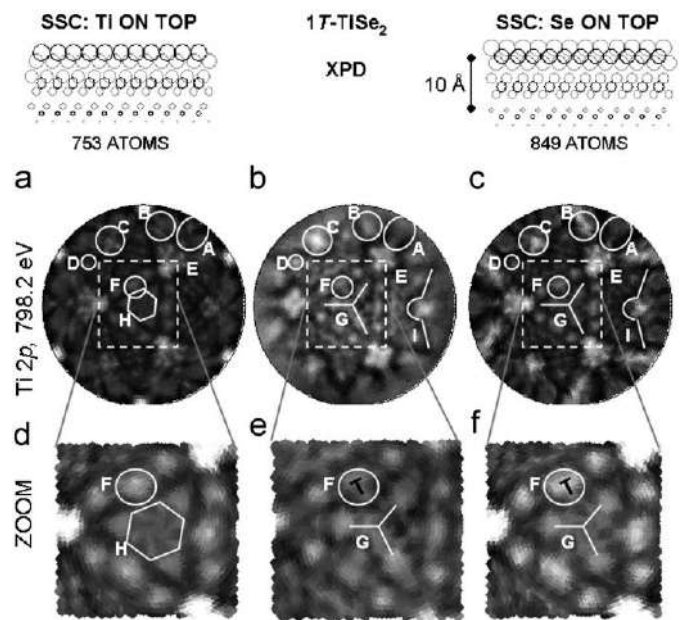


Fig. 2. XPD pattern of 1T-TiSe$_2$ at Ti 2p (kinetic energy of 798.2 eV) core-level (b) is compared to the SSC with the cluster terminated by Ti (a) and Se (c). Linear gray-color scheme is used, with high intensity in white and low intensity in black. Maximum polar angle is $\theta = 88°$. Clusters are illus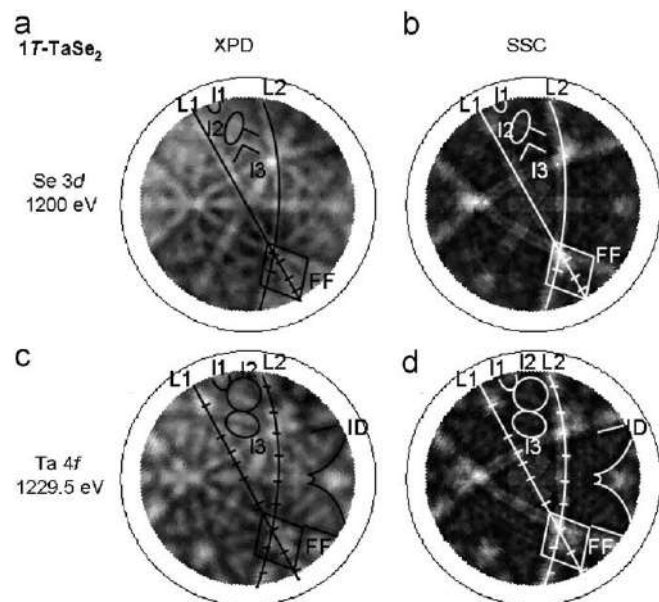trated on top, with Ti atoms in darker and Se in light gray circles, decreasing in radius with the distance from the surface. Zoom of the central parts of the patterns in (a), (b) and (c) is presented with enhanced contrast in (d), (e) and (f), respectively.

In Fig. 2, we present calculations of the two possible surface terminations of the cleaved 1T-TiSe$_2$. One notices immediately that the SSC images are darker than the measured ones, with very strong forward focusing maxima. This is a known disadvantage of the SSC, they over-emphasize the forward focusing peaks. The main features of the diffractograms for both terminations differ in many aspects. The shape of the forward focusing maxima (E) is less compact and intense when Ti atoms are on top (a), and corresponds thus less to the measured XPD pattern (b). The lines originating close to these maxima and continuing towards the outer circle corresponding to the grazing emission (A) are visible only if Se is on top (c), and these lines appear also in the XPD data. Similarly, features B, C

and D are much better reproduced in Fig. 2(c). Feature D does not even exist in the Ti-terminated calculation (a).

Some important differences appear at lower polar angles as well.However, they are hardly visible in the patterns (a), (b), (c).Therefore, a zoom in the near normal-emission area of the diffractograms in (a), (b), (c) is shown in (d), (e), (f). Contrast is enhanced in order to provide better view of the important features. Feature F is shaped like a letter T in the experiment (e) and in the SSC pattern from the Se-terminated cluster (f). In the case of Ti-termination, the intensity within the marked circle F is more round. Finally, the centrum of the patterns, which corresponds to near-normal emission is the most different for the two models of the cleavage plane. While both XPD (e) and SSC from the cluster with Se on top (f) have clearly 3-fold symmetric central feature G, in the centrum of SSC from Ti-terminated cluster one observes 6-fold symmetric feature, encircled by a hexagon H in (d).

In the case of Se emission from different surface terminations (not shown), almost only difference is the appearance of the forward focusing peaks at the grazing emission in the calculations when Se is on top, which is difficult to prove experimentally (low intensity at grazing emission).

Finally, in Figs. 3–5 we present single-scattering simulations (on the right) of the measured XPD patterns (on the left) for $1T$-TaS$_2$, $1T$-TaSe$_2$ and $1T$-TiSe$_2$, respectively. Calculations were done with cleavage plane within the vdW gap. Trigonal symmetry is evident on all diffractograms in Figs. 3–5, as discussed with Fig. 1.

Kikuchi bands are clearly visible in the measured diffractograms and well reproduced by the calculation.



Fig. 4. XPD (left) and SSC (right) patterns on Se 3d (kinetic energy of 1200 eV) and Ta 4f (kinetic energy of 1229.5 eV) core-levels in $1T$-TaSe$_2$. Linear gray-color scheme is used, with high intensity in white and low intensity in black. Maximum polar angle is $\theta = 78°$.
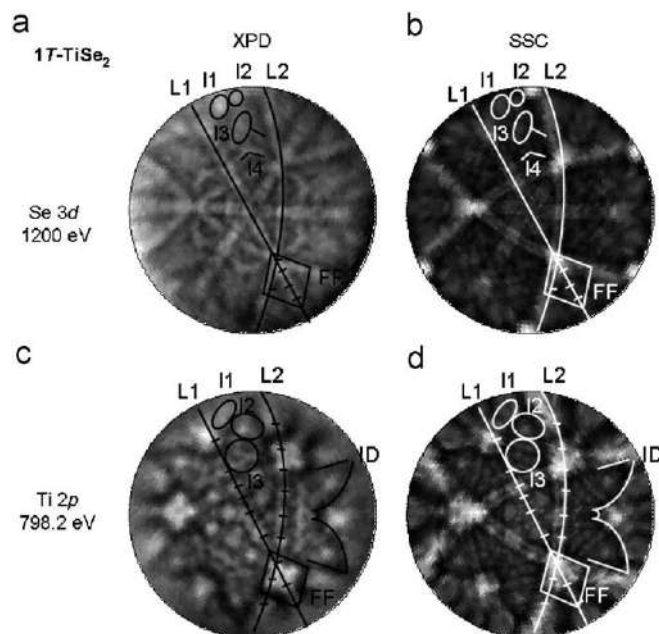


Fig. 5. XPD (left) and SSC (right) patterns on Se 3d (kinetic energy of 1200 eV) and Ti 2p (kinetic energy of 798.2 eV) core-levels in $1T$-TiSe$_2$. Linear gray-color schemeis used, with high intensity in white and low intensity in black. Maximum polar angle is $\theta = 88°$.

The two most prominent ones are marked by L1 and L2. In the XPD patterns on the chalcogen core-level, these lines are almost homogeneous in intensity. Separate maxima which they contain are discernible only close to grazing emission. On the other hand, in the case of metal emission lines L1 and L2 are clearly separated into several intensity peaks, which are also marked by ticks along L1 and L2 in Figs. 3–5(c). Looking at the corresponding SSC,



Fig. 3. XPD (left) and SSC (right) patterns on S 2p (kinetic energy of 1092 eV) and Ta 4f (kinetic energy of 1229.5 eV) core-levels in $1T$-TaS$_2$. Linear gray-color scheme is used, with high intensity in white and low intensity in black. Maximum polar angle is $\theta = 78°$.

we conclude that both the lines in the case of chalcogen emission, as well as their structure in case of metal emission are well reproduced by the simulation.

At the crossing points of the Kikuchi lines, forward focusing maxima appear in the XPD patterns. They are marked by a rhomb in the lower part of the pattern and letters FF. As they appear at relatively high polar angles, some intensity maxima are resolved and marked along the lines L1 and L2 even in the case of chalcogen emission. In Figs. 3–5(a) 4–5 separate intensities are marked along L1 and L2 within the rhomb FF. In Figs. 3–5(c) it is 3 such maxima for all investigated compounds. These maxima are well reproduced in the SSC in Figs. 3–5(b, d). Intensities at the outermost corner of the rhomb, pointing towards the highest polar angles are the most difficult to recognize in the calculations, as the FF peak at the lower polar angles has very strong intensity. The intensity is present, although not as strong as at the lower polar angles.

The 3-fold features in the center of the patterns in Figs. 3–5(a, c) are successfully simulated (b, d). The same holds for the interference shapes between the Kikuchi lines, which are clearly visible even in the calculations, in spite of the intensity-disadvantages of the single-scattering models. These features are marked as I1–3 in Figs. 3–5(c, d) and I1–4 in Figs. 5(a, b). Their shape is less clearly defined than in the case of Kikuchi lines or FF maxima, but they appear in both XPDs and calculations. Finally, all experimental patterns show three intensity depletions in the form of number "3". This is much clearer in the case of metal emission, and has thus been marked only there with the ID line. This line is very well simulated by the SSC, as can be seen in Figs. 3–5(d).

All features from the experimental diffraction images appear in the SS simulated patterns. These features are not identical for the three investigated different compounds, but they are very similar. However, some shortcomings of the SS formalism are clear from thicker and split Kikuchi lines, weak intensity of the highest polar angle FF peak and some extra interference features, which appear in the calculations, but not in the experimental diffractograms.

## 5. Discussion

In the determination of the surface termination of the layered materials, the effectivity of SSC can be compared to the cases of adsorbates, where multiple scattering is expected to be much reduced. Our investigation shows that the calculations with the chalcogen termination give much better description of the measured data than calculations based on the metal-terminated surfaces. One third cleavage possibility exists, also between the metal and the chalcogen planes, leaving the surface terminated by two chalcogen layers. This possibility can be excluded directly, because measured diffractogram on Ti core-level (Fig. 2c) is not more blurred than the Se diffractogram (Fig. 2a) at the grazing emission. This indicates that it is not likely that Ti layer is covered by two extra chalcogen layers.

It turns out that all features from the measured diffractograms are reproduced by the SSC in our study, even without the inclusion of the charge–density wave refined coordinates. This makes us more confident in our choice of SSC instead of computationally more intensive multiple-scattering simulations. Knowing that the strong intensity of the FF peaks in the calculated spectra could dominate in the linear gray-scale of the total pattern and thus diminish totally the intensity of the remaining features, we have relied upon a special intensity normalization procedure [13]. Within this procedure, which is described in the *Experimental* section of this paper, one obtains enhanced intensity at all emission angles, thanks to the polar-angle dependent intensity normalization. In this way it is certain that the manipulation of the gray-scale would not introduce any novelties in the data analysis.

## 6. Conclusion

Successful single-scattering calculations of $1T$-TiSe$_2$, $1T$-TaSe$_2$ and $1T$-TaS$_2$ are presented, exhibiting very good agreement with the experimental diffractograms. The investigation of the Ti emission and calculations for different surface terminations shows cleavage within the van der Waals gap.

## Acknowledgments

## References

[1] M. Bovet, D. Popović, F. Clerc, C. Koitzsch, U. Probst, E. Bucher, H. Berger, D. Naumović, P. Aebi, Phys. Rev. B 69 (2004) 125117.
[2] H. Ding, T. Yokoya, J.C. Campuzano, T. Takahashi, M. Randeria, M.R. Norman, T. Mochiku, K. Kadowaki, J. Giapintzakis, Nature 382 (1996) 51.
[3] Z.-X. Shen, D.S. Dessau, D.S. Marshall, C.H. Park, P. Fournier, A. Kapitulnik, Science 273 (1996) 325.
[4] P. Aebi, J. Osterwalder, P. Schwaller, L. Schlapbach, M. Shimoda, T. Mochiku, K. Kadowaki, Phys. Rev. Lett. 72 (1994) 2757.
[5] C. Fadley, in: R.T. Bachrach (Ed.), Synchrotron Radiation Research: Advances in Surface Science, vol. 1, Plenum, New York, 1990.
[6] R. Fasel, P. Aebi, L. Schlapbach, J. Osterwalder, Phys. Rev. B 52 (1995) R2313.
[7] J. Hayoz, T. Pillo, R. Fasel, L. Schlapbach, P. Aebi, Phys.Rev. B 59 (1999) 15975.
[8] J. Hayoz, C. Koitzsch, D. Popović, M. Bovet, D. Naumović, L. Schlapbach, P. Aebi, Surf. Rev. Lett. 9 (1) (2002) 235.
[9] J. Hayoz, S. Sarbach, T. Pillo, E. Boschung, D. Naumović, P. Aebi, L. Schlapbach, Phys. Rev. B 58 (1998) R4270.
[10] T. Pillo, J. Hayoz, P. Schwaller, H. Berger, P. Aebi, L. Schlapbach, Appl. Phys. Lett. 75 (1999) 1550.

[11] D. Popović, M. Bovet, H. Berger, P. Aebi, Eur. Phys. J.Appl. Phys. 30 (2005) 171.
[12] R. Fasel, P. Aebi, R. Agostino, D. Naumović, J. Osterwalder, A. Santaniello, L. Schlapbach, Phys. Rev. Lett. 76 (1996) 4733.
[13] R. Fasel, Data analysis software XPD plot.
[14] B. Dardel, M. Grioni, D. Malterre, P. Weibel, Y. Baer, F. Lévy, Phys. Rev. B 45 (1992) 1462.
[15] F. Lévy, Y. Froidevaux, J. Phys.: Condens. Matter 12 (1979) 473.
[16] P.A. Lee, Phys. Rev. B 13 (1976) 5261.
[17] S. Kono, S.M. Goldberg, N.F.T. Hall, C.S. Fadley, Phys. Rev. B 22 (1980) 6085.
[18] D. Naumović, A. Stuck, T. Greber, J. Osterwalder, L. Schlapbach, Phys. Rev. B 47 (1993) 7462.
[19] P. Aebi, SSC Software, University of Fribourg, 2001.
[20] P. Aebi, MUFPOT Software, University of Fribourg, 2001.
[21] J.B. Pendry, Low energy Electron Diffraction, Academic Press, London, 1974.
[22] E. Clementi, C. Roetti, At. Data Nucl. Data Tables 14 (1974) 177.
[23] J. Osterwalder, A. Stuck, D.J. Friedman, A. Kaduwela, C.S. Fadley, J.M. de Leon, J.J. Rehr, Phys. Scr. 41 (1990) 990.
[24] R. Trehan, C.S. Fadley, Phys. Rev. B 34 (1986) 6784.
[25] M.P. Seah, W.A. Dench, Surf. Interface Anal. 1 (1979) 2.
[26] C.J. Powell, Surf. Sci. 44 (1974) 29.
[27] R. Fasel, P. Aebi, J. Osterwalder, L. Schlapbach, R.G. Agostino, G. Chiarello, Phys. Rev. B 50 (1994) 14516.
[28] J.A. Wilson, A.D. Yoffe, Adv. Phys. 18 (1969) 193.
[29] J. Osterwalder, E.A. Stewart, D. Cyr, C.S. Fadley, J.M. de Leon, J.J. Rehr, Phys. Rev. B 35 (1987) 9859.

# Two-dimensional states in the electronic structure of Au/ $(\sqrt{3} \times \sqrt{3}) - R30°$-4H-SiC(0 0 0 1)

D. Stoltz [a,*], S.E. Stoltz [b], L.S.O. Johansson [c]

[a] *Kamerlingh Onnes Laboratory, Leiden University, P.O. Box 9504, 2300 RA Leiden, The Netherlands*
[b] *MAX-Lab, Lund University, SE-22100 Lund, Sweden*
[c] *Deptartment of Physics, Karlstad University, SE-65188 Karlstad, Sweden*

## Abstract

We present an angle-resolved photoemission study of the valence band of Au/ $(\sqrt{3} \times \sqrt{3}) - R30°$-4H-SiC(0 0 0 1). Several different two-dimensional states could be identified, depending on the Au coverage and annealing temperature. In the case of silicide at the surface, two-dimensional Shockley-like state is observed for higher coverages, but a potential interface state is observed at low coverages of Au. In the case of a gold film at the surface a true, confined Shockley-type surface state is observed.
© 2007 Elsevier B.V. All rights reserved.

## 1. Introduction

Shockley-type surface state in the L-gap of the Au(1 1 1) surface is since the discovery of states dispersionless with the change of photon energy [1,2], established as a model system for electronic states in two dimensions. Its free-electron like parabolic dispersion is considered a fingerprint of a two-dimensional electron gas. As such, it has been observed after deposition of similar metals on Au(1 1 1) [3,4] or growth of Au films on metals [5] or vicinal semiconductors [6,7]; it has been shown on vicinal Au surfaces [8] or in Au-clusters [9]. Its shape and binding energy carry information about surface energetics, interface and confinement.

Au on Si has been one of the most interesting systems for both applications in electronic devices as for fundamental studies of interface formation and diffusion in the past decades [10–14]. The interest in Au/SiC interface has been growing during the past decade [15–18], as SiC started replacing Si in high temperature, high speed, high power and high voltage sensor and electronic devices [19]. Au/SiC is

a metal/semiconductor system with a small lattice mismatch ($a_{Au(1 1 1)}$=2.89 Å, $a_{4HSiC(0 0 0 1)}$=3.073 Å). However, the Au/SiC interface is rather complex due to high diffusivity of both Au in SiC and Si in Au. It is also sensitive to the annealing temperature. It has been shown that at 1–4 ML Au annealed under 700° a silicide is formed at the surface, while at 5 ML Au annealed at 700° a significant amount of unreacted gold remains on top of the substrate. [18]

The Shockley-state in Au(1 1 1) exists in the inverted sp-band gap due to the boundary conditions at the surface. [20] Quantum-well states in intermetallic systems are confined within the same projected sp bulk band gap. [21,3] On the other hand, semiconductors like 4H-SiC(0 0 0 1) have a real gap across the Fermi level and its position determines the binding energies of the quantum-well and surface states. $(\sqrt{3} \times \sqrt{3}) - R30°$-reconstructed 4H-SiC(0 0 0 1)-surface is the only one which exhibits a surface state within this gap [22].

In this paper we present a systematic study of the changes of the electronic structure of the $(\sqrt{3} \times \sqrt{3}) - R30°$-reconstructed 4H-SiC(0 0 0 1) under deposition of Au and by means of synchrotron radiation based angle-resolved photoelectron spectroscopy. We follow the disappearance of the SiC-surface state and the formation of the d-band of Au together with the Shockley-like surface state.

* Corresponding author. Tel.: +31 71 527 8407.
*E-mail address:* stoltz@physics.leidenuniv.nl (D. Stoltz).

## 2. Experimental

The experiments have been performed at the beamline 33 at the national synchrotron facility MAX-lab in Lund (Sweden). Beamline 33 is bending magnet based and allows for photon energies in the range between 15 and 200 eV. The end station is an angle resolving VG analyzer (ARUPS 10), which was used in this study with angular resolution of $\pm 2°$ and energy resolution of $\leq 100$ meV. The detector is rotatable in two angular degrees of freedom: in the horizontal and in the vertical plane. The sample-manipulator is also rotatable around two axis: the polar and the azimuthal axis. The polar angle was set to give an incidence angle of the light of $45°$. The azimuthal orientation of the sample was monitored by low energy electron diffraction (LEED). The base pressure of the analysis chamber was $4 \times 10^{-11}$ mbar, while that of the preparation chamber was in the lowest $10^{-10}$ mbar region.

The 4H-SiC(0 0 0 1) wafer with $8°$ miscut in the $[11\bar{2}0]$ direction was purchased from Cree. It is high quality (low micropipe) N-type wafer polished on both sides. Precleaning was performed in methanol and by HF (5%) etching before the introduction in the UHV-chamber. *In situ* preparation started with outgassing at $T$ ¡600 °C. A well ordered $3 \times 3$ surface was obtained after 30 min anneal of the sample at $800°$ C in $\sim 2$ ML/5 min Si flux [23–25]. The $(\sqrt{3} \times \sqrt{3}) - R30°$-reconstruction (short $\sqrt{3}$) was obtained by annealing the sample for additional 30 min at $1000°$ C with no Si flux [23–25]. For temperature reading a pyrometer was used, with the emissivity 0.85 [25]. The temperature gradient over the sample was $\sim 50$ °C, which might have led to the onset of $(6\sqrt{3} \times 6\sqrt{3}) - R30°$-reconstruction at the highest temperature end of the sample.

Gold was deposited on the $(\sqrt{3} \times \sqrt{3}) - R30°$-surface from a W-filament carrying a Au-piece at $\sim 0.5$ ML/min. Deposited films were post-annealed at $650–700°$ C (due to the already mentioned temperature gradient) during 5 min. The same emissivity value has been used for the pyrometer readings as in the case of the clean surface. The appearance and the quality of the reconstructions were checked by LEED. The sample was then cooled with liquid nitrogen for the photoelectron spectroscopy measurements. The Au coverages were estimated from the core-level intensities and quartz-microbalance measurements.

Fermi level correction has been performed according to the Fermi edge measurements on the tantalum foil under the same experimental conditions as in the Au/SiC experiment. The intensities have been calibrated with respect to the synchrotron current and the number of sweeps. The FITXPS2 software [26] was used for core-level fits.

## 3. Results and discussion

Fig. 1 presents the development of the valence band (VB) with gold coverage. Spectrum from the $(\sqrt{3} \times \sqrt{3}) - R30°$-4H-SiC(0 0 0 1) ($\sqrt{3}$-4H-SiC) is shown at the bottom with the dashed line. Surface state characteristic for this surface is clearly visible at 1.3 eV binding energy in agreement with Ref. [22]. The $\sqrt{3}$-4H-SiC valence band maximum (VBM) at $\sim 2.3$ eV [22] is also marked on the $\sqrt{3}$-4H-SiC spectrum. At binding energies
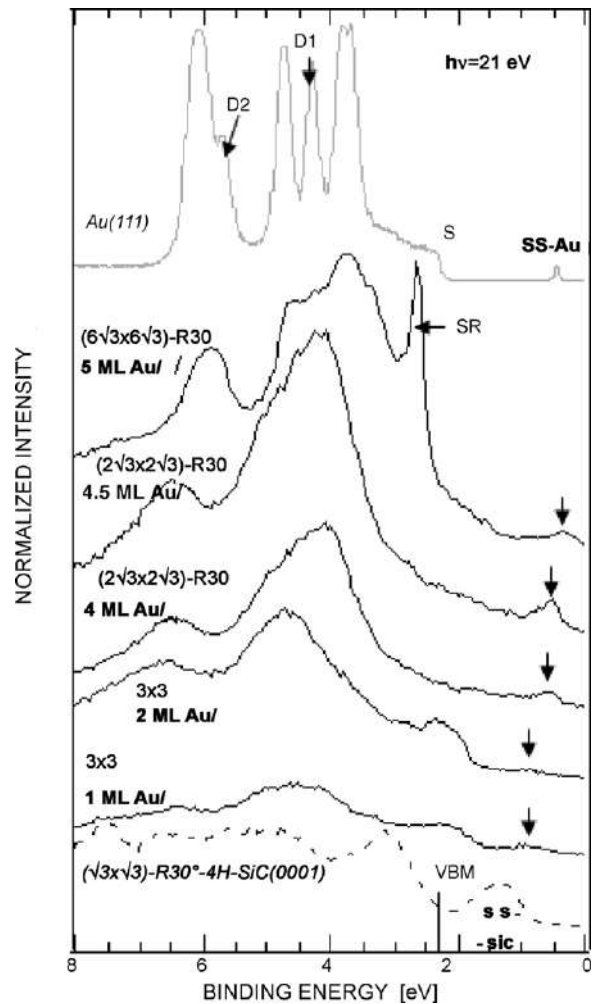


Fig. 1. Normal emission valence band of $(\sqrt{3} \times \sqrt{3}) - R30°$-4H-SiC(0 0 0 1) (dashed), 1–5 ML Au on $(\sqrt{3} \times \sqrt{3}) - R30°$-4H-SiC(0 0 0 1) (black lines) and Au(1 1 1) (grey; taken from Fig. 1 in Ref. [3] at normal emission). The reconstructions are marked. All spectra are measured with photon energy of 21 eV. Au(1 1 1) was measured at 20 K, the rest at 100 K.

higher than VBM the $\sqrt{3}$-4H-SiC valence band states can be observed.

Drastic changes take place when 1 ML of Au is deposited on $\sqrt{3}$-4H-SiC, as can be seen in Fig. 1. With the deposition of gold the surface state of $\sqrt{3}$-4H-SiC and all the other valence band features disappear and the electronic structure changes from the one of $\sqrt{3}$-4H-SiC, towards the one of Au. A spectrum of Au(1 1 1) is shown for comparison as a grey spectrum on the top of Fig. 1, measured with angular resolution of $\pm 0.15°$ and energy resolution of $\leq 3.5$ meV [3].

At $\sim 5$ ML of gold, the d-bands of gold are almost fully developed. D1 and D2 mark herringbone reconstruction related surface resonances in Au(1 1 1) [27] which are not expected to appear on our sample. Another surface resonance (S) [28] could develop for much higher Au coverages. Surface state (SS) of $\sqrt{3}$-4H-SiC is being replaced by a surface state at the binding energy close to that of the SS in pure gold (see arrows at the black spectra). Its appearance suggests that the gold for 5 ML Au has (1 1 1) orientation, as this is the only crystallographic

Table 1
Acronyms used throughout this paper for different surfaces

| Surface | Reconstruction | $T_{anneal}$ | Acronym |
|---|---|---|---|
| 4H-SiC(0 0 0 1) | $(\sqrt{3} \times \sqrt{3}) - R30°$ | – | $\sqrt{3}$-4H-SiC |
| 1 ML Au/ $\sqrt{3}$-4H-SiC | $3 \times 3$ | 675° | 1 ML Au – $3 \times 3$ |
| 2 ML Au/ $\sqrt{3}$-4H-SiC | $3 \times 3$ | 675° | 2 ML Au – $3 \times 3$ |
| 4 ML Au/ $\sqrt{3}$-4H-SiC | $(2\sqrt{3} \times 2\sqrt{3}) - R30°$ | 650° | 4 ML Au – $2\sqrt{3}$ |
| 5 ML Au/ $\sqrt{3}$-4H-SiC | $(6\sqrt{3} \times 6\sqrt{3}) - R30°$ | 700° | 5 ML Au – $6\sqrt{3}$ |

direction in Au exhibiting projected band gap around the $\Gamma$ point (normal emission) [29] and thus allowing for the appearance of the surface states there. The implications for the silicide at the surfaces with 1–4 ML Au are different. Finally, a sharp peak at 2.6 eV binding energy (SR) appears at 5 ML Au on $\sqrt{3}$-4H-SiC with $(6\sqrt{3} \times 6\sqrt{3}) - R30°$ reconstruction and has recently been identified as a surface resonance [17].

When Au is deposited on the $\sqrt{3}$-4H-SiC surface, both gaps of $\sqrt{3}$-4H-SiC and Au determine the energetic range where surface related states can develop. In the Au bandstructure, it is actually the projected sp-gap (parabolic with minimum at $\sim 1.13$ eV at $\Gamma$ [3]) which plays similar role as the VBM in $\sqrt{3}$-4H-SiC, although all VB features in the spectrum of gold are at higher binding energies than the shoulder S at $\sim 2$ eV in Fig. 1.

Different annealing temperatures and gold coverages result in different reconstructions on the surface. [18] Acronyms which will be used for different coverages, instead of the full names describing substrate, adsorbate and the reconstruction, are summarized in Table 1. In the following, we summarize the conclusions from Ref. [18], as they are relevant for the observations made in this manuscript. For 1–4 ML of Au and annealing at 650–675 °C, gold diffuses under the surface and forms a silicide layer. With increasing amount of gold an increasingly large layer of silicide is formed at the surface at annealing temperatures of 650–675 °C. For 5 ML Au – $6\sqrt{3}$ annealed at 700 °C silicide is at the surface, but underneath it and on top of SiC is unreacted Au. For this annealing temperature, gold seggregation replaces silicide formation and silicon-depletion at higher annealing temperatures leads to diminished silicide formation.

Normal emission spectra recorded from the $\sqrt{3}$-4H-SiC surface using photon energies between 17 and 27 eV are shown in Fig. 2 a. A structure located at $\sim 1.3$ eV (full line) shows no $k_\perp$ dispersion, i.e. its binding energy does not change with photon energy. It is assigned, according to the previous studies [22], to emission from a surface state. The position of a valence band maximum (VBM) at $\sim 2.3$ eV [22] is marked by a dashed line. In Fig. 2 b, $k_\parallel$ dispersion of the same state and the rest of the valence band in the $\Gamma$ M direction of the substrate is shown. Some dispersion is visible in Fig. 2 b, but the state is rather flat in the large part of the Brillouin zone (BZ), as reported earlier [22].

At 2 ML Au – $3\times 3$ presented in Fig. 3 a the surface state of $\sqrt{3}$-4H-SiC has disappeared and a new state has appeared in the vicinity of the Fermi level. The gap of the $\sqrt{3}$-4H-SiC surface seems to be closed and the Fermi edge appears in all measured spectra. According to the photon energy scan pre-
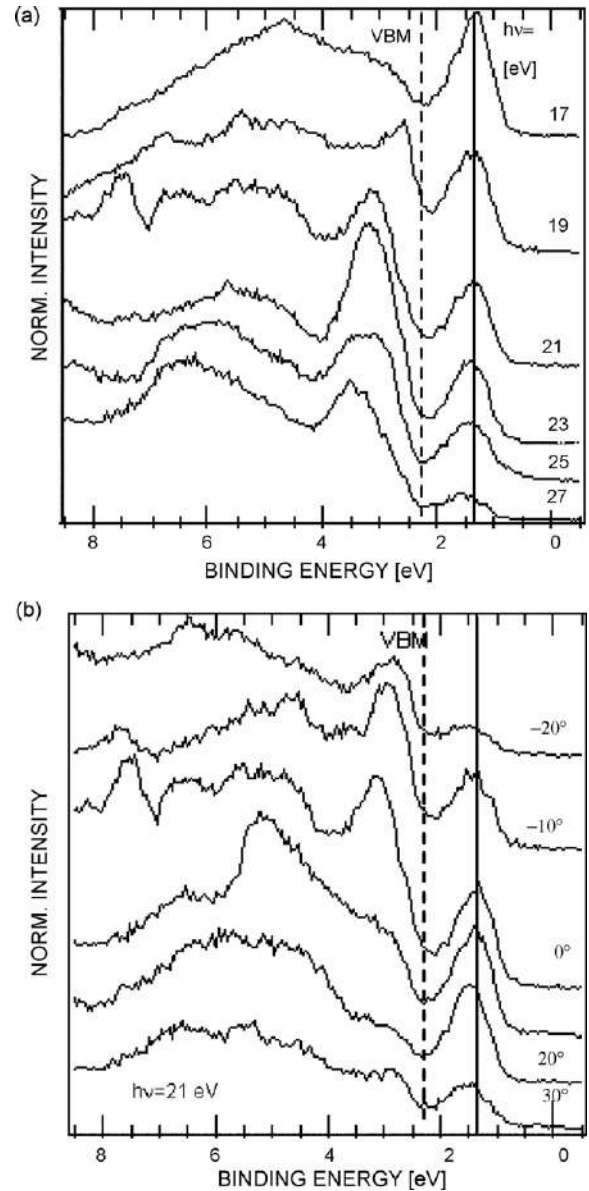


Fig. 2. Spectra of $\sqrt{3}$-4H-SiC taken at (a) normal emission and variable photon energy (marked), (b) in the $\Gamma$M direction of the substrate (emission angles marked) at 21 eV photon energy. All spectra are measured at 100 K.

sented in Fig. 3 b, this state has no $k_\perp$ dispersion, i.e. it is two-dimensional.

This state crosses the Fermi level at the $\Gamma$-point. The nature of this state could be a true interface state, which is allowed to appear on the Au/ $\sqrt{3}$-4H-SiC interface due to very different band structures of the substrate and the adsorbate [30]. The disappearance of this state at higher coverages is in agreement with this. However, other options like a quantum-well state or a surface state cannot be fully disregarded. Nevertheless, it is clear that this state does not originate from the substrate as its steep dispersion is significantly different from the almost flat one of both occupied and unoccupied Mott–Hubbard states of $\sqrt{3}$-4H-SiC [25,31].

At 4 ML Au – 2 $\sqrt{3}$ presented in Fig. 4 the electronic structure near the Fermi level has changed once again. Instead
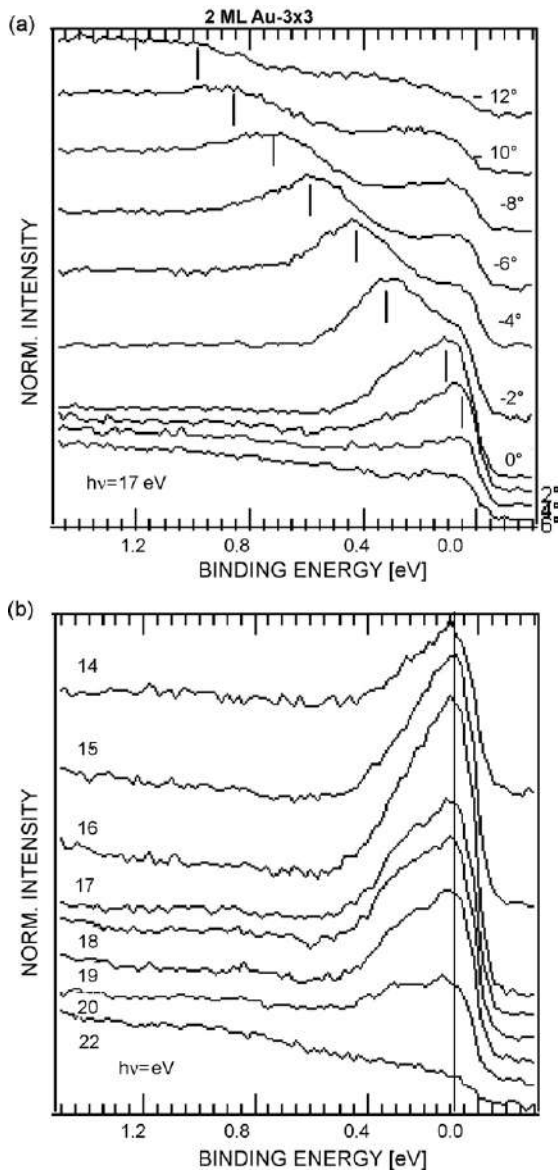
Fig. 3. (a) Spectra from 2 ML Au – 3 × 3 in the ΓM direction of the substrate (emission angles marked) recorded with 17 eV photon energy at 100 K. (b) Spectra from 2 ML Au – 3 × 3 at normal emission and at 100 K taken with different photon energies (marked).
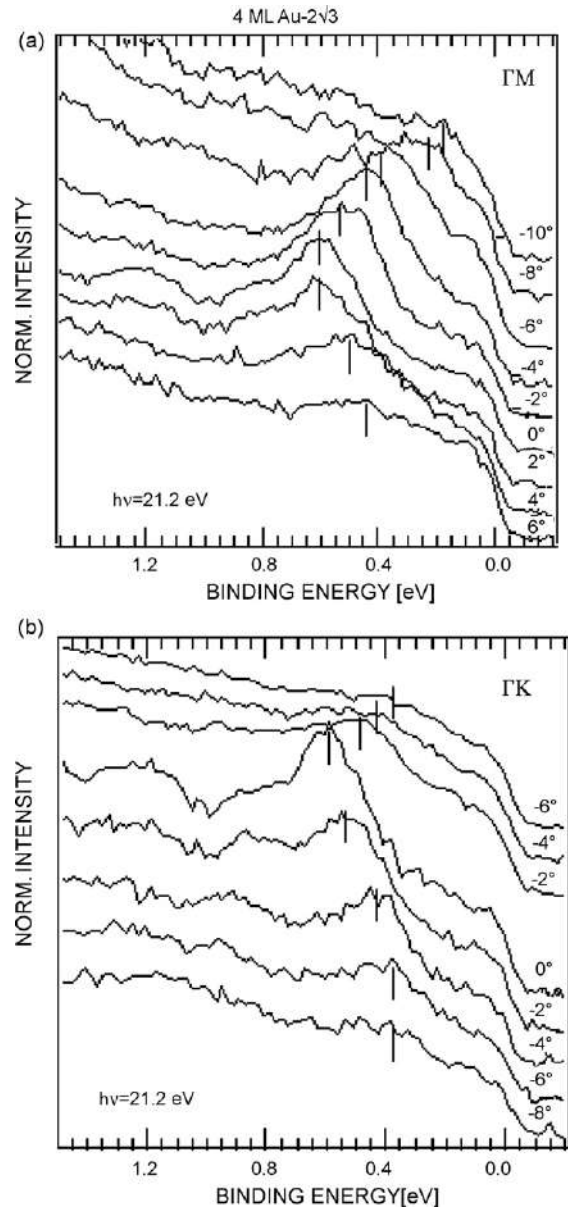


Fig. 4. Spectra from 4 ML Au – 2 $\sqrt{3}$ in the (a) ΓM and (b) ΓK directions of the substrate (emission angles marked) recorded with 21.2 eV photon energy at 100 K.

of the two-dimensional (2D) state shown in Fig. 3, another 2D-state appears in its place. It shows free-electron like parabolic dispersion with positive effective mass, centered at the Γ-point. The dispersion is the same in two different directions of the BZ: ΓM (a) and ΓK (b). This state is very similar to the Shockley-type surface state on the surface of Au(1 1 1). Its disappearance for off normal emission is a fingerprint of a two-dimensional dispersion of a surface state.

The calculated effective mass ($m^*/m_e$) for the parabolic dispersion seen in Fig. 4 a and b is 0.7, compared with 0.26 for the surface state in Au(1 1 1) [3]. Its binding energy is 590 ±20 meV, compared to 487 meV on Au(1 1 1) [3]. The parameters are similar, but not the same as on the Au(1 1 1) surface. However, interface formation study [18] shows that at 4 ML Au – 2 $\sqrt{3}$ Au-silicide forms on the surface on top of the SiC sub-

strate. Without knowing the exact band structure of the silicide, it is not possible to say if this two-dimensional state is a true surface state or a surface resonance. One very good example of a true surface state of Cu becoming a surface resonances in Cu$_3$Au(1 1 1) has been reported earlier by Courths [32].

By inspection of Fig. 4 there could not be noticed any traces of confinement. Our $\sqrt{3}$-4H-SiC sample has a 8° miscut in the [11$\bar{2}$0] direction. This results in ∼ 1000 Å wide terraces on the surface [33]. When resulting energy separation between terrace quantum wells is calculated according to Ref. [8], 0.4 meV is obtained, which obviously does not lead to any observable confinement.

On the other hand, the $2\sqrt{3} \times 2\sqrt{3} - R30°$-reconstruction on the surface, should implement creation of new surface BZ (SBZ) boundaries and backfolding of bands with respect to these

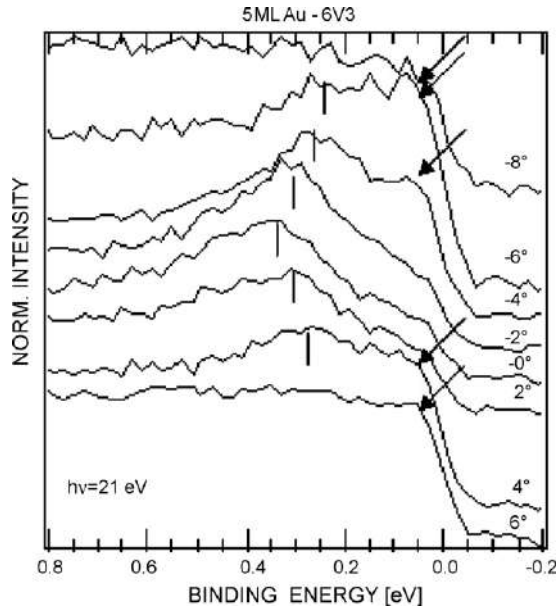Fig. 5. Spectra from 5 ML Au − 6 $\sqrt{3}$ in the ΓM direction of the substrate (emission angles marked) recorded with 21 eV photon energy at 100 K.

boundaries. According to our estimate, the new SBZ boundary should appear at ~0.2 Å$^{-1}$ in both directions (ΓK and ΓM). Fig. 4 does not show any clear backfolding of the surface bands at this point. In our interface study [18], Si is found to form an incomplete surface layer on top of the silicide. Si atoms are thus responsible for the reconstruction and fingerprints of the reconstruction should thus not be expected in the emission coming from the silicide layer, which is underneath the topmost Si and which we consider responsible for the appearance of the observed two-dimensional states.

Finally, electronic structure in the vicinity of the Fermi level for 5 ML Au − 6 $\sqrt{3}$ is presented in Fig. 5. This surface actually consists of unreacted gold on top of the $\sqrt{3}$-4H-SiC substrate and below a thin silicide layer [18]. A two-dimensional state is observed in Fig. 5 with a dispersion resembling a free-electron parabola. Calculating the effective mass ($m^*/m_e$), we obtain 1, compared to 0.26 for Au(1 1 1) [3]. This states binding energy is 343 meV, compared to 487 meV for Au(1 1 1) [3]. Similar binding energy shift of the Shockley-type surface state in Au(1 1 1) has been observed on the (1 1 1) facets of gold clusters [9]. An increased spectral weight at the Fermi level is present at off-normal emission angles and is marked in Fig. 5 by arrows. This can be a consequence of confinement and is similar to spectra at ±3° in Fig. 4 of Ref. [9] on gold clusters. New SBZ due to the $6\sqrt{3} \times 6\sqrt{3} − R30°$-reconstruction on this surface should appear at 0.1 Å$^{-1}$. We do not observe any backfolding of the surface band at that point, which is in agreement with the conclusions of the interface study [18] about the topmost silicide layer.

## 4. Conclusions

We report a systematic study of the electronic structure characteristic of a rather complicated interface reported earlier for Au/ $\sqrt{3}$-4H-SiC [18]. In the silicide layer, which is observed up to 4 ML of Au, a development of an interface state was found to precede a formation of a Shockley-like two-dimensional state, which has been characterized by effective mass and binding energy of its parabolic dispersion. This state could be both a true surface state or a surface resonance. No traces of confinement or surface reconstruction could be seen. In the gold layer, which is formed at 5 ML and a slightly different annealing temperature, a Shockley-like two-dimensional state was also observed, with relevant parameters similar to the ones earlier reported for confined Au. Therefore, we attribute this state to a true surface state.

## References

[1] R. Courths, H.-G. Zimmer, A. Goldmann, H. Saalfeld, Phys. Rev. B 34 (1986) 3577.
[2] S.D. Kevan, R.H. Gaylord, Phys. Rev. B 36 (1987) 5809.
[3] D. Popović, F. Reinert, S. Hüfner, V.G. Grigoryan, M. Springborg, H. Cercellier, Y. Fagot-Revurat, B. Kierren, D. Malterre, Phys. Rev. B 72 (2005) 045419.
[4] H. Cercellier, Y. Fagot-Revurat, B. Kierren, F. Reinert, D. Popović, D. Malterre, Phys. Rev. B 70 (2004) 193412.
[5] F.J. Palomares, M. Serrano, A. Ruiz, F. Soria, K. Horn, M. Alonso, Surf. Sci. 513 (2002) 283.
[6] R. Losio, K.N. Altmann, A. Kirakosian, J.-L. Lin, D.Y. Petrovykh, F.J. Himpsel, Phys. Rev. Lett. 86 (2001) 4633.
[7] J.L. McChesney, J.N. Crain, F.J. Himpsel, R. Bennewitz, Phys. Rev. B 72 (2005) 035446.
[8] A. Mugarza, A. Mascaraque, V. Pérez-Dieste, V. Repain, S. Rousset, F.J.G. de Abajo, J.E. Ortega, Phys. Rev. Lett. 87 (2001) 107601.
[9] I. Barke, H. Hövel, Phys. Rev. Lett. 90 (2003) 166801.
[10] I. Braicovich, C.M. Garner, P.R. Skeath, C.Y. Su, P.W. Chye, I. Lindau, W.E. Spicer, Phys. Rev. B 20 (1979) 5131.
[11] D.K. Sarkar, S. Bera, S. Dhara, K.G.M. Nair, S.V. Narasimhan, S. Chowdhury, Appl. Surf. Sci. 120 (1997) 159.
[12] S.L. Molodtsov, C. Laubschat, G. Kaindl, A.M. Shikin, V.K. Adamchuk, Phys. Rev. B 44 (1991) 8850.
[13] J.-J. Yeh, J. Hwang, K. Bertness, D.J. Friedman, R. Cao, I. Lindau, Phys. Rev. Lett. 70 (1993) 3768.
[14] Y. Haruyama, K. Kanda, S. Matsui, J. Electron Spectrosc. Relat. Phenom. 137-140 (2004) 97.
[15] C. Virojanadara, L.I. Johansson, Surf. Sci. 585 (2005) 163.
[16] C. Virojanadara, L.I. Johansson, Surf. Sci. 600 (2006) 436.
[17] D. Stoltz, S.E. Stoltz, L.S.O. Johansson, Surf. Sci. 601 (2007) 2508.
[18] D. Stoltz, S.E. Stoltz, L.S.O. Johansson, J. Phys. : Condens. Matter 19 (2007) 266006.
[19] J.R. O'Connor, J. Smiltens (Eds.), Silicon Carbide - A High Temperature Semiconductor, Pergamon Press, 1960.
[20] W. Shockley, Phys. Rev. 56 (1939) 317.
[21] T. Miller, A. Samsavar, G.E. Franklin, T.C. Chiang, Phys. Rev. Lett. 61 (1988) 1404.
[22] L.I. Johansson, F. Owman, P. Mårtensson, Surf. Sci. 360 (1996) 478.
[23] K. Heinz, J. Bernhardt, J. Schardt, U. Starke, J. Phys. : Condens. Matter 16 (2004) 1705.

[24] U. Starke, J. Schardt, M. Franke, Appl. Phys. A 65 (1997) 587.

[25] R. Ostendorf, K. Wulff, C. Benesch, H. Merz, H. Zacharias, Phys. Rev. B 70 (2004) 205325.

[26] D.L. Adams, Fitxps2 peak-fitting software, http://www.sljus.lu.se/download.html.

[27] R. Paniago, R. Matzdorf, A. Goldmann, Europhys. Lett. 26 (1994) 63.

[28] H.-G. Zimmer, A. Goldmann, Surf. Sci 115 (1986) 115.

[29] P. Heimann, H. Miosga, H. Neddermeyer, Phys. Rev. Lett. 42 (1979) 801.

[30] T.C. Hsieh, T. Chiang, Surf. Sci. 166 (1986) 554.

[31] C. Benesch, M. Fartmann, H. Merz, Phys. Rev. B 64 (2001) 205314.

[32] R. Courths, M. Lau, T. Scheunemann, H. Gollisch, R. Feder, Phys. Rev. B 63 (2001) 195110.

[33] T. Kihlgren, T. Balasubramanian, L. Walldén, R. Yakimova, Phys. Rev. B 66 (2002) 235422.

ELSEVIER

# Atomic origin of the scanning tunneling microscopy images of charge-density-waves on 1T-TaSe$_2$

D. Stoltz[a,*], M. Bielmann[b], L. Schlapbach[b], M. Bovet[c], H. Berger[d], M. Göthelid[e], S.E. Stoltz[f], H.I. Starnberg[g]

[a]Kamerlingh Onnes Laboratory, Leiden University, P.O. Box 9504, 2300 RA Leiden, The Netherlands
[b]Swiss Federal Lab for Materials Science and Technology (EMPA), CH-8600 Dübendorf, Switzerland
[c]Institut de Physique, Université de Neuchâtel, CH-2000 Neuchâtel, Switzerland
[d]Institut de Physique Appliquée, EPF, 1015 Lausanne, Switzerland
[e]Materialfysik, MAP, KTH-Electrum, SE-16440 Kista, Sweden
[f]MAX-Lab, Lund University, SE-22100 Lund, Sweden
[g]Department of Physics, Göteborg University and Chalmers University of Technology, SE-412 96 Göteborg, Sweden

## Abstract

We show atomically resolved scanning tunneling microscopy (STM) images of charge density waves (CDWs) at room temperature together with angle-resolved photoelectron band-mapping of 1T-TaSe$_2$. By comparing the results of these two techniques, we demonstrate the atomic structure of the CDW-features observed by the STM and atomic origin of the reconstructed band-structure in this material.

## 1. Introduction

The layered transition metal dichalcogenides (TMDs) of the 1T-type have been abundantly investigated in the last decade as quasi-two-dimensional hosts of charge-density waves (CDWs). CDWs offer a playground for studies of interplay between complex structural and electronic changes. On the other hand, the quasi-two-dimensionality of these materials allows simple surface preparation and the straightforward interpretation of the band-mapping in terms of the mapping of the initial bands of the crystals.

Studies of the electronic structure of the TMDs are most of all inspired by the similarity of electronic instabilities in high-temperature superconductors [1,2] and 1T-TMDs [3,4]. The band-structure of 1T-TaSe$_2$ undergoes changes

due to CDWs, the Ta d$_{z^2}^2$-band splits into subbands which follow the periodicity invoked by the reconstruction [4,5]. This establishes the relationship between the structural changes and the electronic band-structure.

The advantage of studying 1T-TaSe$_2$ originates from the fact that it is already in the commensurate CDW phase at room temperature (RT). Scanning-tunneling microcopy (STM) on this compound has sofar revealed the CDW wavelength $\lambda_{CDW} = 12.6$ Å [6], which dominates the images of surfaces with this CDW [7–11]. The atomic height modulation was found to give only minor contribution to the overall $z$ deflection.

In this paper we present atomically resolved RT STM measurements on 1T-TaSe$_2$ in its CDW phase. By tuning the bias voltage of the STM image, we tunnel into different CDW-split subbands of the Ta d$_{z^2}$-band. These subbands can be identified by band-mapping. We demonstrate that they are spatially located on three groups of inequivalent

*Corresponding author. Tel.: +31 71 527 8407.
E-mail address: stoltz@physics.leidenuniv.nl (D. Stoltz).

atoms by visualizing those atoms while tunneling at a bias voltage set to the subbands' binding energy. Furthermore, we demonstrate that atomic corrugation is visible in the CDW-dominated STM images of this material, allowing the interpretation of the CDW-features in terms of the Star-of-David model of the reconstructed Ta-plane.

## 2. Experimental

STM experiments on 1T-TaSe$_2$ have been performed in a UHV system equipped with a UHV AFM/STM scanning probe microscope from Omicron NanoTechnology operating at RT as described elsewhere [12]. The images were taken in constant height mode. Bias voltages are given with respect to the sample, i.e. positive bias means tunneling from occupied states.

Band-mapping experiments have been performed using angle-resolved photoelectron spectroscopy (ARPES) implementing Vacuum Generators ESCALAB Mk II spectrometer at RT with monochromatized He I (h$v$ = 21.2 eV) photons [13] and computer controlled sequential sample rotation [14]. The energy and angular resolution were 20 meV and 0.5°, respectively. The accurate position of the Fermi level ($E_F$) has been determined on a polycrystalline copper sample. Low energy electron diffraction was used to check surface reconstruction, while X-ray photoelectron diffraction was used to determine the sample orientation _in situ_ (accuracy < 0.5°).

Samples of 1T-TaSe$_2$ have been prepared from its constituent elements by reversible chemical reaction with iodine as a transport agent, between 950° (hot zone) and 900° (cold zone) [15]. They were cleaved _in situ_ at pressures in the lower 10$^{-10}$ mbar region.

STM experiments on 2H-TaSe$_2$ have been performed in a constant current mode with a W tip at RT using a variable temperature (VT)-STM from Omicron NanoTechnology. Positive bias means tunneling from occupied states. Samples of 2H-TaSe$_2$ were cleaved _in situ_ at pressures in the lower 10$^{-10}$ mbar region.

## 3. Results

Fig. 1a shows experimental results obtained implementing ARPES along the $\bar{\Gamma}\bar{K}$ direction and up to a binding energy of 1.5 eV. Spectra cover the range between −5° and 20°, which is converted to $k_\parallel$ in the image. The images depict dispersion of the Ta d$_z^2$-band. At the higher binding energies (1.5 eV) the Se 4p band appears energetically close to the Ta d$_z^2$-band primarily in the vicinity of $\bar{\Gamma}$ point. Division of RT band-mapping intensities with the Fermi–Dirac function allows for an extra $5k_B T \approx 130$ meV "visibility" over the Fermi level accomplished in the same way as outlined in Ref. [4].

Fig. 1a shows that the Ta d$_z^2$-band is split into three oscillating subbands (circles). Both the band-splitting and the backfolding of the subbands are CDW-related effects [4,5]. According to the CDW-induced $(\sqrt{13} \times \sqrt{13})R13.54°$
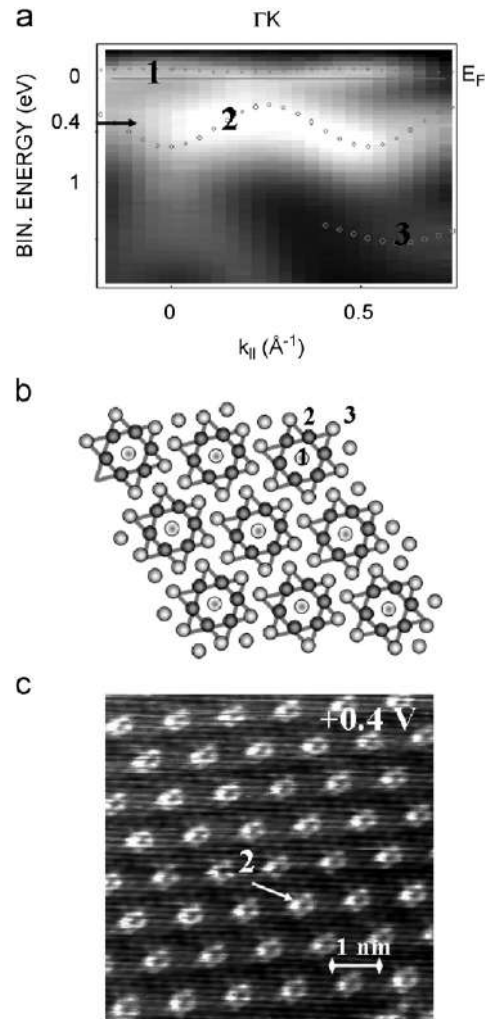


Fig. 1. (a) Band mapping along $\bar{\Gamma}\bar{K}$ of the cleaved 1T-TaSe$_2$ with a photon energy of 21.2 eV at RT. Dark circles represent three new CDW-induced subbands with the new periodicity. High intensity in white. (b) Schematic representation of the Stars-of-David formation in the Ta-plane. (c) STM image of the cleaved 1T-TaSe$_2$ surface taken at RT with 1.2 nA and 0.4 V. The tunneling is achieved in the subband 2 from (a) and it shows atoms marked by 2 in (b). High intensity in white.

reconstruction in the Ta-plane (Fig. 1b), three types of inequivalent atomic positions are introduced in the Star-of-David form: the atom in the center (1), the six atoms constituting the first hexagon around it (2) and the six atoms constituting the outmost hexagon of the star-like cluster (3). These groups are assumed to electronically constitute the subbands of the CDW-split Ta d$_z^2$-band (marked also as 1, 2, 3 in Fig. 1a). However, the photoemission intensity still follows the unreconstructed band-structure, which is treated in detail in Refs. [4,5].

The periodic lattice distortion introduced by the CDW lock-in can be visualized by an STM. Fig. 1c shows 7 nm × 7 nm of the _in situ_ cleaved 1T-TaSe$_2$ surface measured with a bias voltage of 0.4 V (tunneling from the occupied states) and a tunneling current of 1.2 nA. The image shows arrays of white flowerlike patterns with the periodicity of ~12 Å, which is expected for this CDW. If we look at Fig. 1a, the

0.4 eV binding energy corresponds mainly to the second subband (see arrow). It is thus clear that by tunneling from the occupied states of one of the subbands, we can achieve highest intensity on those atoms that electronically contribute to that band. It is important to notice that while Fig. 1a shows photoemission over extended part of $k$-space, STM-tunneling proceeds in the vicinity of the normal emission ($\bar{\Gamma}$). According to Fig. 1c we assign subband 2 to the first six atoms surrounding the central atom of the reconstruction (see arrow). In similar fashion,



a

b

c

Fig. 2. (a) STM image of the cleaved 1T-TaSe$_2$ surface taken at RT with 1.2 nA and 0.2 V. (b) Fourier-filtered image from (a), to exclude the CDW-periodicity. (c) Atomic-resolution image of the cleaved 2H-TaSe$_2$ surface taken at RT with 1.2 nA and −0.76 V. High intensity in white.

tunneling into the first subband reveals that it is located on the central atom (1), while the outermost hexagon (3) contributes the most to the third subband [5].

Fig. 2a shows an STM image of the same surface obtained with a bias voltage of 0.2 V, which corresponds to the tunneling out of the topmost subband (and somewhat out of the second one). It shows the same CDW-periodicity as Fig. 1c, only with the central atoms of the Stars-of-David at highest intensity, while the hexagon formed by the first six atoms around the central one is still visible, but much less intense than in Fig. 1c. The dominant periodicity is the one of the CDW and the unit cell is marked.

However, the interpretation of Fig. 1c in terms of the atomic model of the reconstructed Ta-plane implicitly assumes the presence of the atomic corrugation super-imposed on the CDW pattern in the STM images of the 1T-TaSe$_2$ surface. To prove that this is the case, we have Fourier-filtered Fig. 2a from the CDW periodicity and the result is shown in Fig. 2b. The new pattern becomes obvious here and the relevant unit cell is marked. Comparing this pattern with the one of Fig. 2c obtained on a CDW-free surface of 2H-TaSe$_2$, which has similar lattice constant (3.39 Å compared to 3.47 Å), we conclude that the pattern in Fig. 2b is indeed an atomic lattice. It is thus justified to attribute features from Fig. 1c directly to the atoms of the inner hexagon of the Star-of-David formation.

## 4. Discussion

The slope of the temperature-dependent resistivity in 1T-TaSe$_2$ is metallic at room temperature, at which our measurements were performed. The resistivity is also confirmed to be metallic by our scanning tunneling spectroscopy (STS) measurements (not shown). The conduction charge of the unreconstructed lattice would be equally distributed over all Ta atoms. In the CDW phase we see that the conduction charge is mainly located at the central atom of the Star-of-David cluster, as only the subband located on the central atom is straddling the Fermi level. This can explain the resistivity jump related to the CDW transition. The stability of the CDW phase and the compensation of the lattice distortion energy clearly originate from the energetically lowered bands which are spatially located on the remaining 12 atoms of the Star-of-David cluster and which are completely filled.

Kim et al. [7] were the first to apply STS to investigate fingerprints of the CDW-reconstructed band-structure. STM images of the CDW materials (such as 2H-NbSe$_2$) have also been treated [16] by considering CDW effects on the band-structure and thus, on the tunneling. However, reconstructed band-structure has been assumed in the form of folded, non-split bands. In our study we consider the real reconstructed band-structure, which is measured by ARPES and confirmed by the band-structure calculations. Both band-splitting and back-folding have influence on the formation of such subbands. Tunneling occurs thus
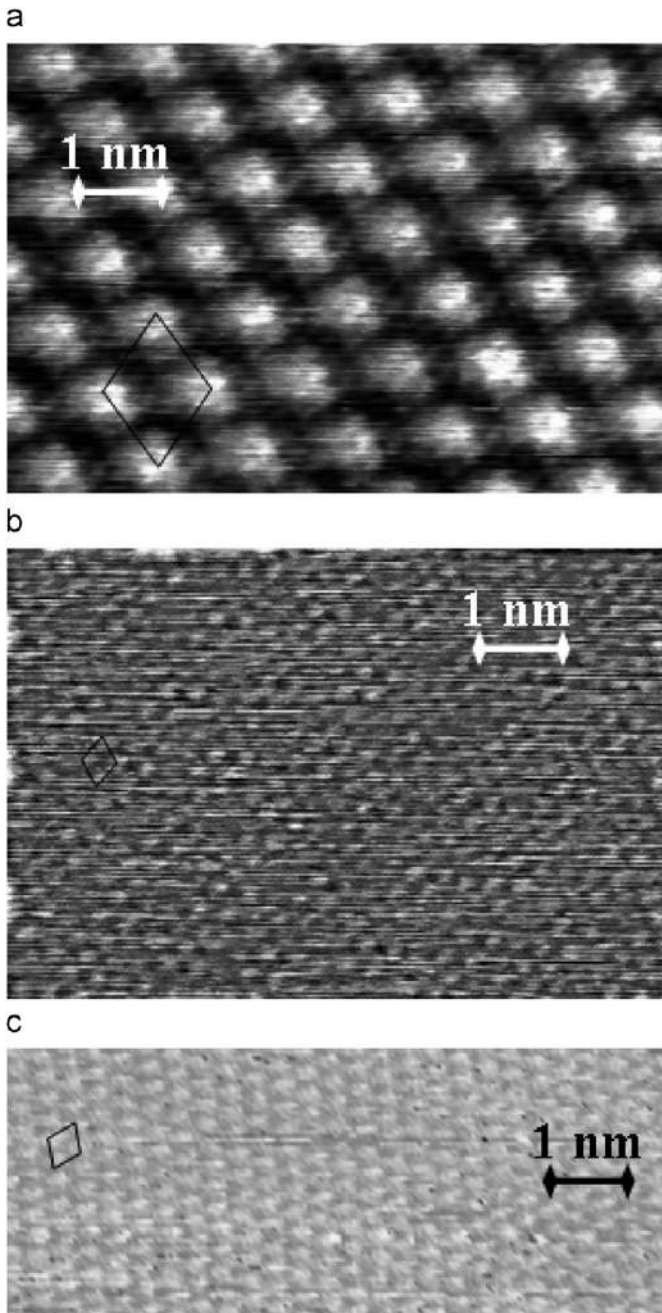
primarily from a subband, in which the binding energy is the same as the bias [5].

## 5. Conclusions

To conclude, band-mapping of 1T-TaSe$_2$ along $\bar{\Gamma}\bar{K}$ reveals CDW induced splitting and folding of the Ta d$_{z^2}$-band into three subbands. Tunneling from separate subbands allows direct visualization of the atoms contributing to CDW-split electronic states. Three groups of inequivalent Ta atoms are giving rise to three new subbands in the reconstructed band-structure of this material. Furthermore, we show that CDW-dominated STM pattern of 1T-TaSe$_2$ has indeed atomic resolution, which allows us to directly attribute atoms from the Star-of-David model to the structures observed by the STM.

## References

[1] H. Ding, T. Yokoya, J.C. Campuzano, T. Takahashi, M. Randeria, M.R. Norman, T. Mochiku, K. Kadowaki, J. Giapintzakis, Nature 382 (1996) 51.
[2] A.G. Loeser, Z.-X. Shen, D.S. Dessau, D.S. Marshall, C.H. Park, P. Fournier, A. Kapitulnik, Science 273 (1996) 325.
[3] T. Pillo, J. Hayoz, H. Berger, M. Grioni, L. Schlapbach, P. Aebi, Phys. Rev. Lett. 83 (1999) 3494.
[4] M. Bovet, D. Popović, F. Clerc, C. Koitzsch, U. Probst, E. Bucher, H. Berger, D. Naumović, P. Aebi, Phys. Rev. B 69 (2004) 125117.
[5] D. Stoltz, M. Bielmann, M. Bovet, L. Schlapbach, H. Berger, Phys. Rev. B 76 (2007) 073410.
[6] C.G. Slough, W.W. McNairy, R.V. Coleman, B. Drake, P.K. Hansma, Phys. Rev. B 34 (1986) 994.
[7] J.-J. Kim, W. Yamaguchi, T. Hasegawa, K. Kitazawa, Phys. Rev. B 50 (1994) 4958.
[8] B. Giambattista, A. Johnson, R.V. Coleman, B. Drake, P.K. Hansma, Phys. Rev. B 37 (1988) 2741.
[9] G. Raina, K. Sater, U. Müller, N. Venkateswaran, J. Xhie J. Vac. Sci. Technol. B 9 (2) (1990) 1039.
[10] W. Han, R.A. Pappas, E.R. Hunt, R.F. Frindt, Phys. Rev. B 48 (1993) 8466.
[11] B. Giambattista, C.G. Slough, W.W. McNairy, R.V. Coleman, Phys. Rev. B 41 (1990) 10082.
[12] P. Ruffieux, O. Gröning, P. Schwaller, L. Schlapbach, P. Gröning, Phys. Rev. Lett. 84 (2000) 4910.
[13] T. Pillo, L. Patthey, E. Boschung, J. Hayoz, P. Aebi, L. Schlapbach, J. Electron Spectrosc. Relat. Phenom. 97 (1998) 243.
[14] P. Aebi, J. Osterwalder, P. Schwaller, L. Schlapbach, M. Shimoda, T. Mochiku, K. Kadowaki, Phys. Rev. Lett. 72 (1994) 2757.
[15] B. Dardel, M. Grioni, D. Malterre, P. Weibel, Y. Baer, F. Levý, Phys. Rev. B 45 (1992) 1462.
[16] W. Sacks, D. Roditchev, J. Klein, Phys. Rev. B 57 (1998) 13118.

# Quasiparticle band dispersion
# in the vicinity of the Fermi surface
# in quasi-two dimensional systems

Dissertation
zur Erlangung des Grades
der Doktorin der Naturwissenschaften
der Naturwissenschaftlich-Technischen Fakultät II
-Physik und Mechatronik-
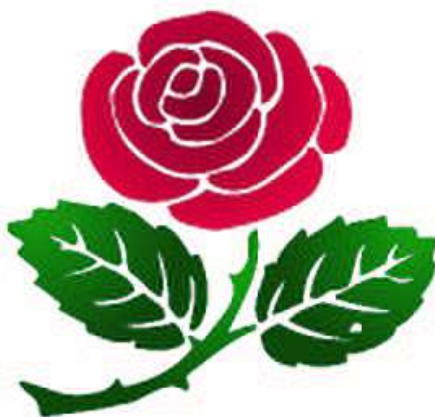Universität des Saarlandes

von

Dunja Popović

Saarbrücken
2004

Tag des Kolloquiums: 11.03.2005.

Dekan:              Prof. Dr. rer. nat. Th. Wichert

Berichterstatter:   Prof. Dr. rer. nat. Dr. h.c. mult. S. Hüfner
                    Prof. Dr. rer. nat. U. Hartmann

Za Oli

# Zusammenfassung

In der vorliegenden Doktorarbeit wurde die Quasiteilchen-Banddispersion nahe der Fermifläche anhand zweier Arten quasi-zweidimensionaler Systeme untersucht: bei den $1T$-Polytypen der Schichtsystem-Übergangsmetalldichalcogeniden (TMD) und bei den Oberflächenzuständen in dünnen Schichten von Silber auf Au(111). Eine gemeinsame Eigenschaft der in dieser Arbeit mittels Photoelektronenspektroskopie untersuchten Systeme ist die Anisotropie ihrer Bandstruktur, die zum quasi-zweidimensionalen Charakter der Anfangszustände führt. Dank dieses Umstands konnte von den Photoemissionspektren eindeutig auf die Anfangsbänder des Kristalls geschlossen werden.

Von den $1T$-TMD-Polytypen sind $TaSe_2$, $TaS_2$ und $TiSe_2$ Verbindungen, in denen Ladungsdichtewellen (CDW) beobachtet werden und $TiTe_2$ ist ein Fermiflüssigkeitsmodellsystem. Als Motivation zur Untersuchung dieser Systeme dienten vor kurzem entdeckte Ähnlichkeiten der CDW- und supraleitenden Grundzustände, die beide über ein Pseudogap am Ferminiveau ($E_F$) verfügen. Andererseits könnte das Fermiflüssigkeitsverhalten von $TiTe_2$ helfen, die Analysemethode für die komplexeren Systeme zu entwickeln.

In dieser Dissertation wurden die hochaufgelösten Photoelektronenspektren von $TiTe_2$ mit einer deutlich besseren Winkel- und Energieauflösung als in den früheren Untersuchungen gemessen. Die Linienformanpassung zeigte, dass die dominante Wechselwirkung in diesem System nicht die - wie in früheren Arbeiten angenommen - Elektron-Elektron-, sondern die Elektron-Phonon-Wechselwirkung ist. Das System ließ sich mittels Elektron-Phonon-Kopplungskonstante $\lambda = 0.2(1)$ und Grenzfrequenz $\omega_D = 20(5)$ meV gut beschreiben; als ein oberer Grenzwert für den Elektron-Elektron-Parameter $\beta$ wurde $0.5$ eV$^{-1}$ bestimmt.

Weiterhin werden die Ergebnisse von winkelaufgelösten Photoemissionexperimenten an $1T$-$TaS_2$ und $1T$-$TaSe_2$ bei Raumtemperatur vorgelegt und mit Dichtefunktionalrechnungen ergänzt. Die Messungen der Fermiflächen in der CDW-Phase sind für die beiden Verbindungen ähnlich und weisen weder die Symmetrie der CDW-hervorgerufenen Brillouin-Zone noch ein eindeutiges Durchkreuzen der Quasiteilchenzustände bei $E_F$ auf. Trotzdem zeigt das Ta $5d_{z^2}$-Band eine eindeutige Modulation, die in beiden Systemen auf Grund der Ladungsdichtewelle entsteht. Das Band wird in drei Subbänder aufgespalten, was durch Bandstrukturrechnungen bestätigt wurde und in Übereinstimmung mit der geometrischen Struktur entsprechend der periodischen Gitterverformung in der CDW-Phase ist. Das oberste Ta $5d_{z^2}$-Subband ist knapp oberhalb von $E_F$ ($TaS_2$), beziehungsweise nahe $E_F$ ($TaSe_2$), thermisch besetzt.

Das beobachtete Verhalten konnte im Rahmen der CDW-rekonstuierten und mit der Spektralfunktion gewichteten Bandstruktur erklärt werden.

Um die eigentliche Größe der van der Waals-Lücke und der inelastischen mittleren freien Weglänge ($\lambda$) dieser Materialien zu untersuchen, wurden Einfachstreurechnungen durchgeführt und mit den Photoelektronenbeugungsversuchen verglichen. Drei Verbindungen wurden untersucht: $TiSe_2$, $TaSe_2$ und $TaS_2$ und deren Beugungsmuster wurden mit $\lambda \approx 10$ Å unter Verwendung des Einfachstreumodells treffend reproduziert. Die Information über die lokale Realraumumgebung, gewonnen mittels der Photoelektronenbeugung, deutet darauf hin, dass die Spaltung der Probe an der van der Waals-Lücke stattfindet.

Andererseits bieten schon geometrisch dünne Edelmetallschichten auf Edelmetallsubstraten die Bedingungen für die Entwicklung stark anisotroper Zustände. Auch Oberflächenzustände in Edelmetallen sind quasi-zweidimensionale Systeme. Die elektronische Lokalisierung kann an den bedeckten oder sauberen Edelmetalloberflächen untersucht werden. Das Wechselspiel der Oberflächen-, der Quantentrog- und der Volumenzustände, sowie deren Volumen- und Oberflächenbeiträge zu den Photoemissionsspektren kann helfen, den Einfluss der intermetallischen Grenzfläche zu bestimmen.

Es wurden detaillierte Untersuchungen der Oberflächenzustandsdispersion in 0-10 ML dünnen Ag-Schichten auf Au(111) mittels Photoelektronenspektroskopie präsentiert. Ungeordnetes Wachstum bei tiefen Temperaturen und Schicht-für-Schicht-Wachstum bei Zimmertemperatur wurden bestätigt. Die Dispersion des $L$-Gap-Shockleyoberflächenzustandes änderte sich monoton von derjenigen des Au zu derjenigen des Ag mit wachsender Schichtdicke. Die Photoemissionsdaten wurden mittels *ab initio* Bandstrukturrechnungen unter Verwendung des WIEN2k-Programms gut reproduziert. Der Vergleich des Verlaufs der Bindungsenergie mit zunehmender Silberbedeckung mit der berechneten Elektronendichte des Oberflächenzustandes wies auf eine Lokalisierung des Oberflächenzustandes auf der Oberfläche hin. Messungen an nur 10 ML Ag auf Au(111) zeigten bereits die $d$-Bandzustände des Ag, obgleich die $sp$-Quantentrogzustände des Silbers immer noch innerhalb der projizierten $sp$-Bandlücke von Gold zu sehen waren.

# Abstract

Quasiparticle band dispersion in the vicinity of the Fermi surface in quasi-two dimensional systems of two types has been studied in this thesis: layered transition metal dichalcogenides (TMDs) of the $1T$-family and surface states in thin silver films on Au(111). The common feature of these different systems is the anisotropy of the band-structure, revealing the quasi-two dimensional character of the initial states, which are investigated by photoelectron spectroscopy. This allows a straightforward interpretation of the photoemission spectra in terms of the mapping of initial bands of the crystal.

Within the $1T$-TMD-polytypes $TaSe_2$, $TaS_2$ and $TiSe_2$ are charge density wave (CDW) materials, and $TiTe_2$ is a Fermi liquid reference compound. The investigation of these systems has been inspired by the recently discovered similarities of the CDW and superconducting ground states, which are both directly related to the pseudogap at the Fermi level ($E_F$). On the other side, Fermi liquid behavior of $TiTe_2$ could help to enlighten the ways to analyze the normal state properties of the high-temperature superconductors.

High-resolution photoelectron spectra of the model Fermi liquid compound $1T$-$TiTe_2$ have been presented in this thesis, with the energy and the angular resolution better than in previous studies. The lineshape analysis of the data shows, that dominant interaction in this system is not electron-electron, as has been assumed so far, but electron-phonon interaction. The system can be optimally described by the electron-phonon coupling parameter $\lambda = 0.2(1)$ and the cut-off energy $\omega_D = 20(5)$ meV; 0.5 eV$^{-1}$ can be taken as the upper limit for the electron-electron interaction parameter $\beta$.

Room temperature angle-resolved photoemission experiments on $1T$-$TaS_2$ and $1T$-$TaSe_2$ are shown in this thesis, complemented by density-functional theory calculations. Fermi surface mapping experiments in the CDW-phase are similar for the two compounds and do not show symmetries due to the CDW-induced new Brillouin zones or quasiparticle crossing. However, the Ta $5d_z^2$ band displays a clear modulation that is related, in both cases, to the CDW. This involves band splitting into three subbands, which is confirmed by the calculations and is in agreement with the geometrical structure after the periodic lattice distortion in the CDW phase. The topmost subband is thermally populated slightly above $E_F$ ($TaS_2$) or close to $E_F$ ($TaSe_2$). The observed behavior can be understood in terms of the CDW-reconstructed spectral-function-weighted band structure.

To investigate the actual size of the van der Waals gap and the inelastic mean free path in these materials, single scattering calculations have been

implemented and compared with the x-ray photoelectron diffraction measurements. Three compounds have been investigated, $TiSe_2$, $TaSe_2$ and $TaS_2$ and their diffractograms have been perfectly reproduced by the single-scattering theory with the inelastic mean free paths of approximately 10 Å. The local real-space environment information of the diffractograms seems to favor the cleavage within the van der Waals gap.

On the other hand, thin films of noble metals on noble metal substrates offer already geometrically the conditions for the development of strongly anisotropic states. Also surface states in noble metals are quasi-two-dimensional systems. The electronic localization within the film and at the surface can be investigated with the growing film thickness, as well as on the clean noble metal surfaces. The interplay of surface, quantum well and bulk states and corresponding bulk and surface contributions to the photoemission observations can help to reveal the intermetallic interface.

A detailed photoemission study of the surface state dispersion in 0-10 ML thin Ag films on Au(111) is presented in this thesis. Disordered growth at low temperatures and layer-by-layer growth at room temperature are confirmed. The dispersion of the $L$-gap Shockley-type surface state undergoes gradual changes from the one of Au towards the one of Ag with increasing layer thickness. The photoemission data have been well reproduced by *ab initio* band structure calculations using the WIEN2k code. The trend of the binding energy with the growing silver coverage is shown to be indicative of the localization of the surface state at the surface by comparison with the calculated electron density of the surface state. Measurements on 10 ML Ag/Au(111) reveal already the $d$-band states of Ag, but one still observes $sp$-related quantum well states of silver within the projected $sp$-band gap of gold.

# List of publications

- D. Popović, D. Naumović, M. Bovet, C. Koitzsch, L. Schlapbach, and P. Aebi
  *Oxidation of Al-Pd-Mn quasicrystal surfaces*
  Surf. Sci. **492/3**, 294 (2001).

- J. Hayoz, C. Koitzsch, D. Popović, M. Bovet, D. Naumović, L. Schlapbach, and P. Aebi
  *Angle-scanned photoemission on $YbH_x$: Relevance for switchable mirrors*
  Surf. Rev. Lett. **9(1)**, 235 (2002).

- M. Bovet, D. Popović, F. Clerc, C. Koitzsch, U. Probst, E. Bucher, H. Berger, D. Naumović, and P. Aebi
  *Psudogapped Fermi surfaces of $1T$-$TaS_2$ and $1T$-$TaSe_2$: A charge density wave effect*
  Phys. Rev. B **69**, 125117 (2004).

- H. Cercellier, Y. Fagot-Revurat, B. Kierren, F. Reinert, D. Popović, and D. Malterre
  *Spin-orbit splitting of the Shockley state in the Ag/Au(111) interface*
  Phys. Rev. B **70**, 193412 (2004).

- D. Popović, M. Bovet, H. Berger, and P. Aebi
  *Fingerprinting substitution sites in $Pb,Dy$-$Bi_2 Sr_2 Ca_1 Cu_2 O_{8+\delta}$ using X-ray Photoelectron Diffraction*
  Eur. Phys. J. Appl. Phys., accepted 2005.

- D. Popović, F. Reinert, B. Eltner, G. Nicolay, U. Probst, E. Bucher, and S. Hüfner
  *High-resolution photoemission investigation of the spectral function of $1T$-$TiTe_2$: Indications for electron-electron and electron-impurity scattering*
  Phys. Rev. Lett., submitted 2005.

- D. Popović, F. Reinert, S. Hüfner, V. G. Grigoryan, M. Springborg, H. Cercellier, Y. Fagot-Revurat, B. Kierren, and D. Malterre
  *High-resolution photoemission on Ag/Au(111): Spin-orbit splitting and electronic localization*
  Phys. Rev. B, to be submitted 2005.

# Introduction

The electronic structure is an important topic in solid state physics to-day. It offers an irreplaceable tool in the most exciting research areas: high-temperature superconductivity [1], new materials [2, 3, 4], organic films [5] or nano-structures [6]. On the one hand, it is a counter-part of the theoretical investigation or band structure calculations and thus indispensable for the scientific progress in this field. On the other hand, electronic properties are also important for the applications, and electronic structure investigation opens a way of communication with the applied physics or even industry. Finally, the most direct tool for the investigation of the electronic properties of solids is photoelectron spectroscopy. [7] The topics investigated in this thesis show how this technique can be implemented in solving some interesting problems in several different solid state fields.

Technological development of the photoelectron spectroscopy in the last couple of decades has enabled access to the band-structure in the vicinity of the Fermi energy, i.e. quasiparticle band dispersion in the case of correlated systems, where one speaks of the free electrons, whose properties are changed by the interaction. [8] Mostly responsible for it is the lowering of the energy and the momentum resolution over almost two orders of magnitude, which made the observations of the surface state spin-orbit splitting [9, 10], band splitting in the charge density wave phases [11] or detailed crystallographic site analysis possible [12].

Special interest in this field was awaken by the quasi-two dimensional systems for two reasons. [13] The anisotropy of the band-structure reveals the quasi-two dimensional character of the initial states, which are investigated by photoelectron spectroscopy. This allows a straightforward interpretation of the photoemission spectra in terms of the mapping of the initial bands of the crystal. [14] On the other hand, one of the most inspiring phenomena of the last decades proves still to be high-temperature superconductivity (HTSC), the most extensively studied compounds showing such a behavior being of layered structure. Two types of quasi-two dimensional systems have been studied in this thesis: layered transition metal dichalcogenides (TMDs) of the $1T$-family and surface states in thin silver films on Au(111).

The study of the $1T$-TMD-polytypes [15, 16, 17] $TaSe_2$, $TaS_2$ and $TiSe_2$, has been influenced by the HTSC in different ways. The first two compounds are charge density wave (CDW) materials, whose ground state in the CDW phase is directly related to the appearance of the pseudogap, which is recently also considered to be a precursor of the HTSC in the Bi-containing compounds. $TiTe_2$ is a Fermi liquid reference compound, which is thus important for the

understanding of the normal state properties of more complex systems, including HTSC.

On the other hand, thin films of noble metals on noble metal substrate offer already geometrically the conditions for the development of quasi-two dimensional states. The strong anisotropy in this system originates from the electronic localization at the surface, which is characteristic for noble metal thin film or substrate surfaces, and related to the existence of the projected band gap. [18] The states developing within this gap are characterized by a complex wave number, meaning that they are damped outside, as well as inside the crystal, and thus do not couple to the bulk states. This localization of the surface state wave function is interesting for the investigation with the growing film thickness in order to learn about the buried intermetallic interface or spatial wave function distribution. The interplay of surface, quantum well and bulk states and corresponding bulk and surface contributions to the photoemission observations has been studied in this thesis, in thin Ag films on Au(111).

Another goal of this thesis is to demonstrate which new domains of solid state research have become accessible by means of high-resolution photoelectron spectroscopy. The development of the state-of-art photoelectron analyzers has triggered the studies of phenomena related to the low-energy scale, where the relevant gaps in the spectral function, flat bands or band-splitting appear. On the other hand, parallel angular detection has enabled convenient data acquiring, especially for the surface states. Similarly, completely automatized and motorized sample rotation, allowed routine Fermi surface mapping and x-ray photoelectron diffraction, serving for both electronic and geometric structure analysis. In this sense is photoelectron spectroscopy an outstanding technique, which can be used to combine the real-space crystallographic information contained in the diffraction patterns of highly energetic photoelectrons with the $k$-space investigations of quasiparticle band dispersions in the vicinity of the Fermi level.

The experiments from this Thesis have been performed on two outstanding measurement set-ups: within the group of Prof. Dr. Dr. h.c. mult. Stefan Hüfner in Saarbrücken (Germany), on the photoemission spectrometer with an excellent energy and angular resolution, and within the group of Prof. Dr. Louis Schlapbach in Fribourg (Switzerland), on a photoemission set-up equipped with the motorized sample manipulator with two degrees of freedom. The scanning tunnelling microscopy (STM) data on TMDs have been gained within the group of Prof. Dr. L. Schlapbach in Fribourg, in collaboration with M. Bielmann. The STM data on Ag/Au(111) have been obtained by Dr. H.

Cercellier in the group of Prof. Dr. D. Malterre in Nancy (France), who has been collaborating with us on this topic. Band-structure calculations using WIEN97 on TMDs have been performed in Fribourg by Dr. M. Bovet and Prof. Dr. P. Aebi. Band-structure calculations using WIEN2k on Ag/Au(111) have been performed in Saarbrücken by Dr. V. G. Grigoryan and Prof. Dr. M. Springborg. Both are used extensively in this work, for comparison with the measurements.

Part one of this thesis is devoted to theoretical and experimental basics of the modern photoemission experiment, with a glance on band-structure calculations. The second part deals with $1T$-materials in the following order: Fermi liquid properties of $TiTe_2$, charge density wave states in $TaS_2$ and $TaSe_2$ and geometrical structure analysis of $TiSe_2$, $TaS_2$ and $TaSe_2$. In the third part surface, quantum well and bulk states in thin silver films on Au(111) are analyzed.

# Table of Contents

# Part I

# Photoelectric effect in experiment and theory

# Chapter 1

# The theory of photoemission

## 1.1 Basic concepts in photoemission

Upon irradiation of a solid with photons, electrons are liberated, called photo-electrons, whose kinetic energy equals the difference of the photon energy and the sum of their binding energy in the material and the surface work function. [19] This effect is known as the photoeffect. The number of electrons at different kinetic energies gives insight into the occupied core levels and valence band states, the experimental technique taking advantage of this fact being known as photoelectron (or photoemission, PE) spectroscopy (PES, PS, or angle-resolved PES, ARPES). The incident radiation can be in the ultraviolet range (5-100 eV, UPS), in the soft x-ray range (100-1000 eV, SXPS) or in the x-ray range (>1000 eV, XPS). The outgoing electrons are detected by the angle- and energy-resolving electron analyzer. [7, 20] This is schematically presented in Fig 1.1. The left side shows occupied core levels and the valence band of the sample from which an electron, bound with binding energy $E_B$, is excited by the light of energy $h\nu$ into a state with kinetic energy $E_K$, where the relation given by Einstein [19] holds (far left). The right side shows measurement result, where peaks of a photoemission spectrum (right) correspond to the occupied electron states of the sample (left). The formula (far right) allows the calculation of the binding energies of the electrons according to the measured kinetic energies and known work function of the analyzer.

With its high sensitivity and resolution, UPS is used to study valence-band and low-binding-energy (shallow) core levels. The UPS spectra of solids show exclusively direct, $k_\parallel$-conserving, transitions. From the energy and momentum distribution of the electrons, one can determine the electronic dispersion curves $E(k)$ in the solid. XPS can be used in the valence band as well as in

the core-level regime, however with the resolution about one order of magnitude worse than that of UPS, except at the synchrotron sources. XPS can be thus used as a chemically sensitive probe of core levels (ESCA–Electron Spectroscopy for Chemical Analysis), for stoichiometry determination [21], for the quantitative analysis of physi/chemisorbed species, surface reactions, diffusion or segregation [21] or alloy formation [22, 23, 24, 25], similar to Auger electron spectroscopy (AES). The information about the density of unoccupied states can be obtained with inverse photoemission spectroscopy (IPES).
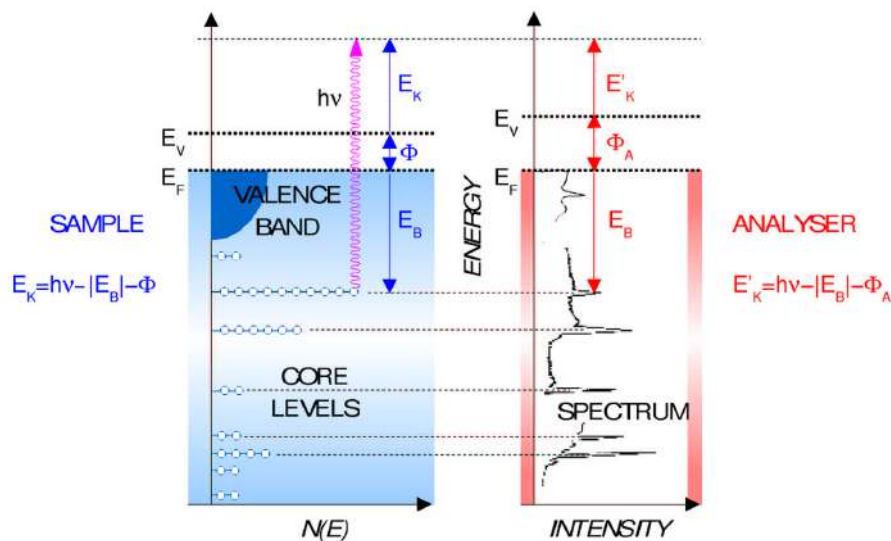


Figure 1.1: Schematic representation of the photoemission experiment.

The characteristics of (photo)electrons for surface spectroscopy or diffraction, by comparison with photons, atoms, neutrons or ions are the following: the escape depth of electrons is only a few Å, which makes them a surface probe of the electronic states; they are easily focused and energetically tunable by electric fields and vanish after detection; their energy and angle can be analyzed by laboratory instruments implementing electric fields.

According to the kinetic theory of gases, with a sticking coefficient $S = 1$ (every molecule or atom impinging on a surface sticks there), a coverage of 1 monolayer (ML) is achieved at a pressure of $10^{-9}$ Torr (1 Torr = 1.333 mbar) in about 1000 seconds (half an hour). For many materials the sticking coefficients are much smaller than one and then a vacuum of $10^{-10}$ Torr is sufficient to perform meaningful experiments over an extended period of time.

The universal electron mean free path $\lambda$ in monolayers as a function of the electron kinetic energy for elements is depicted in Fig 1.2. In the kinetic
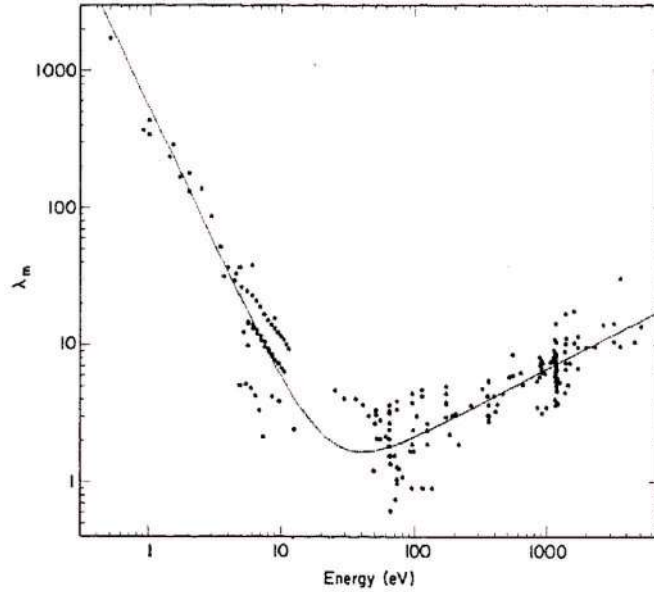
Figure 1.2: Compilation of electron mean free path measurements for elements [26] in monolayers as a function of kinetic energy.

energy range of interest, between about 10 and 2000 eV, the mean free path is smaller than 10 ML, with a minimum approaching one monolayer for kinetic energies of 30–100 eV. Atomically clean surfaces are thus a prerequisite, which is routinely obtainable today in ultra-high vacuum (UHV) conditions. [27] The formula that fits the presented data the best is the 'universal curve' [26, 28]:

$$\lambda_m = 538E^{-2} + 0.41(aE)^{1/2}, \tag{1.1}$$

where $a$ is the monolayer thickness and $E$ kinetic energy. One important consequence of the finite escape depth of the photoelectrons is the variation of the sampled thickness with the rotation angle of the sample with respect to the analyzer (i.e. emission angle), grazing angles being more surface sensitive than normal emission.

The choice of the excitation energy for a certain experiment is problem-specific. The dipole transition matrix element is proportional to an overlap integral between the initial-state wave function and the wave function of the outgoing electron: $M \propto \int \psi_f r \psi_i \mathrm{d}x\mathrm{d}y\mathrm{d}z$. For both the low kinetic energy final state electron and the low angular momentum initial state electron, the variation of the wave function is small over the atomic volume, giving a large dipole matrix element. This means that higher photon energy should be im-

16

plemented to study initial states with higher angular momentum, because it will increase their cross-section.

The final state in a photoemission experiment has a positive hole and can thus be distinctly different from the initial state. It is not always a trivial problem to infer properties of the initial (ground)-state from the final-state spectra. The simplest formulation of the momentum-conservation rule yields that the final-state wave vector $\boldsymbol{k}_f$ equals the initial state wave vector $\boldsymbol{k}_i$ plus a reciprocal lattice vector $\boldsymbol{G}$.

## 1.2 The theory of photoemission

*The three-step model* breaks the PE process up into three distinct and independent processes: (*i*) photoexcitation: the photon is absorbed and an electron is excited into an unoccupied state; (*ii*) this electron travels through the sample to the surface; (*iii*) and finally escapes through the surface into the vacuum where it is detected. A one-step theory actually gives results that are not very different from the conceptually much simpler three-step model. The final state in photoemission process can be viewed as the one where, in contrast to the initial state, one electron has been removed, or a positive potential has been added, which makes substantial difference to the initial state, especially in systems with many degrees of freedom. Therefore, the theory describing PES is a complicated many-body theory. The crucial assumption of the PE-theory is *the sudden approximation* saying that the response of the system to the creation of the photohole is assumed instantaneous and that there is no interaction between the escaping photoelectron and the remaining system, which is valid in the high-energy photoelectron limit or in two-dimensional materials.

The transition probability $w$ per unit time of photoemission process from the $N$-electron initial state $i$ with wave function $\Psi_i$ to the $N$-electron final states $f$ with wave function $\Psi_f$ in the photon field having the vector potential $\boldsymbol{A}$ is calculated by Fermi's Golden rule:

$$w \propto \frac{2\pi}{\hbar} |\langle \Psi_f | \Delta | \Psi_i \rangle|^2 \delta(E_f - E_i - \hbar\omega), \tag{1.2}$$

$$\Delta = \frac{e}{2mc}(\boldsymbol{A} \cdot \boldsymbol{p} + \boldsymbol{p} \cdot \boldsymbol{A}) - e\phi + \frac{e^2}{2mc^2}\boldsymbol{A} \cdot \boldsymbol{A}, \tag{1.3}$$

where $\boldsymbol{A}$ and $\phi$ are the vector and scalar potentials and $\boldsymbol{p}$ the momentum operator $\boldsymbol{p} = i\hbar\vec{\nabla}$. Because of the translational invariance in the solid (surface neglected), for a photoemission process, one retains: $\Delta = (e/mc)\boldsymbol{A} \cdot \boldsymbol{p}$. Radiation of $h\nu$=10 eV has $10^3$ Å wavelength, large compared to the atomic

distances. Therefore **A** can be taken as constant. The commutation relations lead to the equivalence $\langle\Psi_f|\boldsymbol{A}\cdot\boldsymbol{p}|\Psi_i\rangle \propto \langle\Psi_f|\boldsymbol{A}\vec{\nabla}\cdot V|\Psi_i\rangle \propto \langle\Psi_f|\boldsymbol{A}\cdot\boldsymbol{r}|\Psi_i\rangle$, if the Hamiltonian of the electron (e.g., in the solid in the absence of the electromagnetic field) is $H = (\mathbf{p}^2/2m) + V(\mathbf{r})$, meaning that the photoemission of a free-electron gas ($V(\boldsymbol{r}) = const, \nabla\cdot V = 0$) is not possible [7, 29].

In a one-electron view of the core-level PE, the initial-state wave function is written as a product of the orbital $\phi_k$ from which the electron is excited and the wave function of the remaining electrons $\Psi_{i,\mathrm{R}}^k(N-1)$, $\Psi_i(N) = C\phi_{i,k}\Psi_{i,\mathrm{R}}^k(N-1)$. The final state is written as a product of the wave function of the photoemitted electron $\phi_{f,E_{\mathrm{kin}}}$ and that of the remaining $(N-1)$ electrons $\Psi_{f,\mathrm{R}}^k(N-1)$, $\Psi_f(N) = C\phi_{f,E_{\mathrm{kin}}}\Psi_{f,\mathrm{R}}^k(N-1)$. $C$ is the operator that antisymmetrizes the wave function and $R$ stands for remaining. The transition matrix element is obtained as

$$\langle\Psi_f|\boldsymbol{r}|\Psi_i\rangle = \langle\phi_{f,E_{\mathrm{kin}}}|\boldsymbol{r}|\phi_{i,k}\rangle\langle\Psi_{f,\mathrm{R}}^k(N-1)|\Psi_{i,\mathrm{R}}^k(N-1)\rangle, \qquad (1.4)$$

a product of a one-electron matrix element and an $(N-1)$-electron overlap integral. Assuming that the remaining orbitals (passive orbitals) are the same in the final state as they were in the initial state (*frozen-orbital approximation*) $\Psi_{f,\mathrm{R}}^k(N-1) = \Psi_{i,\mathrm{R}}^k(N-1)$ the overlap integral is unity and the transition matrix element is just the one-electron matrix element.

However, it is intuitively clear that the system, after ejection of the electron from orbital $k$ will try to readjust its remaining $N-1$ charges in order to minimize its energy (relaxation). If the final state with $N-1$ electrons has $s$ excited states with the wave function $\Psi_{f,s}^k(N-1)$ and energy $E_s(N-1)$, the transition matrix element will include summing over all possible excited final states:

$$\langle\Psi_f|\boldsymbol{r}|\Psi_i\rangle = \langle\phi_{f,E_{\mathrm{kin}}}|\boldsymbol{r}|\phi_{i,k}\rangle\sum_s c_s, \qquad c_s = \left\langle\Psi_{f,s}^k(N-1)|\Psi_{i,\mathrm{R}}^k(N-1)\right\rangle, \quad (1.5)$$

where $|c_s|^2$ is the probability that the removal of an electron from orbital $\phi_k$ of the $N$-electron ground state leaves the system in the excited state $s$ of the $(N-1)$-electron system. For strongly correlated systems many of the $c_s$ are non-zero. In terms of the PE spectrum, this means that for $s = k$ one has the so-called main line and for the other non-zero $c_s$ additional satellite lines. For the weak correlations $\Psi_{f,s}^k(N-1) \simeq \Psi_{i,\mathrm{R}}^k(N-1)$ and therefore $|c_s|^2 \simeq 1$ for $s = k$ and $|c_s|^2 \simeq 0$ for $s \neq k$, there is only one peak. This allows expressing the photocurrent $I$ detected in a PE experiment as

$$I \propto \sum_{f,i,k}|\langle\phi_{f,E_{\mathrm{kin}}}|\boldsymbol{r}|\phi_{i,k}\rangle|^2\sum_s|c_s|^2\delta(E_{f,\mathrm{kin}}+E_s(N-1)-E_0(N)-\hbar\omega)f_{FD}(\omega,T),$$

$$(1.6)$$

where $E_0(N)$ is the ground state energy of the $N$-electron system, $f_{FD}(\omega, T)$ the Fermi-Dirac distribution and

$$A = \sum_s |c_s|^2 \delta(E_{f,\text{kin}} + E_s(N-1) - E_0(N) - \hbar\omega) \qquad (1.7)$$

*the spectral function.*

Due to the delocalization of the electrons, the electron states in the valence band are wavevector dependent:

$$
\begin{aligned}
I \propto \quad & \sum_{s,i} \left| \left\langle \tilde{\phi}_{f,E_{\text{kin}}} | \boldsymbol{r} | \tilde{\phi}_i \right\rangle \right|^2 \left| \left\langle \tilde{\Psi}_{f,s}(N-1) | \tilde{\Psi}_i(N-1) \right\rangle \right|^2 \\
& \times \frac{1}{\left( k_{i\perp}^{(1)} - k_{f\perp}^{(1)} \right)^2 + \left( k_{f\perp}^{(2)} \right)^2} \delta\left( \boldsymbol{k}_{i\parallel} - \boldsymbol{k}_{f\parallel} + \boldsymbol{G}_{\parallel} \right) f_{FD}(\omega, T) \\
& \times \delta\left( \boldsymbol{k}_i - \boldsymbol{k}_f + \boldsymbol{G} \right) \delta(E_{\text{k}} + E_s(N-1) - E_0(N) - \hbar\omega) \qquad (1.8)
\end{aligned}
$$

In working out the matrix element the periodicity of the Bloch function with respect to $\boldsymbol{G}$, the reciprocal lattice vector has been taken into account. The momentum conservation parallel to the surface shows up separately due to the Fresnel equations. The photoexcited electrons have a relatively short inelastic mean free path within the solid, which is taken into account by assuming a complex wave vector perpendicular to the surface of the solid $k_\perp = k_\perp^{(1)} + i k_\perp^{(2)}$, which leads to a smearing of the momentum conservation. The tilde in wave functions means that the momentum conservation has been worked out.

The points where the three-step model was applied in deriving the formula for the photocurrent in a solid are the following: for photoexcitation of an electron in the solid the matrix element is evaluated between two Bloch states in the solid; propagation of the photoexcited electron to the surface results in a damping of the electron wave described by a complex wave vector; escape of the electron from the solid into the vacuum demanded conservation of $\boldsymbol{k}_{\parallel}$. The three-step model makes the photoemission process quite comprehensible, but a correct treatment of the process requires the introduction of the true final state. For this final state the so-called inverse LEED (Low Energy Electron Diffraction) wave function can be used. [30, 31, 32] In LEED an incoming monochromatic beam of electrons is scattered from the ions in the crystal and the scattered waves sum up to yield the LEED diffraction pattern. If one reverses the direction of the incoming beam, one obtains a monochromatic wave of electrons, which originates from the ions of the crystal, similar to the electron wave produced by the photoemission process.

## 1.3 The photoelectron lifetime

Regarding the photoelectron escaping from the solid into the vacuum, refraction at the solid-vacuum interface ensures the conservation of $k_\parallel$ and the measured spectrum is a $k_\perp$ convolution of the photohole ($A_h$) and photoelectron ($A_e$) spectra [33]. If the photoelectron and photohole spectra have Lorentzian lineshapes with the corresponding widths $\Gamma_e$ and $\Gamma_h$, the total linewidth of the resulting ARPES spectrum will also be a Lorentzian and the width is given by the general expression for the measured photoemission linewidth [14]:

$$\Gamma = \frac{\frac{\Gamma_h}{|v_{h\perp}|} + \frac{\Gamma_e}{|v_{e\perp}|}}{\left| \frac{1}{v_{h\perp}} \left( 1 - \frac{m v_{h\parallel} \sin^2 \theta}{\hbar k_\parallel} \right) - \frac{1}{v_{e\perp}} \left( 1 - \frac{m v_{e\parallel} \sin^2 \theta}{\hbar k_\parallel} \right) \right|}, \tag{1.9}$$

where $\theta$ denotes the polar angle of emission. In the case of normal emission $\theta = 0$, one gets [34, 35]:

$$\Gamma = \frac{\Gamma_h + \left| \frac{v_{h\perp}}{v_{e\perp}} \right| \Gamma_e}{1 - \frac{v_{h\perp}}{v_{e\perp}}}, \qquad v_{e,h\perp} = \frac{\partial E_{e,h}}{\partial k_\perp}. \tag{1.10}$$

The measured linewidth is a linear combination of both electron and hole widths, with the coefficients which depend on details of the band structure, angle and the data acquisition mode. According to Chiang *et al.* [36], $\Gamma$ of the measured spectrum is dominated by $\Gamma_e$, which is typically of the order of 1 eV and thus much larger than $\Gamma_h$, of the order of 0.1 eV.

If the initial state is sufficiently close to the Fermi level, $\Gamma_h \to 0$ and $\Gamma$ is totally determined by the $\Gamma_f$. On the other hand, when $| v_{h\perp} |$ is much smaller than the other velocities, we have for the case of normal emission $\Gamma = \Gamma_h + | \frac{v_{h\perp}}{v_{e\perp}} | \Gamma_e$, or for the vanishing $| v_{h\perp} |$: $\Gamma = \Gamma_h$. For the arbitrary angle this condition follows from the equation (1.9):

$$\Gamma = \frac{\left| \frac{1}{v_{h\perp}} \right| \left[ \Gamma_h + \Gamma_e \left| \frac{v_{h\perp}}{v_{e\perp}} \right| \right]}{\left| \frac{1}{v_{h\perp}} \right| \left| \left( 1 - \frac{m v_{h\parallel} \sin^2 \theta}{\hbar k_\parallel} \right) - \frac{v_{h\perp}}{v_{e\perp}} \left( 1 - \frac{m v_{e\parallel} \sin^2 \theta}{\hbar k_\parallel} \right) \right|} \xrightarrow{| v_{h\perp} | \to 0} \frac{\Gamma_h}{\left| 1 - \frac{m v_{h\parallel} \sin^2 \theta}{\hbar k_\parallel} \right|}, \tag{1.11}$$

yielding finally $C\Gamma_h$, which in the case of normal emission gives exactly $\Gamma = \Gamma_h$, i.e. two-dimensionality of the initial band allows neglecting of the finite photoelectron lifetime in the measured spectrum.

In addition to intrinsic broadening mechanisms, finite angular resolution $\Delta\theta$, for instance, leads to external broadening of the linewidth. Thiery [35]

has developed the following expression for the energy distribution curve (EDC) full-width half-maximum (FMHW):

$$\Gamma = \Gamma_0 + \left| \frac{\hbar^2 k^{Vac^2} \cos\theta(v_{e\perp}v_{h\parallel} - v_{e\parallel}v_{h\perp})}{\hbar k^{Vac}(v_{e\perp} - v_{h\perp}) - m\sin\theta(v_{e\perp}v_{h\parallel} - v_{e\parallel}v_{h\perp})} \right| \cdot \Delta\theta. \qquad (1.12)$$

Th. Kreutz [37] derived the relevant expressions for the angular distribution curves (ADC):

$$\Delta\theta_{Vac}(\Delta\theta^{exp}, \Delta E^{exp}) = \Delta\theta_{Vac} + \frac{\Delta E^{exp}}{\hbar k^{Vac}\cos\theta_{Vac}} \cdot \left| \frac{\frac{1}{|v_{h\perp}|} - \frac{1}{|v_{e\perp}|}}{\frac{v_{h\parallel}}{v_{h\perp}} - \frac{v_{e\parallel}}{v_{e\perp}}} \right| + \Delta\theta^{exp}. \quad (1.13)$$

## 1.4 Band-structure calculations

There are two major non-experimental treatments of the interacting fermion systems: band structure calculations [38] and many-body theories. For the former, the connection with the first-principles in not always apparent, for the second - the applicability to explain the experimental data, the matrix elements being a key problem in explaining optical properties by the one-particle model.

Various different theories will be mentioned in relation to certain problems and we focus now on the first principles calculations. WIEN2k is a program code implementing the full potential linear augmented plane wave (FLAPW) method in performing *ab initio* band-structure calculations. [39, 40, 41, 42, 43, 44, 45, 46, 47] The linearized augmented plane wave (LAPW) method is among the most accurate methods for performing electronic structure calculations for crystals. It is based on the density functional theory (DFT) and the local spin density approximation (LSDA). Exchange and correlation are treated according to the DFT, where one has to calculate the electron density, instead of solving the Schrödinger equation for the wave-function [38]. Two approximations comprise the LSDA [48, 49]: (*i*) the assumption that exchange energy can be written in terms of a local exchange-correlation energy density times the total (spin-up plus spin-down) electron density and (*ii*) the particular form chosen for the local exchange-correlation energy density. Every infinitesimally small volume of the material contributes to the exchange-correlation energy with an amount equal to the contribution of a homogeneous electron gas that occupies that same infinitesimally small volume, and that has the same (overall) charge density as the charge density of the original material in that volume. [42] Several forms of LSDA potentials exist in the literature, recent improvements using the generalized gradient approximation (GGA) [50] are frequently used.

For valence states relativistic effects can be included either in a scalar relativistic treatment or with the second variational method including spin-orbit (SO) coupling with the scalar-relativistic eigenfunctions as basis. Core states are treated fully relativistically. The LAPW method works with a basis set which is especially adapted to the problem. The unit cell is divided into non-overlapping atomic spheres (centered at the atomic sites) and an interstitial region. In these two types of regions different basis sets are used: (*i*) inside atomic sphere a linear combination of radial functions multiplied by spherical harmonics; the coefficients of the linear combination are determined to match (in value and slope) the corresponding basis function of the interstitial region and (*ii*) in the interstitial region a plane wave expansion is used over the reciprocal lattice vectors and the wave vector inside the first Brillouin zone (BZ). Each plane wave is *augmented* by an atomic-like function in every atomic sphere.

The solutions to the Kohn-Sham equations are expanded in this combined basis set of LAPWs according to the linear variation method and the coefficients are determined by the Rayleigh-Ritz variational principle. The convergence of this basis set is controlled by a cut-off parameter $R_{mt}K_{max}$, the product of the smallest atomic sphere radius in the unit cell and the largest $K$ vector has to be 6–9. In its general form of the LAPW method no potential shape approximations are made, a procedure frequently called the "full-potential" method. The "muffin-tin" approximation used in early band calculations corresponds to taking the spherical average inside the spheres and the volume average in the interstitial region. The drawbacks are that many phenomena are not observable using this method, because they are sensitive to the exact shape of the potential. One example for it are the surface core-level shifts [51, 52, 53].

# Chapter 2

# Photoemission experiment

## 2.1 Experimental setup

The experimental set-up in Fribourg represents an extended version of the Vacuum Generators ESCALAB Mk II spectrometer, operating with a base pressure in the low $10^{-10}$ mbar region. XPS, x-ray photoelectron diffraction (XPD) and UPS have been performed in the analysis chamber, equipped with a twin-anode x-rays source (Mg/Si), an ultraviolet (UV) lamp (He/H/Ne) with monochromator [54] and a 150-mm-radius hemispherical electron-energy analyzer with a three-channeltron detection system (Fig 2.1). A motorized manipulator allows sample rotation with two degrees of freedom. [55] All the measurements were carried out at room temperature (RT).

XPS and XPD were performed with Mg K$\alpha$ (h$\nu$ = 1253.6 eV) and Si K$\alpha$ (h$\nu$ = 1740 eV) and a pass energy of 100 eV. The angular resolution was better than 1° full cone acceptance. The spectra have been measured with a pass energy of 100 eV corresponding to an energy resolution of approximately 1 eV. The state-of-the-art XPD measurements have been performed over one night (12h, mostly distributed over several peaks).

ARPES EDCs and Fermi surface mapping (FSM) measurements have been collected at room temperature using monochromatized He I (h$\nu$ = 21.2 eV) photons and the sequential motorized sample rotation. The energy and angular resolution were 20 meV and 0.5°, respectively. A full FSM of a good quality can be obtained within less then an hour, due to the motorization of the measurement set-up. The accurate position of the Fermi level ($E_F$) has been determined on a polycrystalline copper sample. In some cases, the ARPES results have been normalized by the Fermi-Dirac function in order to show states above the Fermi level. Cleanness, quality and reconstruction of the

surface have been checked by PE and LEED. XPD was used to determine the sample orientation *in situ* with an accuracy of better than 0.5°. LEED patterns were recorded with normal incidence and electron energies of 110-120 eV.

STM experiments on 1T-TaSe$_2$ have been performed in a UHV system equipped with a scanning tunnelling microscope OMICRON operating at RT.
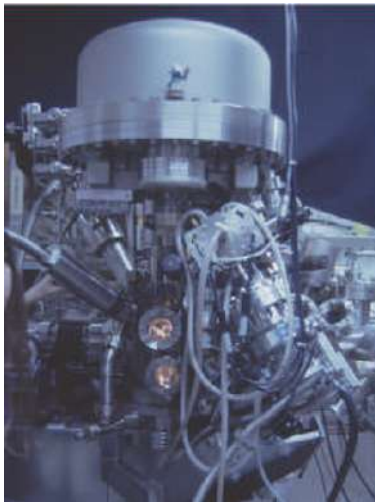


Figure 2.1: Experimental set-up in Fribourg: analysis chamber.

Samples of 1$T$-TaS$_2$ and 1$T$-TaSe$_2$ have been prepared from the elements by reversible chemical reaction with iodine as a transport agent, between 950° (hot zone) and 900° (cold zone) by H. Berger (EPF Lausanne) and Prof. E. Bucher (Konstanz) [56, 57]. 1$T$-TaS$_2$ samples showed clear first-order phase transition at 180 K, indicating very good sample quality. [58] TiSe$_2$ was grown by H. Berger at 500 °C with ICl$_3$ as a transport agent in the presence of a slight Se excess, yielding resistivity ratio $\rho(165K)/\rho(295K) = 3.3$. [59, 60] 1$T$-TiTe$_2$ samples were grown by Dr. U. Probst (Konstanz) by iodine vapor transport and oriented using Laue diffraction. They were cleaved *in situ* at pressures in the lower $10^{-10}$ mbar region by Torr-Seal attached cleavage post (in the case of TiTe$_2$) or scotch-tape (for the others). They have been attached by means of graphite-sprayed Torr-Seal (TiTe$_2$) or silver epoxy (others) on a specially designed sample holder.

The single scattering calculations (SSC) are performed within the "spherical wave model" [61], as previously described in Ref. [62]. All the calculations have been performed at RT with uncorrelated Debye-Waller factor. The phase constants were calculated with the MUFPOT program, which is

24

based on the muffin-tin potential approximation [20], with the wave functions taken from [63]. Both programs have been written by P. Aebi. The radial matrix elements ($R_{l+1}$, $R_{l-1}$ in bohr) and phase shifts ($\sigma_{l+1}$, $\sigma_{l-1}$ in rad) were taken from Ref. [64]: for Ti (798.2 eV) 0.578/2.196/1.958/4.597, for Se (1200 eV) 0.21/1.05/1.769/4.124, for Ta (1229.5 eV) 0.233/1.79/2.544/5.759, for S (1093 eV) 0.362/1.07/1.487/3.505, at the kinetic energies indicated in brackets. Metal emission has been calculated with 6 emitters, chalcogen emission with 36. The inner potential $V_0$, which approximates the potential step from the solid into the vacuum, was set to 10 eV and the average atomic displacements in the bulk and at the surface were taken to be 0.012/0.03 Å$^2$.

Band structure calculations in Fribourg have been performed using the WIEN97 package [65]. For the exchange-correlation potential the GGA was used. [50] For the photoemission process free electron final states were assumed, without introduction of any matrix element effects. For the details of the calculation of the reconstructed structure of $1T$-TaS$_2$, see Reference [66].
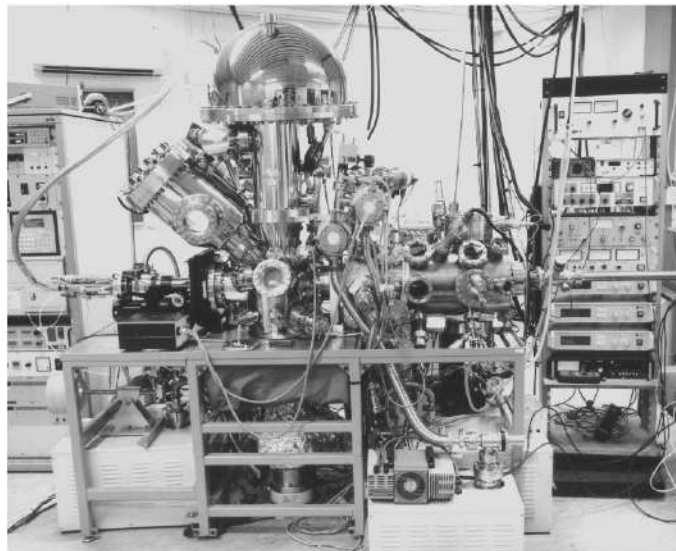


Figure 2.2: Experimental set-up in Saarbrücken.

The photoemission experiments in Saarbrücken have been performed with a SCIENTA SES 200 analyzer (Fig. 2.2) in the angular mode and a monochromatized GAMMADATA VUV-lamp at a photon energy of $h\nu = 21.2$ eV (He I) in the UHV chamber with the base pressure $5 \times 10^{-11}$ mbar. The angle between lamp and analyzer is 45°. The angular mode allows to measure simultaneously all relevant energy and angular positions of the $L$-gap surface state dispersion of pure Au(111) or films of Ag/Au(111). The energy resolution

is $\Delta E = 3.5$ meV, the angular resolution $\Delta\theta \approx \pm0.15°$. [9, 67] The sample temperature of the photoemission data presented here was chosen not below 20–30 K because of an accelerated surface aging at lower temperatures, probably due to hydrogen adsorption. [68] The measuring time was approximately 15 min for one data set of the complete occupied surface state of Au(111) and additional 15 min should be considered for the film preparation.

The surface of the Au(111) was prepared by repeated cycles of Ar$^+$ sputtering and subsequent annealing up to 700 °C. Ag films were evaporated with a triple-evaporator Omicron EFM 3T (with integral flux monitor) from the electron-bombardment heated crucible by setting the emission current at 17 mA and keeping the flux by the feedback-loop at 1 $\mu$A. This corresponds approximately to the application of 690 V high tension and yields evaporation rate of 0.3 Å/min in the high $10^{-10}$ mbar pressure range. The coverage was determined by a quartz-microbalance. The calibration has been checked by a comparison of the band minima of the surface state from our measurements with the ones obtained at surfaces where the coverage has been determined by STM [69].

The STM measurements and additional ARPES measurements on Ag on Au(111) were carried out by Dr. H. Cercellier in Nancy, in a UHV setup composed of a molecular beam epitaxy chamber for the elaboration and characterization of the surfaces, an STM chamber equipped with an Omicron STM1 operating at RT and a photoemission chamber with a high resolution Scienta SES 200 analyzer. The substrate was cleaned by several cycles of Ar$^+$ etching at 2000 V and annealing at 350 °C. The cleanness was checked by STM and AES. The Ag atoms were evaporated from a Knudsen cell operating at $T$=1120 °C at a rate of (0.5-1) ML/min. The ARPES measurements have been performed at the photon energies of $h\nu = 21.2$ eV (He I) or $h\nu = 11.83$ eV (Ar I) and the sample temperature of 80 K.

Band structure calculations on Ag/Au(111) have been performed by Dr. V. Grigoryan using the WIEN2k package [70]. For the exchange-correlation potential the GGA was used. [50] A basis set of 1600 LAPWs and a 100 $k$-points mesh in the irreducible Brillouin zone have been used. SO coupling was included in a second variational step. The surface was modelled by a periodic slab of 23 Au and 1 to 6 Ag layers on the each Au surface, separated by 20 bohr of vacuum. For smaller slabs, the interaction of the two confining surfaces, both via the "bulk" and via the "vacuum" [71], leads to an artificial splitting of the surface state. For a 7-layer slab this splitting is much larger than the SO-splitting of the Au(111) surface state. The size of the system, i.e. 23 layers and 20 bohr vacuum, is chosen in order to produce a splitting of the two surface states below 1 meV, which is two orders of magnitude smaller

than the SO-splitting of Au(111) at $k_F$ (>100 meV). The slab thickness exceeds both decay lengths of Au(111) (3.6 ML) and Ag(111) (12 ML). [72]

## 2.2 Fermi surface mapping

There are several methods for determination of the Fermi surface: de Haas–van Alphen-effect, anomalous skin effect, cyclotron resonance, ultrasonic attenuation. [73] Photoemission is today the method of choice for the Fermi surface mapping, because it does not require high-purity samples or very low temperatures [74]. For the implementation of photoemission for the Fermi surface mapping, crucial was the development of the angle-resolving analyzers. From the angular dependent intensity at a certain kinetic energy, one gets an approach to the crystal wavevector. [74] The parallel component of the wavevector, $k_{\|x} = \sqrt{2m_e/\hbar^2}\sqrt{E_{kin}}\sin\theta$, is up to addition with the reciprocal lattice vector, exactly the parallel wavevector of the initial state, because it remains conserved. [75, 76, 74] The determination of the perpendicular component of the wavevector $k_\perp = k_z$ is because of the refraction at the surface not as easy. [74] One possibility is to assume free electron final states. In that case, the dispersion of the final state is given by $E_f = (\hbar^2/(2m^*))(\vec{k_f} + \vec{G})^2 - V_0 + \phi$, where $m^*$ denotes the effective mass, and one can deduce an expression for the perpendicular component, $k_\perp = \sqrt{2m_e/\hbar^2}\sqrt{E_{kin}\cos^2\theta + V_0}$. This has proved useful for the FSM of the three dimensional metals [74] (Fig. 2.3a). Rewritten in more common dimensions, the above formulas have the following form:

$$k_{\|x}[\overset{\circ}{A}^{-1}] = 0.512 \cdot \sqrt{E_{kin}}\sin\theta\cos\varphi \qquad (2.1)$$
$$k_{\|y}[\overset{\circ}{A}^{-1}] = 0.512 \cdot \sqrt{E_{kin}}\sin\theta\sin\varphi$$
$$k_\perp[\overset{\circ}{A}^{-1}] = 0.512 \cdot \sqrt{E_{kin}\cos^2\theta + V_0}.$$

Whereas $\theta$ denotes the polar angle of emission, $\varphi$ stands for the azimuthal angle, defined in the $xy$ plane, if $z$-axes coincides with the surface normal. For the states with negligible $k_\perp$-dispersion, quasi two dimensional states, the parallel component of the wavevector is sufficient for the detailed description of the initial states (Fig. 2.3 c,d,e).

Modern spectrometers can operate in parallel detection mode, simultaneously collecting photoelectrons as a function of two independent parameters: kinetic energy and angle. [78, 9, 83, 67, 84] A typical dataset for such a measurement consists of the measured intensity $I(E, \theta)$ of the photoelectrons over a certain energy and angular range. One typical data set for non-parallel detection would be one cut through this 2D surface, EDC when it is performed

at the constant wavevector (angle), or MDC (momentum distribution curve) otherwise. Additional to this, there are FSM presentations, like the ones in Fig. 2.3 c,d), where each point presents one $k_\| = (k_x, k_y)$ with the intensity represented in color or grey scale. The points of the images correspond to photoelectron intensities (color or grey-scale) in an energy window around the Fermi level taken as a function of emission angle. The outer circle in Fig. 2.3d) corresponds to grazing emission. Fig. 2.3d) presents an FSM of a high-temperature superconductor. Bi-containing superconductors, as well as the other ones, are normally doped till the metallic normal state is created out of a semi-conducting one. [7] This allows FSM on these compounds. [55] Furthermore, the order parameter in these systems in not isotropic, but most probably of a $d_{x^2-y^2}$ type [7], meaning that the gap (which is the absolute value of the order parameter) opens only at some points in the BZ below $T_c$, enabling again the FSM measurements.

Although the ARPES measurements can cover only certain cross sections of the three-dimensional Fermi surface, the 3D presentations are often used for the calculations (Fig. 2.3b,f) or measurements which can reveal the 3D-structure of the Fermi surface, such as ultrasonic attenuation (Fig. 2.3a) or de Haas-van Alphen effect (Fig. 2.3e). FSM along $k_\perp$ is possible if using ARPES with variable photon energy.
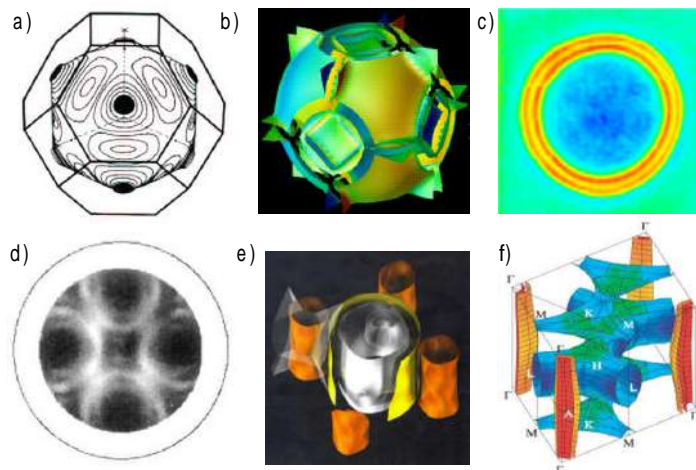


Figure 2.3: Fermi surface of a) Cu, A.B. Pippard [73]; b) Al, J. Chen, T.-S. Choy, S. Hershfield [77] c) surface state on Au(111), F. Reinert [78], d) $Bi_2Sr_2CaCu_2O_{8+x}$, P. Aebi [55], e) $Sr_2RuO_4$, A. P. Mackenzie [79], C. Bergman [80] and Y. Maeno [81], f) $MgB_2$, H.J. Choi [82]

For materials, which do not show clear crossings of the Fermi level, is the definition of the FS very delicate and its determination requires EDC measurements along the FS contours. Luttinger predicted the volume of the FS not to change upon switching the correlation effects on and off. [85] The intensity at the FS of the Fermi liquid is renormalized by a parameter $Z$, as will be shown in Section 4.2, providing the redistribution of spectral weight over the occupied and the unoccupied states. However, if the phase transitions occur, this Luttinger sum rule is no longer valid and a removal of charge carriers from the FS has to be taken into account.

The intensity of an ARPES spectrum can be written in the short form of the Eq. 1.8 as [86]:

$$I(\vec{k}, \omega) = I_0(\vec{k}) f_{FD}(\omega) A(\vec{k}, \omega), \qquad (2.2)$$

where the prefactor includes matrix element effects, $f_{FD}$ is the Fermi-Dirac distribution and $A(\vec{k}, \omega)$ is the spectral function. The momentum distribution function is then given by [87]:

$$n(\vec{k}) = \int_{-\infty}^{+\infty} f_{FD}(\omega) A(\vec{k}, \omega) \, d\omega, \qquad (2.3)$$

which relates $n(\vec{k})$ to the energy-integrated ARPES spectrum. This means that energy-integrated PE intensities should have the shape of the momentum distribution function and has proved useful in the determination of the FS points in the case of high-temperature superconductors [88]. Another possibilities are to fit PE peak positions and extrapolate the dispersion to $E_F$ [89] or to compare the spectra taken at low and high temperatures, as proposed in the $\Delta T$-method [90].

## 2.3    X-ray photoelectron diffraction

Photoelectrons have highly anisotropic angular distribution due to the scattering effects in the final state and this effect is called x-ray photoelectron diffraction. [91, 92, 93] In an x-ray PE experiment the primary photoelectron wave interferes with the one scattered elastically on the surrounding atoms, producing thus an interference pattern which can be detected. This is illustrated in Fig. 2.4. Because of the small mean-free-path of the photoelectrons, only some 3-5 nearest neighbors contribute to the diffraction pattern. Parameters which determine the shape of the interference pattern are the nearest-neighbor distances and angles, chemical type of the emitters and scatterers, relative phases of the primary and secondary waves and kinetic energies of the

emission. [91] The forward focusing effect in the nearest-neighbor directions dominates the kinetic energies above 500 eV, which enables direct "viewing" of the atomic structure of the material under investigation. [94, 95] XPD is used to characterize substitution sites [96], film growth [94, 95, 97, 98, 21] and even phase transitions [99]. It is considered to be a chemically sensitive probe of the real-space local structure around the emitter. [100, 101]
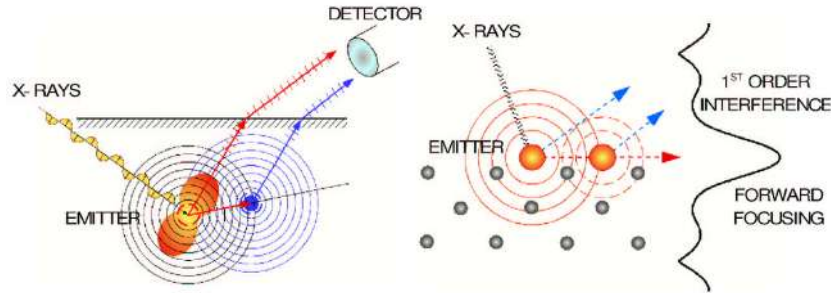


Figure 2.4: Schematic representation of the x-ray photoelectron diffraction. Left: strongly anisotropic angular distribution of emission. Right: Interference of an emitted spherical photoexcited wave with the wave scattered on the nearest neighbor with the central peak termed "forward focusing".

Measured intensities are often represented in a stereographic projection (radial distance of a point from the center is proportional to $\tan(\theta/2)$), as shown in Fig. 2.5. In the center of each plot is normal emission and outer circle corresponds to grazing emission, 90° Along each imaginary circle with the center in the center of the plot, $\theta$ is constant and $\phi$ varies from 0° to 360°. The intensity is presented as a grey-scale plot, with high intensity in white.

The scans presented in Fig. 2.5 were performed on Pb- and Dy-doped $Bi_2Ca_1Sr_2Cu_2O_{8+x}$ (Bi2212, $T_c$=85 K [13]), the most extensively studied bismuth-containing superconductor [102, 103, 104, 105, 106]. It has a layered structure and weak bonding between the Bi-O bilayers results in easy cleavage between these planes. Many different materials have been used to dope the pure Bi2212 in order to influence the charge around the Cu-O planes believed to be responsible for superconductivity or to modify the structure. In this context the question about the influence of dopants on the modulation is interesting as well. Pb substitution of Bi in Bi2212 has led to many studies [107, 108, 109].

For the determination of the effects of dopants on the charge distribution it is very important to know what site the dopant atom is occupying and whether it is distributed homogeneously substituting mainly one element of the host compound or clustering together. XPD proves to be the method of choice for
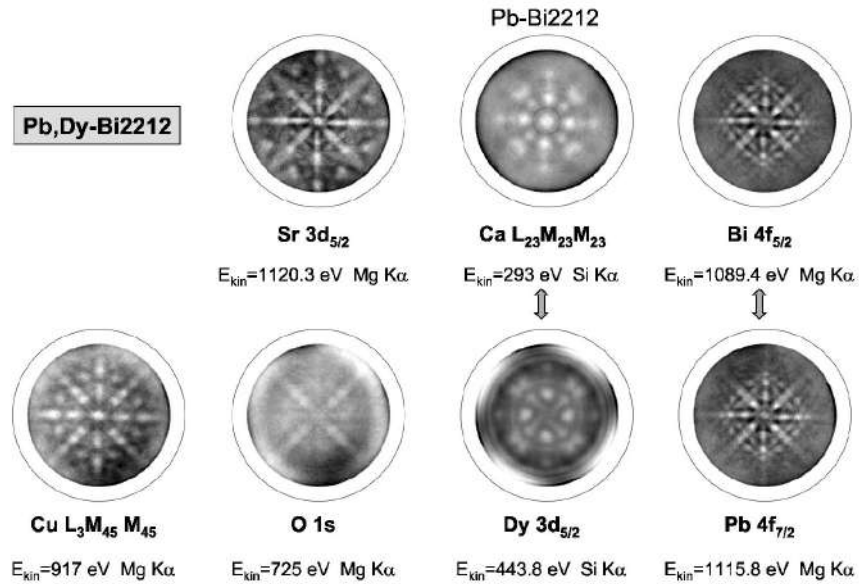
Figure 2.5: XPD patterns on different elements (different kinetic energies) of Bi-Sr-Ca-Cu-O intercalated with Pb and Dy.

substitution site identification. [107, 110, 111, 96, 12] In Fig. 2.5 the occupation sites of Pb,Dy-Bi2212 are presented, fingerprinted by diffractograms. Different elements show diffraction patterns corresponding to their local environment. The patterns of Bi and Pb, as well as the ones of Dy and Ca, taken at similar energies are very similar. This is a straightforward visualization of the fact that Pb atoms substitute Bi and Dy atoms Ca. [12] It should be mentioned that the data on Ca-line have been measured on another sample, Pb-Bi2212, because the Ca in Pb,Dy-Bi2212 was almost completely substituted.

This example was used to demonstrate that XPD can elegantly lead to fingerprinting of the crystallographic sites in complex materials. An often used technique to prove the geometrical interpretation of XPD patterns are single scattering calculations, which neglect the multiple-scattering effects and consider only the changes after one scattering event. [112, 61, 113, 114, 101] This method proved to give nevertheless good qualitative agreement with the measurements, especially in the overlayer systems, where the multiple scattering is excluded. However, the forward focusing intensities in the SSC are overemphasized. On the other hand, the multiple scattering can even lead to

'defocusing' of the diffraction, i.e. reduction of the forward focusing intensity or even appearance of the local intensity minimum. Multiple scattering calculations exist as well, and have been recently successfully implemented to study the structure of complex systems [115].

# Part II

# Electronic and structural properties
# of 1$T$-transition metal
# dichalcogenides

# Chapter 3

# General properties of the 1$T$-family

Transition metal dichalcogenides (TMDs) are compounds with the general formula $MC_2$, where $M$ stands for transition metal of the group IVb, Vb, VIb, VIIb or VIII and $C$ stands for chalcogen: S, Se, or Te. They are further divided into structural subgroups (1$T$, 2$H$, 3$R$, 4$H_a$, 4$H_b$, 6$R$, according to the number of the coupled $CMC$ sandwiches) and the ones of 1$T$-structure will be considered in this thesis.

The octahedral coordination of a metal atom within this structural type is presented in Fig. 3.1a). 1$T$-TMDs are of CdI$_2$ structural type with the space group D$_{3d}^3$ (P$\bar{3}$ml). Due to the tetragonal lattice distortion, the chalcogen atoms are situated slightly below and above the planes set by the lattice constant $c$. The measure of the distortion is $z$ (typically 0.26, depending on the compound [86]), where $zc$ defines the vertical distance between the metal and the chalcogen plane.

Fig. 3.1b) shows a stacking of hexagonally packed atomic planes into $CMC$ sandwiches separated by the van der Waals (vdW) gap. This layered structure makes TMDs very interesting for the problems of strongly correlated materials, in particular because of the similarity with the high temperature superconductors. This layered structure causes anisotropic electronic properties, which make 1$T$-TMDs quasi-2D systems. The preparation technique of these materials relies upon this structure as well: cleaving perpendicular to the surface normal ([001]), within the vdW gap.

Van der Waals bonding is based on the interaction of dipoles or multipoles, permanent or induced ones. It is the dominant type of bonding in crystals of noble gases or molecules (Cl$_2$, CO, bensol). London-interaction between unpolar molecules/atoms, where the potential is given in the form $V \sim \alpha_1 \alpha_2 / r^6$
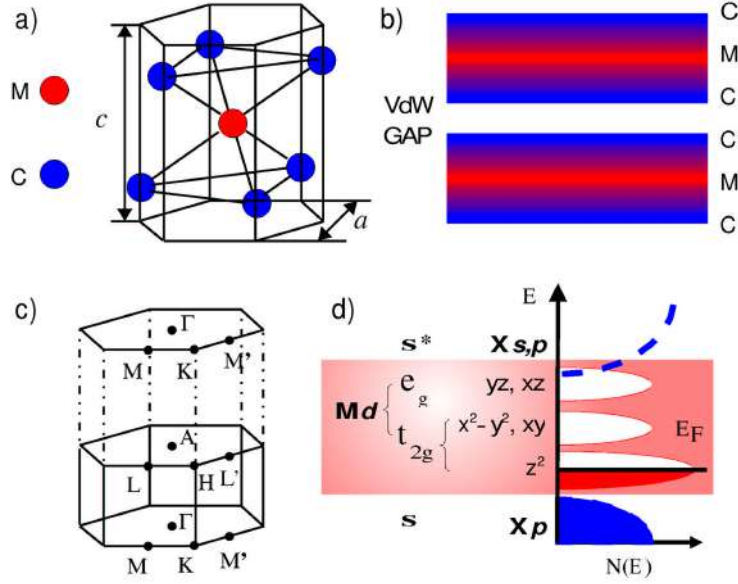
Figure 3.1: Schematic representation of the geometric and the electronic structure of the $1T$-TMDs. a) Coordination of a metal atom. b) Sequence of metal (M) and chalcogen (C) atomic planes separated by van der Waals gap. c) Surface (top) and bulk (bottom) BZ. d) Density of states $N$ vs energy $E$.

[116, 117, 118] (with r being the distance between two molecules or neutral atoms and $\alpha$ their polarisability) as the "actual" van der Waals interaction, which is always attractive. It is the attractive part of the Lennard-Jones potential, defined as $V = A/r^{12} - B/r^{6}$ to describe potential between the neutral atoms, which is attractive at large distances and repulsive at short distances. [119, 120] For a many-particle system, the total energy is obtained as the sum of the two-particle energies and it is typically two orders of magnitude smaller than the covalent one. These tiny binding energies (of the order of $10^{-2}$ eV [120], compared to eV range for the covalent bonding [117]), because of which vdW forces are often termed non-bonding, preserve the characteristics of single atoms and molecules in the crystal.

The largest lattice constants ratio $c/a$ (1.720 [121, 15]) and the largest overlap between metal and chalcogen bands (1.6 eV [122, 123]) in the $1T$-family has $TiTe_2$. This apparent controversy can be explained in terms of van der Waals interaction which decreases with $1/R^{6}$ [116], $R$ being the atomic distance. A larger $c$ corresponds to weaker vdW forces and thus a stronger covalent character of the bonding, similar to what has recently been shown in

calculations [124].

Turning to the electronic structure, we find the surface and the bulk Brillouin zone (BZ) of the $1T$-type presented in Fig. 3.1c). The BZ is hexagonal, but the symmetry of the band structure is only trigonal (difference between M and M', and therefore $\Gamma MLA$ and $\Gamma M'L'A$).

Electronically, TMDs are insulators, semiconductors, semimetals, metals, superconductors. Fig. 3.1d) shows density of states (DOS) as a function of energy for $1T$-TMDs. The chalcogen $p$ bonding ($\sigma$) and antibonding ($\sigma^*$) orbitals are split by a 5-10 eV large gap, which is filled by the metal $d$ orbitals. The crystal field splitting leads to an $e_g$-doublet ($d_{yz}, d_{xz}$) and a $t_{2g}$-triplet ($d_{x^2-y^2}, d_{xy}, d_{z^2}$). The tetragonal distortion of the octahedrally coordinated $MC_6$ removes the degeneration of the triplet. As the remaining metal electrons at $E_F$ are of $d_{z^2}$-symmetry, the material properties will be highly sensitive to the number of $d$ electrons. C$p$ and M$d_{z^2}$ levels are filled. In the simplified ionic picture the chalcogen atoms can reach noble gas configuration by receiving 4 electrons from a metal atom. This leads to the $d^0$ configuration of the metal atoms of the IV-group (semiconducting without the distortion, but semimetallic or metallic with it), or $d^1$ configuration of the metal atoms of the V-group (half-filled band implies metallic behavior). Another important role is played by metallic bonding in these systems. Metallic forces are rather strong, but are considerably diminished in metallic compounds. In transition metal crystals $s$, $p$ and $d$ bands are often mixed. [15] However, the lattice constants of $1T$-compounds TaS$_2$ ($a = 3.365$ Å), TaSe$_2$ ($a = 3.477$ Å), TiSe$_2$ ($a = 3.54$ Å) and TiTe$_2$ ($a = 3.777$ Å) are for respectively 1.9%, 5.3%, 20% and 28% larger than the appropriate metallic lattice constant, which is 2.9508 Å for Ti and 3.3013 Å for Ta. This metallic interatomic difference means that there will be much greater isolation, spatial and energetical, of the $d$-states in TiTe$_2$ then in the rest of the $1T$-family.

The interatomic distances, crystal symmetry and electronic configurations of metal and chalcogen atoms are of great importance, because they influence the metal-chalcogen orbitals overlap, which determines the conducting properties of the material (Fig. 3.1d)). This is more precisely illustrated in Fig. 3.2. In a) bulk band-structure calculations using WIEN97 [70] are presented and the corresponding temperature dependent resistivity curves are shown in b). Arrows A and B in Fig. 3.2a) indicate the M$d_{z^2}$ (red) and C$p$ (blue) bands, respectively. These two bands overlap at $\Gamma$ only for TiTe$_2$; in the case of TaS$_2$ they are separated by 1 eV, consistently with the previously stated largest orbital overlap between metal and chalcogen orbitals in the telluride. $1T$-TiTe$_2$ behaves like a normal metal without phase transition. This is the reason why it is considered a model system for the Fermi liquid (FL) behavior. All
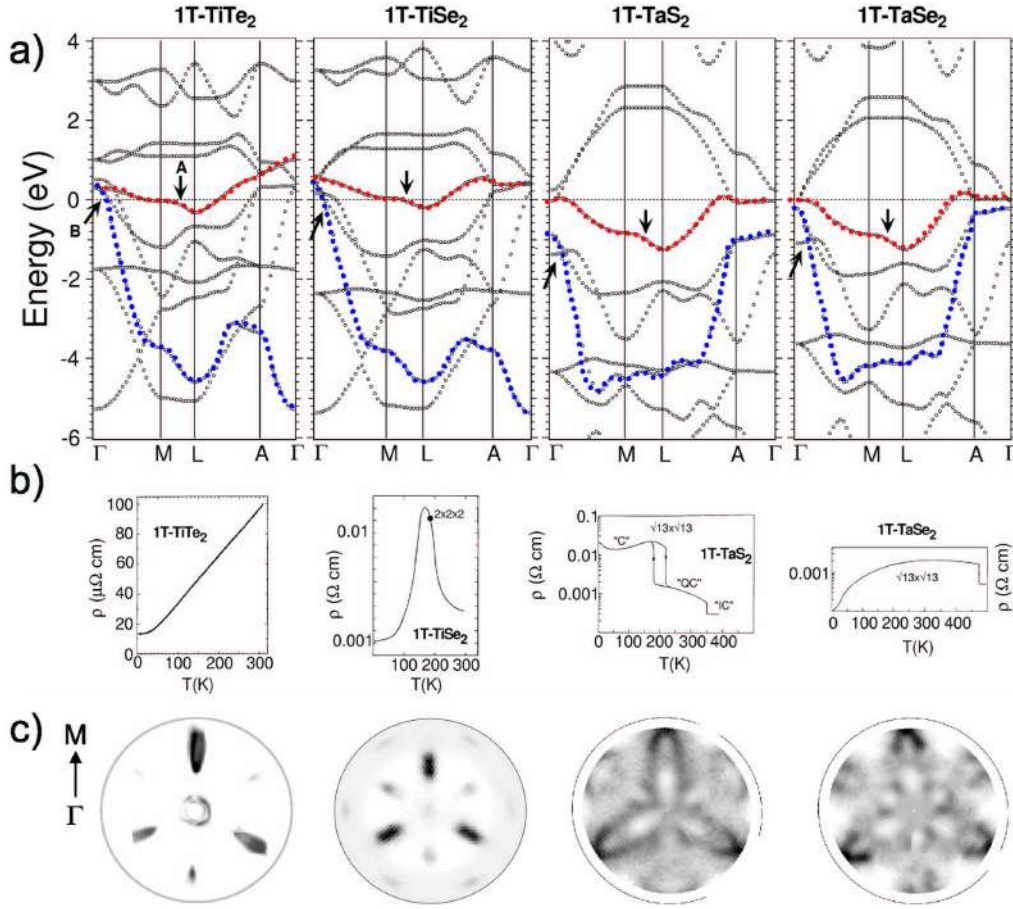
Figure 3.2: 1$T$-TMDs: a) Electronic band structure calculated using WIEN97. b) Temperature dependent resistivity measured by Claessen [125], Lévy [60], DiSalvo [126] and DiSalvo [126]. c) FSM using He I radiation. TiTe$_2$-FSM measured by Eltner [127]. The circle on the TiTe$_2$ FSM marks 35°, on the other ones it marks 90°.

other compounds exhibit phase transitions into different charge-density wave (CDW) phases. For 1$T$-TiSe$_2$ a CDW with a 2×2×2 structural transition locks in slightly before the resistivity peak at 180 K. 1$T$-TaS$_2$ shows multiple transitions. Due to the heaviest metal atom - Ta and the lightest chalcogen atom - S, TaS$_2$ is the most unstable from the four and TiTe$_2$ is the most stable one.

The resistivity curves of TaSe$_2$ and TaS$_2$ reflect considerable differences of the temperature dependent CDW-induced structural evolutions. Undistorted

at high temperature, $1T$-$TaS_2$ has a first phase transition at 1123 K [128] yielding an incommensurate (IC) CDW phase. Below 350 K, the so-called nearly-commensurate (NC) phase consists of commensurate (C) domains separated by incommensurate domain walls [128, 129]; the abrupt resistivity jump at 350 K is followed by a semiconducting-like temperature behavior: the resistivity slightly increases with decreasing temperature. Below a metal-insulator transition (MIT) at 180 K the system enters the C phase, characterized by a resistivity with an order of magnitude higher but, paradoxically, metallic-like slope. The $1T$-$TaSe_2$ with its single phase transition at 473 K gets into the commensurate CDW phase (with the same $(\sqrt{13} \times \sqrt{13})R13.54°$ reconstruction as $1T$-$TaS_2$) with a sudden increase in the resistivity but still with metallic temperature behavior.

Fig. 3.2c) presents FSMs for all four compounds with identical overall structure. Six metal-$d$-band-related ellipsoidal electron pockets are centered on the sides of the hexagonal BZ. Intensity differences between M and M' are due to matrix element effects, reducing the emission along $\Gamma$M' [130, 131] and are common to the $1T$-family [11]. The FS of $TiTe_2$ has been taken at 20 K [127], the other ones at RT. Although $TaSe_2$ and $TaS_2$ are at this temperature in the CDW phase, the spectral weight at the Fermi level follows the shape of the unreconstructed lattice, which will be discussed in detail later.

High energy and angular resolution provide for the first time direct insight in the structure of the angularly extremely narrow electron pockets in $TiTe_2$. [127] This feature does not appear as the homogeneously smeared intensity over an area of an ellipse; a clearly darker elliptical frame is observable instead, defining the contours of the Fermi surface. In the center of the BZ, around $\Gamma$, two visible rings with hexagonal symmetry represent Ti $5p$-related hole pockets, in agreement with the calculations in Ref. [131].

# Chapter 4

# High-resolution photoemission investigation of the spectral function of $1T$-TiTe$_2$

## 4.1 Fermi liquid reference compound $1T$-TiTe$_2$

The concept of the Fermi liquid [8, 132] is one of the corner stones of solid state physics. Stated simply, this concept means that energetically close to the Fermi energy the electrons in a metal can be described as independent particles (quasiparticles) whose properties are renormalized with respect to those of free electrons due to interactions. The main interactions giving rise to the renormalization are the electron-phonon interaction and the electron-electron interaction. The central parameters governing these interactions are the electron-phonon coupling constant $\lambda$ and the electron-electron constant $\beta$.

Photoemission spectroscopy is one of the most direct ways so sample the properties of a Fermi liquid [133], because it measures the spectral function of the system. For kinematic reasons [14] the investigation of the spectral function is most easily performed in a two-dimensional system, as already discussed. This has led to numerous studies of the spectral function on surface states in metallic systems [134, 135, 136, 137], which by their very nature are two-dimensional, and in some quasi-two-dimensional bulk systems, such as $1T$-TiTe$_2$. The first detailed analysis of the spectral function of a Fermi liquid was performed on $1T$-TiTe$_2$. [138] This work was followed up by a number of other investigations, establishing TiTe$_2$ as a Fermi liquid reference system. [139, 90, 131]

Electron-electron interaction was considered in all previous TiTe$_2$-studies

to be the only relevant term of the quasiparticle self-energy. The largest value for $\beta$ obtained so far is 314 eV$^{-1}$ [140], the smallest one 0.5 eV$^{-1}$ [139]. And even the most recent results, obtained with the 8 meV energy resolution on samples with 2 $\mu\Omega$ residual resistivity, assume an additional photoemission linewidth of 17 meV. [139] In this chapter we present high-resolution photoemission data measured with the energy resolution smaller than 5 meV. Using the electron-phonon coupling constant obtained from the temperature dependent line broadening [139], we show that $\lambda$ as small as 0.2 is crucial for the lineshape fit of the photoemission data. On the other hand, $\beta$, which was considered to be the principal parameter in the lineshape studies of TiTe$_2$, plays no significant role. We discuss also the additional photoemission linewidth and it's influence on the fit.

## 4.2   Landau's Fermi-liquid theory

The Landau's Fermi liquid theory offers a successful approach to the interacting particles system based on the single-particle distribution function of a noninteracting system. [141] The starting point of the Landau's theory is *adiabatic* introduction of the interaction, causing gradual transition of the ideal-gas states into the states of the interacting system, the appearance of additional new states not being excluded. This approach was developed rather intuitively by Landau, for the case of weak repulsive forces, but has been later proven to be rigorously correct. The ground state of the interacting system with attractive forces is completely different from the non-interacting one. The states of the interacting system are generally unstable and have rather short lifetime; on the other hand, for the continuous transition from the free-fermion eigenstates to those of the interacting system, we need to turn on the interaction slowly. To menage both these requirements, we need low-lying excited states, very close to the ground state, having a long lifetime. Finally, it is assumed that the ground state of the free particles will become a ground state of the interacting ones.

A quasiparticle added to the real-system ground state is obtained when the particle with the wave vector $k > k_F$ is added to the non-interacting ground state and afterwards the interaction is turned on. The lifetime of this state is long enough only in the vicinity of $k_F$, and the concept of quasiparticles is therefore valid only near the Fermi surface. The distribution function (see Eq. 2.3) can be transferred to the problem of interacting particles, where it gives the distribution of quasiparticles, which is in the ground state the same as the one described for the free fermions. The excitation of the system,
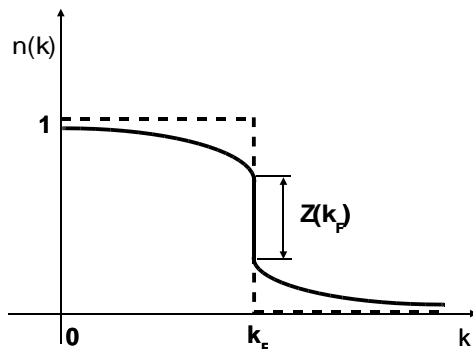
Figure 4.1: Momentum distribution function $n(k)$ for a non-interacting Fermi gas (dashed) and an interacting Fermi liquid (full line) at $T = 0$ K.

determined by the change in the distribution function $\delta n(k) = n(k) - n_0(k)$, must be significant only in the vicinity of the Fermi surface. Therefore it can not be claimed that the ground state consists of $N$ quasiparticles located in the interior of the Fermi surface, because quasiparticle can be at best understood as an elementary excitation near $k = k_F$, leaving the details of the ground state unknown. The energy variation of $\delta E = \sum_k \varepsilon_k \delta n(k)$, where $\varepsilon_k = \delta E / \delta n(k)$ is the first functional derivative and denotes the energy of a quasi-particle. Collective modes of a system are free oscillations of the Fermi surface, similar to that of a liquid drop, giving the name 'Fermi liquid'.

Quasiparticles are characterized by a renormalized energy, a finite lifetime and a renormalized mass $m^*$. The broadening decreases towards the Fermi surface. The electron momentum is no longer a good quantum number, but the momentum distribution $n(\vec{k})$ still exhibits the Fermi-Dirac discontinuity, as illustrated in Fig. 4.1. The discontinuity at $k_F$ of the Fermi-Dirac distribution of the Fermi gas corresponds to the Fermi surface. In the interacting case, spectral weight is decreased at the Fermi surface by a renormalization factor $Z$ and redistributed over $k$.

## 4.3 The electron self-energy

Mathematical way to take interaction into account is adding a so-called complex self-energy $\Sigma(\boldsymbol{k},\omega)$, where $\omega$ denotes the energy, to the single-particle electron energy of a non-interacting system $E^0(\boldsymbol{k})$:

$$\Sigma(\boldsymbol{k}, \omega) = Re\Sigma + iIm\Sigma, \qquad (4.1)$$

41

yielding for the Green's and spectral function:

$$G(\boldsymbol{k}, \omega) = \frac{1}{\omega - E^0(\boldsymbol{k}) - \Sigma(\boldsymbol{k}, \omega)}, \tag{4.2}$$

$$A(\boldsymbol{k}, \omega) = \frac{1}{\pi}|ImG(\boldsymbol{k}, \omega)| = \frac{1}{\pi}\frac{Im\Sigma}{(\omega - E^0(\boldsymbol{k}) - Re\Sigma)^2 + (Im\Sigma)^2}. \tag{4.3}$$

The poles of $G(\boldsymbol{k}, \omega)$ are defined by:

$$\omega_p(\boldsymbol{k}) - E^0(\boldsymbol{k}) - \Sigma(\boldsymbol{k}, \omega_p(\boldsymbol{k})) = 0, \tag{4.4}$$

and give the spectroscopic energies of the interacting system. [141, 142, 133] The pole energy is often written as $\omega_p(\boldsymbol{k}) = Re(\omega_p(\boldsymbol{k})) + iIm(\omega_p(\boldsymbol{k}))$, meaning that the pole occurs at an energy $Re(\omega_p(\boldsymbol{k}))$, with a width $Im(\omega_p(\boldsymbol{k}))$. The real part of the self-energy causes a shift of the maximum of $A(\boldsymbol{k}, \omega)$ from the non-interacting dispersion, whereas the imaginary part yields the finite lifetime of the photohole. The method of Green's functions is one of the most successful in treating interacting particle systems. [133] The approximations here reduce to approximating the self-energy, which is of the similar order of magnitude as the excitation energy, rather than the total energy.

The complete equation for the photocurrent from a crystalline solid is now given (using Eqs. 4.3 and 1.8) by:

$$\begin{aligned}
I(\omega, \hbar\omega) \quad &\propto \sum_{i,f} \frac{Im\sum(\boldsymbol{k}_i)}{(\omega - E^0(\boldsymbol{k}_i) - Re\Sigma(\boldsymbol{k}_i))^2 + (Im\Sigma(\boldsymbol{k}_i))^2} \\
&\times \frac{\left|\tilde{M}_{i,f}\right|^2}{\left(k_{i\perp}^{(1)} - k_{f\perp}^{(1)}\right)^2 + \left(k_{f\perp}^{(2)}\right)^2} \delta\left(\boldsymbol{k}_{i\|} - \boldsymbol{k}_{f\|} + \boldsymbol{G}_{\|}\right) \delta(\boldsymbol{k}_i - \boldsymbol{k}_f + \boldsymbol{G}) \\
&\times \delta(\omega_p(\boldsymbol{k}_f) - \omega_p(\boldsymbol{k}_i) - \hbar\omega) \delta(\omega - \omega_p(\boldsymbol{k}_f) + \phi) \cdot f_{FD}(\omega, T). \tag{4.5}
\end{aligned}$$

For the free-fermions hamiltonian $\hat{H} = \sum_{\boldsymbol{k}\sigma} \varepsilon_k a_{\boldsymbol{k}\sigma}^+ a_{\boldsymbol{k}\sigma}$, with $\varepsilon_k = (\hbar\boldsymbol{k})^2/(2m)$, the single-particle Green's function and the spectral function are [143]:

$$G_\sigma(\mathbf{k}, \omega) = \frac{1}{\omega - \frac{\varepsilon_k}{\hbar} + i\eta_k}, \quad A_k(\omega) = \frac{1}{\pi}\delta(\omega - \omega_k), \tag{4.6}$$

where $\eta_k$ is defined as $\eta_k := \eta \cdot sign(\varepsilon_k - \varepsilon_F)$. $G$ has a pole at $\omega = \varepsilon_k/\hbar - i\eta_k$. The poles correspond to the energies of the quasi-particles, i.e. the elementary excitation spectrum.

In the simplified treatment of a decaying particle with the width $\Gamma$, the corresponding Green's function and the expected Lorentzian form for the spectral function are:

$$G_\sigma(\mathbf{k}, \omega) = \frac{1}{\omega - \frac{\varepsilon_k}{\hbar} + i\Gamma}, \quad A_k(\omega) = \frac{1}{\pi} \frac{\Gamma}{(\omega - \frac{\varepsilon_k}{\hbar})^2 + \Gamma^2}. \quad (4.7)$$

The spectrum of an interacting electron system is by far more complicated. When an appreciable fraction of the spectral strength goes into a relatively strong and narrow peak, this is called a quasiparticle state or an elementary excitation.

## 4.4   Contributions to the self-energy

Self-energy can be written as a sum of contributions from different scattering mechanisms:

$$\Sigma = \Sigma_{e-e} + \Sigma_{e-ph} + \Sigma_{imp}, \quad (4.8)$$

with electron-electron interactions $\Sigma_{e-e}$, electron-phonon interaction $\Sigma_{e-ph}$ and scattering on impurities and crystalline defects $\Sigma_{imp}$. [139]

Electron-electron self-energy is most commonly written in the first order of the Taylor expansion [133]:

$$\Sigma_{e-e}(w) = \alpha w + i\beta[\omega^2 + (\pi k_B T)^2]. \quad (4.9)$$

The data presented in this thesis have been measured at $T$=10 K, which yields 7.3 meV$^2$ ($k_B = 0.08617\frac{meV}{K}$) for the second term in the brackets. For the values of $\beta$ which we apply ($\beta = 0.5$ eV$^{-1}$), this gives an energy independent contribution of 0.004 meV. As this is much smaller than the impurity contribution (14 meV) in the case of TiTe$_2$, it will be neglected.

Electron-phonon self-energy can be written for an isotropic system in the form [144]:

$$\Sigma_{e-ph}(T, w) = \int_{-E_F}^{\infty} d\nu \int_0^{\omega_D} d\omega' \alpha^2 F(\omega') \times \quad (4.10)$$

$$\left[ \frac{1 - f_{FD}(\nu, T) + n_{BE}(\omega', T)}{\omega - \omega' - \nu + i\delta\, sgn(\omega)} + \frac{f_{FD}(\nu, T) + n_{BE}(\omega', T)}{\omega + \omega' - \nu + i\delta\, sgn(\omega)} \right],$$

where $n_{BE}(\omega', T)$ is Bose-Einstein and $f_{FD}(\nu, T)$ Fermi-Dirac distribution, $\alpha^2 F(\omega)$ Eliashberg coupling function, $\omega_D$ a cutoff frequency of the phonon spectrum and $\delta$ an infinitesimal number. According to the Migdal's theorem,

$\Sigma_{e-ph}(k, \omega)$ has been replaced by $\Sigma_{e-ph}(k_F, \omega)$, due to a weak $k$-dependence. Within the Debye model

$$\alpha^2 F(\omega) = \lambda \left( \frac{\omega}{\omega_D} \right)^2, \quad \omega < \omega_D, \tag{4.11}$$

and zero otherwise; $\lambda$ denotes the strength of the electron-phonon interaction. Calculating the integrals at $T = 0$ K with constant $\lambda$, one gets [145, 146]:

$$\begin{aligned} |Im\Sigma_{e-ph}(\omega)| &= \frac{\hbar\lambda\pi|\omega^3|}{3\omega_D^2}, \quad |\omega| < \omega_D \\ &= \frac{\hbar\lambda\pi\omega_D}{3}, \quad |\omega| > \omega_D \end{aligned} \tag{4.12}$$

$$Re\Sigma_{e-ph}(\omega) = -\frac{\lambda\hbar\omega_D}{3} \times \tag{4.13}$$
$$\left[ \left( \frac{\omega}{\omega_D} \right)^3 ln \left| \frac{\omega_D^2 - \omega^2}{\omega^2} \right| + ln \left| \frac{\omega_D + \omega}{\omega_D - \omega} \right| + \frac{\omega}{\omega_D} \right].$$

Influence of disorder can be written in the form

$$\Sigma_{imp} = i\Delta_{imp}(d), \tag{4.14}$$

where $d$ is defect concentration. This term is purely imaginary and can be often regarded as a constant. [135]

## 4.5 Matho and Taylor fits on $k_F$

The equation 4.9 without the last term leads to the following Green's function at $E_{\boldsymbol{k}}$=0 with a simple two-pole structure:

$$G(\boldsymbol{k_F}, \omega) = \frac{Z}{\omega - i0^+} - \frac{Z}{\omega + i/\beta'}, \tag{4.15}$$

where $Z = 1/(1 - \alpha)$ is the quasiparticle weight and $\beta'=\beta Z$.

The so called casual Green's function can be calculated according to the phenomenological Ansatz proposed by Matho [147] and limited here to the second moment expansion:

$$\frac{G(\boldsymbol{k_F}, \omega)}{Q} = \frac{Z}{Q} \frac{1}{\omega - i0^+} + (1 - \frac{Z}{Q}) \frac{1}{\omega - i\Delta}, \tag{4.16}$$

44

where $\beta'=\beta Z=(Q/Z-1)/\Delta$. The background function is assumed to be a Lorentzian, $\Delta$ describes the width of the background spectral function. $\Delta$ is an imaginary part of a complex parameter $\Omega$, which can also have a real part $Q\varepsilon_k$, describing the position of the 'background pole'.

The above two equations have been used for a numerical fit of the experimental data with Taylor or Matho Green's functions. The spectral function calculated with these Green's functions is multiplied by a Fermi distribution at a finite temperature and integrated over a given energy window to simulate the finite angular resolution. The finite energy resolution is simulated through a convolution with a Gaussian of a given full-width half-maximum.

## 4.6 Electron-electron interaction parameter $\beta$

In order to examine the possible range of $\beta$ in TiTe$_2$, we present Taylor and Matho fits with various parameters at $k_F$. Figure 4.2a) shows a $k_F$ spectrum from our best quality TiTe$_2$ sample (blue circles) measured with the energy resolution of 5 meV and after convolution with a 30 meV broadening (black line). The latter curve agrees perfectly with the measurement of Claessen *et al.* [138] (red squares) performed with the energy resolution of 35 meV. This indicates that the difference between the previously measured and our data is only due to instrumental broadening.

The data in Fig. 4.2b) show the insensitivity of the fits with respect to $\beta$. Here the data of Claessen are compared to two fits performed by using an improved theory of Matho (Eq. 4.16) [147] with $\beta'=60$ eV$^{-1}$ (grey dashed) and $\beta'=471$ eV$^{-1}$ (black line) ($\beta' = \beta Z$, where $Z$ describes the renormalization of the $k_F$-step of the $n(k)$ distribution of the interacting system). Although the parameters are very different, the fits are almost identical. In Fig. 4.2c) we show the best data of the present experimental series compared to Taylor fits (Eq. 4.15) with very different electron-electron coupling parameters, namely $\beta=0.005$, 0.5, 1 and 40 eV$^{-1}$, and only slightly varied impurity constant $\Delta_{imp}$ (14-11 meV). The difference in the quality of the fits is hardly noticeable. Finally in Fig. 4.2d) we show again the high-resolution data fitted with the Taylor approximation (red dashed) and the improved Matho theory (blue line). There is hardly any difference in the calculated curves.

The information we get from Fig. 4.2 is that the lineshape fits allow for a wide range of electron-electron coupling parameter and that Taylor and Matho theories prove equally capable of describing the data. The insensitivity to $\beta$ suggests that there may exist other scattering mechanisms, which are more significant for the lineshape fit than the electron-electron interaction.
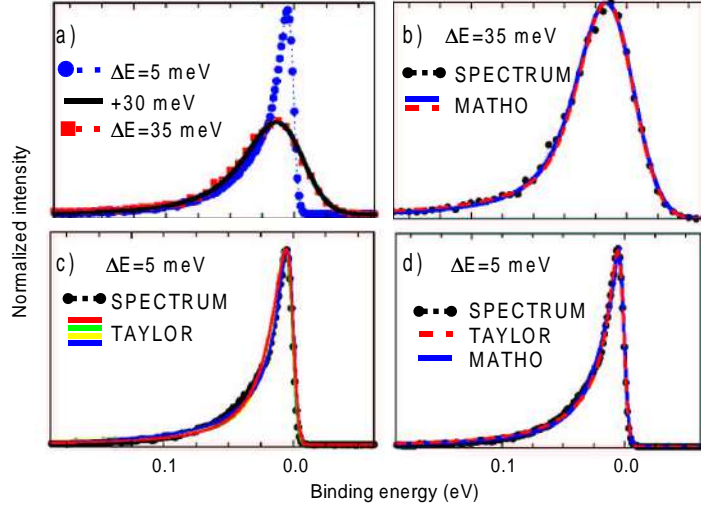
Figure 4.2: Photoemission spectra (circles) of TiTe$_2$ at $k_F$ along $\Gamma$M taken with photon energy 21.2 eV and energy resolution ($\Delta$E) as indicated. a) Data from Claessen [138] (red squares) taken with energy resolution 35 meV, compared with the data taken with energy resolution of 5 meV (blue circles), convoluted with a 30 meV Gaussian (black line). b) Data from Claessen [138], fitted with $\beta' = 60$ eV$^{-1}$ (red dashed) or $\beta' = 471$ eV$^{-1}$ (blue line) by the two-pole fit of the line-shape according to Matho [147]; $T$=20 K. c) Taylor fit of the highest resolution data with $\beta = 0.005, 0.5, 1, 40$ eV$^{-1}$ (respectively: red, green, yellow and blue line); $T$=10 K. d) The highest resolution data fitted my Matho (blue line) or Taylor (red dashed) fit; $T$=10 K.

## 4.7 Electron-phonon coupling constant $\lambda$ and impurity scattering

Electron-phonon coupling is considered to be a dominant scattering mechanism at high temperatures. It has been shown that electron-phonon coupling constant $\lambda$ can be determined from the temperature dependent linewidth [144]:

$$\Gamma_{el-ph}(T) = 2\pi\lambda k_B T, \qquad (4.17)$$

as a slope of the linear part at high temperatures divided by $2\pi k_B$. The linewidth at $k_F$ determined from the photoemission data of Perfetti $et$ $al.$ in a wide range from the lowest temperatures up to the RT is presented in Fig. 4.3. The Debye fit of the data yields both $\lambda = 0.22$, which is a relatively small electron-phonon coupling constant, and $\omega_D = 0.020$ eV. For this reason
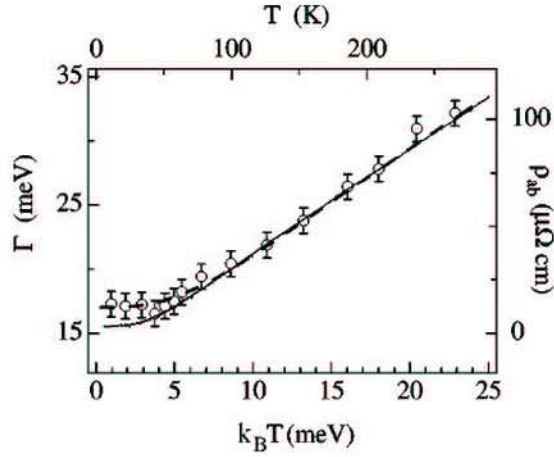
Figure 4.3: Debye-fit of the temperature dependent ARPES linewidth measured at $k_F$ by Perfetti *et al.* [139]

Perfetti *et al.* do not use it for the lineshape fit, but we shall show that even such small $\lambda$ can be crucial for the lineshape fit.

Samples of different quality have also different electron-phonon coupling constants, as shown by resistivity measurements of various TiTe$_2$ samples. [148] The prominent presence of defect modes has been proven by Raman spectroscopy [149] and non-stoichiometry of the samples is considered mainly responsible for them [150, 15]. Ruthenates for instance, which are complex
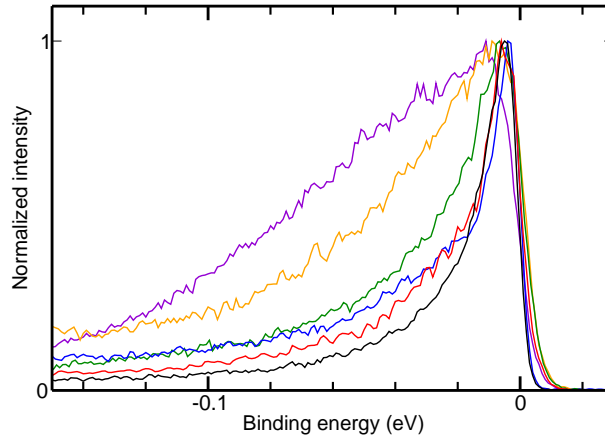


Figure 4.4: Photoemission spectra of different TiTe$_2$ samples taken at $k_F$ along $\Gamma M$ with photon energy 21.2 eV and energy resolution less than 5 meV.

quasi-two dimensional FL systems [151, 152, 153], have residual resistivity 0.1 $\mu\Omega$cm, one order of magnitude smaller than TiTe$_2$ samples measured by Perfetti $et$ $al..$ This supports our finding that the sample quality of TiTe$_2$ is not satisfactory.

In order to emphasize this point we show in Fig. 4.4 spectra for many samples, which had been produced by the same procedure, have been prepared for the measurement and measured under the same conditions. It is obvious that the lineshape and the linewidth deduced from them differ markedly from sample to sample indicating where the problem in the work of TiTe$_2$ lies. These spectra can be reproduced by fits implementing $\Delta_{imp}$ in the range from 10 meV to 200 meV. Larger values of the impurity constant imply smaller relative contribution of the studied interactions in the system and smaller sensitivity to their relevant parameters.

## 4.8  Contributions to the spectral function

We have thus performed a comparative analysis of a series of spectra by taking a self energy consisting of the electron-electron energy, the electron-phonon energy and the inelastic scattering by defects. Fig. 4.5 shows the influence of different interactions on the lineshape fits. The details of the fit are listed in the figure caption. The integration over a window of 4 meV corresponds to our angular resolution of 0.3°. Spectra and calculations are normalized to the same height (1) for all measured angles. Fig. 4.5a) shows a fit with no interaction and just an additional broadening term $\Delta_{imp} = 14$ meV, which will be kept constant in the other fits. Already this fit is surprisingly good although not perfect. Fig. 4.5b) gives a fit with $\lambda = 0$ and $\beta = 0.5$ eV$^{-1}$, which is not very different from the previous one. The optimal fit is presented in Fig. 4.5c), where $\lambda = 0.2$ and $\beta = 0.5$ eV$^{-1}$. The crucial factor for the improved fit quality was the introduction of the electron-phonon interaction. This is obvious from the comparison of Fig. 4.5c) and d), where one sees that removal of $\beta$ almost does not change the fit.

Our values of the electron-electron interaction and the electron-phonon constants [154] are in agreement with the results of Perfetti $et$ $al$ [139], although they have not used both of them for a lineshape fit. Their $\lambda = 0.22$ obtained from the slope of the temperature dependent linewidth agrees very well with our $\lambda = 0.2$ obtained from the lineshape fits of the Ti $3d_{z^2}$-band dispersion along $\Gamma M$. From the series of spectra in Fig. 4.5 we can draw the conclusion that these data sets are not suited to determine $\beta$, the value 0.5 eV$^{-1}$ should be thus considered an upper limit. Also the Debye energy determined from

48

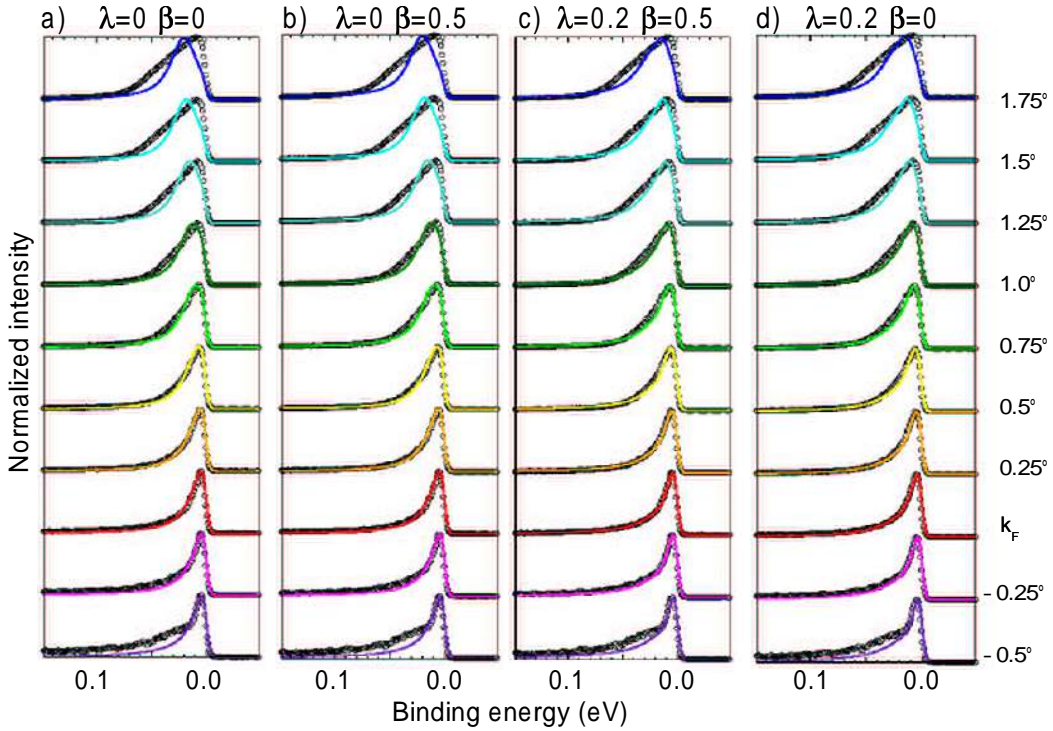Figure 4.5: Photoemission spectra of TiTe$_2$ along $\Gamma$M with photon energy 21.2 eV and energy resolution less than 5 meV (circles) in 0.25°-steps and spectral function calculation (line) with $\lambda$ and $\beta$ in eV$^{-1}$ as indicated above, $\omega_D$=0.020 eV and $\Delta_{imp}$=0.014 eV, integrated due to the finite angular broadening over a 4 meV window, broadened with 5 meV to simulate finite energy resolution and multiplied by a Fermi-Dirac distribution for $T$=10 K.

the fits to be $\omega_D = 0.020$ eV is in agreement with the previously cited values [139, 148, 149] The largest contribution to the line fits, namely the defect scattering contribution, is slightly smaller here (14 meV) than in the work of Perfetti *et al* [139] (17 meV).

Fig. 4.6 demonstrates the importance of the impurity term by a comparison of the data with a theory containing electron-electron ($\beta = 0.5$ eV$^{-1}$) and electron-phonon ($\lambda = 0.2$) interaction, but no defect scattering. In this case it is obvious that the agreement between theory and experiment is poor. The spectral functions of figures 4.6 and 4.5c) differ only in the defect scattering term of 14 meV. For the calculations at $-0.25°$ and $-0.5°$, the quasiparticle peak has just crossed the Fermi level and only a part of it can be seen due to the Fermi-Dirac cut-off in Fig. 4.6. That is why the higher binding energy
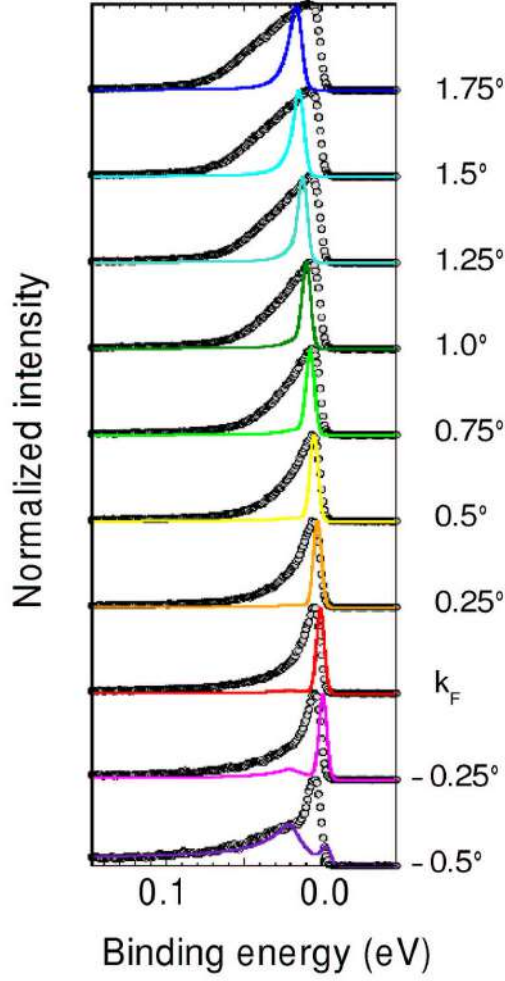
Figure 4.6: Photoemission spectra of TiTe$_2$ along ΓM with photon energy 21.2 eV and energy resolution less than 5 meV (circles) in 0.25°-steps and spectral function calculation (line) with $\lambda$=0.2, $\omega_D$=0.020 eV, $\beta$=0.5 eV$^{-1}$ and $\Delta_{imp}$=0 eV, integrated due to the finite angular broadening over a 4 meV window, broadened with 5 meV to simulate finite energy resolution and multiplied by a Fermi-Dirac distribution for $T$=10 K.

peak gains importance (the data are normalized to the same height). As the quasiparticle peak at 0.5° in Fig. 4.6 is almost completely above the Fermi level, this calculation has not been normalized to the height of the measured peak, but to the measured height at $\approx$ 20 meV, where the strongest calculated peak appears. However, once the data are broadened by 14 meV, the quasiparticle peak appears on the occupied side of the Fermi level, thus diminishing the

relative contribution of the higher binding energy component. This strong difference between the full fit and the underlying spectral function tells that it is absolutely mandatory to reduce the impurity term to the order of the experimental resolution, namely 5 meV or better.

The most important improvement in our approach is the implementation of the Landau-Fermi liquid theory for the electron-phonon system in the presence of Coulomb interactions. Fermi liquid theory has been first developed by Landau [8] to describe Coulomb repulsion between the electrons. Later, Prange and Sachs [155] have derived the Landau theory in the presence of both electron-electron and electron-phonon interactions. Our spectroscopic investigation offers an example for visualization of different contributions in such a general theory.

## 4.9   Conclusion

In conclusion we have been able to get a unique fit of the highly resolved photoemission spectra of $TiTe_2$ including the electron-electron, electron-phonon and electron-defect interactions. The main result of our study is that the electron-phonon coupling in $TiTe_2$, although characterized by a rather small coupling constant $\lambda = 0.2$, is necessary for a good agreement between the fit and the data. Contrary to that, electron-electron scattering, which has been treated as a dominant broadening mechanism in this Fermi liquid reference compound so far, has been shown on the best resolved data to play an insignificant role. The need for a still very large residual broadening for good fits shows the importance of the sample quality for this kind of investigations.

# Chapter 5

# Pseudogapped Fermi surfaces of $1T$-TaS$_2$ and $1T$-TaSe$_2$: A charge density wave effect

## 5.1  Introduction

The mechanism behind high-temperature superconductivity (HTSC) has been recently considered to be directly related to the pseudogap [102, 103] driven by an electronic instability [104]. Similarly, a pseudogap over large portions of the FS has been observed in ARPES experiments on the TMD $1T$-TaS$_2$ instead of a nesting induced partially removed FS in the CDW phase. [156] This new surprising property was questioned to be related to instabilities induced by the underlying Mott localization driven MIT [157, 158] at 180 K. [156] The isostructural $1T$-TaSe$_2$ with its identical CDW at RT appears to be the ideal candidate for further enlightening, as it does not exhibit a bulk MIT at lower temperatures, although it shows a surface MIT [159].

The pseudogap of the superconductors is debated to be a precursor of the actual gap in the electronic spectrum in the superconducting state below T$_c$ [160]. Klemm [160] reports striking similarities between the HTSC pseudogap regime and the behavior of the TMD's and proposes that the pseudogap in the HTSC arises from CDWs and/or spin density waves (SDW) and not from superconducting fluctuations (or preformed pairs).

With their well understood structural properties studied by means of x-ray scattering [161, 128], the two $1T$-TMD-polytypes TaS$_2$ and TaSe$_2$ are of strong interest in the debate on the mechanism driving the charge density wave formation. The quasi-two dimensionality of the geometrical structure,

reflected in the shape of the Fermi surface has been used to explain the CDW formation [16]. However, the X-ray scattering results show a three-dimensional reconstruction of the lattice by the formation of the CDW also along the c-axis. It has been proposed [66] that the necessary interplane coupling between two sandwiches of $1T$-TaS$_2$ at RT occurs as a consequence of the in-plane CDW in the Ta layer. On the other hand, Horiba [162] for $1T$-TaSe$_2$ concludes that the Fermi surface has three-dimensional character due to a large charge transfer between Ta $5d$ and Se $4p$ orbitals. Finally, the debate on where a possible nesting vector on the FS should be placed, is also open.

## 5.2   The 1D electron gas

Compounds of the $1T$-type, except $1T$-TiTe$_2$, show structural instabilities leading to the formation of the superstructures, accompanied by the changes in the electronic structure. The driving mechanism for these changes are CDW concomitant with a periodic lattice distortion (PLD). [163, 118] Density waves (both CDW, first discussed by Fröhlich in 1954 and by Peierls in 1955 and SDW, postulated by Overhauser in 1962) are broken symmetry states of metals, driven by electron-phonon or electron-electron interactions.

Density waves arise in their simplest form in highly anisotropic materials. In a 1D electron gas, with the dispersion relation for electrons in the state $k$ given by $E_k = \frac{\hbar^2 k^2}{2m_0}$, where $m_0$ stands for the free electron mass, and the 1D boundary conditions, the FS consists of two points at $\pm \boldsymbol{k}_F$. The rearrangement of the charge density $\rho$ of the system, expressed in terms of Fourier transform of an induced charge, is proportional to the Fourier transform of a time independent potential $\phi(q)$ describing the external perturbation:

$$\rho^{ind}(\boldsymbol{q}) = \chi(\boldsymbol{q})\phi(\boldsymbol{q}), \tag{5.1}$$

with the proportionality factor $\chi(\boldsymbol{q})$ being the Lindhard response function, defined in $d$ dimensions as

$$\chi(\boldsymbol{q}) = \int \frac{d\boldsymbol{k}}{(2\pi)^d} \frac{f_k - f_{k+q}}{\epsilon_k - \epsilon_{k+q}}, \tag{5.2}$$

where $f_k$ is the Fermi-Dirac distribution.

In a 3D case of a spherical FS, the integral converges and one obtains a finite value for $\chi(2\boldsymbol{k}_F)$. [163] In a 2D case of a circular FS the singularity at $2\boldsymbol{k}_F$ in the response function is not integrable. In a 1D case one has a logarithmic singularity. Assuming linear dispersion relation, we obtain:

$$\chi(\boldsymbol{q}) = -e^2 n(\epsilon_F) \ln \left| \frac{\boldsymbol{q} + 2\boldsymbol{k}_F}{\boldsymbol{q} - 2\boldsymbol{k}_F} \right|, \tag{5.3}$$

with the elementary charge $e$ and the DOS at the Fermi level for one spin direction $n(\epsilon_F)$. For small $\boldsymbol{q}$ one arrives at the Thomas-Fermi approximation, $\chi(\boldsymbol{q}) = -e^2 n(\epsilon_F)$ [163]. This means that the 1D electron gas is unstable against the formation of a density modulation with period $\lambda_0 = \pi/k_F$, which can be a charge- or spin-density wave. This divergence corresponds to the particular topology of the FS, convenient for perfect nesting: one full and one empty state at the same energy, which differ by $\boldsymbol{q} = 2\boldsymbol{k}_F$, give divergent contributions. In higher dimensions is the number of such states significantly reduced, as can be seen in Fig. 5.1 (bottom), leading to the removal of the singularity at $\boldsymbol{q} = 2\boldsymbol{k}_F$.

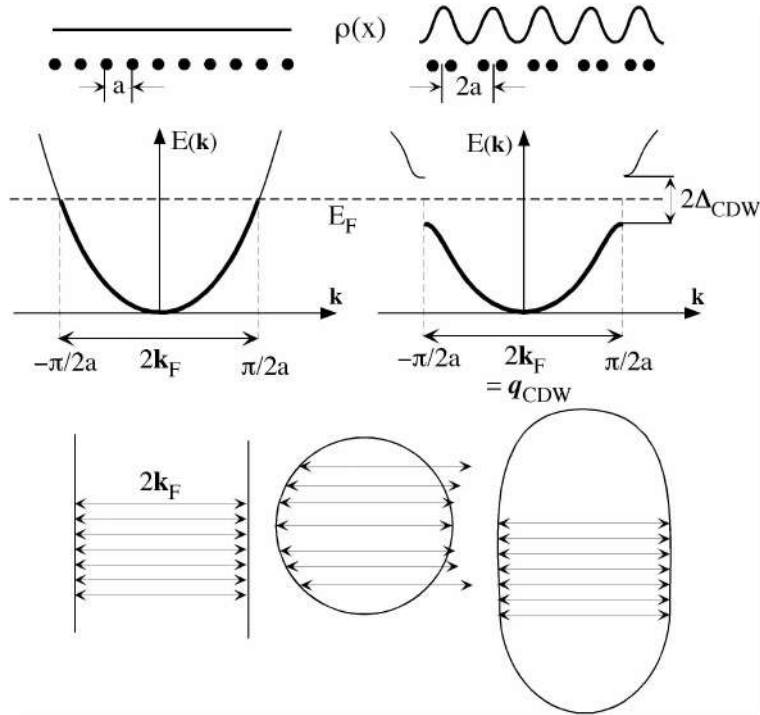The divergent response function leads to various instabilities at low tem-



Figure 5.1: The Peierls transition in 1D. A doubling of the periodicity in real-space halves the extent of the BZ in $k$-space. A gap opens at the BZ boundary lowering the electronic energy and compensating the elastic deformation due to periodic lattice distortion. Bottom: FS topology for a 1D and 2D free electron gas. The arrows indicate pairs of states, one full and one empty, differing by the wavevector $\boldsymbol{q} = 2\boldsymbol{k}_F$. The 2D FS has to exhibit parallel portions in order to be susceptible for an FS nesting scenario based on the 1D model (bottom right).

54

peratures, and a finite transition temperature can be obtained in a simple mean field picture. [163] The broken symmetry ground state at $T = 0$ is a coherent superposition of two possible pair-states, electron-electron and/or electron-hole pairs. For $\boldsymbol{q} = 0$ one obtains electron-electron pairing (the particle-particle or Cooper channel), with the singlet and triplet superconducting ground states according to the Bardeen-Cooper-Schriefer theory (BCS) [164]. For $\boldsymbol{q} = 2\boldsymbol{k}_F$ (the particle-hole or Peierls channel) one obtains CDWs for spin 0 or SDWs for spin 1. All these ground states have a common complex order parameter, which is in the mean field approximation of the CDWs the Peierls gap $\Delta$.
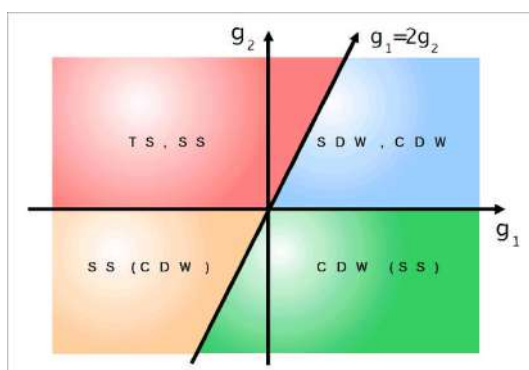


Figure 5.2: The so called g-ology picture: $g_1 - g_2$ (coupling constants) phase space of the 1D electron gas. Various broken symmetry ground states: singlet superconductor (SS), triplet superconductor (TS), CDW or SDW.

In 1D both the Cooper and the Peierls response functions diverge at low temperatures and which one of the states occurs depends on the detailed nature of electron-phonon and electron-electron interactions. These can be weighted by two coupling constants, $g_1$ for the interactions with momentum transfer $\pm 2k_F$ and $g_2$ for the interactions with momentum transfer 0 and a diagram showing the occurrence of the different states is presented in Fig. 5.2. A purely one-dimensional case does not occur in real materials however high the anisotropy may be (chain-structures, for instance, always have interchain coupling); but similarity with the ground states of the $g$-ology diagram is certain for weak interchain interactions.

In the superconducting ground state the gauge symmetry is broken and collective mode leads to a supercurrent in response to $DC$ fields. In the density wave ground state the translational symmetry is broken and the collective modes (phasons and amplitudons) do not contribute to the $DC$ conduction (due to the interaction with impurities and lattice imperfections), and the

opening of a gap at the Fermi level causes the material to become a semiconductor.

## 5.3 The charge density wave ground state

CDWs develop in low-dimensional metals as a consequence of electron-phonon interactions and consist of a periodic charge density modulation coupled by means of electron-phonon interaction with a periodic lattice distortion, both periods being determined by the Fermi wavevector $k_F$. The Fröhlich Hamiltonian of an electron gas can be written in the following form:

$$H = \sum_k \epsilon_k a_k^\dagger a_k + \sum_q \hbar\omega_q b_q^\dagger b_q + \sum_{k,q} g_q(b_{-q}^\dagger + b_q), \qquad (5.4)$$

where the first part describes the electrons, the second part the phonons and the last part the electron-phonon interaction. Annihilation and creation operators for electron states are denoted by $a_k^\dagger, a_k$ and for phonon states by $b_q^\dagger, b_q$, $\omega_q$ are the normal mode frequencies and $g_q$ is the general electron-phonon coupling constant. The coupled electron-phonon system is unstable and this instability has fundamental consequences for both the lattice and the electron gas. The equations of motion in normal coordinates in a 1D case lead to a renormalized phonon frequency $\omega_{ren,q}$ (phonon mode softening, called Kohn anomaly [165]):

$$\omega_{ren,2k_F} = \omega_{2k_F}\sqrt{\frac{T - T_{CDW}^{MF}}{T_{CDW}^{MF}}}, \qquad (5.5)$$

where $T_{CDW}^{MF}$ represents the transition temperature within the mean-field approximation. The softening of the phonon mode at $q = 2k_F$ is evident in 1D, smeared out for 2D and very weak in 3D. For the higher dimensions, the temperature dependence of $\chi(q, T)$ is weak, and for small electron-phonon coupling constants $\omega_{ren,q}$ remains finite at $T = 0$ and there is no phase transition. Below the phase transition, the renormalized phonon frequency is zero, meaning a "frozen" lattice distortion.

This leads to a single-particle gap in the DOS with the magnitude $\Delta$, which is an amplitude of the complex order parameter. The gain in electronic energy ($\propto -\Delta^2 \ln \frac{2E_F}{\Delta}$) is in the weak coupling limit larger than the lattice deformation energy ($\propto \Delta^2$), which leads to the stable CDW ground state. The transition is of the second order. The mean-field transition temperature in the weak-coupling limit ($\epsilon_F \gg \Delta$), is given by

$$2\Delta = 3.52 k_B T_{CDW}^{MF}, \qquad (5.6)$$

where $k_B$ is Boltzmann's constant. This is the same expression as in BCS theory, but it leads here to a periodic charge density variation:

$$\rho(x) = \rho_0[1 + \frac{\Delta}{\hbar v_F k_F \lambda} \cos{(2k_F x + \varphi)}], \qquad (5.7)$$

where $\rho_0$ is the constat charge density in the metallic normal state and $\lambda = \pi/k_F$ the modulation period.

The nesting property of the 1D FS has been shown in the previous section to be of crucial importance for the Peierls instability. Fig. 5.1a) shows a chain of atoms with distance $a$. With one electron per atom, the band is half-filled, i.e. it is filled up to $\pm\pi/2a$, where the BZ extends to $\pm\pi/a$ (left). If the periodicity in real space is doubled (right), the BZ boundary in the reciprocal space shifts to $\pm\pi/2a$. The band is now completely filled up to the new BZ boundary, where the gap opens at the Fermi level through the formation of the standing waves. With 1.5 electrons per atom, for instance, $k_F = 3/4 \cdot \pi/a$ and correspondingly $\lambda = \pi/k_F = 4a/3$. In this way, the elastic deformation energy is compensated by the electronic energy, gained through the lowering of electronic states. This mechanism is called Peierls transition. Two pieces of the FS of a 1D chain can be connected by a nesting vector $\boldsymbol{q} = 2\boldsymbol{k}_F$. This holds also for the 3D crystal consisting of 1D chains (blue bronze $K_{0.3}MoO_3$). But in the spherical FS of the 3D case or the cylindrical ones of the 2D case, it is impossible to connect significantly large FS areas with each other, meaning that the energy gain of such a transition would remain small. However, elliptical or other shapes of the quasi 2D FS enable nesting (see Fig. 5.1, bottom), mostly through the large parallel portions of the FS. A periodic lattice distortion occurs than along the connecting/nesting vector, not necessarily commensurate with the underlying lattice.

## 5.4 Periodic lattice distortion

Main feature of the CDW induced $(\sqrt{13} \times \sqrt{13})R13.54°$ reconstruction in $TaSe_2$ and $TaS_2$ is a star-like clustering (the so-called 'stars of David') in the Ta plane, presented in Fig. 5.3a) [16]. The star of 13 Ta atoms is composed of the central atom (yellow) surrounded by a first shell of 6 (blue), almost equivalent, nearest neighbors and a second shell of 6 (red), almost equivalent, next nearest neighbors. At RT in the NC phase in $TaS_2$, domains of $\approx 70$Å size exist with a structure corresponding to the C-phase, separated by the domain walls, as presented in Fig. 5.3b) [129, 128].

LEED results for $1T$-$TaS_2$ and $1T$-$TaSe_2$ are shown in Fig. 5.4a) and b). Well defined characteristic hexagonal spots of the basic structure are clearly
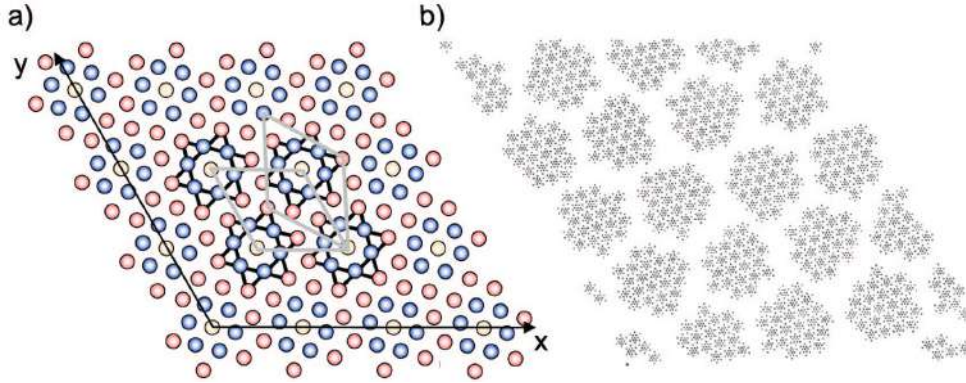
Figure 5.3: a) Two possible CDW reconstructions in the Ta-plane. b) Ta-domains in the $z = 0$ layer in a region of $100 \times 100$ unit cells. Domain-walls are left blank. The modulation is exaggerated 5 times. [128]

present. Each of them is surrounded by the ones of the superstructure. For the $1T$-TaSe$_2$, however, more than one reconstruction is visible (Fig. 5.4b), marked region) due to two domains. Wilson [16] performed electron micrographs of the selenium alloy and also found different domains. They proposed dislocations in a single sandwich, i.e. twin boundaries formed by a Ta atom row separating $\alpha$ and $\beta$ superlattice domains, rotated by respectively $\pm 13.54°$ with respect to the undistorted basic structure. [16] However, they did not show evidence of two domains in $1T$-TaS$_2$, neither does the recent literature, which states the same observations [128, 161].
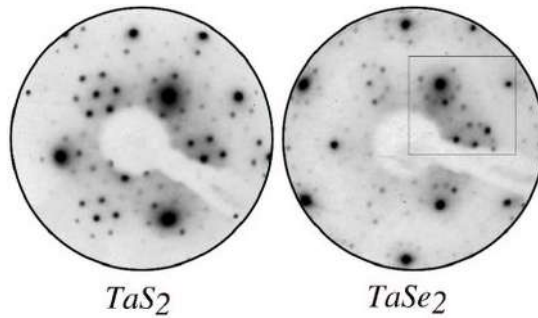


Figure 5.4: LEED patterns of a) $1T$-TaS$_2$ and b) $1T$-TaSe$_2$.

The periodic lattice distortion introduced by the CDW lock-in can be visualized by an STM. [166] Fig. 5.5 shows (20 nm $\times$ 20 nm) of the *in situ* cleaved $1T$-TaSe$_2$ surface measured with the bias voltage 0.2 V and the tunnelling
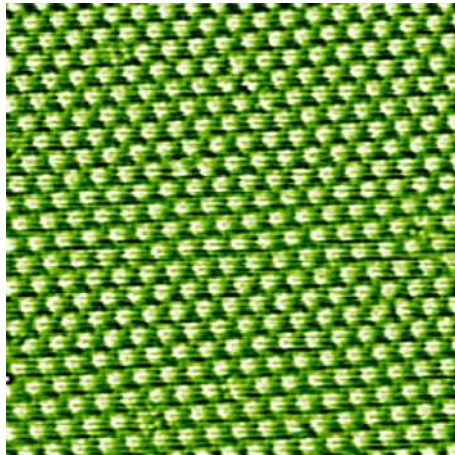
Figure 5.5: STM image of the cleaved $1T$-TaSe$_2$ surface taken with 0.2 V and 1.2 nA. 20×20 nm$^2$.

current 1.2 nA. The Figure shows arrays of white (strong intensity) flowerlike patterns. Their dimensions are about 11 Å, and this corresponds roughly to the diameter of one star drawn schematically in Fig. 5.3a). The structure of the flowers is only recognizable, but not atomically resolved. The periodic repetition of this pattern confirms the presence of the charge density waves.

## 5.5   Fermi surface mapping

In simplified ionic picture both compounds are isoelectronic ($d^1$) and are thus expected to give similar Fermi surface maps. One has to keep in mind that an experimental FSM is not necessarily the actual FS, but a pattern reflecting the anisotropic distribution of the spectral weight of the electrons from the Fermi level. The measured FSMs of TaS$_2$ and TaSe$_2$ are shown in Fig. 5.6a,b. The 1. BZ and the crystallographic directions are marked. The raw data shown in Fig. 5.6a) has its high intensity in the 1. BZ and is three-fold and star-like. Its branches are more unequally weighted for the sulfide. At higher polar angles the intensity decreases but regains strength in the 2. BZ (towards grazing emission).

The intensities have been normalized by the mean azimuthal value, in order to enhance the information close to the grazing angles. The patterns have been mirror-symmetrized with respect to the $\bar{\Gamma}\bar{M}$ to recover the crystal symmetry, which is broken since the unpolarized light points at the sample surface along a non high symmetry direction. The consequent strong, orbital dependent
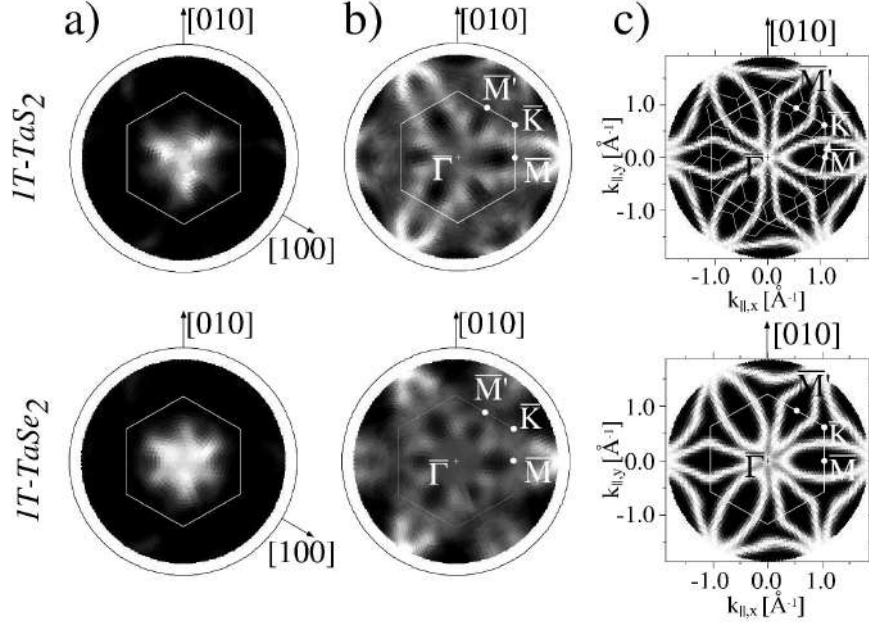
Figure 5.6: FSM with hexagonal unreconstructed BZs and high-symmetry points for both materials. Raw data a) have been normalized by the mean azimuthal value b). FS calculations are given in c). In the c) (top) CDW-induced reconstructed BZ is shown with the possible nesting vector across $\bar{M}$.

polarization effect has been outlined e.g. for copper in Ref. [74]. The influence of polarized light on such photoemission experiments has been discussed in the literature for the $1T$-TaS$_2$, in the case of normal light incidence. [130]

Band-structure calculations of the FS for the undistorted structure in Fig. 5.6c) compared to the experiments taken at RT in the CDW phase in Fig. 5.6b) suggest the $(1 \times 1)$, i.e. unreconstructed character of the electronic structure (see also Fig. 3.2c). In both cases, the simulation is a superposition of two three-ellipse-like flowers, one rotated by 120° with respect to the other. The ellipse gets a strong variation in going through the 1. BZ along $\bar{\Gamma}\bar{M}$', which indicates a weak $k_\perp$-dependence in the unreconstructed electronic structure of these quasi-2D materials. According to Ref. [130], the two flowers are subject to different selection rules in the photoemission process. The $\bar{\Gamma}\bar{M}$ direction is preferred at $E_F$, whereas along $\bar{\Gamma}\bar{M}$', only the beginning of the ellipses is visible, as can be also seen in Fig. 5.6b).

## 5.6 Ta *d*-band dispersion

In order to reveal quasiparticle crossing of the Fermi level, FSM has to be complemented by EDC analysis. The comparison of the experiment with the calculation for the undistorted structure, up to a binding energy of 2 eV, is presented in Fig. 5.7 along the $\bar{\Gamma}\bar{M}$ direction. EDCs presented in Fig. 5.7 are performed on a large polar angle range (50°). Enhanced spectral weight at $E_F$ close to $\bar{\Gamma}$ can be noticed. The Ta 5*d* band in both compounds forms a small hole-like pocket close to $\bar{\Gamma}$ followed by a large electron-like pocket around $\bar{M}$ (see also Fig. 3.2a) and early calculations in Ref. [167]). For 1*T*-TaS$_2$, there is practically no overlap with the S 3*p*, but for 1*T*-TaSe$_2$ at $\bar{\Gamma}$ and $\bar{M}$, the Se 4*p* and the Ta-band are very close. Here, introduction of spin-orbit coupling in the calculation (not shown here) even yields crossing bands. According to the DFT picture, the Ta 5*d* and Se 4*p* wave functions overlap and hybridize, while in the disulfide the Ta 5*d* band is isolated and solely drives
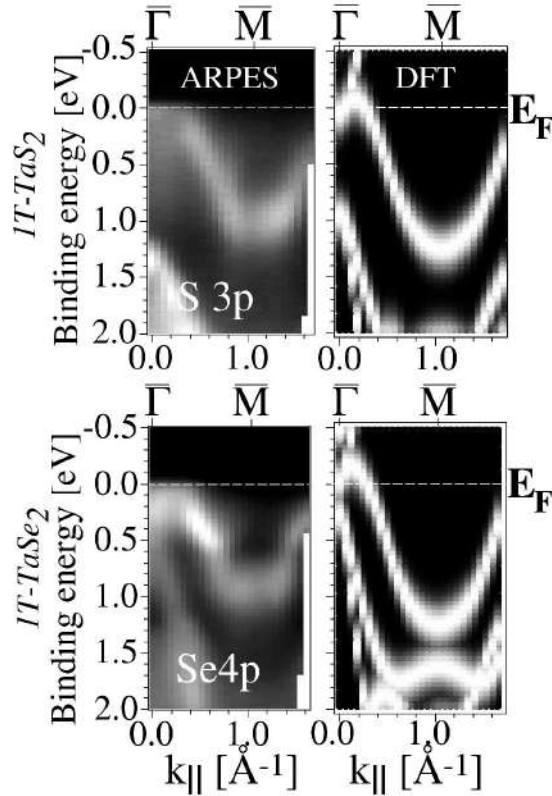


Figure 5.7: ARPES and DFT EDC's.

the electronic properties. This hybridization [162] might play the crucial role in understanding the differences in transport properties of these two materials. The photoemission intensities of the Ta $5d$ band dispersion are, despite the superstructure as detected by x-ray diffraction and LEED, still displaying the band dispersion of the $(1 \times 1)$ undistorted crystal, as can be seen in Fig. 5.7.

The symmetrization procedure, often used for the cuprates [105, 106], offers the most reliable way to determine whether there is a pseudogap or a quasiparticle crossing at the Fermi energy ($\omega=0$), as it removes the perturbative effect of the Fermi-Dirac distribution cut-off, which is important for the weakly dispersive bands at $E_F$. When approaching $E_F$, the quasiparticle peak progressively brings spectral weight closer to it; after crossing it, a dip is expected and this defines the crossing point $k_F$. [106]
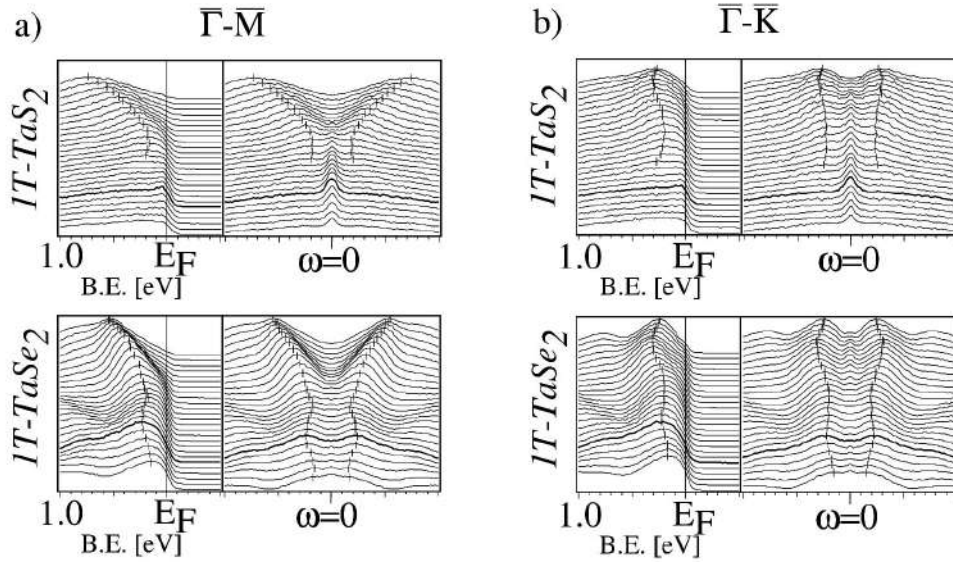


Figure 5.8: Spectra along two high-symmetry directions (left panels) across the normal emission (bold spectrum) and symmetrized data (corresponding right panels) along a) $\bar{\Gamma}\bar{M}$ and b) $\bar{\Gamma}\bar{K}$.

Fig. 5.8 shows measured and symmetrized EDCs taken along a high symmetry directions crossing $\bar{\Gamma}$ ($\bar{\Gamma}\bar{M}$ and $\bar{\Gamma}\bar{K}$). The spectra were taken every degree up to 1 eV binding energy, the spectrum plotted in bold has been measured at the normal ($\bar{\Gamma}$). For the disulfide, the symmetrization leads to a peak, which gradually grows from 10° approaching the normal along $\bar{\Gamma}\bar{M}$ (Fig. 5.8a), or starting from approximately 16° along $\bar{\Gamma}\bar{K}$ (Fig. 5.8b). No clear dip follows the peak, as expected in the case of quasiparticle crossing, behavior which will

be termed pseudogap. For the considered directions, the diselenide seems to be more pseudogapped as judged from the symmetrization peak in Fig. 5.8a,b), with symmetrization peaks confined in a circular region of about 20° centered at the normal. The symmetrization peak shows angular dependence, and the pseudogap seems to grow with larger polar angle. The calculation for the undistorted structure in Fig. 5.7 shows a clear crossing close to $\bar{\Gamma}$, which could not be confirmed by the experiment.

In Fig. 5.8, small bars are drawn on the peaks of the dispersing band. For the S compound, the dispersion is as expected, except that the band surprisingly folds back to higher binding energy after having approached the Fermi level. Along the $\bar{\Gamma}\bar{K}$ direction the dispersion is clearly oscillating. This modulation is even stronger for the diselenide. It indicates that the dispersion of the apparently unreconstructed band structure contains oscillating features due to the CDW.
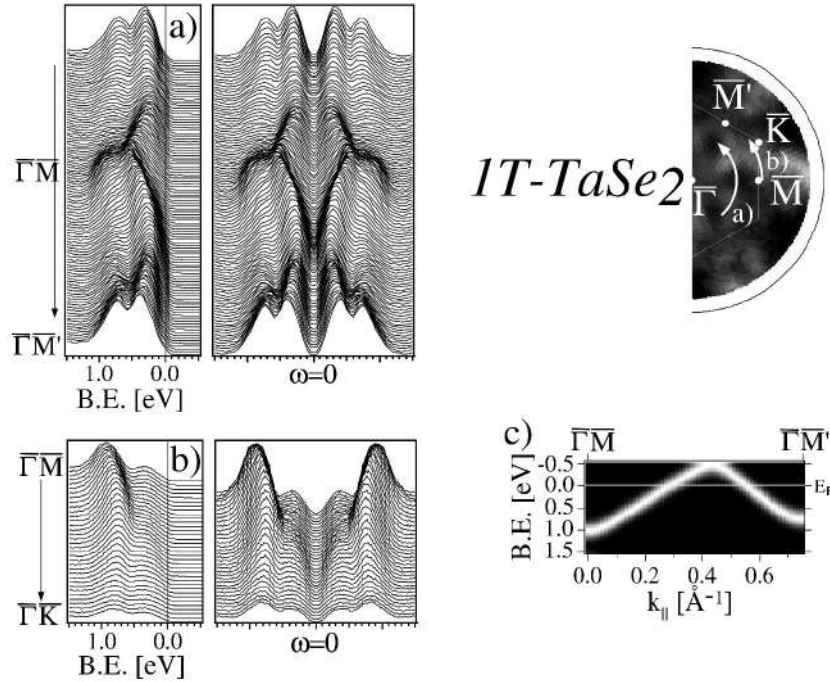


Figure 5.9: Azimuthal scans on $1T$-TaSe$_2$ at two polar angles: a) 20° and b) 32°, as illustrated with the arrows on the FSM (right). c) Simulation for scanning at 20°.

EDC scans along azimuthal angles in order to probe the spectral weight at $E_F$ off normal but also away from the high symmetry directions are pre-

sented in Fig. 5.9. Both samples clearly exhibit the same pseudogap ($1T$-TaS$_2$ measurements are not shown). White arrows indicate the measurement paths on the FSM in Fig. 5.9, right. The first EDCs were taken at a polar angle of 20° (Fig. 5.9a), the second ones at the polar angle of 32° (Fig. 5.9b). The black arrow indicates the order in which the spectra have been collected. The symmetrized results do not have a peak at $\omega = 0$, but the spectral weight is not zero, meaning that there is a pseudogap.

EDCs of Fig. 5.9a) have been simulated with DFT (Fig. 5.9c) between the $\bar{\Gamma}\bar{M}$ and the $\bar{\Gamma}\bar{M}$' directions, which shows one electron-like band. The same pockets are recognizable in the measurement in Fig. 5.9a), but here two subbands disperse, in agreement with Horiba [168], as explained to be a consequence of the CDW formation according to the calculation of Smith [169]. These bands can be also seen at 32° (Fig. 5.9b), where the first subband closer to $E_F$ seems to have decreased intensity with respect to the second one. The conclusions for $1T$-TaS$_2$ are similar, with the difference that the two subbands tend to form a single broad peak, which can be understood by taking into account that the disulfide at RT is composed of C domains with different phases divided by IC domain walls [128] (see Chapter 3 and Section 5.4), thus washing out the CDW features in the band structure.

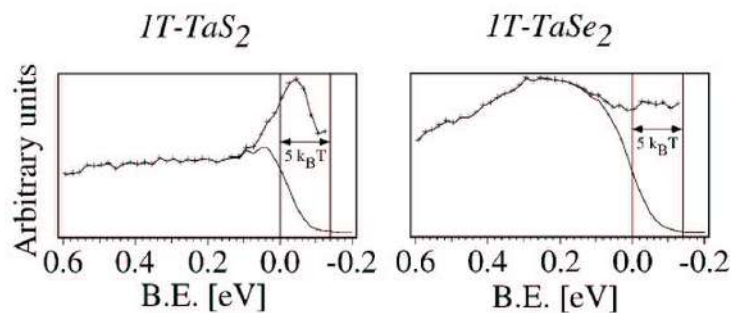## 5.7 Thermal occupation and transport properties



Figure 5.10: Normal emission spectra divided by the Fermi-Dirac function to reveal the thermally excited states (crossed line).

Fig. 5.10 shows thermally excited states in the normal emission spectra in the vicinity of the Fermi level, revealed by the division with the Fermi-Dirac

64

function (FD) up to 140 meV ($5k_BT$) above the chemical potential (small crosses). In Fig. 5.11, the band dispersion has been emphasized by circles, placed on the maximal spectral intensities. Both TMDs show a very flat dispersion close to zero binding energy in the polar angle range near $\bar{\Gamma}$. For $1T$-TaS$_2$ the states lie slightly above the Fermi edge, whereas for $1T$-TaSe$_2$, they are straddling $E_F$. This is visible in both figures and may be of importance for the transport properties. The disulfide needs thermal activation, like in a semiconductor and the diselenide has similar thermal occupation, but still with a band at $E_F$. This explains that both samples, because of the CDW formation, have an increase in resistivity, but different slopes as a function of $T$ at RT: the disulfide has the semiconducting-like slope (negative), and the diselenide the metallic-like one (positive) (see Fig. 3.2b).
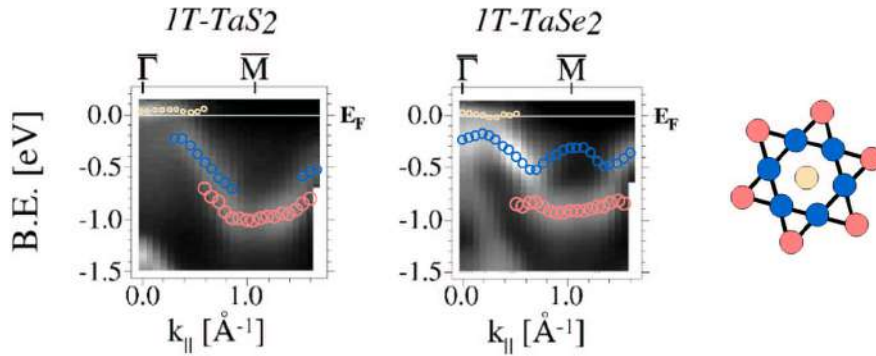


Figure 5.11: Intensity map along $\bar{\Gamma}\bar{M}$ with the circular markers at the local EDC minima.

Figure 5.11 shows the Ta $5d$ band-mapping along $\bar{\Gamma}\bar{M}$. Both materials reveal a modulated dispersion with stronger intensities according to the $(1 \times 1)$ BZ. This modulation is in agreement with the noted oscillatory behavior of the spectral features observed in the EDCs in Fig. 5.8. The Ta-band appears clearly split, and the subbands tend to oscillate, which is stronger for the $1T$-TaSe$_2$. Both effects are due to CDW, as will be discussed in detail in the next Sections.

## 5.8 Reconstructed band-structure calculations of $1T$-TaS$_2$

Fig. 5.12 shows WIEN97 [65] band-structure calculations for the $1T$-TaS$_2$ [66] with the CDW-induced atomic positions measured by x-ray scattering [128].

An approximate commensurate ($\sqrt{13} \times \sqrt{13} \times 3$) superstructure was derived from the refined structural coordinates of the incommensurate structure of the NC phase ($\times 3$ stands for 3 $TaS_2$ sandwiches, but for the computation, only the first sandwich around $z = 0$ was taken). Dotted lines in Fig. 5.12a) present calculated reconstructed band-structure plotted versus a path in the unreconstructed reciprocal space (surface and bulk BZs are illustrated in Fig. 5.12b). A band character analysis indicates that the first seven subbands below the Fermi energy are due to the Ta atoms. Thus the Ta $5d$ band is split by the CDW formation. The uppermost flat subband with a $d_{z^2}$ character moves off from the underlying subbands, disperses in $z$ along $\Gamma A$ and oscillates around $E_F$ at the border of the BZ (along AL).

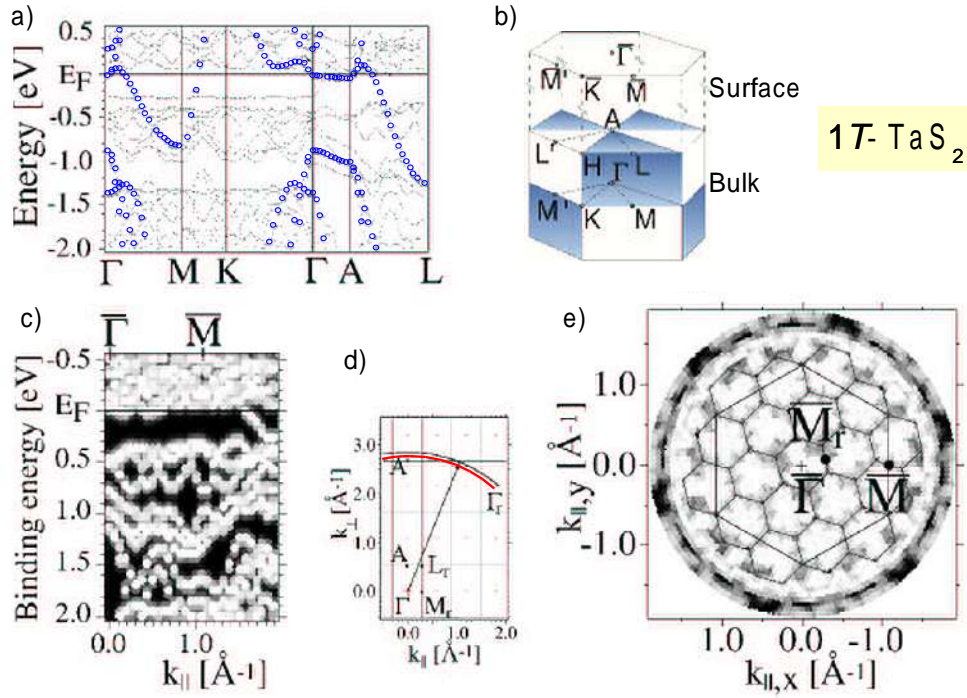Figure 5.12c) shows the simulated EDC along $\Gamma M$ with the $k$-points defined



Figure 5.12: Reconstructed (r) band-structure calculations of $1T$-$TaS_2$ using WIEN97. [11] a) Band dispersion along high-symmetry lines, circular markers (blue) correspond to calculations for the undistorted structure. b) Bulk and surface BZ. c) Band dispersion along $\bar{\Gamma}\bar{M}$ for He I. d) Cut in reciprocal space with free electron final state wave vector for He I. e) FSM with reconstructed BZs.

by a free electron photoemission final state, shown in Fig. 5.12d) up to 60°. A black line was chosen for the Fermi energy and a red one for a binding energy of 2 eV (d). Six subbands can be identified in c), and the uppermost seventh subband straddling $E_F$ and crossing into occupied states at 1.5 Å$^{-1}$. At the normal, the measured $k$-points are closer to A than to Γ, but reach Γ at 60° (d), in agreement with the stated $z$-dispersion of the same band presented in a). Also the experimental bandwidth in Fig. 5.7 (1.3 eV) suggests that PE on the 1$T$-TaS$_2$ probes the BZ off center plane.

In Fig. 5.12e) both, surface reconstructed (13.9° rotated hexagonal lattice) and unreconstructed (large hexagon) BZs have been drawn. The $E_F$ intensities from Fig. 5.12c) are plotted along $\bar{\Gamma}\bar{M}$ on the reconstructed simulated FSM in Fig. 5.12e). The two crossings of $E_F$ just after $\bar{\Gamma}$ in Fig. 5.12c) form the 'flowers' paved FSM in Fig. 5.12e). The 'flowers' clearly follow the grid of the reconstructed higher BZ's. The crossing after $\bar{M}$ in Fig. 5.12c) is also visible at the border of the FSM in Fig. 5.12e).

## 5.9 Electronic structure in the CDW-state

A splitting of the Ta $d$-band into oscillating subbands has been observed in Fig. 5.11 and confirmed by the calculations in the previous Section to be a CDW-induced effect. However, the photoemission intensities are following the unreconstructed band structure, which is visible in the intensity maps of band dispersion (Fig. 5.7) or at the FS (Fig. 5.6) and are thus more similar to the calculations using the unreconstructed structure. This is the reason why the influence of the CDW induced new BZs for the 1$T$-TaS$_2$ has not been observed in the literature [170, 171, 172]. To explain this, Voit [173] has modelled the spectral weight distribution of tight-binding electrons in a solid with competing periodic potentials and shown that the dispersion of the eigenvalues (band structure) follows the reconstructed BZ, but the spectral weight (proportional to the photoemission intensity) follows the unreconstructed band structure. To visualize this, empty circles along the $(1 \times 1)$ dispersion of the disulfide are plotted in Fig. 5.12a), where the PE intensities are supposed to show the underlying subbands and that is exactly observed in the measured band dispersion.

The CDW formation drives the reconstruction of the band structure. The formation of stars of 13 Ta atoms (Fig. 5.3c) with one electron each (in an ionic picture) leads to six subbands with two electrons per band and the top subband which is only half filled, as the calculations in Fig. 5.12a) between 0.2 and 1.0 eV binding energy confirm. The star of 13 Ta atoms is composed

of the central atom surrounded by a first shell of 6, almost equivalent, nearest neighbors and a second shell of 6, almost equivalent, next nearest neighbors. Thus, the subbands may be grouped in 3 manifolds (visible in Fig. 5.11), the first two of them containing 3 subbands and the last one consisting of a single subband. These three manifolds are clearly separated along AL in Fig. 5.12a) and in Fig. 5.12c). The topmost seventh band (which is due to the star center Ta atom) crosses $E_F$ along $\Gamma$A confirming its partial occupation. The FSMs (Fig. 5.6b) can be explained in terms of the $(1 \times 1)$-unreconstructed FS (Fig. 5.6c) weighted with the oscillating behavior of the topmost subband (Fig. 5.12e)). This topmost subband has predominantly $d_{z^2}$ character, which explains the strong intensity drop at higher emission angles due to matrix elements.

The topmost subband is present all over the BZ. Even along $\Gamma$MK$\Gamma$ empty states are very close to $E_F$ everywhere. For this reason there is always spectral weight at $E_F$, whether it is originating from thermal occupation via the Fermi-Dirac distribution or whether states are truly below $E_F$. Since these states are merely straddling $E_F$, a true crossing of a quasiparticle peak can not be observed, but instead a pseudogap behavior displaying an intensity distribution of the spectral weight according to the spectral function with $(1 \times 1)$ symmetry.

## 5.10  The metal-insulator transition

In $1T$-TaS$_2$ at room temperature, the thermal occupation is semiconductor-like, as well as the slope of the temperature-dependent resistivity. As a consequence, there is a temperature above which the thermal excitation is not sufficient anymore to create enough charge carriers, which leads to the Mott MIT. Perfetti [159] reported recently the surface MIT in $1T$-TaSe$_2$ at low temperature. The new CDW induced BZs lead to flattened backfolded bands, i.e. reduced bandwidth ($W$), reducing furthermore $W/U$ ($U$, the onsite Coulomb energy), which is crucial for understanding the activation of a Mott MIT. [159] The stronger overlap of Ta $5d$ and Se $4p$ bands tends to increase $W$, whereas the reduced coordination number at the surface reduces $W$ enabling the phase transition. [159] Below this transition there is still spectral weight remaining at $E_F$ with a possible contribution from the underlying bulk states. This means that at room temperature the electron-phonon interaction determined CDW ground state is responsible for the RT pseudogap formation. At low temperatures, on top of the CDW induced, reduced carrier density, electron-electron correlation becomes dominant at the surface, thus leading to the transition

[159].

## 5.11 The nesting vector

On the search for the driving mechanism of the CDW, nesting conditions can
be inspected at the unreconstructed FS contours, as explained in Sections 5.2,
5.3. The idea behind the Peierls transition in a quasi-one-dimensional system is
to bring the BZ boundary to lie on top of the flat parts of the FS contour. The
unreconstructed Fermi surface contours have an elliptic shape with rather flat
sections close to the $\bar{M}$ point (Fig. 5.6), which can be connected on both sides
of the $\bar{M}$ point according to a quasi-one-dimensional model with long parallel
sections of the FS undergoing a Peierls transition. The length and direction
of a possible nesting vector $q_{CDW}$ appears favorable (see small white arrow in
Fig. 5.6c). But $1T$-systems are not quasi-one-dimensional, but quasi-2D with
three-fold symmetry, making the described scenario impossible. A relatively
long wave length of the periodic lattice distortion yields correspondingly small
new BZs, creating a large number of new zones cutting the FS contours many
times. Furthermore, backfolding of the bands according to the new reciprocal
space structure, yields oscillating behavior of the bands, including the subband
defining the FS. Additionally, splitting of Ta $5d$ band into seven subbands due
to inequivalent atomic positions in the CDW phase, has allowed the system
to lower 6 of the 7 subbands completely below $E_F$, thus gaining electronically
the energy required for the elastic distortion.

## 5.12 Conclusion

In addition to $1T$-TaS$_2$ also $1T$-TaSe$_2$ is shown to be pseudogapped, demon-
strating that the pseudogap is not related to possible fluctuations of the under-
lying MIT. The CDW which has identical symmetry for the two compounds
is found to be responsible for the pseudogap. A detailed PE analysis of the
band-structure of both materials, reveals CDW split features which are con-
firmed by realistic, reconstructed *ab initio* band-structure calculations using
WIEN97. The CDW induced lattice distortion splits the Ta $5d$ band into three
manifolds of seven subbands. One subband is in the vicinity of $E_F$, the others
appear at larger binding energies, thus stabilizing the CDW structure. The
subband close to $E_F$ is straddling the Fermi level and is responsible for the
observed pseudogap behavior since it does not exhibit a clear quasiparticle
crossing in the ARPES spectra, but is creating persistent spectral weight at

$E_F$. The spectral function is modulating the experimental intensities according to the unreconstructed band structure, explaining the apparent absence of spectral features due to the new BZs in FSMs and band mapping experiments.

# Chapter 6

# Structural investigation of the $1T$-TiSe$_2$, $1T$-TaSe$_2$ and $1T$-TaS$_2$ by means of single-scattering calculations and x-ray photoelectron diffraction

## 6.1  Introduction

Layered materials are usually prepared by cleavage perpendicular to the surface normal. In the case of $1T$-TMDs this is assumed to lead to the surface termination within the van der Waals gap, between the chalcogen planes. Interesting electronic properties of layered materials, the cuprates, the ruthenates or the transition metal dichalcogenides, has awaken much interest for their geometrical structure as well. We concentrate here on the XPD patterns and try to reproduce them using the SSC. This proves to be a powerful tool if one wants to investigate the mean free path of the electrons, structural parameters of the system or the termination of the surface.

## 6.2  SSC-simulation of the XPD-patterns

In Fig. 6.1 (left) the cluster which has been used for the single scattering calculations of the diffraction patterns of $1T$-TiSe$_2$ is represented. It contains
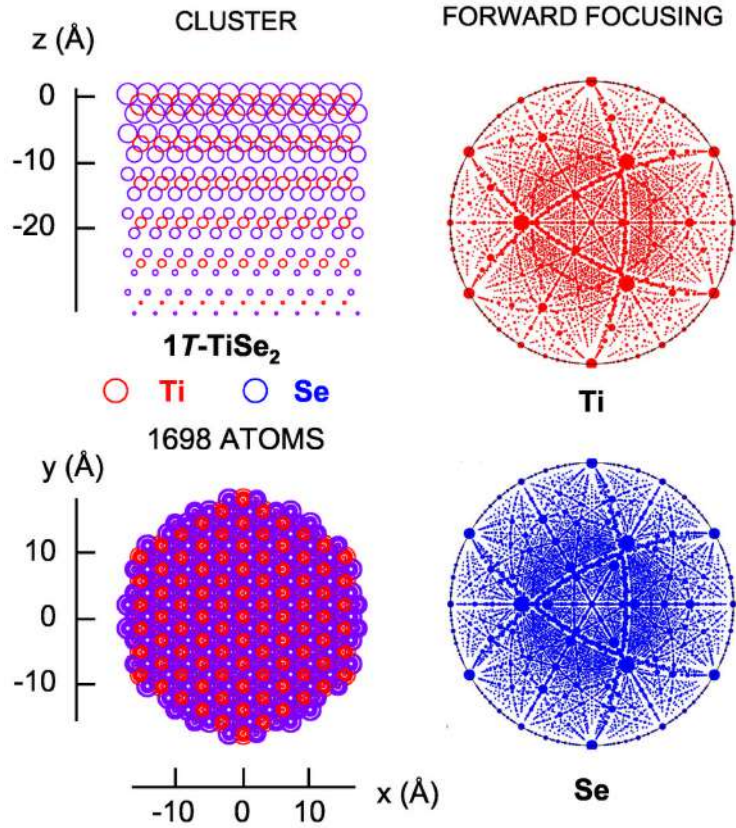
Figure 6.1: Left: cluster used for the single scattering calculations of the diffraction patterns of $1T$-TiSe$_2$ consisting of 1698 atoms. (topview (bottom) and sideview (top)). Ti atoms are presented by red, Se atoms by blue circles. The size of the circles decreases with the distance from the surface. Right: stereographic projection of all the possible forward focusing directions in the cluster depicted on the left, for Ti (top) and Se (bottom).

1698 Ti and Se atoms within the lateral radius of 20 Å (Fig. 6.1 left, bottom) and the total height of some 30 Å (Fig. 6.1 left, top), i.e. six repeated $1T$-sandwiches of chalcogen-metal-chalcogen planes. The clusters of $1T$-TaSe$_2$ (1770 atoms) and $1T$-TaS$_2$ (1877 atoms) were of similar form and size.

On the right side of Fig. 6.1 the stereographic projections of the possible forward focusing directions for Ti (top) and Se (bottom), calculated up to 90°, according to the geometrical structure of the $1T$-TiSe$_2$ and with the help of the depicted cluster, are represented. Trigonal symmetry is dominant and consistent with the crystal symmetry of the $1T$-family. The patterns of Ti and

Se are similar. Larger points correspond to the atoms closer to the surface. If we concentrate on the pattern of Se and observe the edge points of the most prominent inner 'triangle', we see one large point surrounded by the smaller ones, forming together a three-leaf-clover-like shape, which appears also in the measured XPD patterns and which corresponds to the multiple forward focusing possibilities for the emission from the second $1T$-sandwich beneath the surface. One also sees Kikuchi bands, the most prominent ones being along the sides of the 'triangle' and originating from the deeper layers of the $1T$-structure. These bands are also visible experimentally and they exist due to the forward focusing within the close packed crystal layers or planes [174, 175, 176, 177].

Fig. 6.2, Fig. 6.3 and Fig. 6.4 represent measured XPD patterns (on the left) and single scattering calculations (on the right) of $1T$-TaS$_2$, $1T$-TaSe$_2$ and $1T$-TiSe$_2$, respectively. Trigonal symmetry is evident on all diffractograms, as discussed with the Fig. 6.1. Kinetic energy of the measurement and the calculation is noted on the far left. One notices immediately that the SSC images are darker than the measured ones, with very strong forward focusing maxima. This is a known disadvantage of the single scattering calculations, they overemphasize the forward focusing peaks, because the multiple scattering events are neglected (Sections 2.1,2.3). Due to this, there is very little contrast remaining for the fine structure and the image appears rather dark.

The emission of the metal atoms shows three predicted flowerlike shaped forward focusing peaks in all three materials, as well as in TiTe$_2$ [178]. These are well reproduced by the calculation. We have shown through the geometrically calculated forward focusing directions that this is a structural effect due to the multiple scattering possibilities from the layers buried deeper below the surface. Correspondingly, long enough mean free path of the emitted electrons for the calculation is a prerequisite for the appearance of this characteristic shape. The patterns presented in figures 6.2-6.4 are calculated with the mean free path of approximately 10 Å.

Kikuchi bands are clearly visible in the measured diffractograms and well reproduced by the calculation, as well as their fine structure. The six-fold flower in the centrum of the chalcogen-patterns and more three-fold flower in the center of the metal-atom emission patterns are good reproduced. The same holds for the interference shapes outside the Kikuchi lines. The agreement between the measurement and the calculation is outstanding, apart from the relative intensities, which are a known problem of the single scattering models.

In order to illustrate the influence of the choice of the mean free path value in the calculation, we show in Fig. 6.5 the calculated patterns for Ti and Se in $1T$-TiSe$_2$ with the inelastic mean free path of the electrons taken to be
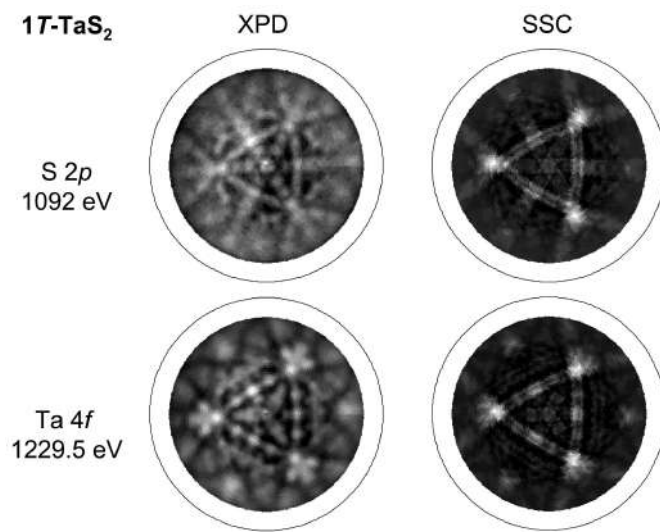
Figure 6.2: XPD (left) and SSC (right) patterns of S $2p$ (kinetic energy of 1092 eV) and Ta $4f$ (kinetic energy of 1229.5 eV) in $1T$-TaS$_2$.
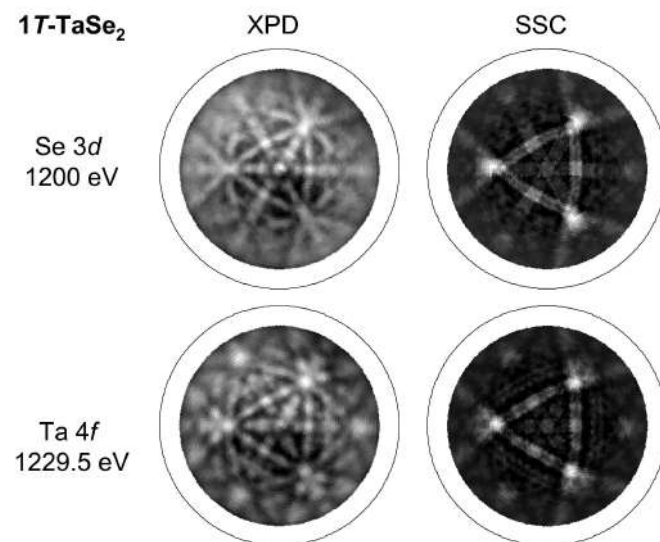


Figure 6.3: XPD (left) and SSC (right) patterns of Se $3d$ (kinetic energy of 1200 eV) and Ta $4f$ (kinetic energy of 1229.5 eV) in $1T$-TaSe$_2$.
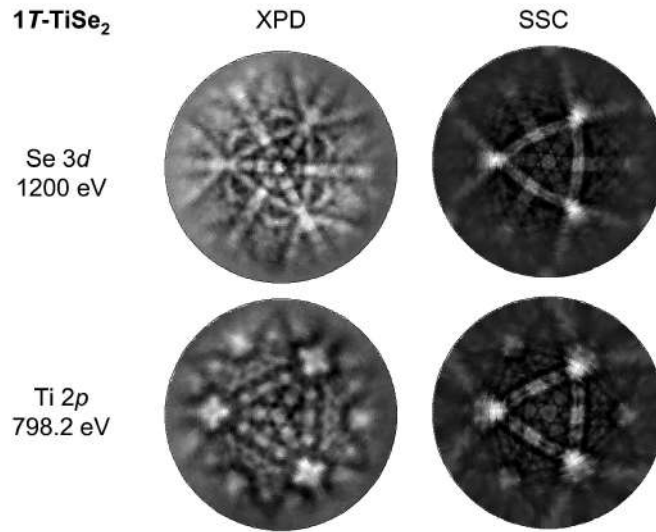
Figure 6.4: XPD (left) and SSC (right) patterns of Se $3d$ (kinetic energy of 1200 eV) and Ti $2p$ (kinetic energy of 798.2 eV) in $1T$-TiSe$_2$.
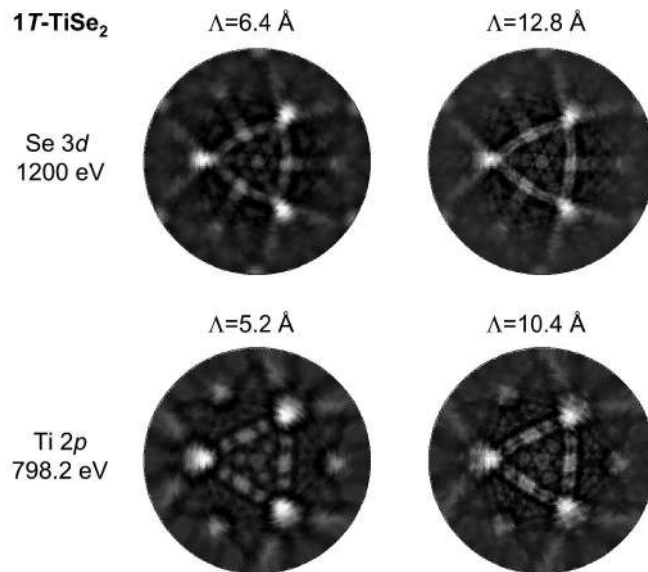


Figure 6.5: SSC patterns of Se $3d$ (kinetic energy of 1200 eV; top) and Ti $2p$ (kinetic energy of 798.2 eV; bottom) in $1T$-TiSe$_2$, calculated with the indicated values of the mean free path.

around 5 Å (left) or 10 Å (right), as was the case in the previous figures. The calculations with the smaller mean free path do not show as rich fine structure as the ones with the larger mean free path. The Kikuchi lines are not as strong, interference details are washed out, and the form of the forward focusing peaks is only roughly reproduced. The three-fold flowers on the edges of the central 'triangle' in the metal emission are fully formed only for the mean free path of 10 Å or more. The same holds for the full development of the Kikuchi bands. Three-fold flowerlike shape of the main FF peaks is due to the electron scattering from the second $1T$-sandwich below the surface and similar holds for the Kikuchi bands. The very fact that we observe them in our XPD images suggests that the mean free path of the electrons is more than one $1T$-sandwich large. We conclude that the inelastic mean free path in these materials is certainly larger than 5 Å and according to our comparison with the SSC patterns, probably around 10 Å. Our investigations show that further increasing of the mean free path does not lead to any significant changes in the calculated pattern.

## 6.3  Cleavage plane and the size of the van der Waals gap

Layered materials are mostly prepared by cleaving perpendicular to the sample surface, assumably within the van der Waals gap, between two chalcogen atomic planes. It is therefore important to investigate if the surface termination really corresponds to the predicted one. In Fig. 6.6 we present calculations of the two possible surface terminations. The corresponding clusters are shown on top. On the left side there is a cleavage between a metal and a chalcogen plane, on the right is the generally assumed cleavage within the gap. Ti and Se atoms are depicted as in the Fig. 6.1, Ti with red and Se with blue circles, decreasing in radius with the distance from the surface. The clusters are approximately only half so large in $z$, as the previously used ones, but since we have proved that the mean free path should be around 10 Å, and we use this value, this size is satisfactory for the calculations considering the termination.

We see that the main features for both terminations are roughly the same, but one notices immediately that the fine structure is very different. Let us observe the Ti emission first and compare the calculated patterns. The shape of the forward focusing maxima is less compact when Ti atoms are on top, and corresponds thus less to the measured XPD pattern. The lines originating close to these maxima and continuing towards the outer circle corresponding to the grazing emission are visible only if Se is on top, and these lines appear
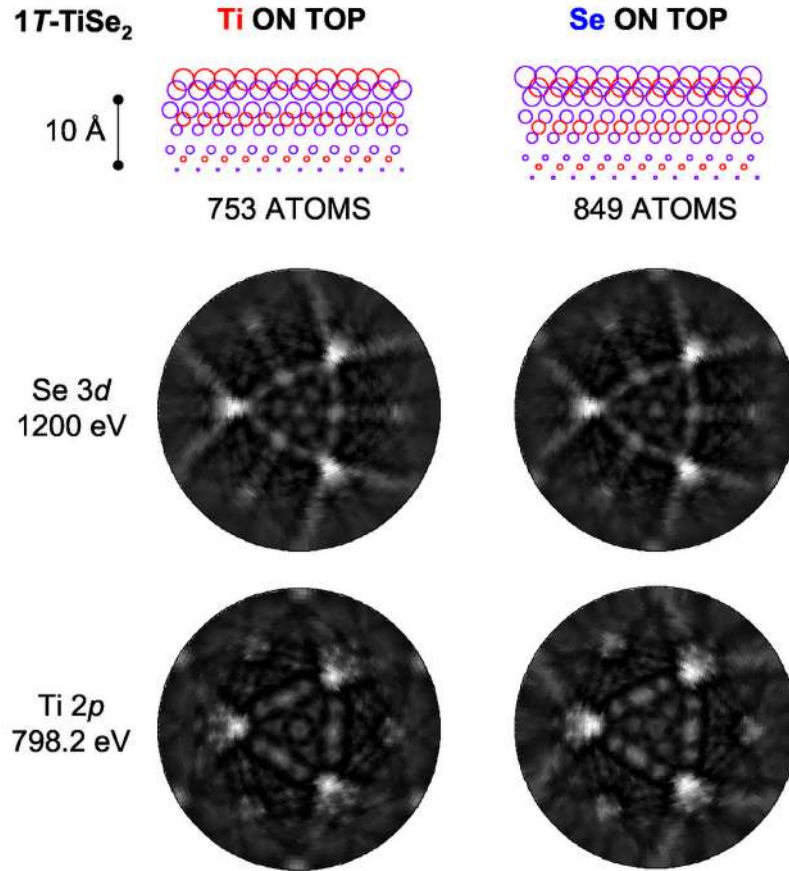
76

Figure 6.6: Top: clusters corresponding to two possible surface terminations in $1T$-TiSe$_2$: Ti on top (left) or Se on top (right). Bottom: SSC patterns of Se $3d$ (kinetic energy of 1200 eV) and Ti $2p$ (kinetic energy of 798.2 eV).

also in our XPD data (see previous figure). The differences in the case of Se emission are not as prominent as those of Ti emission. The main feature by the Se emission is the appearance of the forward focusing peaks at the grazing emission in the case when Se is on top. This is, however, difficult to prove, since our experimental diffractograms are rather blurred at the very grazing emission. We could conclude that the Ti emission suggests that the cleavage is between the chalcogen planes.

Finally, an attempt was made to optimize the agreement between the SSC and the XPD, by changing the size of the gap. In Fig. 6.7 three of five calculated values are presented. The gap is increasing from left to right, and the

value in the middle is the nominal gap size. The corresponding SSCs on a Ti $2p$ kinetic energy (798.2 eV) are shown below. Mean free path of 5 Å has been used for faster calculating, because series of calculations have been performed. With this mean free path, the shape of the forward focusing maxima is not well reproduced, but as we will not focus on this feature now, our choice of the smaller mean free path is still justifiable. If one observes the interference pattern marked with the white ellipse in the Fig. 6.7, one sees remarkable changes in this area with the change of the gap size. The whole interference pattern is absent for the gap smaller than the nominal one, and appears in the expected form first for a gap slightly larger than the nominal. Another feature is the line starting at grazing emission in the direction towards the center of the pattern, ending up before the FF peak (marked with the arrow in Fig. 6.7). This line appears as well only for the gap sizes above the nominal value. It could lead one to conclude that the size of the gap is indeed larger than the nominal one, but one has to be precautious, because SSC is known to overestimate the intensity of the FF peaks. It is thus difficult to draw conclusions from the underestimated intensity of the interference structures.
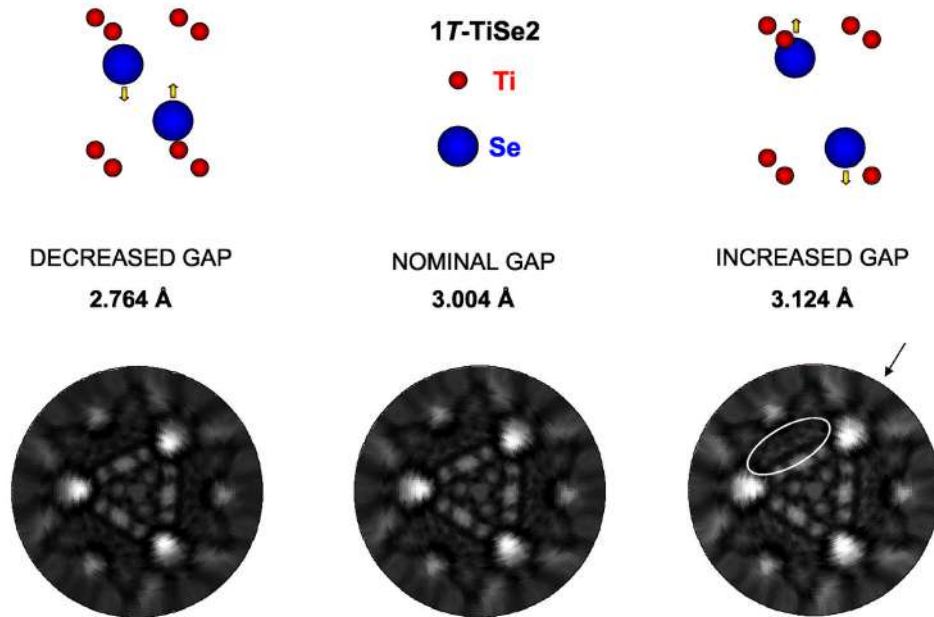


Figure 6.7: SSC patterns for increasing gap size (from left to right) between the chalcogen planes in $1T$-TiSe$_2$, calculated at Ti $2p$ (798.2 eV) emission with the mean free path of 5 Å.

We have performed a detailed and systematic study of the diffraction patterns of the three $1T$-TMDs: $TiSe_2$, $TaSe_2$ and $TaS_2$, on both metal and chalcogen emission lines. In addition to this we have performed series of single-scattering calculations in order to investigate structural properties, mean free path of photoelectrons in these materials or the surface termination. XPD and SSC prove very useful for the determination of the inelastic mean free path, which is approximately 10 Å for the $1T$-family. The determination of the surface termination or the structural analysis are possible, but the large uncertainty is brought by the enhanced intensity of the FF peaks due to neglecting of the multiple scattering in the SSC program and thus diminished intensity of the remaining fine structure of the diffractograms. Combined with the observation of the raw XPD data, SSC is a very useful tool for the mean free path analysis.

## 6.4   Conclusion

Successful single scattering calculations of the three members of the $1T$-family are presented, exhibiting very good agreement with the experimental XPD patterns. Implementing SSC, the optimal value of the mean free path of about 10 Å for these compounds was determined. The investigation of the Ti emission and calculations for different surface terminations confirm cleavage within the van der Waals gap. Finally, changing the structural parameters leads to the changes in the interference pattern in the diffraction images. Although the determination of the termination or the size of the gap could be affected by the disadvantages of the SSC, the mean free path analysis in these materials relies on the form of the FF peaks and can thus successfully be determined by comparison of XPD and SSC.

# Part III

# Surface states in thin silver films on gold

# Chapter 7

# High resolution photoemission study of Ag/Au(111)

## 7.1 Introduction

Shockley-type surface states in the $L$-gap of noble metal (111) surfaces provide a suitable model system for electronic states in two dimensions. Since high-resolution PES has enabled a precise investigation of the intrinsic line width and the spin-orbit splitting of the surface state on Au(111) [78, 83], it has become increasingly interesting to study in which way adsorbates influence it. The localization of the surface states at the surface makes them extremely sensitive to the structural or compositional changes of the surface. [179] The deposition of noble gases like Xe, Kr or Ar in the monolayer regime shows a decrease in substrate surface state binding energy towards the Fermi level and an increase of its spin-orbit splitting up to 30% with respect to the value of pure Au(111). [180] Thin epitaxial films of other noble metals on Au(111) lead to different phenomena due to the existence of their own surface state embedded within their projected bulk band structure. The interplay of the energetics of surface and bulk states determines the binding energies of the observed states in the vicinity of the Fermi level. [181, 182]

Ag/Au(111) is an intermetallic system, exhibiting parallel epitaxy due to a negligibly small lattice mismatch (0.2 %, $a_{Au}$=4.0782 Å, $a_{Ag}$=4.0853 Å). Two peculiarities of Au(111) as a substrate are the so-called herringbone reconstruction of the topmost surface layer (visible also in PE [84], its influence on the Ag film growth will be discussed elsewhere [69]) and the spin-orbit splitting of the Shockley state [78, 83]. The Shockley state in Au(111) exists in the inverted $sp$-band gap due to symmetry breaking by the surface. [183]

Quantum-well states in intermetallic systems are quantized electronic states confined within the same projected $sp$ bulk band gap. [184] High energy resolution enables us to observe the changes that they undergo with the deposition of silver. Complementary to that, the projected band gap and the valence band carry information about the bulk or the substrate.

The interesting question of probing deep interfaces has been investigated in the past by observing the quantum-well states [184] or core-level shifts [185]. It will be shown here that the projected band structure of gold is visible in the data after 10 ML of silver, when the $d$-band of silver is already completely formed. The changes of the surface state are in accordance with the slower development of the $sp$-bands with layer thickness. Whereas the $d$-band shows thus bulk electronic structure of the film, the surface state and the quantum well states offer information about the film thickness and the projected band gap enables a direct visualization of the substrate.

## 7.2 Surface states

Surface states represent electronic states localized due to crystal-symmetry breaking on the surface and they appear in the gaps of the bulk band structure projected on the direction of observation (Fig. 7.1). Their energy vs momentum dispersion is free-electron like, they are quasi-two-dimensional, which ensures the validity of the sudden approximation for the near-Fermi-surface observations (see Sections 1.2,1.3).

Historical development of the surface state concept starts with the theoretical works of Tamm [186, 187], followed by Maue [188], Goodwin [189, 190, 191], Fowler [192], Rijanow [193] and W. Shockley [183], using the Kronig-Penney model [194]. Surface states have been reported on the surfaces of semiconductors and metals, and this thesis considers surface states in thin films of noble metals on noble metals. On these surfaces one distinguishes surface states of Shockley and Tamm type. The generally accepted definition of these two states in the early 1980's [18] is the following: Shockley states are surface states formed by nearly-free $s$ and $p$ electrons, with wave functions extending several layers into solid; whereas Tamm states are $d$-like surface states in transition metals, with atomic-like wave functions localized on surface atoms. An equivalent definition of Zak [18] says that Shockley states appear in a crystal whose surface is a symmetry plane, otherwise one has Tamm surface states. He also showed that if the bands cross to form an inverted gap, which is the case for close atomic configurations, the band symmetry changes. On the other hand, if distorted lattice with no symmetry is assumed, energetically decreasing and

increasing energy levels can not cross. [119] The consequence of the conclusions of Zak is that Shockley states do not require band crossing, i.e. do not exist only in the hybridization gap. [18]
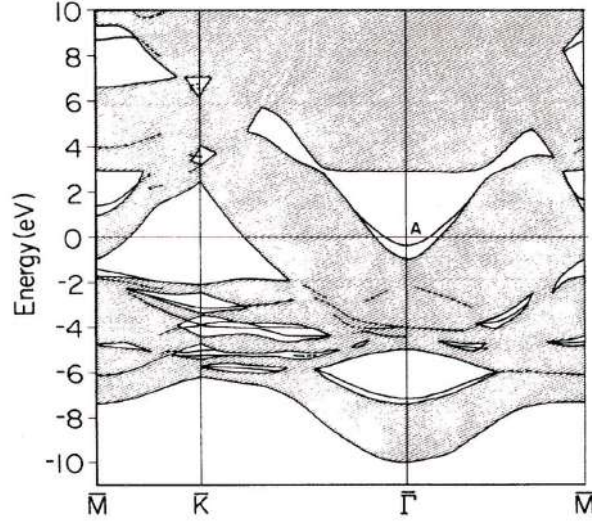


Figure 7.1: Projected band structure of Au(111) (shaded) with the calculated surface states and resonances within the gaps (lines). The surface state treated here is marked with A. [195]

Allowed states of an ideal periodic crystal can be, according to the Bloch's theorem, written in a form:

$$\psi_{\mathbf{k}}(\mathbf{r}) = u_{\mathbf{k}}(\mathbf{r})e^{i\mathbf{k}r}, \tag{7.1}$$

where the function $u_{\mathbf{k}}(\mathbf{r})$ has the three-dimensional periodicity of the crystal lattice and the wave number $\mathbf{k}$ is real, to ensure that the wave function remains finite. The spectrum consists correspondingly from continuous zones and band gaps. In a semi-infinite crystal the forbidden band gaps become allowed, if the wave functions are chosen in such a fashion, to decay from the surface towards the bulk of the crystal. The generalized Blochs formula can be written in the form [196]:

$$\psi_{\mathbf{k}}(\mathbf{r}) = [u_{\mathbf{k}}(\mathbf{r})e^{i\mathbf{k}r}]e^{-\beta r}. \tag{7.2}$$

Inside the crystal, the surface state is an exponentially decaying oscillatory wave function (evanescent) and at the surface, it matches the wave function outside the crystal, as well as its first derivative. [186, 187] Such a wave function has the form $\psi_c$ inside and $\psi_v$ outside the crystal [18]:

$$\psi_c(z) = Ae^{\beta z}\cos(\pi z/a + \delta), z \leqslant 0 \qquad \psi_v(z) = Be^{-k_0 z}, z \geqslant 0. \tag{7.3}$$

where $k_0 = (V_0 - E)^{1/2}, E < V_0$, $V_0$ denotes the constant vacuum potential and constants $\delta$ and $\beta > 0$ are given by $V_0$ and $a$ [18]. The factor $e^{\beta z}$ is the envelope function of the surface state and the decay length of the surface state $\beta^{-1}$ determines its degree of localization at the surface. [72] As the surface state wavefunction decays exponentially in both directions from the surface, the electrons will be bound (localized) at the surface. One may say that $k$ inside the crystal may assume complex values, i.e. $k = \zeta - i\mu$ [18], which give rise to decaying wave functions and energy levels that lie in the gaps between the $k$-real bands of the infinite crystal.

This is presented, in the case of Au(111) in Fig. 7.1. According to the first-principles band structure calculations from Takeuchi *et al.* [195], surface states and resonances can be isolated as those wavefunctions, which are localized at the surface, and their dispersion falls within the band gaps of the projected bulk band structure, which are forbidden for the bulk states.

## 7.3   Growth and morphology of thin Ag films on Au(111)

Due to their confinement at the surface, the Shockley states are very sensitive to the atomic structure or reconstruction of the surface [197], symmetry at the surface [179], periodic steps at the surfaces [198] or the growth mode [199, 200, 182]. At room temperature Ag grows on Au(111)in a layer-by-layer (Frank-van der Merwe) fashion. [201] After a moderate annealing, STM, AES and PES demonstrate an alloying of Au and Ag. The bulk lattice constant of Au and Ag are very close and transmission-electron-microscopy has shown that the interface is abrupt and no interdiffusion occurs at room temperature [202].

Film growth is a non equilibrium process, which depends on both kinematic and dynamic factors. Kinematic condition for layer-by-layer growth is $\gamma_{film} \leqslant \gamma_{substrate} - \gamma_{interface}$, where $\gamma$ denotes surface/interface energy. With the surface free energies of silver and gold (111)-surfaces, which are 0.62 $J/m^2$ and 0.79 $J/m^2$ respectively and the interface energy between -0.39 and -0.10 $J/m^2$ [203], the condition for layer-by-layer growth is fulfilled. Dynamic factors influencing film growth are deposition rate and temperature and exchange and diffusion processes. [179]

The morphology of a 0.5 ML film is illustrated in the STM image in Fig. 7.2. This image shows large Ag islands on Au terraces. The so-called herringbone reconstruction of Au(111) [204, 205, 206] is observed. This $22 \times \sqrt{3}$ reconstruction exhibits parallel zigzag ridges which exist due to stress-induced con-
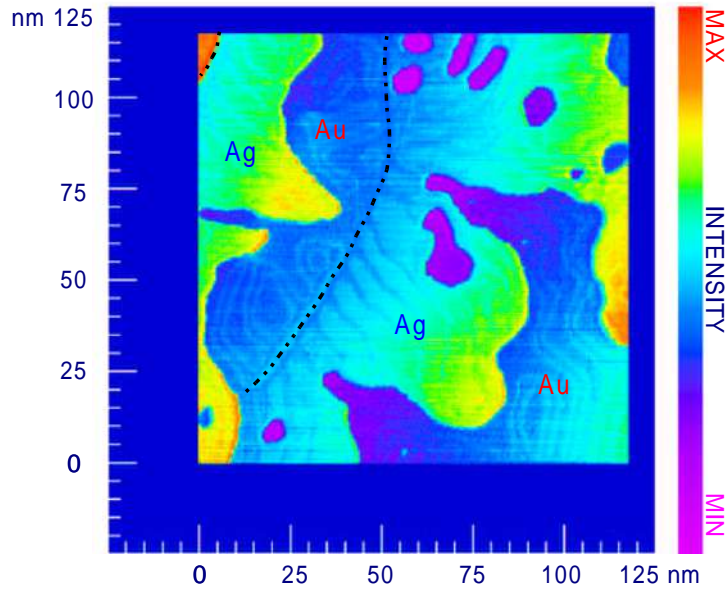
Figure 7.2: STM image of a 0.5 ML Ag-film deposited at room temperature on Au(111), the dotted line represents the step edge of the Au substrate. [69]

tractions [207] connecting hexagonal-closed-packed (hcp) and face-centered-cubic (fcc) regions of the reconstructed first layer. A distortion of the substrate reconstruction is visible in Fig. 7.2 in the vicinity of the Ag islands. Moreover, the corrugation observed on the Ag islands is reminiscent of the Au-herringbone reconstruction. However, it is difficult to conclude if the Au reconstruction still exists below the Ag layer or if the Ag layer itself exhibits a reconstruction similar to the herringbone one. For less than one monolayer, long-shaped islands of Ag can be observed, reminiscent of the underlying herringbone reconstruction, whose influence does not persist further than the first Ag monolayer. [69, 201] The growth of Ag films deposited on Au(111) at RT starts preferentially at the steps of Au-terraces, continuing in a layer-by-layer growth for small coverages. [69, 184, 201]

Parallel with the change of the surface potential induced by an overlayer of silver, a new surface state is observable in the PE data, with characteristic binding energy, effective mass and SO splitting. One surface state corresponds to the substrate or/and each monolayer of the adsorbate, as can be seen in the grey scale dispersion plot $(E(k_\parallel))$ in Fig. 7.3 (top) for 0.5 ML. There we see the surface state of clean gold at the nominal binding energy of 479 meV
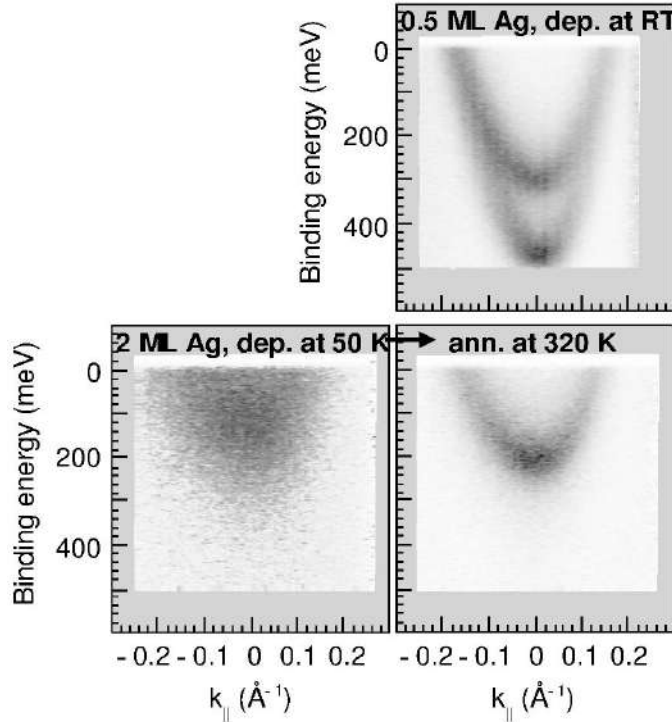
Figure 7.3: Grey-scale plot of the Shockley state for different Ag-film on Au(111) surface preparation conditions measured with He I. Top: 0.5 ML Ag/Au(111) deposited at room temperature, showing layer-by-layer growth. Bottom: 2 ML Ag/Au(111) deposited at 50 K showing disorder (left) and post-annealed at 320 K showing well-ordered surface. Dark represents high photoelectron intensity.

and the surface state of 1 ML Ag/Au(111) at 305 meV. One closed monolayer shows solely one surface state, which will be discussed later. The deposition temperature plays an important role: at room temperature there is enough mobility for the formation of ordered monolayer islands, at low temperatures the Ag-film is highly disordered (Fig. 7.3 bottom left). One finds no well-defined surface-state, but a strongly blurred intensity, due to disorder. After moderate annealing, an ordered epitaxial overlayer is achieved and the surface state corresponding to 2 ML coverage is clearly visible (Fig. 7.3 bottom right).

The best quality of surface states was obtained for the substrate at RT during the Ag deposition. The ionization of the accelerated silver atoms emitted from the evaporator perturbs the interface strongly [208] enough to affect the observation of the SO splitting, i.e. create a less sharp interface, triggering

mechanically and chemically intermixing of silver and gold. For the observation of the decreasing SO splitting in silver films on gold, this problem can be avoided by using a Knudsen cell for evaporation, as will be shown elsewhere [69, 10].

## 7.4 Contributions from surface and bulk to the electronic structure

Fig. 7.4 shows surface and bulk states for pure Au(111) (left) and 10 ML Ag/Au(111) (right) over a wide binding energy (BE) range, from the Fermi level down to 7 eV below. The upper graphs show the surface states marked at their band minimum with a white circle: the first two quantum well states (at 688 meV and 1048 meV BE for a silver covered surface) and, stronger in intensity, the Shockley state (at 479 meV BE left and 84 meV BE right). The surface and quantum well states shift towards lower binding energies with the silver coverage within the limits of the projected bulk band gap of Au(111). The $sp$-gap of Au(111) is visible in Fig. 7.4 as the contrast between bright (within the gap) and dark (projected band structure) areas in the plot and has also been calculated (see Section 2.1), shifted in BE by 120 meV to fit the measurements, and presented in Fig. 7.4 by dark circles.

The lower panels in Fig. 7.4 show the valence band range. Contributions for the Au(111) surface (left) are identified according to Ref. [210, 211] and overlayed by the band-structure calculations from Ref. [209]. The bulk bands are denoted by numbers 2-6, whereas $D_1$ and $D_2$ are surface resonances. Surface resonances differ from surface states because they couple to the Bloch states of the bulk. Their density is thus higher at the surface than in the bulk, but pertains a finite value in the bulk as well, whereas the exponential damping of the surface state density leads to zero after several monolayers. [117] The valence band of 10 ML Ag/Au(111) corresponds perfectly to the overlayed band-structure calculations of pure silver taken from the Ref. [209] Both calculations for silver and gold are taken along ΓK direction, and He I radiation should correspond to $k_\perp$ in the vicinity of Γ [212, 213]. The number and the splitting of the bands are found experimentally, their BEs are somewhat overestimated. Better agreement is possible away from Γ towards L, but as the equivalent of ΓK dispersion is lacking for $k_\perp$ points other than Γ, we decided to show the ΓK calculations. One sees by comparison with the measurements that the Au-bands are absent for 10 ML Ag/Au(111) and that the measured valence band corresponds completely to the one of silver. Although the $d$ bands are already the ones of silver, the upper panel shows the
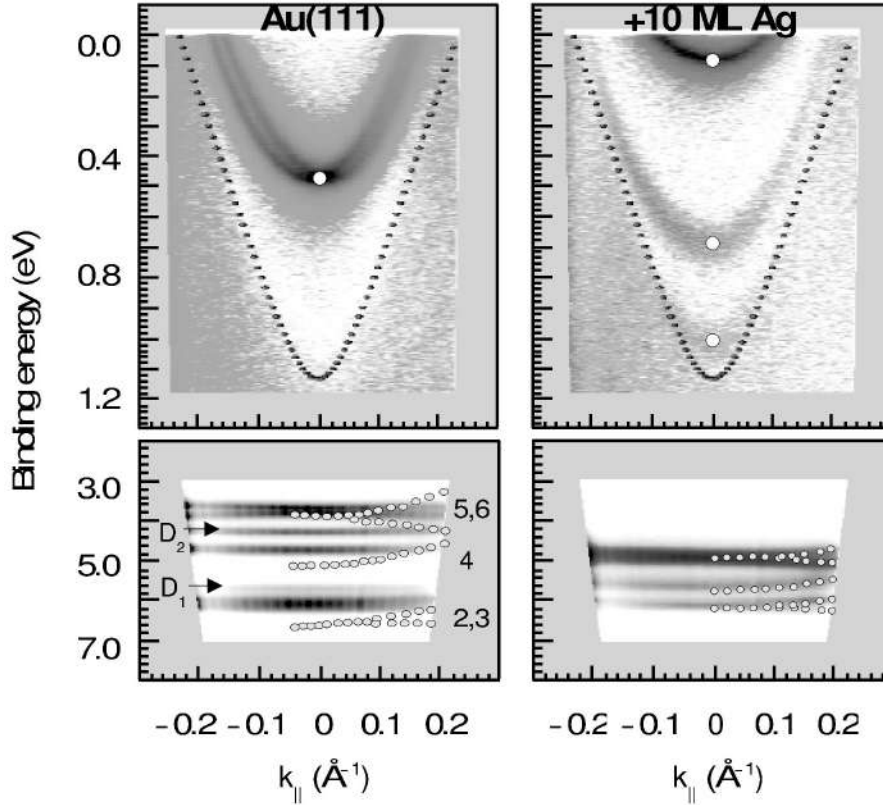
Figure 7.4: Top: Surface state (lower binding energy) and quantum well states (higher binding energies) along $\bar{\Gamma}\bar{K}$ marked by white dots for Au(111) and 10 ML Ag/Au(111). The band-structure calculations of the Au-$sp$-gap have been shifted to fit the measured binding energy for the pure Au(111) and are shown as black circles. Bottom: Valence band; 2-6 are valence bands of the Au(111), $D_1$ and $D_2$ are the surface resonances. White dots represent band-structure calculations for pure Au (left) and Ag (right) by Smith [209]. The measurements have been taken with He I at T=30 K.

$sp$-gap from gold, thus revealing the substrate lying some 30 Å below, which is approximately the thickness of 10 ML of Ag(111). [214] The escape depth for He I is 5-10 Å. [7] The projected band structure of silver will evolve from the quantum-well states, which are also indicative of an overlayer film, and which will reach the characteristic position of the Ag $sp$-gap BE minimum after several tens of monolayers. This is similar to the previously reported "slower" development of the $sp$-bands of the adsorbate by comparison with the $d$-bands [215, 216].

The evolution of the surface state with Ag coverage is depicted in Fig. 7.5. The decrease of the surface state band minimum and the SO splitting and the increase of the effective mass are observable from the values of the Au(111) towards the ones of the Ag(111). The BE and effective mass for the surface state of pure Au(111) are 479 meV and $0.255$ $m_e$, respectively; the ones of silver are 64 meV and $0.397$ $m_e$. [9] Thus one expects a decrease of the binding energy and increase of the curvature with silver coverage on the gold substrate, and that is what we observe. The projected band gap of Au does not change with coverage. The values of the relevant measured and calculated surface state parameters are presented in the Table 7.1. On the measured intensity maps, our band structures obtained with WIEN2k [70](circles; see Section 2.1) have been superimposed. They have been shifted in BE to fit the measurements
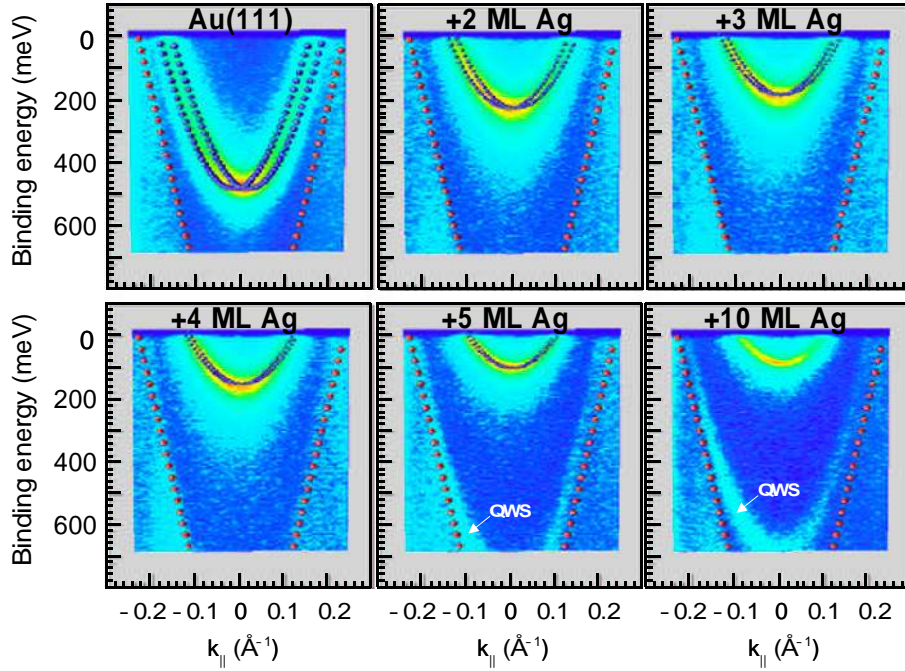


Figure 7.5: Surface state dispersion changes with silver coverage taken with He I. The binding energy of the calculated Au-$sp$-gap (large circles) has been adjusted to the measured value for Au(111). The calculations of the Shockley state (circles) have been shifted for each coverage to fit the measured binding energies.

and the values of the shifts can be read in the Table 7.1. The rigidly shifted calculations agree in effective mass very well with the measurement. For the gap, the calculation for Au(111), shifted to the measured BE minimum of the measured gap on Au(111), has been used for all surfaces (large circles) as a guide for the eye. It yields obviously excellent agreement because the gap does not change up to very high coverages. On the other hand, the calculated "band gap minimum" shows the bulk modes with the lowest binding energy, and these correspond after a couple of monolayers no longer to the projected bands of Au, but to the quantum well states of Ag film. Why is shifting of the calculated bands necessary for the agreement with the measurement will be discussed later.

The first quantum well state is observable within the Au *sp*-gap at 5 ML Ag/Au(111); the second one at 10 ML Ag/Au(111) (Fig. 7.5), in agreement with the previous study [217]. Their line widths are roughly 100 meV, which is slightly more than the estimated 80 meV [184]. Better film preparation procedures can lead to a decrease of the quantum-well-state linewidth to 50 meV. [218] According to the Ref. [184], the 3D-character of the interface could not expand over more than a few monolayers; according to the surface state BE we could state that it should not expand over more than a monolayer. This is another evidence that the SO splitting of the surface state is highly sensitive to the surface and interface quality.

The SO-split surface state parabolas and band gap as calculated are shown in Fig. 7.6. The binding energy and the spin-orbit splitting of the calculated bands represented in Fig. 7.6 are summarized in Table 7.1. All calculations have been performed without structural relaxation, which would have been too much time consuming with the slabs which have been used here. Table 7.1 shows that the shift of approximately 100 meV is necessary in order to achieve agreement between the calculated and the experimental binding energies. This problem is known in the DFT-calculations. [219] The GGA-potential used here is well adapted to describe homogeneous or slightly inhomogeneous electron gas, which could be a reason, why it produces huge discrepancies in the absolute binding energy values in the case of highly inhomogeneous electron density distributions of surface states. [220] The results presented here have qualitative significance.

The changes of the surface state parameters with the coverage are well reproduced by the calculation. One sees in Fig. 7.6, Fig. 7.5 and Table 7.1 that the SO splitting is decreasing and the effective mass increasing with the coverage. According to the experimental data [10], both effective mass and spin-orbit splitting increase exponentially until they reach saturation at approximately 5-10 ML Ag coverage. The work function, on the other hand,
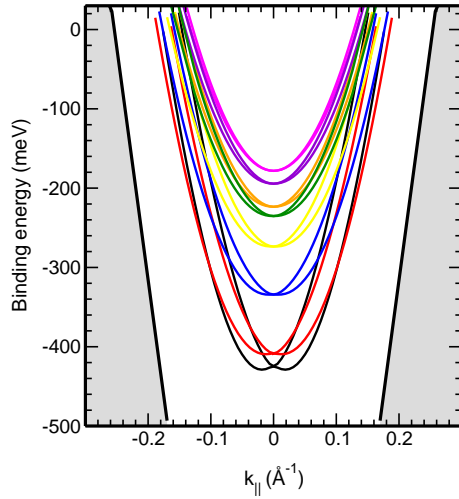
Figure 7.6: Wien 2k band-structure calculations for, from bottom to top, Au(111), 1-6 ML Ag/Au(111) and Ag(111). The calculations have been performed on a 23-layer slab of Au(111) with additional layers of Ag on both sides of the slab and 20 bohr vacuum between the slabs. (See Sections 1.4,2.1) Binding energies are as calculated.

changes rapidly with the first monolayer and reaches saturation at less than

Table 7.1: Binding energy, effective mass and spin-orbit splitting of the surface state for the corresponding coverages of Ag on Au(111) as obtained from the band-structure calculations ($^{th}$) (see Section 2.1) and as measured ($^{exp}$).

| Surface | B.E.$^{th}$ (meV) | B.E.$^{exp}$ (meV) | $m^*/m_e$$^{th}$ | $m^*/m_e$$^{exp}$ [1] | S.O.S.$^{th}$ ($\text{Å}^{-1}$) | S.O.S.$^{exp}$ [1] ($\text{Å}^{-1}$) |
|---|---|---|---|---|---|---|
| Au(111) | 429 | 487 | 0.23 | 0.26 | 0.030 | 0.023 |
| +1 ML Ag | 409 | 305[1] | 0.28 | 0.33 | 0.023 | 0.019 |
| +2 ML Ag | 334 | 222 | 0.32 | 0.34 | 0.019 | 0.015 |
| +3 ML Ag | 274 | 184 | 0.35 | 0.38 | 0.014 | 0.013 |
| +4 ML Ag | 235 | 158 | 0.36 | 0.40 | 0.011 | 0.013 |
| +5 ML Ag | 223 | 98 | 0.36 | 0.41 | 0.009 | 0.010 |
| +6 ML Ag | 194 | 77[1] | 0.37 | - | 0.007 | < 0.010 |
| Ag(111) | 178 | 64 | 0.37 | 0.42 | 0.004 | < 0.010 |

(1) Measured at 90 K [10, 69].

5 ML. [221] The silverlike character of the surface state, which is increasing as the surface state parameters approach the values of pure Ag(111), is thus directly proportional to the number of silver atoms within the sampled thickness. This also confirms the atomic character of the spin-orbit splitting. The calculated SO splitting (Table 7.1) in Ag(111) is 0.004 $\text{Å}^{-1}$, which is very similar to the limit obtained in the Ag films on Au(111) [10], possibly moving the prediction for the SO splitting in Ag towards the limit where it could be observed. If all the surface states are scaled in BE, in such a way that BEs of Au and Ag correspond to the measured ones, there is better agreement with the data, which is visible in Fig. 7.7.
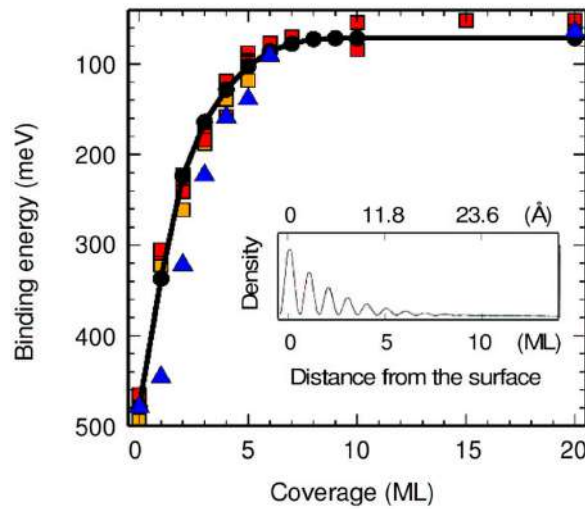


Figure 7.7: Ag-coverage dependent surface state binding energy: experimental data using He I (red squares) and Ar I (orange squares) [10] radiation, band-structure calculations (blue triangles) and electron density of the surface state (see Inset) distributed over discrete numbers of monolayers (black circles and line) both scaled between the binding energies of clean Ag(111) and Au(111) as reference points. The inset shows NFE-calculations of the surface-state electron density perpendicular to the surface by Beckmann [222] for 12 ML Ag/Au(111).

Fig. 7.7 presents the BE trend of the measured and calculated surface state data. Several data sets are displayed (squares), obtained with different film preparation techniques and measured using He I or Ar radiation, in order to get an insight into the data spread which could originate from different surface preparation or coverage calibration. In spite of all differences, the BEs of all the measured surface states agree very well. Beside the measurements, the *ab*

*initio* band structure calculations of the surface state are presented (triangles), scaled linearly between the two reference points as mentioned before. The dependence of the BE on the silver coverage is well reproduced.

The binding energy of the surface state is related to its localization within the surface region because of the exponential damping towards the bulk. [72] The electron density of the surface state from the Au(111) surface covered by 12 ML of Ag, calculated in Ref. [222] in a nearly-free-electron approximation, is displayed in the inset of Fig. 7.7 versus the distance from the surface expressed in monolayers (the thicknesses of Au and Ag monolayers differ quite negligibly). The 12 ML are in accordance with the decay length of the surface state of Ag(111) [72]. Already at 5 ML towards the bulk, most of the signal of the surface state is lost. If maxima of this density curve are taken at discrete numbers of monolayers and scaled between the BEs of Au(111) and Ag(111), one arrives at the black line drawn through the circles in Fig. 7.7. In Fig. 7.7 it demonstrates the BE trend with respect to coverage, which can be understood as the development of the Ag contribution in the BE of the surface state, which is related to the silver coverage in which the density of surface state penetrates. [214] The similarity of Ag and Au lattice constants allows this analogy. It describes the measured binding energies perfectly.

The comparison of the measured and the calculated data is very important, because it allows the identification of the surface/bulk character of the bands. The valence band of 10 ML Ag/Au(111), fits very well with the calculated Ag bulk bands. This is according to the expectations, because the inelastic mean free path of photoelectrons excited with He I does not exceed 10 Å. In this sense, the Ag film is overtaking the role of the half-infinite crystal, and the quantum well states corresponding to it are seen in the calculation as the first bulk modes. And they have partially this role, because of a very large coherence length. On the other hand, their phase shift contains the information about the interface. [184, 223] Shockley states and projected band gap can lead to the same or even more detailed information as the core levels or quantum-well states. The electron density of the surface state has an infinite tail, but the decaying intensity prevents that it couples to the bulk states. We are taking advantage of this property in this work, using the Shockley state for the conclusions about the surface and the projected *sp*-band gap of gold as an indicator of the deep buried interface.

Starting from the general expression for the surface state wavefunction inside the crystal given by Eq.(7.2), the wavefunctions inside the film and the substrate are [72]:

$$\psi_f(\boldsymbol{r};t) = u(\boldsymbol{r})e^{ikz}[e^{\beta_f z} + Ae^{-\beta_f z}], \quad \psi_s(\boldsymbol{r};t) = Bu(\boldsymbol{r})e^{ikz+\beta_s z}, \qquad (7.4)$$
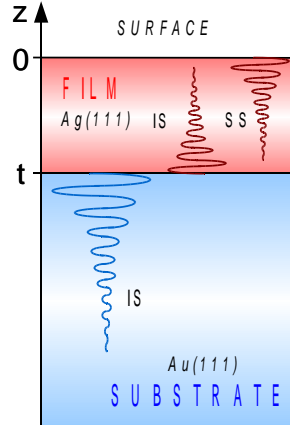
Figure 7.8: Schematic representation of the possible surface and interface states in the case of Ag/Au(111).

where $f$ stands for film ($t < z < 0$) and $s$ for substrate ($-\infty < z < t$) and coefficients $A$ and $B$ can be determined from the continuity of the wavefunction and its derivatives at the substrate-film interface. These formulas are written for the case $u_f \approx u_s = u$, which is justified by the similarity of silver and gold band structures, and they describe two interface and one surface state, which are schematically presented in Fig. 7.8. Under the given condition there can exist only one wave function, to which all the drawn states contribute [72], and this is why only one peak is observed in photoemission experiments. For the $t$-values of the order of $\beta_{f,s}^{-1}$ both $A$ and $B$ are significant and the one state visible in PE is both surface and interface state. It could be therefore said that the film modifies the surface potential and thus the wavefunction of the surface state. The similarity of the electronic structures of silver and gold prevents the formation of a true interface state. [72] This can be qualitatively explained in terms of potential barrier changes: the sample-vacuum potential step in the Ag/Au(111) system is 5 times larger than the work function change at the Ag-Au interface.

## 7.5 Comparison with surface states in other epitaxial systems

The investigated system shows many similarities with the growth of Ag on Cu(111). In both cases we are dealing with a noble metal adsorption on a noble metal surface, where both adsorbent and substrate have a Shockley surface state. Ag grows on Cu(111) also in layer-by-layer fashion for small coverages, and its coverage dependent binding energy of the surface state increases exponentially from the value for pure Cu(111) towards the one of pure Ag(111), reaching the saturation at approximately the same coverage values as in the case of Ag/Au(111). [181, 182] For an "inverted" system, Au/Ag(111), similar monotonic and asymptotic behavior of the surface state parameters has been reported. [216, 72]

On the other hand, $Cu_{0.9}Al_{0.1}(111)$ shows a surface state placed 0.4 eV lower than the one of pure Cu, presumably due to the annealing induced shift of the band gap. [224] In $Cu_3Au(111)$ two surface resonances have been discovered, one at the binding energy of the Cu(111) surface state and another one at -1 eV. [225] The absence of a projected band gap forbids formation of the surface states. Similarly, in the study of Ag films on GaAs(110), the shift of the surface state to 180 meV above the Fermi level is related to the corresponding shift of the $sp$-states und thus induced shift of the bottom of the band gap. [226] These examples illustrate that the interplay of the substrate and adsorbate energetics determines first of all the bulk band gaps, which determine further the appearance, the character or the binding energy positions of the surface states. In the case of Ag/Au(111) is the band gap of Au(111) larger than the one of Ag(111). However, we do not observe the immediate formation of the new gap of the adsorbate bulk band structure. To the contrary, we observe the formation of the quantum-well states, which evolve for very large coverages into the continuum of the projected band structure of silver. The difference between our study and the above mentioned ones is that Ag does not solely change the band structure of Au, but rather develops its own states within it.

Alkali metals lower the work function of the noble metal on which they are adsorbed and shift its surface state towards higher binding energies, as can be seen in the cases of K/Ag/GaAs(110) [226], Cs/Cu(111) [227] or Na/Cu(111) [228]. On the other hand, the deposition of Cs [227, 229], Na [228, 230, 231] or Ba [231] on Cu(111) leads also to a formation of the new states, which are sharp and mostly formed within the band gap of copper, thus being not substrate-independent. In the case of Na, one speaks of a quantum-well state. [232] The band minimum of the surface state is found to shift towards

the Fermi level with increasing film strain and towards larger binding energies with decreasing work function. [233, 226, 228] This can be seen in the measurements of Ag/Si(111) [233], Ag/HOPG [233], Ag/GaAs(110) [226] and Na/Cu(111) [228].

On the other hand, noble gases lower the work function of the substrate [234], as the alkali metals do, but decrease the binding energy of the surface state [180, 235]. The occupied *sp*-derived surface state contributes to the Pauli repulsion towards the closed-shell adsorbates [78, 236], but enhances the bonding interaction of metal adsorbates on metal substrates [236].

For Ag/Au(111) both the surface state and the work function change from the values of Au(111) towards the ones of Ag(111). The work function decreases from the value for Au(111) (5.51 eV) towards the value for Ag(111) (4.56 eV), the binding energy decreases as well, contrary to the reported shifts in the cases of alkali metals on noble metal substrates. Characteristic for epitaxy in this system is that both substrate and adsorbate materials have their own surface states. This means that the adsorbate is not only influencing the potential step at the surface of the substrate, but developing its own surface state. Furthermore, the comparison of the development of the effective mass, spin-orbit splitting and binding energy with the coverage with the development of the work function reveals only qualitative similarity in the case of Ag/Au(111) [221]. The quantitative changes of the character of these parameters from gold to silver can be better described as related to the percentual contributions of Ag and Au to the amount of atoms which is investigated by photoemission. [237, 10]

## 7.6 Conclusion

High-resolution photoemission data of the *L*-gap Shockley states for 0-10 ML of silver on Au(111) are presented, corresponding to a layer-by-layer growth at room temperature. A disordered growth appears at low temperatures, resulting in considerably scattered surface state intensity. The Shockley state exhibits gradual changes with the layer thickness and the values of the relevant surface state parameters, describing the band dispersion, change from the ones of gold towards the ones of silver. Good agreement is achieved between *ab initio* band structure calculations embedded in the WIEN2k code and the photoemission data: the surface state band parameters are well reproduced by the theory, except for the value of the binding energy, which is usually too high in the calculations. The dependence of the binding energy on the thickness of the silver coverage is consistent with the localization of the surface state at

the surface, which is obvious from the comparison of the measurements with the calculated Shockley state electron density. Most importantly, for 10 ML Ag/Au(111) the $4d$ band of Ag(111) is observed, but the quantum-well states have not yet formed a closed continuum as for the Ag $sp$ bulk states. This demonstrates that the PES data is influenced by the substrate through some 30 Å of overlayer, which is more than inelastic mean free path for photoelectrons excited with He I radiation.

# Epilogue

The studies of various phenomena in this thesis have helped to make progress in experimental solid state physics research in two ways. The first one is directly related to the technical challenges, the development and perfection of the measurement methods, through their implementation in solving conceptually new problems. This has been illustrated here for the XPD, an 'old' technique, revived by the proofs of being a powerful tool for the identification of the substitution sites in complex materials or for the 'measurements' of the vdW gaps. Surface phenomena seem to gain more importance, which justifies the research which enables acquiring the information about the surface processes, properties and structure by using surface sensitive techniques, such as photoelectron spectroscopy. Investigation of surface states corresponds partially to this description, showing how interesting electronic states can be used as a tool for viewing the surface or interface structure. In a surprisingly fruitful combination, PES can be used as an electronical and geometrical characterization tool.

Secondly, there are achievements in the fields of band structure studies presented in this thesis. Band structure defines macroscopic properties of the system and its chemical behavior, and PES is the most direct method of investigating it. Layered systems are attracting considerable attention today, because of the convenient preparation techniques, straightforward interpretation of the PE results in terms of initial states and most of all because of the inspiring search for the mechanisms behind the high-temperature superconductivity, which is appearing mostly in the layered systems. The interest for the superconductivity at different $T_c$ values has persisted as one of the most interesting topics over several decades in the solid state physics and it is reasonable to think that it will define future trends as well. TMDs have attracted much interest for their similarities with the HT superconductors and they show interesting phenomena like CDW or pseudogaps. On the other hand, surface states exhibiting spatial localization at the surface are offering an interesting playground since their theoretical prediction in the early thirties until recent first measurements of their spin-orbit splitting and promise to remain a theme of research.

It was one of the goals of this work to show how various exotic phenomena can be addressed by the PES; how an appropriate treatment of the research themes always requires combination of experimental techniques, theory and band-structure calculations; how the relevant energy scale in both CDW-reconstructed band structure or surface state dispersions is today defined by meV; how research of complex systems can open the way for technological

progress and how, in turn, the need to see more in the data is driving technological development. And the motivation for accomplishing it is to learn more about the phenomena in the world around us and the physics we use to describe it.

# Bibliography

[1] A. Damascelli, Z. Hussain, Z. Shen, *Rev. Mod. Phys.* **75**, 473 (2003).

[2] E. Rotenberg, W. Theis, K. Horn, P. Gille, *Nature* **46**, 602 (2000).

[3] D. Naumović, P. Aebi, L. Schlapbach, C. Beeli, K. Kunze, T. A. Lograsso, D. W. Delaney, *Phys. Rev. Lett.* **87**, 195506 (2001).

[4] D. Naumović, P. Aebi, L. Schlapbach, C. Beeli, T. A. Lograsso, D. W. Delaney, *Phys. Rev. B* **60**, R16330 (1999).

[5] E. Umbach, M. Sokolowski, R. Fink, *Appl. Phys. A* **63**, 565 (1996).

[6] M. Corso, W. Auwärter, M. Muntiwiler, A. Tamai, T. Greber, J. Osterwalder, *Science* **303**, 217 (2004).

[7] S. Hüfner, *Photoelectron spectroscopy*, (Springer-Verlag, Germany, 2003).

[8] L. D. Landau, *Soviet Phys. JETP* **3**, 920 (1957).

[9] F. Reinert, G. Nicolay, S. Schmidt, D. Ehm, S. Hüfner, *Phys. Rev. B* **63**, 115415 (2001).

[10] H. Cercellier, Y. Fagot-Revurat, B. Kierren, F. Reinert, D. Popović, D. Malterre, *Phys. Rev. B*, accepted (2004).

[11] M. Bovet, D. Popović, F. Clerc, C. Koitzsch, U. Probst, E. Bucher, H. Berger, D. Naumović, P. Aebi, *Phys. Rev. B* **69**, 125117 (2004).

[12] D. Popović, M. Bovet, H. Berger, P. Aebi, *Eur. Phys. J. Appl. Phys.* (submitted 2004).

[13] H. Ehrenreich, D. Turnbull, Eds., *Superconductivity, quasicrystals and two dimensional physics*, vol. 42, *Solid state physics*, (Academic Press, Inc., San Diego, 1994).

[14] N. V. Smith, P. Thiery, Y. Petroff, *Phys. Rev. B* **47**, 15476 (1993).

[15] J. A. Wilson, A. D. Yoffe, *Adv. Phys.* **18**, 193 (1969).

[16] J. A. Wilson, F. J. D. Salvo, S. Mahajan, *Adv. Phys.* **24**, 117 (1975).

[17] R. L. Withers, J. A. Wilson, *J. Phys. C: Solid State Phys.* **19**, 4809 (1986).

[18] S. G. Davison, M. Stęślicka, *Basic Theory of Surface States*, (Oxford University Press, Oxford–New York, 1992).

[19] A. Einstein, *Ann. Physik* **17**, 132 (1905).

[20] J. B. Pendry, *Low Energy Electron Diffraction*, (Academic Press, London, 1974).

[21] D. Popović, D. Naumović, M. Bovet, C. Koitzsch, L. Schlapbach, P. Aebi, *Surf. Sci.* **492/3**, 294 (2001).

[22] P. Steiner, S. Hüfner, *Acta Metal.* **29**, 1885 (1981).

[23] P. Steiner, S. Hüfner, *Solid State Commun.* **37**, 79 (1981).

[24] P. Steiner, S. Hüfner, *Solid State Commun.* **37**, 279 (1981).

[25] P. Steiner, S. Hüfner, N. Mårtensson, B. Johansson, *Solid State Commun.* **37**, 73 (1981).

[26] M. P. Seah, W. A. Dench, *Surf. Interf. Anal.* **1**, 2 (1979).

[27] H. Lüth, *Surfaces and Interfaces of Solids*, (Springer-Verlag, Germany, 1993).

[28] R. E. Ballard, *J. Electron Spectrosc. Relat. Phenom.* **25**, 75 (1982).

[29] M. Desjonquères, D. Spanjaard, *Concepts in Surface Physics*, (Springer-Verlag, Germany, 1996).

[30] G. D. Mahan, *Phys. Rev. B* **2**, 4334 (1965).

[31] J. B. Pendry, *Surf. Sci.* **57**, 679 (1976).

[32] M. D. Pauli, D. K. Saldin, *Phys. Rev. B* **64**, 075411 (2001).

[33] S. Hüfner, R. Claessen, F. Reinert, T. Straub, V. N. Strocov, P. Steiner, *J. Electron Spectrosc. Relat. Phenom.* **100**, 191 (1999).

[34] J. K. Grepstad, B. J. Slagsvold, I. Bartoš, *J. Phys. F* **12**, 1679 (1982).

[35] T. J. Kreutz, thesis, Universität Zürich, (1981).

[36] E. D. Hansen, T. Miller, T.-C. Chiang, *Phys. Rev. Lett.* **80**, 1766 (1998).

[37] P. Thiery, thesis, Université de Paris-Sud, (1981).

[38] M. Springborg, *Methods of Electronic-Structure Calculations*, Wiley Series in Theoretical Chemistry, (John Wiley and Sons, Ltd, England, 2000).

[39] K. Schwarz, P. Blaha, G. K. H. Madsen, *Comp. Phys. Commun.* **147**, 71 (2002).

[40] D. Singh, *Phys. Rev. B* **43**, 6388 (1991).

[41] G. K. H. Madsen, P. Blaha, K. Schwarz, E. Sjöstedt, L. Nordström, *Phys. Rev. B* **64**, 195134 (2001).

[42] S. Cottenier, *Density Functional Theory and the family of (L)APW-methods: a step-by-step introduction (to be found at http://www.wien2k.at/reg user/textbooks) Instituut voor Kern- en Stralingsfysica, K.U.Leuven, Belgium, 2002.* ISBN 90-807215-1-4.

[43] H. G. Krimmel, J. Ehmann, C. Elsässer, M. Fähnle, J. M. Soler, *Phys. Rev. B* **50**, 8846 (1994).

[44] S. H. Wei, H. Krakauer, M. Weinert, *Phys. Rev. B* **32**, 7792 (1985).

[45] M. Weinert, E. Wimmer, A. J. Freeman, *Phys. Rev. B* **26**, 4571 (1982).

[46] E. Wimmer, H. Krakauer, M. Weinert, A. J. Freeman, *Phys. Rev. B* **24**, 864 (1981).

[47] R. Yu, D. Singh, H. Krakauer, *Phys. Rev. B* **43**, 6411 (1991).

[48] J. P. Perdew, Y. Wang, *Phys. Rev. B* **45**, 13244 (1992).

[49] P. Blaha, K. Schwarz, G. Madsen, D. Kvasnicka, J. Luitz, ***WIEN2k**, An Augmented Plane Wave Plus Local Orbitals Program for Calculating Crystal Properties, User's Guide*, (Karlheinz Schwarz, Techn. Universität Wien, Vienna University of Technology, Austria, November 2001).

[50] J. P. Perdew, K. Burke, M. Ernzerhof, *Phys. Rev. Lett.* **77**, 3865 (1996).

[51] E. Wimmer, M. Weinert, A. J. Freeman, H. Krakauer, *Phys. Rev. B* **24**, 2292 (1981).

[52] H. Krakauer, M. Posternak, A. J. Freean, D. D. Koelling, *Phys. Rev. B* **23**, 3859 (1981).

[53] T.-C. Chiang, D. E. Eastman, *Phys. Rev. B* **23**, 6836 (1981).

[54] T. Pillo, L. Patthey, E. Boschung, J. Hayoz, P. Aebi, L. Schlapbach, *J. Electron Spectrosc. Relat. Phenom.* **97**, 243 (1998).

[55] P. Aebi, J. Osterwalder, P. Schwaller, L. Schlapbach, M. Shimoda, T. Mochiku, K. Kadowaki, *Phys. Rev. Lett.* **72**, 2757 (1994).

[56] B. Dardel, M. Grioni, D. Malterre, P. Weibel, Y. Baer, F. Lévy, *Phys. Rev. B* **45**, 1462 (1992).

[57] B. Dardel, M. Grioni, D. Malterre, P. Weibel, Y. Baer, F. Lévy, *Phys. Rev. B* **46**, 7407 (1992).

[58] E. L. H. Berger. private communications, 2001.

[59] F. Lévy, Y. Froidevaux, *J. Phys.: Condens. Matter* **12**, 473 (1979).

[60] F. Lévy, *J. Phys.: Condens. Matter* **12**, 3725 (1979).

[61] S. Kono, S. M. Goldberg, N. F. T. Hall, C. S. Fadley, *Phys. Rev. B* **22**, 6085 (1980).

[62] D. Naumović, A. Stuck, T. Greber, J. Osterwalder, L. Schlapbach, *Phys. Rev. B* **47**, 7462 (1993).

[63] E. Clementi, C. Roetti, *At. Data Nuc. Data Tables* **14**, 177 (1974).

[64] S. M. Goldberg, C. S. Fadley, S. Kono, *J. Electron Spectrosc. Relat. Phenom.* **21**, 285 (1981).

[65] P. Blaha, K. Schwarz, J. Luitz, ***WIEN97****, A Full Potential Linearized Augmented Plane Wave Package for Calculating Crystal Properties*, (Karlheinz Schwarz, Techn. Universität Wien, Austria, 1999). ISBN 3-9501031-0-4.

[66] M. Bovet, S. van Smaalen, H. Berger, R. Gaal, L. Forró, L. Schlapbach, P. Aebi, *Phys. Rev. B* **67**, 125105 (2003).

[67] G. Nicolay, F. Reinert, S. Schmidt, D. Ehm, P. Steiner, S. Hüfner, *Phys. Rev. B* **62**, 1631 (2000).

[68] G. Nicolay, F. Reinert, F. Forster, D. Ehm, S. S. B. Eltner, S. Hüfner, *Surf. Sci.* **543**, 47 (2003).

[69] H. Cercellier, Y. Fagot-Revurat, B. Kierren, D. Malterre, F. Reinert, *Surf. Sci.* **566**, 520 (2004).

[70] P. Blaha, K. Schwarz, G. K. H. Madsen, D. Kvasnicka, J. Luitz, **WIEN2k**, *An Augmented Plane Wave+Local Orbitals Program for Calculating Crystal Properties*, (Karlheinz Schwarz, Techn. Universität Wien, Austria, 2001). ISBN 3-9501031-1-2.

[71] N. Takeuchi, C. T. Chan, K. M. Ho, *Phys. Rev. B* **43**, 13899 (1991).

[72] T. C. Hsieh, T. Chiang, *Surf. Sci.* **166**, 554 (1986).

[73] W. Harrison, M. Webb, Eds., *The Fermi Surface: Proceedings of an International Conference held at Cooperstown, New York, on August 22-24, 1960*, (John Wiley & Sons, Inc., 1960).

[74] P. Aebi, J. Osterwalder, R. Fasel, D. Naumović, L. Schlapbach, *Surf. Sci.* **307**, 917 (1994).

[75] E. O. Kane, *Phys. Rev. Lett.* **12**, 97 (1964).

[76] R. H. Gaylord, K. H. Jeong, S. D. Kevan, *Phys. Rev. Lett.* **62**, 2036 (1989).

[77] 3D Fermi Srface Site. http://www.phys.ufl.edu/~tschoy/r2d2/Fermi/Fermi.html.

[78] F. Reinert, *J. Phys.: Condens. Matter* **15**, S693 (2003).

[79] A. P. Mackenzie, S. R. Julian, A. J. Diver, G. J. McMullan, M. P. Ray, G. G. Lonzarich, Y. Maeno, S. Nishizaki, T. Fujita, *Phys. Rev. Lett.* **76**, 3786 (1996).

[80] C. Bergman, S. R. Julian, A. P. Mackenzie, S. NishiZaki, Y. Maeno, *Phys. Rev. Lett.* **84**, 2662 (2000).

[81] Y. Maeno, T. Rice, M. Sigrist, *Physics Today* **54**, 42 (2001).

[82] H. Choi, D. Roundy, H. Sun, M. Cohen, S. Louie, *Nature* **418**, 758 (2002).

[83] G. Nicolay, F. Reinert, S. Hüfner, P. Blaha, *Phys. Rev. B* **65**, 033407 (2001).

[84] F. Reinert, G. Nicolay, *Appl. Phys. A* **78**, 817 (2004).

[85] J. M. Luttinger, *Phys. Rev.* **119**, 1153 (1960).

[86] T. Pillo, thesis, Universität Freiburg, Switzerland, (1999).

[87] M. Randeria, H. Ding, J. C. Campuzano, A. Bellman, G. Jennings, T. Yokoya, T. Takahashi, H. Katayama-Yoshida, T. Mochiku, K. Kadowaki, *Phys. Rev. Lett.* **74**, 4951 (1995).

[88] J. C. Campuzano, H. Ding, M. R. Norman, M. Randeria, A. Bellman, T. Yokoya, T. Takahashi, H. Katayama-Yoshida, T. Mochiku, K. Kadowaki, *Phys. Rev. B* **53** (1996).

[89] Z. X. Shen, D. S. Dessau, *Phys. Rep.* **253**, 1 (1995).

[90] L. Kipp, K. Rossnagel, C. Solterbeck, T. Strasser, W. Schattke, M. Skibowski, *Phys. Rev. Lett.* **83**, 5551 (1999).

[91] C. Fadley (ed. R. T. Bachrach), *Synchrotron Radiation Research: Advances in Surface Science*, vol. 1, (Plenum, New York, 1990).

[92] K. Siegbahn, U. Gelius, H. Siegbahn, E. Olson, *Phys. Rev. Lett.* **32a**, 221 (1970).

[93] C. S. Fadley, S. Å. L. Bergström, *Phys. Rev. Lett.* **5**, 375 (1971).

[94] R. Fasel, P. Aebi, J. Osterwalder, L. Schlapbach, R. G. Agostino, G. Chiarello, *Phys. Rev. B* **50**, 14516 (1994).

[95] R. Fasel, P. Aebi, L. Schlapbach, J. Osterwalder, *Phys. Rev. B* **52**, R2313 (1995).

[96] T. Pillo, J. Hayoz, P. Schwaller, H. Berger, P. Aebi, L. Schlapbach, *Appl. Phys. Lett.* **75**, 1550 (1999).

[97] J. Hayoz, T. Pillo, R. Fasel, L. Schlapbach, P. Aebi, *Phys. Rev. B* **59**, 15975 (1999).

[98] T. Greber, J. Wider, J. Osterwalder, *Phys. Rev. Lett.* **81**, 1654 (1998).

[99] J. Hayoz, S. Sarbach, T. Pillo, E. Boschung, D. Naumović, P. Aebi, L. Schlapbach, *Phys. Rev. B* **58**, R4270 (1998).

[100] J. Osterwalder, T. Greber, A. Stuck, L. Schlapbach, *Phys. Rev. B* **44**, 13764 (1991).

[101] D. Naumović, A. Stuck, T. Greber, J. Osterwalder, L. Schlapbach, *Phys. Rev. B* **47**, 7462 (1991).

[102] H. Ding, T. Yokoya, J. C. Campuzano, T. Takahashi, M. Randeria, M. R. Norman, T. Mochiku, K. Kadowaki, J. Giapintzakis, *Nature* **382**, 51 (1996).

[103] Z.-X. Shen, D. S. Dessau, D. S. Marshall, C. H. Park, P. Fournier, A. Kapitulnik, *Science* **273**, 325 (1996).

[104] F. Ronning, C. Kim, D. L. Feng, D. S. Marshall, A. G. Loeser, L. L. Miller, J. N. Eckstein, I. Bozovic, Z.-X. Shen, *Science* **282**, 2067 (1998).

[105] M. R. Norman, H. Ding, M. Randeria, J. C. Campuzano, T. Yokoya, T. Takeuchi, T. Takahashi, T. Mochiku, K. Kadowaki, P. Guptasarma, D. G. Hinks, *Nature* **392**, 157 (1998).

[106] J. Mesot, M. Randeria, M. R. Norman, A. Kaminski, H. M. Fretwell, J. C. Campuzano, H. Ding, T. Takeuchi, T. Sato, T. Yokoya, T. Takahashi, I. Chong, T. Terashima, M. Takano, T. Mochiku, K. Kadowaki, *Phys. Rev. B* **63**, 224516 (2001).

[107] P. Schwaller, P. Aebi, H. Berger, C. Beeli, J. Osterwalder, L. Schlapbach, *J. Electron Spectrosc. Relat. Phenom.* **76**, 127 (1995).

[108] N. Fukushima, M. Yoshiki, *Phys. Rev. B* **50**, 2696 (1994).

[109] N. Fukushima, H. Niu, S. Nakamura, S. Takeno, M. Hayashi, K. Ando, *Physica C* **159**, 177 (1989).

[110] P. Schwaller, P. Aebi, J. Osterwalder, L. Schlapbach, M. Shimoda, T. Mochiku, K. Kadowaki, *Phys. Rev. B* **48**, 6732 (1993).

[111] J. Osterwalder, P. Aebi, P. Schwaller, L. Schlapbach, M. Shimoda, T. Mochiku, K. Kadowaki, *Appl. Phys. A* **60**, 247 (1995).

[112] P. A. Lee, *Phys. Rev. B* **13**, 5261 (1976).

[113] J. J. Barton, S. W. Robey, D. A. Shirley, *Phys. Rev. B* **34**, 778 (1986).

[114] J. M. de Leon, J. J. Rehr, C. R. Natoli, C. S. Fadley, J. Osterwalder, *Phys. Rev. B* **34**, 778 (1986).

[115] J.-C. Zheng, C. H. A. Huan, A. T. S. Wee, M. A. V. Hove, C. S. Fadley, F. J. Shi, E. Rotenberg, S. R. Barman, J. J. Paggel, K. Horn, P. Ebert, K. Urban, *Phys. Rev. B* **69**, 134107 (2004).

[116] B. R. Holstein, *Am. J. Phys.* **69**, 441 (2001).

[117] W. Göpel, C. Ziegler, *Struktur der Materie: Grundlagen, Mikroskopie und Spektroskopie*, (B. G. Teubner Verlagsgesellschaft, Leipzig, 1994).

[118] R. E. Peierls, *Quantum theory of solids*, (Oxford University Press, Oxford, 1955).

[119] W. A. Harrison, *Electronic structure and the properties of solids: The physics of the chemical bond*, (W. H. Freeman and Company, San Francisco, 1980).

[120] P. M. Chaikin, T. C. Lubensky, *Principles of condensed matter physics*, (Cambridge University Press, Cambridge, 2000).

[121] Y. Arnaud, M. Chevreton, *J. Solid State Chem.* **39**, 230 (1981).

[122] A. H. Reshak, S. Auluck, *Phys. Rev. B* **86**, 245113 (2003).

[123] P. Aebi, T. Pillo, H. Berger, F. Lévy, *J. Electron Spectrosc. Relat. Phenom.* **117-118**, 433 (2001).

[124] H. Rydberg, M. Dion, N. Jacobson, E. Schröder, P. Hyldgaard, S. I. Simak, D. C. Langreth, B. I. Lundqvist, *Phys. Rev. B* **91**, 126402 (2003).

[125] R. Claessen. Habilitation, Universität des Saarlandes, (1997).

[126] F. J. DiSalvo, *Solid State Commun.* **23**, 825 (1977).

[127] B. Eltner. Diplomarbeit, Universität des Saarlandes, (2001).

[128] A. Spijkerman, J. L. de Boer, A. Meetsma, G. A. Wiegers, S. van Smaalen, *Phys. Rev. B* **56**, 13757 (1997).

[129] X. M. Wu, C. M. Lieber, *Science* **243**, 1703 (1989).

[130] T. Matsushita, S. Imada, H. Daimon, T. Okuda, K. Yamaguchi, H. Miyagi, S. Suga, *Phys. Rev. B* **56**, 7687 (1997).

[131] K. Rossnagel, L. Kipp, M. Skibowski, C. Solterbeck, T. Strasser, W. Schattke, D. Voß, P. Krüger, A. Mazur, J. Pollmann, *Phys. Rev. B* **63**, 125104 (2001).

[132] D. Pines, P. Nozières, *The Theory of Quantum Liquids*, vol. I, (W. A. Benjamin, Inc., USA, 1966).

[133] L. Hedin, S. Lundqvist, *Solid State Physics*, vol. 23, (Academic Press, Inc., New York, 1969).

[134] M. Hengsberger, D. Purdie, P. Segovia, M. Garnier, Y. Baer, *Phys. Rev. Lett.* **83**, 592 (1999).

[135] M. Hengsberger, R. Fresard, D. Purdie, P. Segovia, Y. Baer, *Phys. Rev. B* **60**, 10796 (1999).

[136] T. Valla, A. V. Fedorov, P. D. Johnson, S. L. Hulbert, *Phys. Rev. Lett.* **83**, 2085 (1999).

[137] F. Reinert, B. Eltner, G. Nicolay, F. Forster, S. Schmidt, S. Hüfner, *Physica B* **351**, 229 (2004).

[138] R. Claessen, R. O. Anderson, J. W. Allen, C. G. Olson, C. Janowitz, W. P. Ellis, S. Harm, M. Kalning, R. Manzke, M. Skibowski, *Phys. Rev. Lett.* **69**, 808 (1992).

[139] L. Perfetti, C. Rojas, A. Reginelli, L. Gavioli, H. Berger, G. Margaritondo, M. Grioni, R. Gáal, L. Fórro, F. R. Albenque, *Phys. Rev. B* **64**, 115102 (2001).

[140] S. Hüfner, T. Finteis, S. Schmidt, G. Nicolay, F. Reinert, Z. Hussain, X. J. Zhou, S. A. Kellar, Z.-X. Shen, *Advanced Light Source Compendium of User Abstracts and Technical Reports* (1999).

[141] P. Nozières, *Theory of interacting Fermi systems*, (W. A. Benjamin, Inc., New York, 1964).

[142] E. N. Economou, *Green's functions in Quantum Physics*, (Springer-Verlag, Germany, 1990).

[143] N. Macris, *Introduction to the techniques for the N-body problem, lecture at the Troisieme Cycle de la Physique en Suisse Romande, EPFL Lausanne, Switzerland (19.-21. 09. 2001)*.

[144] G. Grimvall, *The electron-phonon interaction in metals*, (North-Holland Publishing Co., Cambridge, 1981).

[145] S. Engelsberg, J. R. Schrieffer, *Phys. Rev.* **131**, 993 (1963).

[146] S. LaShell, E. Jensen, *Phys. Rev. B* **61**, 2371 (2000).

[147] K. Matho, *Physica B* **199-200**, 382 (1994).

[148] P. B. Allen, N. Chetty, *Phys. Rev. B* **50**, 14855 (1994).

[149] M. Hangyo, S.-I. Nakashima, A. Misuishi, *Ferroelectrics* **52**, 151 (1983).

[150] C. Riekel, M. Thomas, R. Schöllhorn, *Phys. Stat. Sol. (a)* **50**, K231 (1978).

[151] L. Capogna, A. P. Mackenzie, R. S. Perry, S. A. Grigera, L. M. Galvin, P. Raychaudhuri, A. J. Schofield, *Phys. Rev. Lett.* **88**, 076602 (2002).

[152] S.-I. Ikeda, Y. Maeno, S. Nakatsuji, M. Kosaka, Y. Uwatoko, *Phys. Rev. B* **62**, R6089 (2000).

[153] H. Shaked, J. D. Jorgensen, S. Short, *Phys. Rev. B* **62**, 8725 (2000).

[154] D. Popović, F. Reinert, B. Eltner, G. Nicolay, U. Probst, E. Bucher, S. Hüfner, *Phys. Rev. Lett.* (to be submitted 2004).

[155] P. E. Prange, A. Sachs, *Phys. Rev.* **158**, 672 (1967).

[156] T. Pillo, J. Hayoz, H. Berger, M. Grioni, L. Schlapbach, P. Aebi, *Phys. Rev. Lett.* **83**, 3494 (1999).

[157] P. Fazekas, E. Tosatti, *Phil. Mag. B* **39**, 229 (1979).

[158] P. Fazekas, E. Tosatti, *Physica B* **99**, 183 (1980).

[159] L. Perfetti, A. Georges, S. Florens, S. Biermann, S. Mitrović, H. Berger, Y. Tomm, H. Höchst, M. Grioni, *Phys. Rev. Lett.* **90**, 166401 (2003).

[160] R. A. Klemm, *Physica C* **341** (2000).

[161] G. A. Wiegers, J. L. de Boer, A. Meetsma, S. van Smaalen, *Z. Kristallogr.* **216**, 45 (2001).

[162] K. Horiba, K. Ono, J. H. Oh, T. Kihara, S. Nakazono, M. Oshima, O. Shiino, H. W. Yeom, A. Kakizaki, Y. Aiura, *Phys. Rev. B* **66**, 073106 (2002).

[163] G. Grüner, *Density waves in solids*, (Perseus Publishing, Cambridge, 1994).

[164] J. Bardeen, L. Cooper, J. Schrieffer, *Phys. Rev.* **108**, 1175 (1957).

[165] E. J. Woll, W. Kohn, *Phys. Rev.* **126**, 1693 (1962).

[166] O. Shiino, T. Endo, W. Yamaguchi, H. Sugawara, K. Kitazawa, T. Hasegawa, *Appl. Phys. A* **66**, S175 (1998).

[167] N. V. Smith, M. M. Traum, *Phys. Rev. B* **11**, 2087 (1975).

[168] K. Horiba, K. Ono, H. W. Yeom, Y. Aiura, O. Shiino, J. H. Oh, T. Kihara, S. Nakazono, M. Oshima, A. Kakizaki, *Physica B* **284-288**, 1665 (2000).

[169] N. V. Smith, S. D. Kevan, F. J. D. Salvo, *J. Phys. C: Solid State Phys.* **18**, 3175 (1985).

[170] R. Claessen, B. Burandt, H. Carstensen, M. Skibowski, *Phys. Rev. B* **41**, 8270 (1990).

[171] T. Pillo, J. Hayoz, H. Berger, F. Levý, P. Aebi, L. Schlapbach, *J. Electron Spectrosc. Relat. Phenom.* **101-103**, 811 (1999).

[172] T. Pillo, J. Hayoz, H. Berger, R. Fasel, L. Schlapbach, P. Aebi, *Phys. Rev. B* **62**, 4277 (2000).

[173] J. Voit, L. Perfetti, F. Zwick, H. Berger, G. Margaritondo, G. Grüner, H. Höchst, M. Grioni, *Science* **290**, 501 (2000).

[174] J. Osterwalder, T. Greber, S. Hüfner, L. Schlapbach, *Phys. Rev. B* **41**, 12495 (1990).

[175] J. Osterwalder, E. A. Stewart, D. Cyr, C. S. Fadley, J. M. de Leon, J. J. Rehr, *Phys. Rev. B* **35**, 9859 (1987).

[176] H. Cronacher, *Surf. Sci.* **209**, 387 (1989).

[177] S. Hüfner, J. Osterwalder, T. Greber, L. Schlapbach, *Phys. Rev. B* **42**, 7350 (1990).

[178] T. Straub, thesis, Universität des Saarlandes, Saarbrücken, Germany, (1998).

[179] N. Memmel, *Surf. Sci. Rep.* **32**, 19 (1998).

[180] F. Forster, G. Nicolay, F. Reinert, D. Ehm, S. Schmidt, S. Hüfner, *Surf. Sci.* **532-535**, 160 (2003).

[181] A. Bendounan, Y. Fagot-Revurat, B. Kierren, F. Bertran, V. Yu. Yurov, D. Malterre, *Surf. Sci.* **496**, L43 (2002).

[182] A. Bendounan, H. Cercellier, Y. Fagot-Revurat, B. Kierren, V. Yu. Yurov, D. Malterre, *Phys. Rev. B* **67**, 165412 (2003).

[183] W. Shockley, *Phys. Rev.* **56**, 317 (1939).

[184] T. Miller, A. Samsavar, G. E. Franklin, T.-C. Chiang, *Phys. Rev. Lett.* **61**, 1404 (1988).

[185] T. C. Hsieh, T. Miller, T.-C. Chiang, *Phys. Rev. B* **33**, 2865 (1986).

[186] I. Tamm, *Phys. Z. Sowjet.* **1**, 733 (1932).

[187] I. Tamm, *Z. Phys.* **76**, 849 (1932).

[188] A. W. Maue, *Zeit. f. Physik* **94**, 717 (1935).

[189] E. T. Goodwin, *Proc. Camb. Phil. Soc.* **35**, 205 (1939).

[190] E. T. Goodwin, *Proc. Camb. Phil. Soc.* **35**, 221 (1939).

[191] E. T. Goodwin, *Proc. Camb. Phil. Soc.* **35**, 232 (1939).

[192] R. H. Fowler, *Proc. Roy. Soc.* **A141**, 56 (1933).

[193] S. Rijanow, *Zeit. f. Physik* **89**, 806 (1934).

[194] R. de L. Kronig, W.-G. Penney, *Proc. Roy. Soc.* **A130**, 499 (1931).

[195] N. Takeuchi, C. T. Chan, K. M. Ho, *Phys. Rev. B* **43**, 13899 (1991).

[196] N. W. Ashcroft, N. D. Mermin, *Solid State Physics*, (Saunders College Publishing, USA, 1976).

[197] W. Chen, V. Madhavan, T. Jamneala, M. F. Crommie, *Phys. Rev. Lett.* **80**, 1469 (1998).

[198] A. Mugarza, J. E. Ortega, F. J. Himpsel, F. J. G. de Abajo, *Phys. Rev. B* **67**, 081404 (2001).

[199] R. Fisher, S. Schuppler, N. Fisher, T. Fauster, W. Steinmann, *Phys. Rev. Lett.* **70**, 654 (1993).

[200] R. Fisher, T. Fauster, W. Steinmann, *Phys. Rev. B* **48**, 15496 (1993).

[201] M. M. Dovek, C. A. Lang, J. Nogami, C. F. Quate, *Phys. Rev. B* **40**, 11973 (1989).

[202] Y. Tanisharo, *Surf. Sci.* **111**, 395 (1981).

[203] B. Eisenhut, J. Stober, G. Rangelov, T. Fauster, *Phys. Rev. B* **49**, 14676 (1994).

[204] J. Perdereau, *J. Phys. F* **3**, 798 (1974).

[205] M. A. Hove, *Surf. Sci.* **103**, 189 (1981).

[206] K. G. Huang, D. Gibbs, D. M. Zehner, *Phys. Rev. Lett.* **65**, 3313 (1990).

[207] N. Takeuchi, C. T. Chan, K. M. Ho, *Phys. Rev. B* **43**, 13899 (1991).

[208] A. Schneider, Stuttgart. private communications, 2004.

[209] N. Smith, *Phys. Rev. B* **9**, 1365 (1974).

[210] J. G. Nelson, S. Kim, W. J. Gignac, R. S. Williams, J. Tobin, S. W. Robey, D. A. Shirley, *Phys. Rev. B* **32**, 3465 (1985).

[211] R. Paniago, R. Matzdorf, A. Goldmann, *Europhys. Lett.* **26**, 63 (1994).

[212] P. Wehner, R. Williams, S. Kevan, D. Denley, D. Shirley, *Phys. Rev. B* **19**, 6164 (1979).

[213] K. Mills, R. Davis, S. Kevan, G. Thornton, D. Shirley, *Phys. Rev. B* **22**, 581 (1980).

[214] D. Popović, F. Reinert, S. Hüfner, V. G. Grigoryan, M. Springborg, H. Cercellier, Y. Fagot-Revurat, B. Kierren, D. Malterre, *Phys. Rev. B* (to be submitted 2004).

[215] J. G. Tobin, S. W. Robey, L. E. Klebanoff, D. A. Shirley, *Phys. Rev. B* **35**, 9056 (1987).

[216] F. J. Palomares, M. Serrano, A. Ruiz, F. Soria, K. Horn, M. Alonso, *Surf. Sci.* **513**, 283 (2002).

[217] A. M. Shikin, D. V. Vyalikh, Y. S. Dedkov, G. V. Prudnikova, V. K. Adamchuk, E. Weschke, G. Kaindl, *Phys. Rev. B* **62**, R2303 (2000).

[218] H. Cercellier, Nancy. private communications, 2004.

[219] G. Nicolay, thesis, Universität des Saarlandes, (2002).

[220] V. G. Grigoryan, Saarbrücken. private communications, 2004.

[221] H. Cercellier, thesis, Université Henri Poincaré, Nancy, (2004).

[222] A. Beckmann, M. Klaua, K. Meinel, *Phys. Rev. B* **48**, 1844 (1993).

[223] M. A. Mueller, A. Samsavar, T. Miller, T.-C. Chiang, *Phys. Rev. B* **40**, 5845 (1989).

[224] H. Asonen, M. Pessa, *Phys. Rev. Lett.* **46**, 1696 (1981).

[225] R. Courths, M. Lau, T. Scheunemann, H. Gollisch, R. Feder, *Phys. Rev. B* **63**, 195110 (2001).

[226] C. Jang, H. Yu, X. Wang, C. Shih, P. Ebert, *Phys. Rev. B* **64**, 235410 (2001).

[227] S. Å. Lindgren, L. Walldén, *Solid State Commun.* **28**, 283 (1978).

[228] J. Kliewer, R. Berndt, *Phys. Rev. B* **65**, 035412 (2001).

[229] S. Å. Lindgren, L. Walldén, *Phys. Rev. Lett.* **61**, 2894 (1988).

[230] S. Å. Lindgren, L. Walldén, *Solid State Commun.* **34**, 671 (1980).

[231] S. Å. Lindgren, L. Walldén, *Phys. Rev. Lett.* **59**, 3003 (1987).

[232] J. U. Kliewer, thesis, Technische Hochschule Aachen, (2000).

[233] G. Neuhold, K. Horn, *Phys. Rev. Lett.* **78**, 1327 (1997).

[234] C. Hückstädt. Diplomarbeit, Universität des Saarlandes, (2005).

[235] F. Forster. Diplomarbeit, Universität des Saarlandes, (2002).

[236] E. Bertel, N. Memmel, *Appl. Phys. A* **63**, 523 (1996).

[237] L. Petersen, P. Hedegård, *Surf. Sci.* **459**, 49 (2000).

# Acknowledgments

My greatest thank belongs to my best friend Olivera with her daughter Tina and her mother Trale, Lesnovo, Andon, my little sister Belka, my parents majka Rajka and Gagi, my grandparents Mika, Ljubica and Milan and the rest of our family, because they encouraged me to do my thesis.

I would like to thank Prof. Dr. Dr. h.c. mult. Stefan Hüfner, who gave me the opportunity to continue my PhD in his group at Uni Saarland (Germany) and worked devotedly on two very different research topics with me. In these two years I've enjoyed perfectioning in high resolution photoemission and high level scientific discussion. I am grateful to him for pushing me forward till the end of my thesis. Many thanks also to his wife, Christiane Hüfner.

It was my great pleasure to work under the supervision of Prof. Dr. Friedel Reinert (now Uni Würzburg). I've learned from his practical approaches to solving problems, great experimental, programming and LaTeX skills and very dynamical way of thinking. His creative ideas have contributed significantly to this thesis. I would like to thank him for reading and correcting this work. Many thanks also to his family: his wife Eva and children Mia and Emil.

I am indebted to the people who shared the same machine with me. Brigitte Eltner helped me with coming here, administration, apartment and my first topic - TiTe$_2$. Stefan Schmidt shared his office with me one year long, I have profitted from his broad physics and Linux knowledge and his great experimental know-how. Dr. Dirk Ehm gave me an introduction into Laue technique. Dr. Georg Nicolay helped me with the instrumental calibrations and TiTe$_2$. Frank Forster helped me move in, gave me an introduction to Scienta and DX, as well as valuable tips during my measurements of Ag/Au(111). Conrad Hückstädt was sharing my new offices with me. His enthusiasm has been refreshing for me and his tips in the days of writing the thesis were simply great. I would also like to thank Brigitte's mother and brother, Conrad's sisters, Sigrid, Simone, Silke, Emilie and especially Dr. Angela Munnia. Last, but not least, thanks to Luc Piot, for many times we were on the machine together and for the work we did together for the GRK.

Within the large group of Prof. Hüfner, I could also profit from the contacts with Dr. Paul Steiner, Dr. Remo de Masi, Dirk Reinicke and Dr. Frank Müller. My thanks also to H.-J. Armand, J. Pohla, E. Dobratz, S. Löw, A. Groß, B. Dieter and H. Waack. I appreciate the support of my AP supervisors Dr. A. Klöpperpieper and Dr. H. Schmitt and the support of the groups of Prof. Dr. U. Hartmann and Prof. Dr. K. Jacobs: G. Radu, I. Knittel, A. Englisch, S.

115

HTSC, XPD, SSC. I am also grateful for the very pleasant and fruitful contacts during my last year of thesis in Germany, which includes discussions of the Fribourg data and corrections of some parts of this thesis.

Dr. Marc Bovet and Dr. Christian Koitzsch I thank for working together on one machine and discussing together most of our experimental work. I am indebted to M. Bovet for measuring and analyzing the TMDs and doped Bi2212 samples together. He also gave me an introduction into the WIEN calculations. C. Koitzsch helped me with my SSC calculations and I tried to grow $MgB_2$ films with him. Michael Bielmann performed STM measurements on the $TaSe_2$ and gave me an introduction in this technique. I am also grateful to the other members of the XPD group for many fruitful discussions and tips: Dr. D. Naumović, Dr. O. (especially for the explanations of de Haas-Van Alphen) and P. Groening (especially for the introduction to QUASES), Dr. C. Galli, Dr. P. Ruffieux, Dr. L.-O. Nilsson. Thanks also to: F. Bourqui, Ch. Neururer, O. Raetzo, E. Mooser, M. Zbinden and especially Elisabeth François.

Extremely intensive collaboration with the theoretical groups of Prof. Dr. Dionys Baeriswyl and Prof. Dr. Christiane De Morais Smith, deserves special acknowledgments. Particular thanks to Dr. Lara Benfatto, Mark O. Goerbig and Vladimir Gritsev for many good lessons on strongly correlated systems. I am very grateful to L. Benfatto for the collaboration on the TMDs and the lessons on electron-electron and electron-phonon interactions. Also thanks to A. Capocci, P. Lauretti and J. Wakeling.

I am grateful for the support of Dr. Veronique Trappe, my AP supervisor. My gratitude belongs to Prof. Dr. Peter Schurtemberger, Helene Fueger and Jean Ducotterd for help regarding my transit to Germany. L. Mollet, S. Lenherr and V. Juričić, I. Zečević, I. Borjanović, M. Sremčević, S. and P. Drljača, A. and M. Marinković, M. and Olivier Zappelli have been most kind and most helpful, and I would like to thank them deeply.

The TMD samples have been obtained from H. Berger (EPF Lausanne) and Prof. Dr. E. Bucher (Uni Konstanz). The band structure calculations have been performed by Dr. M. Bovet and Prof. Dr. P. Aebi. Many thanks to Dr. M. Grioni, Dr. L. Perfetti and Dr. Th. Pillo for fruitful discussions on this topic.

For many inspiring discussions, I would like to express my appreciation to Prof. Dr. Thomas Greber and Prof. Dr. Jürg Osterwalder. Many thanks to Prof. Dr. M. Erbudak for inviting me to ETH Zürich. Thanks also to J.-M. Dubois and M.-C. Moissenet.

Finally, I am grateful to Prof. Dr. D. Belić, Dr. M. Popović-Božić and Dr. D. Naumović, for coming to Switzerland.

116

Hiermit erkläre ich an Eides Statt, dass ich die vorliegende Arbeit selbst angefertigt und nur die im Literaturverzeichnis angegebenen Hilfsmittel verwendet habe.

Saarbrücken, den 02. 12. 2004.

Dunja Popović